Roman Teisseyre
Minoru Takeo
Eugeniusz Majewski
Editors

Earthquake Source Asymmetry, Structural Media and Rotation Effects

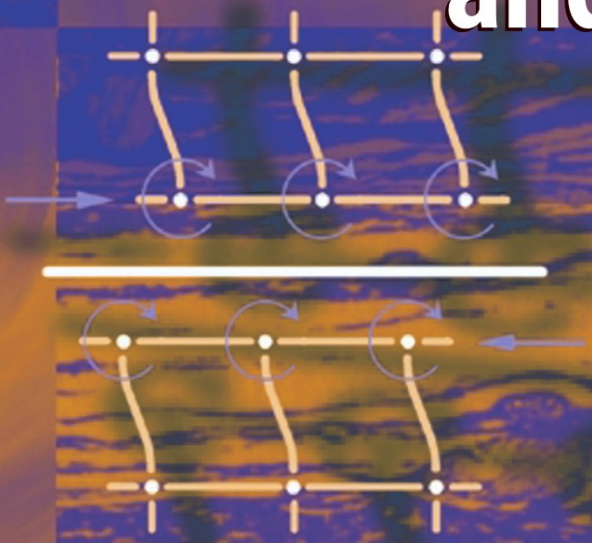

Springer

Roman Teisseyre • Minoru Takeo • Eugeniusz Majewski

Earthquake Source Asymmetry, Structural Media and Rotation Effects

Roman Teisseyre
Minoru Takeo
Eugeniusz Majewski
(Eds.)

Earthquake Source Asymmetry, Structural Media and Rotation Effects

With 223 Figures

Springer

EDITORS:

PROFESSOR ROMAN TEISSEYRE
ASSOCIATE PROFESSOR EUGENIUSZ MAJEWSKI
INSTITUTE OF GEOPHYSICS,
POLISH ACADEMY OF SCIENCES
UL. KS. JANUSZA 64
01-452 WARSAW
POLAND

PROFESSOR MINORU TAKEO
EARTHQUAKE RESEARCH INSTITUTE
UNIVERSITY OF TOKYO
1-1 YAYOI 1-CHOME, BUNKYO-KU
TOKYO 113 0032
JAPAN

E-mail: rt@igf.edu.pl
emaj@igf.edu.pl
takeo@eri.u-tokyo.ac.jp

ISBN 10 3-540-31336-2 **Springer Berlin Heidelberg New York**
ISBN 13 978-3-540-31336-6 **Springer Berlin Heidelberg New York**

Library of Congress Control Number: 2006922187

Springer is a part of Springer Science+Business Media
springeronline.com

Printed in The Netherlands

Cover design: E. Kirchner, Heidelberg
Production: A. Oelschläger
Typesetting: Camera-ready by the Editors

Printed on acid-free paper 30/2132/AO 543210

Preface

When thinking, at the beginning of the new century, on our horizons in seismology, we might return to the old question related to the seismic rotation effects and waves. Seismology, with its spectacular achievements – instrumentation, data processing, seismic tomography and source process theories – remains practically confined to linear ideal elasticity (isotropic or anisotropic). Numerous renown seismologists have tried to go beyond this horizon. As concerns rotation waves, such attempts were inspired by numerous macroscopic observations pointing out the rotation effects, often observed on the ground surface. However, this problem has been apparently closed by Mallet in 1862, who gave the following explanation: rotations of a body on the surface are due to a sequence of impacts of different seismic phases emerging under different angles. Later on, in 1937, Imamura underlined an influence of different inertia moments of an inflicted body. Thus, the surface rotation effects – rotation of some objects on the ground surface – were explained as being caused by the consecutive inclinations and recovery of these objects to the vertical, when hit by the incident seismic body or surface waves. The final position of the object could become slightly twisted in comparison to its former place; the differences between the inertia tensor moments of the object and/or its attachment (as related to friction resistance of binding) to the ground surface play an important role.

At that time, seismic observations were not accurate enough to detect any rotation waves; moreover, from the point of view of ideal elasticity – such waves shall not be observed at all, because rotation motion, even if generated in a seismic source, shall be immediately attenuated. Of course, there remains the displacement rotation component, which differs from zero for shear motion, but in an ideal isotropic elastic body this component attains very small values.

Perhaps some new, but rather isolated, attempts to record the rotation waves were undertaken again in relation to these theoretical predictions. However, most of them failed again because the instrumental tools were not powerful enough.

In the second half of last century, we have observed a spectacular development of mechanics of continua including defects, granular structure and other deviations from the ideal linear elasticity. Special interests were

concentrated on the micropolar and micromorphic continua. In such elastic continua, the real rotations can be accompanied by another kind of axial motion – the twist-bend motion.

We must stress that seismologists share different opinions on the nature of rotation waves. Perhaps, still the majority believes that such rotation motions are not related to inner rotations but are directly related to rotation of displacement field which may reach much higher magnitudes in materials with an internal structure than in homogeneous layers; considering damages in the high buildings, there are many examples indicating enormous increase of rotation effects caused by consecutive impacts of seismic body and surface waves.

The rotation and twist motions are parts of the microdisplacement motion as related to the tensor of microstrain which appears in the generalized continua. In ideal elasticity, any rotation motion is reduced to the displacement vector rotation components, while the twist motion is related to the non-diagonal strain components. In our Monograph, both approaches are discussed.

In the last years, new types of the very sensitive rotation seismographs and the laser/fiber ring interferometers (ring laser gyroscopes and fiber optic gyros), based on the Sagnac principle, opened new abilities of recording techniques.

Real media deviate from the ideal elasticity mainly due to defect content and granular structure; such media will be further called the structured continua. At the same time, some theoretical papers have recently appeared pointing out that the values of the displacement rotation components may be much higher than those predicted by the ideal elastic theory. In both cases, anisotropy shall be also included.

However, apart of the rotation of displacements, in the structured media there may also appear true rotation motions, as independent deformation features. These rotation motions are part of the deformation and rotation tensors, which includes rotation, twist and compression/dilatation motions; together with the displacement vector, these motions form a complete deformation pattern.

The theory of structured continua enhanced our interest in the microdisplacement motions. The microdisplacement fields are produced by the asymmetric pattern of the faulting and friction motions. The slip friction process causes rotation of adjacent grains and any deviations from symmetry lead to a non-zero net rotation motion. Here, we point out the major feature of earthquakes revealed in faulting along the main fault plane. This is the main asymmetry feature of earthquake processes. We may admit that generation of real rotation and twist motions in a source zone is a real fact. However, there remains an open question whether such fields can propa-

gate far from a source or are quickly attenuated when reaching a more consolidated elastic zone. Probably we should confine our considerations to the near-field effects only.

However, we shall again take into account the fact that body and surface seismic waves, when entering a near-surface region, which is characterized by the more complex structure features, may give rise to conjugated microdisplacement motions; hence, rotation and twist waves may again appear due to interaction of the incident seismic waves with the complex features of a near-surface zone. The theories of micropolar and micromorphic media predict some relation between the displacement derivatives and the microdisplacements.

Such considerations inspired us to write a comprehension monograph which may open a new insight into seismological observations and studies. We decided that a subject of such a monograph shall be broad, covering many aspects, beginning from the historical observations, through modern sensors detecting different types of seismic motions, to the advanced theories and models giving us a better insight into the complexity pattern of earthquake source processes. Among other things, further studies on soliton solutions for the events generated in a confined source zone may improve the fracture band models, as introduced by some authors participating in the present task. Also, more attention shall be paid to the anisotropy pattern related to the earthquake source zone.

At last, we shall turn to questions related to the earthquake engineering problems which may arise even due to small rotation motions; the whole problem started because in many cases some twist deformations have been observed on ground surface. And now we shall also examine whether the true rotation or twist motions, however small, can influence some structures senstive to moment of momentum impact.

The book covers, thus, many subjects, enlightened from different points of view, as presented by the individual authors; we tried to collect the individual contributions in such a way as to create a possibly complete coverage of the discussed subjects.

At the end of these considerations, it seems suitable to give a very brief outline of the content of the present Monograph. It is divided into the following six parts:

Part I. MACROSEISMIC ROTATION EFFECTS AND MICROMOTIONS. We discuss the possible causes of the rotation motions and effects in the Earth's interior and on its surface; also we recall some descriptions of the rotation-like damages caused by the historical earthquakes.

Part II. THEORY OF CONTINUA AND FIELDS OF DEFECTS. We present the asymmetric theory of continuous media with defects and anti-

symmetric strains and stresses (as equivalent to the stress moments and related conservation law for moment of momentum); the included introduction to the soliton physics has a particular meaning for the fracturing processes.

Part III. ROTATION MOTIONS, SEISMIC SOURCE MODELS, AND ASYMMETRY OF FRACTURE. We discuss a rotation counterpart in the fracturing process and the related energy release, we approach the problems of complex fracturing and flow phenomena and we face the problems of analysis of the complex seismic motions; further, we present different approaches to fracturing processes and the associated rotation motions in the seismic active regions.

Part IV. EFFECTS RELATED TO MEDIUM STRUCTURES AND COMPLEXITY OF WAVE PROPAGATION. We present some new approaches to the complexity of deformations in the structured and micromorphic media; the non-Riemannian description of deformations is included.

Part V. SEISMIC ROTATIONAL MOTIONS: RECORDING TECHNIQUES AND DATA ANALYSIS. Starting with a historical note, we include the descriptions of some modern measuring systems for rotation, twist and tilt motions, we discuss the gained observations and recordings and we give their tentative analysis.

Part VI. ROTATIONS AND ENGINEERING SEISMOLOGY. We end our Monograph with the problems of the earthquake engineering and strong motions which include the rotation and tilt impacts on high buildings.

Acknowledgement. I would like to express my great thankfulness to the editors of the camera-ready PDF form of manuscripts, Mrs Anna Dziembowska, Mrs Maria Wernik and their staff, for their devoted and laborious work.

Roman Teisseyre

Contents

Contributors

Vladimir AKSENOV
Institute of Physics of the Earth, Russian Academy of Sciences
Bolshaya Gruzinskaya str., 10, Moscow, Russia.

Mariusz BIAŁECKI
Institute of Geophysics, Polish Academy of Sciences
ul. Księcia Janusza 64, 01-452 Warszawa, Poland.

Wojciech BORATYŃSKI
Institute of Geophysics, Polish Academy of Sciences
ul. Księcia Janusza 64, 01-452 Warszawa, Poland
and
Faculty of Mathematics and Information Science,
Warsaw University of Technology
Plac Politechniki 1, 00-661 Warszawa, Poland.

Jiři BUBEN
Institute of Rock Structure and Mechanics
Academy of Sciences of the Czech Republic
V Holešovičkách 41, 182 09 Praha 8, Czech Republic.

Victor G. BYKOV
Institute of Tectonics and Geophysics
Far East Branch of the Russian Academy of Sciences
65 Kim-Yu-Chen St., 680 000 Khabarovsk, Russia.

Heriberta CASTAÑOS
National University of Mexico
UNAM, 04510 Mexico, DF, Mexico.

Alain COCHARD
Department of Earth and Environmental Sciences
Ludwig-Maximilians-Universität
Theresienstr. 41, 80333 München, Germany.

Asher FLAWS
Department für Geo- und Umweltwissenschaften, Sektion Geophysik

Ludwig-Maximilians-Universität München
Theresienstr. 41, 80333 München, Germany.

Graziano FERRARI
SGA Storia Geofisica Ambiente
Via del Battiferro 10b 40129 Bologna, Italy.

Marek GÓRSKI
Institute of Geophysics, Polish Academy of Sciences
ul. Księcia Janusza 64, 01-452 Warszawa, Poland.

Gerhard GRAHAM
Council for Geoscience
Pretoria 0001, South Africa.

Vladimir M. GRAIZER
California Geological Survey
801 K Street, MS 12-32, Sacramento, CA, USA.

Dryver R. HUSTON
Mechanical Engineering, University of Vermont
Burlington, VT, USA.

Heiner IGEL
Department für Geo- und Umweltwissenschaften, Sektion Geophysik
Ludwig-Maximilians-Universität München
Theresienstr. 41, 80333 München, Germany.

Leszek R. JAROSZEWICZ
Institute of Applied Physics, Military University of Technology
ul. Kaliskiego 2, 00-908 Warszawa, Poland.

Marek KACZOROWSKI
Space Research Centre, Polish Academy of Sciences
ul. Bartycka 18A, 00-716 Warszawa, Poland.

Yusuke KAWADA
Department of Geoenvironmental Sciences
Graduate School of Sciences, Tohoku University
Aoba-ku, Sendai 980-8578, Japan.

Andrzej KIJKO
Council for Geoscience
Pretoria 0001, South Africa.

Jan T. KOZÁK
Geophysical Institute, Academy of Sciences of the Czech Republic
14131 Prague 4 – Sporilov, Bočni, Czech Republic.

Zbigniew KRAJEWSKI
Institute of Applied Physics, Military University of Technology
ul. Kaliskiego 2, 00-908 Warszawa, Poland.

Mary LAZARIDOU
Solid Earth Physics Institute, Department of Physics, University of Athens
Panepistimiopolis, Zografos 157 84, Athens, Greece.

Cinna LOMNITZ
National University of Mexico, UNAM
04510 Mexico, DF, Mexico.

Eugeniusz MAJEWSKI
Institute of Geophysics, Polish Academy of Sciences
ul. Księcia Janusza 64, 01-452 Warszawa, Poland.

Takeo MORIYA
Graduates School of Science, Hokkaido University.

Jun MUTO
Department of Geoenvironmental Sciences
Graduate School of Sciences, Tohoku University
Aoba-ku, Sendai 980-8578, Japan.

Hiroyuki NAGAHAMA
Department of Geoenvironmental Sciences
Graduate School of Sciences, Tohoku University
Aoba-ku, Sendai 980-8578, Japan.

Vladimir RUDAJEV
Institute of Rock Structure and Mechanics
Academy of Sciences of the Czech Republic
V Holešovičkách 41, 182 09 Praha 8, Czech Republic.

F. SCHERBAUM
Institut für Geowissenschaften, Universität Potsdam
Karl-Liebknecht-Str. 24/25, 14476 Golm, Germany.

K. Ulrich SCHREIBER
Forschungseinrichtung Satellitengeodäsie der TU- München
Arcisstr. 21, 80333 München, Germany.

B. SCHUBERTH
Department of Earth and Environmental Sciences
Ludwig-Maximilians-Universität
Theresienstr. 41, 80333 München, Germany.

Lech SOLARZ
Institute of Applied Physics, Military University of Technology
ul. Kaliskiego 2, 00-908 Warszawa, Poland.

William B. SPILLMAN Jr.
Physics Department, University of Vermont
Burlington, VT, USA.

Geoffrey E. STEDMAN
Department of Physics and Astronomy, University of Canterbury
Private Bag 4800, New Zealand.

Jerzy SUCHCICKI
Institute of Geophysics, Polish Academy of Sciences
ul. Księcia Janusza 64, 01-452 Warszawa, Poland.

W. SURYANTO
Department of Earth and Environmental Sciences
Ludwig-Maximilians-Universität
Theresienstr. 41, 80333 München, Germany.

Minoru TAKEO
Earthquake Research Institute, University of Tokyo
Zip. 113-0032 1-1-1, Yayoi, Bunkyo-ku, Tokyo, Japan.

Krzysztof P. TEISSEYRE
Institute of Geophysics, Polish Academy of Sciences
ul. Księcia Janusza 64, 01-452 Warszawa, Poland.

Roman TEISSEYRE
Institute of Geophysics, Polish Academy of Sciences
ul. Księcia Janusza 64, 01-452 Warszawa, Poland.

Mihailo D. TRIFUNAC
Department of Civil Engineering, University of Southern California
Los Angeles, CA 90089-2531, USA.

Panayiotis VAROTSOS
Solid Earth Physics Institute, Department of Physics, University of Athens
Panepistimiopolis, Zografos 157 84, Athens, Greece.

A. VELIKOSELTSEV
Forschungseinrichtung Satellitengeodäsie
Technical University of Munich, Fundamentalstation Wettzell
Sackenriederstr. 25, D-93444 Kötzting, Germany.

Alexander V. VIKULIN
Institute of Volcanology and Seismology
Far East Department of Russian Academy of Sciences
Piip Ave. 9, Petropavlovsk-Kamchatsky, 683006, Russia.

D. VOLLMER
Institut für Geowissenschaften, Universität Potsdam
Karl-Liebknecht-Str. 24/25, 14476 Golm, Germany.

J. WASSERMANN
Department of Earth and Environmental Sciences
Ludwig-Maximilians-Universität
Theresienstr. 41, 80333 München, Germany.

Jan WISZNIOWSKI
Institute of Geophysics, Polish Academy of Sciences
ul. Księcia Janusza 64, 01-452 Warszawa, Poland.

Junru WU
Physics Department, University of Vermont
Burlington, VT, USA.

Takahiro YAJIMA
Department of Geoenvironmental Sciences, Graduate School of Science
Tohoku University, Aoba-ku, Sendai 980-8578, Japan.

Zbigniew ZEMBATY
Faculty of Civil Engineering, Technical University of Opole
ul. Mikołajczyka 5, 45-233 Opole, Poland.

PART I

MACROSEISMIC ROTATION EFFECTS AND MICROMOTIONS

1 Development of Earthquake Rotational Effect Study

Jan T. Kozák

Geophysical Institute, Academy of Sciences of the Czech Republic
14131 Prague 4 – Sporilov, Bočni, Czech Republic
e-mail: kozak@ig.cas.cz

Rotational earthquake effects were observed and mentioned by numerous geo-savants in the course of the 19th century. However, it has been often believed that scientific fundaments of this phenomenon were not laid until the end of this century. Indeed, in the latter period many specialized monographs, books and textbooks on geology appeared, in which examples of rotational earthquake displacements were shown, discussed and more or less correctly explained.

However, a closer look into this field reveals that the fundaments of advanced seismological and seismic observations of various earthquake effects, among them rotational ones, had been established much earlier, already in the first half of the 19th century.

It was, e.g. Leopold von Buch (1774-1853) who conducted comprehensive observations on the 1799 Silesian earthquake with the aim to determine the shape and size of the earthquake epicenter zone on the base of civic reports. The pioneer results by von Buch were published in a local journal with limited regional and scientific impact and therefore they soon sunk below the common horizon (Buch 1801 and 1867-1885).

Substantial progress in macroseismic observations, analysis and results' interpretation was reached by (today practically unknown) German mathematician P.N.C. Egen (1793-1844) who made and published an excellent macroseismic analysis of the 1828 North-Rhine earthquake. He, according Günther (1901), is the author of the first "actual macroseismic" map of an earthquake (see Egen 1828).

Further progress in the field was reached by G.H.O. Volger (1822-1897) who presented a thorough and voluminous study on the 1855 Visp, Switzerland, earthquake complemented by an excellent and advanced macroseismic isoseismal map of the event (Volger 1856 and 1857-1858).

In the mid-nineteenth century, the largest move forward in the observation, analysis and explanation of seismic effects – including the rotational ones – must be ascribed to Robert Mallet (1810-1881), author of the famous analytical work on the 1857 Great Neapolitan Earthquake entitled "The First Principles of Observational Seismology" (Mallet 1862). Let us pay a closer attention to his concept.

Modern theoretical and observational seismologists – armed with the last tools of modern theoretical approaches such as nonlinear physics, theory of micromorphic medium, etc. – know that there are more mechanisms or models to explain the observed rotational earthquake effects (see, e.g. Teisseyre and Kozák 2003). Mallet, however, who derived and published his explanation of rotational effects some 150 years earlier, had at his disposal only simple relations of classical mechanics and had to work with the subjects such as, for instance, *earthquake shock* (= seismic wave impact), *emergence angle* (= azimuth and vertical angles of seismic wave arrival), rotated body *mass, gravity, centre of gravity, friction or adherence, centre of adherence, main wave* (= *P* wave), *subordinate* or *second semiphase wave* (= such as *S* wave, surface waves, etc., and also reflected wave phases).

Nevertheless, even with these simple tools Mallet succeeded to formulate two fundamental mechanisms of the rotational seismic effects; let us denote them Rot1 and Rot2. Let us cite the author for the first of them: *Where the body is projected from a base or support with which it has friction or adherence, and the line of the wave transit through its centre of gravity does not also pass through the centre of adherence (that is, the point of the base, and between it and supports, in which all the resting forces, or adherence, etc., may be supposed concentrated), then, besides projection, a movement round a centre of spontaneous rotation within the body will also be impressed* (cit. Mallet 1862).

In such a way the author described a fundamental rotational mechanism, Rot1, of the body subjected to seismic impact turning around the "centre of adherence" (conf. Teisseyre and Kozák 2003).

As concerns rotation of a body in vertical plane, Mallet proposed another mechanism, which consisted in mutual configuration of horizontal component of seismic wave impact and gravity in special situations (see Mallet 1862, fasc edn 1987, vol 1., p 45). In page 78 of the same work Mallet writes: *.....twisting of objects upon their bases such as vases, chimneys, obelisks, etc., of which we shall record many examples.....[were] first explained by myself several years since* (Mallet 1848).

As for the second fundamental mechanism of seismic rotational effects, Rot2, Mallet suggested its explanation by means of "subordinate waves"

consequently emerging under different emergence angles (in comparison with the direct wave) eventually rotating the inflicted body.

By subordinate waves a modern reader would substitute wave phases reflected on inner Earth's boundaries. Let us give a room to the author (cit.): *If the observer look due to south at a square pyramid, for example, whose sides stay cardinal and it be tilted by the first semiphase of a shock from east to west, the pyramid will tilt or rise upon the eastern edge of its base; and if, before it has had time to fall back, it be acted on by another shock from north to south, the pyramid will rotate, upon the bisection or some other point, of the edge on which it momentarily rested, and will hence to come to repose, after having twisted from left to right, or with the hands of a watch* (cit. from Mallet 1862, fasc edn 1987, vol 1, p 376-77).

In principle the second Mallet's mechanism, Rot2, is identical with the one denoted as (b) in the paper by Teisseyre and Kozák (2003). It should be noted that Mallet, far before the type analysis of individual phases of seismic waves was done and accepted, and with a little knowledge on reflecting and refracting boundaries inside the earth, still succeeded to assess the importance of the *subordinate* or *second semiphase* waves for proper explanation of the observed rotational effects of Rot2 type.

In the decades which followed the publication of Mallet's analysis, rotational effects in question gradually appeared in numerous European monographs, geo-encyclopedias and textbooks on geology and geography as a fashion element: more or less detailed explanation of this phenomenon was entirely founded on the concept by Mallet. In most of these writings, individual authors often copied each other in presenting the same examples of rotational effects and even the same illustrations.

One of widely presented manifestations of rotational effects – splitting of stone blocks of the obelisks at the St. Bruno monastery (Italy) and their mutual rotation – can be found, e.g., in Charles Lyell's "Lehrbuch der Geologie*"*. However, Lyell (1833) used this displacement to demonstrate exclusively the obelisks structure disintegration (splitting), not the effects of stone blocks rotation.

Disintegrated blocks of the obelisk at the San Bruno monastery were also commented by Alexander von Humboldt. In his "Kosmos", Humboldt argued against the proposals by Mallet (cit.): *Apparent circular* (rotatorische) *quakes such as these, ...Mallet tried to convert into linear displacement* (see Mallet 1848 and Humboldt 1845-1862).

In the 1870s and 1880s, rotational effects were frequently reported in the papers on individual earthquakes of the time. In his report on the 1872 Central-German earthquake, Karl von Seebach described interaction of seismic waves with two pyramids composed of rectangular wooden blocks of small dimensions located on the writing desk in a building of small fac-

tory in Chomutov town (on Czech/Saxony border, ca 2° from the epicenter): *After passage of seismic waves, the individual wooden blocks were found to be mutually rotated*, see Fig. 1.1. However, the author did not analyze in greater detail the technical parameters of the situation, such as path of seismic waves through the factory edifice towards to the writing desk, friction conditions of the block surfaces, etc. (Seebach 1873, and Gutdeutsch et al. 1992).

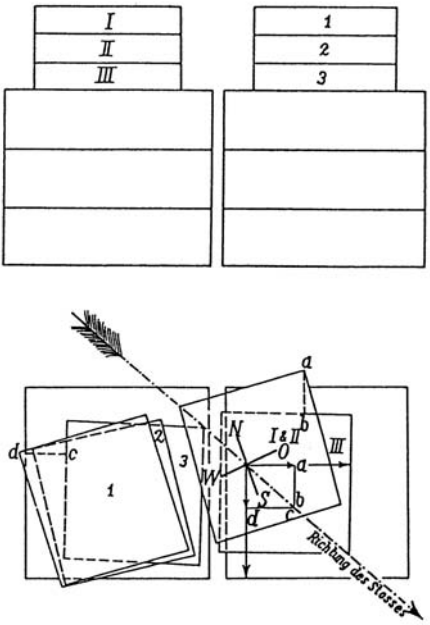

Fig. 1.1 Rotation of the two small pyramids of wooden blocks after the 1872 Central German earthquake (Seebach, 1873)

An experienced Austrian geologist Franz Suess observed and discussed rotational effects when analyzing the 1895 Laibach (Ljubljana) earthquake in Slovenia. He wrote (cit.): *Similarly as for all large earthquakes, also during the Ljubljana quake shifting of block/plate fundaments of columns and tombstones was observed. It is surprising how many different explanations and interpretations of these movements were proposed. Except of Humboldt's* [model of] *rotational earthquakes* (rotatorischen Erdbeben), *also a displacement of a torsion type was suggested, resulting from contemporary effects* [interference] *of direct and reflected waves, or from an elliptic displacement of the Earth particles due to possible interference of secondary transversal waves with the tremors of other type. Seismology has not proceeded enough to allow to decide to which of the above expla-*

nations the truth should be ascribed. However, I myself do not believe that the discussed displacement should be initiated by a single pulse [Stoss]. *More probably, the rotational effects should result from two shocks, following one-shortly-after-the-other, coming from different directions* (Suess 1896, p. 485).

Siegmund Günther in his "Handbuch der Geophysik" writes about *undulatory* or *rotational character* of seismic waves and illustrates it by a classical example – splitting and rotation of the obelisks at the St. Bruno monastery. Günther's interpretation is conform to the one by Mallet (Günther 1897).

Famous obelisk at the St. Bruno monastery was mentioned and its displacements explained also by M. Neumayr in his "Erdgeschichte". The author presents this example together with the other evident rotational earthquake displacements of the time. In this context he writes about earthquake vibration behaviour without more detailed explanation (Neumayr 1897).

In Russia, Ivan S. Mushketov, an eminent Russian seismologist of the turn of the 19th century discussed the rotational effects of earthquakes in his voluminous textbook "Fizicheskaya geologia" ("Physical Geology"). He presented classical examples (such as San Bruno obelisks) together with other examples of this phenomenon observed during recent European and Russian events: author's explanation is also based upon the analysis by Mallet, see Mushketov (1899).

After 1900 – since the type analysis of seismic waves and fundamental principles of their propagation were still not satisfactorily defined and accepted – also common explanation of earthquake rotational effects has not overcome the limits given by simple mechanical approach presented by Mallet. In the series of fundamental books prepared on the new discipline in geo-research, i.e., on seismology, still the old examples of rotational effects (observed during the 1783 Calabria, 1873 Belluno, 1878 West-German, 1895 Ljubljana, 1896 Guatemala, Schönai, Japan, and other famous earthquakes) were presented to illustrate this phenomenon. Out of a long series of publications let us cite at least Sieberg (1904), Jeništa (1906-1907), Lawson et al. (1908), Purkyně (1908), Kafka (1909), Supan (1911). It is worth to note that the observational seismology in this single point appeared a bit behind rapid seismic instrumental progress at that time (e.g. Plešinger and Kozák 2003).

Rotational secondary effects (as seismologists in later decades of the 20th century often named rotational effects) were regarded as marginal phenomena accompanying main seismogenic displacements in numerous works of this period (see, e.g. Janda 1940, and – as a historical reminiscence – Musson 1991 who discussed the early report by Milne 1842).

As concerns both classical mechanical rotation models, Rot1 and Rot2, called sometimes also technical or false models, they remained to serve for physical explanation of rotational phenomena throughout most of the 20th century. One of the reasons of decreasing interest of seismologists in rotational effects in this period lay in common opinion that they have little to do with the modern theory of seismic wave propagation, being more-or-less derived from technical conditions, such as friction, wave interference, etc.

Another mechanism – let us name it Rot3 – relates directly to rotation of displacement field both in an inner source near-zone and in the layers beneath a recording station. The effects related to such a mechanism can much differ in the amplitudes and nature depending on source mechanism and medium structure properties. In the last decades of the 20th century – taking advantage of the advanced continuum mechanics and ray theory and other theoretical achievements on the seismic wave origin and source mechanisms – new models related to this mechanism have been proposed. Many of them are founded on mutual interference of individual wave phases – not yet mutually separated – in the inner seismic source zone. In this situation, the surface Love waves and their horizontal component may, under special conditions, prescribing the properties of the surface zone, contribute to rotational effects in the near-source zone (see, e.g. Takeo and Ito 1997). Mechanism of the Rot3 type will be discussed in detail in several chapters of this monograph.

All three mechanisms, Rot1, Rot2 and Rot3, are derived from mechanical principles of elastic (seismic) wave propagation. Another mechanism (let us denote it Rot4), on the other hand, is linked with the real rotational deformations and the properties of the medium through which the seismic wave propagates. Modern theory of such a medium, usually called as a *micromorphic medium,* was investigated theoretically and also under laboratory conditions, first of all by Polish and Japanese seismologists. It will be demonstrated in other chapters that the advanced theory of micromorphic medium enables to detect rotational component of seismic waves due to wave interaction with the propagation medium treated by the terms of micromorphic description (Moriya and Teisseyre 1999, and Teisseyre et al. 2003).

Mechanism Rot5, recently proposed by Teisseyre (2004), relates to rotation and twist motions; this mechanism is based on additional constitutional bonds between the antisymmetric part of stresses and density of the self-rotation nuclei as being related to an internal friction in a homogenous elastic medium. The antisymmetric stresses correspond to stress moments.

The models Rot3 – Rot5 are derived within the terms of linear physics and elastic wave propagation in an elastic or quasi-elastic medium.

Laboratory and observational research in the last two decades in the field of non-linear medium and non-linear physics based on propagation of non-linear deformational wave, which was performed in cooperation of Russian and Czech seismologists, seems to reveal the existence of a next mechanism, model Rot6, as related to the coherent (self-organized) translation fracture wave. Its physical principles are given in a separate chapter (see Aksenov et al. 1993, and Aksenov 2006).

In our retrospection we can state that after a brilliant analysis of simple mechanics of seismic rotational effects presented by Robert Mallet as early as in 1850s, seismologists had to wait much over hundred years for more sophisticated, more "physical" and more complex explanation of the phenomenon in question, as the relatively recent mechanisms Rot3, Rot 4, Rot5 and especially Rot6 demonstrate. Do these recent models mean the last word in our understanding of the physics of seismic rotational effects?

References

Aksenov V (2006) Rotation wave as rupture mechanism, transfer of rock mass and generation of long period vibrations in fault zone. In: Teisseyre R, Takeo M, Majewski E (eds) Earthquake source asymmetry, structural media and rotation effects. Springer, Berlin (this book)

Aksenov V, Kozák J, Lokajíček T (1993) Nonlinear processes in earthquake foci. Pure and Appl Geophys **140**: 29-47

Buch L von (1801) Nachrichten über das Erdbeben in Schlesien 1799. Der Gesellschaft Natur-forschender Freunde zu Berlin, Neuere Schriften, vol **III,** pp 271

Buch L von (1867-85) Gesammelte Schriften, 4 vols. Publ J Ewald, J Roth und H Eck, Berlin

Egen PNC (1828) Über das Erdbeben in der Rhein- und Niederlanden vom 23. Februar 1828 (Poggendorffs) Annalen der Physik und Chemie 13, Band 89, pp 153

Gutdeutsch R, Grünthal G, Musson RMW (eds) (1992) Historical earthquakes in Central Europe, vol 1. Abh Geol Bundesanst in Wien

Günther S (1897) Handbuch der Geophysik, 2 Bnd. Verlag von Ferdinand Enke, Stuttgart

Günther S (1901) Die ersten Anfänge seismisch-kartograpischer Darstellung. Die Erdbebenwarte, Jahrg I, No 3, Laibach

Humboldt A von (1845-62) Kosmos. Entwurf einer physikalischen Weltbeschreibung, 5 vols. J.G. Cotta, Stuttgart und Tübingen, vol 1, p 212

Janda J (ed) (1940) Large illustrated textbook of natural history, vol VII: Geology (in Czech), Prague

Jeništa J (1906-1907) On seismometers (in Czech). vol **III:** 1, 10-11

Kafka J. (1909) Earthquake (in Czech). F Šimáček, Prague

Lawson et al. (1908) The California earthquake of April 18, 1906. Report of the state earthquake investigation commission, 2 vols and Atlas. Carnegie Institution of Washington, Washington D.C.

Lyell Ch (1833) Lehrbuch der Geologie (transl. from English by K Hartmann), Quedlingburg und Leipzig

Mallet R (1848) [*no title*]. Trans Roy Irish Acad, vol XXI, p 1

Mallet R (1849-50) On worticose shocks and cases of twisting. Meeting Brit Assoc pp 33 and 49. In: Admirality Manual p 213

Mallet R (1862) Great Neapolitan earthquake of 1857. The first principles of observational seismology, vols I-II. Chapman and Hall, London (fasc edn, SGA, Italy 1987)

Milne D (1842) Notices of earthquake-shocks felt in Great Britain and especially in Scotland, with interferences suggested by these notices as to the cause of such shocks. Edinburgh New Phil Journ **32**: 106-127

Moriya T, Teisseyre R (1999) Discussion on the recording of seismic rotation waves, Acta Geophys Pol **47**: 4**,** 351-362

Mushketov IV (1899) Physical Geology (in Russian). IN Ehrlich, St Petersburg

Musson RMW (1991) Pictorial representations of damage in historical British earthquakes. In: Kozák J (ed) Proc. historical earthquakes in Europe, Prague 1989. Geoph Inst Czech Acad Sci, Prague, pp 161-174

Neumayr M (1897) Erdgeschichte, Leipzig und Wien

Plešinger A, Kozák J (2003) Beginnings of regular seismic service and research in the Austro-Hungarian Monarchy, Part II. Studia Geoph et Geod. **47:** 757-791

Purkyně C (1908) Earthquake in Czech. In: Otto J (ed) Common Dictionary, 27 vols. Prague, vol XXVII: 565-571

Seebach K von (1873) Das mitteldeutsche Erdbeben vom 6. Marz 1872. H Haessel, Leipzig

Sieberg A (1904) Handbuch der Erdbebenkunde. F Vieweg u Sohn, Braunschweig

Suess F (1896) Das Erdbeben von Laibach am 14. April 1895. In: Jahrbuch der kaiserlichköniglichen Geologischen Reichsanstalt, 46: 411-890, Wien

Supan A (1911*)* Grundzüge der Physischen Erdkunde. Veit and Comp, Leipzig

Takeo M, Ito HM (1997) What can be learned from rotational motions excited by earthquakes? Geophys J Int **129**: 319-329

Teisseyre R (2004) Spin and twist motions in a homogeneous elastic continuum and cross-band geometry of fracturing. Acta Geophys Pol **52**: 173-184

Teisseyre R, Kozák J (2003) Considerations on the seismic rotation effects. Acta Geophys Pol **51**: 243-256

Teisseyre R, Suchcicki J, Teisseyre KP (2003) Recording the seismic rotation waves: reliability analysis. Acta Geophys Pol **51**: 37-50

Volger GHO (1856) Untersuchungen über das jüngste grosse Erdbeben in Central-Europa. Petermann's Mittheilungen. Justus Perthes, Gotha, année 1856: pp 85-102

Volger GHO (1857-1858) Untersuchungen über das Phänomen der Erdbeben in der Schweiz, Trois partes. Justus Perthes, Gotha

2 Sources of Rotation and Twist Motions

Roman Teisseyre[1], Jan T. Kozák[2]

[1]Institute of Geophysics, Polish Academy of Sciences
ul. Księcia Janusza 64, 01-452 Warszawa, Poland; e-mail: rt@igf.edu.pl

[2]Geophysical Institute, Academy of Sciences of the Czech Republic
14131 Prague 4 – Sporilov, Bočni, Czech Republic
e-mail: kozak@ig.cas.cz

2.1 Introduction

In Chapter 1, some data have been presented on the observed surface rotation effects and related damage caused by strong earthquakes; the rotation effects associated with earthquakes have been described and discussed already in the first theoretical attempts to analyse the seismic wave propagation (see Mallet 1862, Hobbs 1907, Gutenberg 1926, Davison 1927).

Mallet (1862) explained the rotation effects as being due to the incidence of a sequence of seismic phases consecutively emerging under different emergence angles and rotating the inflicted body.

Imamura (1937) proposed to explain the rotation effects by an impact of body waves at the ground surface on objects having different inertia axes; to this explanation, we can add the effects related to possible different adjustments of various parts of the object to its basement or even different friction properties between them.

We can take into account the four main categories of causes leading to the observed/recorded rotation effects:

- Generation of rotation motions in an earthquake source, e.g., due to internal friction processes at the microfracturing and at the macrofault where the nonlinear effects are evidently present; this concerns, in particular, the formation of a coherent fracture translation wave (self -organization) preceding the slip displacement.
- Generation of coupled rotation waves in an underground space beneath the recording station; in a medium with grains or with any kind of

internal structure, as for example that described by the micromorphic or micropolar theories, there may appear the rotation waves coupled to the seismic body waves.

- Effect of counterpart of rotation of the displacement velocities, both in the linear and nonlinear ranges.
- Appearance of the apparent rotation effects caused by a sequence of seismic body or surface waves and the resulting impacts on the objects situated on ground surface (we can call this category a false rotation).

The slip and fracture processes in a seismic source may cause the rotation of grains adjacent to the internal slip planes (Fig. 2.1a). A fracture process is entirely asymmetric, both in the micro- and macroscales. The main fracture may be accompanied by auxiliary perpendicular fracturings frequently appearing later as aftershocks (Fig. 2.1b). Twiss and Gefel (1990) have considered the brittle fault zones composed of rigid grains; the progressive processes in such zones may lead to macrorotations becoming the sources of microspin motions. In the further paper (Twiss et al. 1993), the authors estimated the effect of block rotation in a source on the seismic moment tensor.

The instantaneous process remains asymmetric and can be treated as a source of rotations, which may contain both a proper rotation and a twist motion. The twist motion, similar to shear deformation, represents different rotation shifts for perpendicular directions. At fracturing, the rotations adjacent to the perpendicular microfaults have opposite orientations; hence, when a length of microfault along one direction is greater than that

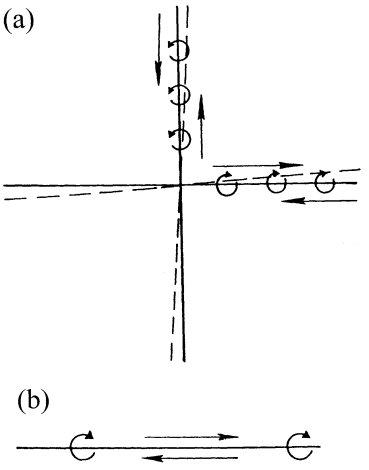

Fig. 2.1 Slip faults and rotation of adjacent grains – scheme of source pattern: (a) symmetric case, (b) asymmetric case

along the other direction, there appears rotation (Fig. 2.2). The rotations are related to internal friction processes.

A microstructure and defect content in a medium (Teisseyre 1973) can be another source of rotations. There are numerous papers on this subject; here, we shall point out the works by Takeo and Ito (1997), and by Teisseyre (2002), which give direct seismological applications. We are entitled to believe that the observations carried out at extremely short distances from seismic sources can reveal such rotation and twist motions. A question whether the rotation motions at a seismic source can propagate in a form of waves through geological layers from such a seismic source to a distant recording station seems still open. Recent theoretical studies (Teisseyre 2004, Boratyński and Teisseyre 2004) and some observational results bring a positive answer to this question. In practice, however, the conditions related to geological structures and to the region near the recording station can be either more or less favourable for detection of rotation waves. The secondary rotation waves are related to coupling between a microstructure and defect content in a medium; in other words, the seismic body and surface waves can give rise, due to interaction with the medium structure, to coupled rotation waves.

The effect of displacement velocity rotation ($\mathrm{rot}\,\dot{u}$) can be roughly estimated using the magnitudes of the observed displacement velocities; when deriving, with the use of the plane wave theory for ideal elastic medium, the rotation by means of time derivative of recorded data we can roughly estimate the effect. Some comparisons between the observed rotation motions and the effect so derived lead to the conclusion that the effect of rotation of displacement motions is small. However, Takeo and

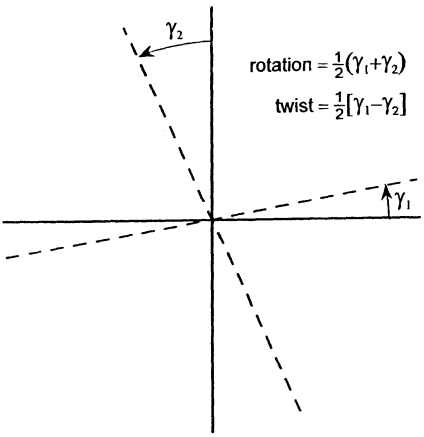

Fig. 2.2 Complex asymmetric pattern: rotation and twist motion

Ito (1997) proved theoretically that an influence of defects, expressed in the framework of the non-Riemannian geometry by torsion and curvature tensors, is such that at short distances the rotation of displacement velocity may be of importance (the near-field rotation effects).

Finally, the incident seismic waves exert direct influence on the objects situated on the Earth's surface; a sequence of incident waves and also the shape and structure of the objects (as expressed by inertia moment tensor) and the properties of the junction with the ground (friction and binding strength) determine the resulting effects. Many, but probably not all historical observations are related to this category.

The rotation and spin motions (related to real rotational deformations) can propagate in a medium with internal defects (dislocation and disclination densities) or even in a homogeneous medium in which, except of the classical constitutive relation between the symmetric strains and stresses, there are additional constitutive relations for the antisymmetric part of stresses and the spin and twist nuclei, as related to rotation of grains and internal friction.

Finally, strong rotational seismic effects (both horizontal and vertical) have been observed right in the epicenter of some shallow earthquakes. An explanation for these effects by the coherent translation wave at a seismic source arising in a self-organization process has recently been proposed (for details see Chapter 17 by V. Aksenov).

It follows from the above classification that individual sources of rotational seismic effects are not equally effective along the whole recording interval from the epicenter to the far-field distances. However, we do not have suitable tools in our hands enabling us to estimate these effects and to make their reliable quantitative comparison.

Many questions related to the rotation waves remain still open: up to now, we have no reliable data on propagation properties (velocity and attenuation) of such waves through geological media and on the influence of distance from source to the recording station; we have no laboratory data on the bonds between the particles or grains related to their mutual rotations and hence on the related elastic constant.

We shall note that the observed macrorotation effects due to large earthquakes may be not entirely caused by the microrotation motions related to seismic waves; we cannot prove, up to now, any unambiguous relation between the macrorotation effects and the microrotation motions observed with very sensitive recording systems.

A better insight into the theories related to rotation and twist micromotions is needed, as outlined further on in this chapter.

2.2 Elements of the Basic Theory

Teisseyre (1973, 1974) attributed the appearence of rotation effects to the seismic wave coupling with micromorphic response of a medium having an internal/granular structure.

We shall, however, account now for different approaches to the continuum description of real bodies: the media with internal structure could be described by micropolar (rotation of grains) or micromorphic (rotation and deformation of grains) theories; the linear, nonelastic media could be described by adequately modified constitutive relations (for example, for thermoelastic bodies or those with plastic relation between stresses and deformation rates). According to Kröner's idea (see Kröner 1981, 1982) we can combine both approaches by introducing the self fields or, in other words, by introducing a distribution of the self-stress or self-strain nuclei. At the same time, we preserve the ideal stress-strain relation. We will follow Kröner's approach which accounts both for the medium structure influence and for the content of defects and nuclei of stresses or deformations.

We introduce the total strains, rotations and distortions related to the displacements and, thus, automatically fulfil the compatibility conditions:

$$E^T = (\nabla u), \quad \omega^T = [\nabla u], \quad \beta^T = \nabla u \ , \tag{2.1}$$

where symbols ( ) and [ ] mean the symmetrized and antisymmetrized products of the elements contained inside them.

We demand that the total fields present the sums of the elastic and self fields:

$$E^T = E + E^S, \qquad \omega^T = \omega + \omega^S, \qquad \beta^T = \beta + \beta^S \ . \tag{2.2}$$

The elastic fields are the observables, the self fields represent distortions related to medium deviations from ideal elasticity and to an influence of other fields (thermal, electric and also that of rotation and friction nature); a sum of elastic and self fields shall result in the field called total, so defined due to obeying the constitutive relation for ideal elasticity.

The stresses (strictly speaking, the symmetric part of stresses, see the text below) remain related to strains by the ideal elastic form of the constitutive relations; in our presentation, such an ideal relation is valid for the total stress and strain fields, so we can write

$$S^T = \lambda I \ \mathrm{tr}\left(E^T\right) + 2\mu E^T \ , \qquad S^T = S + S^S \ , \tag{2.3}$$

while for real media the elastic fields are given as differences between the total and the self-fields, e.g., $E = E^T - E^S$, $S = S^T - S^S$. The self-fields introduce deviations from ideal elasticity (Kröner 1982): defect content, interacting fields and internal nuclei (e.g., dislocation and disclination densities, thermal field, rotation nuclei). The strain and stress elastic fields can be no longer symmetric, and the elastic rotation may become asymmetric too; the constitutive relation for the elastic stresses and strains, as corresponding to that in Eq. (2.3), shall be supplemented by the constitutive relation for the antisymmetric part of strain and stresses. This approach includes also continua with structure, e.g., micropolar or micromorphic continua with internal bonds (the constitutive relations). We will return to these problems in Chapter 4.

After Shimbo (1975, 1995) we can introduce the bonds for the point rotations by assuming that the internal friction along the microslip planes produces the rotation of grains due to the appearance of an antisymmetric part of stresses along such microplanes (Fig. 2.2):

$$\omega_{[..]} = \frac{1}{2\mu^*} S_{[..]} \quad , \tag{2.4}$$

where the material constant μ^* is a new constant different from the shear modulus, and symbol [..] means the antisymmetric part of a tensor.

Another kind of the constitutive relation and the related bonds can be introduced between the stress and rotation moments; under some conditions such an approach can be equivalent to that presented above with antisymmetric stresses and rotations.

The constitutive relation between the rotation field and the antisymmetric stress field can be supplemented with the assumption (Teisseyre 2002) that the elastic rotation relates to the antisymmetric strain and we shall note that the antisymmetric strains and stresses relate directly to the antisymmetric self-strains and self-stresses:

$$\omega_{[..]} = -E_{[..]} \quad \text{and} \quad E_{[..]} = -E^S_{[..]}, \quad S_{[..]} = -S^S_{[..]} \quad . \tag{2.5}$$

While for the twist motion, as given by the symmetric part of the asymmetric rotation tensor, we have to assume that it is equal to the symmetric self-rotation field, and, further, we can assume that the latter is equal to symmetric self-strain field:

$$\omega_{(..)} = -\omega^S_{(..)} \quad , \quad \text{where} \quad \omega^S_{(..)} = -E^S_{(..)} \quad , \tag{2.6}$$

where symbol (..) means the symmetric part of a tensor.

The antisymmetric part of elastic strain and the antisymmetric part of elastic rotation are related to the so-called microdisplacement motions introduced in micromorphic theories by Eringen (1999, and Eringen and Suhubi 1964).

The constitutive relations for the symmetric parts of elastic stresses and strains $E = E^T - E^S_{(..)}$ become, according to Eq. (2.3):

$$S = \lambda I \ \mathrm{tr}\left(E^T\right) + \lambda^* I \ \mathrm{tr}\left(\omega^S_{(..)}\right) + 2\mu E^T + 2\mu^* \omega^S_{(..)} \ , \tag{2.7}$$

where the constants λ^* and μ^* relates to the respective moduli for the microdisplacement motions.

Trace $\mathrm{tr}\left(\omega^S_{(..)}\right)$ presents an influence of diagonal self-strains related to compression/extension of micrograins, which are usually neglected; in such a case we will have

$$S = \lambda I \ \mathrm{tr}\left(E^T\right) + 2\mu E^T + 2\mu^* \omega^S_{(..)} \ . \tag{2.7′}$$

Rotation motions can be explained by theories for media with structures (see: micropolar and micromorphic media; e.g., Eringen and Suhubi 1964, Teisseyre 1973, 1995) or containing defects (see: theories related to the dislocation and disclination densities in continua, e.g., Teisseyre 1995, 2002).

In a near-fracturing state, we can consider, using the theory of elastic beams, the torques acting on bonds in a crystal lattice (Roux 1990, De Arcangelis 1990), as shown in Fig. 2.3. Such torques are conjugated to rotations around nodes; near a percolation threshold the related processes can lead to rotation of some internal rigid microstructures.

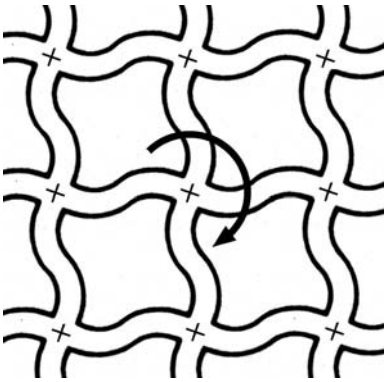

Fig. 2.3 Bending of bonds around the lattice nodes – modified after De Arcangelis (1990)

The sources of rotation motion in a focal source zone can be attributed, as well, to friction processes and grain rotations or to the stress couples connected with the small structural elements (microfaults) permeating such a zone (Teisseyre 1973).

2.3 Recording the Rotation and Twist Motions

Mechanical deformation may contain two independent fields: displacements and rotations; the latter appear when there exist a suitable excitation source and the internal bonds joining rotation motion with a stress moment or with a nonsymmetric part of stresses, like that given by Eq. (2.4). The system used can detect the rotation velocities.

Using the azimuthal array of seismographs, Droste and Teisseyre (1976) derived the first rotation seismograms at the recording site very close (1-3 km) to mine event hypocentres (Droste and Teisseyre 1976; reproduced in Teisseyre 1995, p 625). Figure 2.4 explains the measuring system suitable for estimating the azimuth towards the epicenter: it was a 6-channel azimuth system of horizontal seismographs used to record very close seismic events (at distances ca. 5 km) in a mine in Silesia, Poland. The azimuths as a function of time were determined by two numerical procedures estimating the errors of azimuth determinations in respect to the known position of the epicenter: in the first procedure we assumed that there is no rotation effect, while in the other that the rotation of seismo-

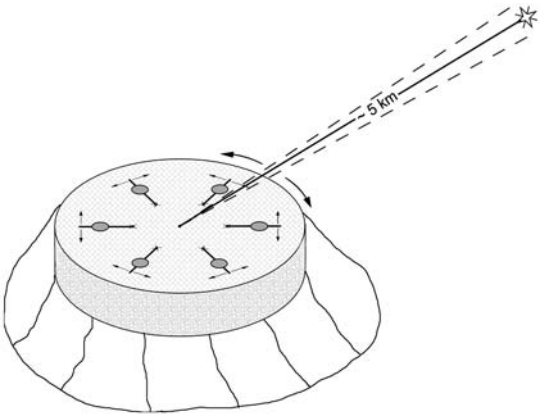

Fig. 2.4 System of the azimuth station. The asterisk denotes the epicenter position; the continuous line indicates the azimuth towards epicenter while the dashed lines mark the range of azimuth variations

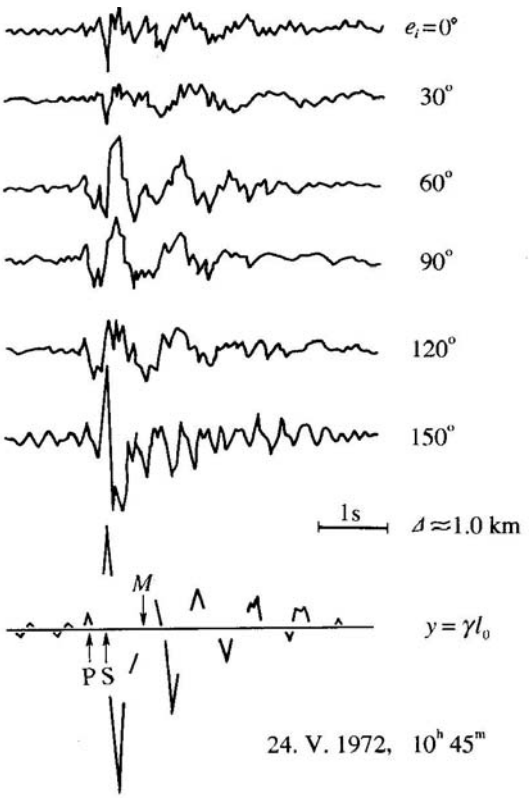

Fig. 2.5 The rotation seismogram derived from the azimuth variations – only for the time moments when their estimations were reliable

graph platform may take place. The method used enabled us to estimate the amplitudes of rotation motion for the moments when the errors for azimuth estimation were smaller than the errors for a fixed position of the platform; the respective time moments coincide with times when amplitudes of the recorded seismic wave were near the maxima. This was probably the first rotation seismogram achieved.

Contemporary systems designated to record the rotation velocities are based either on the very sensitive instruments measuring rotation, like the laser ring interferometers (see Takeo and Ito 1997) or on the rotation seismometer system. The latter consists of the pairs of antiparallel seismographs situated very close to each other (Moriya and Marumo 1998, Moriya and Teisseyre 1999) or suspended on a common axis (see Teisseyre 2002); such systems require a very close identity of the seismograph

responses and enable to record not only the rotation motion but also the twist type motion.

A pair consisting of two pendulum seismometers, aligned antiparallel (e.g., along the *y*-axis, to measure the *x*-component of displacement motion) and having identical responses, permits to measure two velocity fields containing the displacement and rotation velocities:

$$\dot{u}' = \dot{u} + l\left(\frac{\partial \dot{u}}{\partial y} + \dot{\omega}^S_{xy}\right) , \quad \dot{u}'' = \dot{u} - l\left(\frac{\partial \dot{u}}{\partial y} + \dot{\omega}^S_{xy}\right) , \tag{2.9}$$

where l is the reduced length of seismometer pendulum.

A sum of these fields yields displacement velocity, while for the difference of records we arrive at the definition of the microdisplacement tensor (here, the component *xy*):

$$\dot{u} = \frac{1}{2}\left(\dot{u}' + \dot{u}''\right) , \quad \dot{U}_{xy} = \frac{\left(\dot{u}' - \dot{u}''\right)}{2l} = \frac{\partial \dot{u}}{\partial y} + \dot{\omega}^S_{xy} \ . \tag{2.10}$$

The microdisplacements are defined here in relation to the observable values; rotation and twist become defined as

$$\begin{aligned} \frac{1}{2}\left(\dot{U}_{xy} - \dot{U}_{yx}\right) &= \frac{1}{2}\left(\frac{\partial \dot{u}}{\partial y} - \frac{\partial \dot{\upsilon}}{\partial x}\right) + \frac{1}{2}\left(\dot{\omega}^S_{xy} - \dot{\omega}^S_{yx}\right) , \\ \frac{1}{2}\left(\dot{U}_{xy} + \dot{U}_{yx}\right) &= \frac{1}{2}\left(\frac{\partial \dot{u}}{\partial y} + \frac{\partial \dot{\upsilon}}{\partial x}\right) + \frac{1}{2}\left(\dot{\omega}^S_{xy} + \dot{\omega}^S_{yx}\right) \ . \end{aligned} \tag{2.11}$$

Any measuring system detecting rotation motions measures together the velocity displacement and the corresponding component of rotation. We can only estimate the respective influences of these fields by computing the magnitudes of rotation displacement velocities from the records of $\dot{u}$ and $\dot{\upsilon}$ and comparing these magnitudes with the recorded ones related to the observed rotation and twist motions.

The observable quantities $\dot{U}$ relate to the displacement motions and rotations (in Eq. (2.6) we have put $\dot{\omega}^S = -\dot{E}^S$)

$$\begin{aligned} \dot{U}_{(sym)} &= \dot{E}_{(sym)} = \dot{E}^T - \dot{E}^S_{(sym)} = \dot{E}^T + \dot{\omega}^S_{(sym)} \ , \\ \dot{U}_{[antsym]} &= \dot{\omega}_{[antsym]} = \dot{\omega}^T - \dot{\omega}^S_{[antsym]} = \dot{\omega}^T + \dot{\omega}^S_{[antsym]} \ . \end{aligned} \tag{2.12}$$

According to these relations, we can state that the observables relate to elastic stresses or to rotations.

Estimating the order of magnitude of $\partial\dot{u}/\partial y$ and $\partial\dot{\upsilon}/\partial y$ by means of the plane wave approximation and comparing it with the recorded microdisplacement field $\dot{U}$, we have shown that in most cases analyzed so far the space derivatives of displacement motions $\dot{E}^T$ in these relations (Eqs. 2.10–2.12) can be neglected; the observed fields $\dot{U}$ would be comparable, by orders of magnitude, with the estimated orders of $\partial\dot{u}/\partial y$ and $\partial\dot{\upsilon}/\partial y$ only for very small wave velocities. However, in some cases this approximation can be not true.

Finally, we shall return to the question of reliability of recording of the microdisplacement fields $\dot{U}$.

In reality, the responses of the two antiparallel sensors, R', R'', are slightly different; instead of relation (2.9) we shall write

$$\dot{u}' = R' * \dot{\bar{u}} + R' * l\left(\frac{\partial\dot{\bar{u}}}{\partial y} + \dot{\bar{\gamma}}^*_{xy}\right), \qquad \dot{u}'' = R'' * \dot{\bar{u}} - R'' * l\left(\frac{\partial\dot{\bar{u}}}{\partial y} + \dot{\bar{\gamma}}^*_{xy}\right), \tag{2.13}$$

where these convolutions contain now the ground displacement motion, $\dot{\bar{u}}$, and ground rotations $\dot{\bar{\gamma}} = \omega^S$.

For the difference of records we obtain

$$\Delta\dot{u}' = \Delta R * \dot{\bar{u}} + 2R * l\left(\frac{\partial\dot{\bar{u}}}{\partial y} + \dot{\bar{\gamma}}^*_{xy}\right). \tag{2.14}$$

Thus, the seismograph systems record both the microdisplacement motion (hereabove, the second term) and the errors due to differences in responses (the first term). Both terms shall be evaluated and only in the case when the first term is smaller than the second one we can be sure that our records are reliable. Similarly, we shall reconsider relation (2.8) for the second rotation system. Teisseyre et al. (2003), and Nowożyński and Teisseyre KP (2003) proposed a special computation procedure to eliminate such errors related to differences in the responses.

Theoretically, the laser ring interferometers should record only the rotation component, but due to finite dimension of the recording platform there enter the derivatives of displacement motion and an influence of rotation of the velocity displacement will appear.

In the next chapters, several examples of recording of rotation and twist fields are presented. However, as we already mentioned, we shall still keep in mind that no unambiguous relation has been found – up to now – between these microrotation motions (true rotation) and the observed macrorotation effects (true and/or false rotations).

In the last decades, though, some progress in this respect has certainly been achieved. New fundamental ideas have been put forward and basic results of advanced theoretical approach have been obtained in the field of interaction of incident seismic waves with micromorphism and defect content.

Some experiments providing observational confirmation and verification of the studied phenomena have also been made; their first results corroborate the theoretical conclusions and indicate the usefulness of the observational systems.

References

Boratyński W, Teisseyre R (2004) Generalized continuum with defects and asymmetric stresses. Acta Geophys Pol **52**: 185-195

Davison Ch (1927) The founders of seismology. Cambridge Univ Press, Cambridge

De Arcangelis L (1990) Randomness in breaking thresholds (229-260). In: Herrmann HJ and Roux S (eds) Statistical models for the fracture of disordered media. North-Holland, Amsterdam New York

Droste Z, Teisseyre R (1976) Rotational and displacemental components of ground motion as deduced from data of the azimuth system of seismograph. Publs Inst Geophys Pol Acad Sc **97:** 157-167

Eringen AC (1999) Microcontinuum field theories. Vol. I Foundations and Solids. Springer Verlag, New York

Eringen AC, Suhubi ES (1964) Nonlinear theory of simple microelastic solids – I. Int J Eng Sci **2**: 189-203

Gutenberg B (1926) Grundlagen der Erdbebenkunde. Univ. Frankfurt a/M, Frankfurt

Hobbs WH (1907) Earthquakes. Appleton and Co., New York

Imamura A (1937) Theoretical and applied seismology. Maruzen Co., Tokyo

Kröner E (1981) Continuum theory of defects. In: Balian R, Kléman M, Poirier J-P (eds) Les Houches, Session XXXV, 1980, Physique des defauts / Physics of defects. North-Holland Publ Comp, Dordrecht

Kröner E (1982) Continuum theory defects. North-Holland Publ Comp, Dordrecht

Mallet R (1862) Great Neapolitan earthquake of 1857. The first principles of observational seismology, vols I-II. Chapman and Hall, London (Fasc edn, SGA, Italy 1987)

Moriya T, Marumo R (1998) Design for rotation seismometers and their calibration. Geophys Bull Hokkaido Univ **61**: 99-106

Moriya T, Teisseyre R (1999) Discussion on the recording of seismic rotation waves. Acta Geophys Pol **47**: 351-362

Nowożyński K, Teisseyre KP (2003) Time-domain filtering of seismic rotation waves. Acta Geophys Pol **51**: 51-61

Roux S (1990) Continuum and discrete description of elasticity. In: Herrmann HJ, Roux S (eds) Statistical models for the fracture of disordered media, North-Holland, Amsterdam, pp 87-114

Shimbo M (1975) A geometrical formulation of asymmetric features in plasticity. Bull Fac Eng Hokkaido Univ **77**: 155-159

Shimbo M (1995) Non-Riemannian geometrical approach to deformation and friction. In: Teisseyre R (ed) Theory of earthquake premonitory and fracture processes. PWN, Warszawa, pp 520-528

Takeo M, Ito HM (1997) What can be learned from rotational motions excited by earthquakes? Geophys J Int **129**: 319-329

Teisseyre R (1973) Earthquake processes in a micromorphic continuum. Pure appl Geophys **102**: 15-28

Teisseyre R (1974) Symmetric micromorphic continuum: wave propagation, point source solutions and some applications to earthquake processes. In: Thoft-Christensen P (ed.) Continuum mechanics aspects of geodynamics and rock fracture mechanics, D Riedel Publ, Dordrecht-Holland, pp 201-244

Teisseyre R (ed) (1995) Theory of earthquake premonitory and fracture processes. PWN, Warszawa

Teisseyre R (2002) Continuum with defect and self-rotation fields. Acta Geophys Pol **50**: 51-68

Teisseyre R (2004) Spin and twist motions in a homogeneous elastic continuum and cross-band geometry of fracturing. Acta Geophys Pol **52**: 173-183

Teisseyre R, Teisseyre KP, Moriya T, Palangio P (2003) Seismic rotation waves related to volcanic mining and seismic events: nearfield and micromorphic motions. Acta Geophys Pol **51**: 409-431

Twiss RJ, Gefel MJ (1990) Curved slicken fibers: a new brittle shear sense indicator with application to a sheared serpentinite. J Struct Geol **12**: 471-481

Twiss RJ, Souter BJ, Unruh JR (1993) The effect of block rotations on the global seismic moment tensor and the patterns of seismic P and T axes. J Geophys Res **98**: B1, 645-674

3 Some Examples of Rotation Effects: the Tulbagh Earthquake, South Africa

Gerhard Graham, Andrzej Kijko

Council for Geoscience, Pretoria 0001, South Africa
e-mail: kijko@geoscience.org.za

The Southwestern Cape is considered to be one of the regions with the highest level of seismic activity of tectonic origin in South Africa. In this respect, the Tulbagh-Ceres area is of prime interest, as pointed out by the destructive Tulbagh earthquake of 29 September 1969. This earthquake caused severe damages, including rotation of tombstones and memorials in cemeteries in the earthquake-affected towns.

According to Theron (1974), earth tremors have been recorded in the Southwestern Cape as early as 1620. The number of earthquakes recorded in his catalogue for the period 1620-1971 is 73, with at least 7 of them considered to have had local magnitudes M_L between 5.1 and 6.5. The first 300 years of this catalogue contains approximately 23 tremors, against about 53 tremors during its last 50 years. This fact is not considered to indicate increased seismicity in the area, but is rather the result of incomplete recording prior to 1920 and the limited history of observed earthquakes. The catalogue was incorporated into a more complete catalogue by Fernández and Guzmán (1979), covering all events recorded in Southern Africa for the period 1620-1970. It is evident from the Fernández and Guzmán catalogue that the number of recorded events in the Southwestern Cape since 1920 is almost double of that reported by Theron (1974).

A large portion of the Southwestern Cape events in the Fernández and Guzmán (1979) catalogue resulted from the seismicity recorded in the Tulbagh area, especially in the time directly following the large Tulbagh earthquake on 29 September 1969. This earthquake, having a local magnitude M_L of 6.3, was the most destructive earthquake in South African history and was followed by a long sequence of aftershocks, the most severe of which, on 14 April 1970, had M_L of 5.7. A comprehensive report regarding the 1969 earthquake (van Wyk and Kent, 1974) covers aspects such as the geology of the Tulbagh-Ceres area, the seismic history of the Southwestern Cape, macroseismic observations in the meizoseismal areas of the 1969 earthquake, hydrological phenomena associated with the earthquake,

aftershocks of the earthquake, the focal mechanism of the earthquake, geophysical implications of the whole earthquake sequence during 1969-1971, some elements of seismic risk assessment and earthquake-resistant building recommendations.

The worst damage resulting from the Tulbagh earthquake of 29 September 1969 occurred in the northern part of the Tulbagh Valley which is situated close to the epicentre (Keyser, 1974). Severe damage occurred to buildings in the towns of Tulbagh, Wolsely, Ceres and Prince Alfred Hamlet. Damage also occurred in the villages of Saron, Gouda and Hermon as well as in the towns of Worcester and Porterville. Slight damage was observed, in particular, in towns as far away as Stellenbosch which is about 80 km from the epicentre**.** The maximum seismic intensity (in modified Mercalli scale) of VIII was observed during the earthquake in the Tulbagh region. This corresponds to a ground movement of $0.13\ g \leq PGA < 0.26\ g$ according to the intensity–PGA (Peak Ground Acceleration) relation of Trifunac and Brady (1975), where the lower and upper limits of PGA were

Fig. 3.1 The memorial at the cemetery northeast of Tulbagh, some 15-20 km from the 29 September 1969 Tulbagh earthquake epicenter (33.28° S, 19.14° E). The marble pillars supporting the roof with ornaments were rotated by about 10° (Archives of the Council for Geoscience, Pretoria, South Africa)

obtained by substituting the intensity in the intensity-PGA relation by VII½ and VIII½, respectively. The seismic hazard and risk assessment for the Tulbagh area is presented by Kijko et al. (2002, 2003).

Severe damage was observed in many cemeteries in the earthquake -affected towns. In Wolseley, about 20 km from the epicentre**,** more than 50% of the tombstones were toppled over, mostly in westerly direction. A cemetery north-east of Tulbagh experienced less damage. However, a memorial, consisting of a few marble pillars supporting an ornamental roof rotated through about 10°. The roof shifted in south-westerly direction (Keyser, 1974). A photo of this memorial after destruction is shown in Fig. 3.1.

In Ceres cemetery, about 20 km from the epicentre**,** more than 70% of the tombstones collapsed. The majority fell over to the west. Only one fell to the east. Three tombstones rotated anticlockwise through 45° (Keyser, 1974). A spectacular photo of one of the anticlockwise rotated tombstones in the Ceres cemetery is shown in Fig. 3.2.

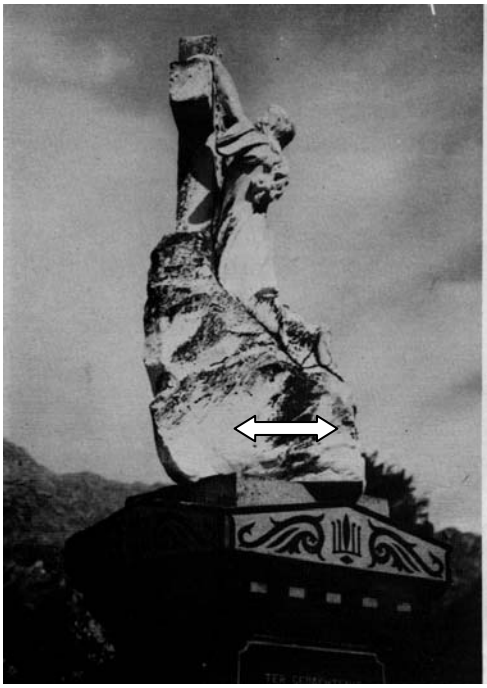

Fig. 3.2 Tombstone in the Ceres cemetery showing anticlockwise rotation through 45 degrees. Source: "Die Aardbewing van 29 September 1969 in die Suidwestelike Kaapprovinsie, Suid-Afrika" Geological Survey, Republic of South Africa, Department of Mines, Seismologiese Reeks 4, 1974, 48 pp"

References

Fernández LM, Guzmán JA (1979) Seismic history of Southern Africa. Geological Survey of South Africa, Seismologic Series 9: 1-38

Keyser AW (1974) The earthquake of 29 September 1969 in the Southwestern Cape Province, South Africa. Geological Survey of South Africa, Seismologic Series 4: 16-22

Kijko A., Retief SJP, Graham G (2002) Seismic hazard and risk assessment for the Tulbagh area, Part I. Assessment of seismic hazard. Natural Hazards **26**: 175-201

Kijko A, Retief SJP, Graham G (2003) Seismic hazard and risk assessment for the Tulbagh area, Part II. Assessment of seismic risk. Natural Hazards **30:** 25-41

Theron JH (1974) The earthquake of 29 September 1969 in the southwestern Cape Province, South Africa. Geological Survey of South Africa, Seismologic Series 4: 12-18

Trifunac MD, Brady AG (1975) On the correlation of seismic intensity scales with the peaks of recorded ground motion. Bull Seism Soc Am **65**: 139-162

van Wyk WL, Kent LE (1974) The Earthquake of 29 September 1969 in the Southwestern Cape Province, South Africa. Geological Survey of South Africa, Seismologic Series 4: 53 pp

PART II

THEORY OF CONTINUA AND FIELDS OF DEFECTS

4 Deviations from Symmetry and Elasticity: Asymmetric Continuum Mechanics

Roman Teisseyre[1], Wojciech Boratyński[1,2]

[1] Institute of Geophysics, Polish Academy of Sciences
ul. Księcia Janusza 64, 01-452 Warszawa, Poland
e-mail: rt@igf.edu.pl

[2] Faculty of Mathematics and Information Science
Warsaw University of Technology
Plac Politechniki 1, 00-661 Warszawa, Poland
e-mail: wbora@mini.pw.edu.pl

4.1 Introduction

The deviations from classical elasticity can be related to the defect distribution (dislocation and disclination densities), thermal excitation, some features of internal structure and different types of nuclei (e.g. electric nuclei, rotation nuclei); other deviations lead to an elasto-plastic behaviour.

The Kröner approach to continua with a distribution of self-field sources is applied to a wide class of deviations from the classical ideal elasticity; the same approach is applied to the theory of continua with asymmetric fields; the related equations of motion are derived. Such an approach replaces other methods based on the constitutive relations specific for each type of the medium considered. In this approach, the reference constitutive relation remains the same, but deviations from the classical ideal elasticity are attributed to different sources, nuclei and defects introduced into continuum theory.

Our considerations extend on deviations from the stress symmetry.

The elastic deformation fields, strain, rotation and distortion, represent real observables; the Kröner continuum with defect distribution of different kinds is based on definitions of the elastic, total and self-fields. We use this approach (see Kröner 1958, 1981) to the elastic theory of continuum deviating from the ideal elasticity and from the stress and strain symmetry; the total stresses and strains remain symmetric while the total rotation remains antisymmetric.

The total fields E^T and ω^T are defined as the fields which can be expressed by means of the displacement field:

$$E_{kl}^{\mathrm{T}} = \frac{1}{2}\left(\frac{\partial u_l}{\partial x_k} + \frac{\partial u_k}{\partial x_l}\right), \qquad \omega_{kl}^{\mathrm{T}} = \frac{1}{2}\left(\frac{\partial u_l}{\partial x_k} - \frac{\partial u_k}{\partial x_l}\right), \qquad \beta_{kl}^{\mathrm{T}} = \frac{\partial u_l}{\partial x_k}, \tag{4.1}$$

while the self-fields represent distribution of internal sources (nuclei) causing the disturbances in the strain and rotation fields. The elastic fields E and ω deviate from total fields due to an influence of the self-fields (Kröner 1958, 1981):

$$E = E^T - E^S, \qquad \omega = \omega^{\mathrm{T}} - \omega^{\mathrm{S}}, \qquad \beta = \beta^{\mathrm{T}} - \beta^{\mathrm{S}}. \tag{4.2}$$

Total fields E^T and ω^T fulfil the compatibility conditions:

$$\varepsilon_{ikm}\varepsilon_{jtn}\frac{\partial^2 E_{mn}^{\mathrm{T}}}{\partial x_k \partial x_t} = 0, \qquad \varepsilon_{ikm}\varepsilon_{jtn}\frac{\partial^2 \omega_{mn}^{\mathrm{T}}}{\partial x_k \partial x_t} = 0.$$

The compatibility conditions for the elastic fields help us to define the incompatibility tensors for elastic and self-fields:

$$\begin{aligned} I_{ij} &= -\varepsilon_{ikm}\varepsilon_{jtn}\frac{\partial^2 E_{mn}}{\partial x_k \partial x_t} = \varepsilon_{ikm}\varepsilon_{jtn}\frac{\partial^2 E_{mn}^{\mathrm{S}}}{\partial x_k \partial x_t}, \\ J_{ij} &= -\varepsilon_{ikm}\varepsilon_{jtn}\frac{\partial^2 \omega_{mn}}{\partial x_k \partial x_t} = \varepsilon_{ikm}\varepsilon_{jtn}\frac{\partial^2 \omega_{mn}^{\mathrm{S}}}{\partial x_k \partial x_t}. \end{aligned} \tag{4.3}$$

These two tensors can be separated into the symmetric and antisymmetric parts (Teisseyre and Boratyński 2003, Boratyński and Teisseyre 2004).

Elastic stresses and strains shall obey some reference constitutive relation; for symmetric fields we assume that such a relation is that of the ideal elasticity:

$$S_{lk} = \lambda\delta_{lk}E_{ss} + 2\mu E_{lk}. \tag{4.4}$$

The elastic and self strains and stresses can be, in general, asymmetric; hence, their anti-symmetric parts shall be mutually compensated to preserve symmetry:

$$E_{[ik]} + E_{[ik]}^{\mathrm{S}} = 0, \qquad S_{[ik]} + S_{[ik]}^{\mathrm{S}} = 0. \tag{4.5}$$

Similarly, the elastic and self rotations are asymmetric and hence their symmetric parts shall be mutually compensated:

$$\omega_{(ik)} + \omega_{(ik)}^{\mathrm{S}} = 0. \tag{4.6}$$

We shall note that the balance law for the antisymmetric stresses and rotations replaces the balance between stress moments and angular momentum.

4.2 Symmetric Stresses: Motion Equations

First, we recall the classic case of symmetric stresses in a continuum with defects (dislocations and disclinations; see Teisseyre 2001); for elastic fields we write the equation of motion expressing divergence of symmetric elastic stresses:

$$\frac{\partial}{\partial x_k} S_{lk} = \rho \frac{\partial}{\partial t} \upsilon_l \,, \qquad \frac{\partial}{\partial t} \upsilon_l = \frac{\partial}{\partial t} \upsilon_l^{\mathrm{T}} - \frac{\partial}{\partial t} \upsilon_l^{\mathrm{S}} \,, \tag{4.7}$$

or

$$\frac{\partial}{\partial x_k} S_{lk} = \rho \frac{\partial^2}{\partial t^2} u_l - \rho \frac{\partial}{\partial t} \upsilon_l^{\mathrm{S}} \,,$$

where υ^S is the plastic velocity. From this relation we obtain, after differentiation and symmetrization:

$$\frac{1}{2}\left(\frac{\partial}{\partial x_k \partial x_s} S_{lk} + \frac{\partial}{\partial x_k \partial x_l} S_{sk} \right) = \rho \frac{\partial^2}{\partial t^2} E_{ls}^{\mathrm{T}} - \rho \frac{1}{2} \frac{\partial}{\partial t} \left(\frac{\partial}{\partial x_s} \upsilon_l^{\mathrm{S}} + \frac{\partial}{\partial x_l} \upsilon_s^{\mathrm{S}} \right), \tag{4.7′}$$

$$\left(\frac{\partial}{\partial x_k \partial x_s} S_{lk} \right)_{(ls)} = \rho \frac{\partial^2}{\partial t^2} E_{ls}^{\mathrm{T}} + \rho \frac{\partial}{\partial t} \left(J_{sl} - \dot{E}_{sl}^{\mathrm{S}} \right) , \tag{4.8}$$

where for the dislocation current J_{sl} we put (Teisseyre 2002)

$$J_{sl} = \frac{\partial}{\partial t} E_{sl}^{S} - \frac{1}{2}\left(\frac{\partial}{\partial x_s} \upsilon_l^{\mathrm{S}} + \frac{\partial}{\partial x_l} \upsilon_s^{\mathrm{S}} \right) . \tag{4.8′}$$

Finally, using relations (4.2) and (4.4) we get

$$\left(\frac{\partial}{\partial x_k \partial x_s} S_{lk} \right)_{(ls)} = \frac{\rho}{2\mu} \frac{\partial^2}{\partial t^2} S_{ls} - \frac{\rho}{2\mu} \frac{\lambda}{(3\lambda + 2\mu)} \delta_{ls} \frac{\partial^2}{\partial t^2} S_{nn} + \rho \frac{\partial}{\partial t} J_{sl} \,. \tag{4.8″}$$

This equation of motion contains on the right-hand side the propagation and diffusion terms.

4.3 Thermal Deformations

Before going into more general considerations we take the case of thermal distortion; the Duhamel–Neuman relation determines the following constitutive law and the motion equation:

$$\frac{\partial}{\partial x_k} S_{lk} = \frac{\partial}{\partial x_k} S^0_{lk}(u) - (3\lambda + 2\mu)\alpha^{\text{ther}} \frac{\partial}{\partial x_l} T = \rho \frac{\partial^2 u_l}{\partial t^2}, \tag{4.9}$$

$$S_{ls} = S^0_{ls}(u) - \delta_{ls}(3\lambda + 2\mu)\alpha^{\text{ther}} T, \tag{4.10}$$

where S^0_{lk} represent stresses for the isothermal case.

Differentiation and symmetrization brings the next relation:

$$\left(\frac{\partial}{\partial x_k \partial x_s} S^0_{lk}(u) \right)_{(ls)} = \rho \frac{\partial^2}{\partial t^2} E^{\text{T}}_{ls} + (3\lambda + 2\mu)\alpha^{\text{ther}} \frac{\partial}{\partial x_l \partial x_s} T. \tag{4.11}$$

Thermal distortions can be described by the dislocation fields (Muskhelishvili 1953, Teisseyre 1986); hence, starting with the constitutive law (4.4) and using relation (4.8) we obtain the equivalent relation:

$$\left(\frac{\partial}{\partial x_k \partial x_s} S_{lk} \right)_{(ls)} = \left(\frac{\partial}{\partial x_k \partial x_s} S^T_{lk}(u) \right)_{(ls)} - \left(\frac{\partial}{\partial x_k \partial x_s} S^S_{lk} \right)_{(ls)}$$
$$= \rho \frac{\partial^2}{\partial t^2} E^{\text{T}}_{ls} + \rho \frac{\partial}{\partial t} J_{sl} - \rho \frac{\partial}{\partial t} \dot{E}^{\text{S}}_{sl}. \tag{4.12}$$

Comparing these two relations for $S^0(u) = S^T(u)$ we obtain the expression for the thermal self-strain and current:

$$E^S_{ls} = \delta_{ls}\alpha^{\text{ther}} T, \quad S^{\text{S}}_{ls} = \delta_{ls}(3\lambda + 2\mu)\alpha^{\text{ther}} T \ , \quad J_{ls} = \delta_{ls}\alpha^{ther}\dot{T}. \tag{4.13}$$

In this manner we arrive also at the total stress field: the Kröner continuum

$$S^{\text{T}}_{ls} = S_{ls} + S^{\text{S}}_{ls} = \delta_{ls}\lambda E_{nn} + 2\mu E_{ls} + \delta_{ls}(3\lambda + 2\mu)E^{\text{S}}_{nn}. \tag{4.14}$$

Comparing (4.13) with the definition of the dislocation current tensor and plastic flow (4.8′) (Teisseyre 2002), we obtain the vanishing of the thermal flow $\upsilon^S_k = 0$.

In a similar way we can define the plastic flow velocities and currents for other sources of distortions, like piezoelectric, anomalous piezoelectric (Teisseyre 2001) and magnetic (Nagahama 2001).

4.4 The Maxwell and Voigt–Kelvin Bodies: Equivalence Theorems

A linear generalized constitutive stress-strain relation for the total fields is as follows:

$$S_{ik}^T + \tau \dot{S}_{ik}^T = \lambda \delta_{ik} E_{ss}^T + 2\mu E_{ik}^T + 2v\dot{E}_{ik}^T \ . \tag{4.15}$$

Such a relation can be written for a sum of the elastic and self-fields (approach of Kröner 1981):

$$S_{ik} + S_{ik}^S + \tau \dot{S}_{ik} + \tau \dot{S}_{ik}^S = \lambda \delta_{ik} E_{SS} + 2\mu E_{ik} + 2\mu E_{ik}^S + 2v\dot{E}_{ik} + 2v\dot{E}_{ik}^S . \tag{4.16}$$

We will search for the definitions of the self-fields which would preserve the ideal elastic relation for the elastic field; we assume here that the trace of self-fields vanishes, $E_{ss} = E_{ss}^T$. Hence, separating these tensors into the axial $\widehat{S}_{ik}$ and deviatoric $\tilde{S}_{ik}$ parts, $\widehat{S}_{ik} = \frac{1}{3}\delta_{ik} S_{ss}$ and $\tilde{S}_{ik} = S_{ik} - \widehat{S}_{ik}$, we can write for the deviatoric fields

$$\tilde{S}_{ik} + \tilde{S}_{ik}^S + \tau \dot{\tilde{S}}_{ik} + \tau \dot{\tilde{S}}_{ik}^S = 2\mu \tilde{E}_{ik} + 2\mu \tilde{E}_{ik}^S + 2v\dot{\tilde{E}}_{ik} + 2v\dot{\tilde{E}}_{ik}^S \ . \tag{4.16'}$$

For the Maxwell body, in particular, we have:

$$\begin{aligned} &\tilde{S}_{ik}^T = 2\mu \tilde{E}_{ik}^T + 2v\dot{\tilde{E}}_{ik}^T \\ \text{and} \qquad &\tilde{S}_{ik} + \tilde{S}_{ik}^{SM} = 2\mu \tilde{E}_{ik} + 2\mu \tilde{E}_{ik}^{SM} + 2v\dot{\tilde{E}}_{ik} + 2v\dot{\tilde{E}}_{ik}^{SM} \ . \end{aligned} \tag{4.17}$$

When the self-stresses and strains are defined as

$$\tilde{S}_{ik}^{SM} - 2\mu \tilde{E}_{ik}^{SM} - 2v\dot{\tilde{E}}_{ik}^{SM} = 2v\dot{\tilde{E}}_{ik} , \tag{4.18}$$

we preserve the ideal elastic relation for the elastic fields.

Similarly, for the Voigt–Kelvin body we have:

$$S_{ik}^T + \tau \dot{S}_{ik}^T = \lambda \delta_{ik} E_{ss}^T + 2\mu E_{ik}^T , \tag{4.19}$$

$$\tilde{S}_{ik} + \tilde{S}_{ik}^{SV} + \tau \dot{\tilde{S}}_{ik} + \tau \dot{\tilde{S}}_{ik}^{SV} = 2\mu \tilde{E}_{ik} + 2\mu \tilde{E}_{ik}^{SV} \ . \tag{4.19'}$$

When defining the self-fields as

$$\tilde{S}_{ik}^{SV} + \tau \dot{\tilde{S}}_{ik}^{SV} - 2\mu \tilde{E}_{ik}^{SV} = -\tau \dot{\tilde{S}}_{ik} \ , \tag{4.20}$$

we obtain again the ideal elastic relation for the elastic fields.

We can combine these results obtaining the complete equivalence between the Kröner approach and the various constitutive relation approach:

$$\tilde{S}^S_{ik} + \tau \dot{\tilde{S}}^S_{ik} - 2\mu \tilde{E}^S_{ik} - 2\nu \dot{\tilde{E}}^S_{ik} = 2\nu \dot{E}_{ik} - \tau \dot{\tilde{S}}_{ik} \quad . \tag{4.21}$$

We will now compare the equations of motion for the two abovementioned approaches describing the distortions from ideal elasticity.

The equation of motion is given by relation (4.7) and the related self-strain, current and plastic velocity join relation (4.8′).

4.5 Asymmetric Fields

The antisymmetric part of self-strains may be related to internal microfrictions (stress moment resistance), while the symmetric part of self-rotations may represent some axial motion, called further on the bend-twist motion.

Already in the micromorphic continuum (Eringen and Suhubi 1964, Eringen and Claus 1970, Eringen and Kafadar 1976), the microstrain can contain its antisymmetric part while the gyration tensor can contain its symmetric part; these peculiarities extend, moreover, on the stresses and stress moments and on the inertia spin tensor (in the latter, some additional asymmetric properties may result from the microinertia tensor).

In this chapter we recall some of our former results for the continuum with defect distribution and we present a uniform continuum with rotation motions – of spin and twist-bend types (Teisseyre 2002, 2004, Teisseyre and Boratyński 2002, 2003, Boratyński and Teisseyre 2004); in our approach we supplement the ideal elasticity constitutive law, the strain-stress relation, by an additional relation joining the rotation tensor and the asymmetric stresses. The asymmetry of fields follows from the antisymmetric stresses introduced by Shimbo (1975, 1995) and Shimbo and Kawaguchi (1976) as related to the friction processes and rotations of grains. Fracture processes develop usually along the main fault plane, giving rise to the initial asymmetry of the fracture pattern; the same concerns the micro-fracturing and internal friction processes. Due to friction, the rotation of grains adjacent to the micro-slip planes causes an appearance of the antisymmetric part of stresses. Owing to the additional constitutive law between the antisymmetric parts of stresses and strains, we can evade an influence of the Hook law, which, when used as a unique law in the ideal elasticity, rules out an existence of rotation waves. Thus, it comes out that the rotation vibrations can, in such an ideal elastic continuum, propagate and be not attenuated.

Already in the micromorphic continuum (Eringen and Suhubi 1964, Eringen and Claus 1970, Eringen and Kafadar 1976, Eringen 1999), the microstrain can contain its anti-symmetric part while the gyration tensor can contain its symmetric part; these peculiarities extend, moreover, on the stresses and stress moments and on the inertia spin tensor (in the latter, additional asymmetric properties may result from the microinertia tensor). The relations for the microstrain and microstress moments can be expressed with the use of notion of the self fields including their symmetric and antisymmetric parts. The motion equations shall be supplemented with that including a balance for stress moments and angular momentum.

Some features of the micromorphic continuum can also be described in the frame of our approach with the properly defined self-fields.

Here, we will also show that even in a uniform continuum, when the rotation of individual particles and the related bond distortions generate antisymmetric stresses, the rotation waves propagate and are not attenuated, similarly as the displacement motion in ideal elasticity.

An alternative way of introducing the rotation motions is to consider a continuum with defect densities (dislocations and disclinations) and/or rotation nuclei (Teisseyre and Boratyński 2003, Boratyński and Teisseyre 2004); see the next chapters.

In our approach, the asymmetry of fields follows from the relation between the antisymmetric stresses and is related to the friction processes and rotation of grains, as introduced by Shimbo (1975, 1995). Fracture processes usually develop along the main fault plane; hence, there appears the initial asymmetry of the fracture pattern (Teisseyre and Kozak 2003); due to friction, the rotation of grains adjacent to the main slip plane gives rise to the antisymmetric part of stresses and the twist-bend tensor. Thus, as we have proposed in our earlier paper, we introduce after Shimbo (1975 and 1995) the bonds for rotation motion as the constitutive relation between the antisymmetric strains; cf. Eqs. (4.5) and (4.6):

$$\omega^{S}_{[lk]} = \frac{1}{2\mu^{*}} S^{\mathrm{S}}_{[lk]} = E^{S}_{[lk]} \,, \tag{4.22}$$

where the constant μ^{*} represents the rotation rigidity of bonds and is related to the inner friction.

We also have to include a counterpart to spin motion – the axial symmetric motion called the bend-twist motion and representing vibrations of the rotation nuclei; we assume that the related strain and rotation self-fields follow the similar relation as given in (4.22). Thus, we can write

$$\omega^{S}_{(lk)} = \frac{1}{2\mu^{*}} S^{\mathrm{S}}_{(lk)} = E^{S}_{(lk)} \quad \text{and} \quad \omega^{\mathrm{S}}_{lk} = E^{S}_{lk} = \frac{1}{2\mu^{*}} S^{S}_{lk} \,. \tag{4.23}$$

Equations of motion for asymmetric fields

In the equation of motion for the continuum with asymmetric fields (Eq. 4.8) the elastic stresses split into the total and self fields with the condition that traces of these tensors remain equal to each other

$$S_{(ik)} = S^T_{ik} - S^S_{(ik)}, \quad S_{(nn)} = S^T_{nn}, \quad E_{(nn)} = E^T_{nn} \,. \tag{4.24}$$

The symmetric parts of the elastic stresses relate to elastic strains according to the constitutive law (4.4) and to self-rotations according to (4.23); we obtain:

$$\left(\frac{\partial}{\partial x_k \partial x_s} (S^T_{(lk)} - 2\mu^* \omega^S_{(lk)}) \right)_{(ls)} = \rho \frac{\partial^2}{\partial t^2} (E^{\mathrm{T}}_{ls} - \omega^{\mathrm{S}}_{ls})$$

$$+ \rho \frac{\partial}{\partial t} J_{ls} \left(\frac{(\lambda+\mu)}{\partial x_l \partial x_s} \frac{\partial^3 u_k}{\partial x_k} + \frac{\mu}{\partial x_k \partial x_k} \frac{\partial^3 u_l}{\partial x_s} - \frac{2\mu^* \partial^2 \omega^S_{(lk)}}{\partial x_k \partial x_s} \right)_{(sl)}$$

$$= \rho \left(\frac{\partial \ddot{u}_l}{\partial x_s} \right)_{(sl)} - \rho \ddot{\omega}^S_{(sl)} + \rho \dot{J}_{(sl)} \,. \tag{4.25}$$

For a homogeneous elastic continuum (vanishing of currents) we obtain

$$\left(\frac{(\lambda+\mu)}{\partial x_l \partial x_s} \frac{\partial^3 u_k}{\partial x_k} + \frac{\mu}{\partial x_k \partial x_k} \frac{\partial^3 u_l}{\partial x_s} - \frac{2\mu^* \partial^2 \omega^S_{(lk)}}{\partial x_k \partial x_s} \right)_{(sl)}$$

$$= \rho \left(\frac{\partial \ddot{u}_l}{\partial x_s} \right)_{(sl)} - \rho \ddot{\omega}^S_{(sl)} \,. \tag{4.26}$$

For the antisymmetric part of elastic stresses we shall take into account the fact that the stress moments and antisymmetric stresses shall enter into the equilibrium conditions; in the homogeneous continuum theory we assume that strain moments relate to the antisymmetric part of strains and, thus, the respective equations reduce to relation between the antisymmetric stresses and antisymmetric strains and rotations (Teisseyre 2002, Teisseyre and Boratyński 2003).

Antisymmetric stresses relate to an internal rotation motion; these stresses become important in zones with higher dislocation densities and their evolution (zones under high stresses) or in zones where microfractures nucleate; in such zones we can expect the presence of rotation nuclei. Considering a slip/fracture process along the tectonic plane, we can try to split our equations of motion into two parts: one describing the dynamic process in which the interaction of defects is confined to the very close vicinity of this plane, and the other relating to radiation in the surrounding

elastic space. This method has been introduced by Teisseyre and Yamashita (1999).

For the antisymmetric stress $S_{[in]}$ we apply the balance law, expressing, on the one hand, the rotation of force $\partial S_{[in]}/\partial x_n$ acting on a body element due to the antisymmetric stresses (rotational moment of forces per infinitesimal arm length corresponding to stress moments), and, on the other hand, the balancing term, the acceleration related to angular momentum:

$$\in_{lki} \frac{\partial}{\partial x_k \partial x_n} S_{[ni]} = \rho \frac{1}{2} \frac{\partial^2}{\partial t^2} \in_{lki} \omega_{[ki]} . \tag{4.27}$$

Equivalently, using the constitutive law (4.22) we obtain:

$$-2\mu^* \in_{lki} \frac{\partial}{\partial x_k \partial x_n} \omega^S_{[ni]} = \rho \frac{1}{2} \frac{\partial^2}{\partial t^2} \in_{lki} \left(\left(\frac{\partial u_i}{\partial x_k} \right)_{[ki]} - \omega^S_{[ki]} \right). \tag{4.28}$$

In this equations there appears the dislocation current which can be alternatively expressed by the dislocation density and its motion velocity, where the latter can be expressed by a difference of stress and stress resistance (Mataga *et al*. 1987, Teisseyre 2001, Teisseyre and Boratyński 2003).

Stress resistance is related to rotational deformations of grains (inner friction), but let us note that also other geometrical objects, the in-plane and out-of-plane deformations of dislocation lines; kinks and jogs (Kocks *et al*. 1975) hamper a motion of dislocations influencing only a coefficient at stress resistance (as the density of the objects increases with increasing dislocation density and its velocity field).

Correspondence to the micropolar theory

In the micropolar theory the motion equation for a stress moment becomes

$$m_{is,s} + \in_{isl} S_{[sl]} + \in_{isl} \rho L_{[sl]} = \rho N \ddot{\omega}^S_{(i)} , \tag{4.29}$$

where the isotropic inertia tensor is proportional to a square of the characteristic length; $m_{is,s}$ are the microstress moments.

When passing to a continuum with the vanishing characteristic length and $m_{is,s} = 0$, this relation becomes only stating that antisymmetric stresses depend on the body couples, e.g., on an internal rotation moments in an earthquake focus:

$$\in_{isl} S_{[sl]} + \in_{isl} \rho L_{[sl]} = 0 , \tag{4.30}$$

while the acceleration of an angular motion $\ddot{\omega}^S_{(i)}$ becomes related to a higher order moments as presented in the previous sections.

Degenerated mechanics

When the displacement motions vanish, we obtain, respectively, from relations (4.26) and (4.27):

$$\left(\frac{\partial \omega^S_{(lk)}}{\partial x_k \partial x_s}\right)_{(ls)} = \frac{1}{V_T^2}\frac{\partial^2}{\partial t^2}\omega^S_{(sl)}\,, \quad \in_{lki}\frac{\partial}{\partial x_k \partial x_n}\omega^S_{[ni]} = \frac{1}{V_R^2}\frac{\partial^2}{\partial t^2}\omega^S_{[l]}\,, \tag{4.31}$$

where $V_T^2 = V_R^2 = 2\mu^*/\rho$ and the velocities for spin and twist waves are equal.

For the spin motion $\omega_{[s]}$ and the bend-twist motion $\omega_{(s)}$ we can write the following conservation laws (Teisseyre 2004):

$$\frac{\partial}{\partial x_k}\omega^S_{[k]} = 0 \quad \text{or} \quad \in_{k\mathbf{mn}}\frac{\partial}{\partial x_k}\omega^S_{[mn]} = 0$$
$$\text{and} \qquad \omega^{\mathrm{S}}_{(\mathrm{s}),\mathrm{s}} = \in_{s\mathbf{mn}}\frac{\partial}{\partial x_s}\omega^S_{(mn)} = -4\pi\Gamma\,, \tag{4.32}$$

where the symbol $\in_{s\mathbf{mn}}$ with the bold indexes means that this antisymmetric tensor is applied without permutation over these indexes.

The conservation law for the bend-twist motion provides a new quantity Γ, which may be related to some source object, called the bending charge; its meaning will be considered in a next chapter.

Relations (4.31) represent the pure bend-twist and spin transverse waves with elastic bonds; there is no attenuation under the usual assumptions as used for ideal elastic body. This case presents a kind of degenerated mechanics; usually, we consider continuum mechanics in terms of the theory with displacement field and without spin motion, but here we have a reverse situation: we have spin and bend-twist motion and no displacement field.

References

Boratyński W, Teisseyre R (2004) Generalized continuum with defects and asymmetric stresses. Acta Geophys Pol **52**: 2, 185-195

Eringen AC (1999) Microcontinuum field theories. Springer, Berlin

Eringen AC, Claus WD Jr. (1970) A micromorphic approach to dislocation theory and its relation to several existing theories, fundamental aspects of dislocation theory. Nat Bur Stand (US), Spec Publ **317**: II, 1023-1040

Eringen AC, Kafadar CB (1976) Polar field theories. In: Eringen AC (ed) Continuum physics, vol 4. Academic Press, New York

Eringen AC, Suhubi ES (1964) Non-linear theory of simple micro-elastic solids – I. Int J Engng Sci **2**: 189-203

Kocks UF, Argon AS, Ashby MF (1975) Thermodynamics and kinetics of slip. Pergamon Press, Oxford–New York, 288 pp

Kossecka E, DeWitt R (1977) Disclination kinematic. Arch Mech **29**: 633-651

Kröner E (1958) Kontinuums Theories der Versetzungen und Eigenspannungen. Ergeb Angew Math, Berlin

Kröner E (1981) Continuum Theory of defects. In: Balian et al (eds) Les Houches, Session XXXV, 1980, Physique des Defauts/Physics of Defects, North Holland Publ Com, Dordrecht

Mataga PA, Freund LB, Hutchison JW (1987) Crack tip plasticity in dynamic fracture. J Phys Chem Solid 48: 985-1005

Muskhelishvili NI (1953) Some basic problems of the mathematical theory of elasticity. P Noordhoff Ltd, Gröningen.

Nagahama H (2001) Gauge theory of dislocational electromagnetic field in earthquake preparation zone. Acta Geophys Pol **49**: 4, 437-448

Shimbo M (1975) A geometrical formulation of asymmetric features in plasticity. Bull Fac Eng, Hokkaido Univ **77**: 155-159

Shimbo M (1995) Non-Riemannian geometrical approach to deformation and friction. In: R Teisseyre (ed) Theory of earthquake premonitory and fracture processes, PWN, Warszawa, pp 520-528

Shimbo M, Kawaguchi M (1976) A note on the asymmetric fields. Bull Fac Eng, Hokkaido Univ **80**: 75-79 (in Japanese)

Teisseyre R (1986) Thermal stresses. In: Teisseyre R (ed) Continuum theories in solid earth physics, PWN, Warszawa – Elsevier, Amsterdam, pp 322-352

Teisseyre R (1997) Dislocation-stress relations and evolution of dislocation fields. Acta Geophys Pol **45**: 3, 205-214

Teisseyre R (2001) Evolution, propagation and diffusion of dislocation fields. In: Teisseyre R, Majewski E (eds) Earthquake thermodynamics and phase transformations in the earth's interior (vol. 76 of International Geophysical Series), Academic Press, San Diego, pp 167-198

Teisseyre R (2002) Continuum with defect and self-rotation nuclei. Acta Geophys Pol **50**: 1, 51-68

Teisseyre R (2004) Spin and twist motions in a homogeneous elastic continuum and cross-band geometry of fracturing. Acta Geophys Pol **52**: 2, 173-183

Teisseyre R, Boratyński W (2002) Continua with self-rotation nuclei: evolution of defect fields and equations of motion. Acta Geophys Pol **50**: 2, 223-229

Teisseyre R, Boratyński W (2003) Continua with self-rotation nuclei: evolution of asymmetric fields. Mech Res Com **30**: 235-240

Teisseyre R, Kozák J (2003) Considerations on the seismic rotation effects. Acta Geophys Pol **51**: 3, 243-256

Teisseyre R, Yamashita T (1999) Splitting stress motion equation into seismic wave and fault-related fields. Acta Geophys Pol **47**: 1, 135-147

5 Degenerated Asymmetric Continuum Theory

Roman Teisseyre, Mariusz Białecki, Marek Górski

Institute of Geophysics, Polish Academy of Sciences
ul. Księcia Janusza 64, 01-452 Warszawa, Poland
e-mails: rt@igf.edu.pl; bialecki@igf.edu.pl

5.1 Introduction

We define the degenerated mechanics as that in which the displacement motions are neglected and only the spin and bend-twist motions can exist as the only independent elastic fields (Teisseyre 2005, Teisseyre et al. 2005). We consider the spin and twist motions in a homogeneous continuum. This case is opposite to that of the classic ideal elasticity. The appropriate constitutive laws support the existence of an elastic response due to the rotational deformations of bonds in a lattice network. We introduce a system of potentials which would help us to understand the waves and geometrical features of degenerated mechanics and its Riemannian geometry.

Figure 5.1 presents the bond deformations related to rotation of grains for a spin motion and for shears. A geometrical description of the other type

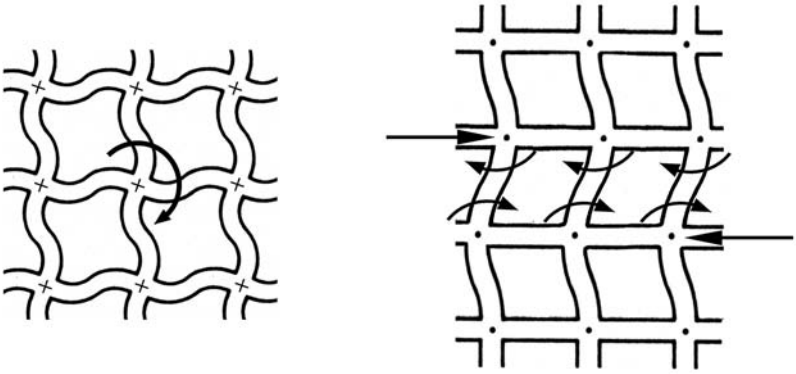

Fig. 5.1 Deformation of the bond caused by rotation of grains for a spin motion (*left*) and for shear strains (*right*)

of axial deformation, the bend-twist (Teisseyre 2004, 2005), will be given at the end of this chapter. The bonds related to rotational deformations can be considered to be weaker than those related to elastic rigidity moduli.

As explained in the former chapter the total rotation is equal to the sum of elastic rotation and self-rotation fields. However, when displacements vanish, the total rotation, as represented by the antisymmetric tensor, vanishes too:

$$\omega_{ki}^{T} = \omega_{ki} + \omega_{ki}^{S} = 0\,, \qquad \omega_{ki} = -\omega_{ki}^{S}\,. \tag{5.1}$$

The antisymmetric part of the self-rotation field, $\omega_{[ki]}^{S} = -\omega_{[ki]}$, gives rise to a proper rotation motion (spin), while its symmetric part, $\omega_{(ki)}^{S} = -\omega_{(ki)}$, relates to the symmetric axial motion called the bend-twist motion. The self-fields related to rotation nuclei ω_{ki}^{S} present the possible sources of rotation processes and bring us to a world of asymmetric continuum. The antisymmetric stresses correspond to stress moments (see Teisseyre 2005).

The bend-twist deformations present the grain deformations caused by elastic strain; however, when considering the grains as the "rigid" points of continuum, such bend-twist deformation converts to a kind of a 3D space curvature, see further on.

In a degenerated continuum, the asymmetric self-rotation is exactly opposite to an asymmetric elastic rotation, $\boldsymbol{\omega}^{S} = -\boldsymbol{\omega}$.

Vector representations of the spin and bend-twist tensors are as follows:

$$\omega_{[s]} = \frac{1}{2}\in_{smn}\omega_{[mn]} = \in_{s\mathbf{mn}}\omega_{[\mathbf{mn}]}\,, \qquad \omega_{(s)} = \in_{s\mathbf{mn}}\omega_{(\mathbf{mn})}\,, \tag{5.2}$$

where we introduced a convention for the bold indexes in the skew-tensor $\in_{s\mathbf{mn}}$ which means that a permutation over these indexes is excluded (no sum over the bold indexes in $\in_{s\mathbf{mn}}\omega_{(\mathbf{mn})}$, so such a product of the antisymmetric and symmetric tensors does not vanish).

The conservation laws for the spin and twist-bend fields can be written as follows:

$$\omega_{[s],s} = 0 \qquad \text{and} \qquad \omega_{(s),s} = 4\pi\Gamma\,. \tag{5.3}$$

Scalar field Γ is defined as a divergence of the bend-twist vector and becomes related to a possible space curvature; such a curvature can represent a matter or its density field.

Considering now the complex field $\omega_s = \omega_{[s]} + \mathrm{i}\omega_{(k)}$, we have the continuity law

$$\iint \in_{kps} (\omega_{[s],p} + \mathrm{i}\omega_{(s),p})\,\mathrm{d}s_k = \iint\left(\frac{\partial}{\mathrm{i}V\partial t}(\omega_{[k]} + \mathrm{i}\omega_{(k)}) + 4\pi I_k\right)\mathrm{d}s_k\,, \tag{5.4}$$

where the current I_k is introduced as related to the scalar field Γ. From this relation we get:

$$\in_{kps} \frac{\partial}{\partial x_p}\omega_{[s]} - \frac{1}{V}\dot{\omega}_{(k)} = 4\pi I_k\,, \qquad \in_{kps} \frac{\partial}{\partial x_p}\omega_{(s)} + \frac{1}{V}\dot{\omega}_{[k]} = 0\,. \tag{5.5}$$

The introduced velocity V is related to the rotation rigidity modulus μ^* as follows:

$$V^2 = 2\mu^*/\rho$$

In these equations, when considering the moving frames, we may assume the relativistic way for a sum of velocities and, therefore, when velocity V will approach c, we obtain a complete similarity between the degenerated mechanics with the formalism of EM theory ($\omega_{[s]} = B_s$, $\omega_{(s)} = E_s$, $I_k = J_k$, $q = \rho$, $V = c$). However, further on we will consider some special cases of the degenerated mechanics being distinctly different.

From relations (5.5) we get the wave equations:

$$\frac{\partial^2}{\partial x_n \partial x_n}\omega_{[k]} - \frac{1}{V^2}\frac{\partial^2}{\partial t^2}\omega_{[k]} = \frac{4\pi}{V} \in_{kps} \frac{\partial}{\partial x_p} I_s\,, \tag{5.6}$$

$$\frac{\partial^2}{\partial x_n \partial x_n}\omega_{(k)} - \frac{1}{V^2}\frac{\partial^2}{\partial t^2}\omega_{(k)} = -\frac{4\pi}{V^2}\dot{I}_k + 4\pi\frac{\partial}{\partial x_k}\Gamma\,. \tag{5.7}$$

However, Eq. (5.7) differs from that derived by Teisseyre (2005) from the motion equations for the symmetric and asymmetric stresses with the displacement and rotation motions existing together; when reducing the above-mentioned motion equations to the case with the vanishing displacement field **u** = 0 (see Eqs. (35) and (37) in Teisseyre 2005) we would obtain the equation different from Eq. (5.7). The explanation of these facts is the following: the former equations, supplemented additionally with some body angular moments $\Omega_{[l]}$ and $\bar{\Omega}_{(k)}$, had the following form:

$$\frac{\partial}{\partial x_n \partial x_n}\omega_{[l]} - \frac{1}{V^2}\frac{\partial^2}{\partial t^2}\omega_{[l]} = \Omega_{[l]}\,, \tag{5.8}$$

$$\left(\frac{\partial \omega_{(lk)}}{\partial x_k\, \partial x_s}\right)_{(sl)} - \frac{1}{V^2}\frac{\partial^2}{\partial t^2}\omega_{(sl)} = \in_{\mathbf{ls}k}\, \bar{\Omega}_{(k)} \tag{5.9}$$

($\in_{\mathbf{ls}k}$: no permutation for **ls**).

Equations (5.8) and (5.9) were derived under the assumption of additional constitutive laws for rotation motion and related stresses, which for the case when the displacement field is neglected reduce to the following:

$$S^S_{[ik]} = 2\mu^* \omega^S_{[ik]} = -2\mu^* \omega_{[ik]}\,, \tag{5.10}$$

$$S^S_{(ts)} = 2\mu^* \omega^S_{(ts)} = -2\mu^* \omega_{(ts)}\,. \tag{5.11}$$

The first of these represents the Shimbo (1975, 1995) law for the antisymmetric stresses and internal friction related to rotation of grains, while the second relates to a strain caused by the grain deformation (the deformable grains constituting the continuum, similar to that of the micromorphic type). The spin motion (5.8) coincides with (5.6) when putting

$$\Omega_{[l]} = \frac{4\pi}{c} \in_{lps} \frac{\partial}{\partial x_p} I_s\,.$$

We have mentioned that the second relation for the bend-twist motion (Eq. 5.9) remains different in an essential way from that derived in the present paper (Eq. 5.7). The only reason is the choice of the constitutive law for bend-twist deformation and self-stress (5.11), having the same form as for the spin field (5.10), as proposed in the former paper (see Eq. 26 in Teisseyre 2005). However, when constructing a consistent theory for the degenerated motion, including the continuity law (5.3), we are forced to introduce, instead of (5.11), the new constitutive law for the symmetric part of rotation tensor and self-stresses:

$$\left(\frac{\partial}{\partial x_s} S^S_{(tn)}\right)_{(ts)} = -2\mu^* \left(\frac{\partial \omega_{(ts)}}{\partial x_n}\right) \tag{5.12}$$

or

$$\left(\delta_{si} S^S_{(tn)}\right)_{(ts)} = -2\mu^* \delta_{ni} \omega_{(ts)} = 2\mu^* \delta_{ni} \omega^S_{(ts)}\,. \tag{5.12a}$$

Such a relation permits to describe properly the space curvature for a medium with non-deformable volume elements (point rigid-grains forming a continuum).

With the new constitutive relation (5.12) we obtain a new form of motion equation

$$\frac{\partial \omega_{(k)}}{\partial x_n \partial x_n} - \frac{1}{V^2}\frac{\partial^2}{\partial t^2}\omega_{(k)} = \bar{\Omega}_{(k)}\,, \tag{5.13}$$

which for $\bar{\Omega}_{(k)} = -\frac{4\pi}{c^2}\dot{I}_k + 4\pi\Gamma_{,k}$ coincides exactly with (5.7).

Antisymmetric potentials for rotation motions

We define a set of 3D vector potentials $\tilde{A}_s$ and $\hat{A}_s$, and the current potentials ψ_s and φ in the following way (Teisseyre et al. 2005):

$$\omega_{[k]} = \in_{kbs} \tilde{A}_{s,b}\,, \quad \omega_{(k)} + \varphi_{,k} = \in_{kbs} \hat{A}_{s,b}\,, \quad \tilde{A}_{s,s} = 0\,, \quad \hat{A}_{s,s} = 0\,, \tag{5.14}$$

$$\frac{4\pi}{V} I_k = \frac{1}{V}\dot{\varphi}_{,k} + \frac{1}{V} \in_{kbs} \psi_{s,b}\,, \qquad \varphi_{,kk} = -4\pi\Gamma\,, \tag{5.15}$$

where we can define the vector current potentials ψ_s and φ acccording to the relation

$$4\pi \in_{ndk} I_{k,d} = -\in_{ndk}\in_{kbs} \psi_{,bd} = \psi_{n,ss}\,, \qquad \psi_{s,s} = 0\,. \tag{5.16}$$

The potentials $\tilde{A}_s$ and $\hat{A}_s$ may be related to the axial motions in the 6D space geometry – see further on. According to the spin and bend-twist motion equations (5.5) and (5.3), we shall put for the potentials defined by Eq. (5.14):

$$\in_{kbs} \tilde{A}_{s,b} - \frac{1}{V}\frac{\partial}{\partial t}\tilde{A}_k = \frac{1}{V}\psi_k\,, \qquad \hat{A}_{b,b} = 0\,, \tag{5.17}$$

$$\in_{kbs} \hat{A}_{s,b} + \frac{1}{V}\frac{\partial}{\partial t}\hat{A}_k = 0\,, \qquad \tilde{A}_{b,b} = 0\,. \tag{5.18}$$

As we know, the tensor of the EM field can be constructed from the EM vector fields, B_s and E_s. In a similar manner we can proceed with the 4D tensor fields $\omega_{\mu\nu}$; according to definitions (5.2) and (5.5), we can write such tensors in the moving frame $x_\mu = \{x_m, \mathrm{i}Vt\}$ as follows:

$$\omega_{\mu\nu} = \omega_{[\mu\nu]} + \mathrm{i}\omega_{(\mu\nu)}\,, \tag{5.19}$$

$$\omega_{\mu\nu} = \begin{bmatrix} 0 & \omega_{[z]} & -\omega_{[y]} & -\mathrm{i}\omega_{(x)} \\ -\omega_{[z]} & 0 & \omega_{[x]} & -\mathrm{i}\omega_{(y)} \\ \omega_{[y]} & -\omega_{[x]} & 0 & -\mathrm{i}\omega_{(z)} \\ \mathrm{i}\omega_{(x)} & \mathrm{i}\omega_{(y)} & \mathrm{i}\omega_{(z)} & 0 \end{bmatrix} + \mathrm{i}\begin{bmatrix} 0 & \omega_{(z)} & -\omega_{(y)} & \mathrm{i}\omega_{[x]} \\ -\omega_{(z)} & 0 & \omega_{(x)} & \mathrm{i}\omega_{[y]} \\ \omega_{(y)} & -\omega_{(x)} & 0 & \mathrm{i}\omega_{[z]} \\ -\mathrm{i}\omega_{[x]} & -\mathrm{i}\omega_{[y]} & -\mathrm{i}\omega_{[z]} & 0 \end{bmatrix}.$$

Now we may construct the complex antisymmetric tensor for potentials $A_{\alpha\beta}$:

$$A_{\alpha\beta} = \tilde{A}_{\alpha\beta} + \mathrm{i}\hat{A}_{\alpha\beta}\,, \tag{5.20}$$

$$A_{\alpha\beta} = \begin{bmatrix} 0 & \tilde{A}_3 & -\tilde{A}_2 & -\mathrm{i}\hat{A}_1 \\ -\tilde{A}_3 & 0 & \tilde{A}_1 & -\mathrm{i}\hat{A}_2 \\ \tilde{A}_2 & -\tilde{A}_1 & 0 & -\mathrm{i}\hat{A}_3 \\ \mathrm{i}\hat{A}_1 & \mathrm{i}\hat{A}_2 & \mathrm{i}\hat{A}_3 & 0 \end{bmatrix} + \mathrm{i}\begin{bmatrix} 0 & \hat{A}_3 & -\hat{A}_2 & \mathrm{i}\tilde{A}_1 \\ -\hat{A}_3 & 0 & \hat{A}_1 & \mathrm{i}\tilde{A}_2 \\ \hat{A}_2 & -\hat{A}_1 & 0 & \mathrm{i}\tilde{A}_3 \\ -\mathrm{i}\tilde{A}_1 & -\mathrm{i}\tilde{A}_2 & -\mathrm{i}\tilde{A}_3 & 0 \end{bmatrix}$$

or

$$A_{\alpha\beta} = \begin{bmatrix} 0 & \overline{A}_3 & -\overline{A}_2 & -\overline{A}_1 \\ -\overline{A}_3 & 0 & \overline{A}_1 & -\overline{A}_2 \\ \overline{A}_2 & -\overline{A}_1 & 0 & -\overline{A}_3 \\ \overline{A}_1 & \overline{A}_2 & \overline{A}_3 & 0 \end{bmatrix}, \qquad \overline{A}_k = \tilde{A}_k + \mathrm{i}\hat{A}_k\,. \tag{5.21}$$

According to (5.17) and (5.18), the tensor $A_{\alpha\beta}$ fulfils the conditions:

$$A_{\alpha\beta,\beta} = \frac{1}{V}\psi_\alpha\,, \qquad \psi_\alpha = \{\psi_k, 0\} \tag{5.22}$$

leading to the wave equations:

$$\Box\tilde{A}_n = \tilde{J}_n\,, \quad \tilde{A}_{s,s} = 0\,, \quad \Box\hat{A}_n = \hat{J}_n\,, \quad \hat{A}_{s,s} = 0\,, \tag{5.23}$$

where

$$\tilde{J}_n = -\frac{1}{V}\in_{ndk}\psi_{k,d}\,, \qquad \hat{J}_k = \frac{1}{V^2}\frac{\partial}{\partial t}\psi_k\,. \tag{5.24}$$

When defining the tensor $J_{\alpha\beta}$

$$J_{\alpha\beta} = \begin{bmatrix} 0 & \overline{J}_3 & -\overline{J}_2 & -\overline{J}_1 \\ -\overline{J}_3 & 0 & \overline{J}_1 & -\overline{J}_2 \\ \overline{J}_2 & -\overline{J}_1 & 0 & -\overline{J}_3 \\ \overline{J}_1 & \overline{J}_2 & \overline{J}_3 & 0 \end{bmatrix}, \qquad \overline{J}_n = \tilde{J}_n + \mathrm{i}\hat{J}_n \tag{5.25}$$

we arrive at the relation

$$\Box A_{\alpha\beta} = J_{\alpha\beta} . \tag{5.26}$$

Applying the operator $\in_{sbn} \partial/\partial x_b$ we obtain Eqs. (5.6) and (5.7).

5.2 Transition to Symmetric Tensor of Potentials

We will present now a way how to arrive at the **symmetric tensor** of potentials in order to combine it with the 4D metric tensor $g^{\alpha\beta}$.

We introduce the new potentials $N_s = \tilde{N}_s + \mathrm{i}\hat{N}_s$ fulfilling the additional conditions:

$$N_s = \in_{skn} \Omega_{n,k} , \quad \Omega_1 = \Theta_{,1} , \quad \Omega_2 = \Theta_{,2} , \tag{5.27}$$

which reduce these potentials to the 2D form: N_S with $S = \{1, 2\}$, as $N_3 = 0$. It also follows from (5.27) that

$$N_{S,S} = N_{1,1} + N_{2,2} = 0 \tag{5.28}$$

and we postulate the following bridge relations to the formerly defined potentials:

$$\in_{kbs} \tilde{N}_{s,b} = \in_{kbs} \tilde{A}_{s,b} , \quad \in_{kbs} \hat{N}_{s,b} = \in_{kbs} \hat{A}_{s,b} . \tag{5.29}$$

With these conditions, we introduce the natural **symmetric tensor** of potentials in the 4D form:

$$N_{\alpha\beta} = \tilde{N}_{\alpha\beta} + \mathrm{i}\hat{N}_{\alpha\beta} , \quad Y_N = \tilde{Y}_N + \mathrm{i}\hat{Y}_N , \tag{5.30}$$

$$\Box N_{\alpha\beta} = \Box \begin{bmatrix} 0 & 0 & -N_2 & -N_1 \\ 0 & 0 & N_1 & -N_2 \\ -N_2 & N_1 & 0 & 0 \\ -N_1 & -N_2 & 0 & 0 \end{bmatrix} = Y^{\alpha\beta} = \begin{bmatrix} 0 & 0 & -Y_2 & -Y_1 \\ 0 & 0 & Y_1 & -Y_2 \\ -Y_2 & Y_1 & 0 & 0 \\ -Y_1 & -Y_2 & 0 & 0 \end{bmatrix}. \tag{5.31}$$

Similarly, we shall define the 2D vector of current potentials η_K which shall fulfil the following bridge relation to the previously defined current potentials ψ_s (Eq. 5.22):

$$-\eta_{1,3} = \in_{2bs} \psi_{s,b}\,, \quad -\eta_{2,3} = \in_{1bs} \psi_{s,b}\,, \quad -\eta_{1,2} - \eta_{2,1} = \in_{3dk} \psi_{k,d} \tag{5.32}$$

and, instead of relations (5.24) for currents $\tilde{J}_N$ and $\hat{J}_N$, we have introduced the new definitions:

$$-\frac{1}{c}\eta_{1,3} = \tilde{Y}_2\,, \qquad \frac{1}{V}\eta_{2,3} = \tilde{Y}_1\,, \qquad \frac{1}{V}\frac{\partial}{\partial t}\eta_N = \hat{Y}_N\,. \tag{5.33}$$

Having these bridge relations we obtain, similarly to (5.22)–(5.24), the following equations for the 4D symmetric potentials for spin and bend-twist motions, $\omega_s = \omega_{[s]} + \mathrm{i}\omega_{(k)}$, and the related current potentials $\eta_\alpha = \{\eta_K, 0, 0\}$:

$$\begin{gathered} \Box\tilde{N}_N = \tilde{Y}_N = -\frac{1}{V}\in_{NdK} \eta_{K,d}\,, \qquad \Box\hat{N}_N = \hat{Y}_N = \frac{1}{V^2}\frac{\partial}{\partial t}\eta_N\,, \\ N_{\alpha\beta,\beta} = \frac{1}{V}\eta_\alpha\,, \qquad \Box N_{\alpha\beta} = Y_{\alpha\beta}\,. \end{gathered} \tag{5.34}$$

We will show, further on, that all these symmetric matrices are the tensors related to the γ-Dirac tensors.

Space curvature and complex metric tensor

The tensor of potentials (5.31) can be written as follows:

$$\begin{aligned} N_{\alpha\beta} = {} & \tilde{N}_1 \begin{bmatrix} 0 & 0 & 0 & -1 \\ 0 & 0 & 1 & 0 \\ 0 & 1 & 0 & 0 \\ -1 & 0 & 0 & 0 \end{bmatrix} + \tilde{N}_2 \begin{bmatrix} 0 & 0 & -1 & 0 \\ 0 & 0 & 0 & -1 \\ -1 & 0 & 0 & 0 \\ 0 & -1 & 0 & 0 \end{bmatrix} \\ & + \hat{N}_1 \begin{bmatrix} 0 & 0 & 0 & -\mathrm{i} \\ 0 & 0 & \mathrm{i} & 0 \\ 0 & \mathrm{i} & 0 & 0 \\ -\mathrm{i} & 0 & 0 & 0 \end{bmatrix} + \hat{N}_2 \begin{bmatrix} 0 & 0 & -\mathrm{i} & 0 \\ 0 & 0 & 0 & -\mathrm{i} \\ -\mathrm{i} & 0 & 0 & 0 \\ 0 & -\mathrm{i} & 0 & 0 \end{bmatrix} \end{aligned} \tag{5.35}$$

or

$$N_{\alpha\beta} = \tilde{N}_1 \in^1 + \tilde{N}_2 \in^2 + \mathrm{i}\hat{N}_1 \in^1 + \mathrm{i}\hat{N}_2 \in^2 = N_1 \in^1 + N_2 \in^2 . \tag{5.36}$$

The complimentary tensors are:

$$\in^3 = \begin{bmatrix} 0 & 0 & 0 & \mathrm{i} \\ 0 & 0 & \mathrm{i} & 0 \\ 0 & -\mathrm{i} & 0 & 0 \\ -\mathrm{i} & 0 & 0 & 0 \end{bmatrix}, \qquad \in^4 = \begin{bmatrix} \mathrm{i} & 0 & 0 & 0 \\ 0 & \mathrm{i} & 0 & 0 \\ 0 & 0 & -\mathrm{i} & 0 \\ 0 & 0 & 0 & -\mathrm{i} \end{bmatrix}. \tag{5.37}$$

The matrices $\in^{\nu}$ fulfil the conditions for the γ-Dirac matrices for the Minkovski-like space:

$$x_\mu = \{x_m, \mathrm{i}Vt\}, \quad \mathrm{d}S^2 = \mathrm{d}x_k \mathrm{d}x_k - V^2 \mathrm{d}t\,\mathrm{d}t , \tag{5.38}$$

$$\in^\alpha \in^\beta + \in^\beta \in^\alpha = 2\eta^{\alpha\beta} . \tag{5.39}$$

However, when disturbing these matrices in the way indicated below

$$\gamma^1 = (1 + N_1) \in^1 , \quad \gamma^2 = (1 + N_2) \in^2 , \quad \gamma^3 = \in^3 , \quad \gamma^4 = \in^4 \tag{5.40}$$

we obtain the known relation for the Dirac matrices:

$$\gamma^\alpha \gamma^\beta + \gamma^\beta \gamma^\alpha = 2g^{\alpha\beta} . \tag{5.41}$$

Thus, we have the complex disturbances N_1 and N_2 as the first order disturbances to the metric tensor:

$$g^{\alpha\beta} \approx \begin{bmatrix} 1+2N_1 & 0 & 0 & 0 \\ 0 & 1+2N_2 & 0 & 0 \\ 0 & 0 & 1 & 0 \\ 0 & 0 & 0 & -1 \end{bmatrix}. \tag{5.42}$$

Note that the tensor $Y_{\alpha\beta}$ can be also built with the help of the Dirac tensors:

$$Y_{\alpha\beta} = \tilde{Y}_1 \in^1 + \tilde{Y}_2 \in^2 + \mathrm{i}\hat{Y}_1 \in^1 + \mathrm{i}\hat{Y}_2 \in^2 \tag{5.43}$$

and we might be able to consider the Einstein-like relations for our degenerated mechanics, but we prefer to avoid such considerations as being, too abstract (see Teisseyre 2005, Teisseyre et al. 2005).

We shall only note that, instead of the 4D presentation, it was also possible to present our relations in the 2D forms with the tensor

$$N_{AB} = \begin{bmatrix} N_2 & N_1 \\ N_1 & -N_2 \end{bmatrix}$$

and with the help of the 2D Pauli tensors

$$\sigma_1 = \begin{bmatrix} 0 & 1 \\ 1 & 0 \end{bmatrix}, \quad \sigma_2 = \begin{bmatrix} 0 & -\mathrm{i} \\ \mathrm{i} & 0 \end{bmatrix}, \quad \sigma_3 = \begin{bmatrix} 1 & 0 \\ 0 & -1 \end{bmatrix}.$$

5.3 Special Case

As we already metioned, our considerations relate the moving frame $x_\mu = \{x_m\ , \mathrm{i}Vt\}$. Let us consider a very special case with vanishing of the currents; according to (5.15) this assumption requires to put

$$\dot{\varphi}_{,k} = 0, \qquad \psi_s = 0, \qquad \eta_S = 0. \tag{5.44}$$

For such a case, our equations become

$$\frac{\partial^2}{\partial x_n \partial x_n}\omega_{[k]} - \frac{1}{V^2}\frac{\partial^2}{\partial t^2}\omega_{[k]} = 0, \quad \frac{\partial^2}{\partial x_n \partial x_n}\omega_{(k)} - \frac{1}{V^2}\frac{\partial^2}{\partial t^2}\omega_{(k)} = 4\pi\frac{\partial}{\partial x_k}\Gamma. \tag{5.45}$$

For the antisymmetric potentials, we shall change Eqs. (5.14) and (5.15) for rotation motions as follows:

$$\begin{aligned} &\omega_{[k]} = \in_{kbs} \tilde{A}_{s,b}\ , \qquad \omega_{(k)} + \varphi_{,k} = \in_{kbs} \hat{A}_{s,b}\ , \\ &\dot{\varphi}_{,k} = 0, \qquad \varphi_{,kk} = -4\pi\Gamma. \end{aligned} \tag{5.46}$$

The potential φ corresponds to the classic gravity-like potential; the field Γ when related to a space curvature can be assumed to be positive-definite.

When introducing the natural symmetric tensor of potentials as before (Eq. 5.31) and the related conditions (5.27)–(5.29), we obtain, instead of (5.34), the following equations:

$$N_{S\beta,\beta} = 0, \qquad \Box N_{\alpha\beta} = 0 \tag{5.47}$$

and, as mentioned above, the complex disturbances N_1 and N_2 which fit the Dirac-type presentation can be combined with the disturbances to metric tensor $g^{\alpha\beta}$ (Eq. 5.42); for the scalar of curvature tensor (3D Riemannian geometry) we obtain for this special case

$$R = h_{\nu}^{\alpha}\Big|_{\alpha}^{\nu} - h_{\nu}^{\nu}\Big|_{\alpha}^{\alpha} = -2\square N_1 - 2\square N_2 = 0\,. \tag{5.48}$$

5.4 Conclusions

The conservation and balance laws for spin and twist fields and the stress-related equations of motion for symmetric and antisymmetric parts of stresses can be treated as source functions describing the spin and twist processes accompanying the fracture processes. For the related rotation waves, of spin and twist type, there is no attenuation as for the ideal elastic waves; these motions are accompanied by the related rotational vibration of the points of continuum.

The degenerated continuum mechanics leads to deformations of the Euclidean space into a Riemannian one and can be described by the complex equations similar, in the form, to that for the EM fields and may, when assuming the special case of the theory, describe also the classic gravity.

With a new constitutive law joining the self-rotations with asymmetric stresses, we can evade an influence of the Hook law, which in the ideal elasticity rules out an existence of the rotation waves, even in a homogeneous elastic continuum. Thus, it is not true that in a homogeneous elastic continuum the rotation vibrations are automatically attenuated and ruled out.

An alternative way to introduce the rotation motions, based on a concept of the asymmetric continuum with dislocation and disclination densities and rotation nuclei, was presented in our former papers (Teisseyre 2001, 2002, Teisseyre and Boratyński 2003); here, we show that even in a uniform continuum such rotational vibrations and waves exist and are not attenuated in contrast to displacement motion in the ideal elasticity.

The other important conclusion is that the influence of rotational processes in earthquake sources outside the fracture is theoretically not attenuated in a homogeneous continuum, unlike in the case of classical ideal elasticity, and the related waves can propagate to distant sites.

Figure 5.2 presents the bending of a flat circuit surface related to a bend-twist deformation as limited to the 2D space but with curvature into the third direction; this is a simplified illustration for the bend-twist deformation of a sphere becoming affected with a Riemannian curvature and a continuum of such points obeys the constitutive law (5.12). An illustration of the considered bending for a 2D continuum is presented in Fig. 5.3. This figure relates to the 2D surface with the axial convexities/concavities

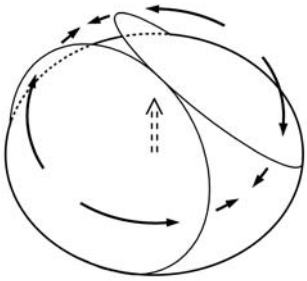

Fig. 5.2 The bending of a flat circuit surface into the perpendicular direction: simplified illustration for the deformation of a sphere affected by a Riemannian curvature

oriented along the perpendicular axis; in a reality we shall apply such a scheme to the 3D space obtaining the bending deformation forming the Riemannian curvature. Such a curvature vanishes for $Y_k = 0$ and $\Gamma = 0$.

In 3D, similar bending-type deformations might be considered for a lattice with two different types of the alternating nodes representing the opposite ions. A bending deformation caused by an electric field will appear on a surface as the alternating knob-convexities and socket-concavities. A slightly different effect will appear when considering an elastic deformation in a lattice with two different types of the alternating nodes characterized by the bonds of different elastic moduli; the respective bendings will appear on a surface with the knobs/sockets (convexities/concavities) of different intensities in an alternating way.

Our relations present a new approach for obtaining the Riemannian description of geometrical deformations related to the bend-twist motions.

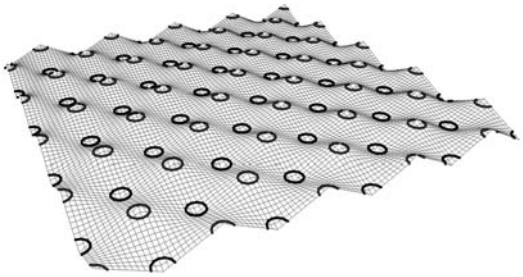

Fig. 5.3 A continuum subject to deformations with axial convexities/concavities as presented in Fig. 5.2; deformation such a 2D surface is a simplified illustration of deformation of the 3D space

References

Kröner E (1981) Continuum theory of defects. In: Balian R, Kléman M, Poirer JP (eds) Physics of defects, (Proc Les Houches XXXV). North Holland Publ Comp, Amsterdam

Shimbo M (1975) A geometrical formulation of asymmetric features in plasticity. Bull Fac Eng Hokkaido Univ **77**: 155-159

Shimbo M (1995) Non-Riemannian geometrical approach to deformation and friction. In: Teisseyre R (ed) Theory of earthquake premonitory and fracture processes. Polish Scientific Publishers PWN, Warszawa, pp 520-528

Teisseyre R (2001) Evolution, propagation and diffusion of dislocation fields. In: Teisseyre R, Majewski E (eds) Earthquake thermodynamics and phase transformations in the earth's interior (vol. 76 of International Geophysical Series). Academic Press, San Diego, pp 167-198

Teisseyre R (2002) Continuum with defect and self-rotation nuclei. Acta Geophys Pol **50**: 1, 51-68

Teisseyre R (2004) Spin and twist motions in a homogeneous elastic continuum and cross-band geometry of fracturing. Acta Geophys Pol **52**: 2, 173-183

Teisseyre R (2005) Asymmetric continuum mechanics: deviations from elasticity and symmetry. Acta Geophys Pol **53**: 2, 115-126.

Teisseyre R, Białecki M (2005) Complex relativity: gravity and electromagnetic fields. arXiv:physics/0506033

Teisseyre R, Boratyński W (2003) Continua with self-rotation nuclei: evolution of asymmetric fields. Mech Res Commun **30**: 235-240

Teisseyre R, Białecki M, Górski M (2005) Degenerated mechanics in a homogeneous continuum potentials. Acta Geophys Pol **53**: 3, 219-230

6 Continuum with Rotation Nuclei and Defects: Dislocation and Disclination Densities

Wojciech Boratyński[1,2], Roman Teisseyre[1]

[1] Institute of Geophysics, Polish Academy of Sciences
ul. Księcia Janusza 64, 01-452 Warszawa, Poland
e-mail: rt@igf.edu.pl

[2] Faculty of Mathematics and Information Science
Warsaw University of Technology
Plac Politechniki 1, 00-661 Warszawa, Poland
e-mail: wbora@mini.pw.edu.pl

6.1 Introduction

In Chapter 4 we have considered rotation motions related to dynamical processes in a homogeneous continuum, and here we will study deformations of rotational type related to a structure of defects in the elastic continuum. A defect distribution may include, among others, the dislocation and disclination densities and rotation nuclei. We take into account two kinds of rotation nuclei as related to the two approaches to the definition of the twist-bend tensor. In this theory, the elastic and self-fields of stresses and strains become asymmetric, while the total fields remain related to displacement field as required by the compatibility conditions. However, the tensor of incompatibility becomes asymmetric.

The antisymmetric stresses play a role of stress moments. We derive the dislocation stress relations and the equations of motion for the symmetric and antisymmetric parts of stresses. Special attention is paid to spin and bend-twist motions.

After Chapter 4 we repeat that according to the Kröner method (Kröner 1981), the elastic strains, rotations and distortions in a continuum with defects can be expressed as a difference between the total and self-fields:

$$\mathbf{E} = \mathbf{E}^{\mathrm{T}} - \mathbf{E}^{\mathrm{S}}, \qquad \boldsymbol{\omega} = \boldsymbol{\omega}^{\mathrm{T}} - \boldsymbol{\omega}^{\mathrm{S}}, \tag{6.1}$$

$$\boldsymbol{\beta} = \boldsymbol{\beta}^{\mathrm{T}} - \boldsymbol{\beta}^{\mathrm{S}}, \qquad \mathbf{S} = \mathbf{S}^{\mathrm{T}} - \mathbf{S}^{\mathrm{S}}.$$

The elastic strains, rotations and stresses become asymmetric and the respective deviations are mutually compensated:

$$\mathbf{E}_{[\,]} + \mathbf{E}^{\mathrm{S}}_{[\,]} = 0\,, \quad \boldsymbol{\omega}_{(\,)} + \boldsymbol{\omega}^{\mathrm{S}}_{(\,)} = 0\,, \quad \mathbf{S}_{[\,]} + \mathbf{S}^{\mathrm{S}}_{[\,]} = 0\,. \tag{6.1a}$$

In our approach, the asymmetry of fields follows from the notion of antisymmetric stresses introduced by Shimbo (1975, 1995) and Shimbo and Kawaguchi (1976) and related to the friction processes and rotation of grains. Fracture processes develop usually along the main fault plane; hence, there appears the initial asymmetry of the fracture pattern (Teisseyre and Kozak 2003); due to friction, the rotation of grains adjacent to the main slip plane gives rise to the antisymmetric part of stresses and the bend-twist deformations.

We define the self-rotation tensor γ by deviations from the total rotation:

$$\gamma_{sn} = \omega^{S}_{sn}\,, \qquad \omega^{T}_{sn} = \omega_{sn} + \omega^{S}_{sn} = \omega_{sn} + \gamma_{sn}\,. \tag{6.2}$$

In our former papers (Teisseyre 2001, Teisseyre and Boratyński 2002) we introduced the following definition of the twist-bend tensor:

$$\tilde{\chi}^{T}_{mq} = \in_{ksq} \frac{\partial \omega^{T}_{mk}}{\partial x_s}\,, \tag{6.3}$$

where again the total field splits into the elastic and self parts

$$\tilde{\chi}^{T}_{mq} = \tilde{\chi}_{mq} + \tilde{\chi}^{S}_{mq}\,. \tag{6.4}$$

The above definition differs from that introduced earlier by Kossecka and DeWitt (1977) and related to gradient of the rotation vector

$$\bar{\chi}^{T}_{mq} = \frac{\partial \omega^{T}_{q}}{\partial x_m} = \frac{1}{2} \in_{nsq} \frac{\partial \omega^{T}_{ns}}{\partial x_m}\,. \tag{6.5}$$

Their definition led, in direct calculations, to vanishing of both the Frank vector (Kossecka and DeWitt 1977) and the disclination density.

These two definitions, (6.3) and (6.5), may describe two different types of rotation nuclei; Kossecka and DeWitt's definition directly leads to the pure rotation nuclei only, while Teisseyre's definition describes nuclei which can undergo the rotation and bend-twist vibrations and includes the non-vanishing Frank vector and disclination density.

The total fields related to these two definitions coincide (apart of the sign):

$$\bar{\chi}^T_{mq} = -\tilde{\chi}^T_{mq} \tag{6.6}$$

hence, we can combine these two kinds of rotation nuclei, putting $-a+b=1$. We obtain

$$\chi^T_{mq} = a\bar{\chi}^T_{mq} + b\tilde{\chi}^T_{mq} = a\frac{\partial \omega^T_q}{\partial x_m} + b\in_{ksq}\frac{\partial \omega^T_{mk}}{\partial x_s} \tag{6.7}$$

or

$$\chi^T_{mq} = a\bar{\chi}^T_{mq} + b\tilde{\chi}^T_{mq} = a\bar{\chi}_{mq} + b\tilde{\chi}_{mq} + a\bar{\chi}^S_{mq} + b\tilde{\chi}^S_{mq}\,, \tag{6.8}$$

where for the material parameters a and b we have $a\in<-1,0>$, $b\in<0,1>$; for $b = 0$ and $a = -1$ we get Kossecka and DeWitt's continuum (Kossecka and DeWitt 1977), while for $a = 0$ and $b = 1$ we have Teisseyre's continuum (Teisseyre 2001).

The incompatibility tensor splits into symmetric and antisymmetric parts; for the symmetric part we write the classical forms (Kossecka and DeWitt 1977):

$$I_{(ij)} = -\in_{ikm}\in_{jtn}\frac{\partial^2 E_{(mn)}}{\partial x_k \partial x_t} = \in_{ikm}\in_{jtn}\frac{\partial^2 E^S_{(mn)}}{\partial x_k \partial x_t}\,, \tag{6.9}$$

$$I_{(pq)} = -\frac{1}{2}\left(\in_{pmk}\frac{\partial \alpha_{qk}}{\partial x_m} + \theta_{pq} + \in_{qmk}\frac{\partial \alpha_{pk}}{\partial x_m} + \theta_{qp}\right), \tag{6.10}$$

where $\boldsymbol{\alpha}$ and $\boldsymbol{\theta}$ are the dislocation and disclination densities, as introduced in the next section.

In the elastic continuum with rotations nuclei we introduce the bonds for point rotations by assuming after Shimbo (1975 and 1995) the antisymmetric stresses related to the friction processes,

$$\gamma_{[lk]} = \omega^S_{[lk]} = E^S_{[lk]} = \frac{1}{2\mu^*}S^S_{[lk]} = -\frac{1}{2\mu^*}S_{[lk]}\,, \tag{6.11}$$

where μ^* is a rotation rigidity modulus.

Similarly, we assume for symmetric parts (cf. Eq. 5.12):

$$\delta_{ni}\gamma_{(ts)} = -\delta_{ni}\omega_{(ts)} = \frac{1}{2\mu^*}\left(\delta_{si}S^S_{(tn)}\right)_{(ts)}\,, \tag{6.12}$$

Hence, combining (6.12) with (6.11) we obtain:

$$\gamma_{mn} = \omega^S_{mn} = E^S_{mn}\,. \tag{6.13}$$

In analogy to relation (6.9), we put for the antisymmetric part of the incompatibility tensor:

$$I_{[ij]} = \in_{ikm} \in_{jtn} \frac{\partial^2 E^S_{[\mathrm{mn}]}}{\partial x_k \partial x_t} = \in_{ikm} \in_{jtn} \frac{\partial^2 \gamma_{[mn]}}{\partial x_k \partial x_t} . \tag{6.14}$$

Our considerations, related to the defect distribution, dislocations, disclinations and rotation nuclei, contain some partial results presented by Kossecka and DeWitt (1977), Teisseyre (2002), Teisseyre and Boratyński (2002, 2003), but some modifications and corrections have been necessary.

When deriving the equations of motion, we follow the approach of Teisseyre and Yamashita (1999) and Teisseyre (2001); the equations of motion split into the symmetric and antisymmetric parts, the latter prevailing on the fracture plane.

6.2 Defect Density Fields

Following Kossecka and De Witt (1977), we define the total disclosure and twist along a closed circuit (the Burgers vector and the Frank vector) as related to the symmetric part of plastic/self strain and self twist-bend tensors:

$$B_l = -\oint \left[E^S_{(kl)} - \in_{lqr} \chi^S_{kq} x_r \right] \mathrm{d}l_k , \qquad \Omega_q = -\oint \chi^S_{kq} \, \mathrm{d}l_k . \tag{6.15}$$

From (15), the dislocation and disclination densities become

$$\begin{aligned} \alpha_{pl} &= -\in_{pmk} \left(\frac{\partial E^S_{(kl)}}{\partial x_m} + \in_{klq} \chi^S_{mq} \right) , \\ B_l &= \iint \left(\alpha_{pl} - \in_{lqr} \theta_{pq} x_r \right) \mathrm{d}s_p , \end{aligned} \tag{6.16}$$

$$\theta_{pq} = -\in_{pmk} \frac{\partial \chi^S_{kq}}{\partial x_m} , \qquad \Omega_q = \iint \theta_{pq} \, \mathrm{d}s_p . \tag{6.17}$$

Further, we obtain

$$\alpha_{pl} = -\in_{pmk} \frac{\partial E^S_{(kl)}}{\partial x_m} - \delta_{pl} \chi^S_{qq} + \chi^S_{lp} . \tag{6.18}$$

From the definitions of the twist-bend tensor (6.6) and (6.7) it follows that:

– for the elastic part

$$\chi_{mq} = a\bar{\chi}_{mq} + b\tilde{\chi}_{mq} = \frac{1}{2}a \in_{nsq} \frac{\partial \omega_{ns}}{\partial x_m} + b \in_{ksq} \frac{\partial \omega_{mk}}{\partial x_s} \ , \tag{6.19}$$

– for the self-part

$$\chi^S_{mq} = a\bar{\chi}^S_{mq} + b\tilde{\chi}^S_{mq} = \frac{1}{2}a \in_{nsq} \frac{\partial \gamma_{ns}}{\partial x_m} + b \in_{nsq} \frac{\partial \gamma_{mn}}{\partial x_s} \ . \tag{6.20}$$

From these relations and with the help of (6.12) and (6.13) we obtain the following formulae for dislocation and disclination densities:

$$\begin{aligned} \alpha_{pl} = & - a \in_{pmk} \frac{\partial \gamma_{[kl]}}{\partial x_m} + \delta_{pl} \in_{qmk} b \frac{\partial \gamma_{qk}}{\partial x_m} \\ & - \in_{pmk} b \frac{\partial \gamma_{lk}}{\partial x_m} - \in_{pmk} \frac{\partial \gamma_{(kl)}}{\partial x_m} \ , \end{aligned} \tag{6.21}$$

$$\theta_{pq} = b \in_{pmk} \in_{qns} \frac{\partial^2 \gamma_{ks}}{\partial x_m \partial x_n} \ , \qquad \frac{\partial \alpha_{pl}}{\partial x_p} + \frac{\partial \chi^S_{qq}}{\partial x_l} - \frac{\partial \chi^S_{lp}}{\partial x_p} = 0 \, , \tag{6.22}$$

with the conditions

$$\frac{\partial \alpha_{pl}}{\partial x_p} + \in_{lpq} \theta_{pq} = 0 \qquad \text{and} \qquad \frac{\partial \theta_{pq}}{\partial x_p} = 0 \, . \tag{6.23}$$

We shall note that, as we have mentioned above, in Kossecka and DeWitt's continuum the direct computation leads to vanishing of disclination velocity; hence, Kossecka and DeWitt (1977) have further assumed that spin velocity $\mathbf{w}$ differs from the time derivative of rotation: $\mathbf{w} \neq \dot{\boldsymbol{\omega}}$. This approach and the assumption that the self twist-bend tensor $\bar{\chi}^S_{mq}$ is not equal to $\partial \omega^S_q / \partial x_m$, leads to another definition of disclination density rate $\dot{\boldsymbol{\theta}}$; however, further on, we follow our simple approach in which $\mathbf{w} = \dot{\boldsymbol{\omega}}$.

Returning to the expressions for the incompatibility tensors, the symmetric (6.10) and antisymmetric (6.14), we can now write

$$I_{pq} = - \left(\in_{pmk} \frac{\partial (\alpha_{qk} - \chi^S_{kq})}{\partial x_m} \right)_{(pq)} - \left[\in_{pmk} \frac{\partial \chi^S_{kq}}{\partial x_m} \right]_{[pq]} \ . \tag{6.24}$$

From the compatibilities for the total fields (see: Kossecka and DeWitt 1977, and Teisseyre 2001) we arrive at deviations for the self-fields which help us to define the related currents; we obtain

– for the dislocation current

$$J_{kl} = -\frac{\partial \upsilon_l^S}{\partial x_k} + \dot{E}^S_{(kl)} + b\dot{\gamma}_{(kl)} + a \in_{kls} \dot{\gamma}_s = \\ = -\frac{\partial \upsilon_l^S}{\partial x_k} + (1+b)\dot{\gamma}_{(kl)} + a\dot{\gamma}_{[kl]}\,, \tag{6.25}$$

where, according to (6.13), $\dot{E}^S_{(kl)}$ is related to the introduced bend-twist motion;

– for the disclination current

$$Y_{kq} = b \in_{nsq} \frac{\partial \dot{\gamma}_{kn}}{\partial x_s} + b \in_{qns} \frac{\partial \dot{\gamma}_{(sk)}}{\partial x_n} = -b \in_{nsq} \frac{\partial \dot{\gamma}_{[ks]}}{\partial x_n}\,. \tag{6.26}$$

The self-twist motions are the sources of disclinations and contribute to the formation of dislocation fields. From these relations, there follow the conservation laws:

$$\dot{\alpha}_{pl} + \in_{pmk} \frac{\partial J_{kl}}{\partial x_m} + \in_{pmk} \in_{klq} Y_{mq} = 0\,, \tag{6.27}$$

$$\theta_{pq} + \in_{pmk} \frac{\partial Y_{kq}}{\partial x_m} - b \in_{pmk} \in_{qns} \frac{\partial^2 \dot{\gamma}_{(ks)}}{\partial x_m \partial x_n} = 0\,. \tag{6.28}$$

The continuity relations are very similar to those obtained by Kossecka and DeWitt (1977), except of the last term in Eq. (6.28).

As to the dislocation current, we may also estimate it independently; according to Teodosiu (1970) and Teisseyre (2001) we obtain

$$J_{pk} = c \in_{qmk} \alpha_{qp} V_m\,, \tag{6.29}$$

where V is the dislocation flow velocity.

Several attempts have been made to estimate such a velocity. Using the expression derived by Mataga *et al*. (1987), we obtain the following equation for the dislocation density flow:

$$V_m = \in_{qmk} \frac{\alpha_{kl}}{|\alpha_{kl}|} \frac{S_{ql} - R_{ql}}{\sqrt{(S-R)^2 + R^2}}\,, \tag{6.30}$$

where S is the stress field; R is the resistance stress, $cB = bR$ (B is the drag coefficient, b is the Burgers vector of dislocation), υ_m and $V_m = \upsilon_m/c$ are, respectively, the dislocation velocity and relative dislocation velocity with respect to the shear wave velocity.

6.3 Dislocation–Stress Relations

For incompatibility tensor we have two equivalent expressions: the one given by Eq. (6.24) and the other obtained from the stress-strain relations (the classical relation for symmetric stresses and Eq. (6.15) for the anti-symmetric stresses with the Poisson ratio ν):

$$I_{pq} = -\in_{pmk} \frac{\partial}{\partial x_m} \in_{qnl} \frac{\partial\left(S_{(kl)} - \frac{\mu}{\mu^*} S_{[kl]} - \frac{\nu}{1+\nu}\delta_{kl} S_{ii} \right)}{\partial x_n} . \tag{6.31}$$

Comparing this expression with (6.24) for the state of equilibrium we can derive from the dislocation-stress relations (cf. Teisseyre 2001; in the paper by Teisseyre 2002, a similar derivation procedure is presented separately for the screw and edge dislocations; however, in the formula for screw dislocations the term $S_{(kl)}$ has been erroneously omitted):

$$\alpha_{sk} - \frac{1}{2}\alpha_{tt}\delta_{sk} = \frac{1}{2\mu} \in_{snl} \frac{\partial\left(S_{(kl)} - \frac{\mu}{\mu^*} S_{[kl]} - \frac{\nu}{1+\nu}\delta_{kl} S_{ii} \right)}{\partial x_n} , \tag{6.32}$$

– for screw dislocations

$$\alpha_{sk} = -\frac{1}{\mu} \in_{snl} \frac{\partial\left(S_{(kl)} - \frac{\mu}{\mu^*} S_{[kl]} \right)}{\partial x_n} , \quad s \to k \tag{6.32a}$$

– for edge dislocations

$$\alpha_{sk} = \frac{1}{2\mu} \in_{snl} \frac{\partial\left(S_{(kl)} - \frac{\mu}{\mu^*} S_{[kl]} - \frac{\nu}{1+\nu}\delta_{kl} S_{ii} \right)}{\partial x_n} , \quad s \neq k . \tag{6.32b}$$

6.4 Equations of Motion

6.4.1 Symmetric stresses

The right-hand side of the equation of motion in a continuum with defects can be expressed by a difference between the total and self accelerations (Kossecka and DeWitt 1977):

$$\frac{\partial}{\partial x_k} S_{lk} = \rho \frac{\partial}{\partial t} \upsilon_l \,, \qquad \frac{\partial}{\partial t} \upsilon_l = \frac{\partial}{\partial t} \upsilon_l^T - \frac{\partial}{\partial t} \upsilon_l^S \,, \tag{6.33}$$

where stresses are understood as the symmetric ones.

Plastic velocity v^S is related to the dislocation velocity, but its symmetrized space derivatives may differ from the rate of plastic strains. Taking the space derivative of this relation and symmetrizing the result we can arrive at

$$\left(\frac{\partial}{\partial x_k \, \partial x_s} S_{(lk)} \right)_{(ls)} = \rho \frac{\partial^2}{\partial t^2} E^T_{(ls)} - \frac{\partial}{\partial t} \left(\frac{\partial}{\partial x_s} \upsilon_l^S \right)_{(ls)}$$

and with the help of (6.1) and (6.25) we get

$$\left(\frac{\partial}{\partial x_k \, \partial x_s} S_{(lk)} \right)_{(ls)} = \rho \frac{\partial^2}{\partial t^2} E_{(sl)} + \rho \frac{\partial}{\partial t} \left(J_{(sl)} - b \dot{\gamma}_{(sl)} \right), \tag{6.34}$$

where the right-hand side contains the propagation and diffusion terms; the dislocation current can be estimated from relations (6.29) and (6.30) while the dislocation density from (6.32).

These equations can be expressed by displacement motion and self rotations; from

$$\left(\frac{\partial}{\partial x_k \, \partial x_s} (S^T_{(lk)} - S^S_{(lk)}) \right)_{(ls)} = \rho \frac{\partial^2}{\partial t^2} E^T_{(ls)} + \rho \frac{\partial}{\partial t} \left(J_{(sl)} - (1+b) \dot{\gamma}_{(sl)} \right)$$

we obtain

$$\left((\lambda + \mu) \frac{\partial}{\partial x_l \, \partial x_s} \frac{\partial u_k}{\partial x_k} + \mu \frac{\partial}{\partial x_k \, \partial x_k} \frac{\partial u_l}{\partial x_s} - 2\mu^* \frac{\partial \gamma_{(sl)}}{\partial x_k \, \partial x_k} \right) =$$

$$= \rho \frac{\partial^2}{\partial t^2} \left(\frac{\partial u_l}{2 \partial x_s} + \frac{\partial u_s}{2 \partial x_l} \right) + \rho \frac{\partial}{\partial t} \left(J_{(sl)} - \dot{E}^{0S}_{(sl)} - (1+b) \dot{\gamma}_{(sl)} \right) \tag{6.35}$$

and for vanishing of displacement motion and other self-fields we obtain for the bend-twist waves (cf. Chap. 4):

$$2\mu^* \frac{\partial \gamma_{(sl)}}{\partial x_k \partial x_k} = \rho(1+b)\frac{\partial^2}{\partial t^2}\gamma_{(sl)}, \qquad V_T^2 = \frac{2\mu^*}{\rho(1+b)}. \tag{6.36}$$

These equations lead further to a classical displacement-type equation with additional source function. The waves presented have no attenuation under the assumptions used for the ideal elastic bodies.

6.4.2 Antisymmetric stresses

For antisymmetric stresses we shall apply the balance law expressing an equality of the change of rotation of force acting on a body element equal to the acceleration of rotation

$$\in_{lki} \frac{\partial}{\partial x_k \partial x_n} S_{[in]} = \rho \frac{\partial^2}{\partial t^2} \in_{lki} \omega_{[ik]}. \tag{6.37}$$

Another form of this equation determines the relation of the total rotations with field $\gamma_{[ki]}$

$$-4\mu^* \frac{\partial}{\partial x_n \partial x_n}\gamma_{[ik]} = \rho \frac{\partial^2}{\partial t^2}\left(\frac{\partial u_i}{\partial x_k} - \frac{\partial u_k}{\partial x_i} - 2\gamma_{[ik]}\right). \tag{6.38}$$

For vanishing displacement motion we obtain for the spin waves the formula, presented already in the former chapter:

$$2\mu^* \frac{\partial}{\partial x_n \partial x_n}\gamma_{[ik]} = \rho \frac{\partial^2}{\partial t^2}\gamma_{[ik]}, \quad V_R^2 = \frac{2\mu^*}{\rho}. \tag{6.39}$$

6.5 Discussion

We have shown that a defect continuum with dislocations and disclinations may lead to structural deformations of rotation type; in a dynamical case these deformations contribute to formation of spin and bend-twist waves.

When assuming that self-rotation fields are the only sources of distortions, it seems possible to estimate the counterparts a and b in the twist-bend tensor. However, this is not exactly true taking into account an arbitrary definition of the bend-twist modulus as equal to the rotation rigidity

modulus in Eq. (6.12). Nevertheless, studying differences of the bend-twist wave velocities (see: Eq. 6.36) for different samples – in the sense of different deformation history, and consequently different defect content – we may relate such velocity differences to the different *b*-values.

References

Kossecka E, DeWitt R (1977) Disclination kinematics. Arch Mech **29**: 633-651

Kröner E (1981) Continuum theory of defects. In: Balian R, Kléman M, Poirer JP (eds) Les Houches, Session XXXV, 1980, Physics of defects, North Holland Publ Comp, Amsterdam.

Mataga PA, Freund LB, Hutchison JW (1987) Crack tip plasticity in dynamic fracture. J Phys Chem Solid **48**: 985-1005

Shimbo M (1975) A geometrical formulation of asymmetric features in plasticity. Bull Fac Eng, Hokkaido Univ **77**: 155-159 (in Japanese)

Shimbo M (1995) Non-Riemannian geometrical approach to deformation and friction. In: Teisseyre R (ed) Theory of earthquake premonitory and fracture processes, pp 520-528, PWN, Warszawa

Shimbo M, Kawaguchi M (1976) A note on the asymmetric fields. Bull Fac Eng, Hokkaido Univ **80**: 75-79 (in Japanese)

Teisseyre R (2001) Evolution, propagation and diffusion of dislocation fields. In: Teisseyre R, Majewski E (eds) Earthquake thermodynamics and phase transformations in the earth's interior (vol 76 of Intern Geophys Series), pp 167-198, Academic Press, San Diego

Teisseyre R (2002) Continuum with defect and self-rotation nuclei. Acta Geophys Pol **50**: 51-68

Teisseyre R, Boratyński W (2002) Continua with self-rotation nuclei: evolution of defect fields and equations of motion. Acta Geophys Pol **50**: 223-229

Teisseyre R, Boratyński W (2003) Continua with self-rotation nuclei: evolution of asymmetric fields. Mech Res Com **30**: 235-240

Teisseyre R, Kozak J (2003) Considerations on the seismic rotation waves. Acta Geophys Pol **51**: 244-256

Teisseyre R, Yamashita T (1999) Splitting stress motion equation into seismic wave and fault-related fields. Acta Geophys Pol **47**: 135-147

Teodosiu C (1970) A dynamic theory of dislocations and its applications to the theory of the elastic-plastic continuum. In: Simmons JA, DeWitt R and Bullough R (eds) Fundamental aspect of dislocation theory, 837-876, Nat Bur Stand US), Sp Publ 317, II.

7 Towards a Discrete Theory of Defects

Mariusz Białecki

Institute of Geophysics, Polish Academy of Sciences
ul. Księcia Janusza 64, 01-452 Warszawa, Poland
e-mail: bialecki@igf.edu.pl

7.1 Introduction

We outline some fundamental principles of description of defects in crystal-like media in terms of a discrete approach instead of widely used continuous one. There are at least two sorts of general arguments supporting the discrete version of the theory of defects. One is connected with physical nature of crystals, which is evidently discrete. Continuum-medium crystal model is a very useful theoretical construction, but it is a kind of idealization. This fact has to be reflected in mathematical structure of the theory. Second, more practical reason, comes from recent significant growth of interest in discrete mathematics and its application in different areas of mathematical physics, quantitative biology and computer sciences. As a result, a lot of new techniques were developed and many obstacles were overcome. Our aim here is to demonstrate a possibility of applying some of them for description of crystal-like media.

In the sequel of this section we introduce basic concepts and point out genesis of our approach. In Sect. 7.2 we introduce notion of discrete description and discuss some differences between it and its continuous counterpart. Section 7.3 is devoted to derivation of a discrete version of Weingarten theorem. In the last section we outline some prospects and consequences of this approach.

The theory of defects (e.g., Kröner 1981) describes physical properties of bodies with internal stresses caused by disturbances in ideal, regular and ordered structure of the medium. Nowadays this theory is well established and found many applications, including those in seismology (Takeo and Ito 1997) and geodesy (Yamasaki and Nagahama 1999a).

Mathematical structure of fundamental equations of the theory of defects is similar to that of the Einstein-Cartan theory of gravitation (Traut-

man 2006, Hehl et al. 1976, Hammond 2002). A comprehensive comparison of these theories is presented by Ruggiero and Tartaglia (2003). A meaningful extension of Einstein-Cartan theory in comparison to the classical Einstein theory of gravitation is to study properties of space-time geometry with nonzero torsion. This makes it attractive for description of rotational effects. One of our prospective aims is to transfer some results into such a general framework (Teisseyre 2002, 2005, Teisseyre and Białecki 2005).

The theory of defects as a rule is formulated within the continuum framework which is usually claimed to be good for geometrical description (eg. Yamasaki and Nagahama 1999b). This continuum could be obtained from crystalline-like lattice by a limiting process, in which ”atoms” are split into smaller ones, so that the overall structure is preserved, but the lattice base is reduced. Such a procedure allows a proper definition of mass and defect densities, with the preservation of crystallographic directions.

The assumption that the lattice constant and other variables could be infinitesimally small provides a significant simplification in many cases. For instance, it is possible to obtain in this way a simple characterization of the Frank vector. The crucial point is that only infinitesimal rotations could obey simple addition law, contrary to non-Abelian nature of rotation group for finite angles. This result strongly depends on infinitesimal size of defects and the rejection of this assumption leads to complicated formulas.

On the other hand, one can recently observe a remarkable development of discrete techniques in mathematical physics. In the theory of integrable systems (called also the soliton theory) it is well known that a single discrete nonlinear equation ”contains” many important nonlinear partial differential equations, which means, they can be derived from this equation taking a suitable limit (Hirota 1981). Nowadays, also discrete geometry, developed in close connection with integrable differential equations, proved to provide fruitful concepts and has their counterparts in classical differential geometry. (For a recent state of theory of discrete integrable systems see Grammaticos et al. 2004.)

It is worth mentioning the important terminological difference between discrete and ultradiscrete objects. For the first ones, the independent variables are discrete, but the dependent ones are continuous. The ultradiscrete, or completely discrete systems, deal with all variables being discrete, and are called cellular automata. (For integrable ultradiscrete systems see, for example, Tokihiro 2004, Doliwa et al. 2003, Białecki and Doliwa 2005.) Notice that the construction of completely discrete theory of defects, allowing only for discrete positions of atoms, is also possible in principle.

The motivation towards a discrete theory of defects is to transfer the development of discrete techniques from mathematics and mathematical physics to material science and to describe crystal-like media as fundamentally discrete objects.

7.2 Towards a Discrete Description

An idea of a geometric description of crystals with defects comes from mapping an undeformed medium to a deformed one. Denote by $\boldsymbol{x} = (x_i, x_j, x_k) \in \mathbb{R}^3$ the Cartesian coordinates of a material point P of undeformed body. After deformation, point P has coordinates $\boldsymbol{x} + \boldsymbol{u}(\boldsymbol{x})$, where $\boldsymbol{u}(\boldsymbol{x})$ is the displacement field which describes the amount and direction of the deformation. So, in a continuous case, we have

$$\boldsymbol{x}' = \boldsymbol{x} + \boldsymbol{u}(\boldsymbol{x}) \ ,$$

where prime indicates the coordinates after deformation. Lets focus our attention on a discrete case. If we denote position of lattice point $P = (n_1, n_2, n_3) \in \mathbb{Z}^3$ by $\boldsymbol{x_n} = \boldsymbol{x}(n_i, n_j, n_k) = (x_i, x_j, x_k) \in \mathbb{R}^3$, one could expect, by analogy,

$$\boldsymbol{x}'_n = \boldsymbol{x}_n + \boldsymbol{u}_a(\boldsymbol{x}_n) \ . \tag{7.1}$$

However, the meaning of this relation is not clear in the presence of defects. Assume that atoms at point P were removed leaving a vacancy. What is the value of the displacement field $\boldsymbol{u}_a(\boldsymbol{x}_n)$ for P in this case? Is it meaningful what is its position after deformation? If we assume that atoms which build a crystal structure are indistinguishable, as vacancies are, we have troubles with the meaning of $\boldsymbol{u}_a(\boldsymbol{x}_n)$. In such a case, an additional definition is required. In the continuous case, one can claim that the set of singular points of this sort is of measure zero and "neglect" them. But when every small value is finite, the situation requires more precise treatment. If we intend to describe the defects, we cannot use the above relation without modifications.

Let us discuss the introduction of a Burgers vector. Denote by B_0 a close circuit consisting of N atoms in undeformed medium, as schematically depicted in Fig. 7.1. When mapped into disturbed medium, the points form a contour which is no longer closed. The failure to close the circuit is given by lattice vector $\boldsymbol{b}$ called local Burgers vector. We assume the definition in which this vector points from the beginning to the end of circuit B. Then we have

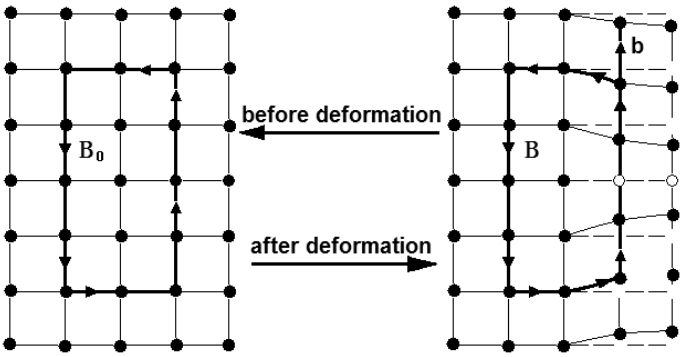

Fig. 7.1 Schematic diagram of *N*-atom circuit before and after deformation

$$\sum \boldsymbol{x}_n = 0 \qquad \text{and} \qquad \sum \boldsymbol{x}'_n = \boldsymbol{b}$$

where we indicate that sums are taken for *N* subsequent atoms forming circuits B_0 and B, respectively. However, to obtain

$$\sum_{B,N} \boldsymbol{u}_a(\boldsymbol{x}_n) = \boldsymbol{b} \ , \tag{7.2}$$

in a way consistent with Eq. (7.1), we cannot assume that atoms along B after vacancy are shifted up for situation presented in Fig. 7.1. In that case, each shifted atom apart from small disturbance $\boldsymbol{u}_a(\boldsymbol{x}_n)$ adds lattice spacings $\boldsymbol{l}_0$. If we consider situation where $\boldsymbol{u}_a(\boldsymbol{x}_n) = 0$ for every point of B (or there is mirror symmetry in crystal with the plane containing the plane of defects and the last point of B is apart from the plane), then we see that $\boldsymbol{b}$ should be of the order of $\boldsymbol{l}_0$ for one vacancy.

We are forced to assume the rule: when crossing the defect point we have to add (or subtract) a lattice spacing $\boldsymbol{l}_0$ and measure $\boldsymbol{u}_a(\boldsymbol{x}_n)$, starting from the next point along the Burgers circuit. This agrees with indistinguishability of atoms in our model. So, instead of Eq. (7.1) we have

$$\boldsymbol{x}'_n = \boldsymbol{x}_n + \delta_D(\boldsymbol{x}_n) + \boldsymbol{u}_a(\boldsymbol{x}_n) =: \boldsymbol{x}_n + \boldsymbol{u}(\boldsymbol{x}_n) \ , \tag{7.3}$$

where

$$\delta_D(\boldsymbol{x}_n) = \begin{cases} 0 & \text{for no defects} \\ +\boldsymbol{l}_0 & \text{for vacancy} \\ -\boldsymbol{l}_0 & \text{for interstice} \end{cases}$$

and $\boldsymbol{l}_0$ pointed in the direction we cross a defect. Notice also that Eq. (7.2) cannot be derived from (7.1) by taking sum of both sides without specifying the meaning of these sums.

The described situation is, in a sense, quite typical, when constructing discrete models. Some difficulties (or differences) could "disappear" when taking a continuum limit. As a rule, there could be many continuous counterparts of a given discrete system, depending on specific settings of taking the limit. From that point of view, discrete cases are basic and allow to control the meaning and mutual dependencies of different parameters of the model.

7.3 Discrete Weingarten Theorem

To demonstrate a possibility of realizing discrete description of defects in crystal-like materials with cubic structure, we will derive a discrete version of the Weingarten theorem. Notice that lattices with non-cubic structures are also under investigation (see Zakrzewski 2005). In this section we will transfer to a discrete case the result described by Kleinert (2006).

Consider a crystal with a half plane layer of lattice sites removed; the configuration is schematically presented in Fig. 7.2. The positions of points are given by

$$\boldsymbol{x}(n_i, n_j, n_k) = (x_i, x_j, x_k) = (x_\alpha) \ .$$

Denote by T_α a shift by one in variable α, for example

$$T_j \, \boldsymbol{x}(n_i, n_j, n_k) := \boldsymbol{x}(n_i, n_j{+}1, n_k) \ ,$$

and by

$$\Delta_\alpha = T_\alpha - 1 \, , \quad \alpha = i, j, k \ ,$$

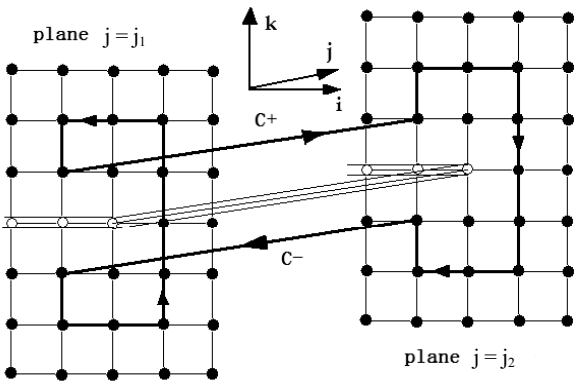

Fig. 7.2 Deformation of lattice with a half plane layer removed

a discrete counterpart of a first derivative in the variable n_α. In the following we will omit dependent variables if they have the same value in all terms of equation. Let us introduce also the symmetric strain field

$$u_{\alpha\beta} := \frac{1}{2}\left[\Delta_\alpha u_\beta + \Delta_\beta u_\alpha\right]$$

and the local rotation field

$$w_{\alpha\beta} := \frac{1}{2}\left[\Delta_\alpha u_\beta - \Delta_\beta u_\alpha\right]$$

which is antisymmetric.

Although the removed layer of atoms has broken the regular structure of crystal, we assume that in the lattice rearranged in this way both sides of cutting surface fit to each other. This implies there is no "jump" in strain and its first derivative when crossing the rearranged surface. So, the physical requirement for the crystal structure along a cutting surface is reflected in the following conditions:

$$\Delta_D u_{\alpha\beta} = 0 \ , \tag{7.4}$$

$$\Delta_D(\Delta_k u_{\alpha\beta}) = 0 \ , \tag{7.5}$$

where Δ_D stands for direction k crossing the singular surface. We would like to point out that the noncommutativity around the defects

$$T_i T_j \boldsymbol{x} \neq T_j T_i \boldsymbol{x} \quad \text{or equivalently} \quad \Delta_i \Delta_j \boldsymbol{x} \neq \Delta_j \Delta_i \boldsymbol{x}$$

is a source of nonzero curvature and torsion (see Kleinert 2006).

Let us investigate the following expression

$$\begin{aligned}&\Delta_D u_i(n_j = j_1) - \Delta_D u_i(n_j = j_2)\\ &\quad := \left[u_i\left(\boldsymbol{x}^+(j_1)\right) - u_i\left(\boldsymbol{x}^-(j_1)\right)\right] - \left[u_i\left(\boldsymbol{x}^+(j_2)\right) - u_i\left(\boldsymbol{x}^-(j_2)\right)\right],\end{aligned}$$

where $\boldsymbol{x}^+$ stands for the upper half space and $\boldsymbol{x}^-$ for lower one. It could be rearranged to

$$\left[u_i\left(\boldsymbol{x}^-(j_2)\right) - u_i\left(\boldsymbol{x}^-(j_1)\right)\right] - \left[u_i\left(\boldsymbol{x}^+(j_2)\right) - u_i\left(\boldsymbol{x}^+(j_1)\right)\right],$$

and then expressed by sums along the contour lines below C^- and above C^+ cutting surfaces

$$\sum_{C^-:j=j_1}^{j_2-1} \Delta_j u_i - \sum_{C^+:j=j_1}^{j_2-1} \Delta_j u_i \ .$$

Using decomposition into symmetric and antisymmetric parts, we get

$$\sum_{C^-:j=j_1}^{j_2-1} \left(u_{ij} - w_{ij}\right) - \sum_{C^+:j=j_1}^{j_2-1} \left(u_{ij} - w_{ij}\right) \ .$$

If for simplicity we assume $n_j(j_1) = 0$ then

$$\sum_{C^+:j=j_1}^{j_2-1} w_{ij}$$

could be written as

$$\sum_{C^+:j=j_1}^{j_2-1} w_{ij} \Delta_j j \ .$$

Integrating this expression by parts (see the Appendix) we arrive at

$$w_{ij}\, n_j\Big|_{j_1=0}^{j_2} - \sum_{C^+:j=j_1}^{j_2-1} (T_j n_j) \Delta_j w_{ij} \ .$$

Using this result, we can write

$$\Delta_D u_i(n_j = j_1) - \Delta_D u_i(n_j = j_2)$$

in the form

$$\begin{aligned} w_{ij}^+(j_2)n_2 - \sum_{C^+:j=j_1}^{j_2-1} \left[u_{ij} + (T_j n_j)\Delta_j w_{ij}\right] - w_{ij}^-(j_2)n_2 - \sum_{C^-:j=j_1}^{j_2-1} \left[u_{ij} + (T_j n_j)\Delta_j w_{ij}\right] \\ = \left[w_{ij}^+(j_2) - w_{ij}^-(j_2)\right] n_2 - \left(\sum_{C^+:j=j_1}^{j_2-1} - \sum_{C^-:j=j_1}^{j_2-1} \right) \left[u_{ij} + (T_j n_j)\Delta_j w_{ij}\right] \\ = \sum_{C^-:j=j_1}^{j_2-1} \left[\Delta_D u_{ij} + (T_j n_j)\Delta_D(\Delta_j w_{ij})\right]. \end{aligned}$$

Since T_i and T_j commute for the undisturbed part of crystal, we obtain

$$\begin{aligned} \Delta_j w_{ij} &= \Delta_j(\Delta_i u_j - u_{ij}) \\ &= \Delta_j \Delta_i u_j - \Delta_j u_{ij} = \Delta_i \Delta_j u_j - \Delta_j u_{ij} = \Delta_i u_{jj} - \Delta_j u_{ii} \ . \end{aligned}$$

Taking into account the physical assumptions, i.e. Eqs. (7.4) and (7.5), we conclude that this integral is equal to zero.

In general, when we allow summation not only along straight path of C^-, we obtain more generally $2\Delta_k w_{ij} = \Delta_k(\Delta_i u_j - \Delta_j u_i) = (\Delta_i\Delta_k u_j + \Delta_i\Delta_j u_k) + (\Delta_j\Delta_k u_i + \Delta_j\Delta_i u_k) + (\Delta_k\Delta_i - \Delta_i\Delta_k)u_j - (\Delta_k\Delta_j - \Delta_j\Delta_k)u_i + (\Delta_j\Delta_i - \Delta_i\Delta_j)u_k$. With commutativity assumption we arrive at $\Delta_k w_{ij} = (\Delta_i u_{kj} + \Delta_j u_{ki})$.

As a result, we obtain that for the difference of "jumps" between two arbitrary points the following relation is valid

$$\Delta_D u_i(2) - \Delta_D u_i(1) = \left(x_j(2) - x_j(1)\right)\left(w_{ij}^-(j_2) - w_{ij}^+(j_2)\right) \ . \tag{7.6}$$

Introducing the rotation matrix

$$\Omega_{ij} := \left(w_{ij}^-(j_2) - w_{ij}^+(j_2)\right)$$

and the rotation vector

$$\Omega_k := \frac{1}{2}\varepsilon_{ijk}\Omega_{ij} \ ,$$

where ε_{ijk} is the antisymmetric symbol of Levi-Civita, we can rewrite Eq. (7.6) in the following form:

$$\Delta_D \boldsymbol{u}(2) = \Delta_D \boldsymbol{u}(1) + \boldsymbol{\Omega} \times \left(\boldsymbol{x}(2) - \boldsymbol{x}(1)\right) \ .$$

This is a discrete version of Weingarten's Theorem. The "jump" of the displacement field crossing the cutting surface can be only a constant vector plus a fixed rotation.

7.4 Prospects

As we have shown in this introductory presentation, it is possible to obtain the equations of continuous theory of defects in a discrete way. Not suprisingly, the relations are exactly the same in both cases. This is not a disadvantage of the discrete approach; in contrary, the first test showed that it retains all results, which proved to be in agreement with measurement and were successfully applied in material sciences. Our hope and motivation is that the discrete version could deal with new phenomena, but reasonable discussion of this topic is impossible at such early stage. Also, it seems very hard to predict applications of this preliminary version of the theory.

However, there are some general guidelines where to look for advantages of this approach. As mentioned in the introduction, the discrete approach proved its unifying and simplifying potential in the theory of integrable systems. So we expect a similar result in the theory of defects.

Discrete theories, with their lack of infinitesimally small amounts, are clear to understand and control, which makes them more comprehensive and promising in education. And last but not least, discrete models are suitable for numerical implementation and could be directly used for computational needs of material engineering and other scientific disciplines applying the theory of defects, including Earth sciences.

Appendix: Discrete Integration by Parts

The discrete version of the integration by parts theorem could be derived in the same way as its continuous counterpart. We start from the Leibnitz rule for differentiation of the product of two functions:

$$\Delta_\alpha(u\cdot v)=\Delta_\alpha u\cdot T_\alpha v+u\cdot\Delta_\alpha v=T_\alpha u\cdot\Delta_\alpha v+\Delta_\alpha u\cdot v\ .$$

Performing sums, one can easily obtain

$$\sum_{C:x_{beg}}^{x_{end}}\Delta_\alpha(u\cdot v)=(u\cdot v)(\boldsymbol{x}_{end})-(u\cdot v)(\boldsymbol{x}_{beg})$$

and for the other side

$$\sum_{C:x_{beg}}^{x_{end}}\Delta_\alpha u\cdot T_\alpha v+\sum_{C:x_{beg}}^{x_{end}}u\cdot\Delta_\alpha v\ .$$

Joining the above expressions we arrive at the desired result.

Acknowledgments. This work is partially supported by Polish Ministry of Science and Information Society Technologies, project 2PO4D 060 28.

References

Białecki M, Doliwa A (2005) Algebro-geometric solution of the dKP equation over a finite field out of a hyperelliptic curve. Commun Math Phys **253**: 157-170

Doliwa A, Białecki M, Klimczewski P (2003) The Hirota equation over finite fields: algebro-geometric approach and multisoliton solutions. J Phys A: Math Gen **36**: 4827-4839

Grammaticos B, Kosmann-Schwarzbach Y, Tamizhmani T (eds) (2004) Discrete integrable systems. Lecture Notes in Physics, vol 644. Springer

Hehl FW, Heyde P von der, Kerlick GD, Nester JM (1976) General relativity with spin and torsion: Foundations and prospects. Rev Mod Phys **48**: 393-416
Hammond TA (2002) Torsiongravity. Rep Prog Phys **65**: 599-649
Hirota R (1981) Discrete analogue of a generalized Toda equation. J Phys Soc Jpn **50**: 3785-3791
Kleinert H (2006) Gravity with torsion (in preparation)
Kröner E (1981) Continuum theory of defects. In: Balian R, Kléman M, Poirer JP (eds) Physics of defects. North Holland Publ Comp, Amsterdam
Ruggiero ML, Tartaglia A (2003) Einstein-Cartan theory as a theory of defects in space-time. Am J Phys **71**: 12, 1303-1313
Takeo M, Ito H (1997) What can be learned from rotational motions excited by earthquakes? Geophys J Int **129**: 319-329
Teisseyre R (2002) Continuum with defects and self-rotation fields. Acta Geophys Pol **50**: 1, 51-68
Teisseyre R (2005) Asymmetric continuum mechanics: Deviations from elasticity and symmetry. Acta Geophys Pol **53**: 2, 115-126
Teisseyre R, Białecki M, Górski M (2005) Degenerated mechanics in homogenous continuum: Potentials for spin and twist. Acta Geophys Pol **53**: 3, 219-231
Tokihiro T (2004) Ultradiscrete systems (cellular automata). In: Grammaticos et al (eds) Discrete integrable systems. Lecture Notes in Physics, vol 644. Springer, pp 383-424
Trautman A (2006) The Einstein-Cartan theory. Encyclopedia of mathematical physics. Elsevier Science Ltd (in print)
Yamasaki K, Nagahama H (1999a) Continuum theory of defects and gravity anomaly. Acta Geophys Pol **47**: 3, 239-257
Yamasaki K, Nagahama H (1999b) Hodge duality and continuum theory of defects. J Phys A: Math Gen **32**: L475-L481
Zakrzewski WJ (2005) Laplacians on lattices. J Nonl Math Phys **12**: 4, 530-538

8 Fault Dynamics and Related Radiation

Wojciech Boratyński[1,2], Roman Teisseyre[1]

[1] Institute of Geophysics, Polish Academy of Sciences
ul. Księcia Janusza 64, 01-452 Warszawa, Poland
e-mail: rt@igf.edu.pl

[2] Faculty of Mathematics and Information Science
Warsaw University of Technology
Plac Politechniki 1, 00-661 Warszawa, Poland
e-mail: wbora@mini.pw.edu.pl

8.1 Introduction

Usually when searching for the fault slip solutions we rely on classical elasticity with the friction constitutive laws introduced according to the experimental data. In spite of the fact that the obtained equations do not theoretically apply to elastic continuum that includes any distribution of defects as objects with their own stress field, the obtained results well explain the observational data.

Instead we may consider an elastic continuum with asymmetric stresses and defects (Teisseyre and Boratyński 2003); such an approach permits to study the defect interactions and elastodynamic solutions describing a slip propagation along a fault and related seismic radiation (Teisseyre and Yamashita 1999).

As explained in the former Chapters 4–6, an elastic asymmetric continuum with defects and rotation nuclei can be analized with the help of the Kröner method with the elastic strains and stresses, $\mathbf{E}$ and $\mathbf{S}$, and corresponding self fields, $\mathbf{E}^S$ and $\mathbf{S}^S$ forming together the total strain and stress fields $\mathbf{E}^T = \mathbf{E} + \mathbf{E}^S$, $\mathbf{S}^T = \mathbf{S} + \mathbf{S}^S$. In this method, we maintain the same type of the stress-strain constitutive relation – that of the ideal elasticity relation. The self fields are related to the internal stresses and their action can replace the role of friction constitutive laws (Teisseyre 2004).

In this chapter we will consider the motion equations for dislocations and disclinations and fracturing phenomena: a process from a glide motion

to fracture slip and the subsequent formation of the soliton wave. Our consideration will end on a relation between the emitted seismic wave and the considered fracturing on a fault plane.

8.2 Fault and Related Stresses

Our problem concerns a fault seismic zone; its plane is defined by $y = x_2 = 0$. Defect accumulation and related induced shears on a fault $S_{12}(x, z)$ are described by the antiplane α_{11}, and inplane α_{31} dislocations; hence, there follows the orientation of the other axes ($x = x_1$, $z = x_3$). The system is surrounded by the intact rocks under stresses S_{11}, S_{22}, S_{33}. A fault plane is defined as that having its rigidity μ_0 smaller than its bulk value μ in the surrounding rocks $\mu_0 < \mu$. Considering the boundary conditions – stress continuity as well as their tangent derivatives – we get on the fault boundary

$$\mu_0 < \mu \rightarrow \alpha_0 \mu_0 = \alpha\mu \rightarrow \alpha_0 > \alpha \tag{8.1}$$

defining a dislocation density jumps up to the greater value along a fault zone.

In 1D (x, t) systems a dislocation density is given as gradient of stresses $\overline{S}$, but a dislocation density is related also to slip δ on a fault plane; both relations lead to the direct relation between slip and local stress on fault:

$$\overline{\alpha} = \frac{1}{\mu}\frac{\partial}{\partial x}\nabla\overline{S}, \quad \overline{\alpha} = \frac{1}{\Lambda}\nabla\delta, \quad \text{hence} \quad \delta = \frac{\Lambda}{\mu}\left(\overline{S} - \tau\right),$$

where τ is the friction, Λ is a certain reference thickness. When computing a dislocation density we count the dislocations comprised in a layer of such a thickness.

8.3 Evolution Equations for Dislocations and Disclinations

The defect conservation laws derived in Chapter 6 do not include the creation and annihilation processes:

$$\text{dislocation density:} \quad \dot{\alpha}_{pl} + \varepsilon_{pmk}\frac{\partial J_{kl}}{\partial x_m} + \varepsilon_{pmk}\varepsilon_{klq}Y_{mq} = 0, \tag{8.2a}$$

disclination density: $$\dot{\theta}_{pq} + \varepsilon_{pmk}\frac{\partial Y_{kq}}{\partial x_m} - b\varepsilon_{pmk}\varepsilon_{qns}\frac{\partial^2 \dot{\omega}^S_{(ks)}}{\partial x_m \partial x_n} = 0\,, \tag{8.3}$$

where **J** and **Y** are the dislocation and disclination currents, respectively.

With $Y_{kq} = -b\varepsilon_{nsq}\dfrac{\partial \dot{\omega}^S_{[ks]}}{\partial x_n}$, and $\theta_{pq} = b\varepsilon_{pmk}\varepsilon_{qns}\dfrac{\partial^2 \omega^S_{ks}}{\partial x_m \partial x_n}$

(b = {0, 1}; see Chap. 4) the relation (8.3) presents the identity. However, the self-rotation field ω^S can be treated as a source term as it may appear due to internal dynamic processes, like earthquakes (cf. Chap 4).

Thus, we can assume that the last term in (8.2a), as the source function term, may include the creation and annihilation of the dislocation pairs; the relation (8.2a) may be written simply as (Teisseyre 2001)

$$\dot{\alpha}_{pl} + \varepsilon_{pmk}\frac{\partial J_{kl}}{\partial x_m} = \Pi_{pl}\,, \tag{8.2b}$$

where Π is a source term, playing a similar role as body forces in usual equation of motion.

The stress-dislocations relation in our system can be written as follows (cf. Chap. 6, Eq. 6.32a):

$$\alpha_{11} = \frac{1}{\mu}\frac{\partial}{\partial z}S_{(12)} - \frac{1}{\mu^*}\frac{\partial}{\partial z}S_{[12]}\,, \tag{8.4a}$$

where the line dislocations are assumed to be parallel to the x-axis; μ^* is the rotation rigidity.

For the inplane case with the we obtain

$$\alpha_{31} = \frac{1}{2\mu}\frac{\partial}{\partial x}S_{(12)} - \frac{1}{2\mu^*}\frac{\partial}{\partial x}S_{[12]}\,, \tag{8.4b}$$

with the line dislocations parallel to the z-axis.

These relations permitts to treat the antiplane and inplane cases in a similar way.

8.4 Motion Equations: Fault and Radiation Parts

Following the results given in Chapter 6, the stress motion equations (6.35) become:

$$\left[\frac{\partial^2}{\partial x_k \partial x_l}\left(\lambda \partial_{ks} E_{ii} + 2\mu E_{(ks)}\right)\right]_{(ls)}$$
$$= \rho \frac{\partial^2}{\partial t^2} E_{(ls)} + \rho \frac{\partial}{\partial t} J_{(ls)} - \rho b \frac{\partial^2}{\partial t^2} \omega^S_{(ls)} \,. \tag{8.5a}$$

A dislocation current and the self-rotation field is practically limited to the fault zone; thus, we can write

$$\left(\frac{\partial^2}{\partial x_k \partial x_s} S_{(lk)}\right)_{(ls)} = \rho\left(\ddot{E}^T_{(ls)} - b\ddot{\omega}^S_{(ls)}\right) + \rho \dot{J}_{(ls)} \,, \tag{8.5b}$$

where for dislocation current (Chap. 6, Eq. 6.29) and velocity in a dynamic range (6.30) we have

$$J_{(ls)} = c(\varepsilon_{mlq}\alpha_{qs})_{(ls)} V_m \,, \quad V_m = \varepsilon_{mij} \frac{\alpha_{ip}}{|\alpha_{ip}|} \frac{S_{(jp)} - R}{R} \,. \tag{8.6}$$

From (8.6) we obtain

$$J_{(12)} = -c \frac{1}{2} \frac{S_{(12)} - R}{R} \left[2\mathrm{abs}\left(\frac{\partial}{\partial z} E_{(12)} + \frac{\partial}{\partial z} \omega^S_{[12]}\right) + \mathrm{abs}\left(\frac{\partial}{\partial x} E_{(12)} + \frac{\partial}{\partial x} \omega^S_{[12]}\right)\right] . \tag{8.7}$$

While for the basic equations for antisymmetric stresses we write after (6.35):

$$\frac{\partial^2}{\partial x_k \partial x_k} S_{[12]} = -2\mu^* \frac{\partial^2}{\partial x_k \partial x_k} \omega^S_{[12]} = \rho \frac{\partial^2}{\partial t^2} \omega_{[12]}$$
$$= \rho \frac{\partial^2}{\partial t^2} \omega^T_{[12]} - \rho \frac{\partial^2}{\partial t^2} \omega^S_{[12]} \,. \tag{8.8}$$

Motion equations in terms of strains become:

$$\frac{\partial^2}{\partial x_1^2} \lambda E_{ii} + \frac{\partial^2}{\partial x_1^2} 2\mu E_{11} + \frac{\partial^2}{\partial x_1 \partial x_2} 2\mu E_{(12)} = \rho \ddot{E}_{11} \,, \tag{8.9a}$$

$$\frac{\partial^2}{\partial x_2^2} \lambda E_{ii} + \frac{\partial^2}{\partial x_2^2} 2\mu E_{22} + \frac{\partial^2}{\partial x_1 \partial x_2} 2\mu E_{(12)} = \rho \ddot{E}_{22} \,, \tag{8.9b}$$

$$\frac{\partial^2}{\partial x_3^2}\lambda E_{ii} + 2\mu\frac{\partial^2}{\partial x_3 \partial x_3}E_{33} = \rho\ddot{E}_{33}\,, \tag{8.9c}$$

$$\lambda\frac{\partial^2}{\partial x_1 \partial x_2}E_{ii} + \left(\frac{\partial^2}{\partial x_1^2} + \frac{\partial^2}{\partial x_2^2}\right)\left(2\mu E_{(12)}\right) + \frac{\partial^2}{\partial x_1 \partial x_2}\left[\mu\left(E_{11} + E_{22}\right)\right]$$
$$= \rho\left(\ddot{E}_{(12)} - b\ddot{\omega}^S_{(12)}\right) + \rho\frac{\partial}{\partial t}J_{(12)}\,. \tag{8.9d}$$

The last equation can be written as

$$\left(\frac{\partial^2}{\partial x_1^2} + \frac{\partial^2}{\partial x_2^2}\right)\left(2\mu E_{(12)}\right) + \lambda\frac{\partial^2}{\partial x_1 \partial x_2}E_{ii} + \frac{\partial^2}{\partial x_1 \partial x_2}\left[\mu\left(E_{11} + E_{22}\right)\right]$$
$$- \rho\ddot{E}_{(12)} + \rho c\frac{\mu}{R}\dot{E}_{(12)}\left[2\mathrm{abs}\left(\frac{\partial}{\partial z}E_{(12)} + \frac{\partial}{\partial z}\omega^S_{[12]}\right)\right.$$
$$\left. + \mathrm{abs}\left(\frac{\partial}{\partial x}E_{(12)} + \frac{\partial}{\partial x}\omega^S_{[12]}\right)\right] = -\rho b\frac{\partial^2}{\partial t^2}\omega^S_{(12)}\,. \tag{8.9e}$$

The fault plane is defined as

$$\mu_0(y) = \mu\left[1 - \varepsilon_0\exp(-ay^4)\right]. \tag{8.10}$$

Hence, an elastic strain field $\mathbf{E}$ can be presented as difference, $\mathbf{E}^T - \mathbf{E}^S$ of the total $\mathbf{E}^T$ field and the self $\mathbf{E}^S = \omega^S$ strain part, and we identify these parts with the fault field $\mathbf{E}^S = \overline{\mathbf{E}}$ and the wave radiation field $\mathbf{E}^T = \tilde{\mathbf{E}}$. Further, we assume that the self strains are only important on a fault plane, and that this field shall rapidly extinct outside the fault plane $y = 0$. Thus, we can put

$$\begin{aligned} E_{(12)}(x,z,t) &= \exp\left(-Dy^4\right)\overline{E}_{(12)}(x,z,t)\,,\\ E_{[12]}(x,z,t) &= \exp\left(-Dy^4\right)\overline{E}_{[12]}(x,z,t) \end{aligned} \tag{8.11}$$

and further:

$$\begin{aligned} \alpha(x,z,t) &= \exp\left(-Dy^4\right)\overline{\alpha}(x,z,t)\,,\\ \gamma(x,z,t) &= \exp\left(-Dy^4\right)\overline{\gamma}(x,z,t)\,,\\ J(x,z,t) &= \exp\left(-Dy^4\right)\overline{J}(x,z,t)\,. \end{aligned} \tag{8.12}$$

As to other components, we take them for the fault and radiation parts:

$$\begin{aligned} E_{11}(x,z,t) &= \exp\left(\mathrm{i}k_x x + \mathrm{i}k_y y + \mathrm{i}k_z z - \mathrm{i}\omega t\right)\tilde{E}_{11}^0 \\ &\quad + \exp\left(-Dy^4\right)\bar{E}_{11}(x,z,t), \\ E_{22}(x,z,t) &= \exp\left(\mathrm{i}k_x x + \mathrm{i}k_y y + \mathrm{i}k_z z - \mathrm{i}\omega t\right)\tilde{E}_{22}^0 \\ &\quad + \exp\left(-Dy^4\right)\bar{E}_{22}(x,z,t), \\ E_{33}(x,z,t) &= \exp\left(\mathrm{i}k_x x + \mathrm{i}k_y y + \mathrm{i}k_z z - \mathrm{i}\omega t\right)\tilde{E}_{33}^0 \\ &\quad + \exp\left(-Dy^4\right)\bar{E}_{33}(x,z,t), \\ E_{12}(x,z,t) &= \exp\left(\mathrm{i}k_x x + \mathrm{i}k_y y + \mathrm{i}k_z z - \mathrm{i}\omega t\right)\tilde{E}_{12}^0 \\ &\quad + \exp\left(-Dy^4\right)\bar{E}_{12}(x,z,t). \end{aligned} \tag{8.13}$$

In a fault plane domain (x, z, t), $y = 0$ the fracturing processes will cause the stress changes while a seismic wave radiation will be observed in the considered (x, y, z, t) domain.

From (8.9) in the (x, y, z, t) domain, outside the fault, we obtain:

$$\left(-k_1^2 + \frac{\omega^2}{a^2}\right)\tilde{E}_{11} - \frac{\lambda}{\lambda+2\mu}k_1^2\left(\tilde{E}_{22} + \tilde{E}_{33}\right) = 0, \tag{8.14a}$$

$$\left(-k_2^2 + \frac{\omega^2}{a^2}\right)\tilde{E}_{22} - \frac{\lambda}{\lambda+2\mu}k_2^2\left(\tilde{E}_{11} + \tilde{E}_{33}\right) - \frac{2\mu}{\lambda+2\mu}k_1k_2E_{(12)} = 0, \tag{8.14b}$$

$$\left(-k_3^2 + \frac{\omega^2}{a^2}\right)\tilde{E}_{33} - \frac{\lambda}{\lambda+2\mu}k_3^2\left(\tilde{E}_{22} + \tilde{E}_{33}\right) = 0, \tag{8.14c}$$

$$\left(-k_1^2 - k_2^2 + \frac{\omega^2}{c^2}\right)\tilde{E}_{(12)} - k_1k_2\left[\frac{\lambda}{2\mu}\tilde{E}_{ii} + \frac{1}{2}\left(\tilde{E}_{11} + \tilde{E}_{22}\right)\right] = 0, \tag{8.14d}$$

where a and c are the P- and S-wave velocities.

On the fault $y = 0$, we put $c = c_0$ in the (x, z, t) domain, and we obtain

$$\left(2\mu\frac{\partial^2}{\partial x_1^2}+2D\mu_0\right)\overline{E}_{(12)}-\rho\frac{\partial^2}{\partial t^2}\overline{E}_{(12)}$$
$$+c_0\rho\frac{\mu}{R}\frac{\partial}{\partial t}\overline{E}_{(12)}\left[2\mathrm{abs}\left(\frac{\partial}{\partial z}\overline{E}_{(12)}+\frac{\partial}{\partial z}\overline{\omega}^S_{[12]}\right)\right.$$
$$\left.+\mathrm{abs}\left(\frac{\partial}{\partial x}E_{(12)}+\frac{\partial}{\partial x}\omega^S_{[12]}\right)\right]=-\rho b\frac{\partial^2}{\partial t^2}\overline{\omega}^S_{(12)}\,, \tag{8.15}$$

where the relations for other components appear to be independent of $\overline{E}_{(12)}$; hence, we put

$$\overline{E}_{11}=0\,,\qquad \overline{E}_{22}=0\,,\qquad \overline{E}_{33}=0\,.$$

For the inplane motion

$$\left(2\mu_0\frac{\partial^2}{\partial x_1^2}+2D\mu_0\right)\overline{E}_{(12)}-\rho\frac{\partial^2}{\partial t^2}\overline{E}_{(12)}$$
$$+\,c_0\rho\frac{\mu}{R}\frac{\partial}{\partial t}\overline{E}_{(12)}\,\mathrm{abs}\left[\frac{\partial}{\partial x}\left(\overline{E}_{(12)}+\overline{\omega}^S_{[12]}\right)\right]=-\rho b\frac{\partial^2}{\partial t^2}\overline{\omega}^S_{(12)}\,, \tag{8.16a}$$

and for the antiplane motion

$$2D\mu_0\overline{E}_{(12)}-\rho\frac{\partial^2}{\partial t^2}\overline{E}_{(12)}$$
$$+2c_0\rho\frac{\mu}{R}\frac{\partial}{\partial t}\overline{E}_{(12)}\,\mathrm{abs}\left(\frac{\partial}{\partial z}E_{(12)}+\frac{\partial}{\partial z}\omega^S_{[12]}\right)=-\rho b\frac{\partial^2}{\partial t^2}\overline{\omega}^S_{(12)}\,. \tag{8.16b}$$

The obtained equations can be written (with $\overline{E}_{(12)}=X$, and $G=\overline{\omega}^S_{[12]}$, $F=-\frac{1}{c_0^2}b\frac{\partial^2}{\partial t^2}\overline{\omega}^S_{(12)}$ the source terms) as follows:

$$\frac{\partial^2}{\partial x^2}X-\frac{1}{c_0^2}\frac{\partial^2}{\partial t^2}X+B\frac{\partial}{\partial t}X\,\mathrm{abs}\left(\frac{\partial}{\partial x}(X+G)\right)+AX=F\,, \tag{8.16a'}$$

$$-\frac{1}{c_0^2}\frac{\partial^2}{\partial t^2}X+2B\frac{\partial}{\partial t}X\,\mathrm{abs}\left(\frac{\partial}{\partial z}(X+G)\right)+AX=F\,, \tag{8.16b'}$$

where c_0 is the shear wave velocity on a fault plane ($\mu=\mu_0$).

The source functions F and G are related to dislocation densities, see Eqs. (8.4a) and (8.4b). Probably the source functions F and G cannot be given independently; for the final moment of the process, the counterparts of the inplane and antiplane motions shall be related to each other on a common plane to approch the equilibrium condition $\operatorname{div} \mathbf{S} \to 0$. In other words, the counterparts of the inplane and antiplane motions are mutually related on a common plane, at least, for a final time moment $t \to t_0$, when

$$\operatorname{div} \mathbf{S}(x, y, z, t_0) \to 0 . \tag{8.16c}$$

Both motions can occur simultaneously, see Fig. 8.1.

Assume that an inplane motion occurs first, forming a fractured segment; its sides parallel to motion direction become formed with the related screw dislocations; we may expect that an antiplane motion might start in a neighbouring segment – see Fig. 8.2 (such a sequence can start reversely: first an antiplane motion and then an inplane one).

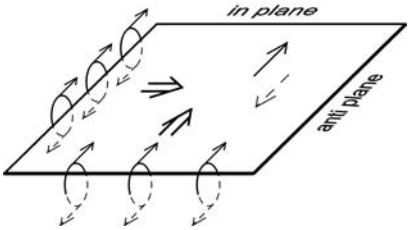

Fig. 8.1 Fault plane: simultaneous inplane and antiplane motions

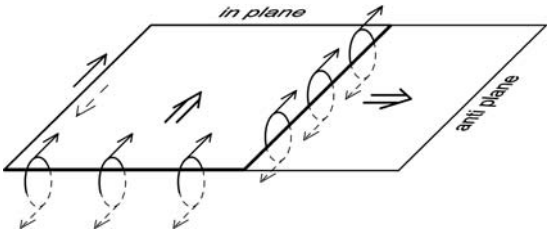

Fig. 8.2 Inplane motion and induced antiplane motion on the neighbouring faults

These motions could be separated by some time interval (shock and aftershock); the related motions described by one of these equations (8.16a') or (8.16b') can start later releasing stresses in an aftershock with the final condition (8.16c).

Of course, these equations can be simply solved separately for the inplane and antiplane motions; when putting for the searched function and

for the source functions $X = X(x, t)$, $F = F(x, t)$ and $G = G(x, t)$, we arrive at the following independent equations:

– inplane

$$\frac{\partial^2}{\partial x^2} X - \frac{1}{c_0^2}\frac{\partial^2}{\partial t^2} X + B\frac{\partial}{\partial t} X \,\mathrm{abs}\left(\frac{\partial}{\partial x}(X+G)\right) + AX = F\,, \tag{8.17a}$$

– antiplane

$$X = X(z,t)\,, \qquad F = F(z,t)\,, \qquad \text{and} \qquad G = G(z,t)\,,$$

$$-\frac{1}{c_0^2}\frac{\partial^2}{\partial t^2} X + 2B\frac{\partial}{\partial t} X \,\mathrm{abs}\left(\frac{\partial}{\partial z}(X+G)\right) + AZ = F\,, \tag{8.17b}$$

where, e.g., the source functions can be given as proportional to sine -terms:

$$G = G_0 \sin\left[\theta(x - Vt)\right], \quad \text{and} \quad F = F_0 \sin\left[\theta(x - Vt)\right],$$

and respectively:

$$G = G_0 \sin\left[\vartheta(z - Wt)\right], \quad \text{and} \quad F = F_0 \sin\left[\vartheta(z - Wt)\right].$$

These equations can be solved numericaly with the assumed intial conditions $X(x, 0) = \sin(x)$ and for $X(x, 0) = x \sin(x)$; some examples of the obtained solutions are presented in Figs. 8.3–8.10 in the domains x: $\{0, \pi\}$, t: $\{0, \pi\}$.

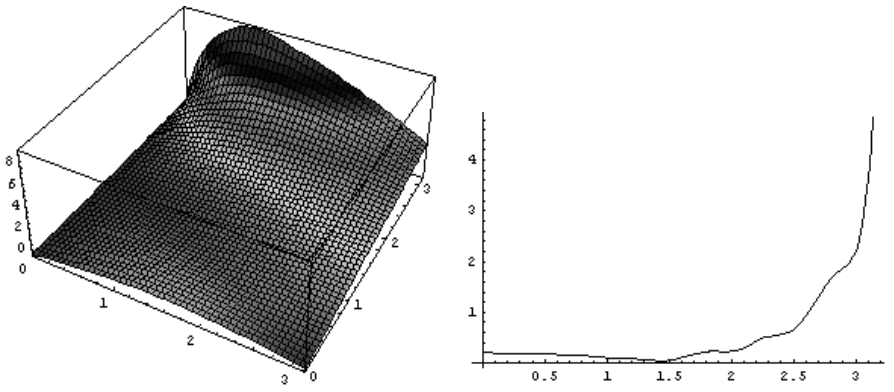

Fig. 8.3 Inplane motion for $X(x, 0) = \sin x$ and $X(0, t) = 0$, $X(\pi, t) = t$. *Left:* 3D plot $X(x, t)$. *Right:* plot for $X(1.5, t)$

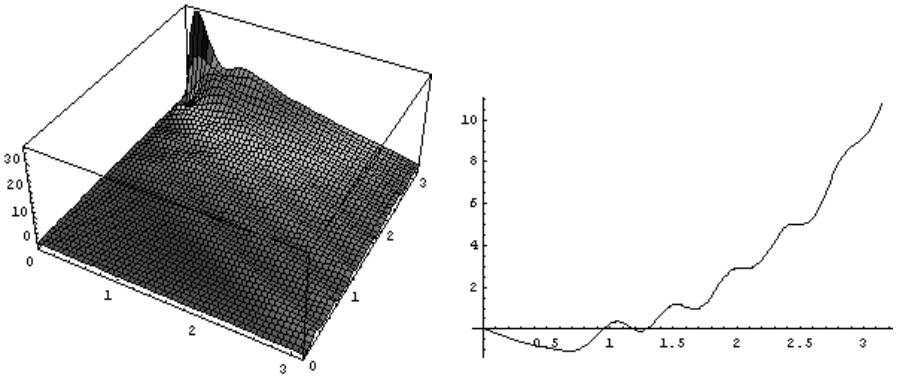

Fig. 8.4 Inplane motion for $X(x, 0) = \sin x$ and $X(0, t) = 0$, $X(\pi, t) = t$. *Left:* 3D plot $\partial/\partial t\, X(x, t)$. *Right:* plot for $\partial/\partial t\, X(1.5, t)$

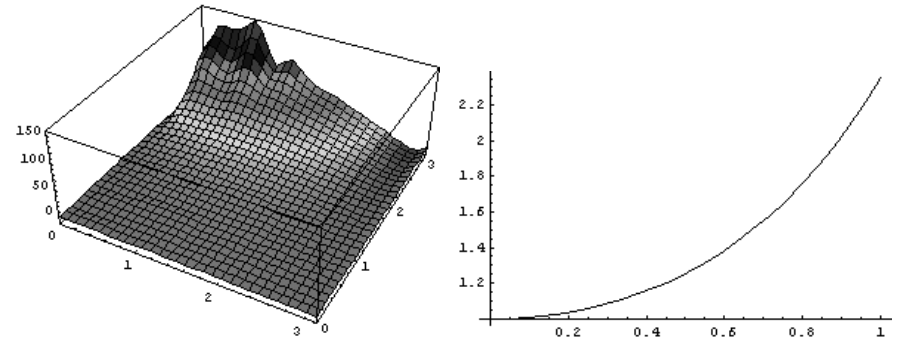

Fig. 8.5 Antiplane motion for $X(x, 0) = \sin x$ and $X(0, t) = 0$, $X(\pi, t) = t$. *Left:* 3D plot $X(x, t)$. *Right:* plot for $X(1.5, t)$

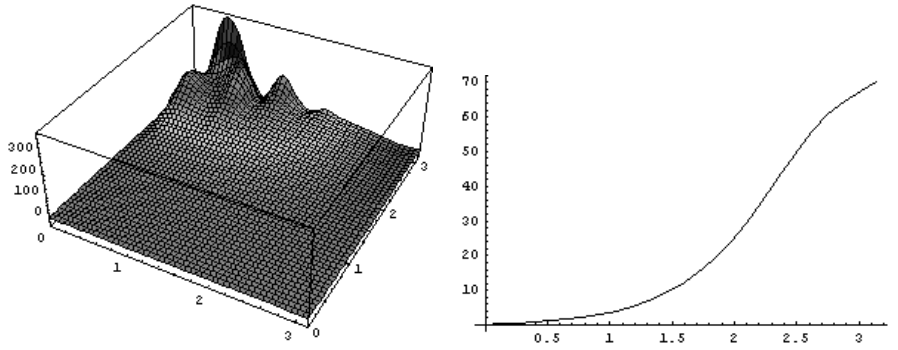

Fig. 8.6 Antiplane motion for $X(x, 0) = \sin x$ and $X(0, t) = 0$, $X(\pi, t) = t$. *Left:* 3D plot $\partial/\partial t\, X(x, t)$. *Right:* plot for $\partial/\partial t\, X(1.5, t)$

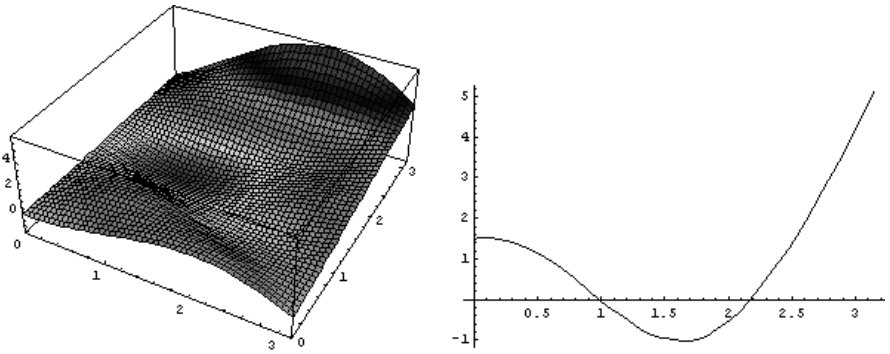

Fig. 8.7 Inplane motion for $X(x, 0) = x \sin x$ and $X(0, t) = 0$, $X(\pi, t) = t$. *Left:* 3D plot $X(x, t)$. *Right:* plot for $X(1.5, t)$

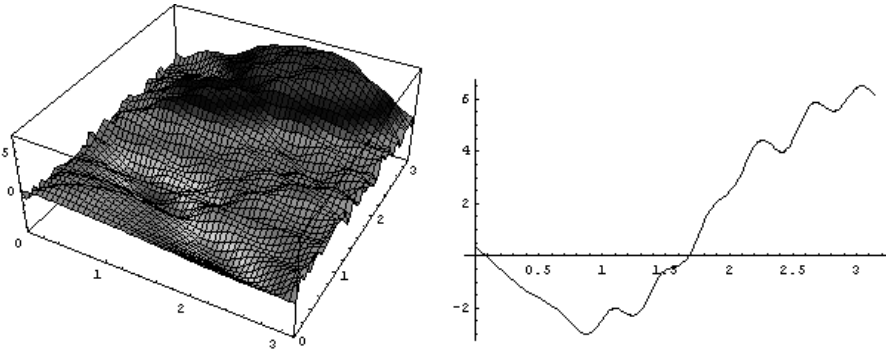

Fig. 8.8 Inplane motion for $X(x, 0) = x \sin x$ and $X(0, t) = 0$, $X(\pi, t) = t$. *Left:* 3D plot $\partial/\partial t\, X(x, t)$. *Right:* plot for $\partial/\partial t\, X(1.5, t)$

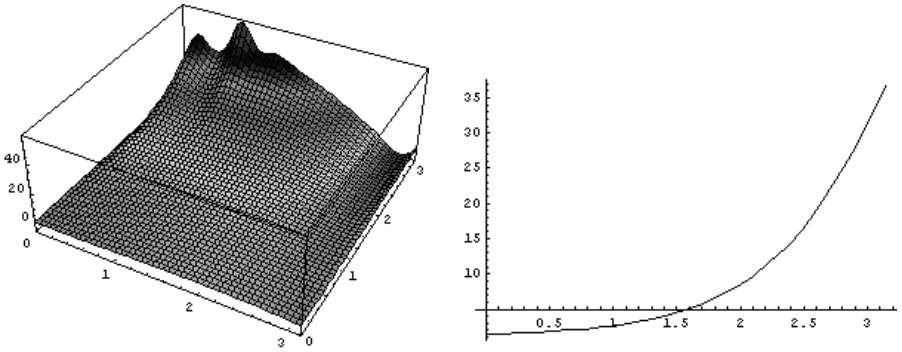

Fig. 8.9 Antiplane motion for $X(x, 0) = x \sin x$ and $X(0, t) = 0$, $X(\pi, t) = t$. *Left:* 3D plot $X(x, t)$. *Right:* plot for $X(1.5, t)$

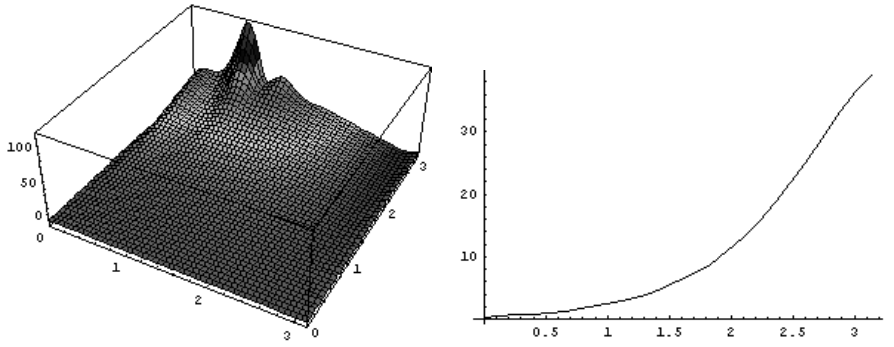

Fig. 8.10 Antiplane motion for $X(x, 0) = x \sin x$ and $X(0, t) = 0$, $X(\pi, t) = t$. *Left:* 3D plot $\partial/\partial t\, X(x, t)$. *Right:* plot for $\partial/\partial t\, X(1.5, t)$

Solutions were obtained with the help of Mathematica Version 5 Program. An additional boundary condition for $X = 0$ is given by $X(0, t) = 0$. The other boundary condition for $x = \pi$ can also be assumed as $X(\pi, t) = 0$, which will corresponds to the motion presented in Fig 8.1, or we can resign from such a restriction allowing further fault propagation as presented in Fig. 8.2.

With the obtained solutions, we can return to the wave equations outside the fault (8.14a, b, c, d), where the known solutions on a fault $X = \overline{E}_{(12)}$ are treated as the boundary/initial conditions for $E_{(12)}$.

8.5 Discussion

The presented approach helps us to better understand a relation between the inplane and antiplane motions; their relation on a common fault becomes evident. For the independent solutions in time (shock and aftershock), we can take the initial condition for equation describing aftershock as that given by the final value of first solution describing main shock.

We shall also recall that the space derivatives of the strains are proportional to the related dislocation densities.

References

Teisseyre R (2001) Evolution, propagation and diffusion of dislocation fields. In: Teisseyre R and Majewski E (eds) Earthquake thermodynamics and phase transformations in the earth's interior. Academic Press, San Diego, pp 167-198

Teisseyre R (2004) Spin and twist motions in a homogeneous elastic continuum and cross-band geometry of fracturing. Acta Geophys Pol **52**: 2, 173-183

Teisseyre R, Boratyński W (2003) Continua with self-rotation nuclei: evolution of asymmetric fields. Mech Res Commun **30**: 235-240

Teisseyre R, Yamashita T (1999) Splitting stress motion equation into seismic wave and fault-related fields. Acta Geophys Pol **47**: 2, 135-147

9 A Review on Friction

Panayiotis Varotsos, Mary Lazaridou

Solid Earth Physics Institute, Department of Physics, University of Athens
Panepistimiopolis, Zografos 157 84, Athens, Greece
e-mail: pvaro@otenet.gr

9.1 Introduction

Tribology is in general the study of adhesion, friction, lubrication and wear of surfaces in relative motion. It seems that the more we learn about tribology the more complex it appears (Urbakh et al. 2004). Recent advances in friction reveal that it plays a major role in diverse systems and phenomena which although at first glance seemed to be unrelated are found to exhibit common features that are shared by all tribological processes in the fields of physics, chemistry, biology, geology and engineering.

In the explanation of the classical laws of friction, e.g., the static friction, force is proportional to the load, and even since the early attempts (Coulomb 1785) the role played by interactions between asperities at the surfaces of solids was emphasized. Furthermore, the idea was put forward (Bowden and Tabor 1950, 1964) that the real contact area is very small and involves such large stresses that a significant plastification occurs. In simple words, one may view a material surface as being rough, consisting of asperities of different sizes which will deform under pressure. Thus, for **static friction**, in the frame of the so-called adhesion model, the friction results from the intermolecular adhesion between two surfaces at the points of contact (e.g., see Bowden and Tabor 1950, 1964). The basic assumption of this model is that when placing one surface on top of another, the deformation will cease when the total yield pressure of the asperities becomes equal to the load of the upper surface divided by the total contact area A_c. This area is usually several orders of magnitude smaller than the apparent area A, e.g., $A_c/A \approx 10^{-6}$ (Johansen et al. 1993); thus, even though the apparent area A may be macroscopic, the actual contact area A_c can be small to such an extent that microscopic randomness may not simply average out. This is the stochastic element that can result in strong fluctuations

of the static friction. Hence, the aforementioned classical friction law, stating that the static friction force is proportional to the load, holds only in an average sense. In the case of **dynamic friction**, as the velocity increases, there will be more momentum transfer into the normal direction, producing an upward force on the upper surface. This results in an increase in the separation between the two surfaces, thus leading to a decrease in the contact area. In the frame of the adhesion model, the decrease of the contact area reflects a reduced adhesion, which qualitatively explains the experimental results. An alternative model, which uses the collisions between the asperities as the dissipation mechanism, was also suggested. However, in spite of their partial success, these two models cannot fully account for the observed (non-linear hysteretic) phenomena (e.g., see Section 9.2). Both models lead to the following picture: If the fluctuations in the static friction are indeed determined by surface area and contact area, then the dynamic friction should fluctuate for the same reasons. This shows that the deterministic friction velocity relations suggested (e.g., see Section 9.3) hold only in an average sense.

Furthermore, there are puzzles even for fully understanding very simple cases. For example, take a coin and launch it across your desk, recording the distance travelled. Now spin the coin about the axis perpendicular to its surface as you launch it; the coin will travel farther, even if we launch it with the same initial velocity. The coin will stop moving and stop spinning at *exactly* the same instant (Farkas et al. 2003). The explanation of such experiments (e.g., see Halsey 2003 and references therein) may be achieved on the basis of the suggestion that the coupled equations, describing how the spinning motion of the coin and its velocity both decrease with time, are highly non-linear (cf. The nonlinear nature of friction in general has been reviewed by Urbakh et al. 2004). It is recently shown (Farkas et al. 2003) that even when considering a coin, the sliding on a table is not a simple system. The frictional mechanics of the coin is governed by material phenomena at scales much smaller than the size of the coin. The well-known laws of friction (i.e., the so-called Amonton's laws) ignore the existence of these complex phenomena at smaller length scales entirely, at the cost of introducing a highly non-linear description of the macroscopic scale of the coin (Halsey 2003).

Finally, we shortly refer to comment on the reason why several attempts have been made to model earthquakes by spring-block systems (with many degrees of freedom). Assume that a block resting on a surface is attached to a spring, the other end of which is pulled at a constant velocity. It has been observed that, at sufficiently slow velocities, the sliding process is not a continuous one, but the motion proceeds by jerks; the contact surfaces "stick" together until (as a result of the gradually increasing pull) there is a

sudden break with a consequent very rapid slip. This behaviour has been termed **stick-slip** motion and is reminiscent of fault seismicity (e.g. Brace and Byerlee 1966, Scholz 1998).

9.2 Stick-Slip Friction of a Granular System. Hysteresis and Precursors

The response of a granular medium to shear forces plays a major role in earthquake dynamics. Slipping events occur along faults which are often separated by a "gouge" filled with sand or other granular material between more rigid regions (Lubkin 1997). The actual time-dependent frictional forces of granular material during brief periods of motion, i.e., individual slip events, have been experimentally studied by Nasuno et al. (1997), who were able to determine force variations within slip events lasting as little as 40 ms. Earlier studies of granular friction have mostly emphasized large systems, high velocity flows, and large normal stress, while Nasuno et al. (1997) measurements allowed direct imaging of particle dynamics and showed a stick-slip behaviour at low velocity across the layer, with a transition to continuous motion at higher velocity gradients (see the caption to Fig. 9.2). Furthermore, they found that the frictional force, within individual slip events, is a multi-valued function of velocity (Fig. 9.2b) and that localized microscopic rearrangements precede (and follow) macroscopic slip events.

The experiment of Nasuno et al. (1997) could be briefly described as follows: A 2mm-thick granular layer consists of spherical glass beads with diameters ranging from 70 to 110 μm. Shear stress was applied, by pushing with a (adjustable stiffness) leaf spring, on a transparent glass cover plate (which was roughened to prevent slip at the plate surface) across the granular layer. A translational stage pushes the spring mount at a speed υ, and the spring deflection was measured as a function of time. Figure 9.1 depicts the results for various velocities: For a relatively low velocity, i.e., $\upsilon \approx 5.67$ μm/s, a stick-slip motion (a) occurs; upon using a stronger spring, the deflections become smaller but the motions remain discrete. Increasing the velocity υ by a factor of 1000 (using the same weak spring as in "a"), the dynamics changed from stick-slip motion to an inertia-dominated oscillation (b). Upon a further increase of velocity, a critical value of υ was reached, and the motion became irregular but continuous.

It seems that the stick-slip motion is a characteristic behaviour but only at low velocities. The **stick-slip phenomena** can be summarized as follows: If k denotes the spring constant and m the mass of the upper plate,

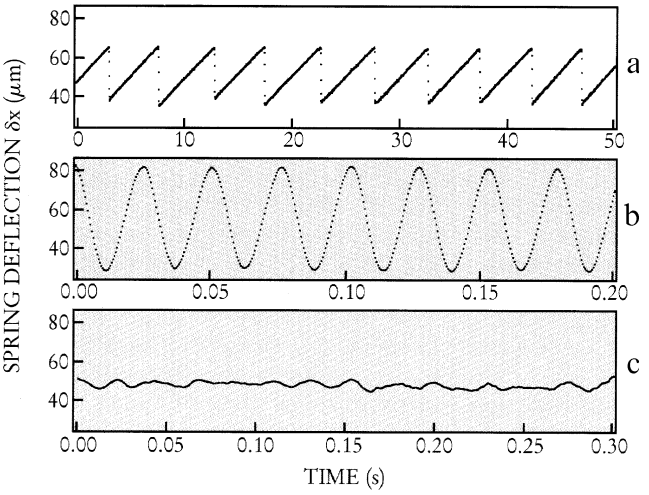

Fig. 9.1 Spring deflection as a function of time according to the experiment of Nasuno et al. (1997): (a) For a relatively low velocity $\upsilon = 5.67$ μm/s, stick-slip motion occurs. When the system sticks, the cover plate is at rest, and the spring deflection increases linearly with time until it applies the maximum static friction force; upon reaching this value, the granular layer cannot sustain the imposed shear stress and the plate suddenly accelerates, while the friction force decreases. When the stress becomes small enough, sticking recurs. (b) When velocity is 1000 times larger, $\upsilon = 5.667$ mm/s, inertia-dominated oscillation occurs. (c) When υ becomes even larger, $\upsilon = 11.33$ mm/s, steady sliding motion with fluctuations occurs (Lubkin 1997)

the slip duration τ_s is comparable to the characteristic inertial time $\tau_{in} = 2\pi\sqrt{m/k}$ (recall that the angular frequency ω is given by $\omega = \sqrt{k/m}$ and $\omega \equiv 2\pi/\tau_{in}$) and is substantially shorter than the time between slip events. The granular flow during slip seems to occur predominantly in the top few layers of the particles. It is important to note that visual observation reveals that the onset of sliding involves fluidization (i.e., transition from a solid state to fluid state, see also Section 9.5) of granular particles in the upper layers. The observed stick-slip motion is almost periodic for a wide range of parameter values. As the pushing velocity υ increases, the mean period T decreases while the slip distance per event remains constant, until the inertia dominated regime is reached, which is depicted in the middle of Fig. 9.1b. The transition from the latter regime to continuous sliding (with fluctuations, see Fig. 9.1c) occurs at a critical value υ_c, which decreases with increasing k and also varies with m. The oscillation amplitude strongly fluctuates near υ_c.

An investigation of what happens during individual slip events is depicted in Fig. 9.2. Figure 9.2a shows the instantaneous sliding velocity versus time for four different pushing speeds ranging from $\upsilon = 56.67$ to 1133.27 μm/s; despite the large variation in the pushing velocity υ (cf. for fixed spring constant and mass), it is remarkable that the four curves coincide and reveal "velocity pulses" as large as 1 cm/s, which last only a short time, i.e., around 40 ms. The instantaneous (normalized) frictional force μ

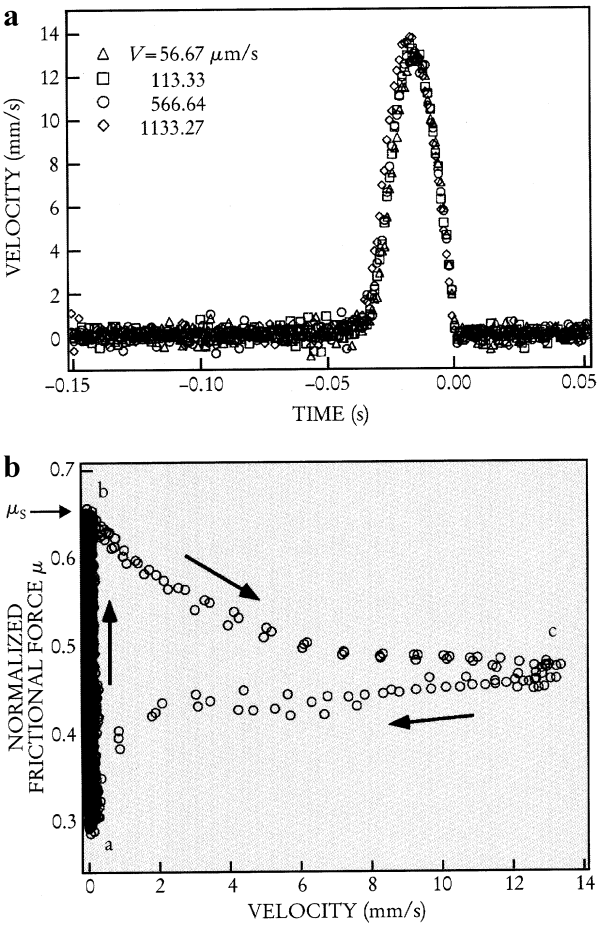

Fig. 9.2 Study of individual slip events, according to the experiment of Nasuno et al. (1997): **(a)** Instantaneous velocity versus time, for four different pushing speeds (the pulses are forced to coincide at the end of each event); **(b)** Instantaneous normalized frictional force for 3 different slip events, which correspond to the same pushing speed $\upsilon = 113$ μm/s (Lubkin 1997)

($\mu = F/mg$, where g stands as usually for the gravity acceleration) *versus* the instantaneous sliding velocity (of the moving plate that has mass m, as mentioned) is depicted in Fig. 9.2b, for three slip events, but for a given pushing speed $\upsilon = 113$ μm/s. An hysteresis loop is observed as follows: The cover plate is at rest at the position "a" and the applied force starts to continuously increase; the frictional force rises (from the position "a" to "b") along the vertical axis and at point "b" the motion begins; between "b" and "c" the plate is accelerating (the velocity increases, but the frictional force decreases) and the velocity reaches its maximum value at "c" (where the frictional force reaches a low value). From "c" to "a", the plate decelerates (until coming to rest), the frictional force remains low (it continues to decrease slowly at first and then rapidly as the slider comes to rest) and does not retrace the first part ("c"→ "b"); the arrows in Fig. 9.2b indicate a hysteresis loop, which is identical for all events in a run. The frictional force is not a single valued function of velocity (memory effects); it is larger for increasing than for decreasing velocity within individual events. One source of the latter difference is that an expansion of the layer during motion occurs, i.e., the measurements show that the layer thickness increases by roughly 15 μm during the slip events; thus a time (about 2 ms) is required for the plate to fall a distance equal to the observed (vertical) dilation of 15 μm.

Imaging the granular layer through a microscope, Nasuno et al. (1997) clarified what happens during apparently quiescent intervals: Significant microscopic rearrangement events occur, during the sticking intervals, and their accumulation leads to creep. By subtracting two adjacent images (cf. the system was photographed at one-second intervals) they observed that *they are not identical, there are regions that have moved* (microscopic slip sites) (Lubkin 1997). The frequency of these microscopic rearrangements of **precursor events** was found to increase dramatically just before a major slip event; thus, before the major events, the precursors were also detectable macroscopically, because they contribute a finite amount of the creep. The accumulated precursors produce a displacement by about 1% as large as that occurring during a slip event.

Stick-slip motion at low speed was also found in recent experiments (quoted by Lubkin 1997) that studied the friction between relatively smooth solids, e.g., a paper sliding on a paper; these experiments also reported creep before a slip event and showed an increase of the coefficient of static friction, when the materials remained in contact.

9.3 Rock Friction

During the last several decades, geophysicists have been trying to explain the energy budget for tectonic faulting, which does not seem to add up (see Marone 2004 and references therein). The main unexplained fact could be summarized as follows: Faults appear more slippery (in other words, less constrained by friction) than has been predicted by theoretical work and laboratory measurements. The latter indicate that the frictional stress faulting (close to the Earth's surface) must be of the order of 50-100 MPa. This reflects that, during faulting, substantial heat should be produced in view of the following fact: when counting the other main energy expenses, i.e., radiation of seismic waves, and the creation of surface area from the production and comminution of "wear material", we find that they are only a small fraction of the total energy dissipation (which is estimated upon considering that the income side of energy budget comes from the driving forces of plate tectonics and the elastic energy stored in the Earth's solid crust). The problem consists in the fact that the expected frictional heat is missing (e.g., Scholz 2000).

It has been suggested long ago, as already mentioned, that earthquakes result from a stick-slip frictional event, and it was assumed that sliding begins when the ratio of shear to normal stress on the surface reaches a value μ_s, **the static friction coefficient**. Once sliding initiates, the frictional resistance decreases and is described through a lower **dynamic friction coefficient** μ_d; this weakening of sliding resistance may, depending on the stiffness of the system, result in a dynamic instability (Scholz 1998). However, according to the recent aspects of rock mechanics (e.g., see Tullis 1996, Scholz 1998), there is an ageing of μ_s (i.e., static friction increases with the time of being static) and a velocity dependence of μ_d (μ_d decreases with increasing slip velocity, but see below); in addition, when the velocity is changed, the transition to the new frictional resistance requires sliding some distance. Thus, within the frame of the new notions, there is now a continuum of varying friction values, while in the old frame the situation was described, as mentioned, in terms only of the static friction μ_S and the dynamic friction μ_d alone.

The current views on the rock friction behaviour could be alternatively summarised as follows: There are two competing effects: the **direct effect** and the **evolution effect**. The former is an initial increase in the resistance to sliding that occurs when the velocity of sliding is abruptly increased (Fig. 9.3); this is termed "the direct effect", because the change of resistance occurs instantaneously and in the same sense as the change in velocity (Tullis 1996). The second effect refers to the fact that, after abrupt

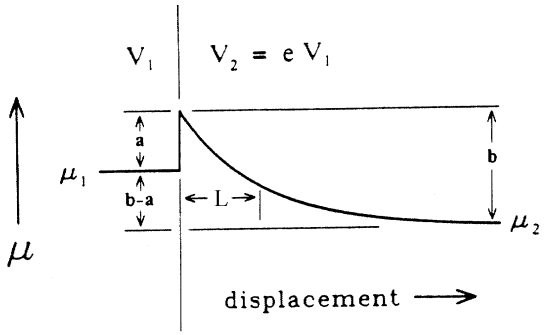

Fig. 9.3 The frictional response *versus* the displacement, when the sliding velocity suddenly increases from a smaller value to a larger one and then is returning to its initial value (Scholz 1998)

changes in velocity, the frictional resistance evolves to a new steady-state resistance over a characteristic slip distance (thus the term "evolution effect"). When sliding is stopped for some period of time (after having attained a steady-state frictional resistance at constant velocity) and then resumed, the resistance climbs up to a peak value, which is larger than the steady-state value prior to the hold, and subsequently decays to the original steady-state value. The peak value increases nearly with the logarithm of the hold time (Fig. 9.4), i.e., surfaces in stationary contact increase in strength with time (thus a re-strengthening of surfaces between slip episodes occurs, without which a repeated unstable slip is impossible); this effect, which is an important aspect of rock friction in terms of application to earthquakes, is known as the **evolution effect**.

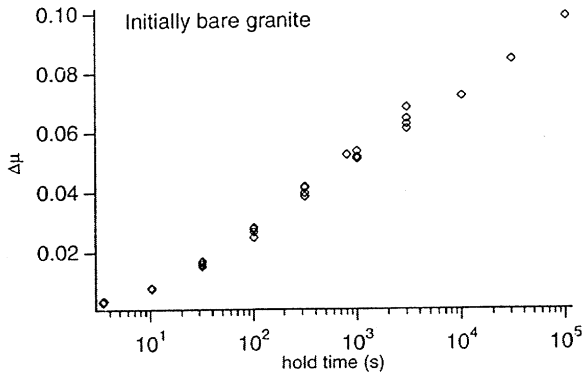

Fig. 9.4 The increasing $\Delta\mu$ of the static friction *versus* the time period of holding static (Tullis 1996)

In summary, laboratory experiments show that the friction of rocks is a function of time, velocity of sliding, and displacement. The processes responsible for these dependencies are still unknown. Furthermore, the following point must be emphasized (e.g., see Tullis 1996): No laboratory experiments in rocks combine the large displacement, high slip rate, high normal stress, and presence of pressurized pore fluids that characterize earthquake slip. This means that the processes that may occur during dynamic slip in earthquakes have not been thoroughly explored experimentally. Chief among these are the shear heating and the associated possible melting or increase in pore fluid pressure. Recent laboratory experiments, that have been performed at high sliding velocities, of the order of m/s (see Section 9.4), which are believed to occur before earthquakes, showed that some of the conclusions deduced from the earlier laboratory measurements cannot be extended to the high velocity regime.

The laboratory observations are described through the so-called rate/state-variable constitutive law. However, when one looks carefully at the details, none of the laws suggested fits all aspects of experimental data and a better law is needed (Tullis 1996). The version of "the rate and state friction law", which is believed to better account for the experimental data (Beeler et al. 1994, Scholz 1998), is the Dieterich–Ruina or "slowness" law, which reads:

$$\tau = \left[\mu_0 + a \ln\left(\frac{\upsilon}{\upsilon_0} \right) + b \ln\left(\frac{\upsilon_0 \theta}{L} \right) \right] \sigma \tag{9.1}$$

where τ denotes the shear stress and σ the effective normal stress (i.e., the applied normal stress minus pore pressure), υ is the slip velocity, υ_0 is a reference velocity and a, b are the material properties (see below); thus, the frictional resistance is described in terms of the so-called base friction μ_0 (the steady-state friction at $\upsilon = \upsilon_0$), nearly independent of rock type and temperature, which is modified by second order effects involving a dependence on sliding velocity and a state variable θ (Scholz 1998); the latter evolves according to

$$\frac{\mathrm{d}\theta}{\mathrm{d}t} = 1 - \frac{\theta \upsilon}{L} \tag{9.2}$$

and hence at the steady state (SS)

$$\theta_{SS} = \frac{L}{\upsilon} \ , \tag{9.3}$$

where L is the critical slip distance, which is usually interpreted as the sliding distance required to renew the contact population and, in this frame, θ_{SS} represents an average "contact lifetime". At steady state, we have

$$\tau = \left[\mu_0 + (a-b) \ln\left(\frac{\upsilon}{\upsilon_0} \right) \right] \sigma \tag{9.4}$$

and a–b could be defined as the velocity dependence of steady-state friction μ_{SS}:

$$a - b = \frac{\partial \mu_{SS}}{\partial (\ln \upsilon)} \ . \tag{9.5}$$

This can be visualised in Fig. 9.3, which schematically shows what happens when the sliding velocity is abruptly increased from a smaller value (the left portion in Fig. 9.3) to a larger one (the right portion); upon the initial application of the velocity increase, there is an "abrupt" increase a in friction, which is followed by a gradual decrease b (the difference in the friction of the two stages is equal to a–b, as shown).

A possible connection of μ_S and μ_d to the parameters a and b could be described as follows: If we define the dynamic friction coefficient μ_d as the steady friction μ_{SS} at velocity υ, and μ_S as the starting friction following a period of time in stationary contact, we have:

$$\frac{\partial \mu_d}{\partial (\ln \upsilon)} = a - b \tag{9.6a}$$

and, for long t:

$$\frac{\partial \mu_S}{\partial (\ln t)} = b \ . \tag{9.6b}$$

If a–$b > 0$, the steady state friction μ_{SS} increases upon increasing velocity υ (see Eq. 9.5); such a system is intrinsically stable. On the other hand, if a–$b < 0$, the value of μ_{SS} decreases upon increasing υ; this is the case which is of interest for earthquakes, because when the applied normal stress σ exceeds a critical value σ_c the sliding is unstable under quasistatic loading. This can be understood on the basis of a spring-slider model (with fixed stiffness k) depicted in Fig. 9.5a in which the slider is assumed to obey Eq. (9.1). Figure 9.5b shows the velocity jump $\Delta\upsilon$, necessary to destabilize the system, *versus* σ. This reveals that if σ exceeds the critical value:

$$\sigma_c = -kL/(a-b) \tag{9.7}$$

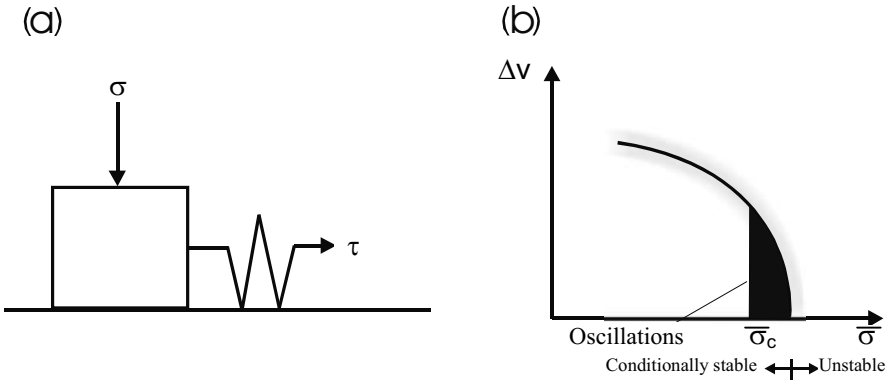

Fig. 9.5a A spring-slider model obeying Eq. (9.1); (b) the velocity jump $\Delta\upsilon$, necessary to destabilize the system, *versus* σ (Scholz 1998)

sliding is unstable with respect to a vanishing incremental velocity perturbation $\Delta\upsilon$ (i.e., a quasistatic loading). If $\sigma < \sigma_c$ the system is in the so-called conditionally stable field, because it is stable under quasistatic loading, but may become unstable under sufficiently strong dynamic loading, i.e., if subjected to a velocity jump $\Delta\upsilon$ exceeding that depicted in Fig. 9.5b. For smaller jumps, at the stability border (close to σ_c, see the shaded region of Fig. 9.5b), sliding occurs by self-sustaining oscillatory motion (Scholz 1998, Heslot et al. 1994). Earthquakes can nucleate only in the regions of a fault which lie within the unstable regime.

Equation (9.7) is derived in the case of the one dimensional spring-slider of Fig. 9.5a. For the two or three dimensional case of a slipping patch of size L, the stiffness k can be written as $k = nG/L$ (Scholz 1998), where G is the shear modulus and n a geometrical factor of the order of unity. This implies that the instability occurs when L reaches a critical size L_c, called the nucleation length, given by (see Eq. 9.7):

$$L_c = \frac{GnL}{(b-a)\sigma} \quad . \tag{9.8}$$

Laboratory observations indicate that stable sliding initiates at a point and then spreads out with an accelerating sliding velocity until the instability arises at L_c. It is not known yet whether such a nucleation occurs at natural faults. Furthermore, the physical significance as well as the scaling of the parameter L, which is of the order of ~10 μm in the laboratory, have not yet been clarified.

9.4 Laboratory Experiments at High Rates of Slip. The Energy Budget for Tectonic Faulting

As already mentioned in the previous section, the dynamics of the tectonic faults that produce earthquakes remains puzzling (Marone 2004) since an energy budged imbalance seems to exist in tectonic faulting. Recent laboratory experiments, however, which will be discussed in this section, when applied to tectonic faults indicate that frictional stress and shear heating may be much lower than expected, thus probably resolving, at least partially, the question of this imbalance.

The friction experiments in rocks mentioned in the previous section have been made at steady-state sliding conditions using velocities of no more than ≈1 cm/s; at such velocities, as mentioned, hysteretic elastic and plastic deformations at the scale of roughness asperities are of significant importance (e.g., see also Caroli and Nozieres 1996, Tanguy and Nozieres 1996, Caroli and Velicky 1997, Bocquet and Jensen 1997). These velocities, however, are orders of magnitude smaller than the sliding velocities which are believed to occur during an earthquake (meters or ten meters per second) and hence the extrapolation of the validity of the aforementioned constitutive laws (especially their velocity weakening dependence) to such velocities is very doubtful. This doubt is strengthened from studies of the physical mechanisms involved in the friction laws, which suggests (e.g. Lomnitz-Adler 1991, Pisarenko and Mora 1994) that different mechanisms (i.e., collisions between asperities and transfer of momentum between the directions parallel and perpendicular to the motion) may become important at large velocities. Furthermore, the results of three laboratory experiments described below started to shed light on what happens at such large velocities:

First, Tsutsumi and Shimamoto (1996, 1997) performed friction measurements on rotating cylindrical samples at velocities up to 1.8 m/s and for slips of several tens of meters. This experiment shows that the behaviour of the friction changes upon increasing the velocity: at small velocities, the friction exhibits a “velocity weakening” regime (thus agreeing with the former friction experiments at small velocities), but this behaviour alters, at larger velocities, to a “velocity strengthening”. At even larger velocities, a “velocity weakening” regime is again found, which seems to be associated to the melting of a very thin layer. This behaviour seems to be in agreement with a “velocity strengthening” behaviour found in recent 3D numerical simulations (Maveyraud et al. 1999); the latter have been performed in the regime of velocities of one meter to ten meters per second

and showed that there is a doubling of the friction coefficient when the velocity increases from 1 to 10 m/s.

Second, Johansen and Sornette (1999) reported the behaviour of the dynamic friction in the high velocity regime (i.e., slip velocities ranging up to $\upsilon_{max} \approx 0.35$ m/s) from an experimental investigation in dry metallic friction. This was a spring-block sliding experiment, performed on a variety of smooth surfaces and revealed that acoustic radiation may control friction in the following sense: Radiation damping is a well-known phenomenon in electromagnetism (e.g., see p. 783 of Jackson 1975), but the corresponding mechanism of dynamic friction due to radiation of phonons had not received much attention. In Varotsos (2004), laboratory measurements have been discussed, which showed that the sound waves emitted by a propagating crack interact with the crack tip and modify the crack velocity. By the same token, in the friction experiments, the acoustic waves – emitted during sliding – lead to a radiation damping feedback; this feedback was found to be important in the range of high slip velocities studied by Johansen and Sornette (1999). Note that Varotsos (2001) showed that the radiation damping force – which is proportional to the derivative of the acceleration – plays a key role in the explanation of the experimental findings in the field measurements of acoustic emission before earthquakes.

Third, Di Toro et al. (2004) reported measurements on quartz rich rock both at low- and high-slip rates. They found that in the former case friction is indeed high in agreement with previous studies, but in the latter case friction drops dramatically as the slip velocity approaches a few mm/s. More precisely, the data indicate an extraordinary progressive decrease in frictional resistance with increasing slip velocity above 1 mm/s; this decrease extrapolates to zero friction at seismic slip rates of ~1 m/s, which might be due to the formation of a thin layer of silica gel on the fault surface. Di Toro et al. suggest that this might explain the low strength of major faults during earthquakes. We note, however, that Marone (2004) pointed out several reasons for caution in extrapolating these laboratory measurements to tectonic faults. Nonetheless, Marone adopted the view that nowadays several lines of evidence point to a high-speed, dynamic weakening of fault zones.

Experiments of Di Toro et al. (2004) suggest that the "weakening" mechanism is connected, as mentioned above, to a thin layer of silica gel acting as grease between the surfaces. An additional key factor in these experiments is the low rate of heat production, which may provide a helpful clue in understanding the balance in the problematic energy budget for faulting since shear heating would be negligible, dissipation of seismic energy would be dominated by radiation of seismic waves and creation of surface area (Marone 2004). In other words, frictional stress and shear

heating are much lower than previously expected, thus implying that the energy imbalance for faulting, described in the beginning of the previous section, probably originates from a non accurate estimation of the energy income rather than of the energy expenses.

The following clarification might be added. Varotsos et al. (2004) recently explained from first Principles why in the Gutenberg–Richter law (stating that the cumulative number of earthquakes $N(>M)$ with magnitude greater than M is given by $N(>M) \sim 10^{-bM}$) the so-called b-value is usually found to be around unity ranging only slightly from region to region. This explanation was achieved just by applying the analysis in the natural time-domain suggested by Varotsos and coworkers (e.g. Varotsos et al. 2001, 2002, Varotsos 2005), without using any adjustable parameter. There is nothing to differentiate the physics of earthquake rupture for small and large earthquakes in such a general scheme. According to the experiment of Di Toro et al. (2004) the onset of "weakening" occurs at only a few mm/s which would be reached even for very small earthquakes. Thus, all earthquakes, small and large ones, would experience considerable dynamic "weakening", while earlier analyses have been predicted on the expectation that it occurs only for earthquakes of magnitude 5 or larger (Marone 2004, Kanamori and Heaton 2000). Hence, it seems that the current aspects coincide with the conclusion that there is no break in earthquake scaling relations.

9.5 Modern Views on Friction. Theoretical Studies

The theoretical approaches introduced to investigate frictional forces in sheared systems can be classified into the following three categories: large-scale molecular dynamics simulations, phenomenological rate-state models and "minimalistic" models. These three theoretical approaches to model friction have been recently reviewed by Urbakh et al. (2004). Simulations of the molecular order and dynamics in thin molecular layers (e.g., Thompson and Robbins 1990) indicated that stick-slip motion is associated with transitions from a static solid state to a sliding fluid state. Furthermore, friction over correlated surfaces has been analysed. Two such studies are now briefly presented below.

First, we report on the memory effects in elasto-plastic models found by Tanguy and Roux (1997). They presented a model where the effective friction law results from the competition of the random interaction potential on the surface and the elastic properties of the solid (reduced to the elastic coupling between the asperity, and the center of mass of the solid). The ef-

fect of a long-range correlated scale-invariant random pinning force on the motion and friction properties of an elastically driven asperity was studied in the quasistatic regime. This study showed that, when the elastic coupling is weak, the macroscopic dynamic behaviour of the asperity can be described as elasto-plastic with a perfectly plastic plateau. The plastic plateau corresponds to statistically stationary sliding. Considering the fact that the macroscopic friction behaviour results from the competition between reversible and irreversible motion due to the multiplicity of equilibrium positions, they obtained a history-dependent behaviour, with marked memory effects over a characteristic length scale. It seems that this length scale is related to the "memory length" L involved in the Eqs. (9.1) to (9.8) of the "rate and state friction law". However, the interconnection of these two "memory lengths" needs further investigation.

Second, we refer to a study of the correlations induced by the dampened motion of a finite-size elastic chain with long range interactions by Tanguy et al. (1998). We clarify that in the case of solid friction, the dynamics of the slider is usually reduced to that of the asperities at the surface of the solid. The competition between the elastic restoring force (originating from the bulk) and the nonlinear pinning force (due to the contact between asperities of different solids) gives rise to multiple stable equilibrium positions. This multistability is responsible for hysteretic behaviour of asperities, when they are driven quasistatically over the pinning centers belonging to the surface of the other solid; the dissipation arises from this hysteretic behaviour. Tanguy et al. (1998) investigated the effect of the long-range elastic couplings on the fluctuations accompanying the average behaviour of an elastic line, driven quasistatically on a substrate with quenched (not changing with time) disorder. A schematic motion of the elastic chain is depicted in Fig. 1 of Tanguy et al. (1998). They considered a (discrete) one-dimensional elastic chain of size L which was discretized into L/d blocks; each point of discretization was called "asperity" and hence the quantity d represents the distance between asperities (in the strong-pinning limit, see below). Each site of the chain was subjected to the following forces: a driving force $F_{\text{ext}}(t)$, a random pinning force (from the interface) (which represents the interaction between the heterogeneous surface and the elastic chain and is always nonlinear), and a long-range elastic force describing the coupling to the other sites of the chain. Tanguy et al. (1998) studied the "strong-pinning" limit, i.e., the case when the couplings are small in comparison to the distortions of the pinning-potential. This study finally showed (more details can be found in Varotsos 2004) that the system organizes after a transient in a stationary state with long -range correlation and the memory of the initial state is lost. Tanguy et al. (1998) identified a crossover time-length t_c above which the uniform dis-

tribution is valid and below which a power-law behaviour (with a non-trivial exponent) is observed. Furthermore, Tanguy et al. (1998) found that for a mix of various couplings, the system exhibits a crossover between a regime controlled by the short-range coupling (at small times and lengths) and a regime controlled by the long range coupling (at large times and lengths).

We finally report on three solutions to the friction problem that have recently been proposed (the first two are briefly reviewed by Kessler 2001).

The first, suggested by Muser et al. (2001), attributes a crucial role to dirt, i.e., the diffuse collection of foreign mobile atoms trapped between the two surfaces. Their numerical stimulations show that these mobile atoms quickly find appropriate gaps between the surfaces, where they become trapped; these atoms then "lock" the two surfaces in place. To move the top surface, it has to be pushed up and over the dirt atoms. An area independent friction coefficient is obtained, for any surface geometry, when an adsorbed layer of mobile atoms is introduced between the surfaces.

The second mechanism was suggested by Gerde and Marder (2001). This is based on the physics of self-healing shear fracture and the basic idea could be simplified as follows (Kessler 2001): Imagine, we want to move a large rug some distance along the floor. Instead of dragging it, a less back-breaking method is to lift the back edge, slide the edge forward a bit and so introduce a ridge in the rug. Pushing on the ridge moves it forwards along the length of the rug, until it reaches the end. The net result is that the rug has been moved. In the fracture considered by Gerde and Marder (mode II crack) the two surfaces remain in close proximity and can come together again and bond, or "re-heal", in their new laterally shifted positions. This re-bonding sets in some distance downstream of the crack edge, so the crack is of finite length. Their model also predicts the minimum shear force required to initiate a propagating crack. Once this minimum force is applied, self-healing cracks are created, causing the surfaces to slide past one another.

The third mechanism was suggested by Rubinstein et al. (2004), who showed that the onset of frictional slip is governed by three different types of coherent crack-like fronts. Two of these fronts, which propagate at subsonic and intersonic velocities, have been also the subject of earlier studies by various groups. Rubinstein et al. show that a third type of front, which propagates an order of magnitude slower, is the dominant mechanism for the rupture of the interface. No sliding occurs until either of the two slower fronts traverses the entire interface.

9.6 Constitutive Friction Law for the Antisymmetric Stresses

It is usually assumed that the dynamic processes along faults are governed by the friction constitutive laws, as discussed in this chapter. However, in a precursory time domain the dynamics of deformations is related to the "inner friction" which hampers a motion of dislocations; such an inner friction is called a stress resistance.

It is worth noting that both kinds of frictions, i.e., the one on a fracture plane and that on a glide plane, may be closely related to rotations of particles/grains adjacent to slip planes; the related macroscopic constants are, of course, different for the two types of friction. Shimbo (1975, 1995) introduced the constitutive law governing the rotation motions as related to the rotation of grains adjacent to the slip planes which results in an appearance of antisymmetric stresses (cf. Teisseyre 2005):

$$\omega_{[lk]} = -\frac{1}{2\mu^*} S_{[lk]} , \qquad \omega^S_{[lk]} = -\frac{1}{2\mu^*} S^S_{[lk]} , \tag{9.9}$$

where $\omega^S_{[lk]}$ is a self-rotation field and the factor μ^* is introduced to indicate that the constitutive parameter related to rotations is different from that related to rigidity μ.

A fracture is usually characterized by an asymmetric fault pattern as manifested by the existence of main fault fracturing. The introduced antisymmetric stresses replace an action of the stress moments and the angular momentum. In our considerations we obtain instead the balance law expressing on the one hand the rotation of force arising from antisymmetric stresses (rot div $S_{[lk]}$) acting on a body element and on the other hand the acceleration of rotation (Teisseyre 2005); in addition, we may introduce here also a body moment of forces related to the source function Π (Teisseyre 2001):.

$$\varepsilon_{lki} \frac{\partial^2}{\partial x_k \partial x_n} S_{[ni]} = \rho \frac{\partial^2}{\partial t^2} \omega_l + \Pi_l$$

or (9.10)

$$\varepsilon_{lki} \frac{\partial^2}{\partial x_k \partial x_n} S_{[ni]} = \frac{1}{2} \varepsilon_{lki} \rho \frac{\partial^2}{\partial t^2} \omega_{[ki]} + \Pi_l \ .$$

It has been proposed that the bonds related to rotation are not as strong as those related to displacement motions and we can expect that the related waves propagate to distant sites (Teisseyre et al. 2003). It seems that the

transition from the precursory, very slow processes to those related to fracturing corresponds to the transition from the microscale motions to the miniscale and collective macroscale motions and fracturings.

Instead of the body source function introduced above, we can introduce a stress moment resistance related to the inner friction (glide motion) and friction (fracturing) processes connected with rotations. As a result, we may expect to get different levels of the stress moment resistance magnitudes and the stress moment resistance $R_{[lk]}$ to be able to introduce into the former relation (instead of the source function). In such a case, the last equation will be written in the new form:

$$\varepsilon_{lki}\frac{\partial^2}{\partial x_k \partial x_n}\left(S_{[ni]} - R_{[ni]}\right) = \frac{1}{2}\varepsilon_{lki}\rho\frac{\partial^2}{\partial t^2}\omega_{[ki]}\ , \tag{9.11}$$

where the following expression for the stress moment resistance

$$R_{[ki]} = R^0_{[ki]}\left[\left(1-\frac{r^0}{R^0}\right)\exp\left(-\frac{\left|\nabla\omega^s\right|}{\alpha^0}\right)+\frac{r^0}{R^0}\right]\frac{\gamma_0}{\gamma_0+\gamma_1\left|\omega^s\right|+\gamma_2\left|\dot{\omega}^s\right|} \tag{9.12}$$

describes the transition from the premonitory to the fracture rebound process (see Teisseyre and Yamashita 1999) and is written in the form presented by Virieux and Madariaga (1982); it included changes of the friction constitutive laws from premonitory exponential to slip nucleation phase (slip weakening) and to dynamic phase (slip rate friction law) (see Varotsos 2004, Teisseyre 2001).

Both approaches, the one in which the variation of stress resistance (Eq. 9.12) directly reduces the antisymmetric stresses, as above, and the other in which this variations enter into the source function (Eq. 9.10), introduce (into the respective relations) some instabilities related to friction and rotation processes.

9.7 Open Questions

Although the dynamics of friction has been studied for hundreds of years, there are many aspects of these everyday processes that are not fully understood. A list of outstanding fundamental questions can be found in the review of Urbakh et al. (2004). Chief among these are: First, the onset of frictional motion (slip), which is central to diverse fields, e.g., physics, mechanics of earthquakes, tribology in general, still awaits for a full explanation despite the aforementioned recent advances. As a second exam-

ple, we refer to the question on whether stick and slip regimes are indicative of different phase states (liquid, solid, glassy) of the confined interfaces.

Another point of central importance is the following: Recently, an entirely new time domain, termed natural time, has been introduced (Varotsos et al. 2001, 2002) as already mentioned above. It is known that Seismic Electric Signals (SES) activities are recorded before major earthquakes (see Varotsos 2005 and references therein). Such a recording signifies that the candidate area entered the critical regime. Upon analyzing the subsequent seismicity in the natural time-domain, we find (Varotsos et al. 2001, Varotsos 2005) that the time of the impending mainshock can be determined with an accuracy of the order of a few days. An application of this procedure to laboratory measurements, in order to find out whether it can approach the onset of frictional slip as well, has not yet been attempted.

References

Beeler NM, Tullis TE, Weeks JD (1994) The roles of time and displacement in the evolution effect in rock friction. Geophys Res Lett **21**: 1987-1990

Bocquet L, Jensen HJ (1997) Phenomenological study of hysteresis in quasistatic friction. J Physique I **7**: 1603-1625

Bowden FP, Tabor D (1950) Friction and lubrication of solids. Part 1. Clarendon Press, Oxford

Bowden FP, Tabor D (1964). Friction and lubrication of solids. Part 2. Clarendon Press, Oxford

Brace WF, Byerlee JD (1966) Stick slip as a mechanism for earthquakes. Science 153: 990-992

Buchel A, Sethna JP (1996) Elastic theory has zero radius of convergence. Phys Rev Lett **77**: 8, 1520-1523

Caroli C, Nozieres P (1996) Dry friction as a hysteretic elastic response. In: Persson BNJ, Tosatti E (eds) Physics of sliding friction. Kluwer Academic Publishers, Dordrecht, pp 27-49

Caroli C, Velicky B (1997) Dry friction as an elasto-plastic response: Effect of compressive plasticity. J Physique I **7**: 1391-1416

Coulomb CA (1785) Theorie des machines simples. Memoire de Mathematique et de Physique de l'Academie Royale, Paris, pp 161-342

Di Toro G, Goldsby DL, Tulis TE (2004) Friction falls towards zero in quartz rock as slip velocity approaches seismic rates. Nature 427: 436-439

Farkas Z, Bartels G, Unger T, Wolf DE (2003) Frictional coupling between sliding and spinning motion. Phys Rev Lett **90**: 248302(4)

Gerde E, Marder M (2001) Friction and fracture. Nature 413: 285-288

Halsey TC (2003) Friction in a spin. Nature 424: 1005-1006

Heslot F, Baumberger T, Perrin B, Caroli B, Caroli C (1994) Creep, stick-slip, and dry friction dynamics: experiments and heuristic model. Phys Rev **E 49**: 4973-4988

Jackson JD (1975) Classical electrodynamics, 2nd ed. John Wiley, New York, 848 pp

Johansen A, Sornette D (1999) Acoustic radiation controls friction: evidence from a spring-block experiment. Phys Rev Lett **82**: 5152-5155

Johansen A, Dimon P, Ellegaard C, Larsen JS, Rugh HH (1993) Dynamic phases in a spring-block system. Phys Rev **E 48**: 4779-4790

Kanamori H, Heaton TH (2000) Microscopic and macroscopic physics of earthquakes. In: Rundle J, Turcotte DL, Kein W (eds) Geocomplexity and the physics of earthquakes, vol 120. AGU Monograph, Washington DC, pp 147-155

Kessler DA (2001) A new crack at friction. Nature 413: 260-261

Lomnitz-Adler J (1991) Model for steadystate friction. J Geophys Res **96**: 6121-6131

Lubkin GB (1997) Experiments find hysterisis and precursors in the stick slip friction of a granular system. Physics Today (September issue), pp 17-19 and references therein

Marone C (2004) Faults greased at high speed. Nature 427: 405-406

Maveyraud C, Benz W, Ouillon G, Sornette A, Sornette D (1999) Solid friction at high sliding velocities: an explicit 3D dynamical smooth particle hydrodynamics approach. J Geophys Res **104**: 28769-28788

Muser MH, Wenning L, Robbins MO (2001) Simple microscopic theory of Amontons's laws for static friction. Phys Rev Lett **86**: 7, 1295-1298

Nasuno S, Kudrolli A, Gollub J (1997) Friction in granular layers: hysteresis and precursors. Phys Rev Lett **79**: 949-952

Pisarenko D, Mora P (1994) Velocity weakening in a dynamical model of friction. Pure Appl Geophys 142: 447-466

Rubinstein SM, Cohen G, Fineberg J (2004) Detachment fronts and the onset of dynamic friction. Nature 430: 1005-1009

Scholz CH (1998) Earthquakes and friction laws. Nature 391: 37-42

Scholz CH (2000) Evidence for a strong San Andreas fault. Geology 28: 163-166

Shimbo M (1975) A geometrical formulation of asymmetric features in plasticity. Bull Fac Eng, Hokkaido Univ **77**: 155-159

Shimbo M (1995) Non-Riemannian geometrical approach to deformation and friction. In: Teisseyre R (ed) Theory of earthquake premonitory and fracture processes, Polish Scientific Publishers, Warszawa, pp 520-528

Tanguy A, Nozieres P (1996) First-order bifurcation landscape in a 2D geometry - The example of solid friction. J Physique I **6**: 1251-1270

Tanguy A, Roux S (1997) Memory effects in friction over correlated surfaces. Phys Rev **E 55**: 2166-2173

Tanguy A, Gounelle M, Roux S (1998) From individual to collective pinning: effect of long-range elastic interactions. Phys Rev **E 58**: 1577-1589

Teisseyre R (2001) Evolution, propagation and diffusion of dislocation fields. In: Teisseyre R, Majewski E (eds) Earthquake thermodynamics and phase transformations in the Earth's interior. Academic Press, San Diego, pp 167-198

Teisseyre R (2005) Asymmetric continuum mechanics: deviations from elasticity and symmetry. Acta Geophys Pol **53**: 2, 115-126

Teisseyre R, Yamashita T (1999) Splitting stress motion equation intoseismic wave and fault-related fields. Acta Geophys Pol **47**: 2, 135-148

Teisseyre R, Suchcicki J, Teisseyre KP, Wiszniowski J, Palangio P (2003) Seismic rotation waves: basic elements of theory and recording. Ann. Geophys. **46**: 4, 671-685

Thompson PA, Robbins M (1990) Origin of stick-slip motion in boundary lubrication. Science 250: 792-794

Tsutsumi A, Shimamoto T (1996) Frictional properties of monzodiorite and gabbro during seismogenic fault motion. J Geol Soc Japan 102: 240-248

Tsutsumi A, Shimamoto T (1997) High-velocity frictional properties of gabbro. Geophys Res Lett 24: 699-702

Tullis TE (1996) Rock friction and its implications for earthquake prediction examined via models of Parkfield earthquakes. Proc Natl Acad Sci USA 93: 3803-3810

Urbakh M, Klafter J, Gourdon D, Israelachvili J (2004) The nonlinear nature of friction. Nature 430: 525-528

Varotsos P (2001) A review and analysis of electromagnetic precursory phenomena. Acta Geophys Pol **49**: 1-42

Varotsos P, Sarlis N, Skordas E (2001) Spatiotemporal complexity aspects on the interrelation between Seismic Electric Signals and seismicity. Practica of Athens Academy 76: 388-415

Varotsos P, Sarlis N, Skordas E (2002) Long range correlations in the electric signals that precede rupture. Phys Rev **E 66**: 011902 (7)

Varotsos P (2004) Fracture and friction: a review. Acta Geophys Pol **52**: 2, 105-142

Varotsos PA (2005) The physics of seismic electric signals. TERRAPUB, Tokyo, 338 pp

Varotsos P, Sarlis N, Skordas E, Tanaka H (2004) A plausible explanation of the b-value in the Gutenberg-Richter law from first Principles. Proc Jpn Acad, Ser. B 80: 283-289

Virieux J, Madariaga R (1982) Dynamic faulting studied by a finite difference method. Bull Seism Soc Am **72**: 345-369

10 Soliton Physics

Eugeniusz Majewski

Institute of Geophysics, Polish Academy of Sciences
ul. Księcia Janusza 64, 01-452 Warszawa, Poland
e-mail: emaj@igf.edu.pl

10.1 Introduction

This chapter is a brief review of some fundamental equations and recent results in the theory of solitons and their applications in physics. The soliton idea is a remarkable mathematical structure based on the integrability of a rather wide class of nonlinear differential equations. Solitons or solitary waves are a special kind of localized waves that propagate undistorted in shape. They are essentially nonlinear waves. We begin with the discovery of a solitary wave on the Edinburgh to Glasgow Canal by J. Scott Russell in 1834 (see Russell 1844, 1895). The solitary waves were known earlier than solitons. Much later, Zabusky and Kruskal (1965) discovered the mathematical structure of solitons. At that time it became clear that there are some intimate connections between these two concepts. While all solitons are solitary waves, the converse is not true; solitons have to satisfy more requirements than solitary waves. Solitons are a very restricted subset of solitary waves. A concept of soliton is very simple on intuitive grounds if we begin our study from solitary waves on shallow water. Ever since Korteweg and de Vries (KdV) first derived their famous equation for water waves in 1895, solitons have been a fascinating and popular area of study in the physics community. This chapter characterises the main features of these waves, and then reviews the fundamental concepts of the theory of nonlinear waves in order to sketch a few key ideas of the theory of solitons. There are approximately one hundred known integrable nonlinear differential equations with soliton solutions, including the KdV equation, the modified Korteweg–de Vries (mKdV) equation, the Kadomtsev–Petviashvili (KP) equation, the nonlinear Schrödinger (NLS) equation, the Boussinesq equations, the Klein–Gordon (KG) equation, and the sine-Gordon (SG) equation. While these investigations reveal general properties of solitons, of importance is the physical insight and applica-

tions of solitary waves in modelling physical phenomena. Zabusky and Kruskal (1965) coined the term “soliton” due to the analogy with particles. The nagging question naturally arises: what is the difference between solitons and solitary waves? The standardized definitions for solitons and solitary waves were not established. Both are colloquially called solitons. There are many different working definitions in the literature describing how to distinguish solitons from solitary waves. These definitions change from author to author. Many authors refer to solitons as special wave pulses that can pass through each other or bounce back from each other (“elastic” interactions), keeping their basic identity and acting as particles. They are non-dispersive localized packets of energy moving with uniform velocity. Solitons resemble extended particles, even though they are solutions of nonlinear wave equations. Solitons are used successfully to model elementary particles in quantum field theories (cf., Rajaraman 1982). Some authors refer to waves which interact “inelastically” as solitary waves. Solitary waves were discovered in many branches of science, such as water dynamics, tsunami waves, optics, plasma, dipole chains, protein chains, dislocations, and seismology. In this chapter, we shall use both terms “soliton” and “solitary wave”, interchangeably.

Solitons can exist in the so-called dispersive media. Most media are dispersive. That is, an initial very small amplitude disturbance in the form of a pulse will, as time evolves, tend to broaden and break up into its individual components. These are simple waves moving with different phase velocities.

The existence of solitons is based on the fundamental assumption that large amplitude disturbances are considered, and it is necessary to invoke a nonlinear theory. Solitons exist because of this nonlinearity and travel with uniform velocity and no distortion in shape. If they collide, they subsequently retain their original shape and velocity. In fact, solitons are the result of the interplay between dispersivity and non-linearity. Namely, for differential equations where both dispersive and nonlinear terms are present, the effects can balance each other in such a way that special solutions called solitary waves or solitons emerge.

This chapter briefly introduces the most famous nonlinear differential equations with soliton solutions, considers rotating solitons, and finally summarizes results on discrete soliton systems (cf., Hirota 1981, Tokihiro 2004). The Box-Ball System (BBS) and its application to the description of soliton motion is also discussed (cf., Toda 1967). General conclusions on soliton stability and applications close the chapter.

10.2 The Discovery of Solitary Waves

In 1834, British engineer J. Scott Russell was riding a horse along the Edinburgh to Glasgow Canal. Suddenly, he noticed something strange. He expressed it in his own words (Russell 1844, 1895): *...the mass of water in the channel...rolled forward with great velocity, assuming the form of a large solitary elevation, a rounded, smooth and well-defined heap of water, which continued its course along the channel apparently without change of form or diminution of speed. I followed it on horseback, and overtook it still rolling on at a rate of some eight or nine miles an hour, preserving its original figure some thirty feet long and a foot to a foot and a half in height*.

This was the first quantitative observation of a water solitary wave and was followed by measurements and laboratory experiments on these nonlinear waves (Drazin 1983, Drazin and Johnson 1989). Russell (1844, 1895) wrote reports summarizing his observations and experiments on solitary waves. He observed that a taller solitary wave propagates faster than a smaller one. In addition, he deduced empirically a formula for the steady velocity v of the solitary wave.

10.3 The Korteweg–de Vries Equation

In 1895 Korteweg and his student de Vries presented a skillful derivation of a solitary wave equation (Korteweg and de Vries 1895). Their starting points were the equations of motion for surface water waves. They simplified these equations under the assumption that the solution propagates in the direction of increasing x. In addition, they assumed that the solution has amplitude A and wavelength λ related to the water depth h by $(A/h) \approx (h^2/\lambda^2) \ll 1$. Starting from *a priori* knowledge concerning an expected solution, Korteweg and de Vries found that a solitary wave would be described by the following nonlinear partial differential equation:

$$\frac{\partial u}{\partial t} + \sigma \frac{\partial u}{\partial x} + u \frac{\partial u}{\partial x} + \frac{\partial^3 u}{\partial x^3} = 0, \tag{10.1}$$

where $\sigma = 0$ or $\sigma = 1$, and $u = u(x, t)$ is the displacement of the water surface from its equilibrium position at location x and time t. Here the units of time and distance were scaled. Equation (10.1) is known as the KdV equation. The nonlinearity is modeled in this equation by the third term that is proportional to displacement, and the dispersion is described by the fourth term that is proportional to the third derivative of displacement. The inter-

play between these two terms is crucial for the formation of solitons. It is noteworthy that this equation does not describe dissipation. However, a soliton is characterized by a stable shape and constant velocity. Emploing a substitution method to Eq. (10.1), Korteweg and de Vries (1895) substituted $u(x,t) = \psi(x - vt)$ and solved the resulting ordinary differential equation for ψ. They obtained a solution in the form of the following soliton

$$u(x,t) = 3(v-1)\,\mathrm{sech}^2\left[\frac{(x - vt)\sqrt{v-1}}{2}\right], \tag{10.2}$$

where v is the constant speed of the soliton.

Figure 10.1 shows a solution to the KdV equation in the form of a single soliton expressed by Eq. (10.2) for particular amplitude. However, this equation also reveals that for i different amplitudes $(v-1)_i$, we can obtain many soliton solutions and i solitons exist here. This multi-soliton solution to the KdV equation is depicted in Fig. 10.2. The solitons have a tendency to form a sequence, with the soliton of the maximum amplitude in the front and the soliton of the smallest amplitude at the rear.

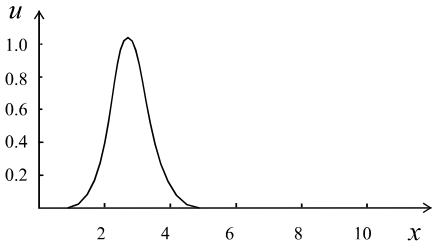

Fig. 10.1 A solution to the KdV equation in the form of a single soliton propagating to the right

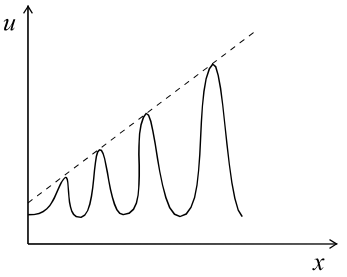

Fig. 10.2 A multi-soliton solution to the KdV equation in the form of a sequence of four solitons moving to the right. The soliton of the maximum amplitude leads the sequence

Many researchers endeavored to generalize the KdV equation in different ways. Some of them accomplished their aims by introducing additional transformations (e.g., Miura 1968) and others introduced an additional space dimension (e.g., Kadomtsev and Petviashvili 1970).

10.4 The Modified Korteweg–de Vries Equation

Miura (1968) and Miura et al. (1968) generalized the KdV equation. As a result, they obtained the so-called modified KdV equation (mKdV) in the form

$$\frac{\partial w}{\partial t} - 6w^2 \frac{\partial w}{\partial x} + \frac{\partial^3 w}{\partial x^3} = 0 . \tag{10.3}$$

After Miura (1968), we define the relationship between the displacement $u(x,t)$ described by the KdV equation and the new function $w(x, t)$ in the form $u = \partial w / \partial x + w^2$. It should be emphasized that the mKdV equation is also analytically solvable.

10.5 The Kadomtsev–Petviashvili Equation

The world we inhabit has 3 (space) +1 (time) dimensions, whereas most of the equations we have been studying have (1+1) dimensions. An interesting question is: what can we learn from these simple equations? Indeed, even one spatial dimension can reveal the most important features of physical phenomena. Depending on the particular physical model, one may describe wave processes in (1+1), (2+1) or (3+1) dimensions.

Kadomtsev and Petviashvili (1970) generalized the KdV equation using two space dimensions by including a y-dependent term in this equation. In such a situation it is reasonable to assume a potential flow (Infeld and Rowlands 2000)

$$\mathrm{u} = \nabla \Psi . \tag{10.4}$$

The Kadomtsev–Petviashvili (KP) equation can be written as

$$\frac{\partial^2 \Psi}{\partial x \partial t} + \frac{\partial \Psi}{\partial x} \frac{\partial^2 \Psi}{\partial x^2} + \frac{\partial^4 \Psi}{\partial x^4} + \frac{\sigma}{2} \frac{\partial^2 \Psi}{\partial y^2} = 0 , \tag{10.5}$$

where $\sigma = \pm 1$.

We can see that this equation is not symmetrical with respect to x and y variables. In contrary, we can observe here that x and y play different parts in this equation, or in other words, they have different weights.

It is noteworthy that if we remove the derivative with respect to x in front of the parenthesis, we obtain the KdV equation inside the parentheses as follows

$$\frac{\partial \Psi}{\partial x}\left(\frac{\partial \Psi}{\partial t}+\Psi\frac{\partial \Psi}{\partial x}+\frac{\partial^3 \Psi}{\partial x^3}\right)+\frac{\sigma}{2}\frac{\partial^2 \Psi}{\partial y^2}=0. \tag{10.6}$$

From the above equation, we can conclude that the KP solitons for $\sigma = 1$ travel in the x direction, but not in the y direction. In most cases they interact elastically, and they separate after the interaction. In addition, they have a zone of mutual interaction at the intersection that is called a virtual soliton. However, for some critical angles of the intersection, the KP solitons interact inelastically and join one another. Such a wave process is called a soliton resonance. The KP solitons for $\sigma = 1$ are stable. They were observed on water surfaces and in plasma physics (Infeld and Rowlands 2000).

The other version of the KP equation for $\sigma = -1$ was also applied in solid state physics, physics of liquids, and other branches of science. Different kinds of solitons were observed, and many elastic interactions between them were described. However, some solitons are not quite stable, they decay after some period of time. The KP equation is also a very interesting area of research for discrete soliton systems (Tokihiro 2004). We shall discuss this problem at the end of this chapter.

10.6 The Boussinesq Equations

Let us write down the first Boussinesq equation

$$\frac{\partial^2 u}{\partial t^2}-\frac{\partial^2 u}{\partial x^2}=\frac{\partial^2}{\partial x^2}\left(u^2+c\frac{\partial^2 u}{\partial t^2}\right), \tag{10.7}$$

where c is a constant coefficient.

The second Boussinesq equation (nonlinear string equation) can be expressed in the form

$$\frac{\partial^2 u}{\partial t^2}-\frac{\partial^2 u}{\partial x^2}=\frac{\partial^2}{\partial x^2}\left(u^2+d\frac{\partial^2 u}{\partial x^2}\right), \tag{10.8}$$

where d is a constant coefficient.

It is noteworthy that the KdV equation and Boussinesq equations are simple reductions of the following equation:

$$\frac{3}{4}\frac{\partial^2 u}{\partial y^2} = \frac{\partial u}{\partial x}\left(\frac{\partial u}{\partial t} - \frac{3}{2}u\frac{\partial u}{\partial x} - \frac{1}{4}\frac{\partial^3 u}{\partial x^3}\right). \tag{10.9}$$

10.7 The Doubly Dispersive Equations

Samsonov (1988) investigated the following nonlinear equation:

$$\frac{\partial^2 u}{\partial t^2} - \frac{\partial^2 u}{\partial x^2} = \varepsilon\frac{\partial^2}{\partial x^2}\left(6u^2 + a\frac{\partial^2 u}{\partial t^2} + b\frac{\partial^2 u}{\partial x^2} + g\frac{\partial u}{\partial t}\right), \tag{10.10}$$

where ε is a small parameter, g is the dimensionless "viscosity", and a and b are constant coefficients. He called it the doubly dispersive equation (DDE), the wave equation describing dispersion and dissipation and having exact solitary solutions.

10.8 The Nonlinear Schrödinger Equation

Let us take a closer look at the most famous nonlinear wave equation in quantum mechanics that puts a great emphasis on the wave amplitude Ψ and its physical interpretations. Namely, we recall the nonlinear Schrödinger (NLS) wave equation. It belongs to the category of soliton equations and reveals multi-soliton solutions. It is also one of the most universal nonlinear differential equations and it was applied in many different branches of science. In general, the NLS equations can describe multi-wave interactions, depending on additional conditions. The cubic NLS equation can be expressed as follows:

$$\mathrm{i}\frac{\partial \Psi}{\partial t} + \frac{\partial^2 \Psi}{\partial x^2} + \frac{\partial^2 \Psi}{\partial y^2} + 2\sigma|\Psi|^2\Psi = 0, \tag{10.11}$$

where $\sigma = \pm 1$.

The above equation also describes dispersive systems. The final form of this equation is the result of the interplay between dispersivity and nonlinearity that determines a different weight of each term. The NLS equation has soliton solutions. These solitons behave in a similar way as the KdV solitons. They are characterized by spatial and temporal stability and collide elastically. Their envelope can describe a simple pulse.

10.9 The Nonlinear Klein–Gordon Equation

The nonlinear Klein–Gordon equation (KG) can be expressed as

$$\frac{\partial^2 u}{\partial t^2} - \frac{\partial^2 u}{\partial x^2} + \frac{\partial}{\partial u}\Psi(u) = 0\,, \tag{10.12}$$

where Ψ is a general nonlinear function of u that may take different forms. For an exponential nonlinearity $\partial\Psi(u)/\partial u = \exp(u)$, Eq. (10.12) was used as a modelling equation for many physical phenomena. For a cubic nonlinearity $\partial\Psi(u)/\partial u = u^3 - u$, Eq. (10.12) also had many applications. For instance, Rajaraman (1982) described the motion of an elementary particle in the framework of the unified field theory by using the nonlinear Klein –Gordon equation in the form

$$\frac{\partial^2 u}{\partial t^2} - \frac{\partial^2 u}{\partial x^2} = Au - Bu^3, \tag{10.13}$$

where A and B are positive constants.

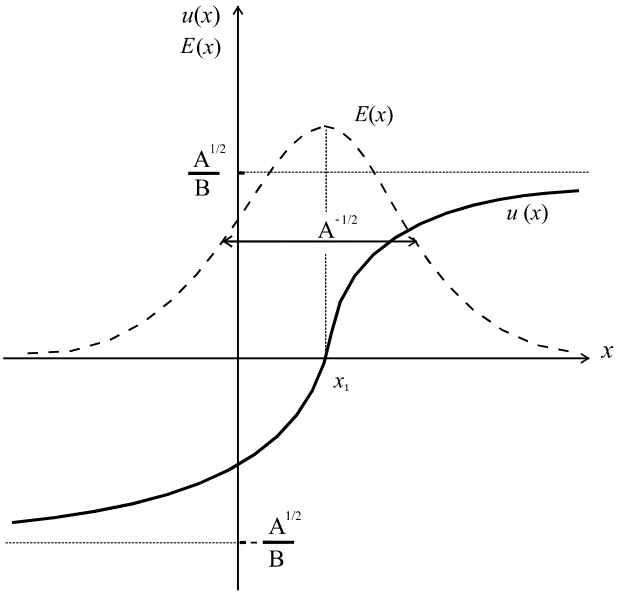

Fig. 10.3 The curve $u(x)$ denotes the static kink solution of the Klein–Gordon equation (10.13). The curve $E(x)$ depicts the energy density of the kink that is localized with a width characterized by $A^{-1/2}$ (modified from Rajaraman 1982)

The soliton solution of this equation is as follows:

$$u(x) = \infty \pm \left(\frac{A^{1/2}}{B} \right) \tanh \left[\frac{A^{1/2}\left(x - x_1\right)}{2^{1/2}} \right]. \tag{10.14}$$

Figure 10.3 displays a soliton solution $u(x)$ of the Klein–Gordon equation (10.13) and the energy density $E(x)$ of the soliton. The solution above the x-axis plotted in Fig. 10.3 is called the "kink" and the one beneath the x-axis the "antikink". The invariance of the solution with respect to translation is clearly visible, since a change in x_1 merely moves the solution along the x-axis.

10.10 The Sine-Gordon Equation

The sine-Gordon equation (SG) is a special case of the Klein–Gordon equation (KG). It was employed in the modelling of many physical processes such as for instance: motion of crystal dislocations in the periodic Peierls potential, motion of charged particles, biological processes like DNA dynamics, magnetic flux in the theory of Josephson junction ladders, Bloch wall motion in magnetic crystals, and two-dimensional models of elementary particles in the unified field theory (Rajaraman 1982). More information concerning soliton applications can be found in Barone et al. (1971), Scott et al. (1973), and Infeld and Rowlands (2000). The sine -Gordon equation can be expressed in the following form:

$$\frac{\partial^2 \phi}{\partial x^2} - \frac{\partial^2 \phi}{\partial t^2} = \sin \phi(x,t). \tag{10.15}$$

10.11 The Inverse Scattering Transform

Processes of evolution of physical phenomena can be described by evolution equations that characterize how some physical variables evolve in time. The evolution equations are usually in the form of a set of nonlinear differential equations with given initial conditions. Most of them are very difficult to solve. Fortunately, some of them have a simple inner structure and can be reduced to linear differential equations that have exact analytical solutions. Due to the fact that these solutions describe physical models and represent applications of mathematics to the real world, they help to stimulate research in this branch of science. There are several mathemati-

cal techniques that can be employed for this task. One of them is the so-called inverse scattering transform (IST), which is a generalization of the Fourier transform. The Fourier transforms are commonly employed to find solutions of linear differential equations. The main advantage of IST is that it reduces nonlinear problems to linear ones. We should recall that the inverse scattering problem is already well known in quantum mechanics. The key idea of this approach is that we have given the asymptotic form for the solution, and our goal is to construct the potential. In this process of constructing an appropriate potential or pseudo-potential, time t is treated as a parameter. When we say that we have given the asymptotic form for the solution, we mean that some features of the solution can be predicted. The key role in the IST is played by the Schrödinger equation. The famous KdV equation and many others can be solved using the IST technique. The IST was formulated by Gardner et al. (1967, 1974). Some more details concerning the IST are presented by Ablowitz and Segur (1981), Newell (1985), and Infeld and Rowlands (2000). The IST method allows us to transform the nonlinear partial differential equation into a linear integral equation that we can solve analytically. In addition, the obtained solutions have a form of solitons. A shortcoming of the method is that $u(x, t)$ and various derivatives must approach zero as $x \to \pm\infty$. Thus, this method gives only some of the solutions of the nonlinear differential equation in question. The IST method excludes periodic solutions and train waves.

10.12 Rotating Solitons

Solitons, in general, can be composed of a single field or of many fields. When a soliton is composed of multiple fields that have different structures, they are called complex solitons or vector solitons. Moreover, there are composite solitons that are made up of optical fields that have different modes of their jointly induced waveguide; in addition, these multimode solitons can be viewed as spatial or temporal solitons. Composite solitons may have different forms. Carmon et al. (2001) presented some observations of (2+1)D composite solitons carrying angular momentum, and rotating throughout propagation. They called them propeller solitons because their planes of equal phase are shaped as propeller blades. Propeller solitons propagate without loss of energy and momentum. These solitons are composed of a bell-shaped mode jointly trapped with a 2D dipole mode rotating in unison. Such solitons can be described by the NLS equation. The envelopes Ψ_1 and Ψ_2 of the NLS equation were described by Carmon et al. (2001) as follows:

$$\mathrm{i}\frac{\partial \Psi_{1,2}}{\partial \zeta} + \frac{\partial^2 \Psi_{1,2}}{\partial \xi^2} + \sigma \frac{\Psi_{1,2}}{\left|\Psi_1\right|^2 + \left|\Psi_2\right|^2} = 0\,, \tag{10.16}$$

where $\sigma = -1$, and ζ denotes the propagation distance.

These types of solitons can describe two-component Bose–Einstein condensates as well. However, in this case the soliton components describe states of the cooled atomic gas in a spherical trap. Carmon et al. (2001) suggest that a vortex-type composite soliton is better suited for these condensates. Figure 10.4 shows a rotating dipole soliton. It is noteworthy that the intensity structure of the soliton components, not only the phase, rotates during propagation.

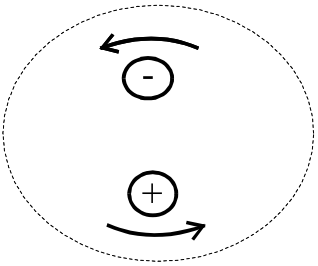

Fig. 10.4 Rotating dipole soliton. The intensity structure of the soliton components rotates throughout propagation

Pigier et al. (2001) observed interactions of a pair of such solitons during their corotation or counterrotation. The rotating solitons exchange the angular momentum between the field components.

The wave function can be found from the NLS equation as a result of numerical approach. Pigier et al. (2001) investigated stability properties

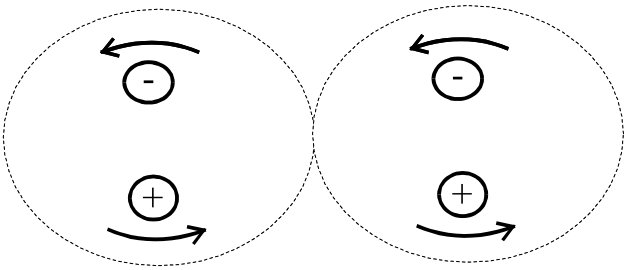

Fig. 10.5 Interactions of two corotating dipole solitons: the input configuration of the dipole mode

and different directions of soliton rotation. They examined the arrangement of two poles and the forces of interaction between the rotating solitons. Figure 10.5 illustrates the interactions (collisions) of two corotating propeller solitons. The above figure shows the input configuration of the dipole mode.

Pigier et al. (2001) studied several cases of interactions (collisions) between dipole-type composite solitons that carry angular momentum. Figure 10.6 illustrates interactions (collisions) of two corotating propeller solitons. This figure shows the output configuration of the dipole mode. From these experiments, Pigier et al. (2001) concluded that during this collision the angular momentum is transmitted from the input solitons to the output solitons. Thus, they found that rotating solitons are very vigorous because they can survive collisions and become rotating solitons again.

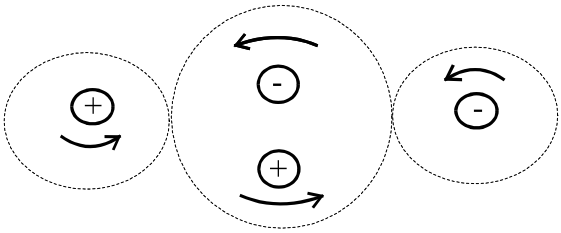

Fig. 10.6 Interactions of two corotating dipole solitons: the output configuration of the dipole mode

10.13 Discrete Soliton Systems

We summarize some results on ultradiscrete soliton systems presented by Tokihiro (2004). Discrete systems may have discrete space coordinates or discrete time or both. Starting from continuous equations, we can obtain a cellular automaton (CA), i.e., a discrete system.

We will discuss a very famous integrable CA, the so-called Box and Ball System (BBS). Takahashi (1991) investigated some soliton systems defined by boxes and balls. Let us consider a sequence of boxes that represent a soliton position. At the initial time, we consider four sequences of balls representing solitons, as depicted in Fig. 10.7. Each sequence of consecutive balls represents one soliton. The length of the sequence represents the soliton amplitude. The empty boxes are treated as inactive cells and boxes with balls are treated as active cells.

As time goes on in discrete steps, the balls move according to the following rules. Balls can move only left to right. First, we move the leftmost ball to its nearest empty box. Next, we move the leftmost ball of the

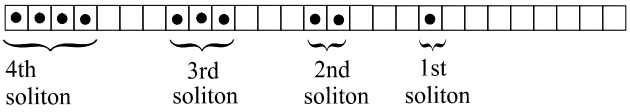

Fig. 10.7 A state of the BBS representing solitons with different amplitudes. The soliton amplitude is directly proportional to the length of the sequence of the balls

remaining balls to its nearest empty box. We move each ball in this order only once until all the balls change their positions. This moving of sequences of balls represents the motions of solitons and is depicted in Fig. 10.8. The Toda lattice is extremely useful in discrete soliton systems, and it is worth noting that the BBS can be applied to the discrete KP equation and to the discrete Toda equation (cf., Toda 1967).

Figure 10.8 describes interactions between solitons during their motion. It can be observed that the phase of solitons represented by balls is shifted after collision. After some time, the soliton with the highest amplitude leads the group of solitons. The amplitudes of the following solitons are thus smaller and smaller. The last soliton in this group has the smallest amplitude. This picture of motion of solitons is in excellent agreement with observations carried out by J. Scott Russell in 1834.

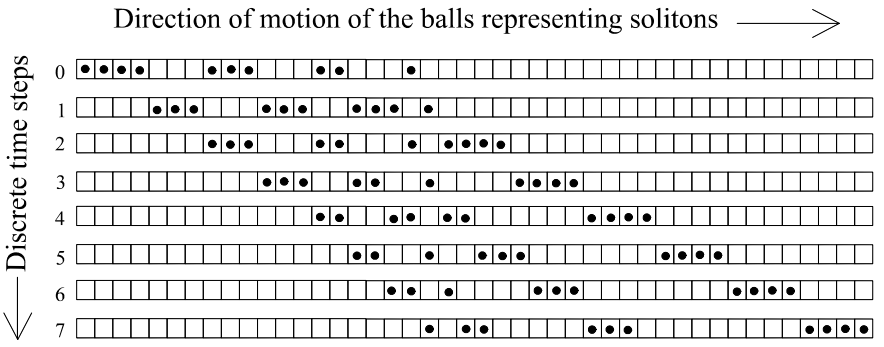

Fig. 10.8 Time evolution of the BBS representing the motion of solitons. The soliton speed is directly proportional to its amplitude (modified from Tokihiro 2004)

Białecki (2005a, b) presented a solution of the cellular automaton associated with the discrete KdV equation, using an algebro-geometric solution of the discrete KP equation over a finite field out of a hyperelliptic curve. Białecki and Doliwa (2005) transferred the algebro-geometric method of construction of solutions of the discrete KP equation to the finite field

case. They employed a Jacobian of the underlying algebraic curve in construction of the solution.

Zabrodin (2004) gave a review of some topics on Hirota's bilinear difference equation (HBDE). This 3D difference equation is helpful in all kinds of discretization procedures for many soliton equations. The key idea of his approach is a discrete version of Zakharov–Shabat equations for *M*-operators in the form of difference or pseudo-difference operators. He considered different approximations of HBDE by 2D equations. Moreover, he discussed discrete versions of the KdV, sine-Gordon, Toda chain, and other aspects of HBDE.

10.14 Conclusions

This chapter presented a few universal nonlinear wave equations with soliton solutions. There are several mathematical methods that can be employed to find such solutions. One of them is the IST, which is a generalization of the Fourier transform. We summarized the IST that can be used to solve the KdV equation and other soliton equations.

The intriguing question naturally arises: why do solitons have such a magnificent structural stability in space and time? A straightforward answer is that they are portions of self-trapped energy that can be carried over a certain distance without loss of energy and momentum. Each soliton equation is associated with an infinite number of constants of motion. Thus, the time evolution of the soliton must be kept within limits.

Perhaps because of the circumstances in which the solitons were discovered, many physicists think of them as massive objects, but the size of solitons can be as small as we like. Thus, solitons can look like point particles. Rajaraman (1982) described the motion of an elementary particle in the framework of the unified field theory by using a soliton solution of the nonlinear Klein–Gordon equation.

Each year, mathematicians, physicists, biologists, and seismologists devote their papers to solitons and their applications. Zorski and Infeld (1992) developed a new soliton equation for dipole chains. They formulated a continuum dynamics of a peptide chain (Zorski and Infeld 1997). Adding to the increase in attention paid to solitons in string theory and astrophysics (rotating black holes) have been the ripple effects of discoveries of new and universal applications of solitons.

References

Ablowitz M, Segur H (1981) Solitons and inverse scattering transform. SIAM, Philadelphia

Barone A, Esposito F, Magee CJ, Scott AC (1971) Riv Nuovo Cim **1**: 227

Białecki M (2005a) Integrable KP and KdV cellular automata out of a hyperelliptic curve. Glasgow Math J **47A**: 33-44

Białecki M (2005b) Integrable 1D Toda cellular automata. J Nonlinear Math Phys, SIDE V Proceedings (accepted)

Białecki M, Doliwa A (2005) Algebro-geometric solution of the discrete KP equation over a finite field out of a hyperelliptic curve. Commun Math Phys **253**: 157-170

Carmon T, Uzdin R, Pigier C, Musslimani ZH, Segev M, Nepomnyashchy A (2001) Rotating propeller solitons. Phys Rev Lett **87**: 14, 143,901-143,904

Drazin PG (1983) Solitons. Cambridge University Press, Cambridge

Drazin PG, Johnson RS (1989) Solitons: an introduction. Cambridge University Press, Cambridge

Gardner CS, Greene JM, Kruskal MD, Miura RM (1967) Method for solving the Korteweg – de Vries equation. Phys Rev Lett **19**: 1095-1097

Gardner CS, Greene JM, Kruskal MD, Miura RM (1974) The Korteweg–de Vries equation and generalizations. VI. Methods for exact solution. Comm Pure Appl Math **27**: 97-133

Hirota R (1981) Discrete analogue of a generalized Toda equation. J Phys Soc Jpn **50**: 3785

Infeld E, Rowlands G (2000) Nonlinear waves, solitons and chaos. Cambridge University Press, Cambridge

Kadomtsev BB, Petviashvili VI (1970) On the stability of solitary waves in weakly dispersive media. Dokl Akad Nauk SSSR 192: 753-756; Sov Phys Dok 15: 539-541

Korteweg DJ, de Vries G (1895) On the change of form of long waves advancing in a rectangular canal and on a new type of long stationary waves. Philos Mag **39**: 5, 422-443

Miura RM (1968) The Korteweg–de Vries equation and generalizations, I. A remarkable explicit nonlinear transformation. J Math Phys **9**: 1202-1204

Miura RM, Gardner CS, Kruskal MD (1968) KdV equations and generalizations II. Existence of conservation laws and constants of motion. J Math Phys **9**: 1204-1209

Newell A (1985) Solitons in mathematics and physics. Society for Industrial and Applied Mathematics, Philadelphia, PA

Pigier C, Uzdin R, Carmon T, Segev M, Nepomnyashchy, Muslimani ZH (2001) Collisions between (2+1)D rotating propeller solitons. Optics Lett **26**: 1577-1579

Rajaraman R (1982) Solitons and instantons: an introduction to solitons and instantons in quantum field theory. North-Holland, Amsterdam

Russel JS (1844) Report on waves. 14th meeting of the British Association Report, York, pp 311-390

Russel JS (1895) The wave of translation in the oceans of water, air and ether. Trubner, London

Samsonov AM (1988) On some exact solutions of nonlinear longitudinal wave equations with dispersion and dissipation. **In:** Crighton DG, Mainardi F (eds) Dispersive waves in dissipative fluids. Proc EUROMECH Coll 240, Bologna, pp 56-57, Tecnoprint, Bologna

Scott AC, Chiu FYF, Mclaughlin DW (1973) The soliton a new concept in applied science. Proc IEEE **61**: 14, 1443-1483

Takahashi D (1991) On some soliton systems defined by boxes and balls. Proc Int Symp Nonlinear Theory its Appl NOLTA 93: p 555

Toda M (1967) J Phys Soc Jpn **22**: 431

Tokihiro T (2004) Ultradiscrete systems (cellular automata). **In:** Grammaticos B, Kosmann-Schwarzbach Y, Tamizhmani T (eds) Discrete Integrable Systems. Springer, Berlin

Zabrodin A (2004) A survey of Hirota's difference equations. ArXiv:solv-int/9704001 v1 30 Mar 1997

Zabusky NJ, Kruskal MD (1965) Interaction of 'solitons' in a collisionless plasma and the recurrence of initial states. Phys Rev Lett **15**: 240-243

Zorski H, Infeld E (1992) New soliton equation for dipole chains. Phys Rev Lett **68**: 1180-1183

Zorski H, Infeld E (1997) Continuum dynamics of a peptide chain. Int J Nonlinear Mechanics **32**: 769-801

PART III

ROTATION MOTIONS, SEISMIC SOURCE MODELS, AND ASYMMETRY OF FRACTURE

11 Rotational Motions Excited by Earthquakes

Minoru Takeo

Earthquake Research Institute, University of Tokyo
Zip. 113-0032 1-1-1, Yayoi, Bunkyo-ku, Tokyo, Japan
e-mail: takeo@eri.u-tokyo.ac.jp

11.1 Introduction

There are many reports about rotations of tombstones and stone lanterns during large earthquakes (e.g. Yamaguchi and Odaka 1974). Only translational ground motions, however, have been observed in instrumental measurements of seismic waves, and quantitative measurements of rotational ground motions have not been made until quite recently. Bouchon and Aki (1982) simulated rotational ground motions near earthquake faults buried in layered media for strike-slip and dip-slip fault models, and obtained a maximum rotational velocity of 1.5×10^{-3} rad/s produced by a buried 30 km long strike-slip fault with slip of 1 m. Their simulation shows that the rotational motions are small compared with the amplitude of the translational motions. The difficulty experienced in measuring of rotational motions excited by earthquakes is caused by a lack of technology for measuring such small rotational motions.

Recently, Nigbor (1994) succeeded in measuring rotational and translational motions using a new angular measurement sensor (Morris 1971) at a surface station during a non-proliferation experiment at the Department of Energy, Nevada Test Site, using a very large (1 kiloton) chemical explosion. The sensor will allow us to measure the rotational ground motions of seismic waves in the near future.

What will rotational motions excited by earthquakes tell us? We will have accurate data for arrival times of *SH* waves, because the rotational component around the vertical axis is sensitive to *SH* waves although not to *P-SV* waves. A vertically heterogeneous, isotropic, elastic medium is the first-order approximation of the Earth's interior, so that we can expect to have a clear *SH*-wave onset in records of the rotational component around the vertical axis. When we try to separate *SH* waves from *P-SV* waves using translational motions, we need to rotate two horizontal components into radial and transverse components. To do this, we have to know the in-

cident directions of seismic waves. Now, we will be able simply to detect onsets of *SH* waves using the rotational component only.

The purpose of this paper is to elucidate another possibility, which is related to seismic sources. The familiar source model of earthquakes is a dislocation model concerned with a discontinuity of displacement across internal surfaces in a continuum, but not with a rotation across the surfaces. The rotation naturally generates rotational seismic waves. Defects in the continuum other than dislocations inclusive of tensile fractures are sources of such rotational motions. Teisseyre (1973) discussed, based on the micropolar theory, the possibility of rotational motions in source processes. There are several theories that deal with elastic continua with internal defects inside (e.g. Kondo 1949a, b, 1957, Bilby et al. 1955, Kröner 1958, Amari 1962, 1968, Mura 1963, 1972, deWit 1973, Kossecka and deWit 1977a, b). Among them, the most general perspective is provided by the geometrical theory of defects (Kondo 1949a, b, 1957). Based upon the theory, we will derive a general expression for rotational motions of seismic waves. This, as well as a general expression for translational motion, completely specifies the seismic waves.

We start with a sketch of the geometrical theory of defects. After outlining the fundamental concepts in Sect. 11.2.1, we present a space-time formulation in Sect. 11.2.2 so that we can treat time-dependent problems. An expression of defects is generalized by using geometrical quantities introduced in these subsections. Two kinds of defects, dislocations and disclinations, play important roles. Interestingly, their motions are closely related with each other, being characterized by continuity equations. Section 11.2.3 is devoted to their derivation, using the space-time of Section 11.2.2. The strain related to earthquakes will be less than 10^{-3}; the magnitude of strain of granite rocks just before brittle fractures was measured in triaxial compression tests (e.g. Mogi 1978). So we can employ a linear approximation to obtain our main result, simple formulae (11.97) and (11.98) for rotational and translational motions excited by earthquakes are used. Finally in Section 11.4, we present a simulation of rotational motion excited by an earthquake, and discuss the possibility of detection in real situations.

11.2 Geometrical Theory of Defects

11.2.1 Fundamental concept

Take an elastic material with internal defects, and cut it into many small pieces free of defects. Then, information on the defects will be reflected in

the relative location of the neighbouring pieces after being relaxed to a strain-free state. Using this idea in the framework of non-Riemannian geometry, a general theory was developed by Kondo (1949a, b, 1953, 1955, 1957), and his successors (e.g. Amari 1962, 1968, 1981, Shiozawa 1980). First we give a sketch of their theory.

Let $x^i (i = 1, 2, 3)$ be a coordinate system in the real Euclidean space E_3 in which a material body M is immersed. The coordinate system can be Cartesian or spherical etc., although it need not be orthogonal. To each point of M we attach the coordinate $x^i (i = 1, 2, 3)$, which the point occupies in E_3. We now have a manifold, hereafter called a material manifold. Let $\mathbf{e}^i(P)$ $(i = 1, 2, 3)$ be the natural bases (vectors directed along the x^i axes) at point P of the manifold. The tangent space T_p is a vector space spanned by the vectors $\mathbf{e}_1(P)$, $\mathbf{e}_2(P)$, $\mathbf{e}_3(P)$.

The material body, in general, is not free from strains, because of external forces applied from the outside or plastic defects existing inside. Take out of the material an element small enough to be free from defects. The element can then be transformed elastically to the strain-free state by cutting it off from the surroundings and releasing it from the constraints of the surroundings. This procedure is named **naturalization**. The states before and after the naturalization are called the **real state** and the **natural state**, respectively (see Fig. 11.1). We assume that the natural state is realized by an affine transformation of the torn small material element.

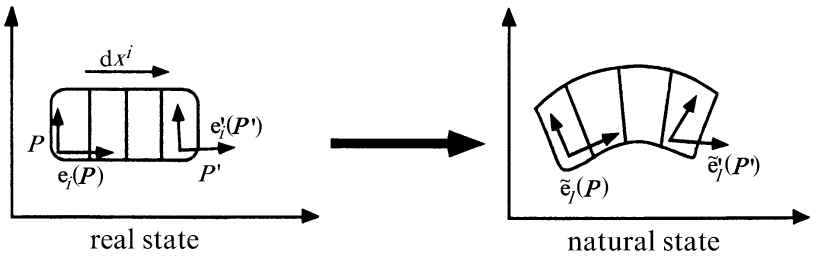

Fig. 11.1 Schematic image of "naturalization"

Suppose the vectors $\mathbf{e}_1$, $\mathbf{e}_2$, $\mathbf{e}_3$ become $\tilde{\mathbf{e}}_1, \tilde{\mathbf{e}}_2, \tilde{\mathbf{e}}_3$, respectively, through naturalization. The squared length $\mathrm{d}s_N^2$ of d$\mathbf{x}$ after naturalization is written as

$$\mathrm{d}s_N^2 = g_{ij}\,\mathrm{d}x^i\,\mathrm{d}x^j\,, \tag{11.1}$$

with

$$g_{ij} = \left(\tilde{\mathbf{e}}_i, \tilde{\mathbf{e}}_j\right), \tag{11.2}$$

which defines a metric tensor in the tangent space T_p. Here $(\tilde{\mathbf{e}}_i, \tilde{\mathbf{e}}_j)$ indicates the inner product in E_3. The summation convention for repeated indices is followed throughout.

Take two points, $P(x^i)$ and $P'(x^i + \mathrm{d}x^i)$, in M. We cut off two neighbouring material elements located around $P(x^i)$ and $P'(x^i + \mathrm{d}x^i)$ from the surroundings, and release them to the natural states. In this process, the two elements are kept connected. By this naturalization, the basis vectors $\mathbf{e}_i$ at P and $\mathbf{e}'_i$ at P' are transformed to $\tilde{\mathbf{e}}_i$ and $\tilde{\mathbf{e}}'_i$, respectively. In general, $\mathbf{e}_i \in T_p$ and $\mathbf{e}'_i \in T_{p'}$ are vectors belonging to different vector spaces, so that they are not comparable. However, we can compare the naturalized vectors $\tilde{\mathbf{e}}_i$ and $\tilde{\mathbf{e}}'_i$ because they are in the same Euclidean space E_3. The difference $\tilde{\mathbf{e}}'_i(P') - \tilde{\mathbf{e}}_i(P)$ is expressed as $\mathrm{d}x^j \Gamma^k_{ji} \tilde{\mathbf{e}}_k$ up to $O(\mathrm{d}x^j)$ with a suitable quantity Γ^k_{ji}. This quantity Γ^k_{ji} enables us to relate two tangent spaces, T_p and $T_{p'}$: the origin of $T_{p'}$ is mapped to $\mathrm{d}\mathbf{x} \in T_p$,

$$\mathrm{d}\mathbf{x} = \mathrm{d}x^i \mathbf{e}_i \,, \tag{11.3}$$

and the basis vector $\mathbf{e}'_i(P')$ is mapped to $\mathbf{e}_i(P) + \mathrm{d}x^j \Gamma^k_{ji} \mathbf{e}_k(P)$ in T_p,

$$\mathrm{d}\mathbf{e}_i = \mathrm{d}x^j \Gamma^k_{ji} \mathbf{e}_k \,. \tag{11.4}$$

Equations (11.3) and (11.4) define an affine connection in the material manifold M, where $\Gamma^k_{ji}(P)$ are called parameters of affine connection. We have thus incorporated the effects of defects into the rules of connection.

We assume that there is no strain gradient between neighbouring naturalized elements, that is, $T_{p'}$ is mapped to T_p by rotation only. This connection is called a metric connection characterized by vanishing of the covariant derivative of the metric tensor g_{ij}:

$$\nabla_k g_{ij} = \partial_k g_{ij} - \Gamma^m_{ki} g_{mj} - \Gamma^m_{kj} g_{mi} = 0 \,, \tag{11.5}$$

where ∇_k and ∂_k denote a covariant derivative and a partial derivative with respect to x^k, respectively.

Let us see what the connection implies. Take a closed circuit L in M which encircles an area Σ passing through a point P, and develop tangent spaces along L using the above connection, as shown in Fig. 11.2. Let $P = P_0, P_1, P_2, \ldots, P_n$ be a sequence of neighbouring points on L. We can map the tangent space T_{P_i} to the tangent space $T_{P_{i+1}}$. By repeating this procedure, the tangent space $T_P = T_{P_0}$ is mapped to T_{P_1}, and then to T_{P_2},

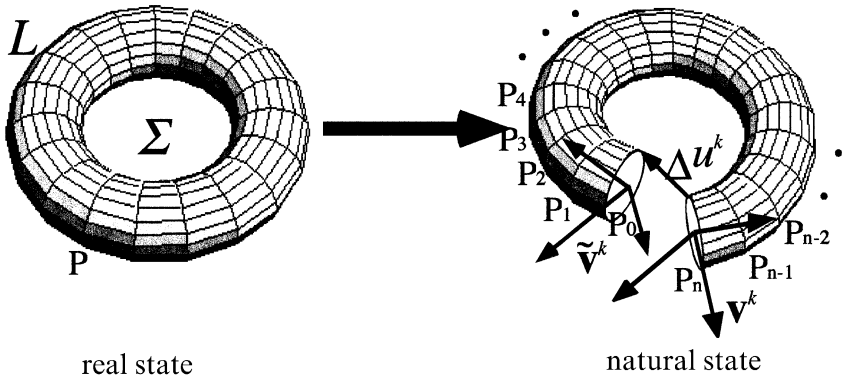

Fig. 11.2 A discrepancy of location Δu^k and a change of vector direction $\Delta \nu^k = \tilde{\nu}^k - \nu^k$ due to "naturalization"

and so on, and finally we have a mapping from T_P onto itself by going round through a loop L. Let the origin of T_P be mapped to a point $\Delta u^k \mathbf{e}_k \in T_P$ and let a vector $\nu^k \mathbf{e}_k$ be mapped to $(\nu^k + \Delta \nu^k)\mathbf{e}_k$. Then, we have

$$\Delta u^k = \int_{\Sigma} S_{ij}^k \, \mathrm{d}f^{ij} \,, \tag{11.6}$$

$$\Delta \nu^k = \frac{1}{2} \nu^l \int_{\Sigma} R_{ijl}^k \, \mathrm{d}f^{ij} \,, \tag{11.7}$$

where the integration is taken over Σ, and $\mathrm{d}f^{ij}$ represents small surface elements of Σ. The quantities S_{ij}^k and R_{ijl}^k in the integrands are a torsion tensor and a curvature tensor, respectively, and are defined by

$$S_{ij}^k = \Gamma_{[ij]}^k \,, \tag{11.8}$$

$$R_{ijl}^k = 2\partial_{[i} \Gamma_{j]l}^k + 2\Gamma_{[i|m|}^k \Gamma_{j]l}^m \,. \tag{11.9}$$

Here [..] denotes the alternation operation applied to indices in [..] except for those in $|..|$. The alternation [...] over p indices is obtained by adding $p!$ signed isomers with permuted indices and by dividing the alternation by $p!$, where the sign is positive if the permutation is even and negative if odd. If indices have to be singled out, the sign $|\ |$ is used; for example,

$$P^{\omega}_{[\chi\lambda|\mu|\nu]} = \frac{1}{6}\left(P^{\omega}_{\chi\lambda\mu\nu} + P^{\omega}_{\lambda\nu\mu\chi} + P^{\omega}_{\nu\chi\mu\lambda} - P^{\omega}_{\chi\nu\mu\lambda} - P^{\omega}_{\nu\lambda\mu\chi} - P^{\omega}_{\lambda\chi\mu\nu} \right). \tag{11.10}$$

Equations (11.8) and (11.9) are written explicitly as

$$S^{k}_{ij} = \Gamma^{k}_{[ij]} = \frac{1}{2}\left\{ \Gamma^{k}_{ij} - \Gamma^{k}_{ji} \right\}, \tag{11.11}$$

$$R^{k}_{ijl} = 2\partial_{[i}\Gamma^{k}_{j]l} + 2\Gamma^{k}_{[i|m|}\Gamma^{m}_{j]l} = \partial_i \Gamma^{k}_{jl} - \partial_j \Gamma^{k}_{il} + \Gamma^{k}_{im}\Gamma^{m}_{jl} - \Gamma^{k}_{jm}\Gamma^{m}_{il} . \tag{11.12}$$

The relations (11.6) and (11.7) allow for the following physical interpretations. Let us cut a loop of small material elements from the surroundings along L. This forms a ring, which cannot in general be put in the natural state without cutting it further into a non-ring form. When we cut the ring at point P and release the strain, we have a sequence of naturalized elements, which does not form a ring in the natural state (see Fig. 11.2). The discrepancy of position Δu^k is given by Eq. (11.6) and the change $\Delta \nu^k$ of the vector ν^k is given by Eq. (11.7). The defect due to the torsion tensor is called the dislocation, which is commonly used in earthquake source models. The curvature tensor, on the other hand, gives another defect called disclination.

We further introduce two strain tensors, a strain tensor e_{ij} and a rotational strain tensor γ_{ijk} defined by

$$e_{ij} = \frac{1}{2}\left(a_{ij} - g_{ij} \right), \tag{11.13}$$

$$\gamma_{ijk} = \Lambda_{i[jk]} - \Gamma_{i[jk]} , \tag{11.14}$$

where $a_{ij} = (\mathbf{e}_i, \mathbf{e}_j)$ is a metric tensor in E_3, agreeing with δ_{ij} in case of the Cartesian coordinates. In Eq. (11.14), Γ_{ijk} is defined as $\Gamma_{ijk} = g_{pk}\Gamma^{p}_{ij}$, and

$$\Lambda_{ijk} = \frac{1}{2}\left\{ \partial_i a_{jk} + \partial_j a_{ik} - \partial_k a_{ij} \right\}. \tag{11.15}$$

The strain tensor e_{ij} represents how the material element at P is deformed from the natural state: the difference between the length in the real state and the one in the natural state is given as

$$(a_{ij}\,\mathrm{d}x^i\,\mathrm{d}x^j)^{1/2} - (g_{ij}\,\mathrm{d}x^i\,\mathrm{d}x^j)^{1/2} \approx e_{ij}\,\mathrm{d}x^i\,\mathrm{d}x^j .$$

On the other hand, antisymmetric part of $\mathrm{d}x^m\Gamma^{k}_{mi}g_{kj}$ shows the relative rotation between the two bases at P and P' in the natural state. $\Lambda_{i[jk]}$ is the

corresponding quantity when there are no defects, so that γ_{ijk} contains information on the intrinsic rotation between two neighbouring elements in the natural state.

The torsion tensor and the curvature tensor can be rewritten in terms of the strain tensor and the rotational strain tensors as

$$S_{ij}^{k} = -\gamma_{[ij]k} - \partial_{[i} e_{j]k} , \tag{11.16}$$

$$R_{ijlk} = -2\partial_{[i}\gamma_{j]lk} - 2g^{rs}\gamma_{[i|kr|}\gamma_{j]ls} . \tag{11.17}$$

The compatibility condition of e_{ij} and γ_{ijk} is characterized by vanishing of the torsion and the curvature tensors: $S_{ijk} = R_{ijlk} = 0$. The compatibility condition in linear approximation means that there exist a vector u_i and a tensor ω_{ij} such that

$$e_{ij} = \partial_{(i} u_{j)} , \tag{11.18}$$

$$\gamma_{ijk} = \partial_i \omega_{jk} + \partial_i \partial_{[j} u_{k]} , \tag{11.19}$$

where $(\cdot)$ and $[\cdot]$ mean mixing and alternation, respectively. The mixing $(\ )$ over p indices is effected in the same way as the alternation except that the sign is always positive. For example,

$$P^{\omega}_{(\chi\lambda|\mu|\nu)} = \frac{1}{6}\left(P^{\omega}_{\chi\lambda\mu\nu} + P^{\omega}_{\lambda\nu\mu\chi} + P^{\omega}_{\nu\chi\mu\lambda} + P^{\omega}_{\chi\nu\mu\lambda} + P^{\omega}_{\nu\lambda\mu\chi} + P^{\omega}_{\lambda\chi\mu\nu}\right), \tag{11.20}$$

and Eq. (11.15) is written as

$$e_{ij} = \frac{1}{2}\left(\partial_i u_j + \partial_j u_i\right). \tag{11.21}$$

11.2.2 Space-time formulation

We extend the formulation in the previous section to deal with moving defects. We add a time axis to the Euclidean space E_3 to make a 4-D Euclidean space E_4. Each point of a deformed material can be marked with a 4-D coordinate system $x^{\mu}(\mu = 0, 1, 2, 3)$, where $x^0 = t$ and $x^i(i = 1, 2, 3)$ denote the time and the space coordinates, respectively. We then have a 4-D material manifold M. Hereafter, the Greek indices run over both the time and the space coordinates, while Roman indices run over the space coordinates only, unless otherwise stated.

Let $\mathbf{e}_\mu(P)\,(\mu = 0, 1, 2, 3)$ be the natural basis at point P of the manifold M. The tangent space T_p is a vector space spanned by the vectors $\mathbf{e}_\mu(P)\,(\mu = 0, 1, 2, 3)$. Note that $\mathbf{e}_0(P)$ is a unit vector of the x^0-axis, so is independent of P and is always perpendicular to $\mathbf{e}_i(P)$.

The connections between the neighbouring tangent spaces T_p and $T_{p'}$ of $P(x^\lambda)$ and $P'(x^\lambda + \mathrm{d}x^\lambda)$ are defined by

$$\mathrm{d}\mathbf{x} = \mathrm{d}x^\mu \mathbf{e}_\mu \,, \tag{11.22}$$

$$\mathrm{d}\mathbf{e}_\mu = \mathrm{d}x^\nu \Gamma^\kappa_{\nu\mu} \mathbf{e}_\kappa \,, \tag{11.23}$$

through the naturalization as in the previous subsection. Since we deal with the non-relativistic case, we define the naturalization involving time as follows. Let $\tilde{\mathbf{e}}_\mu(P)$ be a result of the naturalization of $\mathbf{e}_\mu(P)$. First, vectors $\tilde{\mathbf{e}}_i$ remain in E_3; that is, $(\tilde{\mathbf{e}}_i, \tilde{\mathbf{e}}_0) = 0$. Second, by Galilei transformation, the vector $\mathbf{e}_0 + v^i \mathbf{e}_i$ indicating the motion of P with the velocity $v^i = v^i(P)$ is naturalized to a unit vector of the time axis, $\mathbf{i}_0 = (1, 0, 0, 0)$, representing a state without motion. In other words,

$$\tilde{\mathbf{e}}_0 + v^i \tilde{\mathbf{e}}_i = \mathbf{i}_0 \,. \tag{11.24}$$

We can easily get

$$\Gamma^0_{\mu l} = 0 \,, \tag{11.25}$$

using the relation $(\mathrm{d}\tilde{\mathbf{e}}_l, \tilde{\mathbf{e}}_0) = 0$. From Eq. (11.24), $\mathrm{d}\tilde{\mathbf{e}}_0$ can be expressed as

$$\mathrm{d}\tilde{\mathbf{e}}_0 = -\partial_\mu v^k \mathrm{d}x^\mu \tilde{\mathbf{e}}_k - v^k \mathrm{d}\tilde{\mathbf{e}}_k = -\left\{\partial_\mu v^k + v^l \Gamma^k_{\mu l}\right\} \mathrm{d}x^\mu \tilde{\mathbf{e}}_k \,. \tag{11.26}$$

Remembering that the relation

$$\mathrm{d}\tilde{\mathbf{e}}_\mu = \mathrm{d}x^\nu \Gamma^\kappa_{\nu\mu} \tilde{\mathbf{e}}_\kappa \,, \tag{11.27}$$

holds by definition, we have

$$\mathrm{d}\tilde{\mathbf{e}}_0 = \mathrm{d}x^\mu \Gamma^0_{\mu 0} \tilde{\mathbf{e}}_0 + \mathrm{d}x^\mu \Gamma^k_{\mu 0} \tilde{\mathbf{e}}_k \,. \tag{11.28}$$

Comparing Eqs. (11.20), (11.21), and (11.23), we have

$$\Gamma^0_{\mu\nu} = 0 \,, \tag{11.29}$$

$$\Gamma^k_{\mu 0} = -\partial_\mu v^k - v^l \Gamma^k_{\mu l} \,. \tag{11.30}$$

The metric tensor defined by $g_{\mu\nu} = (\tilde{\mathbf{e}}_\mu, \tilde{\mathbf{e}}_\nu)$ is expressed as

$$g_{\mu\nu} = \begin{pmatrix} 1 = \nu^k \nu_k & -\nu_1 & -\nu_2 & -\nu_3 \\ -\nu_1 & g_{11} & g_{12} & g_{13} \\ -\nu_2 & g_{21} & g_{22} & g_{23} \\ -\nu_3 & g_{31} & g_{32} & g_{33} \end{pmatrix}. \tag{11.31}$$

We define, in the same manner as the 3-Dl case, a torsion tensor and a curvature tensor as

$$S^\kappa_{\mu\nu} = \Gamma^\kappa_{[\mu\nu]}, \tag{11.32}$$

$$R^\kappa_{\mu\nu\lambda} = 2\partial_{[\mu}\Gamma^\kappa_{\nu]\lambda} + 2\Gamma^\kappa_{[\mu|\rho|}\Gamma^\rho_{\nu]\lambda}, \tag{11.33}$$

and a strain tensor and a rotational strain tensor as

$$e_{\mu\nu} = \frac{1}{2}\left(a_{\mu\nu} - g_{\mu\nu}\right), \tag{11.34}$$

$$\gamma_{\mu\nu\kappa} = \Lambda_{\mu[\nu\kappa]} - \Gamma_{\mu[\nu\kappa]}. \tag{11.35}$$

Here

$$\Lambda_{\mu\nu\kappa} = \frac{1}{2}\left\{\partial_\mu a_{\nu\kappa} + \partial_\nu a_{\mu\kappa} - \partial_\kappa a_{\mu\nu}\right\}, \tag{11.36}$$

and $a_{\mu\nu} = (\mathbf{e}_\mu, \mathbf{e}_\nu)$ is a metric tensor; the components relating to time axis are $a_{00} = 1$ and $a_{i0} = a_{0i} = 0$. A 4-D counterpart of Eqs. (11.16) and (11.17) now reads:

$$S_{\mu\nu\kappa} = -\gamma_{[\mu\nu]\kappa} - \partial_{[\mu}e_{\nu]\kappa}, \tag{11.37}$$

$$R_{\mu\nu\lambda\kappa} = -2\partial_{[\mu}\gamma_{\nu]\lambda\kappa} - 2g^{\rho\sigma}\gamma_{[\mu|\kappa\rho|}\gamma_{\nu]\lambda\sigma}. \tag{11.38}$$

We note that the 3-D components of the torsion and curvature tensors defined above agree with those in previous subsection because $\Gamma^0_{\mu\nu} = 0$. We also note that the connection is a metric connection in the 4-D sense, $\nabla_k g_{\mu\nu} = 0$, by virtue of Eqs. (11.5), (11.29), and (11.30).

From the definition of the strain tensor, $e_{\mu\nu}$, and Eq. (11.31), we have

$$e_{00} = \frac{1}{2}\left(a_{00} - g_{00}\right) = \frac{1}{2}\left(1 - 1 - \nu^k \nu_k\right) \approx 0, \tag{11.39}$$

$$e_{0k} = \frac{1}{2}\left(a_{0k} - g_{0k}\right) = -\frac{1}{2}g_{0k} = \frac{1}{2}v_k \,. \tag{11.40}$$

From the definition of $\gamma_{\mu\nu\kappa}$, $\gamma_{\mu 0\kappa}$ is represented as

$$\gamma_{\mu 0\kappa} = \frac{1}{2}\left\{g_{\kappa\lambda}\Gamma^{\lambda}_{\mu 0} - g_{\lambda 0}\Gamma^{\lambda}_{\mu\kappa}\right\} \approx -\frac{1}{2}\partial_{\mu}v_k \,, \tag{11.41}$$

which gives a gradient of the velocity.

11.2.3 Density and current tensors of defects

In this section we confine ourselves to linear problems where higher-order terms of geometrical quantities are negligible. We will derive systematically the results that were obtained based on a linear theory of elasticity by Mura (1963, 1972, 1982), deWit (1973), and Kossecka and deWit (1977a, b) and so on. First we introduce two density tensors, α^{ij} for dislocation and θ^{ij} for disclination, using the torsion tensor (11.37) and the curvature tensor (11.38) as follows:

$$\alpha^{ij} = \varepsilon^{ilk} S^{j}_{lk} \Big/ \sqrt{g} \,, \tag{11.42}$$

$$\theta^{ij} = \varepsilon^{ilk}\varepsilon^{jmn} R_{klmn} \Big/ 4g \,. \tag{11.43}$$

Here and in the following ε_{ijk} is Eddington's epsilon:

$$\varepsilon_{ijk} = \varepsilon^{ijk} = \begin{cases} 1 & \text{if } ijk \text{ is an even permutation of } (1, 2, 3) \\ -1 & \text{if } ijk \text{ is an odd permutation of } (1, 2, 3) \\ 0 & \text{otherwise} \end{cases} \tag{11.44}$$

and $g = \det(g_{ij})$. The meanings of α^{ij} and θ^{ij} will be clear from the relations (11.6) and (11.7). Since $\varepsilon^{ijk} \Big/ \sqrt{g}$ behaves as a tensor under the 3-D transformation, $t \to t' = t$, $x \to x' = x'(x)$, so do α^{ij} and θ^{ij}. The inverse relations of Eqs. (11.42) and (11.43) are written as

$$S^{j}_{lk} = \frac{1}{2}\sqrt{g}\,\varepsilon_{ilk}\,\alpha^{ij} \,, \tag{11.45}$$

$$R_{klmn} = g\,\varepsilon_{ikl}\,\varepsilon_{jmn}\,\theta^{ij} \,. \tag{11.46}$$

Their current tensors I^{n}_{m} and J^{n}_{m} are defined as

$$I_m{}^n = S_{m0}{}^n = -S_{m0}{}^n , \tag{11.47}$$

$$J_m{}^n = \frac{1}{2}\varepsilon^{npq} R_{m0pq} \Big/ \sqrt{g} . \tag{11.48}$$

Let us now derive continuity equations in linear approximation, which will justify the above introduction. Hereafter we assume that the coordinate system x^i is Cartesian. From Bianchi's identities, the following equations are fulfilled by the torsion and curvature tensors (Schouten 1954),

$$\nabla_{[\omega} R_{\nu\mu]\lambda}{}^{\kappa} = 2S_{[\omega\nu}{}^{\rho} R_{\mu]\rho\lambda}{}^{\kappa}, \infty \tag{11.49}$$

$$R_{[\nu\mu\lambda]}{}^{\kappa} = 2\nabla_{[\nu} S_{\mu\lambda]}{}^{\kappa} - 4S_{[\nu\mu}{}^{\rho} S_{\lambda]\rho}{}^{\kappa} , \tag{11.50}$$

and an identity for the curvature tensor under the metric connection: $R_{\nu\mu(\lambda\kappa)} = 0$. From the definition of the curvature tensor, it is obvious that $R_{(\nu\mu)\lambda}{}^{\kappa} = 0$. The connection treated in this paper is metric $(\nabla_\nu g_{\mu\lambda} = 0)$, so we have $R_{\nu\mu(\lambda\kappa)} = 0$ (Schouten 1954). Equation (11.50) becomes

$$R_{[\nu\mu\lambda]}{}^{\kappa} = 2\partial_{[\nu} S_{\mu\lambda]}{}^{\kappa} , \tag{11.51}$$

if we neglect terms of order higher than $0(\Gamma_{ij}^k)$. Employing this equation, we obtain

$$\partial_p \alpha_m^p = \partial_p \varepsilon^{pij} S_{ijm} = 6\partial_{[1} S_{23]m} = \frac{1}{2}\varepsilon^{klp} R_{klpm} . \tag{11.52}$$

From Eq. (11.43), we have the relation:

$$\varepsilon_{ipq}\theta^{pq} = \frac{1}{4}\varepsilon_{ipq}\varepsilon^{pkl}\varepsilon^{qrs} R_{klrs} = -\frac{1}{2}\varepsilon^{klp} R_{klpm} , \tag{11.53}$$

if we use $g = 1$ for the Cartesian coordinate system and $R_{\nu\mu(\lambda\kappa)} = 0$. Then, we have the relation

$$\partial_p \alpha_i^p + \varepsilon_{ipq}\theta^{pq} = 0 . \tag{11.54}$$

Employing a formula for Eddington's epsilon

$$\varepsilon^{ijk}\varepsilon^{lmn} = gg^{pl}g^{qm}g^{rn}\begin{vmatrix} \delta_p^i & \delta_q^i & \delta_r^i \\ \delta_p^j & \delta_q^j & \delta_r^j \\ \delta_p^k & \delta_q^k & \delta_r^k \end{vmatrix} , \tag{11.55}$$

we see θ^{ij} defined by Eq. (11.43) agrees with the Einstein tensor G^{ji}

$$G^{ji} = R^{ji} - \frac{1}{2} R g^{ji} , \tag{11.56}$$

in a 3-D space. Here $R^{ji} = g^{kj} g^{mi} R_{km}$, $R_{km} = R_{pkm}{}^{p}$ and $R = R_{p}{}^{p}$. The Einstein G^{ji} generally satisfies

$$\nabla_i G_j{}^{i} = -3 S_{[jk}{}^{r} R_{i]rl}{}^{k} g^{il} . \tag{11.57}$$

Hence, neglecting the higher-order terms, we have

$$\partial_i \theta^{il} \approx 0 . \tag{11.58}$$

The formula (11.57) is obtained from Eq. (11.49) in three dimensions, i.e. the indices run over space coordinates 1, 2, 3, as follows. Multiplied by $\delta_{\kappa}{}^{\nu}$ and contracting along ν, the left-hand side term of Eq. (11.49) becomes

$$\delta_{\kappa}{}^{\nu} \nabla_{[\omega} R_{\nu\mu]\lambda}{}^{\kappa} = \frac{1}{3} \left(\nabla_{\omega} R_{\mu\lambda} + \nabla_{\kappa} R_{\mu\omega\lambda}{}^{\kappa} - \nabla_{\mu} R_{\omega\lambda} \right) , \tag{11.59}$$

where $R_{\mu\lambda} = R_{\kappa\mu\lambda}{}^{\kappa}$. Again, multiplying by $g^{\mu\lambda}$ and contracting along μ, the term on the left-hand side becomes $-\frac{2}{3} \nabla_{\mu} \left(R_{\omega}{}^{\mu} - \frac{1}{2} R \delta_{\omega}{}^{\mu} \right)$, where $R = R_{\mu}{}^{\mu}$. When we apply the same procedure to the term on the right-hand side of Eq. (11.49), it becomes $2 S_{[\omega\kappa}{}^{\rho} R_{\mu]\rho\lambda}{}^{\kappa} g^{\mu\lambda}$. Because $G_{\omega}{}^{\mu} = R_{\omega}{}^{\mu} - \frac{1}{2} \delta_{\omega}{}^{\mu} R$, we get Eq. (11.57) in three dimensions.

Let Eq. (11.42) be partially differentiated with respect to time:

$$\partial_0 \alpha_k{}^{m} = \varepsilon^{mij} \partial_0 S_{ijk} = -2 \varepsilon^{mij} \partial_i I_{jk} - \varepsilon^{mij} R_{i0jk} + \frac{1}{2} \varepsilon^{mij} R_{ij0k} . \tag{11.60}$$

Here, the relation $R_{[0ij]}{}^{k} = 2 \partial_{[0} S_{ij]}{}^{k}$ deduced from Eq. (11.51) is used. From the definition of $J_i^{\,n}$ we have the following expression:

$$\varepsilon_{njk} J_i^{\,n} = R_{i0jk} . \tag{11.61}$$

Then, Eq. (11.60) can be rewritten as

$$\partial_0 \alpha_k^{m} + \varepsilon^{mij} \left(2 \partial_i I_{jk} + \varepsilon_{njk} J_i^{\,n} \right) = \frac{1}{2} \varepsilon^{mij} R_{ij0k} . \tag{11.62}$$

Neglecting the higher-order terms in Eq. (11.38) and using Eq. (11.41), the following relation holds:

$$R_{ij0k} = \frac{1}{2}\left(\partial_i \partial_j \nu_k - \partial_j \partial_i \nu_k\right) = 0\,, \tag{11.63}$$

and, finally, we have

$$\partial_0 \alpha_k^m + \varepsilon^{mij}\left(2\partial_i I_{jk} + \varepsilon_{njk} J_i^n\right) = 0\,. \tag{11.64}$$

In linear approximation, we have from Eq. (11.49) that

$$\partial_{[\omega} R_{\nu\mu]\lambda\kappa} = 0\,, \tag{11.65}$$

and it follows that

$$\partial_0 R_{ijpq} = -\partial_i R_{j0pq} - \partial_j R_{0ipq}\,. \tag{11.66}$$

Let θ^{mn} be partially differentiated with respect to time:

$$\partial_0 \theta^{mn} = \frac{1}{4}\varepsilon^{mij}\varepsilon^{npq}\partial_0 R_{ijpq} = -\varepsilon^{mij}\partial_i J_j^n\,, \tag{11.67}$$

then we have

$$\partial_0 \theta^{mn} + \varepsilon^{mpq}\partial_p J_q^n = 0\,. \tag{11.68}$$

Therefore, the continuity equations take form of

$$\partial_0 \alpha_k^m + \varepsilon^{mij}\left(2\partial_i I_{jk} + \varepsilon_{njk} J_i^n\right) = 0 \quad \text{and} \quad \partial_0 \theta^{mn} + \varepsilon^{mpq}\partial_p J_q^n = 0 \tag{11.69}$$

and the dislocation tensor and disclination tensor are related to each other by

$$\partial_p \alpha_i^p + \varepsilon_{ipq}\theta^{pq} = 0 \quad \text{and} \quad \partial_i \theta^{il} \approx 0\,. \tag{11.70}$$

Here we note that the geometrical theory presents more general framework than the dislocation theory: dislocation is a defect accompanied by the vanishing of curvature tensor R_{ijlk} and is sometimes called a plasticity of distant parallelism.

We will rewrite the above expression using the strain tensor e_{ij} and the rotational strain tensor γ_{ijk} for later convenience. In general, the deformation is not completely elastic but partly plastic, so we decompose the tensors into elastic and plastic components as

$$e_{ij} = e_{ij}^E + e_{ij}^*\,, \tag{11.71}$$

$$\gamma_{ijk} = \gamma^{E}_{ijk} + \gamma^{*}_{ijk} , \tag{11.72}$$

where the superscripts E and $*$ denote the elastic part and the plastic part, respectively. When defects are present, a displacement field has a discrepancy and a change of vector on a defect surface, as shown in Fig. 11.2, which are given by Eqs. (11.6) and (11.7) in general. Therefore, it is found that the spatial derivative of displacement has a singularity on the defect surface, and this singular part is found to be plastic parts of these strain tensors. When no defects are present, the plastic fields are compatible, i.e. the plastic parts of these strain tensors can be derived from a plastic displacement, u^{*}_{j}, and a plastic tensor, ω^{*}_{jk}, using Eqs. (11.18) and (11.19) which satisfy the compatibility conditions, $S_{ijk} = R_{ijlk} = 0$. We sometimes conventionally introduce the total displacement u_j and ω_{jk} satisfying Eqs. (11.18) and (11.19), even when e^{*}_{ij} and γ^{*}_{ijk} do not vanish. It should be noted, however, that u_j and ω_{jk} are no longer single-valued functions because of the incompatibility. This is easily understood in the dislocation model of earthquake: u_j is discontinuous on the fault plane. The above convention will be permitted as long as multivaluedness does no harm (see Sect. 11.3).

Because the elastic deformation satisfies the compatibility conditions, e^{E}_{ij} and γ^{E}_{ijk} do not contribute to the torsion tensor and the curvature tensor. Therefore, neglecting the higher-order terms, the torsion tensor and the curvature tensor are written as

$$S_{ijk} = -\gamma^{*}_{[ij]k} - \partial_{[i} e^{*}_{j]k} , \tag{11.73}$$

$$R_{ijlk} \approx -2\partial_{[i}\gamma^{*}_{j]lk} . \tag{11.74}$$

Substituting Eqs. (11.73) and (11.74) into Eqs. (11.42) and (11.43), we have

$$\alpha^{i}_{j} = -\varepsilon^{ipq}\left(\varepsilon_{qjn}\kappa^{*n}_{p} + \partial_{p} e^{*}_{qj}\right), \tag{11.75}$$

$$\theta^{ij} = -\varepsilon^{ipq}\partial_{p}\kappa^{*j}_{q} , \tag{11.76}$$

where

$$\kappa^{*j}_{i} = \frac{1}{2}\varepsilon^{jpq}\gamma^{*}_{ipq} \quad \text{or} \quad \gamma^{*}_{ijk} = \varepsilon_{jkp}\kappa^{*p}_{i} . \tag{11.77}$$

The current densities I_{mn} and J_m^n are similarly given by

$$I_{mn} = \frac{1}{2}\left(\varepsilon_{mnl}\kappa_0^{*l} + \partial_0 e_{mn}^0 - \partial_m \nu_n\right), \tag{11.78}$$

$$J_m^n = -\partial_m \kappa_0^{*n} + \partial_0 \kappa_m^{*n}. \tag{11.79}$$

11.3 Formulation of Rotational and Translational Motions Due to Earthquakes

In order to develop equations for seismic waves from buried plastic deformations, we shall describe such sources in terms of a transformational (or stress-free) strain introduced in the source volume. This problem is a generalization of Eshelby's "transformation problem" to an anisotropic medium and an inhomogeneous stress-free strain (Eshelby 1957). We note here that the concept of the transformational strain in Eshelby (1957) is identical with the plastic strain of this paper. Similar approaches have been made by Mura (1972, 1982), deWit (1973), Kossecka and deWit (1977a, b), etc., who gave displacements and distortions caused by dislocations and/or disclinations in a linear elastic continuum. Kossecka and deWit (1977b) proposed a simple expression for the rotational velocity of a distribution of moving dislocations and disclinations. However, they assumed the existence of a "plastic velocity" whose physical meaning was not clear.

Since we are interested in the ground motions excited by an earthquake, we assume that there exists a bounded region V_S outside of which defects vanish and the material deforms elastically. It should be noted that an earthquake is an internal process of the Earth, and the displacement field excited by an earthquake has a quiescent past. In this section, we will derive a simple formula for rotational motion caused by an earthquake.

To help understand the following formal derivation, let us briefly illustrate Eshelby's recipe of how to implement defects in the material. First, we separate the source material V_S by cutting along the surface S enclosing V_S and removing V_S from the surroundings. Second, we let the source material undergo plastic strain (stress-free strain) which causes deformation without changing the stress within V_S. Third, we apply extra surface tractions or fictitious body forces that will restore the source volume to its original shape. Then, we put the source material back in the hole and weld the material across S, removing the extra tractions or fictitious body forces on S, and find the resulting displacement caused by the plastic strain. So,

the moral of Eshelby's method is that a defect described by the plastic strain e^*_{kl} can be simulated by the extra traction given by $-C^{ijkl}e^*_{kl}n_j$ or the fictitious body force given by $-C^{ijkl}\partial_j e^*_{kl}$ where C^{ijkl} is a tensor of elastic constants (e.g. Aki and Richards 1980).

The above procedure is simply done as follows. Keeping in mind that e^*_{kl} is stress-free, we apply Hook's law,

$$\sigma^{ij} = C^{ijkl}e^E_{kl}\,, \tag{11.80}$$

together with $\partial_{(k}u_{l)} = e^E_{kl} + e^*_{kl}$ to the equation of motion without body forces:

$$\rho\partial_0\partial_0 u^i = \partial_j\sigma^{ij}\,. \tag{11.81}$$

Here ρ is the density of the medium. The tensor C^{ijkl} is a symmetric tensor with respect to the *i* and *j* indices ($C^{ijkl} = C^{jikl}$) due to a symmetric characteristic of elastic stress, and with respect to the *k* and *l* indices ($C^{ijkl} = C^{ijlk}$) due to a symmetric characteristic of elastic strain. Therefore, we obtain the equation of motion as follows:

$$\rho\partial_0\partial_0 u^i = C^{ijkl}\left(\partial_j\partial_k u_l - \partial_j e^*_{kl}\right). \tag{11.82}$$

Using Green's function $G_{ni}(x, t-\tau; \xi, 0)$, a seismic displacement (translational motion) generated by a plastic strain can be expressed as

$$u_n(x,t) = -\int_{-\infty}^{\infty}\mathrm{d}\tau\int C^{ijkl}\partial_j G_{ni}(x,t-\tau;\xi,0)\,e^*_{kl}(\xi,\tau)\,\mathrm{d}V(\xi)\,, \tag{11.83}$$

after integration by parts. Green's function $G_{ni}(x, t-\tau; \xi, 0)$ satisfies an equation of motion

$$\rho\partial_0\partial_0 G^i_n = C^{ijkl}\partial_j\partial_k G_{\ln} + \delta^i_n\delta(x-\xi)\,\delta(t-\tau)\,, \tag{11.84}$$

and represents the *n*th component of the displacement resulting from a unit impulse source of the *i*th component applied at $x = \xi$, and $t = \tau$ (e.g. Aki and Richards, 1980). δ^i_n and $\delta(x-\xi)$ or $\delta(t-\tau)$ denote Kronecker's delta and delta functions, respectively. Differentiating Eq. (11.83), we have

$$\begin{aligned}\partial_m u_n(x,t) &= -\int_{-\infty}^{\infty}\mathrm{d}\tau\int C^{ijkl}\partial_m\partial_j G_{ni}(x,t-\tau;\xi,0)\,e^*_{kl}(\xi,\tau)\,\mathrm{d}V(\xi)\\ &= -\int_{-\infty}^{\infty}\mathrm{d}\tau\int C^{ijkl}\partial_j G_{ni}(x,t-\tau;\xi,0)\,\partial_{m'}e^*_{kl}(\xi,\tau)\,\mathrm{d}V(\xi),\end{aligned} \tag{11.85}$$

where we have used integration by parts with respect to space and the boundary condition that the plastic strain (e^*_{kl}) vanishes outside of V_S. The partial differentiation with respect to τ or the mth component of ξ is explicitly shown by an index with a prime, for example, $\partial_{0'}$ and $\partial_{m'}$. From Eq. (11.75), we have

$$-\partial_{m'} e^*_{kl} = \varepsilon_{pmk}\left(\alpha^p_l - \kappa^{*p}_l\right) - \partial_{k'} e^*_{ml} + \varepsilon_{lmk}\kappa^*, \tag{11.86}$$

where $\kappa^* = \kappa^{*i}_i$, from which it follows that

$$\begin{aligned}
\partial_m u_n(x,t) &= \int_{-\infty}^{\infty} \mathrm{d}\tau \int C^{ijkl}\partial_j G_{ni}(x,t-\tau;\xi,0) \\
&\quad \times \left\{\varepsilon_{pmk}\left[\alpha^p_l(\xi,\tau) - \kappa^{*p}_l(\xi,\tau)\right] - \partial_{k'} e^*_{ml}(\xi,\tau)\right\}\mathrm{d}V(\xi) \\
&= \int_{-\infty}^{\infty} \mathrm{d}\tau \int \varepsilon_{pmk} C^{ijkl}\partial_j G_{ni}(x,t-\tau;\xi,0) \\
&\quad \times \left[\alpha^p_l(\xi,\tau) - \kappa^{*p}_l(\xi,\tau)\right]\mathrm{d}V(\xi) + e^*_{mn}(x,t) \\
&\quad - \int_{-\infty}^{\infty} \mathrm{d}\tau \int \rho\partial_0\partial_0 G^l_n(\boldsymbol{\xi},t-\tau;x,0) \times e^*_{ml}(\xi,\tau)\mathrm{d}V(\xi),
\end{aligned} \tag{11.87}$$

where we have used integration by parts again and the symmetric property of C^{ijkl}. Here, a reciprocal relation of Green's function, $G^l_n(x,t-\tau;\xi,0) = G^l_n(\xi,t-\tau;x,0)$, is also employed. The second term on the right-hand side of Eq. (11.87) vanishes because we assume the plastic strain outside the source volume (V_S) to be zero. The partial differentiation of Eq. (11.83) with respect to time yields

$$\begin{aligned}
\partial_0\partial_m u_n(x,t) &= \int_{-\infty}^{\infty} \mathrm{d}\tau \int \varepsilon_{pmk} C^{ijkl}\partial_j G_{ni}(x,\tau;\xi,0)\partial_0 \alpha^p_l(\xi,t-\tau)\mathrm{d}V(\xi) \\
&\quad - \int_{-\infty}^{\infty} \mathrm{d}\tau \int \varepsilon_{pmk} C^{ijkl}\partial_j G_{ni}(x,\tau;\xi,0)\partial_0 \kappa^{*p}_l(\xi,t-\tau)\mathrm{d}V(\xi) \\
&\quad + \partial_0 e^*_{mn}(x,t) - \int_{-\infty}^{\infty} \mathrm{d}\tau \int \rho\partial_0\partial_0 G^l_n(\xi,\tau;x,0) \\
&\quad \times \partial_0 e^*_{ml}(\xi,t-\tau)\mathrm{d}V(\xi).
\end{aligned} \tag{11.88}$$

The first term (I_1) on the right-hand side of the above equation can be rewritten using Eq. (11.66) as

$$\begin{aligned}
\mathrm{I}_1 &= -\int_{-\infty}^{\infty}\mathrm{d}\tau\int\varepsilon_{pmk}C^{ijkl}\partial_j G_{ni}\varepsilon^{prs}\left\{2\partial_{r'}I_{sl}+\varepsilon_{qsl}J_r^q\right\}\mathrm{d}V \\
&= -2\int_{-\infty}^{\infty}\mathrm{d}\tau\int I_{kl}C^{ijkl}\partial_m\partial_j G_{ni}\mathrm{d}V - 2I_{mn} \\
&\quad +2\int_{-\infty}^{\infty}\mathrm{d}\tau\int\rho\partial_0\partial_0 G_n^l I_{ml}\mathrm{d}V+\int_{-\infty}^{\infty}\mathrm{d}\tau\int C^{ijkl}\varepsilon_{qml}J_k^q\partial_j G_{ni}\mathrm{d}V\,, \qquad (11.89)
\end{aligned}$$

where we also use the relations

$$\varepsilon_{pmk}\varepsilon^{prs}=\delta_m^r\delta_k^s-\delta_m^s\delta_k^r\,, \qquad (11.90)$$

$$C^{ijkl}\partial_k\partial_j G_{ni}=\rho\partial_0\partial_0 G_n^l-\delta_n^l\delta(\xi-x)\delta(t-\tau)\,, \qquad (11.91)$$

and

$$\varepsilon_{qkl}C^{ijkl}J_m^q=0 \qquad (\text{due to } C^{ijkl}=C^{ijlk})\,. \qquad (11.92)$$

From Eq. (11.58), we have a relation

$$\partial_j\kappa_0^{*k}=-J_j^k+\partial_0\kappa_j^{*k}\,. \qquad (11.93)$$

Substituting this equation into the integrand of the second term (I_2) on the right-hand side of Eq. (11.88), we have

$$\begin{aligned}
\mathrm{I}_2 &= -\int_{-\infty}^{\infty}\mathrm{d}\tau\int C^{ijkl}\varepsilon_{pmk}J_l^p\partial_j G_{ni}\mathrm{d}V-\int_{-\infty}^{\infty}\mathrm{d}\tau\int C^{ijkl}\varepsilon_{pmk}\partial_{l'}\kappa_0^{*p}\partial_j G_{ni}\mathrm{d}V \\
&= -\int_{-\infty}^{\infty}\mathrm{d}\tau\int C^{ijkl}\varepsilon_{qml}J_k^q\partial_j G_{ni}\mathrm{d}V+\varepsilon_{pmn}\kappa_0^{*p} \\
&\quad -\int_{-\infty}^{\infty}\mathrm{d}\tau\int\varepsilon_{pml}\rho\partial_0\partial_0 G_n^l\kappa_0^{*p}\mathrm{d}V\,. \qquad (11.94)
\end{aligned}$$

Finally, Eq. (11.88) is written as

$$\begin{aligned}
\partial_0\partial_m u_n(x,t) &= -2\int_{-\infty}^{\infty}\mathrm{d}\tau\int C^{ijkl}\partial_m\partial_j G_{ni}(x,\tau;\xi,0)I_{kl}(\xi,t-\tau)\mathrm{d}V(\xi) \\
&\quad -\left\{2I_{mn}(x,t)-\partial_0 e_{mn}^*(x,t)-\varepsilon_{pmn}\kappa_0^{*p}(x,t)\right\} \\
&\quad +\int_{-\infty}^{\infty}\mathrm{d}\tau\int\rho\partial_0\partial_0 G_n^l(\xi,\tau-\tau;x,0) \\
&\quad \times\left\{2I_{ml}(\xi,\tau)-\partial_{0'}e_{ml}^*(\xi,\tau)-\varepsilon_{pml}\kappa_0^{*p}(\xi,\tau)\right\}\mathrm{d}V(\xi)\,. \qquad (11.95)
\end{aligned}$$

The second term on the right-hand side of Eq. (11.95) is zero because defects are limited in V_S and x is outside of V_S. The integrand of the third term can be simplified using Eq. (11.78), and Eq. (11.95) is rewritten as follows:

$$\begin{aligned}\partial_0\partial_m u_n(x,t) = &-2\int_{-\infty}^{\infty}\mathrm{d}\tau\int C^{ijkl}\partial_m\partial_j G_{ni}(x,t-\tau;\xi,0)I_{kl}(\xi,\tau)\mathrm{d}V(\xi)\\ &-\int_{-\infty}^{\infty}\mathrm{d}\tau\int\rho\partial_0\partial_0 G_n^l(\xi,t-\tau;x,0)\partial_{m'}\nu_l(\xi,\tau)\mathrm{d}V(\xi)\,.\end{aligned} \tag{11.96}$$

This equation is a generalized version of Eq. (38.36) in Mura (1980). We have, then, a simple expression for the rotational velocity of a seismic wave as follows:

$$\begin{aligned}\partial_0\omega^q(x,t) &= \frac{1}{2}\left[\nabla\times\partial_0\mathbf{u}\right]^q\\ &= -\int_{-\infty}^{\infty}\mathrm{d}\tau\int\varepsilon^{qmn}C^{ijkl}\partial_m\partial_j G_{ni}(x,t-\tau;\xi,0)I_{kl}(\xi,\tau)\mathrm{d}V(\xi)\\ &-\frac{1}{2}\int_{-\infty}^{\infty}\mathrm{d}\tau\int\varepsilon^{qmn}\rho\partial_0\partial_0 G_n^l(x,t-\tau;\xi,0)\partial_{m'}\nu_l(\xi,\tau)\mathrm{d}V(\xi)\\ &= -\frac{1}{2}\int_{-\infty}^{\infty}\mathrm{d}\tau\int\varepsilon^{qmn}C^{ijkl}\partial_m\partial_j G_{ni}(x,t-\tau;\xi,0)\\ &\times\left\{\gamma_{0kl}^*(\xi,\tau)+\partial_{0'}e_{kl}^*(\xi,\tau)-\partial_{k'}\nu_l(\xi,\tau)\right\}\mathrm{d}V(\xi)\\ &-\frac{1}{2}\int_{-\infty}^{\infty}\mathrm{d}\tau\int\varepsilon^{qmn}\rho\partial_0\partial_0 G_n^l(\xi,t-\tau;x,0)\partial_{m'}\nu_l(\xi,\tau)\mathrm{d}V(\xi)\,.\end{aligned} \tag{11.97}$$

On the other hand, the velocity of translational motion is written as

$$\partial_0 u_q(x,t) = -\int_{-\infty}^{\infty}\mathrm{d}\tau\int C^{ijkl}\partial_j G_{qi}(x,t-\tau;\xi,0)\partial_{0'}e_{kl}^*(\xi,\tau)\mathrm{d}V(\xi)\,. \tag{11.98}$$

These two equations show that we can estimate the tensors γ_{0kl}^*, $\partial_k\nu_l$ using the translational and rotational motions of seismic waves simultaneously.

11.4 Possibility of Estimating a Rotational Strain Tensor Due to an Earthquake

To get information about γ_{0kl}^* and $\partial_k\nu_l$ due to an earthquake based on observed seismic waves, it is necessary that γ_{0kl}^* and $\partial_k\nu_l$ appearing in

Eq. (11.97) have a magnitude equal to or higher than $\partial_0 e^*_{kl}$. Let us estimate their magnitudes in a simple case. In this section, we also assume that the coordinate system x^i is Cartesian.

From Eqs. (11.6), (11.7), (11.45), and (11.46), the discrepancy Δu_j and the change $\Delta \bar{\nu}_k$ of a vector $\bar{\nu}_k$ due to defects are rewritten as

$$\Delta u_j = \int_\Sigma S_{pqj}\, \mathrm{d}f^{pq} = \int_\Sigma \alpha^i_j\, \mathrm{d}\Sigma_i\,, \tag{11.99}$$

$$\Delta \bar{\nu}_k = \frac{1}{2}\bar{\nu}^l \int_\Sigma R_{pqlk}\, \mathrm{d}f^{pq} = \frac{1}{2}\bar{\nu}^l \int_\Sigma \varepsilon^{ipq} R_{pqlk}\, \mathrm{d}\Sigma_i = \bar{\nu}^l \int_\Sigma \varepsilon_{jlk}\theta^{ij}\mathrm{d}\Sigma_i\,, \tag{11.100}$$

where $\mathrm{d}f^{pq} = \varepsilon^{ipq}\mathrm{d}\Sigma_i \big/ \sqrt{g}$ and $\mathrm{d}\Sigma_i$ is the i th component of the area vector of Σ. Now, we consider a simple model of an earthquake such that a material below a surface S has been plastically displaced with respect to a material above S by a constant amount which represents a rigid motion; the upper plane (denoted by S^+) slips by a constant Burgers vector $\mathbf{b}^*$ relative to the lower plane (denoted by S^-), and S^+ twists against S^- by a constant Frank vector $\boldsymbol{\Omega}^*$ at point $\boldsymbol{x}_0$ (see Fig. 11.3).

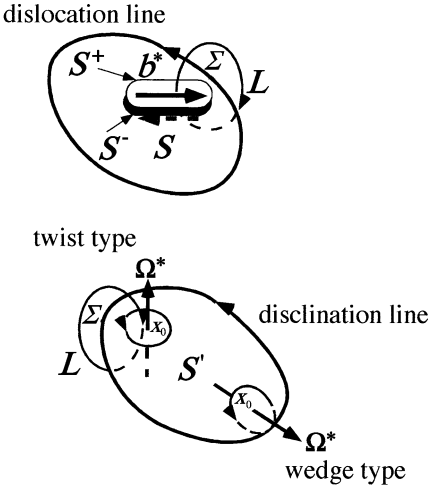

Fig. 11.3 Schematic figures of dislocation (upper) and disclination (lower). The dislocation line is defined as a part of the boundary of a slip plane S. The disclination line is created by twisting surface S'^+ against surface S'^- by rotation angle $\boldsymbol{\Omega}^*$ at point $\mathbf{x}_0$. L is a Burgers circuit. When vector $\boldsymbol{\Omega}^*$ is normal to S', the disclination is of a twist type, and it is of a wedge type when $\boldsymbol{\Omega}^*$ is on S'

We will derive expressions for the dislocation tensor α^{ij} and the disclination tensor θ^{ij} in the case of a constant Burgers vector **b** and a constant Frank vector **Ω**. Since the discrepancy Δu_j and the change $\Delta \bar{\nu}_k$ of a vector $\bar{\nu}_k$ are related to the Burgers vector b_j and the Frank vector Ω^i by

$$\Delta u_j = b_j + \left[\mathbf{\Omega} \times \left(\mathbf{x} - \mathbf{x}_0\right)\right]_j , \tag{11.101}$$

$$\Delta \bar{\nu}_k = \left(\mathbf{\Omega} \times \bar{\mathbf{\nu}}\right)_k = \varepsilon_{ijk} \mathbf{\Omega}^i \bar{\nu}^j , \tag{11.102}$$

by comparing these with Eqs. (11.99) and (11.100), we have formulae relating α^{ij} and θ^{ij} to b_j and Ω^j:

$$\Delta \bar{\nu}_k = \varepsilon_{jlk} \mathbf{\Omega}^j \bar{\nu}^l = \bar{\nu}^l \varepsilon_{jlk} \int_\Sigma \theta^{ij} \mathrm{d}\Sigma_i ; \tag{11.103}$$

therefore

$$\mathbf{\Omega}^j = \int_\Sigma \theta^{ij} \mathrm{d}\Sigma_i , \tag{11.104}$$

and

$$\begin{aligned} b_j = \Delta u_j - \left[\mathbf{\Omega} \times \left(\mathbf{x} - \mathbf{x}_0\right)\right]_j &= \int_\Sigma \alpha_j^i \mathrm{d}\Sigma_i - \varepsilon_{jmn} \int_\Sigma \theta^{im} \left(x^n - x_0^n\right) \mathrm{d}\Sigma_i \\ &= \int_\Sigma \left[\alpha_j^i - \varepsilon_{jpq} \theta^{ip} \left(x^q - x_0^q\right)\right] \mathrm{d}\Sigma_i . \end{aligned} \tag{11.105}$$

Introducing ϕ_p^{*l} and β_{ij}^* satisfying

$$\alpha_j^i = -\varepsilon^{ipq} \left(\partial_p \beta_{qj}^* + \varepsilon_{qjn} \phi_p^{*n}\right), \tag{11.106}$$

$$\theta^{ij} = -\varepsilon^{ipq} \partial_p \phi_q^{*j} , \tag{11.107}$$

and defining $\pi_{pqn}^* = \varepsilon_{qnl} \phi_p^{*l}$, we have

$$\Omega^j = -\oint_L \phi_i^{*j} \mathrm{d}L^i , \tag{11.108}$$

$$b_j = -\oint_L \left[\beta_{ij}^* - \varepsilon_{jpq} \phi_i^{*p} \left(x^q - x_0^q\right)\right] \mathrm{d}L^i , \tag{11.109}$$

where we have used Stoke's theorem.

We see, the integrand of the first term on the right-hand side of (11.95) reads

$$I_{mn} = \frac{1}{2}\left(\pi^*_{0mn} + \partial_0 \beta^*_{mn} - \partial_m \nu_n\right), \tag{11.110}$$

where

$$\phi^{*j}_i = -\delta_i(S)\Omega^{*j}, \tag{11.111}$$

$$\beta^*_{ij} = -\delta_i(S)\left\{b^*_j + \varepsilon_{jpq}\Omega^{*p}\left(x^q - x^q_0\right)\right\}, \tag{11.112}$$

$$\pi^*_{0kl} = \varepsilon_{klq}\phi^{*q}_0 = -\varepsilon_{klq}\partial_0\left\{\Omega^{*q}\delta(S)\right\}. \tag{11.113}$$

Here $\delta_i(S)$ is defined by

$$\delta_i(S) = \int_S \delta(x-\xi) n_i \, \mathrm{d}S(\xi) = \int_S \delta(x-\xi)\mathrm{d}S_i. \tag{11.114}$$

It is straightforward to check that Eqs. (11.111) and (11.112) satisfy (11.108) and (11.109) if we note that

$$\int_S \delta^i(L)\mathrm{d}S_i = \int_L \delta_i(S)\mathrm{d}L^i = \begin{cases} 1 & \text{if } L \text{ crosses } S \text{ positively,} \\ 0 & \text{if } L \text{ does not cross } S, \\ -1 & \text{if } L \text{ crosses } S \text{ negatively,} \end{cases} \tag{11.115}$$

because the curve L crosses the surface S once as shown in Fig. 11.3. Here $\delta^i(L)$ is defined by

$$\delta^i(L) = \int_L \delta(x-\xi) t_i \, \mathrm{d}L(\xi) = \int_L \delta(x-\xi)\mathrm{d}L^i. \tag{11.116}$$

During the last decade, waveform inversion of strong motion and teleseismic data excited by earthquakes have been used to determine the spatial and temporal variations of slip on the fault plane (e.g. Hartzell and Heaton 1983, Kikuchi and Fukao 1987, Takeo 1988), clarifying that the slip distribution on the fault plane of large earthquakes is generally very complex. The spatial resolution of the slip distribution obtained in these inversions is more than a few kilometers at best; the resolution depends on the minimum wavelength of the seismic waves employed in the inversion. Now, we assume that the Burgers vector is constant in the region S whose length-scale is shorter than 10^3 m, because we have no information about slip distributions in source areas smaller than several square kilometers. The order of $\mathbf{\Omega}^*$ is not clear because the value related to an earthquake has not been obtained until now. One possible rotational deformation during an

earthquake is a tensile fracture at an end of the fault plane, as illustrated in Fig. 11.4. Let us assume that the order of $\mathbf{\Omega}^*(O(\mathbf{\Omega}^*))$ is 10^{-2} radian ($\approx 1^o$) and the area (S') concerning this phenomenon is an order of magnitude less than the area of the fault plane (S), i.e., $S' \approx S \times 0.1$. The spatial variation of slip velocity (v_l) also has a large uncertainty due to the lack of observations. It seems, however, reasonable to assume that the spatial scale of variation is not shorter than the scale of S. Taking appropriate values for other parameters: $O(b_j^*) \approx 1\,\mathrm{m}$, $O(v_l) \approx 1\,\mathrm{m \cdot s^{-1}}$ and O (Eq. 11.114) $\approx 1\,\mathrm{km^{-1}}$, we get $O(\pi_{0mn}^*) \approx 10^{-3}$, $O(\partial_0 \beta_{mn}^*) \approx 10^{-3}$ and $O(\partial_m v_n) \approx 10^{-3}$ This result shows that π_{0mn}^*, $\partial_m v_n$ and $\partial_0 \beta_{mn}^*$ have similar orders of magnitude, and it is possible to estimate π_{0mn}^* and $\partial_m v_n$, i.e., γ_{0mn}^* and $\partial_m v_n$ using the translational and rotational motions of seismic waves simultaneously.

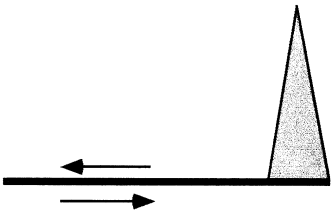

Fig. 11.4 Schematic image of a tensile fracture at edges of a fault plane

The resolution of the new angular sensor (Morris 1971, Nigbor 1994) is limited by internal sensor noise of about 3×10^{-4} rad/s, the value obtained in a field observation on the Izu peninsula, Japan. In order to estimate the magnitude of an earthquake whose rotational ground motion can be observed by the angular sensor, we calculate the rotational and translational velocities excited by an earthquake with a seismic moment of 10^{18} N·m buried 5 km deep. The focal mechanism is a vertical strike-slip fault: only dislocation is taken into account in this case. The reflection-transmission

Table 11.1 Velocity structures used in the simulation of rotational and translational ground motions

V_P [km/s]	V_S [km/s]	ρ [kg/m^3]	Depth [km]	Q_P	Q_S
2.80	1.30	2.30×10^3	0.00	200	100
5.60	2.90	2.50×10^3	2.70	400	200
6.00	3.40	2.60×10^3	6.10	500	230
6.80	4.00	3.00×10^3	19.00	600	270

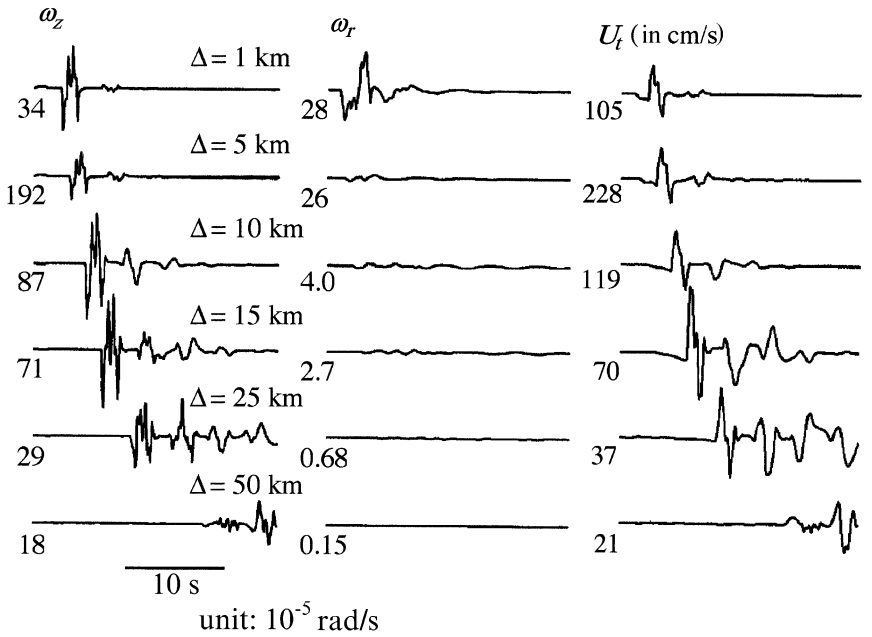

Fig. 11.5 Synthetic ground velocities of rotational and translational components at six stations of different hypocentral distances, Δ. The number attached to each trace is the peak-to-peak amplitude of each of ground velocities. ω_z, ω_r and u_t denote a rotational velocity around the vertical axis, the one around the radial axis, and a translational velocity of transverse direction, respectively

matrices (Kennett and Kerry 1979) and the discrete wavenumber method (Bouchon 1981) are used in the calculation of ground motion, assuming the anelastic layered half-space structure listed in Table 11.1. Figure 11.5 represents the rotational and translational ground velocities at stations that are in line along the strike direction of the fault plane. The rotational velocity around the vertical axis (ω_z) has a maximum value of 2×10^{-3} rad/s at the hypocentral distance of 5 km. This simulation shows that this angular sensor will be able to record rotational motion excited by an earthquake of moment magnitude 6 (seismic moment: 10^{18} N·m) up to a hypocentral distance of 25 km.

11.5 Conclusions

We extend the dislocation model of earthquakes to cover phenomena generated by rotational motions in the source area. The extended model includes defects, dislocations and disclinations, which are shown to be com-

pletely characterized by geometrical quantities, a torsion tensor and a curvature tensor. We derive a set of continuity equations among densities of dislocation and disclination and their currents.

Employing the continuity equations, we derive a simple expression for the rotational velocity of seismic waves. Combining the rotational motions of seismic waves with the translational motions, we can estimate the tensors γ^{*}_{0mn} and $\partial_m v_n$, i.e., the rotational strain tensor and the spatial variation of slip velocity. These quantities will be large at the edges of a fault plane due to spatially rapid changes in slip on the fault and/or a formation of tensile fractures. We estimate from a simulation that the angular sensor now available will detect the rotational motions from earthquakes with magnitude 6 or larger if the hypocentral distance is shorter than 25 km.

Acknowledgments. This research was partially supported by Grant-in -Aid for Scientific Research (B), the Ministry of Education, Science, Sports and Culture, Japan.

References

Aki K, Richards PG (1980) Quantitative seismology: theory and methods. Freeman WH and Co, San Francisco CA.

Amari S (1962) On some primary structures of non-Riemannian plasticity theory. Memoirs of the Unifying Study of the Basic Problems in Engineering Sciences by Means of Geometry **3** D: 163-172

Amari S (1968) A geometrical theory of moving dislocations and anelasticity. Memoirs of the Unifying Study of the Basic Problems in Engineering Sciences by Means of Geometry **4** D: 284-295

Amari S (1981) Dualistic theory of non-Riemannian material manifolds. Int J Engng Sci **19**: 1581-1594

Bilby BA, Bullough R, Smith E (1955) Continuous distribution of dislocations: A new application of the method of non-Riemannian geometry. Proc Roy Soc London **A231**: 263-273

Bouchon M (1981) A simple method to calculate Green's functions for elastic layered media. Bull Seism Soc Am **71**: 959-971

Bouchon M, Aki K (1982) Strain, tilt, and rotation associated with strong ground motion in the vicinity of earthquake faults. Bull Seism Soc Am **72**: 1717-1738

deWit R (1973) Theory of disclinations: II. Continuous and discrete disclinations in anisotropic elasticity. J Res Nat. Bureau Standards **77A**: 49-100

Eshelby JD (1957) The determination of the elastic field of an ellipsoidal inclusion and related problems. Proc Roy Soc London **A241**: 376-396

Hartzell SH, Heaton TH (1983) Inversion of strong ground motion and teleseismic waveform data for the fault rupture history of the 1979 Imperial Valley, California, earthquake. Bull Seism Soc Am **73**: 1553-1583

Kennett LN, Kerry NJ (1979) Seismic waves in a stratified half-space. Geophys J Roy astron Soc **57**: 557-583

Kikuchi M, Fukao Y (1987) Inversion of long-period P-waves from great earthquakes along subduction zones. Tectonophysics **144**: 231-247

Kondo K (1949a) A proposal of a new theory concerning the yielding of materials based on Riemannian geometry, I. J Jpn Soc Appl Mech **2**: 123-128

Kondo K (1949b) A proposal of a new theory concerning the yielding of materials based on Riemannian geometry, II. J Jpn Soc Appl Mech **2**: 146-151.

Kondo K (1953) On the geometrical and physical foundations of the theory of yielding. Proc 2nd Jpn Nat Congr Appl Mech: 41-47

Kondo K (1955) Non-holonomic geometry of plasticity and yielding. Memoirs of the Unifying Study of the Basic Problems in Engineering Sciences by Means of Geometry **1** D: 453-572

Kondo K (1957) Geometry of deformation. Appl Math, B7-b, Iwanami Co, Tokyo

Kossecka E, deWit R (1977a) Disclination kinematics. Archives Mech **29**: 633-651

Kossecka E, deWit R (1977b) Disclination dynamics. Archives Mech **29**: 749-767

Kröner E (1958) Kontinuumstheorie der Versetzungen und Eigenspannungen. Springer-Verlag, Berlin-Göttingen-Feidelberg

Minagawa S (1983) Continuum mechanics for an imperfect crystal. Zairyo Kagaku **20**: 54-59

Mogi K (1978) Dilatancy of rocks under general triaxial stress states with special reference to earthquake precursors. J Phys Earth **25**: Suppl S 203-S 217

Morris HD (1971) Angular acceleration measurements for geokinetic stability. AIAA Guidance, control and fright mechanics conference, Hofstra University, Hempstead, NW: No. 71-909

Mura T (1963) Continuous distribution of moving dislocations. Phil Mag **8**: 843-857

Mura T (1972) Semi-microscopic plastic distortion and disclinations. Arch Mech Stos **24**: 449-456

Mura T (1982) Micromechanics of defects in solids. Kluwer Academic Pub Co, Dordrecht, Netherlands

Nigbor RL (1994) Six-degree-of-freedom ground-motion measurement. Bull Seism Soc Am **84**: 1665-1669

Schouten JA (1954) Ricci-Calculus, 2nd. Springer Verlag, Berlin Göttingen Heidelberg

Shiozawa K (1980) Theory of distributed dislocations in continuum. In: Oominami M (ed) Micromechanics of solids, Orm Co, Tokyo, Japan

Takeo M (1988) Rupture process of the 1980 Izu-Hanto-Toho-Oki earthquake deduced from strong motion seismograms. Bull Seism Soc Am **78**: 1074-1091

Teisseyre R (1973) Earthquake processes in a micromorphic continuum. Pure Appl Geophys **102**: 15-28

Yamaguchi R, Odaka T (1974) Field study of the Izu-Hanto-oki earthquake of 1974. Special Bull Earthq Res Inst, Univ Tokyo **14**: 241-255

12 Ground Rotational Motions Recorded in Near-Source Region of Earthquakes

Minoru Takeo

Earthquake Research Institute, University of Tokyo
Zip. 113-0032 1-1-1, Yayoi, Bunkyo-ku, Tokyo, Japan
e-mail: takeo@eri.u-tokyo.ac.jp

12.1 Introduction

Only translational ground motions have been observed in instrumental measurements of seismic waves, and quantitative measurements of rotational ground motions have not been made until quite recently. Nigbor (1994) succeeded in measuring rotational and translational motions using a new angular measuring sensor (Morris 1971) at a surface station during a non-proliferation experiment at the Nevada Test Site. Spudich et al. (1995) also estimated a rotational ground motion excited by the 1992 Landers earthquake (M = 7.4) at the UPSAR seismograph array about 400 km northwest of the epicenter. Stedman et al. (1995) observed a rotational ground motion around the vertical axis using a Ring Laser Gyro. This motion was excited by an earthquake of magnitude 6.3 at Kelburn, Wellington, New Zealand, whose epicentral distance is more than 200 km. Nobody has, however, succeeded in recording a strong ground rotational motion in the near-source region of earthquakes until now.

Bouchon and Aki (1982) simulated rotational ground motions near earthquake faults buried in layered media for strike-slip and dip-slip fault models, and obtained a maximum rotational velocity of 1.5×10^{-3} rad/s produced by a buried 30 km long strike-slip fault with slip of 1 m. On the other hand, employing the geometrical theory of defects, Takeo and Ito (1997) obtained a general expression for rotational motions of seismic waves as a function of parameters of source defects. They made it clear that a rotational strain tensor and a spatial variation of slip velocity can be estimated combining the rotational motions with the translational motions. These quantities will be large at edges of a fault plane due to spatially rapid changes in slip on a fault plane (Takeo and Ito 1997). Therefore,

near-source rotational motions produce much detailed information on rupture processes of earthquakes.

During an earthquake swarm at offshore region of Ito in Izu peninsula, Japan, we succeeded in recording rotational ground motions in the near-source region of earthquakes. The purpose of this paper is to report the characteristics of the rotational ground motions excited by the earthquakes.

12.2 Observational System

The observational system consists of a triaxial translational sensor, a triaxial rotational sensor, and a six-channel digital recorder. The translational and rotational motions are measured by a Kinemetrics FBA-23 triaxial accelerograph, and by a Systron Donner MotionPak triaxial gyro sensor, respectively. These sensors are similar to those of the recording system designed by Nigbor (1994). Full-scale outputs of the translational sensor and the rotational sensor are ±1 G and $\pm 8.73 \times 10^{-1}$ rad/s, respectively. The translational sensor has flat frequency response to translational acceleration from DC to 50 Hz. The rotational sensor has flat frequency response to rotational velocities around three axes perpendicularly intersecting each other from DC to 75 Hz.

The digital data logger is a REF TEK 72A-08 DAS which has a three-channel, 24-bit resolution digitizer and a three-channel, 16-bit resolution digitizer. The signals from the rotational sensor are digitized by the 16-bit resolution digitizer, and those from the accelerograph are digitized by the 24-bit resolution digitizer. The sampling rate of this logger is 20 samples/s under a continuous recording mode. This observational system has been installed at Cape Kawana (KAW), about 4.5 km southeast of Ito, and near Cape Shiofuki (SOF), about 2.5 km east of Ito, since October 1996.

12.3 Near-Source Ground Rotational Motions

The earthquake swarm started on 2 March, 1997, and lasted for 24 days: the source area lay about 3 km east of Cape Kawana extending for about 5 km in the east-west direction. Figure 12.1 shows epicenters of earthquakes with magnitudes larger than 3.5 that occurred from 2 March 15:00 to 7 March 15:00. During this swarm, 13 events excited large rotational ground motions exceeding the internal noise level of the rotational sensor at KAW. The observational system operated at SOF had a trouble and could not record ground motions.

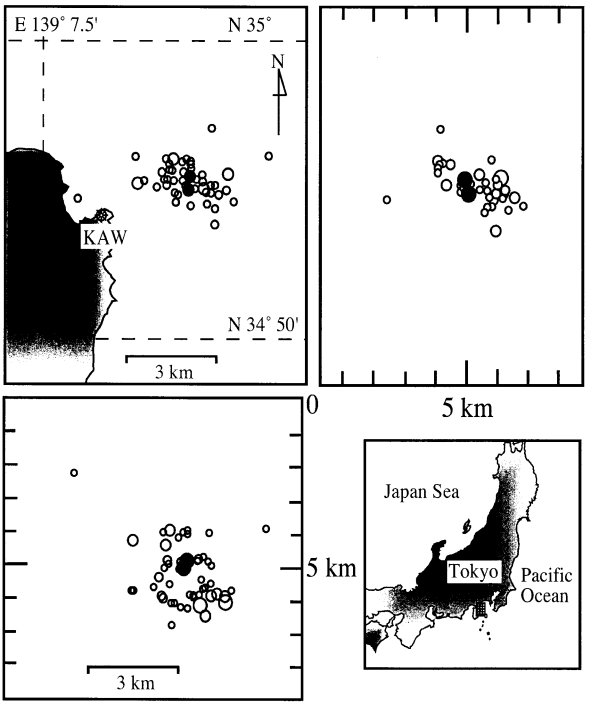

Fig. 12.1 Epicenters of earthquake swarm from 2 March 15:00 to 7 March 15:00 at offshore Ito in Izu peninsula, Japan. The earthquakes with magnitudes larger than 3.5 are shown. The hatched area in the bottom panel on the right-hand side represents the offshore Ito. KAW is a station where an observational system for rotational and translational motions is installed. The closed circles represent the epicenters of the largest and the second largest events of the earthquake swarm.

The largest earthquake with a magnitude of 5.7 occurred at 3:51 GMT on 4 March. Figure 12.2 shows the triaxial translational velocities and the triaxial rotational velocities excited by the largest event and the second largest event which occurred at 14:09 GMT on 3 March, whose epicenters are shown in Fig. 12.1. These translational velocities are obtained by numerically integrating the accelerograms. The largest amplitude of rotational velocity observed at KAW during this swarm is 2.6×10^{-2} rad/s around the east-west axis, i.e. tilt in the north-south direction, which was excited by the second largest event. The maximum rotational velocity excited by the largest event is 5.9×10^{-3} rad/s around the north-south axis, i.e. tilt in the east-west direction. The peak to peak amplitude of acceleration at KAW during the largest event is 3 m/s^2, whereas that of the second largest event is 8 m/s^2. These large rotational velocities are accompanied by the large accelerations. The G sensitivity of the sensor (sensitivity to transla-

tional acceleration) provided by the manufacturer is less than 3.5×10^{-4} rad/s/G, so that the errors in the rotational velocities due to large translational motions are less than 1.1×10^{-4} rad/s for the largest event, and 2.9×10^{-4} rad/s for the second largest event. These errors are about two orders in magnitude smaller than the signals in both cases.

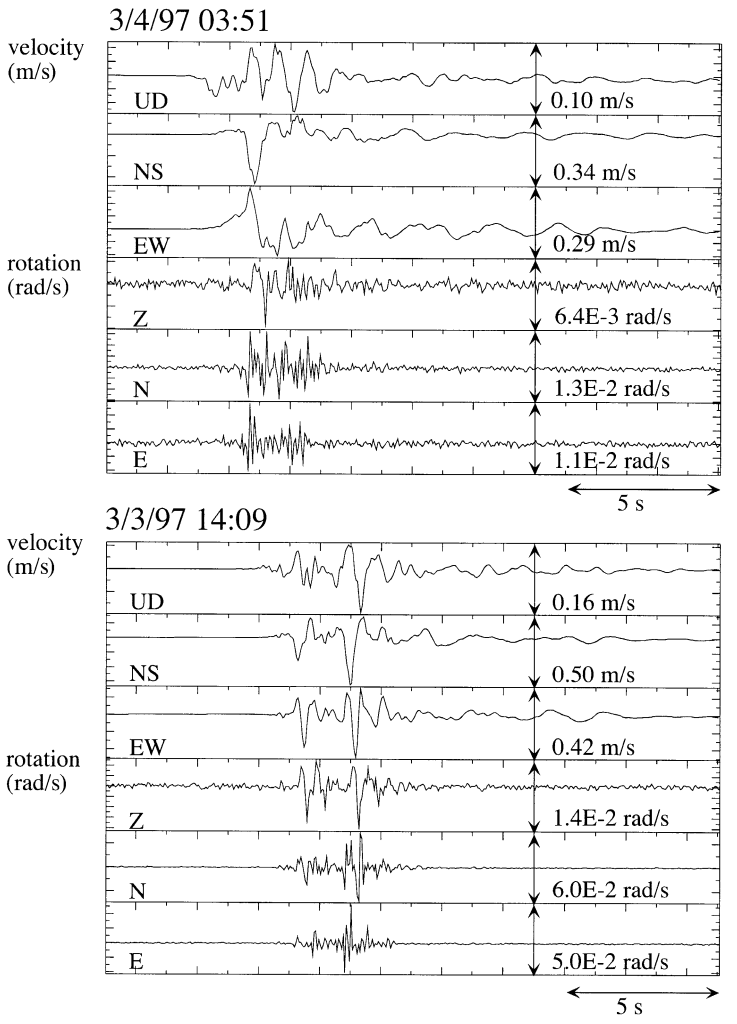

Fig. 12.2 Triaxial translational velocities and triaxial rotational velocities excited by the largest event (upper panel) and the second largest event (lower panel), respectively. The epicenters are represented by closed circles in Fig. 12.1

The rotational velocities around the horizontal axes seem to be dominated by relatively higher frequency than those around the vertical axis. The Nyquist frequency of the recording system is 10 Hz. The frequency dominating the rotational velocities around the horizontal axes, i.e. tilts, is only a little lower than the Nyquist frequency of the recording system, so that quantitative evaluation of the tilts is very difficult. Therefore, we focus on the rotational motion around the vertical axis and present a preliminary analysis concerning the source process of the largest event in the next section.

12.4 Discussion

The seismic moment of the strike-slip fault model used in Bouchon and Aki (1982) was about $8\text{x}10^{18}$ N·m, and the rotational velocity around the vertical axis of $1.5\text{x}10^{-3}$ rad/s was produced at a station 1 km away from the fault. The seismic moments of the largest and the second largest events of the swarm are $1.2\text{x}10^{17}$ N·m and $2.7\text{x}10^{16}$ N·m (Hayashi, personal communication, 1997). These values are two orders in magnitude smaller than that of the simulation model employed by Bouchon and Aki (1982). The maximum rotational velocities around the vertical axis at KAW are, however, about $3.3\text{x}10^{-3}$ rad/s for the largest event and about $8.1\text{x}10^{-3}$ rad/s for the second largest event. KAW lies about 3.3 km away from the both epicenters. The observed rotational velocities are several times larger than the simulation result, in spite of these smaller seismic moments and greater epicentral distances.

What caused the large discrepancy between the observation and the simulation? During the last decade, waveform inversion analyses have clarified that the slip distribution on the fault plane of large earthquakes is generally complex (e.g. Hartzell and Heaton 1983, Kikuchi and Fukao 1987). One possible answer is that the large rotational velocities are caused by heterogeneity of slip velocity on the fault.

Takeo and Ito (1997) derived a general expression for rotational velocities of seismic waves as a function of the geometrical quantities: torsion tensor and curvature tensor. Neglecting the term which dominates only in the high-frequency range, we get a simple expression as follows:

$$\partial_0 \omega^q(\mathbf{x},t) \approx -\int_{-\infty}^{\infty} \mathrm{d}\tau \int \varepsilon^{qmn} C^{ijkl} \partial_m \partial_j G_{ni}(\mathbf{x},t-\tau;\xi,0)\, I_{kl}(\xi,\tau)\, \mathrm{d}V(\xi)\,. \qquad (12.1)$$

The velocity of translational motion is written as

$$\partial_0 u_q(\mathbf{x},t) = -\int_{-\infty}^{\infty} \mathrm{d}\tau \int C^{ijkl}\partial_j G_{qi}(\mathbf{x},t-\tau;\xi,0)\partial_{0'} e^*_{kl}(\xi,\tau)\,\mathrm{d}V(\xi)\,, \qquad (12.2)$$

where C^{ijkl}, I_{kl}, e^*_{kl} and ε^{qmn} are the tensor of elastic constants, the current tensor of defect, the plastic strain, and Eddington's epsilon, respectively. Green's function G_{ni} (x, t–τ; ξ, 0) satisfies the equation of motion

$$\rho\partial_0\partial_0 G^i_n = C^{ijkl}\partial_j\partial_k G_{ln} + \delta^i_n\delta(\mathbf{x}-\xi)\delta(t-\tau)\,, \qquad (12.3)$$

where δ^i_n and $\delta(\mathbf{x}-\xi)$ or $\delta(t-\tau)$ denote Kronecker's delta and delta functions, respectively. I_{kl} is simply given by

$$I_{kl} = \frac{1}{2}(\gamma^*_{0kl} + \partial_{0'} e^*_{kl} - \partial_{k'} v_l)\,, \qquad (12.4)$$

where $\partial/\partial\tau \equiv \partial_{0'}$ and $\partial/\partial\xi_m \equiv \partial_{\mathrm{m}'}\cdot\ \gamma^*_{0kl}$, and v_l are the plastic part of a rotational strain tensor and the slip velocity, respectively. For further details of these tensors, the reader should refer to Takeo and Ito (1997). These equations show that not only the plastic strain but also the rotational strain and the spatial variation of slip velocity at earthquake sources directly generate rotational components in seismic waves. On the other hand, translational motions in seismic waves are only excited by the plastic strain as shown in Eq. (12.2), which can be transformed into a dislocation in case of a simple fault model (Takeo and Ito 1997). Bouchon and Aki (1982) took into account only rotational motions excited by dislocations on the fault plane, and did not evaluate the direct excitation of rotational motions due to a spatial variation of slip velocity and due to rotational strains. The contribution of a spatial variation of slip velocity is another possible answer to the question posed in the head of the previous paragraph.

Since the radiation patterns of seismic waves due to the second and the third terms on the right-hand side of Eq. (12.4) are different from each other, we can estimate how to change slip velocities spatially even in case of a point source approximation using rotational and translational motions at several stations around the source area. In the present case, however, we cannot estimate the spatial variation uniquely, because the rotational motions were recorded at KAW only. Therefore, we apply a simple point source model to evaluate the rotational velocity around the vertical axis during the largest event. The distribution of epicenters just after the largest event suggests that the nodal plane of the focal mechanism striking in the direction of N154°E is the fault plane of the largest event (see Fig. 12.3). First, we calculate the rotational velocity around the vertical axis at KAW using the focal mechanism shown in Fig. 12.3 with the seismic moment

of 1.2×10^{17} N·m. The seismic-moment-rate function is assumed to be an isogonal trapezoid as shown in Fig. 12.4. We assume that t_1 and t_2 are 0.2 s and 0.8 s, respectively; these values are obtained by trial and error fitting of the pulse width of the strong motion records. The reflection-transmission matrices (Kennett and Kerry 1979) and the discrete method (Bouchon 1981) are used in the calculation of ground motion, assuming the anelastic layered half-space structure listed in Table 12.1.

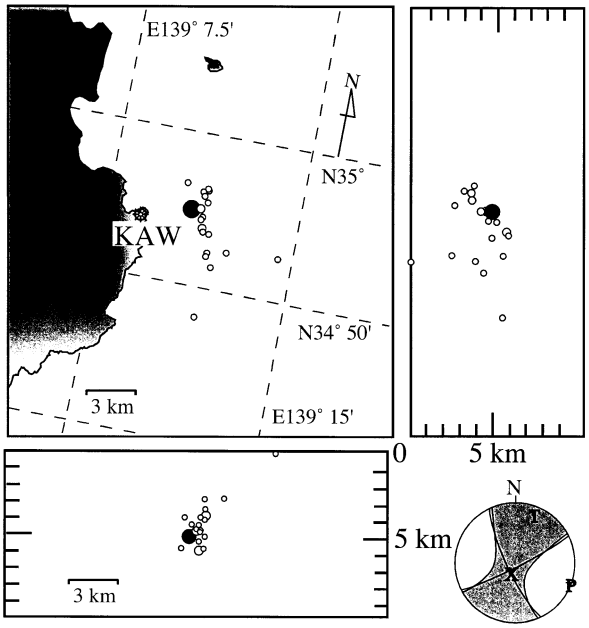

Fig. 12.3 Seismicity just after the largest event and the focal mechanism of the largest event obtained using near-field strong motion records (Hayashi, personal communication, 1997). The focal mechanism is plotted on the lower hemisphere. The epicenters with magnitudes larger than 2.5 which occurred on 4 March from 3:51 to 4:59 are shown

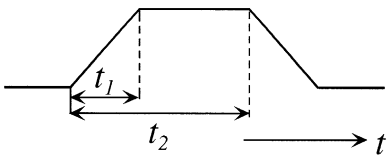

Fig. 12.4 The source-time function of PS1 used in the waveform calculation. The time constants t_1 and t_2 approximately correspond to the rise time of dislocation and the time for the rupture front to propagate through the fault, respectively

Table 12.1 Velocity structure used in the calculation

V_P [km/s]	V_S [km/s]	ρ [g/cm^3]	h [km]	Q_P	Q_S
1.95	0.23	2.00	0.00	50	30
2.05	0.48	2.00	0.04	50	30
2.15	0.73	2.00	0.08	50	30
2.25	0.98	2.00	0.12	50	30
2.60	1.30	2.00	0.16	100	50
4.20	2.20	2.30	0.36	300	200
5.30	3.10	2.50	1.86	500	300
6.00	3.46	2.70	4.30	1000	500
6.80	3.93	3.00	15.0	1000	500
7.80	4.50	3.20	30.0	2000	1000

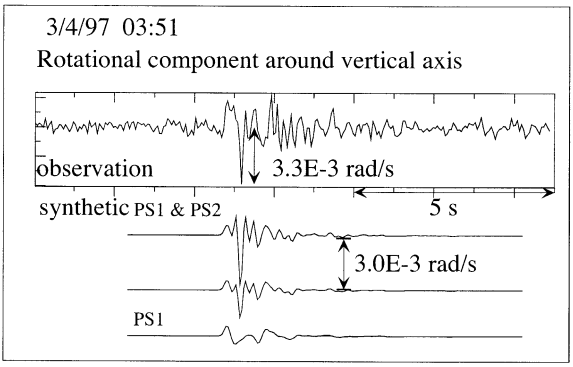

Fig. 12.5 Comparison of observed rotational velocity around the vertical axis at KAW with synthetics calculated for a simple model composed by two point sources. An upper trace of the synthetics is the rotational velocity considering the full contribution of PS1 and PS2. A second trace represents the rotational velocity which takes into account PS1 and only the contribution of the spatial variation of slip velocity in PS2. The bottom trace is the rotational velocity excited by PS1. In this calculation, we consider that PS2 lies at the southeastern edge, but the synthetic for PS2 is calculated for the same epicentral distance with PS1. However, the synthetic for PS2 using the epicentral distance 1 km longer than that of PS1 differs little from the previous one

The bottom trace in Fig. 12.5 is the rotational velocity excited by this point source. The peak amplitude of the synthetic is about one seventh of the

observation. The first half cycle of the synthetics has a similar waveform with the observation, but the waveform in the later part is quite different from the observation, which has a large spiky pulse.

We employ another point source which represents a spatial variation of slip velocity in a small region. Hereafter, we denote the former point source by PS1, and the latter by PS2. The first term on the right-hand side of Eq. (12.4) will vanish when we assume a flat fault plane in a homogeneous medium (Takeo and Ito 1997). Then, we consider the excitation of rotational motion due to the second term ($\partial_0 e^*_{kl}$) and the third term ($\partial_k v_l$) of Eq. (12.4) in PS2. The largest event is dominated by the left-lateral strike-slip motion with the strike direction of N154°E. Here, we assume a simple case of the spatial variation of slip such that the left-lateral strike-slip velocity decreases rapidly as we go to the edge of the fault. The duration of the spiky pulse appeared in the observation is about 0.1 s. The isosceles triangle with a base length of 0.1 s is employed as a source-time function of PS2. This duration of the source time corresponds to the spatial extent of about a hundred meters along the rupture direction assuming the rupture velocity of 3 km/s. We assume that the magnitude of the third term, $\mu \int \partial_k v_l \, dV$ (μ is the rigidity), is $1\text{x}10^{16}$ N·m/s, and that the source material satisfies the Poisson relation ($\lambda = \mu$). Then, the third term along the strike direction of N154ºE can be transformed to the components of the source-tensor as follows:

$$\begin{pmatrix} 2.62 & 0.79 & 0.0 \\ 0.79 & 1.38 & 0.0 \\ 0.0 & 0.0 & 1.0 \end{pmatrix} \cdot 1 \times 10^{16} \tag{12.5}$$

Based on this model, we calculate the rotational velocity around the vertical axis.

The second term on the right-hand side of Eq. (12.4) excites not only the rotational velocity through Eq. (12.1) but also the translational velocity through Eq. (12.2). For the second term, we use the same source-time function as that of the third term, and assume that the seismic moment of this limited region is $1\text{x}10^{16}$ N·m. Because this source time has short duration, the second term excites large spiky translational velocities of 0.5 m/s and 0.3 m/s on the NS and EW components of the translational velocity at KAW, respectively. The observed translational velocities, however, do not have such large amplitudes. Therefore, $1\text{x}10^{16}$ N·m is the supremum of the seismic moment concerned with the second term of Eq. (12.4) in PS2.

Changing the time lag between PS1 and PS2, we calculate the synthetic rotational velocity and compare it with the observation. When the time lag

is 0.3 s, we get a best fit between the synthetics and observation, as shown in Fig. 12.5. The second trace of the synthetics in Fig. 12.5 represents the rotational velocity which takes into account PS1 and only the contribution of the spatial variation of slip velocity in PS2 which lies at the southeastern edge of the fault. The spatial variation of slip velocity along the fault at the northwestern edge has the opposite sign to that at the southeastern edge. Then, the spiky pulse of the rotational velocity shown in the second trace has the reverse sign when PS2 lies at the northwestern edge. The upper trace of the synthetics in Fig. 12.5 is the rotational velocity considering the full contribution of PS1 and PS2 in the case when PS2 lies at the southeastern edge. The synthetic reproduces the observation well. When PS2 lies at the northwestern edge, the spiky pulses excited by the second term and by the spatial variation of slip velocity will cancel each other. If the spatial variation of slip velocity is small and the large pulse is excited only by the second term of Eq. (12.4), PS2 must have the seismic moment of 2×10^{16} N·m. However, this source also excites the translational velocity with amplitude larger than 1 m/s which was not observed. Therefore, the large spatial change of slip velocity should occur rapidly during the rupture process of the largest event. The time lag of 0.3 s corresponds to the spatial separation of about 1 km between PS1 and PS2 assuming the rupture velocity of 3 km/s. Then, we can estimate that PS2 lies about 1 km southeast of PS1 or the hypocenter; in other words, the fault slip stopped rapidly about 1 km southeast of the hypocenter.

In the region of the eastern coast of Izu peninsula, many young and small submarine volcanoes are identified (Hamuro et al. 1980), and a submarine eruption occurred on 13 July 1989, during an earthquake swarm at the eastern offshore Ito which started on 30 June 1989. A shallow reflection survey in this region reveals that there are several old dyke formations whose P wave velocity is higher than that of the surrounding media (Kasahara et al. 1991). These old dyke formations are one of the candidates of barriers which make the slip stop rapidly. A similar rupture process was inferred for the largest earthquake of the 1989 earthquake swarm at the eastern offshore Ito (Takeo 1992). Of course, this simple model is not a unique one to explain the large rotational velocity observed at KAW, but is a candidate for the rupture model of the largest event.

Acknowledgments. The author expresses his gratitude to S. Ide, W. Nakayama, I. Nishidomi, K. Imanishi, N. Hayashi, H. Aoyama, and I. Ogino who kindly supported the observation. I acknowledge the careful reviews by two anonymous reviewers, all of whom provided useful criticisms and suggestions. This research was partially supported by Grant-in-Aid for

Scientific Research (B), the Ministry of Education, Science, Sports and Culture, Japan.

References

Bouchon M (1981) A simple method to calculate Green's functions for elastic layered media. Bull Seism Soc Am **71**: 959-971

Bouchon M, Aki K (1982) Strain, tilt, and rotation associated with strong ground motion in the vicinity of earthquake faults. Bull Seism Soc Am **72**: 1717-1738

Hamuro K, Aramaki S, Kagami H, Fujioka K (1980) The Higashi-Izu-oki submarine volcanoes, Part 1. Bull Earthq Res Inst Tokyo Univ **55**: 259-297 (in Japanese)

Hartzell SH, Heaton TH (1983) Inversion of strong ground motion and teleseismic waveform data for the fault rupture history of the 1979 Imperial Valley, California, earthquake. Bull Seism Soc Am **73**: 1553-1583

Kasahara K, Yamamizu F, Ikawa T, Kuroda T, Takahashi A (1991) Reflection profiles of active volcanic region, the east coast of Izu peninsula. Earth Monthly **13**: 145-153 (in Japanese)

Kennett L N, Kerry NJ (1979) Seismic waves in a stratified half-space. Geophys J R astr Soc **57**: 557-583

Kikuchi M, Fukao Y (1987) Inversion of long-period P waves from great earthquakes along subduction zones. Tectonophysics **144**: 231-247

Morris HD (1971) Angular acceleration measurements for geokinetic stability. Paper presented at AIAA Guidance, Control and Flight Mechanics Conference, Hofstra University, Hempstead NY, No. 71-909, Aug. 16-18, 1971.

Nigbor RL (1994) Six-degree-of-freedom ground-motion measurement. Bull Seism Soc Am **84**: 1665-1669

Spudich P, Steck LK, Hellweg M, Fletcher JB, Baker LM (1995) Transient stresses at Parkfield, California, produced by the *M* 7.4 Landers earthquake of June 28, 1992: Observations from the UPSAR dense seismograph array. J Geophys Res **100**: 675-690

Stedman GE, Li Z, Bilger HR (1995) Sideband analysis and seismic detection in a large ring laser. Applied Optics 34: 5375-5385

Takeo M (1992) The rupture process of the 1989 offshore Ito earthquakes preceding a submarine volcanic eruption. J Geophys Res **97**: 6613-6627

Takeo M, Ito HI (1997) What can be learned from rotational motions excited by earthquake? Geophys J Int **129**: 319-329

13 Fracture-Band Geometry and Rotation Energy Release

Roman Teisseyre, Marek Górski, Krzysztof P. Teisseyre

Institute of Geophysics, Polish Academy of Sciences
ul. Księcia Janusza 64, 01-452 Warszawa, Poland; e-mail: rt@igf.edu.pl

13.1 Introduction

In this chapter we recall some basic ideas of the Earthquake Dislocation Theory (Droste and Teisseyre 1959, Teisseyre 1961, 1964, 1970) and Fracture Band Model (Teisseyre 1996, 1997, Teisseyre and Wiejacz 1993, Teisseyre et al. 2001) in order to obtain a better insight into the problem of fracturing under different load conditions, including the earthquake premonitory and rebound phases. A counterpart of the rotation processes and rotation energy release explains fragmentation process and permits to estimate the efficiency of different fracturing modes.

13.2 Earthquake Dislocation Theory

We will start with recalling some elements of the elastic dislocation theory (e.g., Eshelby et al. 1951, Nabarro 1951, Kröner 1981):

– Dislocation notion in its physical meaning is related to disorder in a crystal lattice caused by a slip along a certain glide plane by a lattice spacing (lattice constant λ); as a result, the lattice disorders appear only at the edges of the glide, while along a glide the continuity is preserved. This notion differs essentially from a geological dislocation like fault.

– Dislocated area with a constant slip value (the Burgers vector) $\Delta u = \lambda$, along its surface, is bounded at its edges by the dislocation line, called in physics just a dislocation (only such a line represents a real physical object in a crystal lattice).

– The elastic energy is concentrated around a dislocation line and is a source of elastic deformation, decreasing with distance from the dislocation.

– Dislocations can have different signs (orientation of slip vector as related to the normal of the dislocated area); the dislocations of opposite signs attract each other (tendency to join the respective two dislocated areas), while dislocations of the same sign repel each other; a dislocated area is bounded at its opposite edges by the dislocations of opposite sign.

– An external stress field acts on a dislocation line; when this load overpasses a certain limit (stress resistance), the opposite dislocations move in the opposite directions (the Koehler force).

– Under an external load the dislocations having the same sign and situated on a common plane, may form a dislocation array; this happens when the dislocations moving in the same direction are, at the first leading dislocation, stopped by some barrier (obstacle), with a greater stress resistance.

– The dislocations grouped in an array form a concentration of stress field $S = n_A S_0$ (S_0 is the external stress load, n_A is the number of dislocations) and when the concentration of stresses is very high, such an array well approximates a dislocation with the slip $n_A \lambda$.

– The stress field of an array, with a sufficiently great number of dislocations entering it, exactly approximates the field of a crack tip.

– At the other side of the obstacle, the travelling array can meet the opposite array; the external forces and additionally the attraction of the opposite arrays may break the barrier and the strains of the two arrays will be mutually canceled, and their energies will be released; a related dynamic process becomes manifested by formation of a micro-crack.

Recall now the basic elements of the Earthquake Dislocation Theory (Droste and Teisseyre 1959, Teisseyre 1961, 1964, 1970):

– The early premonitory time-domain: formation of the dislocation arrays of different signs, interaction between the arrays, generation of the micro-cracks accompanied with the respective energy releases (transition from quasi-static to dynamic processes and from stress resistance to friction).

– The advanced premonitory time-domain: interaction between the tips of microcracks of opposite orientations (signs); mutual annihilation of the respective crack tips leading to expansion of the cracks, formation of bigger and bigger cracks; formation of fragments of slip fracturing (macrocracks, fragmentation); development of a rapid dynamic process along the planes with the slip fragments, in which the fragmented parts join together in a main fault (an earthquake); the possible aftershocks. These processes may develop along two perpendicular planes, but in reality, due to the fact that any geological space is extremely complex, one main fracture plane is

usually formed first, and an asymmetric geometry pattern of the resulting faults remains.

In this theory, an energy release is explained by the mutual annihilations of the strain energies of the opposite groups of defects: dislocation arrays, tips of microcracks, tips of cracks and those of fragments (macrocracks).

13.3 Earthquake Thermodynamics and Fracture Band Model

The basic elements of the fracture band model in a 2D simplification (Teisseyre 1996, 1997, Teisseyre et al. 2001):

– In an earthquake preparation zone, besides the basic lattice, we expect an existence of a super-lattice caused by the interactions between the densely distributed dislocations (a dislocation super-lattice can be associated with an internal structure, band of the old slip planes or the slip plane fragments).

– We assume that for the super-lattice constant Λ we can put $\Lambda \gg \lambda$.

– We expect that in earthquake preparation zone the super-lattice may be very irregular. In order to make it more coherent we define, at desired places, the vacant dislocations; a difference between the best fitted regular super-lattice and the real one defines a number of the vacant dislocations.

– The thermodynamics of a super-lattice (Teisseyre 2001) is based on the Gibbs formation energy $\hat{g}^f$ for a vacant dislocation and the related expression for an equilibrium number of vacant dislocations is

$$\hat{n}_{eq} = \frac{1}{\Lambda^3} \exp\left(-\frac{\hat{g}^f}{kT} \right).$$

– For a fracture model we assume for simplicity a disc model of an earthquake volume

$$\Delta V = \pi R^2 D . \tag{13.1}$$

– In the fracture band model, we assume that a band of slips is active both during the premonitory time-domain and during the fracture process; the respective motions appear as glide motions (dislocation slips) and as fracturing (fracture slip).

– We assume that a local shear stress before an earthquake can be estimated by the value of the related stress drop (Teisseyre 2001)

$$S = A \Delta S , \tag{13.2}$$

where we shall note that this assumption follows from the studies of series of earthquakes (see Teisseyre 1996, Teisseyre and Wiejacz 1993).

– The Burgers dislocation vector b (slip vector) is assumed to be given by the product of the number of dislocations in an array and the lattice constant

$$b = \Delta u = N\lambda ,$$

where the number of dislocations entering an array may be estimated to be proportional to the shear local field; hence, according to the former assumption we can put

$$N = B\Delta S \tag{13.3}$$

and we get

$$b = \Delta u = B\lambda \Delta S = \frac{B}{A}\lambda S .$$

– For a band of shear planes, an equivalent value shall be multiplied by ratio of a band width D and super-lattice constant Λ (Fig. 13.1):

$$b = \Delta u = B\lambda \Delta S\frac{D}{\Lambda} = \frac{B}{A}\lambda S\frac{D}{\Lambda}. \tag{13.4}$$

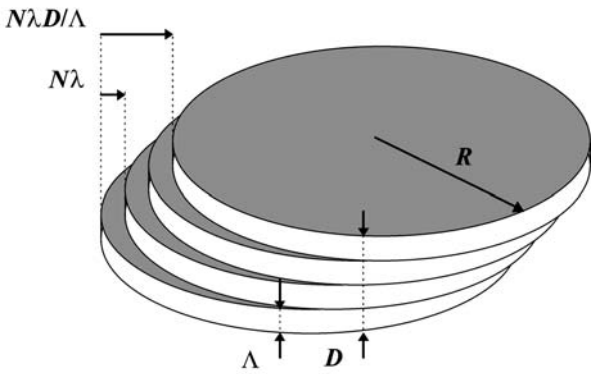

Fig. 13.1 Shear band model

– Finally, for a seismic scalar moment we obtain the expression

$$M^0 = \mu b\Delta s = \mu B\frac{\lambda}{\Lambda}\Delta S\left(\pi R^2 D\right) , \tag{13.5}$$

where for the given M^0, ΔS, R and assumed constants μ, λ, Λ we can find a source thickness D.

– For the total energy release we get the formulae

$$\Delta E = \frac{1}{2\mu} S \Delta S \left(\pi R^2 D\right), \quad \Delta E = \frac{A}{2\mu} (\Delta S)^2 \left(\pi R^2 D\right), \tag{13.6}$$

where the second relation follows from the above-mentioned empirical relation (13.2).

Using the observational data $\Delta E^{rad}, \Delta S, R$ and the thickness D estimated from the seismic moment (13.5), we may estimate the total energy release (13.6).

– The estimated total energy release can be compared with the Boltzmann expression for the energy release

$$\Delta E = \frac{kT}{\lambda^3} \left(\hat{\Delta} \pi R^2 D\right) \tag{13.7}$$

as defined by the volume of the broken bonds, with $\hat{\Delta}$ being the source damage parameter. However for the band model we shall define, instead of the elementary volume element λ^3, the element related to both the crystal lattice and super-lattice $\Lambda\lambda^2$. We get instead of (13.7):

$$\Delta E = \frac{kT}{\Lambda\lambda^2} \left(\tilde{\Delta} \pi R^2 D\right) \tag{13.8}$$

and hence the redefined damage parameter $\tilde{\Delta}$ can be estimated.

– The seismic efficiency can be now estimated as follows:

$$\eta = \frac{\Delta E^{rad}}{\Delta E} = \frac{2\mu \, \Delta E^{rad}}{A(\Delta S)^2 \left(\pi R^2 D\right)} \, . \tag{13.9}$$

– The shear band fracture model can be generalized to the form including the action of tensile stresses (Teisseyre et al. 2001).

Some thermodynamic considerations related to the presented fracture band model are presented in paper by Teisseyre (2001).

13.4 Elastic Rotation Energy

A density of strain energy for the case of asymmetric fields (see Chapter 3) can be written as

$$\varepsilon = \frac{1}{2} S_{ik} E_{ik} = \frac{1}{2}\left(S_{ik}^T - S_{ik}^S\right)\left(E_{ik}^T - E_{ik}^S\right), \tag{13.10}$$

where this expression contains also the elastic rotation energy.

This formula can be considered separately for the axial and deviatoric fields; for any tensor F we can write:

$$\hat{F}_{ik} = \frac{1}{3} F_{ss}\,\delta_{ik}, \qquad \tilde{F}_{ik} = F_{ik} - \frac{1}{3} F_{ss}\,\delta_{ik}, \tag{13.11}$$

and on this basis we consider the cases of compression, shears and rotations separately.

We assume that the diagonal terms $\hat{S}_{ss}$, $\hat{E}_{ss}$ of the total fields are equal to those of the elastic fields; this means that the self fields are zero in the axial/deviatoric representation: $\hat{S}_{kk}^S = 0$, $\hat{E}_{kk}^S = 0$.

The energy densities can be written as

$$\varepsilon = \frac{3\lambda + 2\mu}{2}\left(\frac{\partial u_k}{\partial x_k}\right)^2 \qquad \text{for the compression case, and}$$

$$\varepsilon_{(\,)} = \frac{1}{2}\tilde{S}_{(ik)}\tilde{E}_{(ik)} = \frac{1}{2}\left(S_{(ik)}^T - S_{(ik)}^S\right)\left(E_{(ik)}^T - E_{(ik)}^S\right)$$

or

$$\varepsilon_{(\,)} = \frac{1}{2} S_{(ik)} E_{(ik)} = \mu\left(\frac{\partial u_k}{\partial x_i}\right)_{(ik)}\left(\frac{\partial u_k}{\partial x_i}\right)_{(ik)} + \mu^* \omega_{(ik)}^S \omega_{(ik)}^S, \tag{13.12}$$

for the shear case,

where referring to Chapter 3 we use the following assumption for the self -rotation field: $E_{(ik)}^S = \omega_{(ik)}^S$, μ^* is the rotation rigidity (Shimbo 1995, Teisseyre and Boratyński 2003). Hence, here and further on we neglect the cross terms as formed by the independent fields, like $\left(\frac{\partial u_k}{\partial x_i}\right)_{(ik)} \omega_{(ik)}^S = 0$.

The density of the rotation elastic energy is

$$\varepsilon_{[\,]} = \frac{1}{2} S_{[ik]} E_{[ik]} = \mu\left[\frac{\partial u_k}{\partial x_i}\right]_{[ik]}\left[\frac{\partial u_k}{\partial x_i}\right]_{[ik]} + \mu^* \omega_{[ik]}^S \omega_{[ik]}^S . \tag{13.13}$$

We shall underline that the elastic rotation energy is included only when assuming the constitutive law joining rotations with the antisymmetric stresses. This expression corresponds to the density of angular motion energy when putting for the constitutive law for the antisymmetric part of stresses and for the self-fields the following relations:

$$S_{[ik]} = 2\mu^* \left[E^T_{[ik]} - E^S_{[ik]} \right], \quad S^S_{[ik]} = 2\mu^* \omega^S_{[ik]}, \quad \omega^S_{[ik]} = E^S_{[ik]} \tag{13.14}$$

as already postulated in Chapters 3 and 5.

13.5 Cross-Band Fracturing Model and Rotation Processes

During the precursory time-domain and during a seismic event we can consider the same system of glide and slip planes as defined for the band model. The cross band model (see Teisseyre 2004) consists of two perpedicularly oriented shear plane systems: one greater with the characteristic parameters R, D and the other smaller, with parameters r, d (Fig. 13.2, also compare Fig. 13.1).

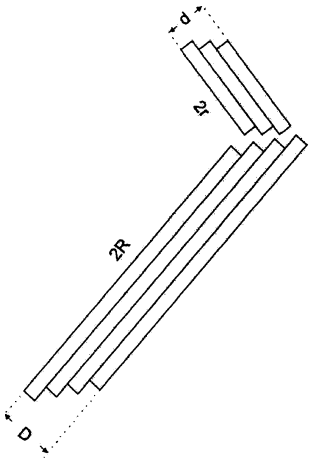

Fig. 13.2 Two systems of the band planes

Taking the slip values on the parallel and perpendicular planes as related to the dislocation arrays, we put according to (13.4) for slips on the parallel (main) planes and on the perpendicular planes:

$$\Delta u^{\parallel} = \lambda \Delta N^{\parallel} \frac{D}{\Lambda} = B^{\parallel} \frac{\lambda}{\Lambda} D \Delta S, \quad \text{and}$$
$$\Delta u^{\perp} = \lambda \Delta N^{\perp} \frac{d}{\Lambda} = B^{\perp} \frac{\lambda}{\Lambda} d \Delta S, \tag{13.15}$$

where the parameters $B^{\parallel}$ and $B^{\perp}$ determine an asymmetry of the fracture pattern:

$$\Delta N^{\parallel} = B^{\parallel} \Delta S, \qquad \Delta N^{\perp} = B^{\perp} \Delta S \ .$$

We relate these slips with the stress drop during a considered seismic event.

For the band model describing the systems of the parallel (main) planes and perpendicular planes we may define the seismic moment, stress release, and rotation release or the drop of the angular seismic moment. Such expressions contain both the classic energy release and the elastic rotation energy release, assuming that stress drops contain both symmetric and antisymmetric parts: $\Delta S = \Delta S_{( )} + \Delta S_{[ ]}$.

For the seismic moment generalized in such a way, and its release, we obtain:

$$M^{\parallel} = S^{\parallel} D(\pi R^2), \quad \Delta M^{\perp} = S^{\perp} d(\pi r^2), \quad \text{and}$$
$$\Delta M^{\parallel} = D \Delta S(\pi R^2), \quad \Delta M^{\perp} = d \Delta S(\pi r^2)$$

or according to Eqs. (13.2), (13.6), and (13.15):

$$\Delta M^{\parallel} = \frac{A}{B^{\parallel}} \frac{\Lambda}{\lambda} \Delta N^{\parallel} (\pi R^2) = D \Delta S(\pi R^2), \quad \text{and}$$
$$\Delta M^{\perp} = \frac{A}{B^{\perp}} \frac{\Lambda}{\lambda} \Delta N^{\perp} (\pi r^2) = d \Delta S(\pi r^2). \tag{13.16}$$

With $\omega^{\parallel} = \frac{\sum \Delta u^{\parallel}}{\Lambda} = N^{\parallel} \frac{D\lambda}{\Lambda^2}$ and $\omega^{\perp} = \frac{\sum \Delta u^{\perp}}{\Lambda} = N^{\perp} \frac{d\lambda}{\Lambda^2}$ we obtain the expressions for elastic rotation energy release:

$$\Delta E^{\parallel}_{[ ]} = \Delta M^{\parallel} \omega^{\parallel} = \frac{A}{B^{\parallel}} \frac{\Lambda}{\lambda} \Delta N^{\parallel} (\pi R^2) N^{\parallel} \frac{D\lambda}{\Lambda^2} = N^{\parallel} \frac{D\lambda}{\Lambda^2} D \Delta S(\pi R^2),$$

(13.17)

$$E^{\perp}_{[ ]} = \Delta M^{\perp} \omega^{\perp} = \frac{A}{B^{\perp}} \frac{\Lambda}{\lambda} \Delta N^{\perp} (\pi r^2) N^{\perp} \frac{d\lambda}{\Lambda^2} = N^{\perp} \frac{d\lambda}{\Lambda^2} d \Delta S(\pi r^2).$$

The energy release expressions presented here correspond to the previously defined density of elastic rotation energy (13.14).

Compression and induced shears $S_{[12]} = S_{[21]}$

Under the assumption $\Delta V = 0$ we can reexamine Dietrich's (1978) compression experiments, which leads to the conclusion that for the precursory shear stress $S_{12}^{pre} > 0$ (as induced by the confining pressure) we arrive at coseismic rebound compensation of shears by the rebound stress $S_{12}^{reb} < 0$ (signs are defined arbitrarily):

$$S_{12}^{pre} + S_{12}^{reb} \approx 0 . \tag{13.18}$$

With the antisymmetric stresses induced by a rotation process as shown in Fig. 13.3, we can propose the following reinterpretation:

– local induced shear stresses are antisymmetric: $S_{12} > 0$ and $S_{12} < 0$;

– for stresses on the parallel plane $\parallel$ (which will become the main fracture plane) we have

$$S_{12}^{\parallel pre} > 0 , \qquad S_{12}^{\parallel reb} < 0 ; \tag{13.19}$$

– for rotations (on the main plane $\parallel$ we have ($\omega_{(ik)}^{S} = \gamma_{(ik)}$)

$$\gamma^{\parallel pre} \rightarrow \text{clockwise} , \qquad \gamma^{\parallel reb} \rightarrow \text{anticlockwise} ; \tag{13.20}$$

– for stresses on an auxiliary, perpendicular plane $\perp$ we have

$$S_{21}^{\perp pre} < 0 , \qquad S_{21}^{\perp reb} > 0 ; \tag{13.21}$$

– for rotations on an auxiliary, perpendicular plane $\perp$ we have

$$\gamma^{\perp pre} \rightarrow \text{clockwise} , \qquad \gamma^{\perp reb} \rightarrow \text{anticlockwise} . \tag{13.22}$$

Precursory rotations associated with slips or dislocations are opposite to that related to coseismic process and both preserve their sense on perpendicular planes.

The repeated precursory processes lead to a number of the microfracturings finally forming a fragmentation pattern. On the presented figures, here and further, we explain schematically a possible pattern of premonitory distributions of the dislocations arrays or microcracks; a rebound process follows such a scheme leading to a cumulative process of energy release.

To relate the stress acumulation S to defect densities, we recall the basic relation $S = nS_0$ for the dislocation array in an equilibrium (supported by the external stress S_0). This relation comes from interaction of the dislocations (densities α_i represented here by the stress gradients ∇S_i) pushed by the external field S_0 to the first blocking dislocation; S is the resulting stress accumulation at the place of the first dislocation:

$$S = \int_0^n \nabla S_i \mathrm{d}i = \int_0^x \frac{\partial}{\partial x} S \, \mathrm{d}x \ . \tag{13.23}$$

In our case, we have no initial shear field but only compression: due to the lower value of shear resistance we have to assume that inside a body there appear regions with the induced shear stresses of opposite signs (as a result, we get the induced antisymmetric shear stress).

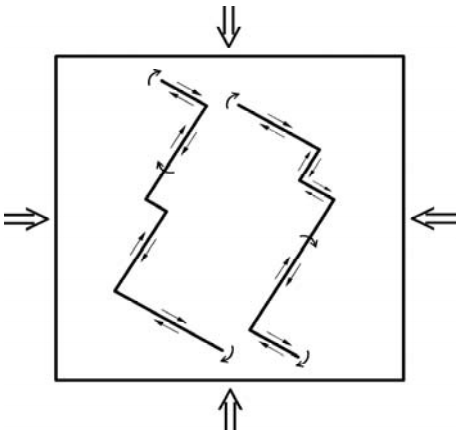

Fig. 13.3 Compression: induced shear stresses of opposite signs on perpendicularly orientated planes; a common sense of rotations

According to the band-model, the shear stress is related to the concentration of induced dislocations (in the number N^{ind}, n^{ind}, respectively): the induced shear stressess are asymmetric, $S = An$, hence, the stresses at these planes can be related to dislocation densities (Fig. 13.2):

– on the parallel plane $\parallel$:

$$S^{\parallel pre} \approx AN^{\parallel ind} \propto \alpha^{\parallel ind} \ , \quad S^{\parallel reb} \approx -AN^{\parallel ind} \propto -\alpha^{\parallel ind} \ , \tag{13.24}$$

– on the perpendicular plane $\perp$:

$$S^{\perp pre} \approx -An^{\perp ind} \propto -\alpha^{\perp ind} \ , \quad S^{\perp reb} \approx An^{\perp ind} \propto \alpha^{\perp ind} \ . \tag{13.25}$$

The signs of dislocations of these planes can be different, depending also on the position of their wedge, but a common sense of rotations shall be preserved on these planes.

Earthquake process and its energy release relates to a coalescence of dislocation arrays of opposite signs; also that part of energy release which depends on drop of moment of momentum depends on dislocation coalescence process; it can be expressed by the rotation release.

For a total shear release on the two planes we can demand at a compression (with the signs as in Eq. 13.19)

$$\Delta S^{\parallel pre} + \Delta S^{\parallel reb} \approx 0\,, \quad \Delta S^{A\perp pre} + \Delta S^{A\perp reb} \approx 0 \tag{13.26}$$

while for an instantaneous, rebound, shear stress drop and the total shear stress drop we get

$$\begin{gathered}\Delta S^{\parallel reb} \approx -A\Delta N^{\parallel ind}\,, \quad \Delta S^{\perp reb} \approx A\Delta n^{\perp ind}\,, \\ \Delta S^{reb} \approx -A\left(\Delta N^{\parallel ind} - \Delta n^{\perp ind}\right).\end{gathered} \tag{13.27}$$

Thus, the total shear stress drop for compression process can be, in such a case, relatively small; the real stress drop relates to non-shear components.

The coseismic rotations are opposite to the precursory rotations; it is the coseismic, rebound process that brings the release of rotation. According to (13.16) and (13.17), the total rotation releases at the $\parallel$ and $\perp$ planes the precursory and rebound processes become:

$$\Delta M^{\parallel pre} + \Delta M^{\parallel reb} \approx 0\,, \quad \Delta M^{\perp pre} + \Delta M^{\perp reb} \approx 0\,. \tag{13.28}$$

The final instantaneous rotation release for coalescence process on both planes and the total one are as follows:

$$\begin{gathered}\Delta M^{\parallel reb} \approx -\frac{A}{B}\frac{\Lambda}{\lambda}\Delta N^{\parallel ind}\,, \quad \Delta M^{\perp reb} = -\frac{A}{B}\frac{\Lambda}{\lambda}\Delta n^{\perp ind}\,, \\ \Delta M^{reb} = \Delta M^{\parallel reb} + \Delta M^{\perp reb} = -\frac{A}{B}\frac{\Lambda}{\lambda}\left(\Delta N^{\perp ind} + \Delta n^{\perp ind}\right),\end{gathered} \tag{13.29}$$

where A and B are the adequate proportionality coefficients.

Comparing this result with that for the related stress drop (13.27) we find that at the compression load the related energy releases for the induced shears are relatively smaller (a difference of stress drops related to parallel and perpendicular systems) than for the rotation related moment drops (a sum of moment drops). Under a compression load the rotation processes in fragmentation and fracturing play an essential role.

External shear load $S_{12}^0 = S_{21}^0$

For symmetric fields, in a similar way as above, we may put at the main, parallel plane $\parallel$ and at the perpendicular planes $\perp$ (Fig. 13.4):

$$S_{12}^{\parallel pre} > 0\,, \quad S_{12}^{\parallel reb} > 0\,, \quad S_{21}^{\perp pre} > 0\,, \quad S_{21}^{\perp reb} > 0\,, \tag{13.30}$$

$$\gamma^{\parallel pre} \rightarrow \text{clockwise}\,, \quad \gamma^{\parallel reb} \rightarrow \text{anticlockwise}\,, \tag{13.31}$$

$$\gamma^{\perp pre} \rightarrow \text{clockwise}\,, \quad \gamma^{\perp reb} \rightarrow \text{anticlockwise}\,. \tag{13.32}$$

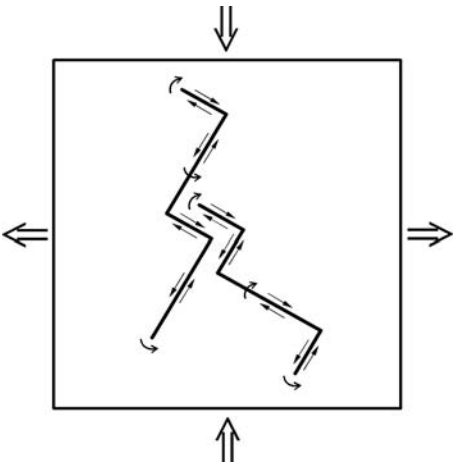

Fig. 13.4 External shears: shear motion on perpendicularly orientated planes; an opposite sense of rotations

For the regional shearing field $S^0(S_{12}^0 = S_{21}^0)$, the effects of processes at the main shearing and at auxiliary, perpendicular planes are (on both planes, $\parallel$ and $\perp$):

$$S^{\parallel pre} \approx S_0 + AN^{\parallel pre} \propto \alpha^{\parallel pre}\,, \quad S^{\parallel reb} \approx S_0 + AN^{\parallel reb} \propto \alpha^{\parallel reb}\,, \tag{13.33}$$

$$S^{\perp pre} \approx S_0 + An^{\parallel pre} \propto \alpha^{\parallel pre}\,, \quad S^{\perp reb} \approx S_0 + An^{\parallel reb} \propto \alpha^{\parallel reb}\,. \tag{13.34}$$

The shear stress drops on both planes, $\parallel$ and $\perp$, and the total shear stress drop is, respectively:

$$\Delta S^{\parallel} \approx A\,\Delta N\,, \quad \Delta S^{\perp} \approx A\,\Delta n\,, \quad \Delta S^{reb} \approx A(\Delta N + \Delta n)\,. \tag{13.35}$$

The signs of rotation release on these planes are opposite; for instantaneous rotation release we get expression with a relatively smaller value (comparing to the former case)

$$\Delta M^{reb} = -\frac{A}{B}\frac{\Lambda}{\lambda}\left(\Delta N^{\perp} - \Delta n^{\perp}\right). \tag{13.36}$$

Comparing this result with that for the related stress drop (13.35) we find that at a shear load the related energy releases for the shears are relatively greater (a sum of stress drops related to parallel and perpendicular systems) than for the rotation related moment drops (a difference of moment drops). Under a shear load the shear processes play the main role in fragmentation and fracturing.

Compression and shear load $S_{11}^0 < S_{22}^0$

Assuming $S_{11}^0 < S_{22}^0$ we can present the initial stress state as a combination of the two cases presented above: $\tilde{S}_{22}^0 = S_{11}^0$ and $S_{12}^0 = S_{21}^0 = \frac{1}{2}(S_{22}^0 - S_{11}^0)$ (Fig. 13.5).

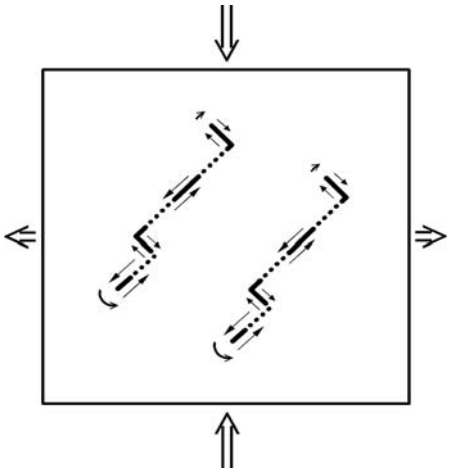

Fig. 13.5 Compression and shear load: asymmetric shears and differentiated rotations

Such a combination leads to: (a) bigger precursory phenomena (sum of the precursory shear and induced shear); and (b) smaller shears on perpendicular planes (difference of precursory and induced shears).

Hence, there follows a rule for earthquake asymmetry faulting (even independent of any previous stick-slips):

– a combined shear stress drop becomes

$$\Delta S^{reb} \approx A[\Delta N + \Delta N^{ind} + \Delta n - \Delta n^{ind}], \tag{13.37}$$

– an instantaneous rotation release becomes

$$\Delta R^{reb} \approx -B[\Delta N + \Delta N^{ind} - \Delta n + \Delta n^{ind}]. \tag{13.38}$$

Thus, for momentum and moment of momentum releases for the 2D band fracture model we obtain

$$\Delta M = A\pi[R^2 D(\Delta N + \Delta N^{ind}) + r^2 d(\Delta n - \Delta n^{ind})], \tag{13.37′}$$

$$\Delta M^{\omega} = -B\pi[R^2 D(\Delta N + \Delta N^{ind}) + r^2 d(-\Delta n + \Delta n^{ind})]. \tag{13.38′}$$

13.6 Conclusions

The fracture processes are determined by stress load and local stress concentrations due to accumulation of dislocations and partial mutual dislocation annihilations. In such processes, the formation of dislocation arrays and microcracks related to the premonitory processes and its rebound event plays an essential role. Additional counterpart of stress moments appears due to the antisymmetric stresses related grain rotations and due to stress moments formed by the fracturing pattern.

Rotations at source zones help to understand geometry of fracturing and releases of stress and rotation counterparts as a result of precursory and rebound processes.

References

Eshelby JD, Frank FC, Nabarro FRN (1951) The equilibrium of linear arrays of dislocations. Philos Mag **42**: 351-364

Dietrich JHJ (1978) Preseismic fault slip and earthquakes prediction. J Geophys Res **83**: (B8) 3940-3954

Droste Z, Teisseyre R (1959) The mechanism of earthquakes according to dislocation theory. Sci Rep Tohuku Univ, Ser 5 Geophys **11**: 55-71

Kröner E (1981) Continuum theory of defects. In: Balian R, Kléman M, Poirer JP (eds) Physics of defects (Proc Les Houches, XXXV), North Holland Publ Comp, Amsterdam

Nabarro FRN (1951) The synthesis of elastic dislocation fields. Philos Mag **42**: 1224-1231

Shimbo M (1995) Non-Riemannian geometrical approach to deformation and friction. In: Teisseyre R (ed) Theory of earthquake premonitory and fracture processes, PWN, Warszawa, pp 520-528

Teisseyre R (1961) Dynamic and time relations of the dislocation theory of earthquakes. Acta Geophys Pol **9**: 3-58

Teisseyre R (1964) Dislocation systems and their interaction inshock sequence. Acta Geophys Pol **12**: 23-36

Teisseyre R (1970) Crack formation and energy release caused by the concentration of dislocations along fault planes. Tectonophysics **9**: 547-557

Teisseyre R (1996) Shear band thermodynamical earthquake model. Acta Geophys Pol **44**: 219-236

Teisseyre R (1997) Shear band thermodynamical model of fracturing with a compressional component. In: Gibowicz S, Lasocki S (eds) Rockburst and seismicity in mines, pp 17-21, Balkema, Rotterdam-Brookfield

Teisseyre R (2001) Shear band thermodynamic model of fracturing. In: Teisseyre R, Majewski E (eds) Earthquake thermodynamics and phase transformations in the earth's interior. Academic Press, San Diego-Tokyo.

Teisseyre R (2004) Spin and twist motions in a homogeneous elastic continuum and cross-band geometry of fracturing. Acta Geophys Pol **52**: 173-183

Teisseyre R, Boratyński W (2003) Continua with self-rotation nuclei: evolution of asymmetric fields. Mech Res Commun **30**: 235-240

Teisseyre R, Wiejacz P (1993) Earthquake sequences: stress diagrams. Acta Geophys Pol **41**: 85-100

Teisseyre R, Teisseyre KP, Górski M (2001) Earthquake fracture-band theory. Acta Geophys Pol **49**: 463-479

14 Rotation Motions: Recording and Analysis

Krzysztof P. Teisseyre, Jerzy Suchcicki

Institute of Geophysics, Polish Academy of Sciences
ul. Księcia Janusza 64, 01-452 Warszawa, Poland; e-mail: kt@igf.edu.pl

14.1 Introduction

Rotation motions can be classified as those associated to the body seismic waves (displacement-related component and micromorphic component) and those which form independent fields (pure rotation and twist waves); see Chaps. 4–6. The equipment that records rotation motions may use various sensors, like the Sagnac-effect based gyroscopes (see Chaps. 11, 12, 29, 30, 31, 37), seismometers (Chaps. 15, 32, 33, 34), tiltmeters (Chap. 36) or rotation sensors (Chap. 35).

In this Chap. we present some records obtained with a system of two horizontal seismometer pairs, each containing two pendulums suspended on a common axis and aligned in opposite directions. The pairs were oriented perpendicular to each other. The system was constructed by J. Suchcicki (see Teisseyre et al. 2003). Its ability has been improved by some numerical procedures normalizing the signals at the antiparallel channels. The errors caused by the inevitable small differences in seismograph responses have been estimated and a reliability of recordings was tested in many ways: by filtering in the time domain (using some data obtained from the same equipment as a reference, see Nowożyński and Teisseyre KP 2003), or by numerical filtering procedure in the frequency domain and the learning procedure for filters (Teisseyre R et al. 2003a, b).

Any serious analysis of rotation wave records would require, first of all, the existence of a network of recording stations; however, up to now, only few rotation-recording stations do exist, and these use various sensors. There is also a need for a more advanced theory describing propagation and reflection of the rotation waves. Such an advanced approach should follow the development of the classical seismology, starting with hodographs and separation of phases of rotation motions.

The independent rotation waves may travel with different, rather lower velocities than those related to the body waves. This is due to the different material constants that describe the stress response to rotational deformations. Such constants enter in the constitutive relation between the stress moments (or equivalently, the antisymmetric stresses) and angular motion (see Chaps. 4–6). To better understand the role of pure rotation and twist, we shall take into account the fact that rotation of particles or grains induces antisymmetric stresses (equivalent to stress moments). We expect the rotation rigidity (see Chap. 5) to be smaller than the rigidity modulus; hence, we could expect the late arrivals of the related rotation waves. To discover such late arrivals we shall start with hodographs for near field and gradually extend the required time interval of registrations. A first trial of such a near field hodograph is presented by Jaroszewicz et al. in Chap. 31. However, we shall also take into account an interrelation between the displacement motion and rotation, which may lead to a kind of coupling of these motions; this is, among other things, discussed in this chapter.

14.2 Examples of Records and Their Preliminary Analysis

In this chapter we present some examples of rotation wave recordings, and their preliminary analysis. All the cases chosen were analyzed in the frequency range of 2.6-43 Hz, some cases being studied also in the low frequency range: 0.3-3 Hz.

The main part of our analysis is based on the data from l'Aquila Observatory (central Italy). Twenty four cases were chosen, for which good quality of rotational components has been obtained; good quality means that the seismic event is seen not only in the plots of the so-called **initial data** (displacement velocity V, after its correction by filtration), but in the plots of rotational motions ($\sim \Delta V/2l_0$, where l_0 is the reduced length of the seismometer) as well. Data acquisition took place in 2002; the chosen cases belong to the local seismic events.

Among the events recorded in l'Aquila, the nearest occurred at a distance of 6.9 km, while the five most remote ones at a distance of about 40 km from the measuring site in the Castello Cinquecentesco in the town of l'Aquila. The maxima of initial signals, V_{max} , appear to lie between 75 μm/s (for the seismic event nearest to the station) and 1 μm/s. The calculated rotation motions achieved maximum values from 15.7 to 0.37 μrad/s, depending on the case.

In all the cases except of four, the twist motions have slightly greater amplitudes than the spin ones (the four cases for which the spin curve had

a higher maximum value belong to a few cases of low intensity of initial and rotational signals, and high noise content in the latter). Generally speaking, with increasing distance, the signals relating to the seismic event, at both the spin and the twist plots, were less distinct from the noise.

In the tectonic seismic events encountered near l'Aquila we found some discrepancy and shift between the curves of the displacement velocity signals (shown here after filtration and normalisation) and the curves of rotation motion, especially profound at the beginning of the seismic event. The rotational motions were often unexpectedly large.

Here we present the results for the three cases: one from the l'Aquila Observatory **(**Fig. 14.1); one for an earthquake in Podhale region (southern Poland, 30 November 2004 at 17:18; Fig. 14.2); and a seismic event in the mine in southern Poland (Upper Silesian mining region; Fig. 14.3). The latter two events were registered at the Ojców Observatory, southern Poland.

To study the differences between the displacement velocity curves and the rotational ones, and to analyse the course of seismic records, we introduce index T, defined as a mean of the absolute values of differential signals.

$$T = \frac{1}{2}\left(\frac{\Delta V_{12}}{2l_0} + \frac{\Delta V_{34}}{2l_0} \right), \quad \Delta V_{12} = V_1 - V_2 \ , \ \Delta V_{34} = V_3 - V_4 \ .$$

The plots of this mean (lower curves in Figs. 14.1.b, 14.2b, 14.3.b; also Figs. 14.1d, 14.2d and 14.3d) were compared to the curves of mean absolute values of the displacement velocity signals

$$\bar{U} = \frac{1}{4}\left(|V_1| + |V_2| + |V_3| + |V_4| \right)$$

seen in the upper portions of the same figures. Subsequently, on the basis of variation in shape and amplitude of both curves, we computed, for short time intervals, the new indices R_m defined as follows:

$$R_m = \sum T^2 \Big/ \sum \bar{U}^2 \ .$$

Index R_m is analogous to the indices R_1 and R_2 used in the study of differential motions at the Pasterze Glacier (see Chap. 15 and the references therein).

While analysing the l'Aquila data, indices R_m were in each case calculated for three time intervals: one at the beginning of seismic event, one somewhere in the middle and the last in that part where oscillations start to decline. Usually such an interval was 60 samples long (which corresponds

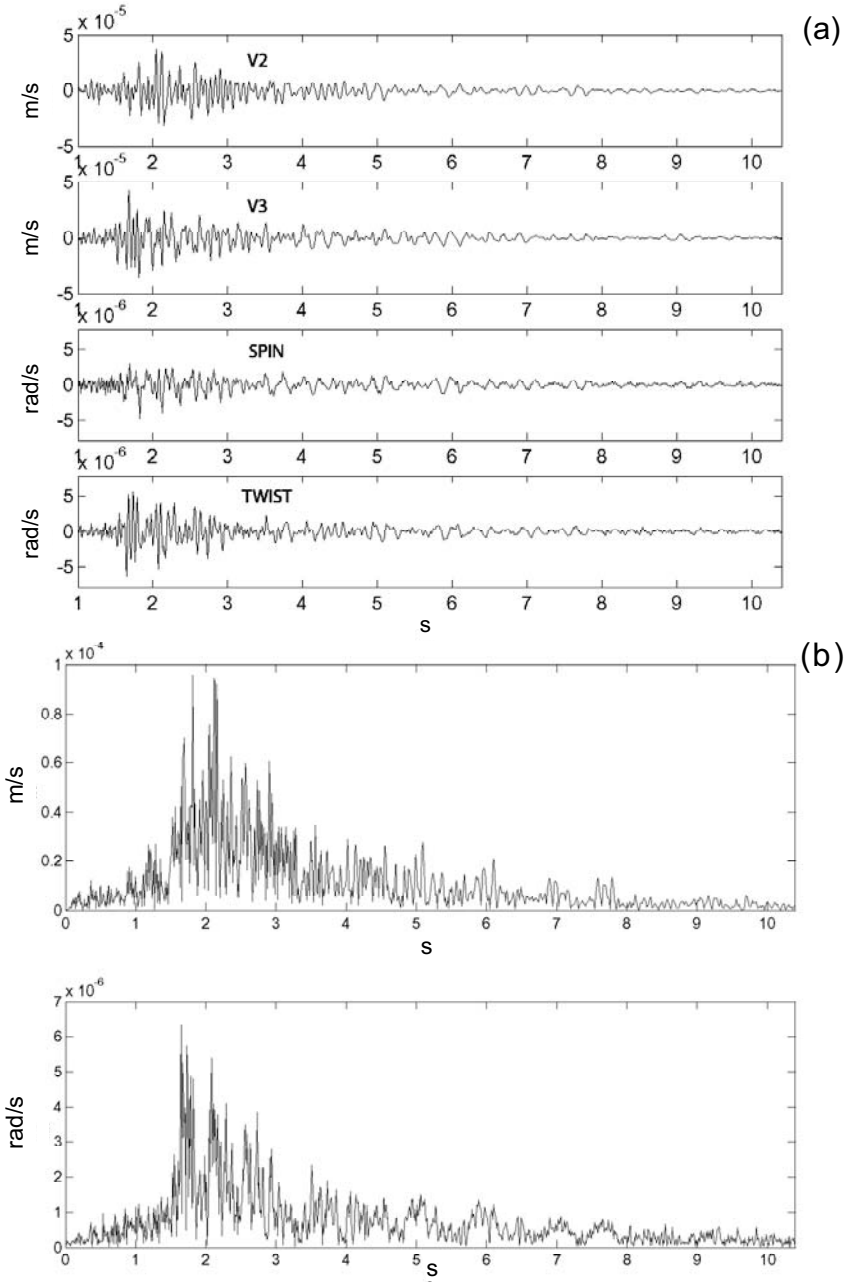

Fig. 14.1a, b Seismic event recorded at l'Aquila Observatory (20 Aug 2002, 13:50, Aquilano region) for normal frequency range (2.6-43 Hz): (a) displacement velocities V_2 and V_3, spin, twist; (b) mean absolute velocities of displacement $\bar{U}$ (*top*) and mean absolute values of rotational motions (*bottom*)

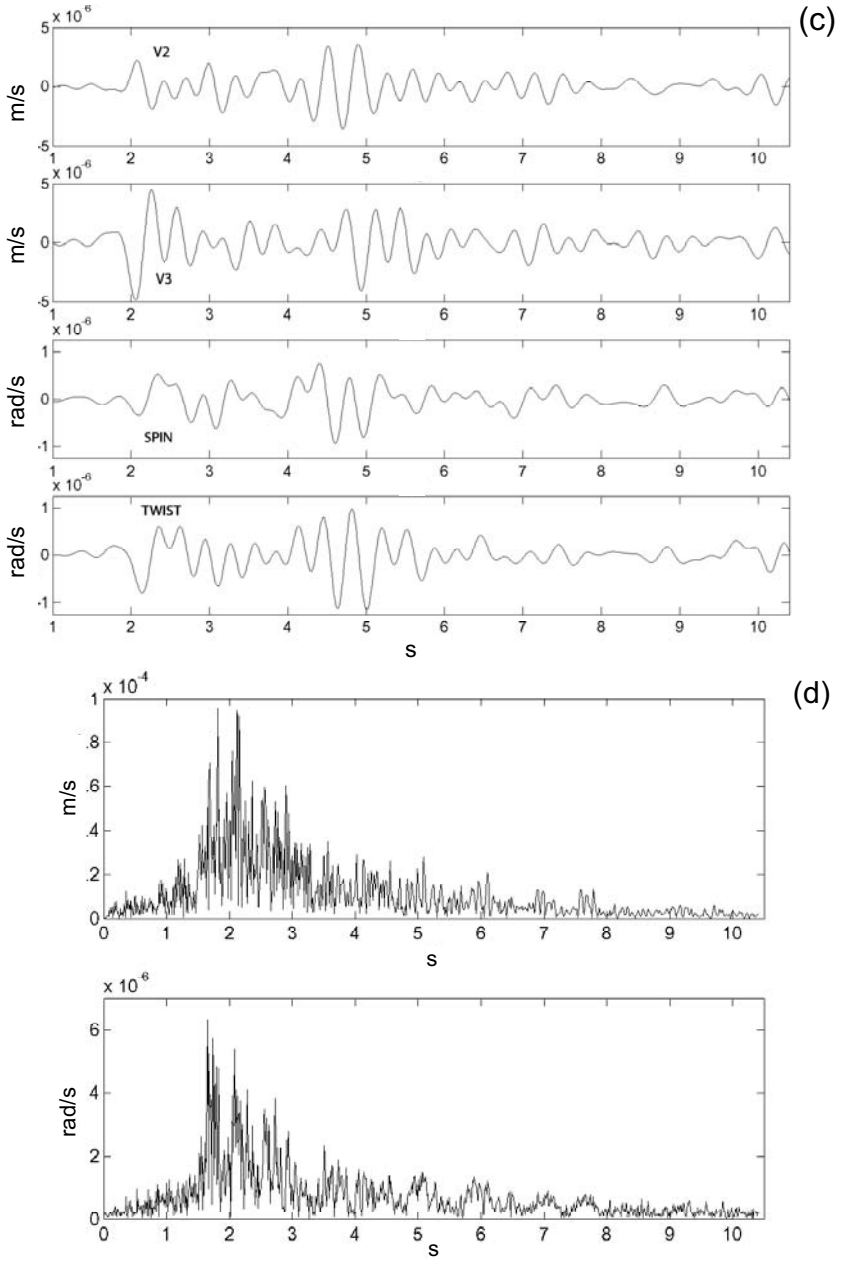

Fig. 14.1c, d Seismic event recorded at l'Aquila Observatory (20 Aug 2002, 13:50, Aquilano region) for low frequency range (0.3-3 Hz): (c) displacement velocities V_2 and V_3, spin, twist; (d) mean absolute velocities of displacement $\bar{U}$ (*top*) and mean absolute values of rotational motions (*bottom*)

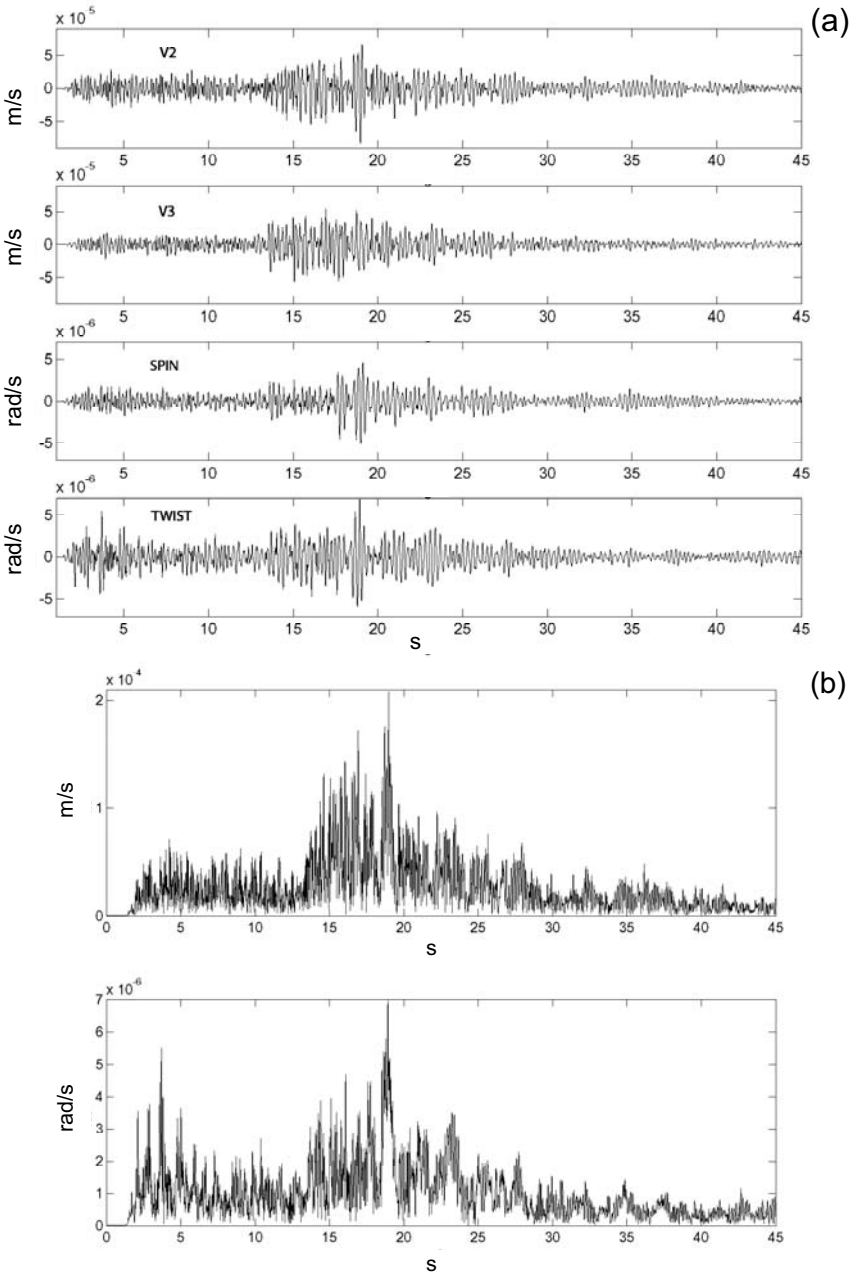

Fig. 14.2a, b Earthquake recorded at Ojców Observatory (30 Nov 2004, 17:18, Podhale region) for normal frequency range (2.6-43 Hz): (a) displacement velocities V_2 and V_3, spin, twist; (b) mean absolute velocities of displacement $\bar{U}$ (*top*) and mean absolute values of rotational motions (*bottom*)

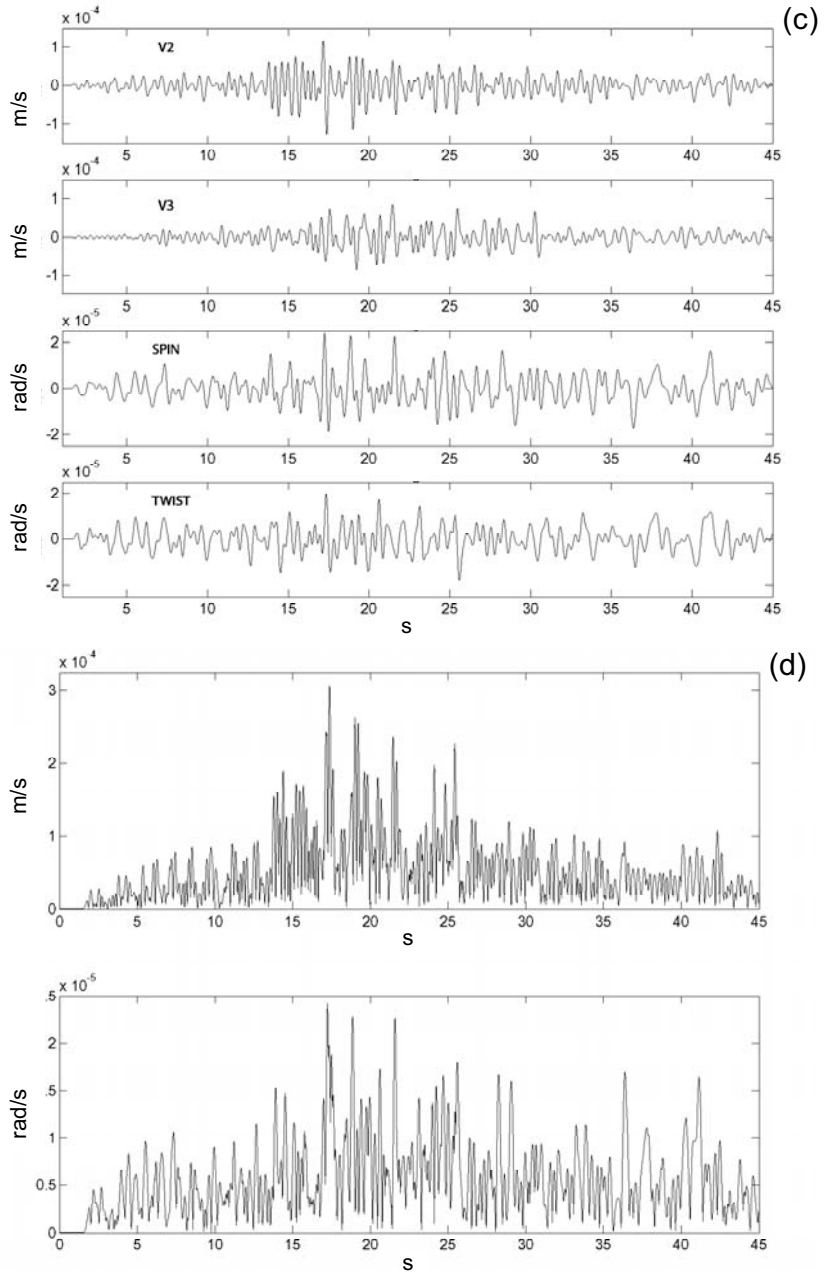

Fig. 14.2c, d Earthquake recorded at Ojców Observatory (30 Nov 2004, 17:18, Podhale region) for low frequency range (0.3-3 Hz): (c) displacement velocities V_2 and V_3, spin, twist; (d) mean absolute velocities of displacement $\overline{U}$ (*top*) and mean absolute values of rotational motions (*bottom*)

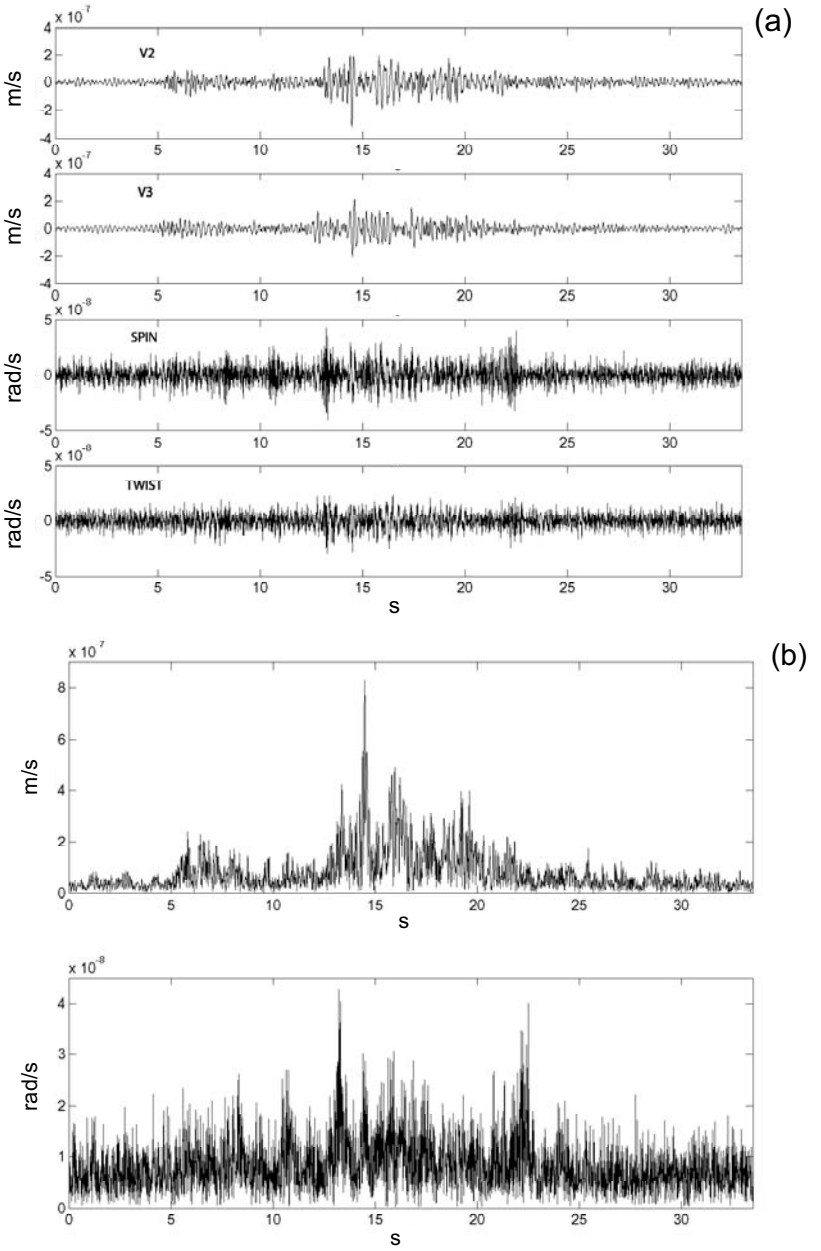

Fig. 14.3a, b Mining seismic event recorded at Ojców Observatory (22 Mar 2004, 23:48, the region of Upper Silesia) for normal frequency range (2.6-43 Hz): (a) displacement velocities V_2 and V_3; spin, twist; (b) mean absolute velocities of displacement $\bar{U}$ (*top*) and mean absolute values of rotational motions (*bottom*)

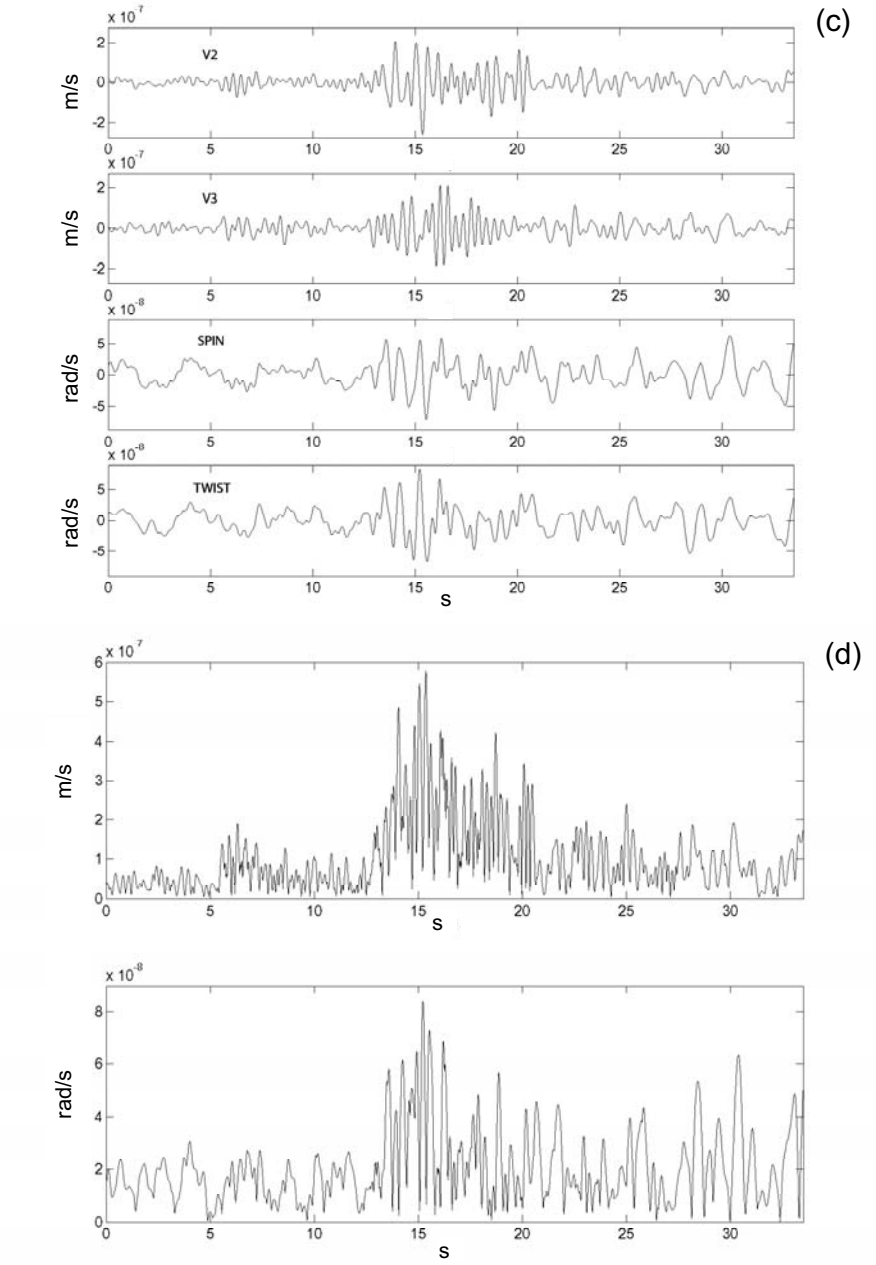

Fig. 14.3c, d Mining seismic event recorded at Ojców Observatory (22 Mar 2004, 23:48, the region of Upper Silesia) for low frequency range (0.3-3 Hz): (c) displacement velocities V_2 and V_3, spin, twist; (d) mean absolute velocities of displacement $\bar{U}$ (*top*) and mean absolute values of rotational motions (*bottom*)

to 0.6 s). In most cases, the results obtained had the following characteristic feature: indices R_m calculated for the first and the last interval were greater than for the middle one, and the first had the greatest value. This result, emphasising temporal variation of the wave generation in the source, is not shown here. For simplicity, we only show, in Fig. 14.4a, the means of those three indices, denoted by squares. The same figure shows also maxima of rotational motion for the same cases (absolute values), denoted by asterisks. Both kinds of resulting data are ordered by the maximum (absolute) value of displacement velocity, V_{max}.

Next, we have normalized the maximum amplitudes (V_{max}) to the related epicentral distances. A damping effect is not included, but the distances considered are not drastically different. Then we put again these experimental results in Fig. 14.4b, but rearranged according to new values at the abscissa. Now, the R_m-means are shown as triangles, and rotation motion maxima – as small five-pointed stars. We return to the obtained picture in the discussion.

Beside the above-mentioned discrepancy between the curves, the rotation motions compared with the displacement motions differ also in minute

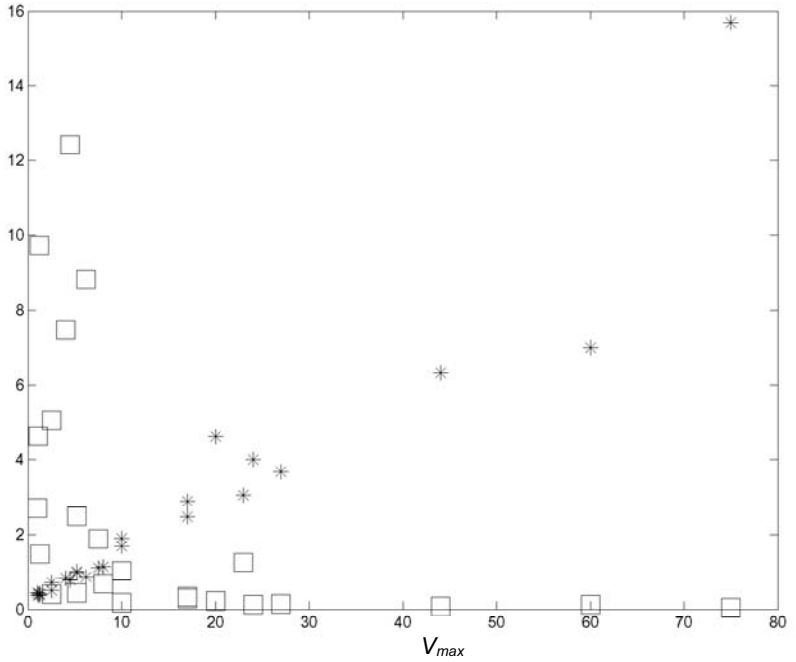

Fig. 14.4a Analysis of 24 seismic events recorded at l'Aquila; normal frequency range. Mean indices R_m (squares) and maxima of rotation motions amplitude (asterisks) *versus* maxima of displacement velocity

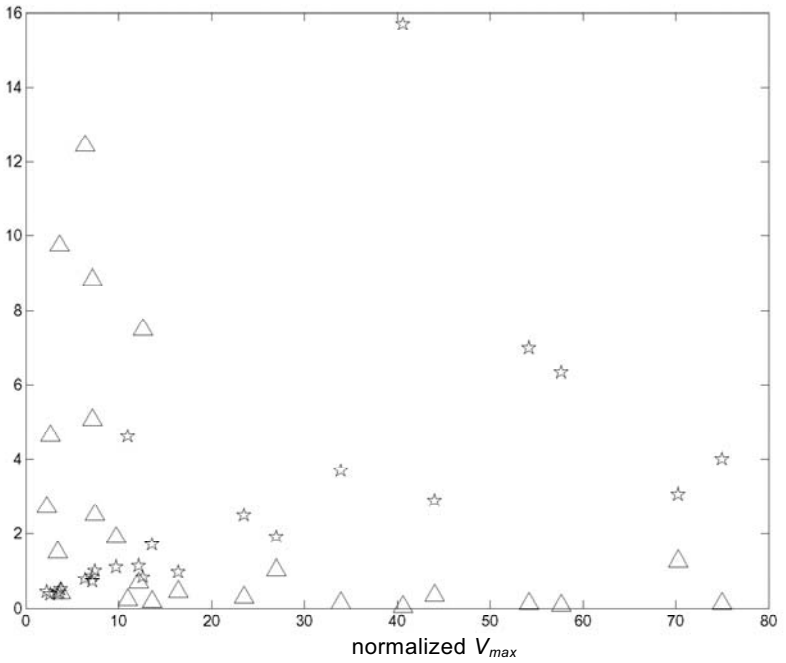

Fig. 14.4b Analysis of 24 seismic events recorded at l'Aquila; normal frequency range. Mean indices R_m (triangles) and maxima of rotation motions amplitude (stars) *versus* distance-normalized maxima of displacement velocity

details – micro-differences look like results of a phase-shift on the way of seismic waves from the source to the station. Comparing the plots of $\bar{U}$ and T, we noticed that the same holds for the means.

Similar observations are drawn from the analysis of an earthquake in the Podhale region. This seismic event had longer duration; therefore, finding the details of differences between separate curves is more difficult.

Interestingly enough, an analysis of the same cases in the low frequency range (0.3-3 Hz), gives surprisingly different course of the studied event. We observed slightly later arrivals of distinct peaks, as compared to the results of analysis in normal (2.6-43 Hz) frequency range, especially visible in the plots of mean values ($\bar{U}$ and T, compare Fig. 14.1d with Fig. 14.1b). Also the general shape of recorded event is different; relatively high-amplitude oscillations persist for longer time than in the higher frequencies.

For the mining events (see Fig. 14.3), the rotation motions are more similar to the displacement fields, although we still find all the above-mentioned differences: between curves of initial and differential data, and

between results obtained at low frequencies and in the normal frequency range. Here, the number of studied cases was small; nevertheless, it seems that the results of the mining events registered at Ojców have more in common with the results for mining events obtained at Książ Observatory (in Sudety Mts., southern Poland), than with the results of analysis of tectonic earthquakes.

14.3 Discussion

According to the analysis of l'Aquila data, we may tentatively state that, during the seismic event, the short intervals with the high content of rotations interlace with intervals with a relatively low content of rotation waves. These results fit to a slip-rotation scheme of fracturing, presented in Chap. 13. Accordingly, we may say that a slip step unlocks a rotation step occurring with some delay; and *vice versa*: a rotation step is followed by a slip. A possible support for this hypothesis comes from an analysis of seismic events recorded at the Pasterze Glacier (Chap. 15). In the course of differential motion, obtained from this research, we have also noticed some precursory signals directly prior to the record of the event.

Experimental evidence from l'Aquila shows that there exist a hyperbolic relation $V_{max} \cdot R_m$ = constant (see Figs. 14.4a, b). After the distance-normalisation of the abscissa, its relation with the indices R_m still resembles a hyperbole, but now the values of mean R_m in the higher-amplitude part of the plot are greater than before. These relations refer to situation closer to the source, and we see that the smaller the displacement amplitude (for a given case), the bigger the part of energy emanated as rotations. We may say: in smaller earthquakes, relatively bigger portions of energy release through rotational waves, and this relation has a hyperbolic character. However, it is still too early for any definite statements about the rotational aspect of seismicity around l'Aquila.

Note that a picture similar to that in Fig. 14.4a was found for the seismic events occurring in Pasterze Glacier, studied in the frequency range of 3-15 Hz (see Chap. 15). For the glacier events, however, no distance-normalised values could be calculated, as we do not know the distances from the measuring site to the sources of registered seismic events. A few glacial cases were analysed also in the frequency range of 0.3-3 Hz, and then no relation between V_{max} and indices R_1 or R_2 was found.

In the seismic events occurring in mines, studied so far, the generation of rotation motion is apparently more strictly bounded to the course of „regular" seismic waves generation. This may be explained by smaller

confining pressure in mines, as compared to the foci of tectonic earthquakes. Under the conditions present in the mine, no large rotations are needed to unlock the slip movement.

To come upon conclusions, some discrepancies were found between rotational and „classic" seismic motions emitted from the tectonic shock. The discrepancies were much milder in the cases of mining tremors. But we cannot make any firm statement about an influence of the local material micromorphism on the results obtained at a given station, because outcomes of detailed analyses are still sparse. Therefore, we must take into account the fact that the rock media between the source and the measuring station may distort the shape of rotation curves, to an unknown extent. For example, the minute time-differences between local peaks of displacement and rotational motions (these are seen after stretching the time scale) might reflect the processes in the source, but might also be results of phase-shift in the material between the focus and the measuring equipment.

The low-frequency seismic waves seem to travel somewhat slower than the waves of higher frequencies (this is especially clearly seen in the diagrams showing rotation motions), but we cannot decide yet, whether this is a source-effect or an effect of rock media influence.

We hope that further studies, with the networks of rotational seismic stations, will solve these, and many more questions.

References

Nowożyński K (2004) Estimation of magnetotelluric transfer functions in the time domain over a wide frequency band. Geophys J Int **158**: 32-41

Nowożyński K, Teisseyre KP (2003) Time-domain filtering of seismic rotation waves. Acta Geophys Pol **51**: 1, 51-61

Teisseyre R, Suchcicki J, Teisseyre KP (2003a) Recording the seismic rotation waves: Reliability analysis. Acta Geophys Pol **51**: 1, 37-50

Teisseyre R, Suchcicki J, Teisseyre KP, Wiszniowski J, Palangio P (2003b) Seismic rotation waves: basic elements of theory and recording. Annals Geophys **46**: 4, 671-685

15 Glacier Motion: Seismic Events and Rotation/Tilt Phenomena

Marek Górski, Krzysztof P. Teisseyre

Institute of Geophysics, Polish Academy of Sciences
ul. Księcia Janusza 64, 01-452 Warszawa, Poland
e-mails: mgorski@igf.edu.pl; kt@igf.edu.pl

15.1 Introduction

The many-year seismic monitoring of the Hans Glacier (South Spitsbergen) made it possible to associate seismic events with dynamic processes taking place in the glacier and related to its movements. The first registrations of seismic events in the Hans Glacier were made by Roman Teisseyre in the summer season of 1962 (Lewandowska and Teisseyre 1964). The study of seismic events on the Hans Glacier are based on two sources of recording. The first is the incessant recording of ice seismicity on the seismological station (HSP) at the Polish Polar Station Hornsund (Górski 1997). The other is the seasonal seismic survey carried out on the Hans Glacier. The results from the Hans Glacier were compared with analogous studies in the Antarctic and an Alpine glacier.

The study of rotation waves which were generated and propagated in ice was initiated in the Hans Glacier region in 2000 (Teisseyre et al. 2004). The study was continued at the Pasterze Glacier in the Austrian Alps.

There are two main types of seismic events generated in glaciers: icequakes (Fig. 15.1) related to the release of stresses accumulated in ice, and ice-vibrations (Fig. 15.2) of a relatively long duration and relatively low frequency spectrum (dominant frequencies of 2-12 Hz).

15.2 Icequakes

Observations of icequakes on the Hans Glacier lead to the conclusion that the recorded seismicity can be related to the release of stresses in the marginal zone of the glacier, on the boundary between the two parts of the

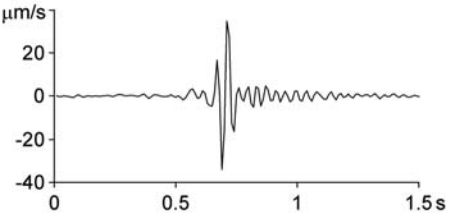

Fig. 15.1 Icequake event recorded on the Pasterze Glacier at 14:32 on 28 August 2005

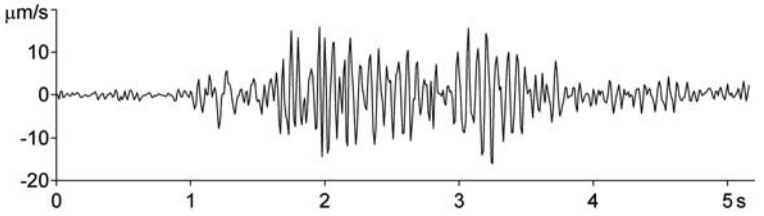

Fig. 15.2 Ice-vibrations event recorded on the Pasterze Glacier at 16:12 on 29 August 2005

glacier: the part which is strongly associated with rocky environment and the other which constitutes the glacier's main stream. This can be seen in Fig. 15.3, in which we show the location of foci of icequakes recorded in two measurement series (Górski 2003). Icequakes are associated with regions of large gradient of ice movement velocity, rather than with the large value of ice flow velocity itself (Fig. 15.4). The figure shows a comparison of the location of epicenters of icequakes with magnitudes greater than –0.7, with the annual mean distribution of ice flow velocity at the glacier surface. The seismically active region is situated in the marginal zone of the glacier along the western border of the maximally cracked region; in this place the gradient (on a transverse profile) of the glacier velocity in its annual movement is large. The glacier's bottom in this area is at depths from 0 to over 50 m below sea level.

Spectral parameters of icequake foci have been determined for the series of events recorded at the Hans Glacier. The calculations were based on Brune's model. A comparison was made of icequake series recorded in different seasons (Górski 2003). A comparison of the seismic moment–focal radius and seismic moment–seismic energy relationships for spring and summer seasons point to seasonal changes of physical parameters of ice or focus structure. Figure 15.5 shows, for the event series of Fig. 15.3, the relation between the seismic moments and the source radii: lines of

constant stress drop are marked. For comparison, we also present in this figure (gray-colour area), the groups of various earthquakes and mining tremors in South Africa gold mines (Abercrombie and Leary 1993). The ellipse represents the region occupied by icequakes recorded in an Antarctic shelf glacier (Osten-Woldenburg 1990). The radii of icequakes are in the range of 10–100 m. It is seen in the figure that the location of points corresponding to the same values of the seismic moment for earthquakes differs from that for icequakes. Icequakes are shifted towards greater values of focus radii. This is a consequence the different physical properties of ice and rocks.

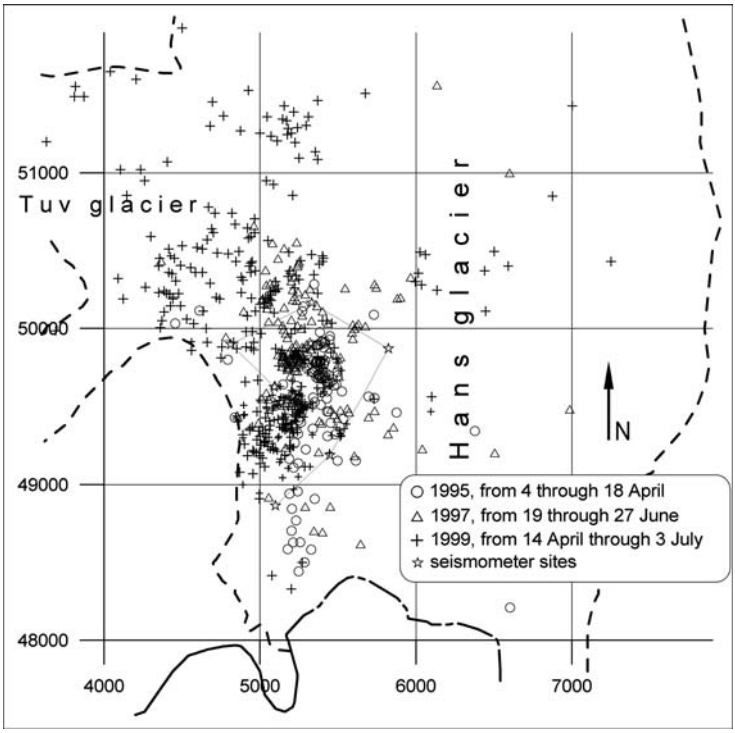

Fig. 15.3 Location of icequake epicentres of three series at the Hans Glacier and seismometer sites. The glacier's margin is marked by a broken line

15.3 Ice Vibrations

Vibration-type events accompany glaciodynamical processes in the main glacier flow area (Fig. 15.4). These vibrations are most probably related

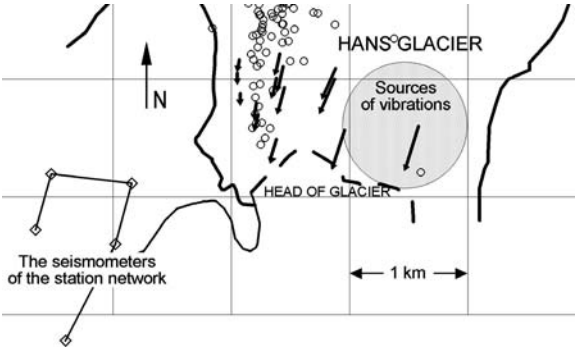

Fig. 15.4 Location of icequakes epicenters (circles) recorded in the Hans Glacier in April 1995 (Górski 1997). Arrows are the vectors of annual glacier motion velocity (Jania 1992)

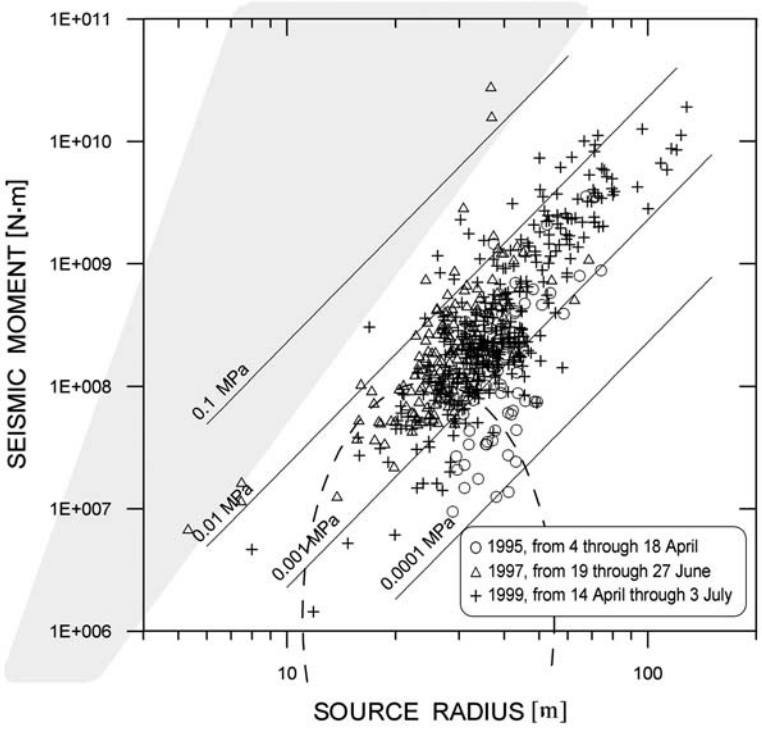

Fig. 15.5 Seismic moment v*s*. source radius. The circles, triangles and crosses mark icequake series recorded in the Hans Glacier. The lines labeled 0.0001, 0.001 and 0.1 MPa represent the respective constant stress drops. The gray area represents the location of groups of various earthquakes and mining tremors in South Africa gold mines, ellipse indicates icequakes recorded in Antarctic shelf glacier

to the processes occurring in the bottom zone of glacier and to displacements of glacier parts due to gravity or uplift forces. Of interest is an analysis of these events in terms of coherent seismic waves in the glacier movement zones (self-organization processes).

Spectral analysis of the recorded vibrations indicates that there exists a relation between their period and the scale of dynamic processes within the glacier (Górski 2004). Spectra of vibration-type seismic events contain characteristic resonance frequencies related to the scale of dynamic processes within the glacier.

The measurements were made with the use of continuous recording and large sampling frequency, which enabled a full interpretation of the generation process of seismic events in the glacier, those of vibration-type in particular. The recordings made from April to August 2002 by an array of seismometers placed directly on surface of the Hans Glacier enabled us to fairly accurately locate the vibration-generating area. In Fig. 15.4 this area is shaded. The major part of the analysed material are the records of seismo-glacial events at the Hornsund station. Owing to the refinement of digitalisation of analog seismograms, a valuable comparative material was obtained from the vibration seismograms recorded by one of the authors at Huron Glacier of the Antarctic Peninsula (Fig. 15.6). Vibrations recorded at the Hans Glacier in Spitsbergen are shown in Fig. 15.7. Vibrations recorded at the Hans Glacier in Spitsbergen are also compared to the events of the same type recorded at Pasterze Glacier in the Alps (Fig. 15.8).

15.3.1 Relation between rotation/tilt phenomena and the Pasterze Glacier seismic events

Measurements on the Pasterze Glacier, Austria, have been performed by means of one rotation seismograph system in September 2003, and two such systems in September 2005. Each of the systems consists of two vertical seismometers (Fig. 15.9), their horizontal pendulums being aligned in opposite directions. Such a pair permits to record vertical displacements, and also a rotation/tilt around horizontal axis, as the difference between records from two separate sensors (cf. Chapter 14 by Teisseyre KP and Suchcicki, and Chapter 33 by Wiszniowski). The two systems were oriented perpendicularly enabling to record rotations around two independent horizontal axes. Each of the rotation/tilt motions is a complex one: it is a sum of the spin and twist motions (see Chapters 3 and 4) and also may include the tilt variation component. We have no separate source of knowledge about variations of the glacier's surface tilt below the recording systems, so the signal differences are referred to **the rotation/tilt motion**.

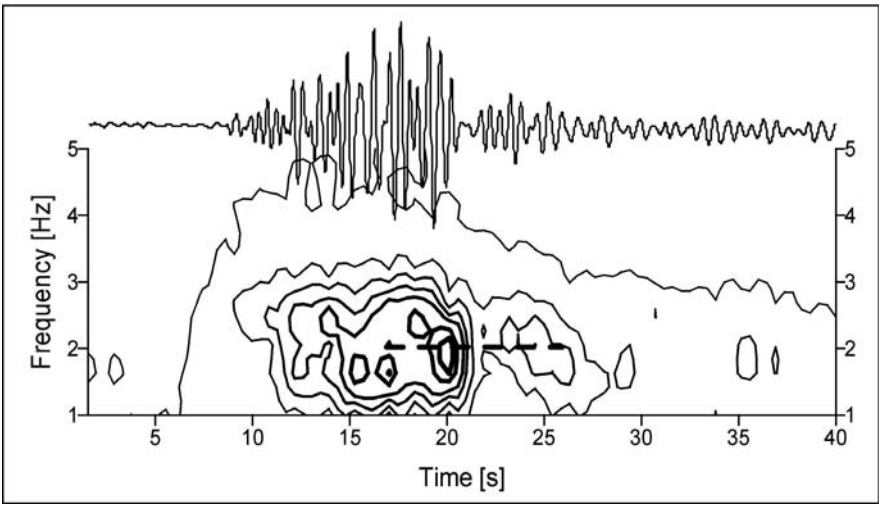

Fig. 15.6 Ice vibration event recorded on the Huron Glacier at 03:15 on 15 January 1991. The displacement seismogram recorded on the glacier is shown on top. The lower diagram presents the isolines of the spectrum; broken line denotes the dominant frequency

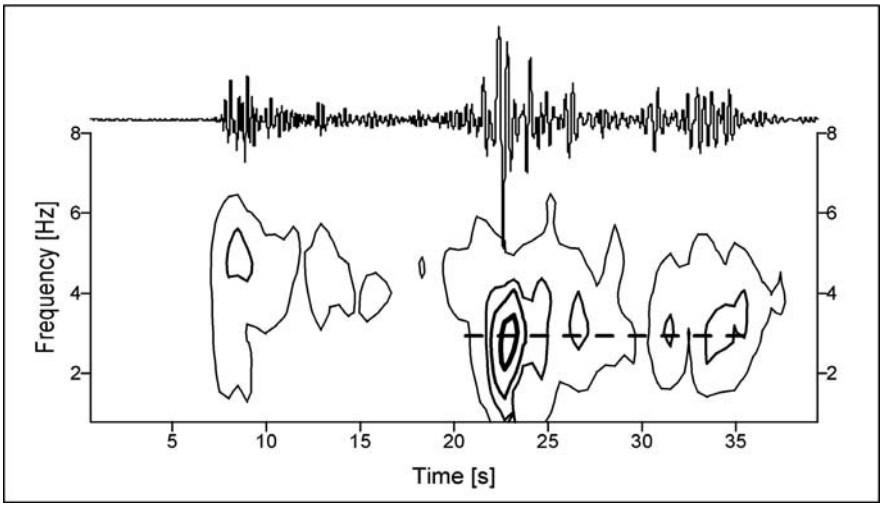

Fig. 15.7 Ice vibration event recorded on the Hans Glacier at 06:35 on 21 August 2002. The displacement seismogram recorded on the glacier is shown on top. The lower diagram presents the isolines of the spectrum; broken line denotes the dominant frequency

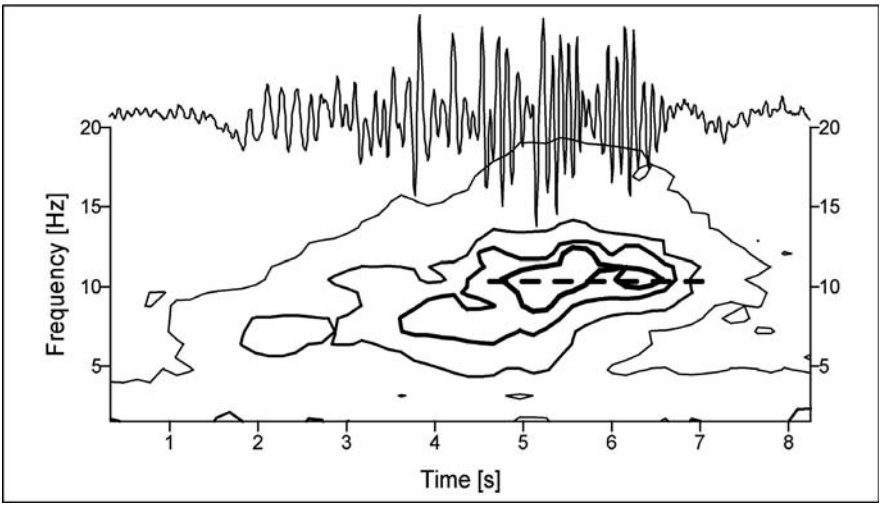

Fig. 15.8 Ice vibration event recorded on the Pasterze Glacier at 00:53 on 30 September 2003. The displacement seismogram recorded on the glacier is shown on top. The lower diagram presents the isolines of the spectrum; broken line denotes the dominant frequency

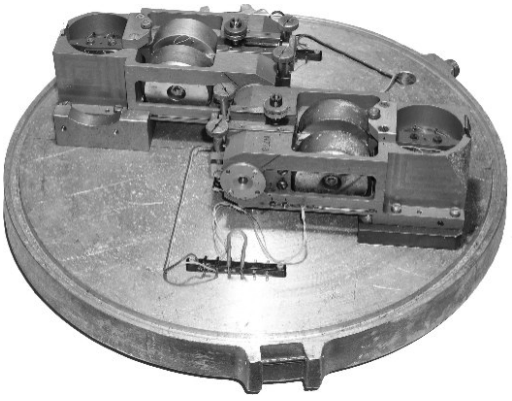

Fig. 15.9 Horizontal rotation system constructed from two vertical seismometers suspended on a common axis and aligned in the opposite directions (construction: J. Suchcicki, see Wiszniowski et al. 2003; phot.: A. Skrzyński)

The rotation/tilt phenomena recorded on the Pasterze Glacier indicated a distinct activity observed during the whole recording experiment.

For analysis of seismic events, we have chosen single tremors and in some cases two or more tremors; the total number of analysed cases is 39. We estimate that from the data collected in 2005, most of the usable se-

quences were taken into account; those with a high noise level were excluded from further study.

The recorded displacement velocities are called **initial data**, in contrast to the **differential data**, which mean the rotation/tilt. Differential data are defined as the differences between the filtered signals from two parallel but oppositely oriented pendulum sensors, divided by the reduced distance between them.

The maximum amplitudes of the displacement velocity for a given shock were generally in the range of 1.8-26 μm/s; two smaller events were included, which will be mentioned later.

An analysis of results shows that on the surface of glacier the relation between seismic displacement oscillations and the differential motions is complex (it seems to be much more complex than in rock media); the records show an almost constant rotation/tilt activity related to the glacier responses to the accumulated strains caused by glacier deformations and flow.

Studying the diagrams containing both the initial and differential data, we have distinguished several types of glacier responses revealing different correlations between the initial and differential data:

- an almost perfect correspondence: the seismic event is clearly seen both in the plots of the initial data and of differential ones; the influence of noise is negligible;
- a good agreement: the event is still clearly visible on the differential components, but the influence of noise is high;
- in one of the differential signals, the seismic event may be distinguished with ease, while in the other it is not so;
- in differential signals, the seismic events are invisible, or at least hard to find.

As mentioned above, the glacier seismic events include the icequakes and the ice vibrations (see Figs. 15.1 and 15.2). Typical examples of analysed cases including vertical displacement velocities and rotation/tilt motions are shown in Figs. 15.10–15.15. From the initial recordings, only two channels are shown, because channel V2 is visually indistinguishable from V1, and V4 from V3. The initial data are always shown unfiltered.

In general, stronger seismic events are characterized by rather good agreement between vertical displacement velocities and the shape of differential data; the three strongest events belong to the first type. Their maximum amplitudes were 26 μm/s, 20 μm/s and 18 μm/s; the fourth reached an amplitude of 14 μm/s which was found also in two cases of worse initial-differential data correspondence. On the average, stronger

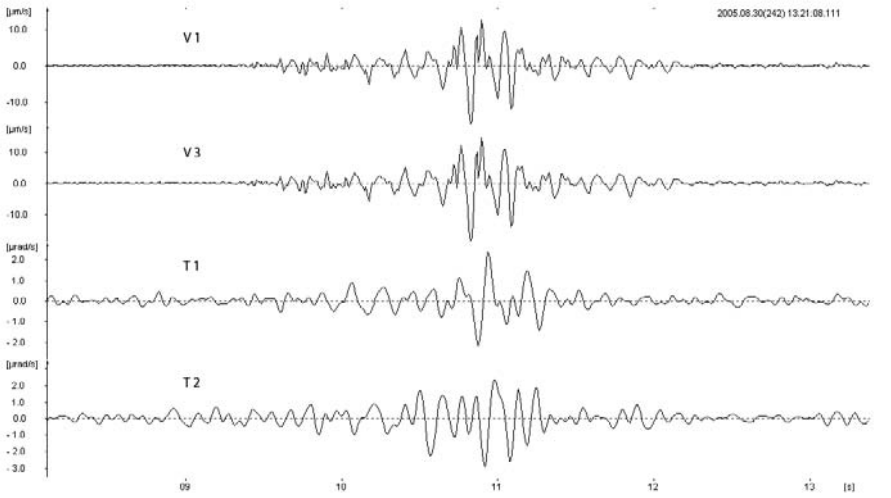

Fig. 15.10 Event on the Pasterze Glacier, 30 August 2005, 13:21. Channels V1 and V3 present the vertical displacement velocities; channels T1 and T2 present rotation/tilt motions around two horizontal axes

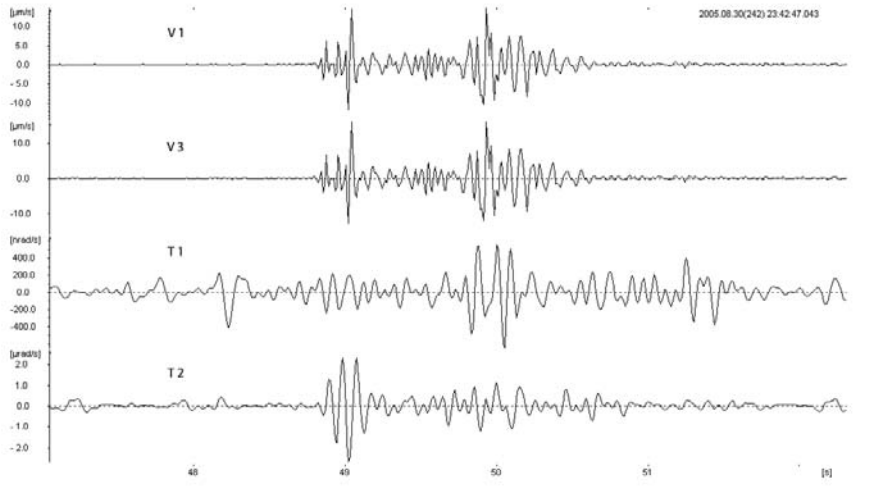

Fig. 15.11 Event on the Pasterze Glacier, 30 August 2005, 23:42. Channels V1 and V3 present the vertical displacement velocities; channels T1 and T2 present rotation/tilt motions around two horizontal axes

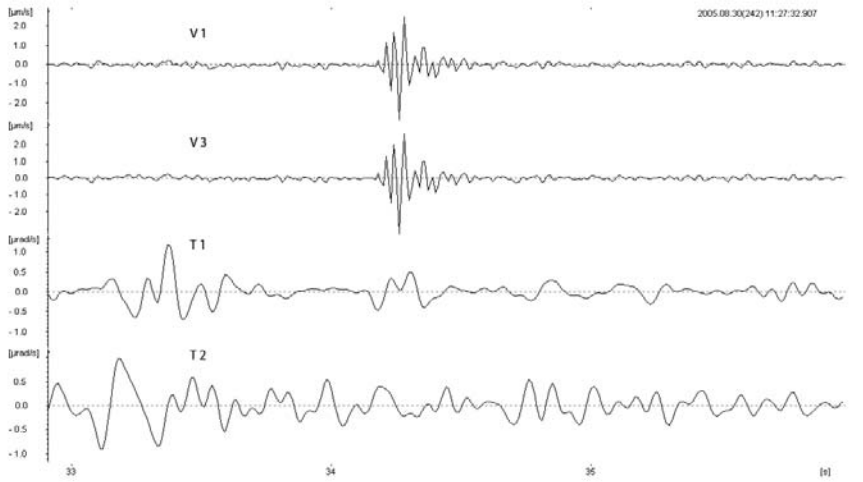

Fig. 15.12 Event on the Pasterze Glacier, 30 August 2005, 11:27. Channels V1 and V3 present the vertical displacement velocities; channels T1 and T2 present rotation/tilt motions around two horizontal axes

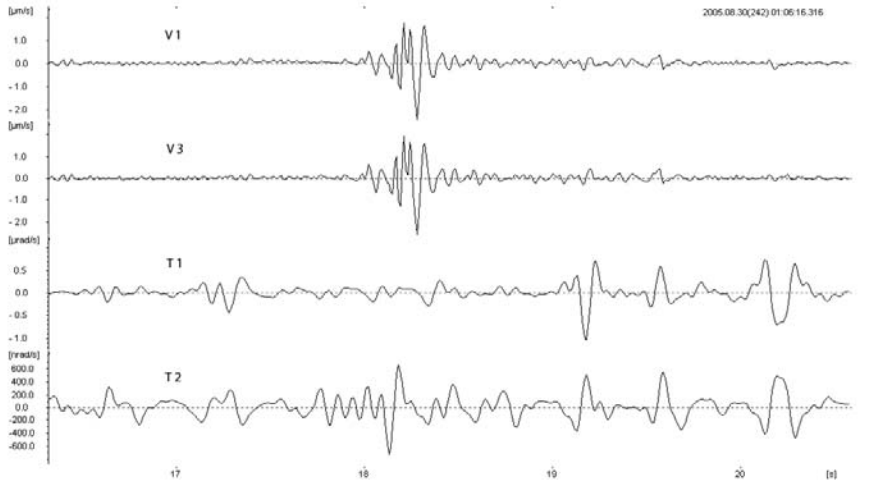

Fig. 15.13 Event on the Pasterze Glacier, 30 August 2005, 01:06. Channels V1 and V3 present the vertical displacement velocities; channels T1 and T2 present rotation/tilt motions around two horizontal axes

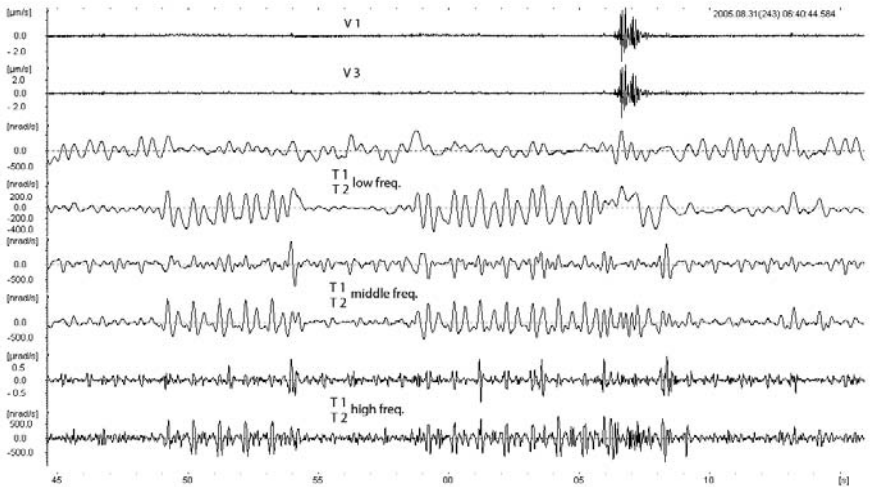

Fig. 15.14 Event on the Pasterze Glacier, 31 August 2005, 06:41. Channels V1 and V3 present the vertical displacement velocities; channels T1 and T2 present rotation/tilt motions around two horizontal axes for the 0-3, 1-5 and 3-15 Hz frequency ranges

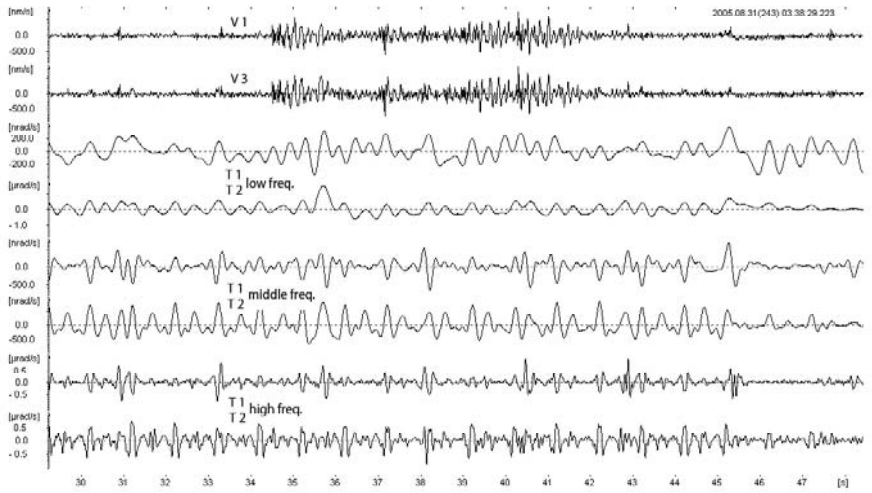

Fig. 15.15 Pasterze Glacier, 31 August 2005, 03:38. Seismic event of long-time, low-amplitude, ascribed to the ice vibration class. Differential motion curves are poorly correlated with those of the displacement motions. Channels V1 and V3 present the vertical displacement velocities; channels T1 and T2 present rotation/tilt motions around two horizontal axes for the 0-3, 1-5 and 3-15 Hz frequency ranges

events contain a relatively smaller contribution of the rotation/tilt motions, when analysed in the higher frequencies range.

All initial data were pass-band filtered in the 3-15 Hz range. Ten cases were analysed also in the 0.3-3 Hz range and additionally in the 1-5 Hz range (Figs. 15.14 and 15.15); these cases were chosen because a high content of low frequency undulations was visible in the initial data. Cases shown in Figs. 15.14 and 15.15 belong to this group, other cases were analysed only in the higher-frequency part of the spectrum.

In many cases, curves showing rotation/tilt correspond to the curves of initial data, especially for the strongest seismic events. Weaker seismic events, and probably those which occurred at a greater distance from the measuring site, showed more varied differential motions, as compared to the initial signals.

Icequakes of short-duration recorded at a close distance revealed a poor agreement of rotation/tilt motions with the initial data presenting displacement motion (see Fig. 15.14). This is especially marked in low frequencies.

For all the cases analysed in low frequencies, differential motions appear smaller than those obtained in an analysis in high frequencies, and bear less resemblance to the displacement motions.

In order to make more precise analysis, we have calculated indexes R_1 and R_2 for a given interval, showing relation between mean rotation/tilt motion (squared) and the mean filtered displacement motion (squared), for each seismometer pair separately:

$$R_1 = \frac{\Sigma T_1^2}{\Sigma \bar{U}_1^2}, \qquad R_2 = \frac{\Sigma T_2^2}{\Sigma \bar{U}_2^2},$$

where

$$T_1 = \frac{|V_1 - V_2|}{2l_0}, \qquad T_2 = \frac{|V_3 - V_4|}{2l_0},$$

$$\bar{U}_1 = \frac{|V_1| + |V_2|}{2}, \qquad \bar{U}_2 = \frac{|V_3| + |V_4|}{2},$$

V_i are the displacement velocities recorded with separate sensors and $2l_0$ is the reduced distance between two sensors within a pair. Such indexes are compatible with the ratio R used in the analysis of data collected at the Pasterze Glacier in 2003 (Teisseyre KP et al. 2004.). These indexes were calculated for each of analysed cases, and always the case included the time interval of the seismic event and some short intervals before and after

it. For presentation purposes, somewhat longer time-windows are shown in Figs. 15.14 and 15.15.

Our analysis with the help of the calculated indexes R_1 and R_2 reveals that for higher frequencies the indexes decrease with increasing displacement motions. This is shown in Fig. 15.16, together with a positive correlation between maximum rotation/tilt amplitudes and those of the displacement velocities. For low frequencies, no such correlations were found (see Fig. 15.17).

Indexes R_1 and R_2 calculated for the frequency range 3-15 Hz lie generally in the range 0.07-2.6. Differences between R_1 and R_2 are in many cases large. The strongest event, that of 26 μm/s amplitude, was analysed only in this higher-frequency part of the spectrum; indexes calculated for this case are amongst the lowest: $R_1 = 0.18$; $R_2 = 0.32$. The indexes calculated for low frequencies (0.3-3 Hz) are more uniform for each case; they lie in the range of 1.1-7.6.

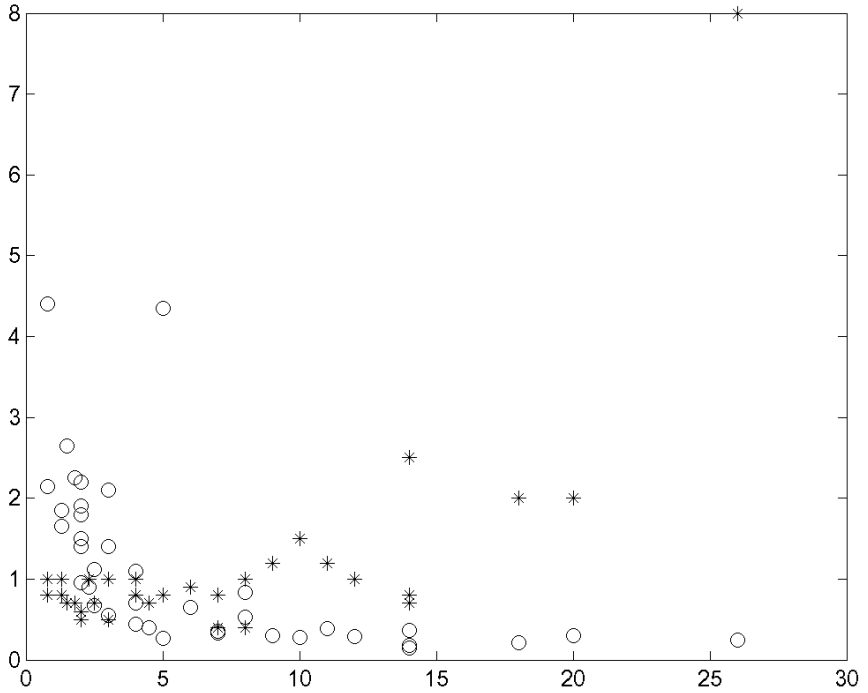

Fig. 15.16 Maximum amplitudes of displacement velocity signals *vs*. maximum amplitude of differential signal in μrad/s (asterisks), and mean value of R_1 and R_2 (circles). Pasterze Glacier, 2005; data analysed in the 3-15 Hz range

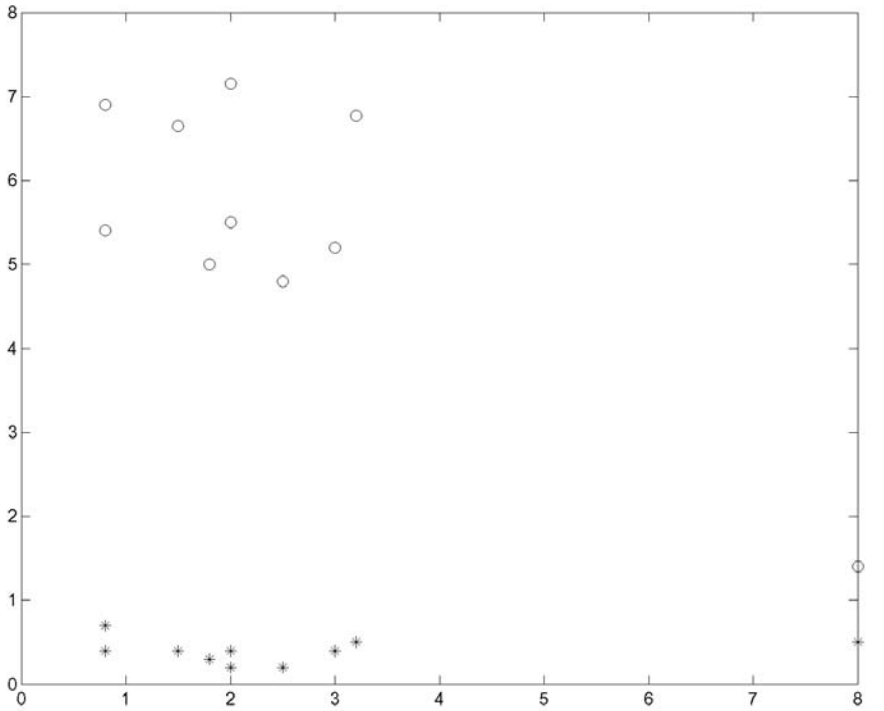

Fig. 15.17 Maximum amplitude of the displacement velocity signals signals *vs*. maximum amplitude of differential signal in μrad/s (asterisks), and mean value of R_1 and R_2 (circles). Pasterze Glacier, 2005; data analysed in the 0.3-3 Hz range

Two events clearly stand out; these are the smallest ones, whose maximum amplitudes were about 0.8 μm/s while the neighbouring noise was reaching 0.1-0.2 μm/s. In the first of these cases, the indices for higher frequencies are the greatest: $R_1 = R_2 = 5.4$; for low frequencies we obtained $R_1 = 6.7$ and $R_2 = 6.6$. The second event, which occurred 37 minutes later, also shows a large content of rotation/tilt motions, as the indices are again relatively large: $R_1 = 1.9$, $R_2 = 2.4$, and for low frequencies $R_1 = 6.4$, $R_2 = 7.3$.

We must remember that each time the window selected comprised, beside the recording of the event, also a certain sequence of just noise, before and after the seismic event. This noise might influence the results to some extent; on the other hand, the rotation/tilt activity appears frequently in the time periods without icequakes.

Similar index R, calculated for some analysed cases belonging to the data collected on the Pasterze Glacier in 2003 (Teisseyre KP 2004), are

several times smaller. Maybe, the wider spectrum of those analysed data is the cause of such a profound difference, but this requires further research.

15.3.2 Transient quiescence in rotation motion or a variable geometry?

The lack of distinct correspondence of differential motions with the initial data, revealed in many cases, is worth consideration. Let us assume that this disagreement between the curves is systematic. Indeed, in many such cases some strong fluctuations are seen on rotation/tilt plots before and after the seismic event, and they might well be related to the event. Also, a marked difference between two rotation/tilt channels and a certain quiescence in these channels is seen, being more visible in one of them (to emphasise this, the same case was shown in Fig. 15.14, with the frequency ranges for rotations/tilts: 0-3, 1-5, and 3-15 Hz).

We find two possible explanations. First, rotational noise is usually present in the creeping glacier; these tiny motions facilitate the flow. When they are in a certain area blocked for some reason, the stress reaches higher values and an icequake occurs. This would be similar to the well-known seismic quiescence in a tectonically active region, but in a much shorter time scale. In this explanation, the above-mentioned special undulations before and after the icequake would be the signs of blocking and unblocking of the creep-and-rotation activity in the area.

Such a hypothesis assumes that the curve of differential motions reflects the preseismic activity in the focus lying at a small distance from the measurement site. These fluctuations might be a sign of preparation for rupture or slip process, and after the event they result in smaller motions in the focal area; during the seismic event itself, the majority of rotation/tilt motions becomes only two-dimensional, and this may be also the reason why rotational waves have a relatively smaller amplitude at this moment.

More precise analysis, using several time windows (before, during, or after the shock) would probably enlighten the problem of disagreement between initial and differential motion curves, so often observed in the research at glaciers. We have made the first attempt: we calculated indexes R_1 and R_2 once more for two already investigated cases (Figs. 15.14 and 15.15), but not for the same time intervals as previously, but in four or six time-windows separately. Two time-windows were chosen for periods of noise. In the first case, the seismic event was relatively short (see Fig. 15.14) and was taken into analysis as a whole. In the analysis of the second case (see Fig. 15.15), the seismic event was divided into three parts of equal length. The last time-window was used to analyse the period just

after the seismic event. In each time-window, indexes R_1 and R_2 were calculated for two spectral ranges: 0.3-3 and 3-15 Hz. For low frequencies, all the obtained indices lie in a very narrow range: 4.9-7.8. For higher frequencies, the time interval when the shock was visible in initial data differs from time intervals before and after the seismic event. In the first case, $R_1 = 0.27$ and $R_2 = 0.5$ for the event and outside the seismic event these indices were in the range 4.6-5.8. In the second, ice-vibration case, during the shock these indices appeared to be in the range of 1.05-1.78, and for time outside the seismic shock the range was 3.6-5.9. Therefore we may conclude that (a) the relative weakness of high-frequency differential motions during the seismic event is proved, (b) the long-duration seismic event of the ice vibration character appeared to be similar to other events, despite its resemblance to the exaggerated noise (whatever it might be). Such conclusions are in agreement with the general picture seen in Figs. 15.16 and 15.17.

15.4 Discussion

The results obtained show that in glaciers we observed probably more complex relations between the seismic events (icequakes and vibrations) and rotation/tilt phenomena. The rotation/tilt phenomena have always been present at the investigated glaciers. They may be signs of the ice flow. However, also opposite interpretation may be true: these tiny movements may facilitate the creep. Even the character of rotational/tilt noise, so often different for different orientations of sensors, also points to the complexity of seismic field at glaciers surface; such a complexity would be hard to detect with single sensors.

Seismic events in ice are also rich in rotational compounds, especially at low frequency range (0-5 Hz). The differential data, calculated for many sensors, bring new information on the complex glacier responses to stress.

To obtain deeper knowledge of dynamic processes occurring in the glacier, more systems to record rotational/tilt data should operate on it simultaneously. Probably this would also help to refine some methods of analysis.

We shall notice that the rotation/tilt activity might be different in cooler glaciers. It is also possible that the same or similar phenomena associated with relations between the glacier rotation noise and glacier flow exist in the tectonic regions of Earth's crust and mantle. In the case of rocks, such a flow-related noise would be limited only to very low frequencies and would be detectable only with instruments of a very high sensitivity. How-

ever, at deep parts of the seismotectonic regions, at elevated temperatures, the situation might be again similar to that in glaciers.

Acknowledgement. Part of visual analysis and calculations has been done with the help of computer programs and procedures written by Jan Wiszniowski (including time corrections).

References

Abercrombie R, Leary P (1993) Source parameters of small earthquakes recorded at 2.5 km depth, Cajon Pass, Southern California: Implication for earthquake scaling. Geophys Res Lett **20**: 1511-1514

Górski M (1997) Seismicity of the Hornsund region, Spitsbergen: icequakes and earthquakes. Publs Inst Geophys Pol Acad Sci **B-20**: 308, 1-77

Górski M (2003) Icequakes in Hans Glacier, Spitsbergen: source parameters of icequake series. Acta Geophys Pol **51**: 4, 399-407

Górski M (2004) Predominant frequencies in ihe spectrum of ice-vibrations events. Acta Geophys Pol **52**: 4, 457-464

Jania J (1992) Some results of glaciological research – Hansbreen. In: Field Workshop on Glaciological Research in Svalbard, University of Silesia, V/19-V/34

Lewandowska H, Teisseyre R (1964) Investigations of the ice microtremors on Spitsbergen in 1962. Biul Inf Komisji Wypraw Geof PAN 37: 1-5

Osten-Woldenburg H (1990) Icequakes on Ekstrom ice shelf near Atka bay, Antarctica. J Glaciol **36**: 31-36

Teisseyre KP, Górski M, Suchcicki J (2004) Seismic events and rotation waves in the Hans Glacier, Spitsbergen, and Pasterze Glacier, Austria. Acta Geophys. Pol. **52**: 4, 465-476

Wiszniowski J, Skrzyński A, Suchcicki J (2003) Recording rotations with a pendulum seismometer: A sensor with reduced sensitivity to linear motions. Acta Geophys Pol **51**: 4, 433-446

16 Rotational Energy and Angular Momentum of Earthquakes

Eugeniusz Majewski

Institute of Geophysics, Polish Academy of Sciences
ul. Księcia Janusza 64, 01-452 Warszawa, Poland
e-mail: emaj@igf.edu.pl

16.1 Introduction

Motions in the earthquake source can be translational, rotational, rolling, vibrational, and rocking. The importance of the study of rotational motions occurring in the earthquake source stems from the fact that these motions may provide information regarding the structure as well as energy states of the source. This chapter estimates a rotational energy generated by rotational motions in the earthquake sources. We derived here general expressions for rotational energy of an earthquake in terms of dimensions of the earthquake source and of the total slip on the fault. In addition, the angular momentum generated in the earthquake source was considered.

16.2 Modelling the Rotational Motions Excited in Earthquake Sources as Rolling Motions

We consider here a simple model of an earthquake source composed of two tectonic plates and a large, round fragment of rock (shaped as a solid cylinder) between them. The tectonic plate A moves from right to left, but the tectonic plate B stays at rest. At the same time, the large, round fragment of rock rolls from right to left. The rolling motion of the solid cylinder is a combination of purely translational and purely rotational motions. The rotation of the largest fragment of rock is conveyed to other, smaller rock fragments that rotate as well. Thus, in the earthquake source there are many rotating fragments of rocks that are the sources of seismic rotation waves. Figure 16.1 shows the schematic picture of a simple model of a rolling motion in the earthquake source.

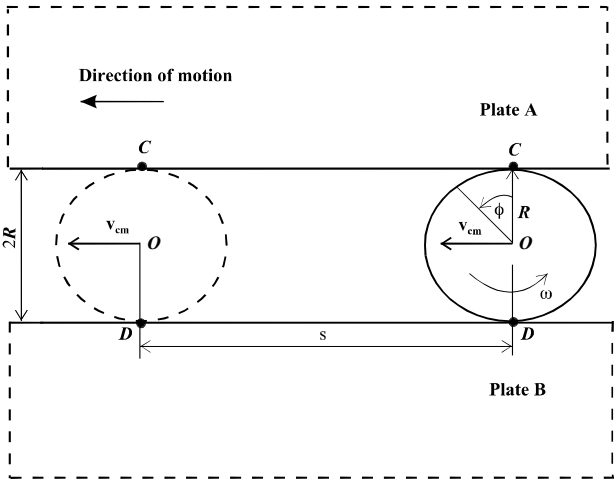

Fig. 16.1 A simple model of rolling motion generated in the earthquake source. Due to the motion of tectonic plate A during an earthquake, the round fragment of rock shaped as a cylinder rolls from right to left. We assume here that plate B is at rest. The rolling motion is a combination of a translational motion over a distance *s* and a pure rotation in the counterclockwise direction

16.3 Rolling in the Earthquake Source as Translation and Rotation Combined

Our starting point in exploring the rotational energy is to assume a rolling motion in the earthquake source. Here we consider only a solid rock cylinder that rolls smoothly along a tectonic plate surface; that is, the cylinder rolls without slipping or bouncing on the plate surface. Note that the center of the cross-section of the cylinder moves along a straight line parallel to the plate surface. A point on the cylinder's rim moves along a curve called a cycloid. However, we can treat this motion as a superposition of translation of the cylinder's central axis and rotation of the rest of the solid cylinder around that axis. If we observe the cross-section of the cylinder in Fig. 16.1 as it rolls along the tectonic plate, we can see the center of mass *O* of the circle (cross-section of the cylinder) moves from right to left at constant speed v_{cm}. The point *D* on the plate B where the circle makes contact with the plate surface also moves from right to left at speed v_{cm} , so that point *O* remains directly above point *D*. During a time interval *t*, both *O* and *D* move from right to left by a distance *s*. We assume here that this distance is equal to the total tectonic slip on a fault during an earthquake.

The cylinder rotates through an angle ϕ about central axis, with the points of the cylinder that were touching the plate B at the beginning of t moving through arc length s. We can express the arc length s in terms of the rotation angle ϕ:

$$s = \phi R \ , \tag{16.1}$$

where R is the radius of the solid cylinder. The linear speed v_{cm} of the center of mass of this uniform cylinder is $\mathrm{d}s/\mathrm{d}t$. The angular speed ω of the cylinder about central axis is $\mathrm{d}\phi/\mathrm{d}t$. Thus, differentiating Eq. (16.1) with respect to time yields

$$v_{cm} = \frac{\mathrm{d}\phi}{\mathrm{d}t} R = \omega R \ , \tag{16.2}$$

where ω is the angular speed of the cylinder.

Every point on the cylinder rotates about central axis with angular speed ω. Bearing in mind that the motion of the cylinder rolling smoothly over a plate surface can be decomposed into purely rotational and purely translational motions, we can observe that the bottom part of the cylinder at point D is stationary and the top part at point C is moving at speed $2v_{cm}$, thus twice faster.

16.4 The Kinetic Energy of Rolling in the Earthquake Source

Let us now calculate the kinetic energy of the rolling cylinder in the earthquake source. If we treat the rolling as a pure rotational motion about an axis through the point D on the bottom plate in Fig. 16.1, then we obtain

$$K = \frac{1}{2} I_D \omega^2 \ , \tag{16.3}$$

where I_D is the rotational inertia of the cylinder about the axis through point D, and ω is the angular speed of the cylinder. Using the parallel-axis theorem for the rotational inertia, we obtain

$$I_D = I_{cm} + m R^2 \ , \tag{16.4}$$

where I_{cm} is the cylinder's rotational inertia about an axis through its center of mass (central axis), and m is the mass of the solid cylinder. Combining Eqs. (16.4) and (16.3), we obtain

$$K = \frac{1}{2} I_{cm} \omega^2 + \frac{1}{2} m R^2 \omega^2 \ . \tag{16.5}$$

Using Eq. (16.2) gives the relation

$$K = \frac{1}{2} I_{cm} \omega^2 + \frac{1}{2} m v_{cm}^2 \ . \tag{16.6}$$

The physical interpretation of the first term in the above equation is that it describes the kinetic energy of the cylinder's rotation about an axis through its center of mass, and the second term can be interpreted as the kinetic energy of the translational motion of the cylinder's center of mass.

If we assume that plate B is at rest and only plate A is moving, its speed will be twice larger than the speed of the cylinder's center of mass. The plate's speed equals the time derivative of the slip function, i.e., $\dot{s} = v$. The mass of the cylinder of length h is $m = \pi R^2 h \rho$. Thus, the kinetic energy generated in the earthquake source in terms of the slip rate is as follows:

$$K = \frac{1}{2} \pi \rho h R^4 + 2 \pi \rho h R^2 \dot{s}^2 \ , \tag{16.7}$$

where ρ is the material density of the rock cylinder.

The above formula determines the kinetic rotational energy generated in the earthquake source in terms of the source dimensions and the tectonic slip rate. Here $2R$ is the distance between tectonic plates and h is the length of the rolling cylinder.

When the rock cylinder rolls at constant velocity, it has no reason to slide at the contact point D, and thus the frictional force is zero there. However, when a net force is accelerating or decelerating the rolling motion of the cylinder, then that force generates acceleration a_{cm} of the cylinder's center of mass along the direction of the tectonic fault. It also generates an angular acceleration or deceleration α of the cylinder. These accelerations can generate sliding motions of the cylinder at point D. These motions create a frictional force between the cylinder and the plate at point D. When the cylinder does not slide, the static frictional force $\mathbf{F}_s$ is created, and the cylinder is rolling smoothly. We can then express the magnitude of the linear acceleration a_{cm} in terms of the angular acceleration α by taking a time derivative of Eq. (16.2). Consequently, on the left side of this equation, we obtain $\mathrm{d}v_{cm}/\mathrm{d}t$ that is equal to a_{cm}, and on the right side we obtain $\mathrm{d}\omega/\mathrm{d}t$ that is equal to α. Thus, in the case of smooth rolling we obtain the following relation:

$$a_{cm} = R\alpha \ . \tag{16.8}$$

When the cylinder slides and the net force is not zero, then the kinetic frictional force $\mathbf{F}_k$ acts at point D. In such a case, the motion is not smooth rolling, and Eq. (16.8) is not valid for this motion. The kinetic frictional force will be discussed in Section 16.6.

16.5 Modelling Purely Rotational Motions in the Earthquake Source

Now let us consider a model of purely rotational motions in the earthquake source depicted in Fig. 16.2. Particularly, one can infer spin motions of the solid cylinder (Teisseyre 1973, 2004). We can also imagine such a situation that both tectonic plates will move in opposite directions and oscillate along the fault at the same time. During such a process, the tectonic plates vibrate in the opposite directions and the cylinder is in a twist motion. We can combine these two simple motions of tectonic plates together and obtain a resulting motion of the cylinder with two components: twist and spin motions.

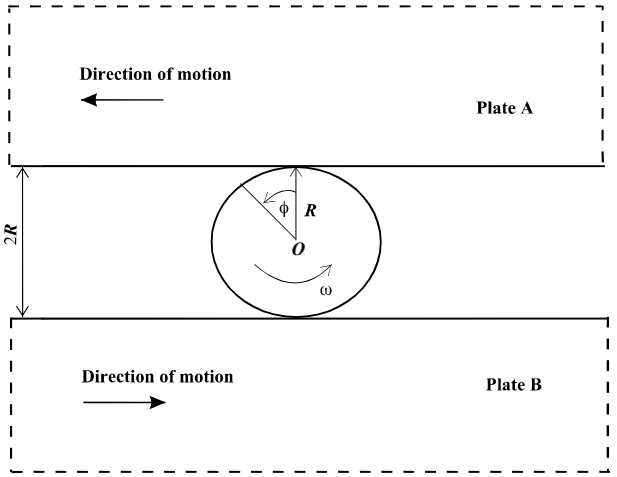

Fig. 16.2 A model of purely rotational motions generated in the earthquake source. Due to the motion of tectonic plates A and B in opposite directions during an earthquake, the round fragment of rock shaped as a cylinder rotates counterclockwise. This situation corresponds to spin motions of the rotating cylinder. If the tectonic plates move back and forth, then the cylinder may have twist motions

16.6 The Torque and Angular Momentum of the Earthquake Source

The torque is equal to the vector representing the cylinder's diameter perpendicular to the plate cross the kinetic frictional force between the cylinder and a tectonic plate:

$$\boldsymbol{\tau} = 2\mathbf{R} \times \mathbf{F}_k \ . \tag{16.9}$$

We can also write that $\tau = I_{cm}\,\alpha$. The angular momentum of the solid rock cylinder about central axis can be expressed as

$$M = I_{cm}\,\omega = \frac{1}{2} m R^2 \omega = \frac{1}{2} \pi \rho h R^4 \omega \ . \tag{16.10}$$

Since we use the solid rock cylinder to model rotations in the earthquake source, the magnitude of the seismic angular momentum generated in the source is as follows:

$$M = \frac{1}{2} \pi \rho h R^4 \omega \ . \tag{16.11}$$

For 3D space rotation, the dynamical law corresponding to the law $\mathbf{F} = \mathrm{d}\mathbf{p}/\mathrm{d}t$, is that the torque vector is the rate of change with time of the angular momentum vector

$$\boldsymbol{\tau} = \mathrm{d}\mathbf{M} / \mathrm{d}t \ . \tag{16.12}$$

If we take a vector sum of all external torques over all grains or blocks in the earthquake source, the external torque acting in the source is the time rate of change of the total angular momentum:

$$\boldsymbol{\tau}_{ext} = \mathrm{d}\mathbf{M}_{total} / \mathrm{d}t \ . \tag{16.13}$$

For a rotational motion in the source, one can calculate the work

$$W = \int_{\phi_1}^{\phi_2} \tau \, \mathrm{d}\phi \ . \tag{16.14}$$

Consequently, one can find the power P for rotational motion in the earthquake source as

$$P = \dot{W} = \tau \dot{\phi} = \tau \omega \ . \tag{16.15}$$

16.7 Modelling Rotational Motions in the Earthquake Source as a Turbulence of Grains and Blocks Between Moving Tectonic Plates

Now let us model the rotational motions in the earthquake source as turbulence of grains and blocks between moving tectonic plates. This model is depicted in Fig. 16.3. Such an approach will allow us to look at the problem of rotational energy from a broader perspective. The turbulent flow is in general rotational. We can describe turbulence in the framework of a micropolar theory of fluent media (Eringen 1966, 2001). It was found that there is some correspondence between plastic flow of solids and motions in micropolar fluids. Our aim is to estimate the angular momentum of such a turbulent motion of grains and blocks in the earthquake source.

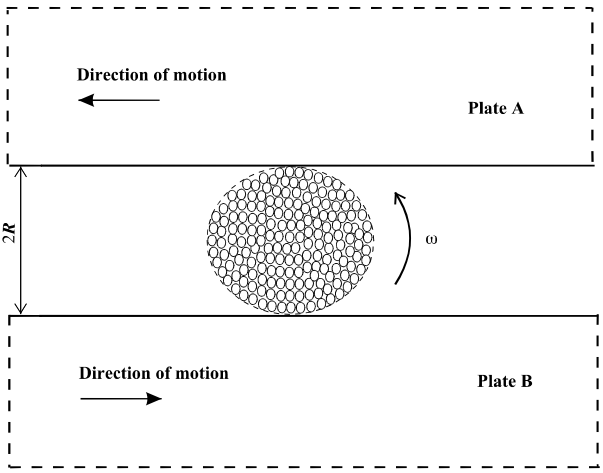

Fig. 16.3 A model of rotational motions in the earthquake source as a turbulence of grains and blocks between moving tectonic plates. The grains and blocks rotating counterclockwise at the angular speed ω form the vortex

In order to describe turbulence, we have to consider the problem at two levels: macroscopic and microscopic (Teisseyre and Majewski 2001, 2002, Nikolaevskiy 2003). Thus, we need two linear scales: the external scale L, and the internal scale Λ. We also need to consider a macrovolume ΔV and a microvolume dv. The macrovolume and microvolume are displayed schematically in Fig. 16.4. The equations describing the microscopic level are usually differential equations. A complete description of turbulence requires a separate set of equations for the description at the microscopic

level and another set of equations describing processes at the macroscopic level. The key idea here is that a small eddy (an element of turbulent mesostructure) reveals its own dynamics as a structure element rotating at its own spin velocity. In order to describe the behaviour of such a system of rotating objects, one has to formulate the angular momentum balance for a macrovolume. This angular momentum is taken about a mass center of the macrovolume ΔV.

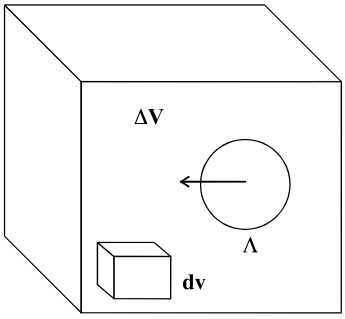

Fig. 16.4 Microscopic and macroscopic levels of description of the turbulence. Here dv denotes the microvolume, and Λ – the internal scale, ΔV – the macrovolume (modified from Nikolaevskiy 2003)

One can write the angular momentum balance in the form (Nikolaevskiy 2003):

$$\frac{\partial}{\partial t}<\varepsilon_{kmn}\rho u_n r_m> + \frac{\partial}{\partial X_m}<\varepsilon_{kmn}\rho u_n r_p u_m>_m + \varepsilon_{kpn}<\rho u_n u_p>_p$$
$$= \frac{\partial}{\partial X_m}<\varepsilon_{kmn}\sigma_{mp} r_p>_p + \varepsilon_{kpn}<\sigma_{np}>_p + <\varepsilon_{kpn} r_p F_n>, \quad (16.16)$$

where $<>$ denotes the average, ε_{kmn} is the Levi-Civita alternating tensor, ρ is the material density, u_i are the velocity components, σ_{mp} are the viscous stress components, F_n are the components of the mass force, x_m and X_m are the microscale and macroscale coordinates, respectively, and $r_m = x_m + X_m$ is a radius-vector relative to the mass center of the elementary volume.

It is assumed that the macrovolume ΔV contains i eddies. The spatial averaged angular momentum of one eddy is defined as

$$< M_k > = < \varepsilon_{kpn}\rho u_n r_p > . \quad (16.17)$$

16.8 Conclusions

This chapter briefly presented a few models of rotational motions in the earthquake source. At first, rolling motions were considered and the kinetic energy of rolling was formulated. The second model deals with purely rotational motions. The kinetic energy, work, power, and angular momentum for this model were expressed in terms of earthquake dimensions and the total tectonic slip on the fault. The third model treats rotational motions in the earthquake source as turbulence of grains and blocks between moving tectonic plates. A general approach to the turbulence was discussed. A balance equation for the angular momentum was shown. An angular momentum for a small turbulent eddy was defined.

References

Eringen AC (1966) Theory of micropolar fluids. J Math Mech **16**: 622-729

Eringen AC (2001) Microcontinuum field theories, II: Fluent media. Springer, New York

Nikolaevskiy VN (2003) Angular momentum in geophysical turbulence. Kluwer, Dordrecht

Teisseyre R (1973) Earthquake processes in a micromorphic continuum. Pure Appl Geophys **102**: 15-28

Teisseyre R (2004) Spin and twist motions in a homogeneous elastic continuum and cross-band geometry of fracturing. Acta Geophys Pol **52**: 173-183

Teisseyre R, Majewski E (eds) (2001) Earthquake thermodynamics and phase transformations in the earth's interior. Academic Press, San Diego

Teisseyre R, Majewski E (2002) Physics of earthquakes. In: Lee WHK, Kanamori H, Jennings PC, Kisslinger C (eds) International handbook of earthquake & engineering seismology, Part A. Academic Press, San Diego, pp 229-235

17 Bend-Rotation Wave as a Mechanism of Macroseismic Effects

Vladimir Aksenov

Institute of Physics of the Earth, Russian Academy of Sciences
Bolshaya Gruzinskaya str., 10, Moscow, Russia
e-mail: aksenovv1@yandex.ru

17.1 Introduction

Instrumental measurements in epicentral zones of earthquakes and especially on outcropped faults are still relatively rare. This also concerns macroseismic observations during strong earthquakes. Issues regarding faulting kinematics, distribution of effective forces, accelerations and other parameters of near-surface seismic process, and, consequently, the focus mechanisms in the case of their outcropping, are still insufficiently studied. Macroseismic observations and measurements that are available show various effects. We put a special attention to the following macroseismic observations: eruption of soil and hard rock with overturning in air; bouncing of heavy blocks with simultaneous shifting 2-5 m aside; overturning of soil and ground blocks with 180º rotation along horizontal axis (Bolt 1978, Nikonov 1992). In Japan, movement of rectangular ledger blocks immediately near a fault formed at the graveyard was noted (Nikonov 1992). It is essential that ledger stones were of standard size, and stood vertically on pins fixed in underlying horizontal slabs; the pins remained undamaged, whereas vertical slabs have been displaced along the fault to the opposite wall of the fault. Hence, not a mere shear movement but slab tossing in air by some angle to the horizon took place.

Interesting data can be found in the publication by Popova (1990). During Kudmdag earthquake (March 14, 1983) in the South-Western Turkmenia, with $M = 5.4$, $I = 8$, and focus depth $h = 3$ km, a 20 km long fault cropped out crossing the settlement built on a plane. Engineering -seismologic study revealed strengthening of shocking force by 0.5-0.7 (comparing to average values for the settlement) in strips along the fault, 150-400 m wide on one side, and 75-200 m wide on the other side of the fault. For earthquakes with high magnitude and intensity, the width of

zones with strengthened impact along outcropping faults increases significantly. So, for earthquakes of epicentral intensity of 9-10, the width of the zone of highest intensity at the fault amounts to 2-6 km (Popova 1990). We draw special attention to the measurements which showed differences with distance in acceleration values recorded by accelerographs; a representative example is here the Rudbar earthquake in North Iran (20 June 1990, $M_s = 7.7$). At this event, a 80-km long fault ripped on the surface in three areas; the left-lateral shifts had the horizontal extent of 0.6 m (maximum), and the vertical extent up to 0.95 m (Berberian et al. 1992). The peak accelerations recorded at different distances from the focus and fault plane are listed in Table 17.1.

Table 17.1 Peak accelerations of the Rudbar event of 20 June 1990

Site	Distance [km]		Acceleration g	
	from epicenter	from fault	vertical	horizontal
Abbar	47	8	0.23	0.65
Kazvin	80	50	0.09	0.19
Abbar	77	75	0.06	0.13
Tonekabon	130	95	0.03	0.11
Karai	182	148	0.03	0.06

It is seen that the values of vertical and horizontal accelerations increase exponentially up to 0.65g when approaching the ripped fault at a distance of 8 km, so that the value of 2g was possibly achieved at the fault's edges. Many authors have noted clear features of non-linearity of intense soil movements in the zone of tectonic faults (Aksenov et al. 1992, 1993, Aksenov and Lokajiček 1997, Li et al. 1994). The following features were observed in all reports:

– low-frequency oscillations (0.4-1.5 Hz),
– high-amplitude monochromatic coherent oscillations,
– low velocity of phase range of 160-180 m/s with duration of up to 5 minutes.

All these three features have been observed only in a zone adjacent to the tectonic fault. Moreover, the distance from the fault walls where the non-linear effects are observed depends on the earthquake magnitude. It is important to note that there is a rather sharp boundary of the space beyond which all non-linear effects disappear (Li et al. 1994). Presentation of

models of mechanisms for all non-linear effects mentioned above, including rupture mechanism, involves many problems. Basing on theoretical works on non-linear dynamics (Lyapunov 1892, Poincare 1928, Mandelshtam 1950, Nicolis 1986), laboratory experiments and field studies, the author suggests a model based on bend-rotation waves as a mechanism of fracturing and macroseismic effects.

17.2 Experimental Data

First of all, it is necessary to select oscillation parameters describing seismic soil movement to investigate dependence of the selected parameters on energy (magnitude), motion or destruction type, and distance from registration point to the tectonic fault. Determination of the mechanism causing macroseismic effects is the foremost issue. The following parameters have been selected as the main oscillation parameters: A – amplitude characterizing the signal intensity; τ – pulse width (the parameter of the assemblage of curves delineating envelope of oscillations); f_0 – dominant frequency (or period) of oscillations; S – spectrum width.

The author used a laser vibrometer with flat characteristic from 0.1 Hz to 0.5 MHz. Models of three types were built, as shown in Fig. 17.1: the barrier model A (fine sandstone, coarse sandstone); the enclosed fault model B (perspex); and the open fault model C (granite).

The barrier model A consisted of a parallelepiped with sides of 20×30×10 cm. On sides, direct cuts at an angle of 45 degrees were made, leaving a barrier of 3 cm in the center. The sample loading was performed along vertical axis until the moment of the barrier destruction. Recording by the laser vibrometer was carried out in the center of the barrier. Figure 17.2 shows time pulse records for model A (tracks 1, 2, 3 – fine sandstone; 4, 5, 6 – coarse sandstone); pulse amplitude spectra are presented below. Tracks 1 and 4 are the typical records of pulses corresponding to beginning of the barrier destruction. Pulses are short, with low amplitude. They have high -frequency spectra. Dominant frequency is hard to isolate. The spectrum width is 60 kHz. We observe a typical interference of waves from independent oscillation sources.

At increasing load (axial pressure P) we obtain different pulse shapes; tracks 2 and 5 and their spectra reflect qualitative transition of the system to another state. Amplitudes, i.e., the signal intensity, increased sharply, as well as the pulse width did. The base frequency of 80 kHz for track 2 is isolated. That for track 5 is 115 kHz. The spectrum width is 10 kHz in both cases. Sidebands are present in the spectra. Such spectra occur in the case

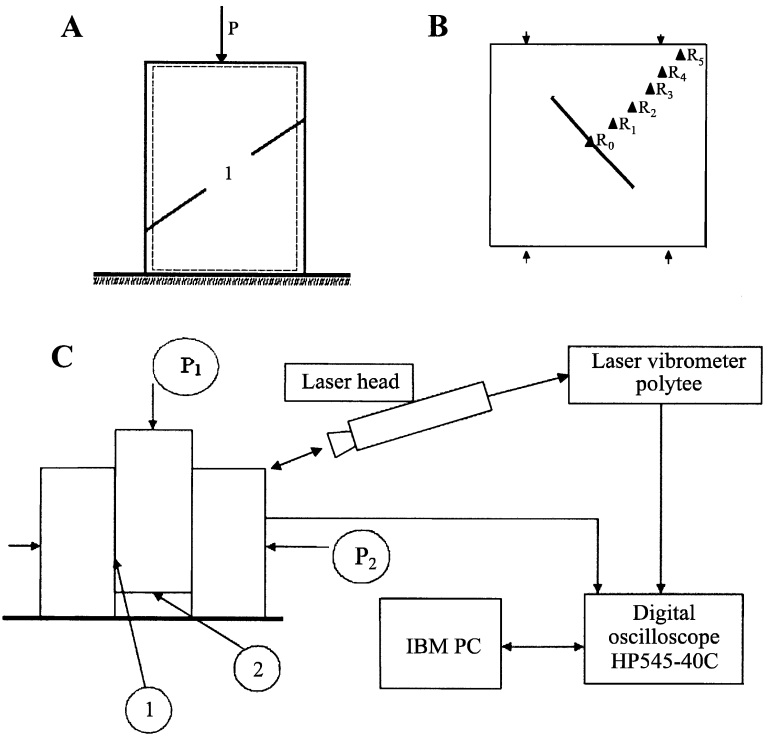

Fig. 17.1 The three models: A – barrier model (P is the axial pressure, 1 denotes the 2D luminous reflectance point); B – enclosed fault model (R_0–R_5 are the 2D luminous reflectance points); C – open fault model (P_1 is the axial pressure, P_2 is the lateral pressure, 1 and 2 are the 2D luminous reflectance points of waves from independent oscillation sources)

of modulated oscillations. Let us consider a simple amplitude-modulated oscillation. Initially, we had oscillations of the carrier frequency: $Y = a_0 \sin(\omega_0 t + \phi_0)$, and a modulating oscillation $1 + mf(t)$, where $f(t)$ is the modulating function, m is the parameter characterizing the affection level. As a result of some operation, called "modulation", both these oscillations are multiplied, yielding: $x = a_0 [1 + mf(t)] \sin(\omega_0 t + \phi_0)$. Then, the carrier frequency is marked in the spectrum, and the modulating frequency is available on sides. This is true for periodic functions only. In case of non-periodic modulating function, i.e., inharmonic oscillations, continuous sidebands will be observed in the spectrum instead of side lines.

Tracks 3 and 6 (further increase of load) are examples of time oscillation records registered before the final destruction of the barrier. The am-

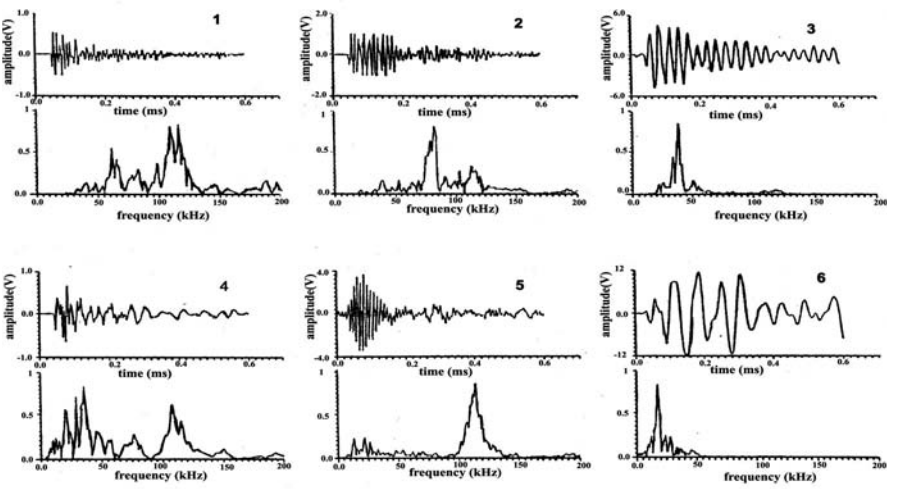

Fig. 17.2 Barrier model A, the wave shapes and spectra. Tracks 1-3 – fine sandstone, tracks 4-6 – coarse sandstone

plitudes and pulse widths are at maximum. The dominant frequency radically shifted to the low-frequency region. The period increases twofold for track 3, and sevenfold for track 6. The width of spectra sharply contracts, thus showing the coherence of oscillations.

The evolution of pulses and their spectra raises a number of questions. Which of the parameters of appearing fault (destruction of the barrier) causes this evolution? This problem can be solved with the help of the theory of nonlinear dynamic systems. As follows from Nicolis (1986), if n independent oscillators with unit amplitude interfere in some point of space, then the total energy is proportional to the sum of energies of each oscillator:

$$W \approx \left|\sum E_i\right|^2 ,$$

$$W \approx \left(\sum_{i=1}^{n} \cos\phi_i\right)^2 + \left(\sum_{i=1}^{n} \sin\phi_i\right)^2 = n + 2\sum_{i\neq j}^{n(n-1)/2} \cos\varepsilon_\sigma , \qquad (17.1)$$

where $\varphi_i - \varphi_j = \varepsilon_\sigma$; for all φ equal (complete coherence), $\varepsilon_\sigma = 0$, and the energy becomes

$$W \approx n + (n-1)n = n^2 . \qquad (17.2)$$

If phases are independent and distributed uniformly, then φ has Simpson's distribution (in the interval from -2π to $+2\pi$), and the energy of incoherent oscillators is

$$W \approx \left\{ n + \sum_{\sigma=1}^{n(n-1)} \cos\varepsilon_\sigma \right\} = n + \frac{n(n-1)}{2\pi} \int_0^{2\pi} \cos\varepsilon_\sigma \mathrm{d}\varepsilon_\sigma = n \ . \qquad (17.3)$$

So, it can be stated that the total energy density is proportional to the second power of the number of oscillators n^2 (coherence) provided that the phases of all n oscillators are equal. If phases of oscillators are random and uniformly distributed over some, 2π long interval, then the total energy density is proportional to the number of oscillators n (incoherence). Thus, if only 10 out of 100 oscillators are coherent, then these 10 oscillators "behave" like the remaining ones, and are able to synchronize the rest of oscillators. Of course, in the most abundant case we deal with time-limited partial coherence.

Enclosed fault model B: In the perspex plate of 15×15×1.5 cm size, a cut was made in the center at an angle of 45º presenting "a fault" of 4 cm length. Under vertical pressure, the "fault" walls shift to opposite sides relative to each other making cyclic motion of the **stick–slip** type. Surface oscillation recording points R_0–R_5 (Z-component) were placed on the straight line perpendicular to the "fault" with spacing of 10 cm. Recorded pulses shape and their spectra are shown in Fig. 17.3. At R_0, a single unipolar pulse is recorded. Noteworthy is the high amplitude of the pulse, its small width, very low dominant frequency (610 Hz) and small width (τ = 0.001 s). The spectrum width is small as well. Typically, a single pulse of arbitrary shape has continuous spectrum within the frequency interval in which the period stays long as compared to the pulse length. At increasing frequency, when the period T becomes comparable with the pulse length τ, function S (spectrum) starts to decrease. As to the spectrum width, according to Mandelshtam (1950), Charkievich (1953), and Nicolis (1986), the bell-shaped pulse exhibits a number of remarkable features. Out of all pulses of random shape, the maximum energy is concentrated in the bell-shaped pulse. Its spectrum width is minimal, i.e. the wave is coherent. In other words, high energy is concentrated in such a pulse in short time interval. Then, at points R_2–R_5 we have ordinary elastic oscillations with wide spectra. R_1 is like a transitional point, and the distance R_0–R_1 can be called the zone of the pulse existence (action) with all the consequences.

The open fault model C consists of three blocks subject to lateral pressure P_2. The medium block makes shear movements under vertical pres-

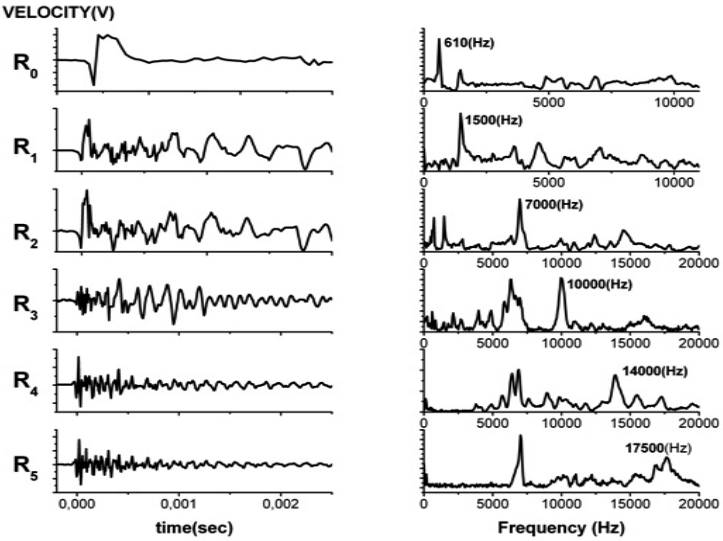

Fig. 17.3 The barrier model B: pulse shapes and their spectra

sure P_1. The objective of the experiment was to thoroughly study physics and "kinematics" of a shear movement. The laser vibrometer recorded oscillations (both velocity and displacement) directly on the contact surface of the "fault", point 1 (see Fig. 17.1).

At point 2 we recorded the total movement of the block relative to the support surface. Shapes of pulses recorded at point 1 (contact surface of the fault wall), and at point 2 (the total displacement of the block) are presented in Fig. 17.4. The shape of pulses approaches the bell-type one. Pulse width amounts to $\tau = 0.01$ s. Thus, the shear movement generates a pulse, and *vice versa*, a bell-shaped pulse generates shear movement. According to Mogi (1985), localization of deformation occurs at fault's walls before shear movement. This local deformation was registered by Mogi (1985) by strain gage; however, the kinematics of the movement itself could not be registered for technical reasons.

Upon combining the results of Mogi and the author's own experiments, we can propose the bend-rotation wave (BRW) model, or, more specifically: *Bend rotation wave as a mechanism of shear movement, macroseismic effect, and ripping of tectonic fault's seam (rapture mechanism)*. Let us consider a flexible thread lying on the support surface. A local deformation occurs due to shear stress (Mogi 1985), see Fig. 17.5. The thread rests on a flat support at its non-deformed sections. The deformation grows up to some value, and then the wave starts motion toward the zone of lower stresses. After moving over some interval ΔX relative to the support

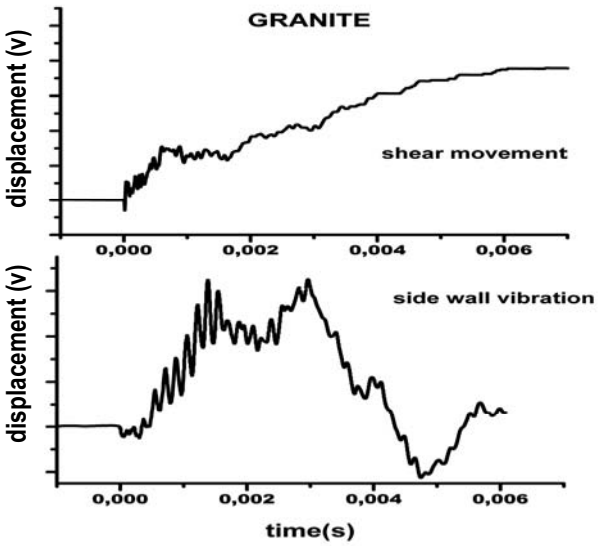

Fig. 17.4 The open fault model C. The upper track – the total movement of the block. The lower track – the pulse recorded on the side of contact surface of the fixed block

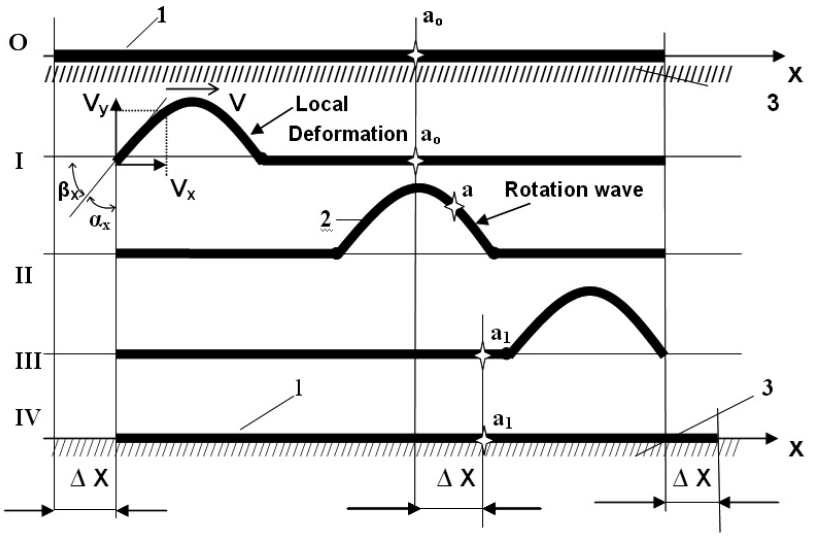

Fig. 17.5 Fracturing process and formation of the bend-rotation wave; motion of an arbitrary point *a* on fracture plane is shown and a final slip ΔX is indicated

surface, it transits to the position a_1 being in resting state. Thus, upon entering the wave, each point of the body makes wave incremental movement and the entire body translates over the support surface.

For better understanding the mass wave transfer as a physical phenomenon, we present the diagram of discreet wave motion of the linear density. Figure 17.6 shows the macroparticle displacements under the influence of a wave of increased density (compression) and a wave of decreased density (tensile). During motion of the wave with increased density, a macroparticle velocity vector v_a coincides with the vector of the wave with decreased density, under the influence of which macroparticle a_i shifts by $+\Delta x_i$. On the other hand, the velocity vector v_a in the wave with decreased density is directed oppositely, and the macroparticle a_i shifts by $-\Delta x_i$. The main feature of this motion is a chain process of small displacements of adjacent particles of the body subjected to the wave propagation. The wave propagates continuously, and the body's particle moves in a pulse manner. Thus, a moving wave (compression or tension) serves as a mechanical transformer of continuous motion into discrete one. Let us show that the de formed section of the thread being in the wave moves without friction relative to the support (Fig. 17.5).

The wave velocity is $V_y = V \sin\alpha_x$, so $V_x = V\sqrt{(1-\cos\alpha_x)^2 + \sin^2\alpha_x}$ at $\alpha_x \to 0$, $V_x = 0$; $V_y = V$, i.e., when the wave leading edge enters, point a_0 has a velocity whose vector is directed perpendicularly upward, and at the

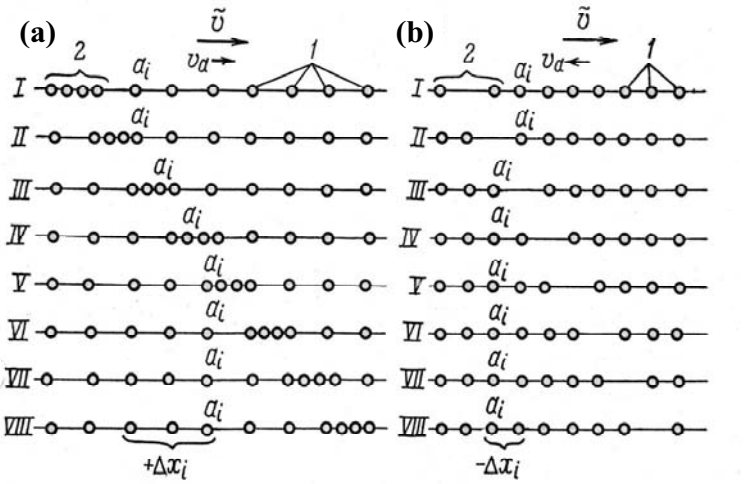

Fig. 17.6 Diagram of macroparticle displacements a_i under the influence of compression wave (a) and tensile wave (b). 1 – macroparticles, 2 – compressional wave in part (a) and tensile wave in part (b)

end of the wave trailing edge – perpendicularly downward to the contact surface. Such a wave is called the bend-rotation wave, since the non-deformed thread that enters the wave before the leading edge deforms (undergoes compression or depression), and is carried by the wave to the end of the trailing edge where the deformation is removed.

17.3 Field Observations

As already mentioned, a number of recordings which have been performed in-site, so almost in the focus, is extremely low, especially at walls of faults. But there are facilities creating laboratory conditions for earthquake registration. Such facilities comprise underground gas storages, which are of particular environmental hazard. Figure 17.7 presents layout of an underground gas storage, coordinates of earthquakes, and dates of the strongest earthquakes (M = 1.69-1.24 as recorded in the region of Příbram of Czech Republic, in 1999–2001). The strongest earthquakes occurred in June and January. This fact can be explained as related to the period of gas injection (June) and the period of gas extraction (January). The difference between maximum and minimum pressures amounts to 9 MPa. The rock enclosing the gas storage is under variable load and, accordingly, shear stresses. As Revuzhenko (2000) showed, ordered structures are formed in homogenous medium under alternate load.

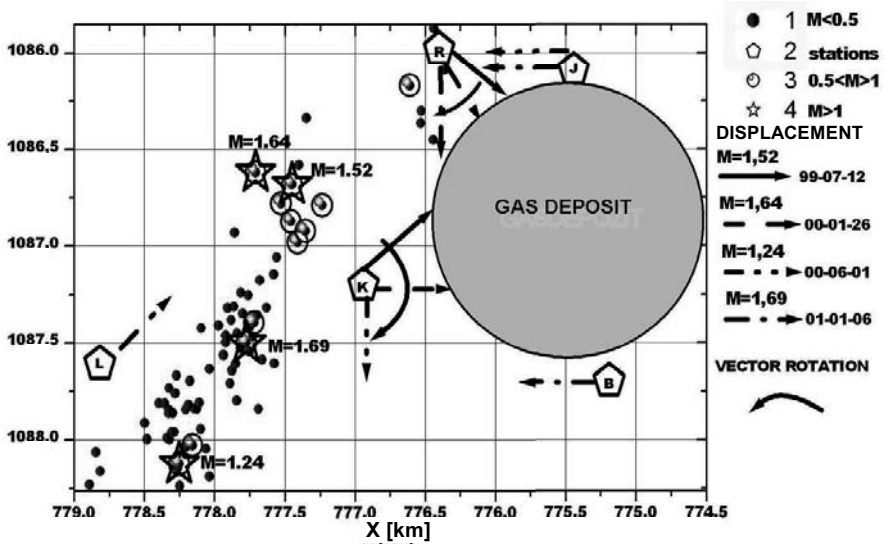

Fig. 17.7 Layout of the underground gas storage

These structures move relative to each other under shear stresses, thus forming faults. Figure 17.8 shows the seismograms for event $M = 1.24$ for stations L, K, J. Figure 17.9 shows the use of 3 Hz low pass filter to iden-

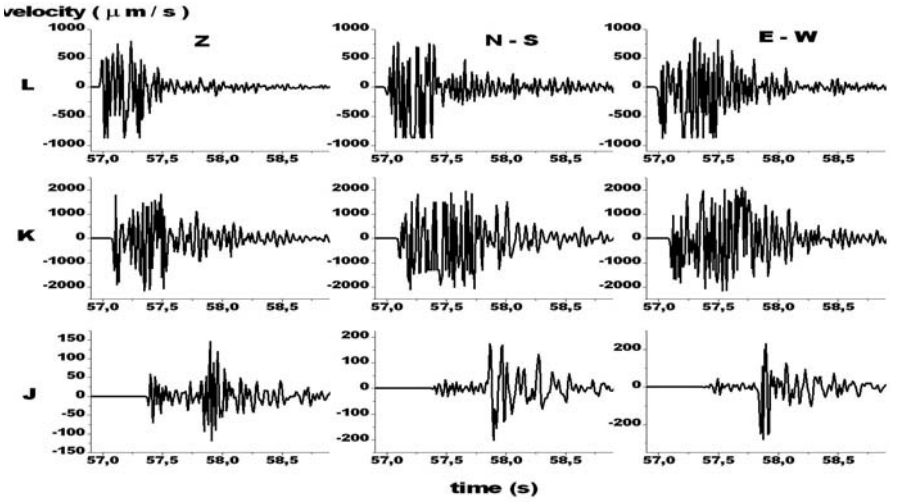

Fig. 17.8 Records of the seismic event $M = 1.24$ for three stations

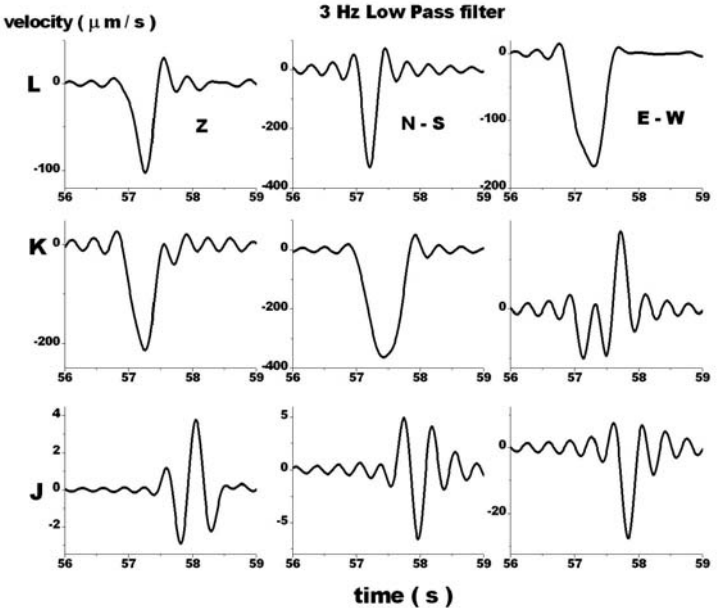

Fig. 17.9 Waves forms after filtration (3 Hz low pass filter)

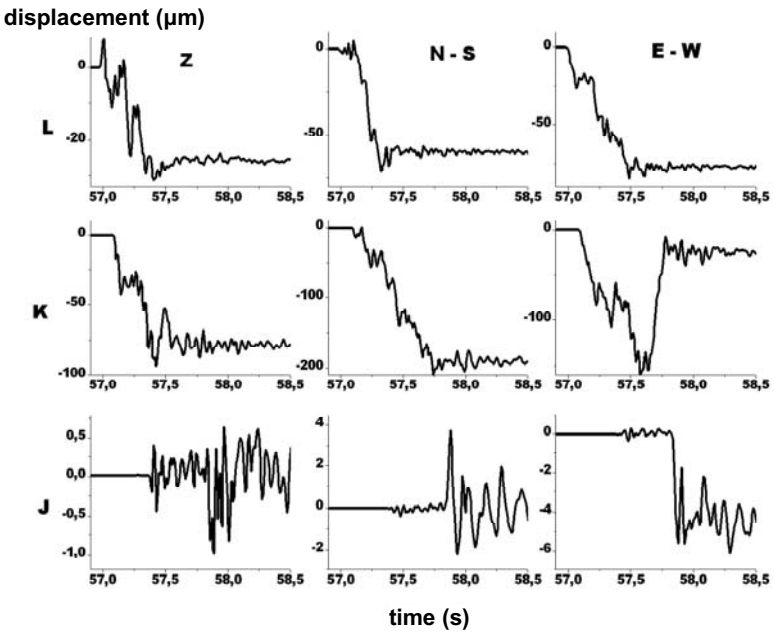

Fig. 17.10 Recorded displacements (after integration, seismic event $M = 1.24$) for the three components at the three stations

tify low-frequency component of the seismic signal. As a result, monopolar pulses can be derived. Amplitudes of signals on non-filtered seismograms (2-fold) at stations L and K are rather different, but become equal after filtration. Figure 17.10 shows displacements at the same stations. At L and K, displacements greatly differ from each other; station L is closer to the focus (Fig. 17.7), the distance being 700 m, but the displacement is 3 times smaller than that at station K. This confirms the conclusions made by Li et al. (1994); station K is situated at the fault wall. At station K, acceleration reached 0.3g. For stations K and R, rotation of displacement vector was found, i.e. vector of sum of two components (N-S, E-W) was changing its direction from event to event. As a result, residual displacement obtained rotational nature, and "rotational" dislocation occurred.

17.4 Conclusions

Basing on the model of bend-rotation wave (BRW), it seems possible to interpret non-linear and macroseismic effects as the effect of BRW on the medium. The BRW parameters (amplitude A, pulse width τ, velocity V) are

determined by local deformation. As experiments have shown, when the lateral pressure increases (Fig. 17.1, open fault model C), the pulse width τ increases too, from $\tau = 0.001$ to 0.02 s. For the gas storage (K station, E–W component, Fig. 17.9), τ reaches 0.6 s. Due to long period, the BRW can create modulation. At passing of "rotation wave", modulation involves n oscillators. Under «BRW» action, oscillators in the wave are synchronized, and their total energy is proportional to n^2 (Nicolis 1986). The oscillation period grows too. Therefore, the released energy and the BRW pulse width are directly proportional. BRW is a 3-dimensional wave, and buildings, boulders, etc are affected with impact, related to a rotating vector (Fig. 17.5). However, the BRW amplitude is spatially limited, and, as a consequence, macroseismic effects are observed in a limited zone along the tectonic fault.

Acknowledgements. I wish to thank Tomas Lokajiček and Vladimir Rudajev of the Institute of Rock Structure and Mechanics, Academy of Sciences of the Czech Republic.

References

Aksenov V, Kozak J, Rudajev V, Lokajiček T (1992) Seismic source self-organizing. Acta Montana **A89**: 89-110

Aksenov V, Kozak J, Lokajiček T (1993) Nonlinear process in earthquake foci. Pure appl geophys **140**: 29-47

Aksenov V, Lokajiček T (1997) Influence of nonlinear processes in seismic foci on released energy. Pure appl geophys **149**: 337-355

Berberian V, Qorashi V, Jackson JA, Priestley K, Wallace T (1992) The Rudbar-Tarom earthquake of June 1990 in NW Persia: preliminary field and seismological observations and its tectonic significance. BSSA **82**: (4) 1726-1755

Bolt B (1978) Earthquakes. A primer. WH Freeman and Company, San Francisco

Charkievich, AA (1953) Spectra and analysis. GITTL, Moscow (in Russian)

Li Y, Aki K, Adams D, Hasemi A (1994) Seismic guided waves trapped in the fault zone of the landers. California J Geophys Res **99**: (B6) 11705-11722

Lyapunov AM (1892) Fundamental problems of movement stability. Kharkov Math Soc (in Russian)

Mandelshtam, LI (1950) Complete collection of works, vol III. Izd Acad Nauk, Moscow, pp 89-178 (in Russian)

Mogi K (1985) Earthquake prediction. Academic Press, Tokyo

Nicolis JS (1986) Dynamics of hierarchical systems, an evolutionary approach. Springer Verlag, Berlin-Heidelberg

Nikonov A (1992) On extreme seismic velocities. Dokl RAN 323: 70-73 (in Russian)

Poincare A (1928) Sur les courbes definies par une equation differentiele. Ocuures VI, Paris
Popova E (1990) Macrocosmic data. Nauka 31: 135-137
Revuzhenko AF (2000) Mechanics of elastoplastic media and nonstandard analysis. Izd Novosib Univ, Novosibirsk (in Russian)

18 Solitary Waves in Crustal Faults and their Application to Earthquakes

Victor G. Bykov

Institute of Tectonics and Geophysics, Far East Branch of the Russian Academy of Sciences, 65 Kim-Yu-Chen St., 680 000 Khabarovsk, Russia
e-mail: bykov@itig.as.khb.ru

18.1 Introduction

The problem related to crustal fault dynamics consists of identification of the processes and parameters that are responsible for sliding regimes in the faults. The concepts according to which the transition from creep to stick-slip along the crustal fault, in most cases accompanied by a tectonic earthquake, is caused by geometrical inhomogeneities of fault surfaces, a decrease of friction in some segments of the fault and by anomalies of the pore pressure, are considered to be conventional (Ben-Zion and Rice 1995). The deformational waves propagating along the faults and excited by elastic-rebound in the foci of the past earthquakes may also initiate seismic slips in crustal faults (Ulomov 1993).

The deformational waves detected from changes in the geophysical fields (Nikolaevskiy 1998) are accompanied by migration of seismic activity in a number of cases (Ulomov 1993). The existence of these waves is known to be confirmed in the course of experimental studies of slow deformation processes in the crust (Nevskiy 1994). A lot of direct and indirect evidences (Nikolaevskiy 1996) show that slow tectonic deformations are propagating as solitary waves – solitons. For this reason, theoretical studies (Garagash 1996, Nikolaevskiy 1996, Nikolaevskiy and Ramazanov 1986) aimed at developing mathematical models that lead to soliton-like solutions and, at the same time, reflect the main features of wave deformation process occurring in the crust are of topical interest.

In this chapter it is shown that local deformation effects at the mesoscopic level related to decrease of friction at the contacts of inhomogeneous fault surfaces may cause solitary waves of activation whose evolution leads to macroscopic processes as seismic slips in crustal faults. The model

suggested describes the dynamics of relative displacements of fault surfaces including retarding and accumulation of energy necessary to provide a stick-slip process. As it is well known, the stick-slip is a necessary element to provide seismic events inside the earthquake focus. Analysis is made of asperity and friction effects in the fault on the evolution of velocity of waves of activation and also the amplitude and frequency of periodical load on fault dynamics. A relative role of different processes in the initiation of seismic slip is investigated.

18.2 Observational Evidence

The concept of the deformational (tectonic) waves generated in the Earth is based on the results of the study of spatio-temporal density distribution and processes of crustal deformation. The results of observation of the oriented earthquake migration of direct and indirect in-situ measurements of deformational waves or of their indications are most comprehensively shown and analyzed by Mogi (1968), Nersesov et al. (1990), Barabanov et al. (1994), Kasahara (1979), and Nikolaevskiy (1998).

Quantitatively, the deformational wave processes are displayed in the rate of the earthquake foci migration and the presence of geophysical field anomalies close to the faults. In conventional approach, the most characteristic rates of these processes and the corresponding waves can be divided into two groups (two scales of manifestation): global tectonic waves and deformational waves generated in the faults.

The global tectonic waves with velocities of 10-100 km/year are observed in the following phenomena: the oriented migration of large earthquakes (Stein et al. 1997); seismic velocity anomalies (temporal variations of seismic wave velocities, travel-times and time discrepancies) (Nevskiy et al. 1987); changes of the underground water table along the fault zone due to waves (Barabanov et al. 1994); deformographic measurements (Ishii et al. 1979); cyclic migration of aseismic gaps in the Earth's mantle (Nikolaevskiy 1998); oscillation motions of seismic reflectors (Bazavluk and Yudakhin 1993, Bormotov and Bykov 1999). Movement of slow tectonic deformations occurs along the deep faults in a narrow "corridor" (~100 km) (Nevskiy et al. 1989).

Rapid migration of seismic activity occurring in vast areas prior to or after large earthquakes testifies indirectly about the existence of the deformational waves with velocities of 1-10 km/day generated in the faults (Hill et al. 1995, Barabanov et al. 1994). The seismic activity can be detected from the observable radon, electrokinetic and hydrogeodynamic

signals (Nikolaevskiy 1998), and exciting of the stress-and-strain waves at the explosion and vibration slips in initiation in the fault zone (Ruzhich et al. 1999). Geophysical signals have a shape of solitary waves and are propagating along the crustal faults (Nikolaevskiy 1998).

18.3 Mathematical Model of Deformation Process

The model includes two most important mechanisms providing interaction of the fault surfaces: friction, simulated by introduction of gouge viscosity in the fault, and geometrical inhomogeneities which are characterized by ratio of scales of asperity and sinusoidal parts of the internal fault surfaces, and external load. Thus, we now postulate the following equation:

$$\frac{\partial^2 U}{\partial \xi^2} - \frac{\partial^2 U}{\partial \tau^2} = \sin U + \alpha \frac{\partial U}{\partial \tau} + \gamma(\xi)\delta(\xi - L)\sin U + \sigma(\tau), \qquad (18.1)$$

where $U = 2\pi u/a$, $\xi = \pi x/ap$, $\tau = \pi\omega_0 t/p$, $p^2 = a^2 D/4mgh$, $\omega_0^2 = D/m$, $\alpha \approx a\mu/d\Delta\rho\sqrt{gh}$, $\gamma = H/L$, U is the displacement of blocks located periodically along the fault length; a is the distance between the block centers; D is the tangential contact stiffness; m is the mass of the block; h is the distance between the block centers of the adjacent block layers; g is the gravity acceleration; μ is the viscosity of the layer between the blocks; d is the diameter of the circular contact of the blocks; Δ is the layer thickness; ρ is the density of the block material; α and γ are the parameters of friction and inhomogeneity, respectively; H, L are the height of asperities and the distance between them normalized to ap/π; $\delta(\xi)$ is the Dirac delta-function and $\sigma(\tau)$ is the function which reflects the external load at the contact of the fault surfaces. Figure 18.1 shows schematic presentation of the fault surfaces.

The left-hand side of the generalized sine-Gordon equation (18.1) corresponds to the wave operator applied to the relative displacement of the fault surfaces. In the right-hand side of Eq. (18.1) the first term characterizes the "restoring" force, originating due to shear along the sinusoidal-homogeneous surfaces of the fault; the second one – the friction force, which is proportional to the velocity relative to displacement; the third term corresponds to corrections for inhomogeneities which are distributed at a distance apL/π; the fourth one describes the initiation external load on the fault.

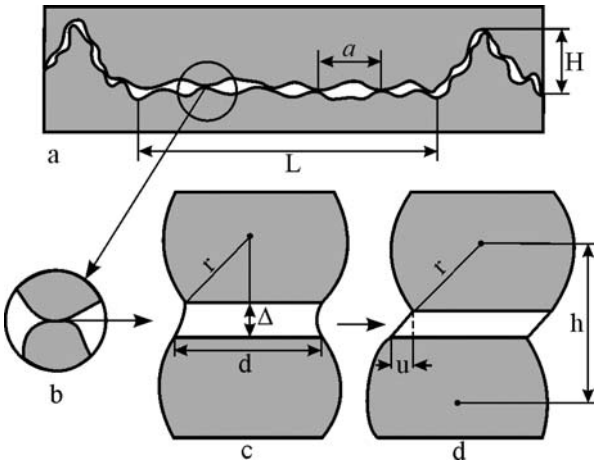

Fig. 18.1 Schematic diagram showing a change in contact between fault surfaces (a) and a change in the geometry of blocks contact (b-d): $a \approx 2r$, r is the radius of blocks

The expression for parameter α is obtained proceeding from the concepts of stick-slip (Dieterich 1987, Sleep 1995) and theory of dimension. Friction parameter α is mainly dependent on the average sizes of the blocks on the fault surface and also on the viscosity of the gouge, and assumes the values 0.01-1.0.

Inhomogeneity coefficient γ is equal to ratio of height H of the asperity to length L of the sector of the sinusoidal-inhomogeneous surface and characterizes regular point asperities of the relief of the fault surfaces. This element of the model reflects the fractal structure of the fault surfaces in the first approximation. Variation of the inhomogeneity coefficient γ is possible in the range from 0 to 1.0. The zero value means a complete absence of "cohesions" distinguished at the sinusoidal surface. The inhomogeneity coefficient value equal to 1.0 means coincidence of the height of the point asperity with the amplitude of the sinusoid.

Note that the effect of block rotation suggests an explanation for the sinusoidal character of the "restoring" forces (Nikolaevskiy 1996).

Integration of Eq. (18.1) has been made by the McLaughlin–Scott approximation method (Solerno et al. 1983), and numerical realization has been performed by the Runge-Kutta-Felberg scheme (Forsythe et al. 1977). The parameters of the medium were as follows: $\rho = 3\text{x}10^3$ kg/m^3, $D = 10^4$-10^6 N/m, $g = 9.8$ m/s^2, $r = 0.1$-1.0 m, $a = h = 2r$. Computation has been carried out with variation of the parameters of friction α and

inhomogeneity γ, which characterize the state of the contact at the fault, and also the value of $\sigma(\tau)$, that determines the external load.

18.4 Solitary Wave of Fault Activation

Profile of velocity v of the particles (Fig. 18.2) on the fault surfaces has a shape of the soliton $v(x,t) = v_{max}\mathrm{sech}(x–V_\alpha t)$, moving along the fault with a velocity V_α. Variation of friction parameter α in the sine-Gordon equation clears up significantly the reasons for variations of velocity V_α of the solitary wave in the crustal fault, as well as the consequences related to this variation. Value of velocity v of a particle on the fault surface is dependent on the state of the contact, that is, the value of the parameter α. It follows from the computations that in the case of low V_α, the value of v is insignificant and the stable sliding (creep) occurs. For the relatively high values of velocity V_α^{max} (of the order of 1-10 m/s) we obtain the soliton profile $v \sim 0.1$-1 m/s and the stepwise profile (kink) $u(x, t)$ (see Fig. 18.2). A similar relationship for dynamic characteristics but without time shift of the maxima of V_α and v can be obtained by analytical solution of the canonic sine-Gordon equation for a solitary wave in homogeneous fault without friction.

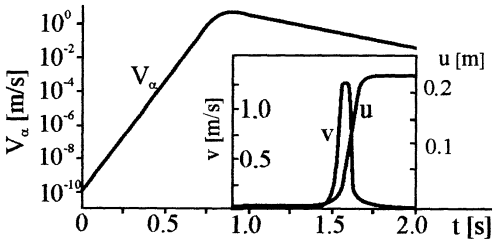

Fig. 18.2 Evolution of velocity V_α of wave of activation, displacement u and slip velocity v in the fault

Time interval between the peak values of V_α and v depends on the parameters α and γ. The moment of time when V_α attains the maximum value V_α^{max} always occurs earlier as compared to the calculated time of $v_{max.}$ Time lags between the transmitting of the solitary wave with the maximum velocity value and displacement u_{max} are stipulated by friction and inhomogeneities in the fault. The possibility of attaining high values of the relative slip gives grounds for calling the wave $v(V_\alpha)$ the solitary wave of

fault activation. The velocity maximum for the wave of activation, depending on the values of the chosen contact stiffness D in the faults does not exceed 10-100 m/s, that differs noticeably from velocities for the seismic waves, so from those for the deformational ones.

18.5 Evolution of Waves of Fault Activation

Velocity amplitude for the wave of activation increases to the value of about 0.9-1.8 m/s with subsequent transition to the stationary regime with the values $V_\alpha^{st} \approx 10^{-4}$-$10^{-2}$ m/s (Fig. 18.3), corresponding to the velocities of the deformational waves at inhomogeneity coefficient $\gamma = 0.1$-0.3 and a decrease of friction parameter α to 0.04. The creep regime is observed at $t = 11.0$-14.0 s. In the case of $\gamma > 0.3$, stability is acquired far later and V_α^{st} may have the values of the order of 10^{-6}-10^{-13} m/s. The value of V_α^{st} decreases with increase of γ, which is a result of the additional friction: the asperities make impediments at sliding more often, and retarding of the wave of activation is enhanced (the sliding is damped). Also, a transition of the system to the "fault is locked" regime is possible when $V_\alpha \to 0$.

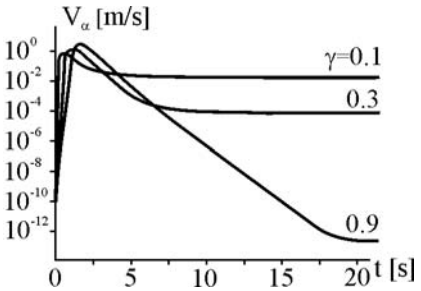

Fig. 18.3 Evolution of velocity V_α of wave of activation at different values of inhomogeneity coefficient γ and $\alpha = 0.04$

The greater the value of parameter γ ("cohesion" of the fault surfaces when other parameters are constant), the greater the velocity maximum of the wave of activation and the quicker the process of acquiring the stationary regime of activation. Thus, at the beginning of the stable sliding regime the inhomogeneities contribute to accumulation of greater elastic energy which is determined in dimensionless form by the component $(1+\gamma)\sin U$ in Eq. (18.1), and, vice versa, then they contribute to the fastest damping of the sliding. A long period of time is required to obtain V_α^{max} at an increase of α and decrease of γ.

Computation of fault dynamics shows that instability of sliding may be caused by a sharp decrease of the friction parameter which leads to an increase in the velocity of the wave of activation, and, consequently, in the slip velocity for the fault surfaces. Change in the sliding regimes dependent on the fault parameters occurs from 10 s ($\alpha = 0.04$, $\gamma = 0.1$) to 45 s ($\alpha = 0.01$, $\gamma = 0.1$).

18.6 Effect of Periodical Change of Friction in the Fault

Evolution of velocity V_α of the wave of activation in the fault depends on the friction parameter α. This parameter has a periodically changing component α_1 that corresponds to the regime of the cyclic perturbation contribution in some segments of the fault. Then the parameter α in Eq. (18.1) is transformed in $\alpha = \alpha_0 + \alpha_1 \sin(\tau/\eta)$, where α_0, α_1, η are some constants.

Results of computation of Eq. (18.1) at $\sigma(\tau) = 0$, $\eta = 10^2$, for varying α_0, α_1, and γ, show (see Fig. 18.4) that the maximum of velocity V_α is attained at t = 2-8 s from the perturbation moment, the time interval within which V_α corresponds to a slip 1-5 s. In fact, in real faults the sliding time is a value of the order of seconds at large earthquakes (Carlson 1991).

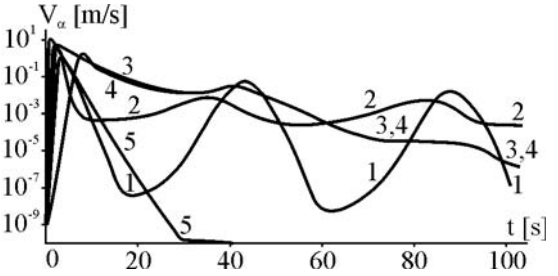

Fig. 18.4 Evolution of velocity V_α of wave of activation for different parameters of the state of contact for curves: (1) $\alpha_0 = 0.02$, $\alpha_1 = 0.09$, $\gamma = 0.9$; (2) $\alpha_0 = 0.09$, $\alpha_1 = 0.09$, $\gamma = 0.9$; (3) $\alpha_0 = 0.01$, $\alpha_1 = 0.01$, $\gamma = 0.9$; (4) $\alpha_0 = 0.01$, $\alpha_1 = 0.01$, $\gamma = 0.1$; (5) $\alpha_0 = 0.02$, $\alpha_1 = 0$, $\gamma = 0.9$

If the inhomogeneity parameter is constant, $\gamma = 0.9$, the maximum value of V_α is registered at the same time moment, but curves 1, 2 and 3 differ in amplitude: the minimum value of V_α corresponds to the maximum friction parameter α_0 (Fig. 18.4). Curves 3 and 4, computed at different γ and equal to α_0, α_1, at the time moment t = 30 s are merging and become indiscernible

further. It also follows from Fig. 18.4 that with increasing γ the maximum value of V_α is attained much earlier. At small α_0 and α_1 (curves 3 and 4) the velocity V_α is attenuating gradually to zero. At the higher values of α_0 and α_1 (curves 1 and 2), V_α acquires the periodical regime with velocities close to those of quick deformational waves reaching 1-10 km/day (Nikolaevskiy 1998). Evolution of V_α is represented by curve 5 without periodically changing additional friction ($\alpha_1 = 0$). This computation corresponds to a single generation of the solitary wave with transition of the system in the "fault is locked" regime.

Figure 18.4 shows that periodical generation of waves of activation with the velocities commensurable with those for the deformational waves is possible only under a certain state of the contacts of fault surfaces, that is, a combination of the friction and inhomogeneity parameters.

From this it follows that Eq. (18.1) can be applied for modelling of the seismic process at the appropriate choice of the corresponding parameters. Similar cyclic changes in the slip velocity and displacement in the fault zone were obtained due to periodical variations of stress (Dieterich 1987) and pore pressure (Sleep 1995) in the models of unstable sliding.

The increase in amplitude α_1 of the periodical friction component leads to a decrease in the maximum velocity value v of the seismic slip in the fault if other parameters of the model are constant. On the contrary, the increase of inhomogeneity parameter γ, which characterizes "cohesion" of the fault surfaces, causes the amplitude increase of velocity $v_{\max}$ of the seismic slip.

18.7 Effect of Periodical Change of External Load

Seismoactive faults undergo permanent external initiation effects of stress changes due to Earth tides, deformational waves from earthquakes or hydrological factors. Being active, these faults can generate oscillations, thus affecting other faults. Initiation of seismic slip may start because of inhomogeneity of physical properties along the faults due to constant external load.

We will simulate initiation of external load on the fault by including in Eq. (18.1) another periodical function $\sigma(\tau) = \sigma_0 \sin(\Omega\tau)$, where σ_0 and Ω are the dimensionless amplitude and frequency of the external load, the friction parameter α being constant. The instable slip being not affected by the external load, following (Sobolev et al. 1995), will be further called a

natural slip, while that initiated by the additional periodical external load – the initiated one.

The profile of velocity V_α of a solitary wave (curves 2 and 3) propagating along the fault differs sharply from the profile of velocity in the case with the natural slip (curve 1) (Fig. 18.5a). Within the initial part of velocity curves V_α the shape of the curves coincides for all the cases, but it has significant distinctions after the velocity maximum is attained. At higher frequencies (curve 3), V_α represents a periodical curve simulated by a descending part of the velocity curve V_α, which is computed in the absence of the source of external load (curve 1). The low-frequency ($\Omega = 0.1$) external load causes smoother changes of V_α, and the internal friction in the fault is not capable of compensating to the full extent the influence of the external load (Fig. 18.5a).

It follows from Fig. 18.5b that the first initiated slip occurs earlier at any frequency of the external load as compared to the natural one (curve 1). For this version of the computation, the time interval ΔT between $V_\alpha^{\max}$ and $v_{\max}$ is larger for the natural slip (curve 1) than for the initiated one (curves 2 and 3). This time, the interval increases with increasing frequency of the external load. The maximum velocity values of the wave of activation V_α, as well as those of slip velocity $v_{\max}$, correspond to the minimum frequency of the external sinusoidal load ($\Omega = 0.1$).

The time delay of the initiated dynamic slip decreases with increasing amplitude of the external load (Fig. 18.6). This agrees well with laboratory

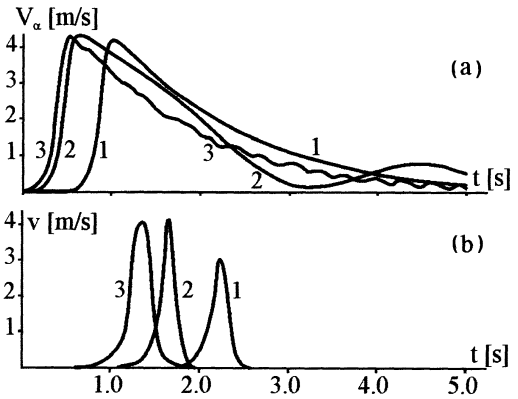

Fig. 18.5 Evolution of velocity of wave of activation V_α (a), and slip velocity v (b) at natural (1) and initiated (2, 3) slips. Parameters: $\alpha = 0.04$, $\gamma = 0.9$; $\sigma_0 = 0$ and $\Omega = 0$ for curve 1; $\sigma_0 = 0.01$ and $\Omega = 0.1$ for curve 2, $\sigma_0 = 0.01$ and $\Omega = 1.0$ for curve 3

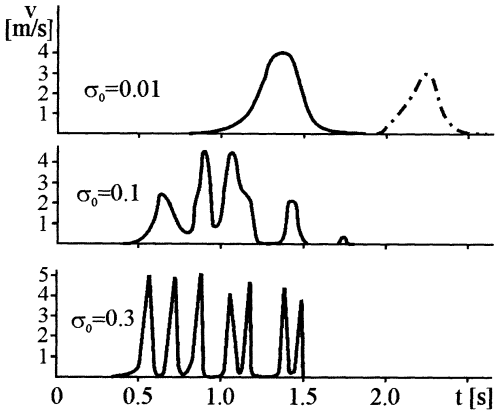

Fig. 18.6 Change of velocity of initiated slip v at constant frequency of external load $\Omega = 1.0$ and different amplitudes of load σ_0. The dot-dash line – natural slip velocity profile. Parameters: $\alpha = 0.04$, $\gamma = 0.9$

(Sobolev et al. 1991) and field (Ruzhich et al. 1999) experiments. A number of slips occur instead of one slippage, and the velocity amplitude of the first slip is the maximum one. The slip velocity amplitudes and the time intervals between them are not equal. The values of velocity maxima coincide for almost all these seismic slips. The slip velocities are weakly dependent on the amplitude σ_0 of the external load (Figs. 18.6 and 18.7). The number of slips is proportional to the amplitude of the load. The number of slips increases with an increase in the frequency of the constant sinusoidal load, while the time interval between the successive slips decreases (Fig. 18.6). This also coincides with the experiments (Ruzhich et al. 1999, Sobolev et al. 1995).

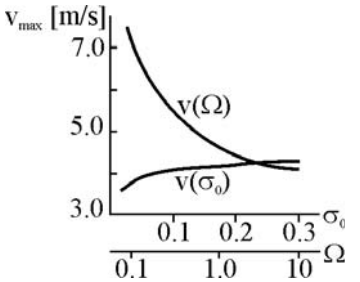

Fig. 18.7 Dependence of slip velocity maximum v_{max} in the fault on the frequency Ω ($\sigma_0 = 0.1$) and the amplitude σ_0 ($\Omega = 10$) of the external load. Parameters: $\alpha = 0.04$, $\gamma = 0.9$

A decrease in the frequency of the external load Ω leads to a significant amplitude increase in the slip velocity (Fig. 18.7). This is of particular importance if we take into consideration that the process is starting to be extremely sensitive to the external load at the final stage of earthquake preparation. Thus, we can consider the external load on the fault as an amplification of the wave of activation by the deformational waves with different frequency, radiated by an impact, explosion or earthquake.

It follows from the computed characteristics of the slips with different physical and mechanical parameters of the fault that the intensity and amplitude of the velocity of the initiated slip depend on the state of contacts of fault surfaces.

18.8 Conclusions

1. The generalized sine-Gordon equation can be applied for modeling peculiarities of fault dynamics. In fact, contribution of perturbation in the sine-Gordon equation in the form of friction and inhomogeneities leads to the solutions of the solitary-like waves that can be interpreted as the waves of fault activation.

2. The value of velocity for these waves regulates the sliding regime in the fault. The value of $v_{\max}$ of the wave of activation increases with increasing velocity V_α of the wave. The slip velocity increases sharply for the wave velocity V_α of 1 m/s and higher, and the values of displacement u are compatible with the displacements of the fault surfaces that are observed for earthquakes.

3. At definite values of friction and inhomogeneity parameters, α and γ, the solitary wave "acquires" the stationary regime with the values of $V_\alpha \sim 10^{-4}$-10^{-1} m/s or 10 km per day that correspond to the deformational waves. Earthquakes may be a source for deformational waves. These waves, migrating along the fault, may trigger the subsequent seismic events.

4. Periodical changes in the friction parameter in the generalized sine-Gordon equation (18.1), which models, for example, the weakening of the fault due to cyclic fluid flow, lead to a periodical generation of waves with the velocities characteristic of the observed deformational waves.

5. External periodical loading is the effective mechanism of the initiation of unstable dynamic slip. The external high-frequency load is probable to initiate the fault activation, but it does not provide periodical generation of the deformational waves and manifestation of seismic slips, as in the case with the cyclically changing friction inside the fault.

6. It is just the frequency of external loading that influences mainly the intensity of fault initiation, that is, the value of ν_{max} and the time interval between them. The amplitude increase of the sinusoidal external loading leads to a reduction in the time delay of the initiated stick-slip.

Acknowledgment. This research was supported by the Russian Basic Research Foundation (Grant 04-05-97001).

References

Barabanov VL, Grinevskiy AO, Belikov VM, Ishankuliev GA (1994) Migration of the crustal earthquakes. In: Nikolaev AV (ed) Dynamic processes in the geophysical medium. Nauka, Moscow, pp 149-167 (in Russian)

Bazavluk TA, Yudakhin FN (1993) Deformation waves in earth crust of Tien-Shan on seismological data. Dokl Akad Nauk **329**: 565-570 (in Russian)

Ben-Zion Y, Rice JR (1995) Slip patterns and earthquake populations along different classes of faults in elastic solids. J Geophys Res **100**: 12,959-12,983

Bormotov VA, Bykov VG (1999) Seismological monitoring of the deformation process. Geol Pacific Ocean **18**: 17-25

Carlson JM (1991) Time intervals between characteristic earthquakes and correlations with smaller events: An analysis based on a mechanical model of a fault. J Geophys Res **96**: 4255-4267

Dieterich JH (1987) Nucleation and triggering of earthquake slip: effect of periodic stresses. Tectonophysics **144**: 127-139

Forsythe GE, Malcolm MA, Moler CB (1977) Computer methods for mathematical computations. Prentice Hall, Englewood Cliffs, New York

Garagash IA (1996) Microdeformation of the prestress discrete geophysical media. Dokl Akad Nauk **347**: 95-98 (in Russian)

Hill DP, Johnston MJS, Langbein JO, Bilham R (1995) Response of Long Valley caldera to the M_w = 7.3 Landers, California, earthquake. J Geophys Res **100**: 12,985-13,005

Ishii H, Takagi A, Suzuki S (1979) Characteristic movement of crustal deformation in Northeast Honshu, Japan. Gerlands Beitr Geophys **88**: 163-169

Kasahara K (1979) Migration of crustal deformation. Tectonophysics **53**: 329-341

Mogi K (1968) Migration of seismic activity. Bull Earth Res Inst Tokyo Univ **46**: 53-74

Nersesov IL, Lukk AA, Zhuravlev VI, Galaganov ON (1990) On propagation of strain waves in the crust of South Middle Asia. Fizika Zemli **5**: 102-112 (in Russian)

Nevskiy MV (1994) Extra long period waves of deformations on the lithosphere plate boundaries. In: Nikolaev AV (ed) Dynamic processes in the geophysical medium. Nauka, Moscow, pp 40-55 (in Russian)

Nevskiy MV, Morozova LA, Zhurba MN (1987) The effect of propagation of the long-period strain perturbations. Dokl Akad Nauk **296**: 1090-1093 (in Russian)

Nevskiy MV, Morozova LA, Fuis GS (1989) Long-period strain waves. In: Sadovskiy MA (ed) Discrete properties of the geophysical medium. Nauka, Moscow, pp 18-33 (in Russian)

Nikolaevskiy VN (1996) Geomechanics and Fluidodynamics: with Applications to Reservoir Engineering. Kluwer Acad Publish, Dordrecht Boston London

Nikolaevskiy VN (1998) Tectonic stress migration as nonlinear wave process along earth crust faults. In: Adachi T, Oka F, Yashima A (eds) Proc of the Fourth Intern. Workshop on Localization and Bifurcation Theory for Soils and Rocks, Gifu, Japan, 28 Sept. - 2 Oct. 1997. AA Balkema, Rotterdam, pp 137-142

Nikolaevskiy VN, Ramazanov TK (1986) Generation and propagation of tectonic waves along deep faults. Fizika Zemli **10**: 3-13 (in Russian)

Ruzhich VV, Truskov VA, Chernykh EN, Smekalin OP (1999) Recent movements in the fault zones of Pribaikalia and mechanisms of their initiation. Geo Geofiz **40**: 360-372 (in Russian)

Sleep N (1995) Ductile creep, compaction, and rate and state dependent friction within major fault zones. J Geophys Res **100**: 13,065-13,080

Sobolev GA, Koltsov AV, Andreev VO (1991) Effect of oscillation triggering in modelling of earthquake. Dokl Akad Nauk SSSR **319**: 337-341(in Russian)

Sobolev GA, Ponomarev AV, Koltsov AV (1995) Excitation of vibrations in a model of seismic source. Fizika Zemli **12**: 72-78 (in Russian)

Solerno M, Soerensen MP, Skovgaard O, Christiansen PL (1983) Perturbation theories for sine – Gordone soliton dynamics. Wave Motion **5**: 49-58

Stein RS, Barka AA, Dieterich JH (1997) Progressive failure on the North Anatolian fault since 1939 by earthquake stress triggering. Geophys J Int **128**: 594-604

Ulomov VI (1993) Seismogeodynamic activization waves and the long-term prediction of earthquakes. Fizika Zemli **4**: 43-53 (in Russian)

19 Seismic Rotation Waves: Spin and Twist Solitons

Eugeniusz Majewski

Institute of Geophysics, Polish Academy of Sciences
ul. Księcia Janusza 64, 01-452 Warszawa, Poland
e-mail: emaj@igf.edu.pl

19.1 Introduction

This chapter describes seismic rotation waves that can be excited by rotational motions in earthquake sources. The existence of rotational motions excited by earthquakes was proposed by Teisseyre (1973). He considered theoretical aspects of this phenomenon in the framework of the mechanics of a micromorphic continuum. The micromorphic continuum allows for rotational motions of each microvolume of a continuum, so the behaviour of rocks and granular media during an earthquake can be modelled by this theory.

Bouchon and Aki (1982) recorded simulated rotational ground motions in the near-source region. Takeo and Ito (1997) applied the Kondo geometrical theory of defects and derived a general expression for rotational motions of seismic waves as a function of parameters of source defects. The ground rotational motions were observed and recorded by Nigbor (1994), Spudich et al. (1995), Stedman et al. (1995), McLeod et al. (1998), Spillman et al. (1998), Takeo (1998), and Igel et al. (2005). The measurements carried out by Takeo (1998) were recorded in the near-source region of earthquakes. The measurements by Spillman et al. (1998) were carried out far from an earthquake source (200 km and more). Trifunac and Todorovska (2001) estimated the rotational component of seismic waves from linear translations. It is noteworthy that other tectonic, volcanic, mining, and land sliding events can be a source of rotational motions as well. Rotational motions in the earthquake source can excite seismic rotation waves. The seismic rotation waves were recorded by Teisseyre et al. (2003).

Rotational effects occurring on the ground surface can be caused by the propagation of seismic rotation waves. These waves may rotate buildings,

towers, memorials, tombstones, bridges, and other objects situated on the Earth's surface. There is a great deal of observational evidence of this kind of seismic activity on the Earth's surface. Rotational waves are very dangerous for tall buildings (Zembaty and Boffi 1994). These buildings are very sensitive to angular momentum carried by rotation waves. They are designed according to special building codes that take into account seismic rotational motions. Moreover, incident seismic rotation waves interact with the geological structures (e.g., granular medium) and may lead to their softening, degradation, damage or fracture. Geological media with rotational degrees of freedom (e.g., the so-called "liquid sands") are extremely sensitive to any rotational motions or vibrations.

The aim of this chapter is to investigate the seismic rotation waves. We are particularly interested in seismic rotation waves that have a form of solitons. Thus, we have to consider nonlinear waves. The wave nonlinearity introduces a new possibility that the rotation wave speed may depend on the magnitude of a rotation vector. In such a case, the wave width and amplitude are modulated during the process of propagation (Hanyga 1986). Its profile changes as a function of the magnitude of a rotation vector. We will show that seismic rotation waves may take a form of solitary waves. The solitary waves or solitons are self-trapped packets of energy that propagate without loss of energy and momentum. The solitary wave is a result of the balance of nonlinearity (due to finite deformations and elastic features of the medium) and dispersion (due to the microstructure of the medium).

19.2 Modelling the Rotational Motions Excited in Earthquake Sources

We consider here a simple model of an earthquake source composed of two tectonic plates and a large, rounded fragment of rock (shaped as a cylinder) between them. The tectonic plate A moves from right to left, while the tectonic plate B moves from left to right. At the same time, the large, rounded fragment of rock rotates counterclockwise. The rotation of the largest fragment of rock is conveyed to other, smaller rock fragments that rotate as well. Thus, in the earthquake source there are many rotating fragments of rocks that are the sources of seismic rotation waves. Figure 19.1 shows the schematic picture of the mechanism that excites rotational motions in the earthquake source. One can infer spin motions of the solid cylinder and imagine a situation in which both tectonic plates move in opposite directions, oscillating along the fault at the same time. During such

a process, the tectonic plates vibrate in opposite directions and the cylinder is in a twist motion. We can combine these two simple motions together and obtain a resulting motion of the cylinder with two components: twist and spin motions.

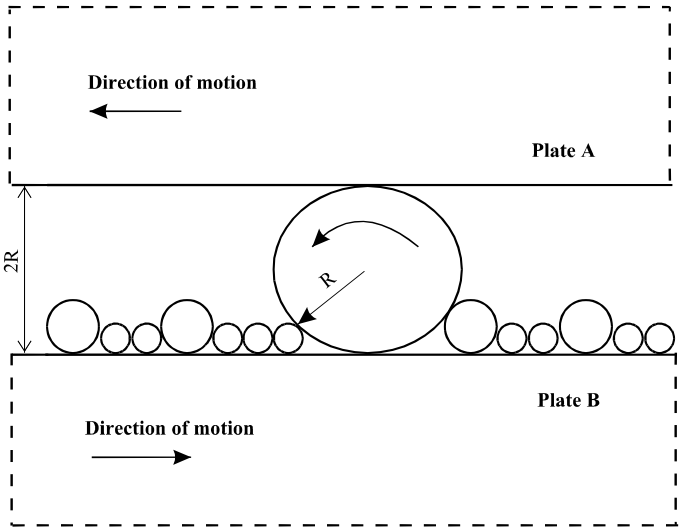

Fig. 19.1 A simple model of rotational motions excited in the earthquake source. Due to the motion of tectonic plates A and B in opposite directions during an earthquake, the largest, round fragment of rock rotates counterclockwise. It also conveys its rotational motion to other, smaller fragments of rocks. As a result, many fragments of rock rotate and become sources of seismic rotation waves

19.3 Seismic Rotation Waves: *PR* and *SR* Waves

The rotational motions generated in the earthquake source can excite seismic rotation waves that propagate to the Earth's surface. We distinguish two kinds of seismic rotation waves: (i) longitudinal rotation waves, i.e., *PR* waves, and (ii) shear rotation waves, i.e., *SR* waves. The *PR* wave has a rotation vector parallel to the direction of the wave propagation. In turn, the *SR* wave has a rotation vector perpendicular to the direction of the wave propagation. These seismic rotation waves are illustrated in Fig. 19.2. It should be added that when one makes measurements of the *PR* waves on the Earth's surface, it is easy to see the intimate relations between *PR* waves and *SH* waves since both waves involve rock particles

vibrating in the same plane. Similar intimate relations can be seen between the *SR* waves and *SV* waves measured on the Earth's surface.

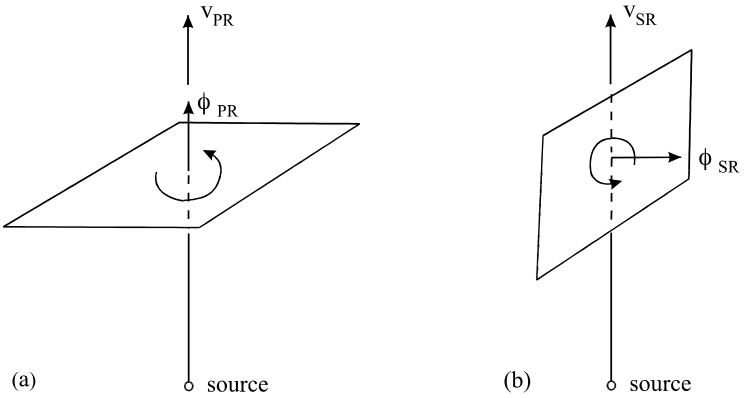

Fig. 19.2 Illustration of the seismic rotation waves excited in the earthquake source. (a) The seismic *PR*-wave. Here the direction of the rotation vector ϕ_{PR} is parallel to the direction of wave propagation v_{PR}. The rotations take place in the plane perpendicular to the direction of wave propagation. (b) The seismic *SR*-wave. Here the rotation vector ϕ_{SR} is perpendicular to the direction of wave propagation v_{SR}. The rotations take place in the plane parallel to the direction of wave propagation

We should also mention another important classification of rotation waves. From the point of view of rotational symmetry, the rotation waves can be divided in two groups: spin waves, and twist waves.

19.4 The Slow Tectonic Rotation Waves

Seismic rotation waves propagate faster in solid rocks and much slower in fractured media along tectonic faults. Thus, in solid rocks far away from earthquake faults the seismic rotation waves propagate with velocities roughly comparable with velocities of other seismic waves propagating in the Earth's interior. The so-called "slow" seismic rotation waves propagate in fractured rock media along earthquake faults with a velocity of about 250-300 km/year (Nikolaevskiy 1996, 1998). They are excited by past earthquakes and can trigger new earthquakes on the fault (cf., Chap. 17 by Aksenov and Chap. 18 by Bykov). Thus, the "slow" seismic rotation waves (called also "deformational waves") have the form of solitons and can be viewed as a mechanism triggering earthquakes on the faults. Such a slow rotation soliton is usually accompanied by a transverse wave.

19.5 Hamilton's Principle

The "action" S is defined by a momentum multiplied by a distance minus an energy multiplied by time

$$S = \mathbf{p} \cdot \mathbf{x} - E\,t\,, \tag{19.1}$$

where $\mathbf{p}$ is the momentum, $\mathbf{x}$ is the distance vector, E is an energy and t is time. However, we can also define the "action" S as the volume integral of the kinetic energy density K, minus the potential strain energy density P, minus the potential of external volume forces B, plus the surface integral of surface forces W and Z acting on displacements u and on rotations $\phi\hat{\theta}$, respectively, and the whole expression integrated over the time interval $[t_1, t_2]$

$$S = \int_{t_1}^{t_2} \left[\iiint_V \left(K - P - B\right) \mathrm{d}V + \iint_{\partial V} \left(Wu + Z\phi\hat{\theta}\right) \mathrm{d}A \right] \mathrm{d}t\,, \tag{19.2}$$

where

$$K - P - B = L\,, \tag{19.3}$$

and L is the volume density of the Lagrange function.

Bearing in mind that the kinetic and potential energies, as well as other variables are time-dependent, for each different possible path of integration one gets a different result for the "action". Our aim is to find such a path in space for which the result is the smallest number. Thus, we seek the least action. Hamilton's Principle can be viewed as a Principle of Least Action on intuitive grounds. We assume that the earthquake processes in the source follow Hamilton's Principle. Starting from this Principle, we shall derive fundamental equations for seismic rotation waves. Before we proceed, we have to formulate basic constitutive equations for the micropolar elastic rock medium that can describe rotations.

19.6 A Rock Medium Modelled as a Nonlinear Micropolar Elastic Continuum

In order to describe seismic rotation solitons, we have to consider a nonlinear rock medium with rotational degrees of freedom, nonlinear deformations, and nonlinear seismic waves. Thus, we have to take into consideration both, the physical and geometrical sources of nonlinearity. First of all, we have to assume finite deformations. In the formulae for measures

of strains, relative distortions and microdistortions as functions of displacements, we have to retain the nonlinear terms

$$\begin{aligned} E_{ij} &= \frac{1}{2}\left(u_{i,j} + u_{j,i} + u_{k,i}u_{l,j}\right), \\ \gamma_{kl} &= \frac{1}{2}\left(u_{k,l} + \phi_{kl} + u_{k,i}\phi_{il}\right), \\ \chi_{ijk} &= \phi_{ij,k} + u_{l,i}\phi_{lj,k}\ , \end{aligned} \tag{19.4}$$

where E_{ij} is the Cauchy-Green tensor of elastic strain, γ_{kl} is the relative distortion tensor (Nowacki 1970), χ_{ijk} is the microdistortion gradient, and ϕ_{ij} is the rotation tensor (Nowacki 1977, Eringen 1999).

The kinetic energy density can be expressed as follows:

$$K(t) = \frac{1}{2}\rho(\dot{\mathrm{u}}\cdot\dot{\mathrm{u}} + j\dot{\boldsymbol{\phi}}\cdot\dot{\boldsymbol{\phi}})\,. \tag{19.5}$$

The potential strain energy density is

$$P(t) = P_E + P_\gamma\ , \tag{19.6}$$

where

$$P_E = \frac{1}{2}\left[\lambda E_{kk}E_{ll} + (\mu+\kappa)E_{kl}E_{kl} + \mu E_{kl}E_{lk}\right], \tag{19.7}$$

$$P_\gamma = \frac{1}{2}\left(\alpha\gamma_{kk}\gamma_{ll} + \beta\gamma_{kl}\gamma_{lk} + \gamma\gamma_{kl}\gamma_{kl}\right). \tag{19.8}$$

From Hamilton's Principle

$$\delta L + \tilde{\delta} A = 0\,, \tag{19.9}$$

one can obtain a set of fundamental Euler equations. Here $\tilde{\delta} A$ denotes an elementary work produced by external forces during a virtual displacement. These equations are the coupled partial differential equations describing the wave propagation processes. From the variation calculus one can obtain (Samsonov 2001, Erofeyev 2003)

$$\begin{aligned} \frac{\partial L}{\partial u_j} = {} & \frac{\partial}{\partial x_n}\frac{\partial L}{\partial u_{j,n}} + \frac{\partial}{\partial t}\frac{\partial L}{\partial \dot{u}_j} - \frac{\partial^2}{\partial x_n^2}\frac{\partial L}{\partial u_{j,nm}} \\ & - \frac{\partial^2}{\partial x_n \partial t}\frac{\partial L}{\partial \dot{u}_j} + \frac{\partial^3}{\partial x_n^3}\frac{\partial L}{\partial u_{j,knm}}\ , \end{aligned} \tag{19.10a}$$

$$\frac{\partial L}{\partial \phi_{mn}} = \frac{\partial}{\partial x_i}\frac{\partial L}{\partial \phi_{mn,i}} + \frac{\partial}{\partial t}\frac{\partial L}{\partial \dot{\phi}_{mn}} - \frac{\partial^2}{\partial x_i^2}\frac{\partial L}{\partial \phi_{mn,ij}} - \frac{\partial^2}{\partial x_i \partial t}\frac{\partial L}{\partial \dot{\phi}_{mn,i}} + \frac{\partial^3}{\partial x_i^3}\frac{\partial L}{\partial \phi_{mn,ijk}} \ . \qquad (19.10b)$$

19.7 The Nonlinear Field Equations

We consider a micropolar elastic continuum that allows rotational deformations. Rotation waves can propagate in such a medium. Micropolar effects are important in the excitation and propagation of seismic rotation waves. In order to reveal these effects, and the new physical properties described beyond and above the seismic *P* and *S* waves, here we examine the dispersion of plane seismic waves in an isotropic micropolar elastic Earth. These considerations may be also helpful for experimental observations to determine the micropolar elastic constants for rock media.

From Hamilton's Principle in the form of Eq. (19.2), after some calculations and additional assumptions, one can obtain nonlinear field equations. The field equations of a micropolar elastic solid Earth may be expressed in the vectorial form

$$(\lambda + 2\mu + \kappa)\Delta \mathbf{u} - (\mu + \kappa)\nabla \times \nabla \times \mathbf{u} + \kappa \nabla \times \boldsymbol{\phi} - \rho \ddot{\mathbf{u}} = \mathbf{N}_1 \ , \qquad (19.11)$$

$$(\alpha + \beta + \gamma)\Delta \boldsymbol{\phi} - \gamma \nabla \times \nabla \times \boldsymbol{\phi} + \kappa \nabla \times \mathbf{u} - 2\kappa \boldsymbol{\phi} - \rho \mathbf{j} \ddot{\boldsymbol{\phi}} = \mathbf{N}_2 \qquad (19.12)$$

where Δ is the Laplacian, ∇ is the gradient operator, $\mathbf{u}$ is the displacement vector, $\boldsymbol{\phi}$ is the rotation vector, λ and μ are Lamé's constants, κ is the Mooney constant, α, β and γ are elastic constants of microrotation, ρ is the material density, $\mathbf{j}$ is the inertia vector for the macrovolume, $\mathbf{N}_1$ and $\mathbf{N}_2$ are the vectors that include nonlinear terms.

19.8 The Linear Seismic Rotation Waves

Disregarding the nonlinear terms ($\mathbf{N}_1 = \mathbf{N}_2 = 0$), the field equations (19.11) and (19.12) can be decomposed into scalar and vector wave equations by introducing scalar potentials (*F*, *R*) and vector potentials $\mathbf{U}$, $\boldsymbol{\Phi}$ (Eringen 1999),

$$\begin{aligned} \mathbf{u} &= \nabla F + \nabla \times \mathbf{U}\,, \\ \boldsymbol{\phi} &= \nabla R + \nabla \times \boldsymbol{\Phi}\,, \end{aligned} \tag{19.13}$$

where $\nabla \mathbf{U} = 0$ and $\nabla \boldsymbol{\Phi} = 0$.

Equations (19.11) and (19.12) are satisfied if

$$\begin{aligned} V_P^2\,\Delta F - \ddot{F} &= 0\,, \\ V_{PR}^2\,\Delta R - \psi^2 R - \ddot{R} &= 0\,, \end{aligned} \tag{19.14}$$

$$\begin{aligned} & V_S^2\,\Delta \mathbf{U} + \frac{1}{2}\mathbf{j}\psi^2 \nabla \times \boldsymbol{\Phi} - \ddot{\mathbf{U}} = 0\,, \\ & (V_{SR}^u)^2\,\Delta \boldsymbol{\Phi} - \psi^2 \boldsymbol{\Phi} + \frac{1}{2}\psi^2 \nabla \times \mathbf{U} - \ddot{\boldsymbol{\Phi}} = 0\,, \\ & (V_{SR}^l)^2\,\Delta \boldsymbol{\Phi} - \psi^2 \boldsymbol{\Phi} + \frac{1}{2}\psi^2 \nabla \times \mathbf{U} - \ddot{\boldsymbol{\Phi}} = 0\,, \end{aligned} \tag{19.15}$$

where

$$\begin{aligned} & V_P^2 = \frac{\lambda + 2\mu + \kappa}{\rho}\,, \qquad V_S^2 = \frac{\mu + \kappa}{\rho}\,, \qquad V_{PR}^2 = \frac{\alpha + \beta + \gamma}{\rho j}\,, \\ & (V_{SR}^u)^2 = \frac{\gamma}{\rho j}\,, \qquad (V_{SR}^l)^2 = \frac{\gamma - 2\kappa}{\rho j}\,, \qquad \psi^2 = \frac{2\kappa}{\rho j}\,. \end{aligned} \tag{19.16}$$

Here V_P, V_S, V_{PR}, V_{SR}^u, V_{SR}^l are the magnitudes of phase velocities of the seismic *P*, *S*, *PR*, upper *SR*, and lower *SR* waves, respectively, and ψ is a constant.

We consider here plane harmonic waves, thus we have

$$(F, R, \mathbf{U}, \boldsymbol{\Phi}) = (g, h, W, Z)\exp[\mathrm{i}(\mathbf{k}\,\mathbf{x} - \omega t)]\,, \tag{19.17}$$

where $\mathbf{k}$ is the wave-vector and ω is the angular frequency.

The above equation allows us to formulate dispersion relations ω *vs.* $\mathbf{k}$. After investigations of the dispersion relations we can conclude that there are five different seismic waves propagating with five different phase velocities.

- A longitudinal displacement wave propagates with the phase velocity V_P. This will be called the seismic *P* wave (*P*).
- A longitudinal rotation wave propagates with the velocity V_{PR}. This will be called the seismic *PR* wave (*PR*).
- A vector wave with phase velocity V_S. This will be called the seismic shears wave (*S*).

– Two vector waves coupled with *S* wave that propagate with the phase velocities V_{SR}^{u} and V_{SR}^{l}. They will be called the upper and lower seismic shear rotation waves (*SR*), respectively.

Dispersion relations are sketched in Fig. 19.3. Except of the *P* wave, all waves are dispersive. The asymptotes of *PR*, *SR*, and *S* waves are depicted by broken lines. The asymptote of the *PR* wave is $V_{PR}\,k$, the asymptote of the *S* wave is $V_S\,k$ and the asymptotes of the upper and lower *SR* waves are $V_{SR}^{u}\,k$ and $V_{SR}^{l}\,k$, respectively.

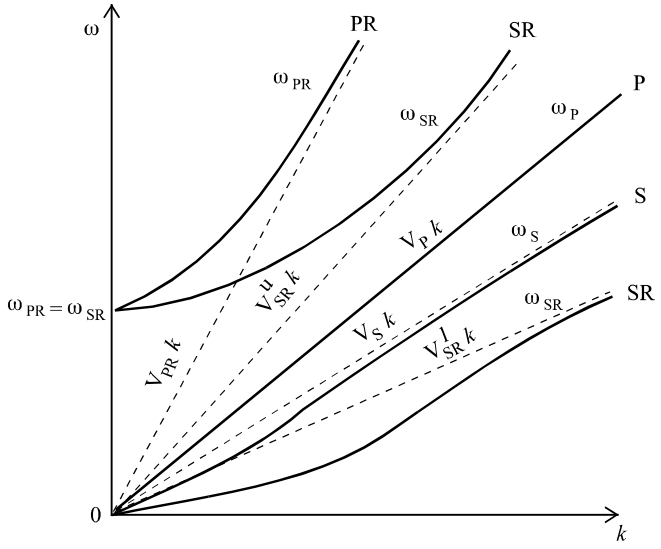

Fig. 19.3 Dispersion curves of seismic waves near $k = 0$ in a micropolar elastic Earth. *P* denotes the seismic *P* wave, *S* – the seismic *S* wave, *PR* – the seismic *PR* wave and *SR* – the seismic *SR* wave

19.9 The Nonlinear Seismic Rotation Waves

In order to formulate a set of field equations of nonlinear micropolar elasticity, we should specify the nonlinear terms $\mathbf{N}_1$ and $\mathbf{N}_2$ in (19.11) and (19.12). However, they are long and tedious expressions. Due to the space limitations, we confine ourselves to the final results. We can solve this nonlinear problem for particular cases of wave interactions as a collinear propagation of *P* waves and of *PR* waves. We can also consider a collinear

propagation of *P* waves and *SR* waves. In this way, we will display some interesting physical phenomena that are lost in the linear theory. As a result, we can reduce the nonlinear field equations (19.11) and (19.12) to the following set of equations for coupled normal waves

$$b_1\left(\xi^{(3)}\right)^3 + b_2\xi^{(3)} + b_3\xi^{(3)}_{xx} + \mathrm{i}\dot{\xi}^{(3)} = \frac{(V^u_{SR})^2}{6}\left(\frac{\rho j}{\kappa}\right)^{1/2}\partial^2_{xx} \times\left[\left(\xi^{(1)} + \xi^{(2)} + \xi^{(3)}\right) + \left(\zeta^{(1)} + \zeta^{(2)}\right)\right], \tag{19.18}$$

$$\dot{\xi}^{(1,2)} \pm V^l_{SR}\xi\xi_x^{(1,2)} \pm c_1\xi^{(1,2)}_{xx} \pm c_2\xi^{(1,2)}_{xxx} = \mp\frac{V_P^2}{V_{SR}}\partial_x \left[\left(\xi^{(1)} + \xi^{(2)} + \xi^{(3)}\right)\cdot\left(\zeta^{(1)} + \zeta^{(2)}\right)\right], \tag{19.19}$$

$$\dot{\xi}^{(1,2)} \pm V_P\zeta_x^{(1,2)} = \mp\frac{V_P}{2}\partial_x \left[\left(\xi^{(1)} + \xi^{(2)} + \xi^{(3)}\right) + 6\left(\zeta^{(1)} + \zeta^{(2)}\right)^2\right] \tag{19.20}$$

where b_1, b_2, b_3, c_1, and c_2 are constants.

A similar procedure was developed by Erofeyev (2003) in a context of acoustic waves. We can see that the left side of (19.18) contains a nonlinear Schrödinger (NLS) equation and describes a dispersion branch off the upper seismic *SR* wave. In addition, the left side of (19.19) contains the Korteveg-de Vries-Burgers (KdVB) equations and describes a dispersion branch off the lower seismic *SR* wave. These two equations have solitary solutions. In a similar way, by retaining terms with higher order derivatives, we can obtain the doubly dispersive equation (DDE) as a branch of the lower *SR* wave.

Now we will pay attention to a collinear propagation of seismic *P* waves and *PR* waves. To this end, we will focus on the paper by Maugin and Miled (1986) who studied one-dimensional rotation waves. They found solitary waves modelling the motions of ferromagnetic and ferromagnetic domain walls. We will outline their work and apply it to seismology. They considered finite elastic deformations and used a Lagrangian frame-of-reference. Due to the fact that the transverse components of the displacement vector are equal to zero and the axis of rotation is the *X* axis, we can write (cf., Eringen 1999)

$$x = X + U(\mathrm{X},t), \qquad y = Y, \qquad z = Z, \tag{19.21}$$

$$\chi_{kK} = \begin{bmatrix} 1 & 0 & 0 \\ 0 & \cos\phi & -\sin\phi \\ 0 & \sin\phi & \cos\phi \end{bmatrix}, \tag{19.22}$$

where U is the axial displacement and $\phi(X, t)$ is the rotation angle about the X axis.

The deformation tensor E_{KL} and Wryness tensor Γ_{KL} are given by

$$E_{KL} = x_{k,K}\chi_{lL} = \begin{bmatrix} 1+\dfrac{\partial U}{\partial X} & 0 & 0 \\ 0 & \cos\phi & -\sin\phi \\ 0 & \sin\phi & \cos\phi \end{bmatrix}, \tag{19.23}$$

$$\Gamma_{KL} = \frac{1}{2}\in_{KLM}\chi_{kM,L}\chi_{kN} = \begin{bmatrix} \dfrac{\partial\phi}{\partial X} & 0 & 0 \\ 0 & 0 & 0 \\ 0 & 0 & 0 \end{bmatrix}. \tag{19.24}$$

We specify constitutive equations in the form

$$T_{Kl} = \frac{\partial\Psi}{\partial C_{KL}}\chi_{lL}, \qquad M_{Kl} = \frac{\partial\Psi}{\partial\Gamma_{LK}}\chi_{lL}, \tag{19.25}$$

where Ψ is the free energy. For isotropic solids, Ψ is a function of the invariants of E_{KL} and Γ_{KL}. For a second-degree polynomial, it has the form (cf. Eringen 1999)

$$\Psi = \frac{1}{2}\lambda\left(1+U_{,x}+2\cos\phi\right)^2 + \frac{1}{2}\Big[\mu\left(1+U_{,x}\right)^2 + 2\cos^2\phi - \sin^2 + \frac{\mu+\kappa}{2}\Big[\left(1+U_{,x}\right)^2 + 2\cos^2\phi + \sin^2\phi\Big] + \alpha\left(\phi_{,x}\right)^2. \tag{19.26}$$

After some calculations (for details, see: Maugin and Miled 1986, Eringen 1999) the final equations may be written in nondimensional forms:

$$\frac{\partial^2\bar{U}}{\partial t^2} - V_{PR}^2\frac{\partial^2\bar{U}}{\partial X^2} = \alpha\frac{\partial}{\partial\bar{X}}\left(\cos\frac{\phi}{2}\right), \tag{19.27}$$

$$\frac{\partial^2 \phi}{\partial r^2} - \frac{\partial^2 \phi}{\partial X^2} - \sin\bar{\phi} = e\sin\frac{\bar{\phi}}{2} + b\frac{\partial^2 \bar{U}}{\partial X}\sin\frac{\phi}{2}, \tag{19.28}$$

where: $\bar{\phi} = 2\phi, \quad r = \omega_M t, \quad \bar{X} = X/\delta, \quad \bar{U} = U/\sqrt{J},$

$$\omega_M^2 = \frac{2(2\lambda+\mu)}{\rho_0 J}, \qquad \delta^2 = \frac{\alpha}{2(2\lambda+\mu)}, \qquad e = \frac{2\lambda}{2\lambda+\mu},$$

$$V_{PR}^2 = \frac{J}{\alpha}\left(\lambda+2\mu+\kappa\right), \qquad \alpha = \frac{\left(\lambda+2\mu+\kappa\right)\sqrt{2J}}{\sqrt{\alpha(2\lambda+\mu)}},$$

$$b = \frac{2\lambda\sqrt{2J}}{\sqrt{\alpha(2\lambda+\mu)}}.$$

Maugin and Miled (1986) showed that the coupled nonlinear equations (19.27) consist of a d'Alembert equation and a double sine-Gordon equation for ϕ. Finally, we have explicit solutions for the seismic *PR* wave in the form of a rotation soliton and for the axial displacement in the form of the longitudinal displacement soliton

$$\phi_{PR} = 4\tan^{-1}\left(\sqrt{-p}\sinh\xi\right), \tag{19.29}$$

$$U = \frac{2a}{\omega^2 - \omega_{PR}^2}\left[\frac{1}{\sqrt{-1-p}}\tan^{-1}\left(\sqrt{-p-1}\tanh\xi\right)\right] + U_0, \tag{19.30}$$

where

$$p = \frac{1}{4\left(\omega^2 - q^2\right)}\left(e + \frac{ab}{\omega^2 - \omega_{PR}^2}\right). \tag{19.31}$$

19.10 Dispersion Curves and Rotation Solitons

Now we collect our results and plot them in Fig. 19.4. One can see dispersion curves of different seismic waves and rotation solitons branching off the curves corresponding to rotation waves. On the horizontal axis we have the wave vector **k**, and on the vertical axis we have the wave number ω. This means that for a critical value of the wavelength/grain size ratio, we can expect a branching seismic rotation soliton.

The seismic rotation solitons are depicted in Fig. 19.4 in the form of broken lines. They branch off dispersion curves of seismic rotation waves.

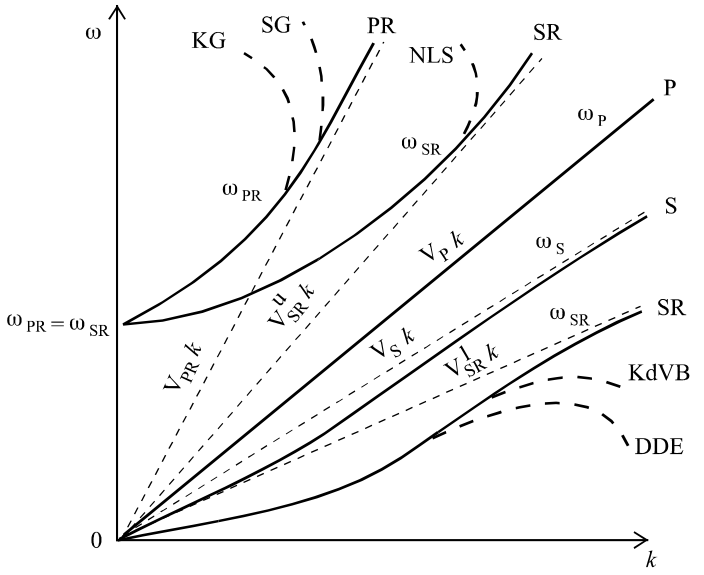

Fig. 19.4 Seismic rotation solitons branching off dispersion curves for seismic waves in a micropolar Earth. *P* denotes the seismic *P* wave, *S* – the seismic *S* wave, *PR* – the seismic *PR* wave, *SR* – the seismic *SR* wave; KG – the Klein –Gordon rotation soliton, SG – the sine-Gordon rotation soliton (both branching off the *PR* wave branch); NLS – Schrödinger's soliton branching off the upper *SR* wave branch; and KdVB – the Korteveg–de Vries–Burgers rotation soliton, DDE – the DDE rotation soliton (both branching off the lower *SR*-wave branch)

19.11 The Seismic Rotation Solitons in the Degenerated Continuum

19.11.1 The seismic spin and twist solitons described by the DDE equation

In Chapter 5, a theory of the degenerated asymmetric continuum is developed, in which the displacement motions vanish, and only rotational motions are retained. Both the spin motions characterized by antisymmetric fields and the bend-twist motions characterized by symmetric fields have been considered (cf. Teisseyre 2004). Now we write equations for seismic spin and twist rotational waves in the form of the DDE equations:

$$\frac{\partial^2 \phi_{[s]}}{\partial t^2} - V_{PR}^2 \frac{\partial^2 \phi_{[s]}}{\partial x^2} = \varepsilon^2 \left(a_1 \frac{\partial^4 \phi_{[s]}}{\partial x^2 \partial t^2} + a_2 \frac{\partial^4 \phi_{[s]}}{\partial x^4} + a_3 \frac{\partial^2}{\partial x^2} \left(\phi_{[s]}^2 \right) \right), \quad (19.32a)$$

$$\frac{\partial^2 \phi_{(t)}}{\partial t^2} - V_{PR}^2 \frac{\partial^2 \phi_{(t)}}{\partial x^2} = \varepsilon^2 \left(b_1 \frac{\partial^4 \phi_{(t)}}{\partial x^2 \partial t^2} + b_2 \frac{\partial^4 \phi_{(t)}}{\partial x^4} + b_3 \frac{\partial^2}{\partial x^2} \left(\phi_{(t)}^2 \right) \right), \quad (19.32b)$$

where the velocities for spin and twist waves are equal $V_{PR}^2 = 2\mu^* / \rho$, μ^* is the rotation rigidity, ρ is the material density, ε is a small parameter, and a_i and b_i (i = 1, 2, 3) are constant coefficients. The DDE equation was investigated by Samsonov (1988). He called it the doubly dispersive equation (DDE), describing dispersion and dissipation and having exact solitary solutions. In our case, the seismic spin soliton has the form

$$\phi_{[s]} = A m_{[s]}^2 \cosh^{-2}(m_{[s]}\theta), \quad (19.33)$$

where $A = 6(a_{10}a_2 + a_3)/a_4$ and $\theta = x - V_{ph}t$, and V_{ph} is the phase velocity of the wave, $m_{[s]}$ is the parameter to be defined by the substitution of the above solution into Eq. (19.32a).

Correspondingly, the seismic twist soliton has the form

$$\phi_{(t)} = A m_{(t)}^2 \cosh^{-2}(m_{(t)}\theta), \quad (19.34)$$

where $A = 6(b_{10}b_2 + b_3)/b_4$, and $m_{(t)}$ is the parameter to be defined by the substitution of the above solution into Eq. (19.32b).

19.11.2 The seismic spin and twist solitons described by the Klein–Gordon equation

Now let us describe the seismic spin and bent-twist waves by using the Klein–Gordon equation in the form:

$$\frac{\partial^2 \phi_{[s]}}{\partial t^2} - \frac{\partial^2 \phi_{[s]}}{\partial x^2} = A\phi_{[s]} - B\phi_{[s]}^3 \ , \quad (19.35)$$

$$\frac{\partial^2 \phi_{(t)}}{\partial t^2} - \frac{\partial^2 \phi_{(t)}}{\partial x^2} = \Gamma \phi_{(t)} - Y\phi_{(t)}^3 \ , \quad (19.36)$$

where the variable t was scaled, and A, B, Γ, and Y are positive constants. Upon choosing $\phi(x_0) = 0$, the soliton solutions of these equations are as follows:

$$\phi_{[s]}(x) = \pm\left(\frac{A^{1/2}}{B}\right)\tanh\left[\frac{A^{1/2}\left(x-x_1\right)}{\sqrt{2}}\right], \tag{19.37}$$

$$\phi_{(t)}(x) = \pm\left(\frac{\Gamma^{1/2}}{Y}\right)\tanh\left[\frac{\Gamma^{1/2}\left(x-x_1\right)}{\sqrt{2}}\right]. \tag{19.38}$$

Figure 19.5 illustrates the relationship between the seismic spin and twist solitons $\phi_S(x)$ and $\phi_T(x)$. These curves were obtained as kink solutions to the Klein-Gordon equations (19.10) and (19.11). In addition, the energy densities $E_S(x)$ and $E_T(x)$ of the seismic spin and twist solitons were depicted. It is noteworthy that the energy curves have pulse-like profiles.

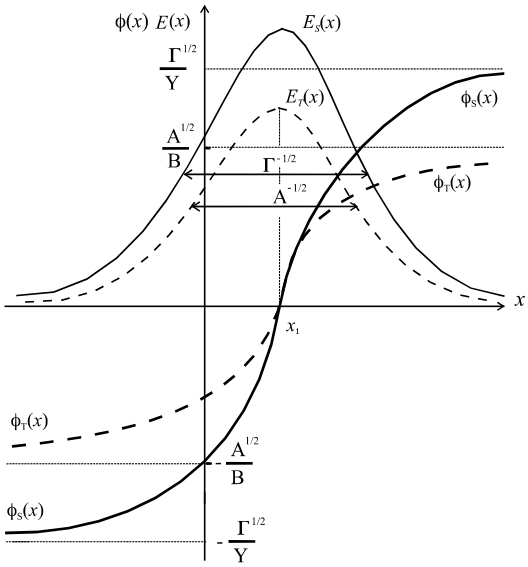

Fig. 19.5 The curves $\phi_S(x)$ and $\phi_T(x)$ display the seismic spin and twist solitons obtained as kink solutions of the Klein-Gordon equations (19.37) and (19.38), respectively. The curves $E_S(x)$ and $E_T(x)$ depict the energy densities of the spin and twist solitons that are localized with their widths characterized by $A^{-1/2}$ and $\Gamma^{-1/2}$, respectively

19.11.3 The seismic spin soliton described by the sine-Gordon equation

Let us model the seismic spin wave by using the sine-Gordon (SN) equation in the form

$$\frac{\partial^2 \phi}{\partial t^2} - \frac{\partial^2 \phi}{\partial x^2} = -\sin \phi(x,t)\,, \tag{19.39}$$

where the variable t is scaled. This equation has a solitary solution in the form

$$\phi = 4\tan^{-1}\left[\exp\frac{(\pm x - ht)}{\sqrt{1-h^2}}\right], \tag{19.40}$$

where $h = \sqrt{d^2 - 1}/d$. Thus, Eq. (19.40) describes a seismic spin soliton.

Figure 19.6 is the illustration of the seismic spin soliton modelled by the sine-Gordon equation (19.39). Solutions to the sine-Gordon and the Klein –Gordon equations have "kink" profiles. In order to obtain pulse profiles, it is necessary to plot derivatives of the solutions.

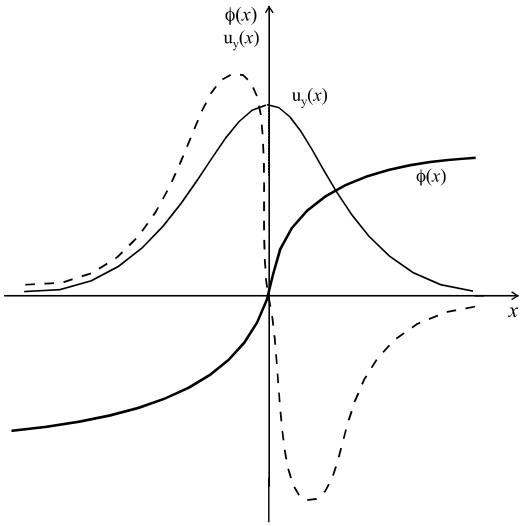

Fig. 19.6 The curve $\phi(x)$ displays the seismic spin wave modelled by the kink solution of the sine-Gordon equation (19.39). The curve u_y depicts the corresponding transverse displacement. The broken line displays the spatial derivative of the transverse displacement with respect to variable x

19.12 Conclusions

This chapter briefly presented the main results concerning seismic rotation waves and seismic rotation solitons, namely spin and twist solitons. A model of micropolar elastic medium was applied due to the fact that such a

medium allows rotational motions. Hamilton's Principle was the starting point of our considerations. Based on this principle, nonlinear forms of wave equations were formulated and analyzed. On the basis of different methods of solving, we pointed out that the nonlinearity of wave equations and nonlinearity of the rock medium are essential factors for modelling the behavior of these waves in the Earth's interior. The first conclusion can be drawn that the seismic rotation waves can branch into seismic rotation solitons. Due to the fact that solitons can propagate without any loss of energy, these waves are extremely important carriers of seismic energy and they can trigger new earthquakes. Thus, the information or the message carried by seismic rotation solitons – as we will call the seismic solitary waves – is very strong, because it starts from the earthquake source and reaches a recording station without any loss of information. We will show that these seismic rotation solitons (spin and twist solitons) traveling throughout different rock media can modify their amplitudes and widths in such a way that their energy (or carried information) is not lost. It is safe to say that the rotation waves carry crucial information concerning the earthquake source processes. We can also say that the rotation waves carry information about the properties of rocks beneath the seismic station. Now, a new challenge emerges: how can we decipher this information? The nagging question naturally arises: what are the circumstances at which the seismic rotation waves branch into seismic rotation solitons? So far, we do not have a complete and definite answer to this question. We know only that there is a critical value of the ratio of a wavelength over the grain size, in which a soliton is branching from the seismic rotation wave. The problem is so complex that many factors and mechanisms can be responsible for the branching and the formation of solitons. Thus, the research on seismic rotation solitons is essential for investigating the propagation of seismic waves and helps understand mechanisms triggering earthquakes.

References

Bouchon M, Aki K (1982) Strain, tilt, and rotation associated with strong ground motion in the vicinity of earthquake faults. Bull Seism Soc Am **72**: 1717-1738

Eringen AC (1968) Theory of micropolar elasticity. In: Liebovitz H (ed) Fracture vol 2, Academic Press, New York

Eringen AC (1999) Microcontinuum field theories, I: Foundations and solids. Springer, New York

Erofeyev V (2003) Wave processes in solids with microstructure. World Scientific, Singapore

Hanyga A (1986) Seismic waves in the Earth. PWN–Elsevier, Warszawa–Amsterdam

Igel H, Schreiber KU, Flaws A, Schuberth B, Velikoseltsev A, Cochard A (2005) Rotational motions induced by the M8.1 Tokachi-oki earthquake, September 25, 2003. Geophys Res Lett **32**: L08309, doi:10.1029/2004GL022336

Maugin DA, Miled A (1986) Solitary waves in micropolar elastic crystals. Int J Engng Sci **9**: 1477-1499

McLeod DP, Stedman GE, Webb TH, Schreiber U (1998) Comparison of standard and ring laser rotational seismograms. Bull Seism Soc Am **88**: 1495-1503

Nigbor RL (1994) Six-degree-of-freedom ground-motion measurement. Bull Seism Soc Am **84**: 1665-1669

Nikolaevskiy VN (1996) Geodynamics and fluidodynamics. Kluwer, Dordrecht

Nikolaevskiy VN (1998) Nonlinear modelling of geomaterials and self-organizing phenomena. In: de Borst R, Giessen E (eds) Material instabilities in solids, J Wiley, New York

Nowacki JP (1977) Theory of disclinations in elastic Cosserat media. Arch Mech **29**: 531-545

Nowacki W (1970) Theory of micropolar elasticity. Udine Courses & Lectures No 25, Springer-Verlag, Wien

Samsonov AM (1988) On some exact solutions of nonlinear longitudinal wave equations with dispersion and dissipation. In: Crighton DG and Mainardi F (eds) Dispersive Waves in Dissipative Fluids. Proc EUROMECH Coll 240, Bologna, 56-57, Tecnoprint, Bologna,

Samsonov AM (2001) Strain solitons in solids and how to construct them. Chapman & Hall/CRC, London

Spudich P, Steck LK, Hellweg M, Fletcher JB, Baker LM (1995) Transient stresses at Parkfield, California, produced by the M 7.4 Landers eartquake of June 28, 1992: Observations from the UPSAR dense seismograph array. J Geophys Res **100**: 675-690

Stedman GE, Li Z, Bilger HR (1995) Sideband analysis and seismic detection in a large ring laser. Applied Optics **34**: 5375-5385

Spillman WB Jr, Huston DR, Wu J (1998), Very long gauge length fiber optic seismic event detectors. Proceedings of the SPIE 3555: 311-321

Takeo M (1998) Ground rotational motions recorded in near-source region of earthquakes. Geophys Res Lett **25**: 789-792

Takeo M, Ito HI (1997) What can be learned from rotational motions excited by earthquake? Geophys J Int **129**: 319-329

Teisseyre R (1973) Earthquake processes in a micromorphic continuum. Pure Appl Geophys **102**: 15-28

Teisseyre R (2004) Spin and twist motions in a homogeneous elastic continuum and cross-band geometry of fracturing. Acta Geophys Pol **52**: 173-183

Teisseyre R, Suchcicki J, Teisseyre KP (2003) Recording the seismic rotation waves: reliability analysis. Acta Geophys Pol **51**: 37-50

Trifunac MD, Todorovska M (2001) A note on the useable dynamic range of accelerographs recording translation. Soil Dyn Earth Engng **21**: 275-286

Zembaty Z, Boffi G (1994) Effect of rotational seismic ground motion on dynamic response of slender towers, Europ Earthquake Engng **8**: 3-11

20 Earth Rotation, Elasticity and Geodynamics: Earthquake Wave Rotary Model

Alexander V. Vikulin

Institute of Volcanology and Seismology
Far East Department of Russian Academy of Sciences
Piip Ave. 9, Petropavlovsk-Kamchatsky, 683006, Russia
e-mail: vik@kcs.iks.ru

20.1 Introduction

Properties of seismicity such as grouping of earthquakes in space and time, their seismic energy and migration have been determined in the recent decades. All these properties point to the wave nature of seismic process. The data available indicate that the earthquakes and some processes on a planetary scale (atmospheric processes, variations of planet rotation, nutation of the Earth's pole, heliophysical parameters, cosmic factors, etc.) are correlated to the character of stress fields in the areas of earthquake foci.

The block character of seismically active strata is confirmed in many papers, among others those related to the vortex tectonics (e.g., Wezel 1986) and it has been proved that the Earth has very strong non-linear properties. It has also been shown that the laws of seismicity in the belts can be described with analytical methods by means of non-linear wave equations (Zhuravlev 1983, Lyubushin 1991, Nikolaevsky 1996).

The main conclusion of such a hierarchical approach is a strong non-linearity of differential equations describing the seismic process.

Thus, analytical models pretending to form an adequate description of the seismic process must contain strong non-linear wave equations, whose coefficients are determined by the structural properties of medium and seismicity (Vikulin 2003).

In this chapter, we present a rotational wave model of seismic processes within the Pacific margin that is related to the assumption of seismofocal blocks rotating due to internal sources. An analytical expression is obtained for the energy of seismofocal block interaction. Explanation is given for the velocity spectrum of seismicity migration. It is shown that the

known dislocation models of tectonic earthquake source are an extreme case of the rotational model when the source-block interaction can be neglected. A possibility of using the rotational model to the problem of tectonic movement is discussed.

The new model presented here differs from the "local" Reid's principle and supplements Reid's theory with an interaction mode.

20.2 Hypothesis

There are many geological, geophysical and seismological data that point to the rotational movement of the Earth's crust blocks and lithospheric plates. The vortex-related structures have been recognized in the material from all geologic periods at the Earth and surfaces of other planets and their satellites (Lee 1928, Melekestsev 1979, Wezel 1986, Mandeville 2000, Vikulin 2004).

Structural maps of the lithosphere show that the rotation traces of different blocks can be regarded as manifestations of vortex-related processes in a geological medium. Vortex and ring structures of tectonic nature are distributed over the whole surface of the Earth (Scheidegger 1982, Kulakov 2003, Vikulin 2004, Xie Xin-sheng 2004). The same structures have been detected on Mars (the period of rotation being 24.5 hours) and have not been traced on the "slowly" rotating planets (Mercury – 59 days, Venus – 243 days) and satellites (Moon – 30 days) (Melekestsev 2004). This analogy gives grounds for assuming that accumulation and release of stresses within each of the elementary seismofocal blocks forming the largest earthquake sources is also caused by rotation of the planet (Vikulin and Ivanchin 2000), or at least related to it. This assumption is confirmed by geological evidence of the seismofocal block rotation in Ecuador and in the central part of Aleutian Islands in the Miocene-Pliocene (Daly 1989, Geist et al. 1988), in China, Caucasus, and in other regions in the Pliocene, Quaternary and Miocene (Xie Xin-sheng 2004), and by the data supporting the connection between seismicity and rotation of the planet (Chao and Gross 1995).

Thus, the angular momentum of a block or a plate on a rotating planet must be compensated by the force moment; on the other hand, such a force moment can be related to an elastic field arising around the rotating volume (blocks or plates); hence, we face a problem of how to calculate the stress field in the areas of rotating hard blocks.

20.3 Stress Field Related to Rotation of Hard Bodies

To approach the solution of our problem we will consider several stages as discussed below (Vikulin 2003, Vikulin and Ivanchin 2000, Vikulin and Krolevetz 2002). We consider a sphere block with radius R_0, elastically coupled with its surrounding medium (matrix), and subjected to laws of the classical elasticity theory.

1. The main idea based on the results of laboratory experiments and theoretical studies of polycrystalline body samples for real conditions is as follows. Some volume V (the seismofocal block) inside the rotating body acquires – due to internal forces – an impulse momentum **M**. Due to rotation of the surrounding matrix, a change of the direction of this impulse momentum is expected and shall be compensated by a force moment $\mathbf{K} = d\mathbf{M}/dt$. Therefore, the rotation of seismofocal block results in elastic stress field excited around the block by the corresponding force moment.

2. We consider two systems of coordinates which can rotate around the common axis; the axis Z in the first system is assumed to be parallel to the axis of rotation Ω of the matrix (Earth) and directed from the south to the north pole, while the axis $\tilde{Z}$ of the second system is put parallel to the impulse momentum **M** after its turn by the angle β as caused by the elastic coupling of rotated seismofocal volume V in respect to the matrix. The center of both systems of coordinates is put in the gravity centre of the volume V (Fig. 20.1).

The next mental experiment is made in order to determine the elastic stress excited in a matrix around the seismofocal volume V.

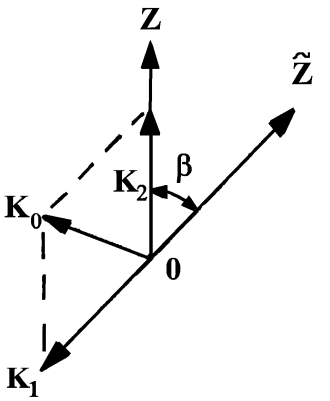

Fig. 20.1 Two systems of coordinates rotating around the common axis by angle β. Axis Z is parallel to the axis of the body rotation Ω and directed from the south pole to the north pole

At first we stop rotation of the volume V applying an elastic stress σ_1 with the force moment $\mathbf{K_1}$, directed towards negative direction of the axis $\widetilde{Z}$; kinetic rotation energy of the volume V transforms entirely into the potential energy of the elastic stress σ_1. Then we allow the seismofocal volume V to rotate with the whole matrix; there appears an elastic stress σ_2 with the force moment $\mathbf{K_2}$, directed parallel to the positive axis (Fig. 20.1). In other words, the kinetic energy the volume V

$$W = \frac{1}{2}\mathbf{I}\,\Omega^2 \tag{20.1}$$

transforms into the elastic energy with the stress tensor σ_1. Here $\mathbf{I}$ is the inertial moment of the volume V, Ω is the angular rotational velocity of the matrix (the Earth); when the considered volume V starts to rotate again conformably with the matrix, the same kinetic energy is produced due to the elastic stress σ_2.

As stated above, we consider the seismofocal block V as a sphere; its inertial moment does not depend on the selection of the rotation axis. The equality of the kinetic and potential energies leads to the equality $|\mathbf{K}_1| = |\mathbf{K}_2|$. When these vectors differ, the required force moment $\mathbf{K_0}$ appears as a result of the rotation of the volume V in the non-inertial coordinate system: $\mathbf{K_0} = \mathbf{K_2} - \mathbf{K_1}$. Its module is found to be (Fig. 20.1):

$$|\mathbf{K}_0| = 2|\mathbf{K}_1|\sin\beta/2 \quad . \tag{20.2}$$

It is to be noted that our approach differs essentially from other analogous approaches. Let us recall, for example, that according to Xie Xin-sheng (2004), the "rotational tectonic stress field is the result of non-uniform motion of matter and dissymmetrical force actions in the nature", while according to Mandeville (2000), "most geological changes and structural features in the crust of the Earth are created by changes in the location of the spin axis and cyclical variations in Chandler's wobble in response to the gravity of the Moon and the Sun".

3. According to the assumptions presented above, the spherical (radius R_0) seismofocal volume V, elastically coupled with its surrounding matrix, becomes rotated due to internal sources. The origin of the coordinates x_i is put in the centre of the volume V. The axis $x_3 = Z$ (Fig. 20.1) is parallel to the axis Ω. To determine the elastic displacement field $\mathbf{U}$ around the rotational volume V, we shall solve the equation of elastic equilibrium (Landau and Lifshits 1987):

$$\text{grad div}\,\mathbf{U} - \chi\ \text{rot rot}\,\mathbf{U} = 0\,, \tag{20.3}$$

where $\chi = (1-2\nu)/2(1-\nu)$, and ν is Poisson's ratio; we apply zero boundary conditions in the infinity:

$$\mathbf{U} \to 0 \quad \text{with} \quad r = \left(x_1^2 + x_2^2 + x_3^2\right)^{1/2} \to \infty \tag{20.4}$$

and the forces acting on the surface of the volume V put as equal to zero

$$F_i = \int_S \sigma_{ij}\, \mathrm{d}S_i = 0 \ . \tag{20.5}$$

The force moment independent of the size of volume V is

$$K_i = \int_S x_k e_{ikl} \sigma_{lj}\, \mathrm{d}S_j \neq f(R_0)\,, \tag{20.6}$$

where σ_{ij} is the stress tensor, e_{ikl} is Levi-Civita's symbol, the surface integral is over a surface of volume $V(R_0)$; the summation is according to repeating indexes.

Solution to the problem (20.1)–(20.6) has been given by Vikulin and Ivanchin (2000) and Vikulin (2003) in the spherical coordinate system (r, φ, ψ), with the origin of coordinates $r = 0$ in the centre of volume V, the angle φ lying in the plane normal to the rotational axis of the block V, and the angle ψ coinciding at $\psi = \pi/2$ with the axis of rotation of volume V. In the domain $r \geq R_0$, the displacement field $\mathbf{U}$ and stress field σ become as follows:

$$U_r = U_\psi = 0, \quad U_\varphi = -3Ar^2 \sin\psi \ , \tag{20.7}$$

$$\sigma_{r\varphi} = \sigma_{\varphi r} = \frac{3}{2} AG\, r^{-3} \sin\psi \ , \tag{20.8}$$

where G is the shear modulus, A is the constant which will be determined below. The other components of the stress tensor are equal to zero.

When putting the field determined in Eq. (20.8) into relation (20.6) for the force moment which creates the elastic field, we obtain

$$K_{1z} = \int_0^{\pi} \int_0^{2\pi} \sigma_{r\varphi} r^3 \sin\psi\, \mathrm{d}\psi\, \mathrm{d}\varphi \ . \tag{20.9}$$

The other components of the force moment are equal to zero: $K_{1x} = K_{1y} = 0$ (Fig. 20.1).

4. The density of the elastic stress energy, W , can be written as follows: $W = \sum\left[\lambda/2(\varepsilon_{ij}\delta_{ij})^2 + G\varepsilon_{ij}^2\right]$, where λ is the uniform compression module,

ε_{ij} is the deformation, δ_{ij} is the Kronecker symbol. To obtain the elastic energy W stored in the matrix (region $r \geq R_0$) we perform the integration:

$$W = \frac{9}{2} A^2 G \int_{R_0}^{\infty} \int_0^{\pi} \int_0^{2\pi} r^{-4} \sin\psi \, \mathrm{d}r \, \mathrm{d}\psi \, \mathrm{d}\varphi = 4\pi A^2 G R_0^{-3} \ . \tag{20.10}$$

The elastic energy W is created by the force moment $\mathbf{K_1}$ (or K_{1z} in Eq. 20.9). Putting the elastic energy W equal to the kinetic energy (20.1), with inertial moment of the sphere $I = 8/15 \, \pi\rho R_0^5$, we obtain

$$A = R_0^4 \Omega \left(\rho / 15G\right)^{1/2} \ , \tag{20.11}$$

where ρ is the average density of the body.

Thus, by means of Eqs. (20.2) and (20.9)–(20.11) the force moment which excites the elastic field around the rotational volume V, and its energy, are determined from the following relations:

$$K = -6\pi^2 \Omega R_0^4 (\rho / 15G)^{1/2} \sin\beta/2 \ , \tag{20.12}$$

$$W = 16/15 \ \pi\rho \Omega^2 R_0^5 \ \sin^2\beta/2 \ . \tag{20.13}$$

By means of relations (20.2), (20.7), (20.8), and (20.11), the field of the displacement **U** and the stress field σ become:

$$U_r = U_\theta = 0, \ \ U_\varphi = -3R_0^4 r^{-2} \Omega (\rho/15G)^{1/2} \sin\psi \sin\beta/2 \, , \ r \geq R_0 \, , \tag{20.14}$$

$$\sigma_{r\varphi} = \sigma_{\varphi r} = 3/2 \ R_0^4 r^{-3} \Omega (\rho/15G)^{1/2} \sin\psi \sin\beta/2 \, , \ r \geq R_0 \, . \tag{20.15}$$

The other components of the stress tensor are equal to zero.

5. The estimations obtained show a good agreement between the theoretical values inferred from the rotational model (20.12)–(20.15), and the experimentally observed parameters characteristic of the largest Pacific earthquakes. Let us assume the model parameters: ρ = 3 g/cm^3, $G = 10^{11}$ N/m^2, $\Omega = 7.3\times10^{-5}$ rad/s and the radius of the elementary spherical seismofocal block $R_0 \approx 100$ km. Its volume is equal to the average source of oval (elliptical) shape in the energy class of the largest Kurile-Kamchatka and Japan earthquakes. Then any four parameters, namely: displacement $U \approx$ 10 m, stress release $\sigma \approx$ 100 bar, seismic moment $M_0 \approx 10^{29}$ dyne·cm, seismic energy radiation $W \approx 10^{17}$ J and angle $\beta \approx 10^{-4}$ rad (i.e., $\approx 10^{-2}$ degree) are automatically inferred from relations (20.12)–(20.15).

Thus, the estimates obtained employing the rotational model for parameters related to the Pacific largest earthquake sources are seis-

mologically and physically substantiated. Moreover, a possibility to describe comprehensively and analytically some physical quantities using our unique model points to the advantages of this model as compared to the known dislocation models for tectonic earthquake sources.

20.4 Interaction Between Seismofocal Blocks

The rotational model explains the earthquake source interaction, as discussed further on, as being related to the source migration (Duda 1963, Mogi 1968). In compliance with the concepts of our model, stresses generated around the seismofocal block are accumulated in the space surrounding it; on the other hand, the seismofocal zone, as part of the lithosphere where the seismic processes occur, is a chain of seismofocal blocks – sources of the largest earthquakes. For this reason, in the rotational model, the stress accumulation in any part of the lithosphere is stipulated either by displacement of a closely located block or by the adjacent seismofocal blocks.

To determine the energy of seismofocal block interaction, let us make use of the proportionality of elastic energy to the strain square. The elastic energy for the model of two blocks can be written as

$$\int (a+b)^2 \mathrm{d}V = G\left(\int a^2 \mathrm{d}V + \int b^2 \mathrm{d}V + 2\int ab\,\mathrm{d}V \right) ,$$

where a and b are the elastic deformations caused by the rotation movements of the first and second blocks, respectively; the integration is extended over the whole volume of the body. The first and second integrals on right-hand side are the elastic energies; each of them is calculated by formulae (20.13). The third integral determines the form of the energy of interaction W_{int} between the first and the second blocks:

$$W_{\mathrm{int}} = 2G\int ab\,\mathrm{d}V \ .$$

This energy of the elastic interaction between two spherical blocks with radii R_1 and R_2 and centers at a distance r from each other was analytically determined as (Vikulin and Ivanchin 2000)

$$W_{\mathrm{int}} = (3/2)\pi\rho\Omega^2 R_1^4 R_2^4 r^{-3}\cos\phi \ , \qquad (20.16)$$

where ϕ is the angle between the force moments of elastic fields around each of the blocks. A ratio of the interaction energy W_{int} to the block's "own" energy W for $R_1 \approx R_2 \approx R_0$, can be estimated using relations (20.13) and (20.16) as follows:

$$\frac{W}{W_{\text{int}}} = \frac{45(R_0/r)^3 \cos\phi}{32(\sin\beta/2)^2} = \delta \ .$$

One can see that the maximum distance between blocks at $\cos\phi \approx 1$, when the interaction energy is close to the block's own energy ($\delta = 1$), is given by the expression $r_0 \approx 2\beta^{-2/3} R_0 \approx (10^2 \div 10^3) R_0$. Thus, in this way the elastic fields created around rotating blocks became capable of remote action (Vikulin and Duda 2001). Such rotary elastic fields allow us to estimate the properties of a chain of blocks.

20.5 Chain of Blocks: Application to Pacific Margin Seismic Belt

Let us consider the seismic processes occurring within the Pacific margin (Vikulin 2003, Vikulin and Ivanchin 2000). We assume for simplicity that the seismofocal region volume consists of a one-dimensional chain of interacting blocks of similar size. Each block is characterized by the inertia moment **I** and a similar volume $V = 4/3\pi R_0^3$. We can write the equation of motion for the block as

$$\mathbf{I}\,\frac{\partial^2 \beta}{\partial t^2} = \mathbf{K} + \mathbf{K}_{\text{int}} \ ,$$

where **K** is the force moment corresponding to the elastic stress field excited around the block, independent of its interaction with other blocks in the chain, and is given by (20.12); $\mathbf{K}_{\text{int}}$ is the force moment responsible for interaction of the block with other blocks in the chain.

It is necessary that quantity $\mathbf{K}_{\text{int}}$ be proportional to the elastic energy accumulated around the block, $V \cdot \partial^2 \beta / \partial z^2$, and consequently to the energy accumulated for the other blocks in the chain. For the latter, we choose the value equal to the average linear density of the elastic energy accumulated for the chain of blocks *w*. Here *z* is the coordinate along the source chain. Thus, we obtain

$$\mathbf{K}_{\text{int}} = w \frac{\partial^2 \beta}{\partial z^2} \ .$$

The final equation of motion for the block with in the coordinate *z* and time interval *t* can be written as the sine-Gordon (SG) equation (Vikulin and Ivanchin 2000):

$$\frac{\partial^2\theta}{\partial\xi^2} - \frac{\partial^2\theta}{\partial\eta^2} = \sin\theta \ ,$$

where we define the non-dimensional coordinates $\theta = \beta/2$, $\xi = k_0 z$, $\eta = c_0 k_0 t$, and constants c_0 and k_0 representing the velocity and wave number of the process.

In the case of quasi-linear approximation (linearized SG equation), when the length of the exciton wave (like an "usual" elastic *S* wave) may be taken equal to the size of rotating block (Nikolaevsky 1996), we obtain the following expression for the value of the characteristic seismotectonic propagation velocity:

$$c_0^2 = 3\sqrt{15}/8\pi^2\, \Omega R_0 \sqrt{G/\rho} \approx V_R V_S \ ,$$

where $V_R = \Omega R_0$ and $V_S = \sqrt{G/\rho}$ mean the values of the centrifugal and *S*-wave velocities. It can be seen, in the framework of the suggested model, that c_0 is related to the value of the Earth's angular rotation. Thus, the name for the model, as given by the authors, is the wave rotary model. Using the above parameters we can find $c_0 \approx 1$ cm/s.

Soliton's solutions of SG equation are well known (e.g. Davydov 1982): the energy of solitons increases monotonically from zero to c_0, which is the maximum velocity.

In a long chain of blocks, the influence of its ends may be not considered, our soliton solutions have two peculiarities. The first peculiarity corresponds to the "zero" solution, when the block chain moves as a whole, without any deformation (Vikulin and Krolevetz 2002). The second peculiarity is the following: the non-linear properties of a solution are not connected with a discontinuous structure of chain but with non-linear properties of the medium. A seismic belt is considered as an analogue of the chain of the blocks.

In the frame of the rotary model, all the observed values of the Pacific earthquakes migration velocities as functions of elastic energy *E* (magnitude *M*) are explained (Fig. 20.2). Earthquake migration along the seismic belt (global migration) corresponds to the soliton's **solution I** of the model's SG equation. The maximum value of soliton global migration velocity (under $M \to M_{\max} \approx$ 8-8.5) is equal to $V_0 \approx c_0$. The soliton's **solution I** may be written down as (Vikulin and Ivanchin 2000)

$$\log L \approx 0.4 \log V \ . \qquad (20.17)$$

Here L (in km) is the length of earthquake foci with the magnitude *M*.

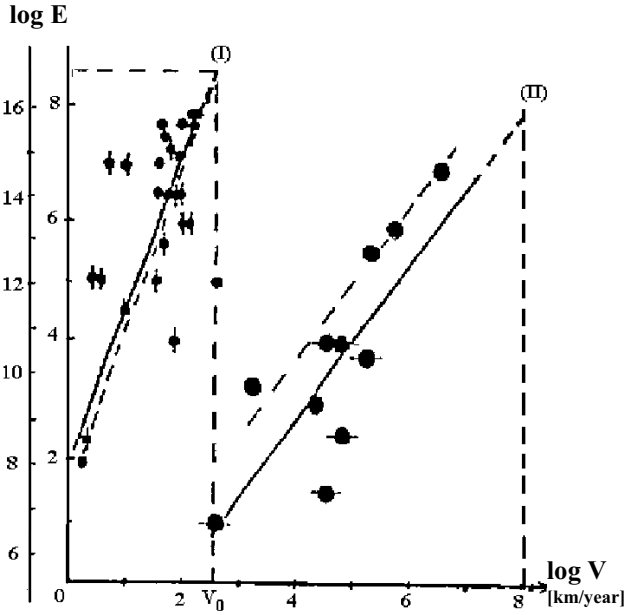

Fig. 20.2 The values of the Pacific earthquake migration speeds along the seismic belt. The determined dependencies $M(V)$: soliton's **solution I** and exciton's **solution II**. The dashed lines – the dependencies which were obtained earlier (Vikulin and Ivanchin 2000). V_0 is the characteristic velocity of the process defined by the parameters of the model; V_S is the velocity of the S wave

The migration of foreshocks and aftershocks within an earthquake focus is described by the exciton's solution of the model SG equation (**solution II**, Fig. 20.2). The "zero" exciton's solution (the movement of the seismic belt as a whole) describes quantitatively the Earth's nutation (Vikulin and Krolevetz 2002). The limit (under $M \rightarrow M_{max} \approx$ 8-8.5) velocity value for an exciton's solution of model SG equation is close to the S-wave velocity (**solution II**, Fig. 20.2).

It is possible, in the frame of the rotary model, to search for solutions concerning the allocation of seismic energy in the earthquake foci.

20.6 Friction and Irregularities of Block Rotation: Rotation Mechanics of Earthquake Foci

Taking into account friction and irregularities of block's rotation, the equation of block's movement in a chain reduces to an indignant Sine-Gordon equation, ISG (Vikulin et al. 2000):

$$\frac{\partial^2\theta}{\partial\xi^2} - \frac{\partial^2\theta}{\partial\eta^2} = \sin\theta + \alpha\frac{\partial\theta}{\partial\eta} + \mu\delta(\xi)\sin\theta \ ,$$

where α is a friction coefficient, μ is a parameter characterizing the force which stimulates the block's rotation, $\delta(\xi)$ is the delta function. The solutions for X, V and $\dot{\theta}$ for the parameters $\alpha \approx 0.1\text{-}1$ and $\mu \approx 10^{-4}\text{-}10^{-2}$, close to real breaks, are shown in Fig. 20.3. Here X is the distance covered by the wave, V is the wave velocity and $\dot{\theta}$ is the deformation velocity.

Numeral investigation of the solutions allowed us to establish the existence of conservation laws. Firstly, the solution of the ISG equation describes the effect corresponding to the process of seizure of the wave by the block: $X_{asymptotic} \to R_0$ (Fig. 20.3), and, consequently, to the process of interaction between the seismofocal block and the tectonic wave. Such a process of interaction contains the three specific phases: foreshock (first maximum of $\dot{\theta}$), aftershock (second maximum of $\dot{\theta}$) and the main shock between them (maximum of V, minimum of $\dot{\theta}$).

Secondly, the tectonic wave has a spinning polarization. The theoretical formula for the wave momentum with its numeral estimation and the formula for the seismic moment with its numeral value, become equal.

Thirdly, during the foreshock stage the elastic field „turns" relative to the considered block. The angle of this turn can be in the microscopic mo-

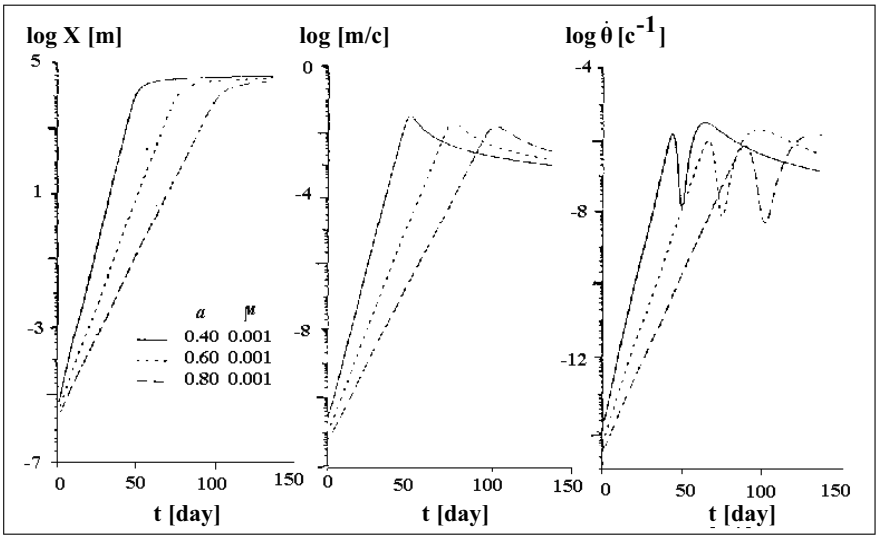

Fig. 20.3 The solutions of the indignant sine-Gordon equation (Vikulin et al. 2000)

dels related to an appearance of disclinations (rotational dislocations) as an analogue to a plane fracturing dislocation models (≈ 45°).

Fourthly, the limit (max.) exciton solution corresponding to the linearized ISG equation (Fig. 20.2: **solution II**, the point $M_{max} - V_S$) is close to the usual elastic wave, with velocity V_{max} and length L_{max} equal to a seismic *S*-wave velocity ($V_{max} \to V_S$) and the length of a seismofocal block $L_{max} = L(M \to M_{max})$; see relation (20.10).

The available data show that the earthquake foci models based on the near-action Reid principle (Reid 1911) can be considered as a particular case of the rotary model when the interaction between the earthquake foci is equal to zero.

20.7 Some Consequences

1. The one-dimensional SG equation is known to belong to the class of integrable equations, for which there exist the Lagrange function and conservation laws. Thus, the interaction energy of the chain of all blocks (E_{int}) is equal to the doubled kinetic energy E_{kin} of the system (from virial theorem: $E_{int} = 2E_{kin}$). The seismic wave energy spreading out from earthquake foci can be, in a first approximation, compared to the kinetic energy. Then, in accordance with the virial theorem, for the model of two blocks, the value of seismic energy of the greatest earthquake must be equal to the half of the interaction energy $E_{int} = W_{int}$ determined from (20.16). In reality, the model of two blocks is similar to the case of "doubled" shocks of the Great Kamchatka 1952, $M = 8.5$ earthquake. Its foci can be represented by two aftershock areas, each of 200-250 km size, 150-200 km apart from each other. The available published examples of multiple earthquakes data are collected in Vikulin (2003). On the basis of these data, putting $R_1 \approx R_2 = R_0 \approx 100$ km, $r \approx 4R_0$, $\phi = \pi$, we obtain from (20.16) the seismic energy $E_{int} = E \approx 10^{17\text{-}18}$ J, that is known to be close to the instrumentally registered values of seismic energy of greatest earthquakes.

It should be noticed that the seismic energy determined in this way, namely

$$E = 3/256\, \pi \rho \Omega^2 R_0^5 \neq f(G) \tag{20.18}$$

coincides with the numerical factor from (20.13), the expression for the elastic field energy of the rotating block. Also, the obtained seismic energy is independent of the elastic modulus *G*. Physically this means that the rotary mechanism allows "to inject" into the hard medium such a quantity of elastic energy that it can exceed its shear strength.

A possibility of determining the earthquake elastic energy value (20.18) may allow us to construct the earthquakes statistics (the statistical seismology) based on the rotary model.

2. The relation between tectonics and the problem of rotational movement is not new (Lee 1928, Melekestsev 1979, 2004, Wezel 1986, Mandeville 2000, Xie Xin-sheng 2004). In the light of rotary concept, the plates as well as the "elementary" seismofocal blocks are surrounded by fields of elastic stresses (Vikulin 2004, Tveritinova and Vikulin 2005).

Analytically, the problem of elastic stress fields arising in the whole body of a rotating planet with its turning plates and blocks has not been solved yet; it is necessary to check the adaptability of the rotary concept to tectonic problems. To this end, we analyze the data characterizing the plate sizes and the spreading velocity of the rifting zones of the Pacific. The results are shown in Fig. 20.4; the line on this figure is estimated by the least-squares method:

$$\log L = (0.4 \pm 0.1) \log V + (3.2 \pm 0.3) \ .$$

The dependence obtained is near to the soliton block relation (20.17).

Our result shows that the rotary concept can be applied in principle to the tectonic problems, connected with the calculation of elastic stresses fields round the moving plates. The value of elastic energy corresponding to such a rotary interaction can exceed greatly the theoretical shear strength.

3. One can believe that in this way we can approach the forecast of the strength of the medium. The possibility for quantitative description of the

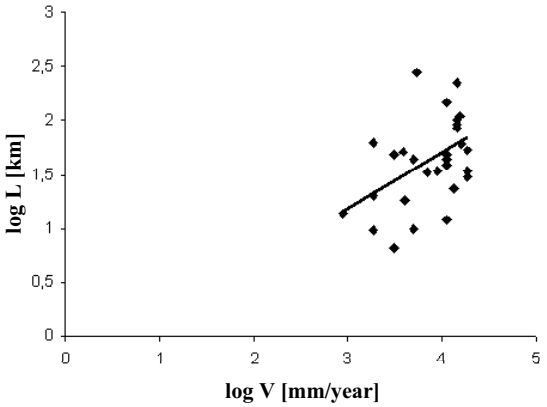

Fig. 20.4 Data showing the existence of dependence between the length of plates (log$L$ in km) and the velocity of spreading-rifting (log$V$ in mm/year) along their boundaries (Tveritinova and Vikulin 2005)

foreshock and aftershock stages of the seismic cycle (Fig. 20.3) allows us to create a kind of earthquake prediction theory, containing the timing of events and their foci locations, which is more deterministic than statistic in character.

As we can see, the rotary wave seismic model, explaining remote action effect between earthquake's foci, may open new ways for the solution to the earthquake prediction problem. To this end, it would be necessary, firstly, to improve the presented theoretical approach and, secondly, to develop a network of stations recording rotation waves, in place of the existing single stations of such a character (e.g. Huang 2001, Takeo 1998).

In the frame of the rotary model, the nature of interaction between seismicity and the solar activity cycles could be studied, as the seismicity and its relation to the moment of momentum of blocks become related to the "complex dynamics of all the solar system" (Timashev 2003).

4. Some aspects of the presented model in relation to geomechanical problems can also be discussed. The analysis of natural stress fields based on the results of measurements in mines on the territory of North Eurasia indicates that the whole body of the Earth's crust is self-organizing in each moment of time. Such structures can be described by means of the "pendulum" waves (Kurlenya and Oparin 2000) that are per se the tectonic solitons.

Strong explosions (including the volcanic ones) do not radiate the rotation/torsion waves. Thus, solutions of the related problems of the recognition of explosions can be supported by recording the torsional oscillations (Baumgard et al. 2001).

5. The rotary wave model, utilizing the concept of stresses and force moments, was constructed in the frame of classical elasticity theory. In our approach, we did not need the concept of elasticity theories (Nowacki 1975) based on Cosserat's continuum (Cosserat and Cosserat 1909). It can be noted that the Cosserat's elasticity theory, in contrast to the classic elasticity theory (Landau and Lifshits 1987) is purely mathematical (Nikolaevsky 1995). We think that this can be of consequence for only one reason: the space in relation to asymmetrical tensor shall be considered as anisotropic (Vikulin and Ivanchin 2002).

20.8 Conclusions

It turns out that the idea of the Earth crust block which might rotate due to the internal sources, brings some new productive tools. In the frame of our

and other models it became possible to get quantitative description of the wide spectrum of geophysics phenomena (Lee 1928, Melekestsev 1979, 2004, Wezel 1986, Kurlenya and Oparin 2000, Mandeville 2000, Kulakov 2003, Tveritinova and Vikulin 2005, Vikulin 2000, 2002, 2003, 2004, Vikulin et al. 2000, Vikulin and Duda 2001, Vikulin and Ivanchin 2002, Vikulin and Krolevetz 2002, Xie Xin-sheng 2004). Thus, the basis of a new school, "the vortex dynamics of the lithosphere", is founded.

The relations between tectonic vortex movement intensity and planet's rotation, as analyzed above, might be extended onto a search for similar relations in the domain of atmosphere vortex movements, like cyclones, on the Earth and planets.

Finally, we believe that the nature of vortex movements is connected with some more "deep" parameters related to the fine matter structure; such relations might become recognized along with the development of seismic technology of sufficiently high precision to study elastic nonlinear waves of spinning polarization.

Acknowledgments. The author is grateful to S. Duda and R. Teisseyre for help and discussions on the problems of the paper.

References

Baumgard DR, Ryaboy V, Gusev AA, Vikulin AV (2001) Calibration of the IMS station at Petropavlovsk (PET) on Kamchatka Peninsula and other IMS stations in the transition zone from Eastern Eurasia to the Pacific ocean. Third Workshop on IMS Location Calibration, NORSAR, Oslo, Norway, 23-27 April, 2001

Chao BF, Gross RS (1995) Changes in the Earth's rotational energy induced by earthquakes. Geophys J Int **122**: 776-783

Cosserat E, Cosserat F (1909) Theorie des corps deformables. Hermann, Paris

Daly MC (1989) Correlation between Nazca-Farallon plate kinematics and forearc basin evolution in Ecuador. Tectonics **8**: 4, 769-790

Davydov AS (1982) Solitons in quasi-one-dimensional molecular structures. Usp Fiz Nauk (Moscow) **138**: 4, 603-644 (in Russian)

Duda SJ (1963) Strain release in the Circum-Pacific belt, Chile 1960. J Geophys Res **68**: 5531-5544

Geist EL, Childs JR, Scholl DW (1988) The origin of summit basins of the Aleutian ringe: implications for block rotation of an arc massif. Tectonics **7:** 2, 327-341

Huang B-S (2001) Evidence for azimuthal and temporal variations of the rupture propagation of the 1999 Chi-Chi, Taiwan, earthquake from dense seismic array observations. Geophys Res Lett **28**: 3377-3380

Kulakov A (2003) Morphostructure and evolution of the eastern margin of Asia. The new confirmation of the expanding earth theory. In: Scalera G, Jacob KH (eds) Why expanding earth? INGV Publisher, Roma, Italy, pp 275-296

Kurlenya MV, Oparin VN (2000) Problems of nonlinear mechanics, II. Physical -Engineering Creation of Mineral Product Inst of Mining of SB RAS, Novosibirsk 4: 3-26 (in Russian)

Landau LD, Lifshits EM (1987) Elasticity theory. Nauka, Moscow, pp 248 (in Russian)

Lee JS (1928) Some characteristic structural types in Eastern Asia and their bearing upon the problems of continental movements. Geol Mag **66**: 422-430

Lyubushin AA Jr (1987) Hierarchical model of seismic process. Fiz Zemli 11: 43-52 (in Russian)

Mandeville MW (2000) An outline of the principles of vortex tectonics. http: //www.aa.net/~mwm

Melekestsev IV (1979) The vortex volcanic hypothesis and some prospects for its application. In: Problems of deep magmatism. Nauka, Moscow, pp 125-155 (in Russian)

Melekestsev IV (2004) Significance of vortexes in the origin and existence of the Earth. In: Vortex-related events of the geological processes. KGPU, Petropavlovsk-Kamchatsky, pp 25-70 (in Russian), www.kcs.iks.ru

Mogi K (1968) Migration of seismic activity. Bull Earthquake Res Inst **46**: 175-203

Nikolaevsky VN (1995) Mathematical modelling of deformation and seismic waves. Doklady of RAS **341**: 3, 403-405 (in Russian)

Nikolaevsky VN (1996) Geomechanics and fluidodynamics. Kluwer, Boston, pp 448

Nowacki W (1975) Elasticity theory. Mir, Moscow, pp 872 (in Russian)

Reid HF (1911) The elastic rebound theory of earthquakes. Univ Calif Publ Bull Dep Geol 6: 413-444

Rikitake T (1967) Geophysical and geological data in and around the Japan Arc. Japanese National Report for the UMP, Tokyo

Sato H (1973) A study of horizontal movement of the crust. Bull Geograph Survey Inst **19**: 1, 89-130

Scheidegger AE (1982) Principles of geodynamics. Springer-Verlag, Berlin

Takeo M (1998) Ground rotational motions recorded in near-source region of earthquakes. Geophys Res Lett **25**: 789-792

Timashev SF (2003) On basic principles “New dialogue with Natura”. In: Nikolaev AV (ed) Problems of geophysics of the 21st century, vol 2. Nauka, Moscow, pp 104-141 (in Russian)

Tveritinova TYu, Vikulin AV (2005) Geological and geophysical signs of vortex structures in geological medium. Bull Kamchatka Regional Association “Educational Scientific Center” Earth Sciences 5: 59-77 (in Russian), http://www.kcs.iks.ru

Vikulin AV (ed) (2000) Far East seismicity problems. KEMSD, Petropavlovsk -Kamchatsky, pp 318 (in Russian)

Vikulin AV (2002) Solitary tectonic waves of rotational deformation as a result of planet's rotation. Geophys J (Kiev) **24**: 4, 90-101 (in Russian)

Vikulin AV (2003) Physics of wave seismic process. KSPU, Petropavlovsk -Kamchatsky, pp 150 (in Russian), http://www.kcs.iks.ru

Vikulin AV (ed) (2004) Vortex-related events of the geological processes. KSPU, Petropavlovsk-Kamchatsky, pp 297 (in Russian) http://www.kcs.iks.ru

Vikulin AV, Duda S (2001) Long-period motion by earthquakes. In: Problems of seismicity of the Far East. Proceedings of III-d scientific conference, Khabarovsk, pp 24-26 (in Russian)

Vikulin AV, Ivanchin AG (2000) Rotational model of seismic process. Geol Pac Ocean **15**: 1225-1240

Vikulin AV, Ivanchin AG (2002) Rotation and elasticity. Probl Materials Science **1:** 29, 435-441 (in Russian)

Vikulin AV, Krolevetz AN (2002) Seismotectonic processes and the Chandler oscillation. Acta Geophys Pol **50**: 395-411

Vikulin AV, Bykov VG, Luneva MN (2000) Nonlinear deformation's waves in rotational model of seismic process. Calculating Technologies (Novosibirsk) **5**: 1, 31-39 (in Russian)

Wezel F-C (1986) The Pacific island arcs: produced by post-orogenic vertical tectonics? In: Wezel F-C (ed) The origin of arcs. Elsevier, Amsterdam, pp 529-566

Xie Xin-sheng (2004) Discussion on rotational tectonics stress field and the genesis of circum-Ordos landmass fault system. Acta Seism Sinica **17**: 4, 464-472

Zhuravlev VI (1983) Modelling of seismic process by autoregression equation. In: Tentative seismology, Nauka, Moscow, pp 99-108 (in Russian)

PART IV

EFFECTS RELATED TO MEDIUM STRUCTURES AND COMPLEXITY OF WAVE PROPAGATION

21 Seismic Rotation Waves in the Continuum with Nonlinear Microstructure

Eugeniusz Majewski

Institute of Geophysics, Polish Academy of Sciences
ul. Księcia Janusza 64, 01-452 Warszawa, Poland
e-mail: emaj@igf.edu.pl

21.1 Introduction

The aim of this chapter is to derive a nonlinear equation for seismic rotation waves. To this end, we apply the theory of a linear elastic microstructure formulated by Mindlin (1964) and its nonlinear generalization developed by Engelbrecht and Pastrone (2003). The problem of seismic rotation waves in the continuum with nonlinear microstructure is considered here at two levels. We start with some balance equations employing a macroscopic stress that plays a crucial part in exciting seismic *P* waves and seismic rotation waves. We consider a nonlinear microstructure, which is determined by microrotations and microforces of interactions. In the microstructure we emphasize its nonlinearity resulting from a nonlinear term in the free energy function. Fundamental equations of the nonlinear microstructure are finally applied to the derivation of a nonlinear equation for seismic rotation waves. This equation describes double dispersion. These rotation waves are the waves that are excited by rotational motions in the earthquake source. At first, we divide the stresses and forces into two groups: macroscopic and microscopic. Next, we assume an additive decomposition of the total macroscopic stresses, microstresses, and interaction microforces into elastic and self-parts (plastic parts). The elastic parts of stresses and forces are our main field of interest. These stresses and forces are expressed in terms of the free energy function. At the first stage, a linear form of this function is considered. From this linear form of the free energy, we derive a linear equation of the seismic rotation waves. At the second stage, we add merely one cubic term containing a spatial derivative of rotation. We consider a collinear propagation of the nonlinear seismic *P* waves and the nonlinear seismic rotation waves. As a result, we obtain a nonlinear equation describing the seismic rotation waves propa-

gating in the solid Earth, which is modeled as a continuum with nonlinear microstructure. The concept of microstructure is, to some extent, similar to the concept of the dislocation superlattice applied to earthquake thermodynamics (Majewski and Teisseyre 1997). In addition, the spinel lenses in anticracks considered by Majewski and Teisseyre (1998) form a certain material microstructure.

21.2 Additivity of Elastic and Self-Parts of Stresses, Microstresses, and Interaction Microforces

Our starting point in exploring the seismic rotation waves is to assume an additivity of the elastic and self-parts of stresses, microrotations, and microforces in the following form (Teisseyre and Majewski 2001, 2002):

$$\mathbf{S}^T = \mathbf{S} + \mathbf{S}^S\,, \quad \boldsymbol{\varphi}^T = \boldsymbol{\varphi} + \boldsymbol{\varphi}^S\,, \quad \boldsymbol{\varsigma}^T = \boldsymbol{\varsigma} + \boldsymbol{\varsigma}^S\,, \tag{21.1}$$

where $\mathbf{S}^T$ is the Piola-Kirchhoff total stress, $\mathbf{S}$ is the Piola-Kirchhoff elastic stress, $\mathbf{S}^S$ is the Piola-Kirchoff self-stress, $\boldsymbol{\varphi}^T$ is the total microstress, $\boldsymbol{\varphi}$ is the elastic microstress, $\boldsymbol{\varphi}^S$ is the self-microstress, $\boldsymbol{\zeta}^T$ is the total interaction microforce, $\boldsymbol{\zeta}$ is the elastic interaction microforce, and $\boldsymbol{\zeta}^S$ is the interaction self-microforce. The self-parts can be treated as internal variables of the material continuum (Majewski 1993).

21.3 The Macroscopic and Microscopic Balance Equations

We outline here basic concepts of the theory of microstructure in linear elasticity constructed by Mindlin (1964) and its nonlinear generalization proposed by Engelbrecht and Pastrone (2003). Let us now write the macroscopic momentum balance equation in the form

$$\int_{\partial B} \mathbf{S}\mathbf{n}\,\mathrm{d}A + \int_B \mathbf{F}_{\mathrm{L}}\,\mathrm{d}V = \frac{\mathrm{d}}{\mathrm{d}t}\int_B \mathbf{p}\,\mathrm{d}V\,. \tag{21.2}$$

The microscopic balance of momentum can be written as

$$\int_{\partial B} \boldsymbol{\Phi}\mathbf{n}\,\mathrm{d}A + \int_B \left(\mathbf{F}_{\Lambda} + \boldsymbol{\Upsilon}\right)\mathrm{d}V = \frac{\mathrm{d}}{\mathrm{d}t}\int_B \vartheta\,\mathrm{d}V\,, \tag{21.3}$$

where B is the solid body volume under consideration, ∂B is the outer surface of the solid body B, $\mathbf{n}$ is the unit normal vector, $\mathbf{S}$ is the Piola-Kirchhoff macrostress tensor, $\boldsymbol{\Phi}$ is the microstress tensor, $\mathbf{F}_{\mathrm{L}}$ and $\mathbf{F}_{\Lambda}$ are

the body macroforces and microforces, respectively, Υ is the interaction microforce, $\mathbf{p} = \rho \dot{\mathbf{x}}$ is the linear macromomentum, ρ is the mass density, and $\dot{\mathbf{x}}$ is the macroscopic velocity, $\vartheta = I\dot{\upsilon}$ is the micromomentum, where I is the inertia tensor and $\dot{\upsilon}$ is the microscopic velocity.

From Eqs. (21.2) and (21.3), one can obtain the following one-dimensional relationships (Engelbrecht 1997, Eringen 1999, Engelbrecht and Pastrone 2003):

$$\rho u_{tt} = S_x + F_L \,, \tag{21.4}$$

$$I\upsilon_{tt} = \varphi_x + \varsigma + F_\Lambda \,, \tag{21.5}$$

where u is the magnitude of the displacement, and the subscripts x, t denote spatial and time derivatives, respectively.

In order to simplify Eqs. (21.4) and (21.5), we neglect the body forces and replace υ_{tt} by ϕ_{tt}, where ϕ is the rotation. Thus, we obtain the following set of equations:

$$\rho u_{tt} = S_x \,, \tag{21.6}$$

$$I\phi_{tt} = \varphi_x + \varsigma \,. \tag{21.7}$$

We assume a free energy function in the form

$$\Psi = \Psi\left(u_x, \phi, \phi_x\right), \tag{21.8}$$

where u_x is the spatial derivative of the longitudinal displacement, ϕ is the rotation, and ϕ_x is the spatial derivative of the rotation.

The elastic components of the quantities defined by Eqs. (21.1), can be expressed in terms of the free energy

$$S = \frac{\partial \Psi}{\partial u_x} \,, \qquad \varphi = \frac{\partial \Psi}{\partial \phi_x} \,, \qquad \varsigma = \frac{\partial \Psi}{\partial \phi} \,. \tag{21.9}$$

At first, let us consider the free energy function with quadratic terms

$$\Psi = \frac{1}{2} a u_x^2 - b\phi u_x + \frac{1}{2} c\phi^2 + \frac{1}{2} d\phi_x^2 \,, \tag{21.10}$$

where a, b, c and d are constant coefficients.

With help of the above relations, Eqs. (21.6) and (21.7) will take the following form:

$$\rho u_{tt} = a u_{xx} - b\phi_x \,, \tag{21.11}$$

$$I\phi_{tt} = d\phi_{xx} - bu_x + c\phi\,. \tag{21.12}$$

The above set of wave equations can be interpreted as a collinear propagation of the seismic *P* wave and the seismic rotation wave.

We use the following dimensionless quantities:

$$U = u/U_0\,, \qquad X = x/L\,, \qquad T = t\,V_P/L\,, \tag{21.13}$$

where V_P is the magnitude of velocity of the seismic *P* wave, $V_P^2 = a/\rho$, in addition, U_0 and L are constant intensity and wavelength of the initial excitation. We must also introduce a scale parameter Λ of the microstructure, and two more dimensionless parameters $\varepsilon = \Lambda^2/L^2$, $\delta = U_0/L$. After Engelbrecht and Pastrone (2003), we write for the inertia $I = \rho\Lambda^2 I_0$, and for the stress parameter $d = \Lambda^2 d_0$, where I_0 is dimensionless and d_0 has the stress dimension. As a result, Eqs. (21.11) and (21.12) take the form

$$U_{TT} = U_{XX} - b_0\phi_X\,, \tag{21.14}$$

$$\varepsilon a I_0 \phi_{TT} = \varepsilon d_0 \phi_{XX} - b\delta U_X + c\phi\,, \tag{21.15}$$

where $b_0 = b/a$.

Equation (21.15) can be solved for U_X as follows:

$$U_X = \frac{c}{b\delta}\phi + \frac{\varepsilon}{b\delta}\left(d_0\phi_{XX} - aI_0\phi_{TT}\right)\,. \tag{21.16}$$

Now, we differentiate Eq. (21.16) twice with respect to X

$$U_{XXX} = \frac{c}{b\delta}\phi_{XX} + \frac{\varepsilon}{b\delta}\left(d_0\phi_{XX} - aI_0\phi_{TT}\right)_{XX}\,, \tag{21.17}$$

and differentiate Eq. (21.16) twice with respect to time

$$U_{XTT} = \frac{c}{b\delta}\phi_{TT} + \frac{\varepsilon}{b\delta}\left(d_0\phi_{XX} - aI_0\phi_{TT}\right)_{TT}\,. \tag{21.18}$$

We differentiate Eq. (21.14) with respect to X

$$U_{TTX} = U_{XXX} - b_0\,\phi_{XX}\,. \tag{21.19}$$

Let us assume that $U_{XTT} = U_{TTX}$, and write the above equation in the form

$$U_{XTT} = U_{XXX} - b_0\,\phi_{XX}\,. \tag{21.20}$$

Substituting (21.17) and (21.18) into (21.20), we obtain a linear equation for seismic rotation waves in the form

$$\phi_{TT} = (1-\eta)\phi_{XX} + \varepsilon\left[\frac{1}{c}\left(\Re_{XX} - \Re_{TT}\right)\right], \tag{21.21}$$

where $\eta = \delta b b_0 / c$, and

$$\Re_{XX} = \left(d_0\phi_{XX} - aI_0\phi_{TT}\right)_{XX}, \tag{21.22}$$

$$\Re_{TT} = \left(d_0\phi_{XX} - aI_0\phi_{TT}\right)_{TT}. \tag{21.23}$$

Equation (21.21) describes the linear seismic rotation wave in a solid Earth with microstructure. The wave velocity is different here than in the continuum without microstructure due to the presence of the coefficient η. The parameter ε plays the crucial part here. The influence of the microstructure on the macrostructure is directly proportional to the value of parameter ε. This parameter depends on the ratio of micro- and macroscales that are depicted in Fig. 21.1. This equation reveals the so-called double dispersion, because of the appearance of the spatial and time fourth order derivatives ϕ_{XXTT} and ϕ_{TTTT}, which are present in the terms $\Re_{XX}$ and $\Re_{TT}$. These results are, to some extent, similar to the results obtained by Maugin (1999).

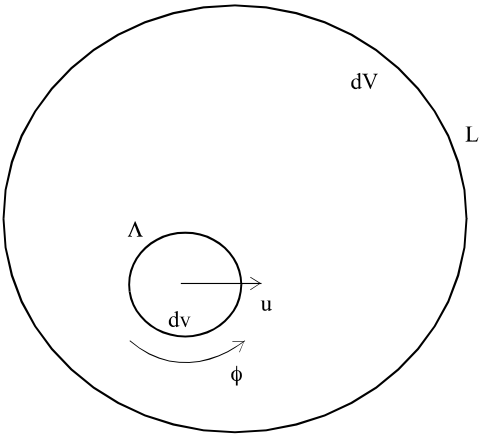

Fig. 21.1 Microscopic and macroscopic levels of description of the excitation of seismic waves. Here dv denotes the microvolume, Λ the internal scale in the microvolume, ϕ the direction of rotation of the microvolume, u the direction of the longitudinal displacement of the microvolume; and dV denotes the macrovolume and L the macroscopic scale in the macrovolume

21.4 The Nonlinear Microstructure

In order to keep the model simple, the macroscopic description is still linear. However, in the microstructure, after Engelbrecht and Pastrone (2003), we add a cubic term to the expression (21.10) for the free energy function. Thus, one can obtain

$$\Psi = \frac{1}{2}au_x^2 - b\phi u_x + \frac{1}{2}c\phi^2 + \frac{1}{2}d\phi_x^2 + \frac{1}{3}e\phi_x^3 . \tag{21.24}$$

Now, instead of (21.11) and (21.12), we have

$$\rho u_{tt} = au_{xx} - b\phi_x , \tag{21.25}$$

$$I\phi_{tt} = d\phi_{xx} + e\phi_x\phi_{xx} - bu_x + c\phi . \tag{21.26}$$

where $e = \Lambda^2 e_0$, and e_0 is constant.

Using the dimensionless quantities, we can write the above equations in the form:

$$U_{TT} = U_{XX} - b_0\phi_X , \tag{21.27}$$

$$\varepsilon a I_0\phi_{TT} = \varepsilon d_0\phi_{XX} + \varepsilon e_0\phi_X\phi_{XX} - \delta b U_X + c\phi . \tag{21.28}$$

One can solve the last equation for U_X as follows:

$$U_X = \frac{c}{\delta b}\phi + \frac{\varepsilon}{\delta b}\left(d_0\phi_{XX} - aI_0\phi_{TT} + e_0\phi_X\phi_{XX}\right) . \tag{21.29}$$

Now, we differentiate the above equation twice with respect to X

$$U_{XXX} = \frac{c}{\delta b}\phi_{XX} + \frac{\varepsilon}{\delta b}\left(d_0\phi_{XX} - aI_0\phi_{TT} + e_0\phi_X\phi_{XX}\right)_{XX} , \tag{21.30}$$

and differentiate twice with respect to time

$$U_{XTT} = \frac{c}{\delta b}\phi_{TT} + \frac{\varepsilon}{\delta b}\left(d_0\phi_{XX} - aI_0\phi_{TT} + e_0\phi_X\phi_{XX}\right)_{TT} . \tag{21.31}$$

We differentiate Eq. (21.27) with respect to X

$$U_{TTX} = U_{XXX} - b_0\phi_{XX} . \tag{21.32}$$

Now, we assume that $U_{XTT} = U_{TTX}$, and write the above equation in the form:

$$U_{XTT} = U_{XXX} - b_0 \phi_{XX} \,. \tag{21.33}$$

Inserting (21.30) and (21.31) into (21.33), we obtain a nonlinear equation for seismic rotation waves in the form:

$$\phi_{TT} = (1-\eta)\phi_{XX} + \varepsilon\left[\frac{1}{c}\left(\tilde{\Re}_{XX} - \tilde{\Re}_{TT}\right)\right], \tag{21.34}$$

where $\eta = \delta b b_0 / c$, and

$$\tilde{\Re}_{XX} = \left(d_0\phi_{XX} - aI_0\phi_{TT} + e_0\phi_X\phi_{XX}\right)_{XX}, \tag{21.35}$$

$$\tilde{\Re}_{TT} = \left(d_0\phi_{XX} - aI_0\phi_{TT} + e_0\phi_X\phi_{XX}\right)_{TT}. \tag{21.36}$$

The nonlinear wave properties are displayed in the last terms of expressions (21.35) and (21.36).

It is interesting to compare the nonlinear wave equation (21.34) with the DDE equation derived by Samsonov (2001) in the form:

$$U_{TT} = b_1 U_{XX} + \varepsilon^2\left[b_2 U_{XXTT} + b_3 U_{XXXX} + b_4 (U^2)_{XX}\right]. \tag{21.37}$$

The above equation describes double dispersion and dissipation and has a solitary solution.

21.5 Conclusions

This chapter presented a few ideas concerning the continuum with nonlinear microstructure. Such a continuum allows the propagation of nonlinear seismic rotation waves. These are the waves that are excited by rotational motions in the earthquake source. We considered a collinear propagation of the seismic *P* waves and the seismic rotation waves. As a result, we obtained a nonlinear equation describing the seismic rotation waves propagating in the solid Earth modeled as the continuum with nonlinear microstructure. We found that the influence of microstructure is visible in affecting the wave velocity. The microstructure provides us with the formalism that is essential in the description of double dispersion. The derived nonlinear equation reveals the interplay between the nonlinearity and dispersion. It is noteworthy that the continuum is linear at the macroscopic level, but nonlinear at the microscopic level. Finally, we compared the nonlinear wave equation for rotation waves with the DDE equation derived by Samsonov (2001) for longitudinal waves in the solid rod. The DDE

equation has a solitary solution. The main difference between the DDE equation and the equation derived here consists in the appearance of fourth time derivatives in the latter equation and their absence in the DDE. We conclude that the equation derived here describes a different type of double dispersion than the DDE equation. The equation for rotation waves is more sensitive to time derivatives.

References

Engelbrecht J (1997) Nonlinear wave dynamics: complexity and simplicity. Kluwer, Dordrecht

Engelbrecht J, Pastrone F (2003) Waves in microstructured solids with nonlinearities in microscale. Proc Estonian Acad Sci Phys Math **52**: 12-20

Eringen AC (1999) Microcontinuum field theories. I Foundations and solids. Springer, New York

Majewski E (1993) Thermodynamic approach to evolution. In: Teisseyre R, Czechowski L, Leliwa-Kopystynski J (eds) Dynamics of the earth's evolution, Vol 6 Teisseyre R (ser ed): Physics and evolution of the earth's interior. Elsevier, Amsterdam, New York.

Majewski E, Teisseyre R (1997) Earthquake thermodynamics. Tectonophysics **277**: 219-233

Majewski E, Teisseyre R (1998) Anticrack-associated faulting in deep subduction zones. Phys Chem Earth **23**: 1115-1122

Maugin GA (1999) Nonlinear waves in elastic crystals. Oxford University Press, Oxford

Mindlin RD (1964) Micro-structure in linear elasticity. Arch Ration Mech Anal **16**: 51-78

Samsonov AM (2001) Strain solitons in solids and how to construct them. Chapman & Hall/CRC, London

Teisseyre R, Majewski E (eds) (2001) Earthquake thermodynamics and phase transformations in the earth's interior. Academic Press, San Diego

Teisseyre R, Majewski E (2002) Physics of earthquakes. In: Lee WHK, Kanamori H, Jennings PC, Kisslinger C (eds) International handbook of earthquake & engineering seismology, Part A. Academic Press, San Diego, pp 229-235

22 Tectonic Solitons Propagating Along the Fault

Eugeniusz Majewski

Institute of Geophysics, Polish Academy of Sciences
ul. Księcia Janusza 64, 01-452 Warszawa, Poland
e-mail: emaj@igf.edu.pl

22.1 Introduction

The aim of this chapter is to determine two types of tectonic solitons excited in the earthquake source and propagating along the fault: longitudinal self-distortion (plastic) solitons and shear self-distortion solitons. The Earth's interior is modeled as an elasto-plastic continuum. We summarize a few results of the gauge theory of elasto-plastic continuum with dislocations that was formulated by Kadic and Edelen (1983), Edelen and Lagoudas (1988), Lagoudas (1989), Lagoudas and Edelen (1989). Elasto-plastic waves were investigated by Erofeyev (2003). He derived two soliton equations that describe elastic longitudinal and plastic shear distortion solitons. The problem of sine-Gordon solitons propagating along the fault was considered by Nikolaevskiy (1996). We outline his work and employ the solitons to the description of processes occurring on the fault. Teisseyre and Yamashita (1999) pioneered the method of splitting the stress motion equations into wave and fault-related parts. We apply their method in order to determine the solitons propagating along the fault. The first type of obtained solitons are the seismic longitudinal self-distortion Klein –Gordon's solitons that were formulated by splitting a soliton equation for elastic longitudinal distortions into a field part and the fault-related self -part. The solitons of the second type are the seismic shear self-distortion Schrödinger's solitons that also propagate along the fault.

22.2 Seismic Waves in the Continuum with Dislocations

Let us denote the displacement vector by $\mathbf{u}(x, t)$. We also assume that the total stress and total distortion can be decomposed into the elastic and self-fields (plastic fields) as follows (Teisseyre 2004):

$$S^T = S + S^S, \qquad \beta^T = \beta + \beta^S . \tag{22.1}$$

We limit our considerations to translational defects only, so the internal variable (Majewski 1993) can be described by the self-distortion tensor β_{ij}^S (Eringen 1999, Teisseyre and Majewski 2001, 2002).

In the framework of the gauge field theory applied to the medium with dislocations, the fundamental equations are obtained by variation of the gauge invariant Lagrangian. In the case of elastic and self-deformations, Lagrangian L^T consists of two parts (Panin 1995, Erofeyev 2003)

$$L^T = L + L^S . \tag{22.2}$$

The first part describes the kinetic energy of total displacements minus the potential energy of elastic fields in the medium. It can be expressed as

$$L = \int \left[\frac{1}{2}\left(\rho \frac{\partial u_i}{\partial t}\frac{\partial u_i}{\partial t} \right) - \frac{\lambda}{2}\left(\frac{\partial u_i}{\partial x_i} - \beta_{ii}^S \right)\left(\frac{\partial u_k}{\partial x_k} - \beta_{kk}^S \right) \right.$$
$$\left. - \frac{\mu}{2}\left(\frac{\partial u_k}{\partial x_i} - \beta_{ki}^S \right)\left(\frac{\partial u_i}{\partial x_k} - \beta_{ik}^S \right) - \frac{\mu}{2}\left(\frac{\partial u_i}{\partial x_k} - \beta_{ki}^S \right)\left(\frac{\partial u_k}{\partial x_i} - \beta_{ik}^S \right) \right] \mathrm{d}V , \tag{22.3}$$

where ρ is the medium density, λ and μ are Lamé's constants, $\mathrm{d}V$ is the differential volume.

The second part describes the kinetic minus the potential energy of dislocations. It can be written in the form

$$L^S = \int \left(\frac{B}{2}\frac{\partial \beta_{km}^S}{\partial t}\frac{\partial \beta_{km}^S}{\partial t} - \frac{C}{2}\alpha_{km}\alpha_{km} \right) \mathrm{d}V , \tag{22.4}$$

where B and C are the medium constants; B is proportional to the effective mass of dislocations in a unit volume, C is proportional to the self-energy of dislocations. The tensor of dislocation density α_{km} is determined as follows:

$$\alpha_{km} = \in_{kij} \frac{\partial \beta_{jm}^S}{\partial x_k} . \tag{22.5}$$

The medium is assumed to be plastically incompressible, i.e. under the self-deformation the following relations hold:

$$\mathrm{Tr}\left[\beta_{ij}^S \right] = \beta_{ii}^S = 0 . \tag{22.6}$$

The dissipation is determined by the Rayleigh function

$$\Re = \eta \frac{\partial \beta_{ij}^S}{\partial t} \frac{\partial \beta_{ij}^S}{\partial t} = \eta I_{ij} I_{ij} \,, \tag{22.7}$$

where

$$I_{ij} = \frac{\partial \beta_{ij}^S}{\partial t} \tag{22.8}$$

is the dislocation stream tensor, and η is the dissipation coefficient.

After Erofeyev (2003), we can recall the equations of motion of elasto-plastic continuum obtained as a result of taking a variation of Lagrangian (22.1) and dissipation function (22.7)

$$\rho \frac{\partial^2 u_i}{\partial t^2} = \frac{\partial S_{ik}}{\partial x_k}, \qquad B \frac{\partial^2 \beta_{ij}^S}{\partial t^2} = S_{ij}^S - 2\eta \frac{\partial \beta_{ij}^S}{\partial t}, \tag{22.9}$$

where the elastic stress tensor is expressed as follows:

$$S_{ij} = \mu \left(\frac{\partial u_i}{\partial x_j} + \frac{\partial u_j}{\partial x_j} - \beta_{ji}^S - \beta_{ij}^S \right) + \lambda \delta_{ij} \frac{\partial u_k}{\partial x_i} \,, \tag{22.10}$$

and the self-stress tensor takes the form

$$S_{ij}^S = S_{ij} - \gamma S_{ij} + C \left(\frac{\partial^2 \beta_{ij}^S}{\partial x_k \partial x_k} - \frac{\partial^2 \beta_{kj}^S}{\partial x_k \partial x_i} \right), \tag{22.11}$$

where γ is a Lagrange factor, which can be determined from Eq. (22.5)

$$\gamma = \left(\lambda + \frac{2}{3} \mu \right) \frac{\partial u_k}{\partial x_k} - \frac{C}{3} \frac{\partial^2 \beta_{ki}^S}{\partial x_k \partial x_i} \,. \tag{22.12}$$

After Erofeyev (2003), we write equations (22.9) in the following form:

$$\rho \frac{\partial^2 u_p}{\partial t^2} - \lambda \frac{\partial^2 u_q}{\partial x_p \partial x_q} - \mu \left(\frac{\partial^2 u_p}{\partial x_q \partial x_q} + \frac{\partial^2 u_q}{\partial x_q \partial x_p} \right) + \mu \left(\frac{\partial \beta_{pq}}{\partial x_q} + \frac{\partial \beta_{qp}}{\partial x_q} \right) = 0 \,, \tag{22.13a}$$

$$B \frac{\partial^2 \beta_{pq}}{\partial t^2} - C \left(\frac{\partial^2 \beta_{pq}}{\partial x_k \partial x_k} - \frac{\partial^2 \beta_{jq}}{\partial x_j \partial x_p} \right) - \lambda \frac{\partial u_i}{\partial x_i} \delta_{pq} - \mu \left(\frac{\partial u_p}{\partial x_q} + \frac{\partial u_q}{\partial x_p} \right) + \mu \left(\beta_{pq} + \beta_{qp} \right) + 2\eta \frac{\partial \beta_{pq}}{\partial t} - \gamma \delta_{pq} = 0 \,. \tag{22.13b}$$

22.3 Seismic P waves

Erofeyev (2003) was seeking solutions of Eqs. (22.13a,b) in the form of travelling harmonic waves as

$$\begin{pmatrix} u_p \\ \beta_{pq} \end{pmatrix} = \begin{pmatrix} u_p^{(0)} \\ \beta_{pq}^0 \end{pmatrix} \exp(\mathrm{i}\omega t - \mathrm{i}kx) .$$

Usually, it is assumed that the angular frequency ω is real and the wave vector **k** is complex, i.e.,

$$\mathbf{k} = \mathrm{Re}\,\mathbf{k} + \mathrm{Im}\,\mathbf{k} ,$$

where the real part is responsible for the wave propagation and the imaginary part for the wave damping. Erofeyev (2003) considered nonlinear problems of elasto-plastic wave propagation. He investigated a collinear propagation of plain waves along the x_1-axis with zero dissipation ($\eta = 0$). From some calculations concerning longitudinal waves, after assuming that $u_{2,3} = 0$, he obtained:

$$\rho \frac{\partial^2 u_i}{\partial t^2} - \frac{\partial}{\partial x_1}\left[(\lambda + 2\mu)\left(\frac{\partial u_1}{\partial x_1} - \beta_{11}^S \right) + 3(\lambda + 2\mu) \times \left(\frac{\partial u_1}{\partial x_1} - \beta_{11}^S \right)^2 \right] = 0 , \quad (22.14a)$$

$$B \frac{\partial^2 \beta_{11}^S}{\partial t^2} - (\lambda + 2\mu)\left(\frac{\partial u_1}{\partial x_1} - \beta_{11}^S \right) + 3\left(\frac{\lambda}{2} + \mu \right)\left(\frac{\partial u_1}{\partial x_1} - \beta_{11}^S \right)^2 = 0 . \quad (22.14b)$$

If one differentiates the first equation with respect to x_1 and subtracts the second equation from the first one, then one will obtain an equation describing elastic distortion

$$\frac{\partial^2 \beta_{11}}{\partial t^2} + \frac{(\lambda + 2\mu)}{B} \beta_{11} + \frac{(\lambda + 2\mu)}{B} (\beta_{11})^2 - \frac{\partial^2}{\partial x_1^2}\left[\frac{(\lambda + 2\mu)}{\rho} \beta_{11} + \frac{(\lambda + 2\mu)}{\rho} (\beta_{11})^2 \right] = 0 , \quad (22.15)$$

where the elastic distortion is defined as $\beta_{11} = \dfrac{\partial u_1}{\partial x_1} - \beta_{11}^S$.

Equation (22.15) differs from the wave equation by one dispersion and two nonlinear terms. To estimate the value of each term Erofeyev (2003) introduced dimensionless variables $x = x_1 / \Lambda$, $\tau = tV_P / \Lambda$, $\wp = \beta_{11} / \beta_0$. Here Λ and β_0 are characteristic wavelength and amplitude of the elastic distortion wave, respectively. Equation (22.15) can be reduced to

$$\frac{\partial^2 \wp}{\partial \tau^2} - \frac{\partial^2 \wp}{\partial x^2} + l\wp + \aleph_1 \wp^2 - \aleph_2 \frac{\partial^2}{\partial x^2}\left(\wp^2\right) = 0, \tag{22.16}$$

where $l = \Lambda^2 \rho / B$ is the parameter characterizing dispersion, $\aleph_1 = \beta_0 \Lambda^2 \rho / B$ and $\aleph_2 = \beta_0$ are the parameters characterizing nonlinearity.

Using the values for the wave number $\Lambda \approx 10\sqrt{C/\mu}$, Erofeyev (2003) obtained $l / \aleph_1 \approx 1/\beta_0$, $l / \aleph_2 \approx 30.95/\beta_0$ and $\aleph_1 / \aleph_2 \approx 30.95$. He concluded that with such a choice of parameters the nonlinearity with coefficient $\aleph_2$ can be neglected. As a result, Erofeyev (2003) described the propagation of longitudinal elastic distortion wave in the form

$$\frac{\partial^2 \wp}{\partial \tau^2} - \frac{\partial^2 \wp}{\partial x^2} + l\wp + \aleph_1 \wp^2 = 0. \tag{22.17}$$

This is a soliton equation. Equation (22.17) has a solitary solution in the form of slowly propagating soliton of elastic distortion.

22.4 Splitting the Elastic Distortion Soliton Equation into Seismic and Fault-Related Soliton Equations

Teisseyre and Yamashita (1999) split the stress motion equations into seismic wave and fault-related fields (see Chap. 8). We apply this method to Eq. (22.17) and split the equation for elastic distortion solitons into seismic soliton and fault-related soliton equations. Equation (22.17) is nonlinear and superposition methods do not apply here; nevertheless, the elastic distortion field on a fault is small, because the self-distortion field is dominant, thus, in the limit, we can assume that the self-distortion field along the fault is almost equal to the total distortion field during an earthquake process. The equation for self-distortion obtained as a result of splitting Eq. (22.17) can be treated as an approximation.

An elastic distortion $\wp$ can now be presented as the difference $\wp^T - \wp^S$ between the total $\wp^T$ field and the self $\wp^S$ distortion part, which is as-

sumed to rapidly decrease away from the fault plane. We can identify these parts with a radiation field $\wp^T = \tilde{\wp}$ and a fault-related field $\wp^S = \overline{\wp}$. After splitting, the first equation for the field takes the form

$$\frac{\partial^2 \tilde{\wp}}{\partial \tau^2} - \frac{\partial^2 \tilde{\wp}}{\partial x^2} + l\,\tilde{\wp} + \aleph_1 \tilde{\wp}^2 = 0\,. \tag{22.18}$$

The fault-related equation for the self-distortion will be as follows:

$$\frac{\partial^2 \overline{\wp}}{\partial \tau^2} - \frac{\partial^2 \overline{\wp}}{\partial x^2} + l\,\overline{\wp} + \aleph_1 \overline{\wp}^2 = 0\,. \tag{22.19}$$

The above two equations have soliton solutions. These solitons are longitudinal seismic waves. The latter equation describes the tectonic soliton that can be excited by past earthquakes and may propagate slowly along the fault to trigger new earthquakes. Figure 22.1 depicts the splitting the elastic distortion soliton equation into seismic soliton and fault-related soliton equations.

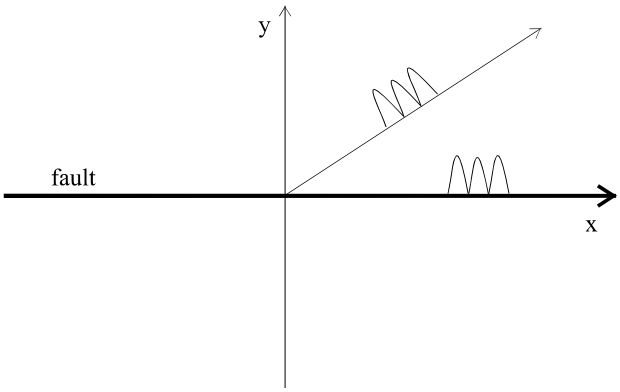

Fig. 22.1 Illustration of the splitting the elastic distortion soliton equation into seismic soliton and fault-related soliton equations

22.5 Seismic S Waves

From some calculations concerning shear waves, after assuming that $u_1 \equiv 0$, Erofeyev (2003) arrived at the following equations:

$$\rho \frac{\partial^2 u_2}{\partial t^2} - \frac{\partial}{\partial x_1}\left[\mu\left(\frac{\partial^2 u_2}{\partial x_1} - \beta_{21}^S\right)\right] = \frac{\partial}{\partial x_1}\left[\left(\lambda + 2\mu\right)\left(\frac{\partial u_2}{\partial x_1}\right)^3\right], \tag{22.20a}$$

$$B\frac{\partial^2 \beta_{21}^S}{\partial t^2} - C\frac{\partial^2 \beta_{21}^S}{\partial x_1^2} - \mu\left(\frac{\partial u_2}{\partial x_1} - \beta_{21}^S\right) = 0\,. \tag{22.20b}$$

One can evaluate $\partial u_2/\partial x_1$ from the second equation and substitute the expression obtained into the first equation differentiated with respect to x_1. That allows reducing Eqs. (22.20a, b) into one equation

$$\begin{aligned}
&\frac{\partial^2 \beta^S}{\partial \tau^2} + \frac{V_0^2}{V_S^2}\frac{\partial^4 \beta^S}{\partial x^4} - \left(1 + \frac{V_0^2}{V_S^2}\right)\frac{\partial^4 \beta^S}{\partial x^2 \partial \tau^2} + \frac{\partial^4 \beta^S}{\partial \tau^4} \\
&\quad = \frac{u_0^2 \rho}{B}\frac{V_P^2}{V_S^2}\frac{\partial^2}{\partial x^2}\left[\left(\frac{\partial^2 \beta^S}{\partial \tau^2} - \frac{V_0^2}{V_S^2}\frac{\partial^2 \beta^S}{\partial x^2}\right)^3\right. \\
&\quad + 3\left(\frac{\partial^2 \beta}{\partial \tau^2} - \frac{V_0^2}{V_S^2}\frac{\partial^2 \beta}{\partial x^2}\right)^2 \beta^S \\
&\quad \left. + 3\left(\frac{\partial^2 \beta^S}{\partial \tau^2} - \frac{V_0^2}{V_S^2}\frac{\partial^2 \beta^S}{\partial x^2}\right)(\beta^S)^2 + (\beta^S)^3\right],
\end{aligned} \tag{22.21}$$

where $V_0^2 = C/B$ and the following dimensionless variables were introduced:

$$x = x_1\sqrt{\frac{\rho}{B}}\,, \quad \tau = tV_S\sqrt{\frac{\rho}{B}}\,, \quad v = \frac{u_2}{u_0}\,, \quad \beta^S = \frac{\beta_{21}^S}{u_0}\sqrt{\frac{B}{\rho}}\,. \tag{22.22}$$

Erofeyev (2003) was seeking a solution of Eq. (22.22) in terms of harmonic wave with amplitude and phase slowly changing in time and space

$$\beta^S(x,t) = \Psi(\varepsilon x, \varepsilon t)e^{i(\omega t - kx)} + c.c.\,, \tag{22.23}$$

where $\Psi(x, t)$ is the complex amplitude, *c.c.* denotes the complex conjugate, ω and k satisfy the dispersion relations

$$\omega^4 - \left(1 + \frac{V_0^2}{V_S^2}\right)\omega^2 k^2 - \omega^2 + \frac{V_0^2}{V_S^2}k^4 = 0\,, \tag{22.24}$$

$$\frac{\dfrac{\partial \Psi}{\partial x}}{k\Psi} \approx \frac{\dfrac{\partial \Psi}{\partial \tau}}{\omega \Psi} \approx \varepsilon \ll 1\,. \tag{22.25}$$

After some calculations, Erofeyev (2003) arrived at the equation of quasi -harmonic wave envelope. The envelope evolution is described by nonlin-

ear Schrödinger's (NLS) equation in coordinates $\tau = \varepsilon t, \quad \xi = x - v_g t$ moving with the group velocity $v_g = \mathrm{d}\omega/\mathrm{d}k$

$$\mathrm{i}\frac{\partial \Psi}{\partial \tau} + \frac{\partial v_g}{\partial k}\frac{\partial^2 \Psi}{\partial \xi^2} - \alpha |\Psi|^2 \Psi = 0, \tag{22.26}$$

where

$$\alpha = \frac{\alpha_0 V_P^2}{V_S^2\left[-4\omega^3 + 2\omega k^2\left(1 + \frac{V_0^2}{V_S^2}\right) + 2\omega\right]}, \tag{22.27}$$

$$\alpha_0 = 3k^2\left(\omega^6 - 30\frac{V_0^2}{V_S^2}\omega^4 k^2 + 3\frac{V_0^4}{V_S^4}\omega^2 k^4 - \frac{V_0^6}{V_S^6}k^6 - 3\omega^4 + 6\frac{V_0^2}{V_S^2}\omega^2 k^2 - 3\frac{V_0^4}{V_S^4}k^4 - 3\frac{V_0^2}{V_S^2}k^2 + 3\omega^2 - 1\right). \tag{22.28}$$

Equation (23.26) is a fault-related nonlinear Schrödinger's equation that describes shear self-distortion solitons. This type of equation usually has multi-soliton solutions. This means that many solitons can be excited and may propagate slowly along the fault.

Figure 22.2 depicts the shear self-distortion soliton propagating along the fault. This soliton is a solution of nonlinear Schrödinger's equation (22.26).

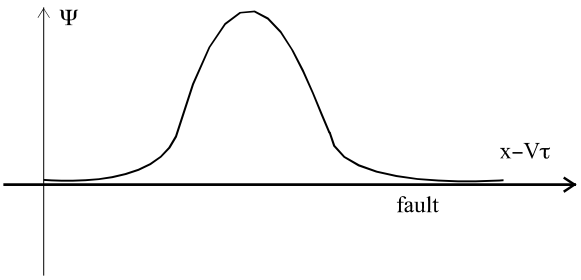

Fig. 22.2 Illustration of Schrödinger's soliton of shear self-distortion propagating along the fault

22.6 Conclusions

We summarized briefly a few results of the gauge theory of an elasto-plastic continuum with dislocations. Two soliton equations for elastic and

self-distortions were presented by Erofeyev (2003). Here, these results were applied to modeling tectonic solitons propagating along the fault. The first soliton equation for longitudinal elastic distortions was considered and split into seismic soliton and fault-related tectonic soliton equations. The second soliton equation derived by Erofeyev (2003) describes shear self -distortion solitons, thus it was already in the fault-related form. Both solitons can propagate slowly along the fault and trigger earthquakes.

References

Edelen DGB, Lagoudas DS (1988) Gauge theory and defects in solids. North -Holland, Amsterdam

Eringen AC (1999) Microcontinuum field theories, I: Foundations and solids. Springer, New York

Erofeyev VI (2003) Wave processes in solids with microstructure. World Scientific, Singapore

Kadic A, Edelen DGB (1983) A gauge theory of dislocations and disclinations. Lecture Notes in Physics 174. Springer-Verlag, Heidelberg

Lagoudas DC (1989) A gauge theory of defects in media with microstructure. Int J Engng Sci **27**: 237-249

Lagoudas DC, Edelen DGB (1989) Material and spatial gauge theories of solids. Int J Engng Sci **27**: 411-431

Majewski E (1993) Thermodynamic approach to evolution. In: Teisseyre R, Czechowski L, Leliwa-Kopystynski J (eds) Dynamics of the earth's evolution, Vol 6: Teisseyre R (ed) Physics and evolution of the earth's interior. Elsevier, Amsterdam, New York.

Majewski E, Teisseyre R (1997) Earthquake thermodynamics. Tectonophysics **277**: 219-233

Nikolaevskiy VN (1996) Geomechanics and fluidodynamics. Kluwer, Dordrecht

Panin VE (ed.) (1995) Physical mesomechanics. vol I, II. Nauka, Novosibirsk

Teisseyre R (2004) Spin and twist motions in a homogeneous elastic continuum and cross-band geometry of fracturing. Acta Geophys Pol **52**: 2, 173-183

Teisseyre R, Majewski E (2001) (eds) Earthquake thermodynamics and phase transformations in the earth's interior. Academic Press, San Diego

Teisseyre R, Majewski E (2002) Physics of earthquakes. In: Lee WHK, Kanamori H, Jennings PC, Kisslinger C (eds) International handbook of earthquake & engineering seismology, Part A. Academic Press, San Diego, pp 229-235

Teisseyre R, Yamashita T (1999) Splitting stress motion equations into seismic wave and fault-related fields. Acta Geophys Pol **47**: 2, 135-147

23 Complexity of Rotation Soliton Propagation

Eugeniusz Majewski

Institute of Geophysics, Polish Academy of Sciences
ul. Księcia Janusza 64, 01-452 Warszawa, Poland
e-mail: emaj@igf.edu.pl

23.1 Introduction

This chapter deals with complexity of seismic rotation soliton propagation. It describes an excitation of seismic rotation solitons as a result of a collinear propagation of a seismic *P* wave and a seismic rotation wave. We assume that the solid Earth's interior is modeled as a micropolar medium filled with uniformly distributed defects in the form of disclinations. Our starting point is a set of coupled nonlinear differential equations for the seismic *P* wave and for the amplitude of the rotation angle oscillations.

23.2 Preliminary Assumptions

We consider a continuum with defects. There are many examples of crystal lattice defects as: vacancies, impurities, dislocations, and disclinations, to name just a few. The self-fields, mentioned above, are created as a result of dislocations (during translational motions) and disclinations (during rotational motions). Dislocations are the results of incompatibility of the strains, and disclinations are the results of incompatibility in the rotation. According to Teisseyre and Boratyński (see Chapter 4), and Teisseyre and Białecki (see Chapter 6), the evolution equations for disclinations and dislocations can be written in the following forms:

$$\dot{\theta}_{pq} + \in_{pmk} \frac{\partial Y_{kq}}{\partial x_m} - b \in_{pmk} \in_{qns} \frac{\partial^2 \dot{\phi}^S_{(ks)}}{\partial x_m \partial x_n} = 0 \qquad (23.1a)$$

for disclination density,

$$\dot{\alpha}_{pl} + \in_{pmk} \frac{\partial J_{kl}}{\partial x_m} + \in_{pmk} \in_{klq} Y_{mq} = 0 \qquad (23.1b)$$

for dislocation density.

From the first equation (23.1a), we can infer a direct connection between disclination density rate $\dot{\theta}_{pq}$ and the self-rotation rate $\dot{\phi}^{S}_{ks}$. The both variables can be treated as internal variables in the continuum with defects (cf., Majewski 1993, Majewski and Teisseyre 1997, 1998, Teisseyre and Majewski 2001, 2002)

23.3 Seismic Rotation Solitons

Deformation dynamics of the continuum with dislocations and disclinations was discussed in Eringen (1999) and Teisseyre (2001). We introduce the following assumptions concerning the continuum with disclinations. We consider a collinear propagation of the seismic *P* wave and a seismic rotation wave in a micropolar continuum with uniform disclination distribution. In addition, we assume that the disclinations are not interacting with each other.

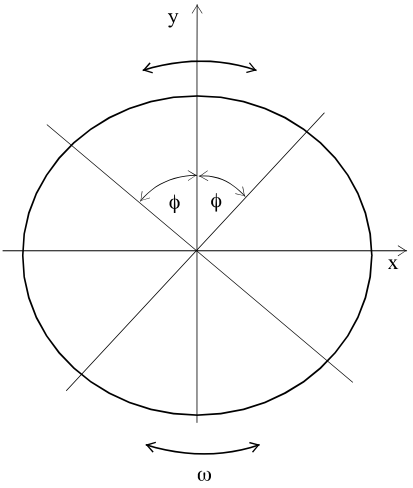

Fig. 23.1 Illustration of the amplitude of the rotation angle oscillations during the propagation of the seismic rotation soliton

Due to the fact that the propagating seismic *P* wave is longitudinal, we can express the longitudinal stress *S* exerted on the disclination as

$$S = \left(\lambda + 2\mu + \kappa\right)u_x + \left(\lambda + 2\mu + \kappa\right)\theta\phi\,, \tag{23.2}$$

where λ and μ are the Lamé constants, κ is the elastic Mooney constant, u_x is the spatial derivative of the longitudinal displacement, θ is the discli-

nation density, ϕ is the rotation angle (Nowacki W 1970, Nowacki JP 1977, Eringen 1999, Teisseyre 2001, 2004).

A seismic plane *P*-wave propagation in the micropolar medium with defects along the *x*-axis can be described using the following set of coupled nonlinear differential equations

$$\rho_0 u_{tt} - (\lambda + 2\mu + \kappa) u_{xx} = \theta(\lambda + 2\mu + \kappa)\phi_x + b_1 (u_x^2)_x , \tag{23.3a}$$

$$I\phi_{tt} - b_2 (\lambda + 2\mu + \kappa)(u_x - \theta\phi) = b_3\phi^2 - b_4\phi , \tag{23.3b}$$

where u is the component of the displacement vector along the x-axis direction, I is the rotational inertia, b_1, b_2, b_3, and b_4 are constant coefficients, ρ_0 is the initial density of the material, V_P is the magnitude of the seismic *P*-wave velocity and $V_P^2 = (\lambda + 2\mu + \kappa)/\rho_0$.

Equation (23.3a) is formulated for the longitudinal displacement due to the propagation of a plane seismic *P* wave in the medium with disclinations. Equation (23.3b) is formulated for the amplitude of the rotation angle oscillations. A similar set of differential equations was considered by Erofeyev and Pegushin (2003, 2004) for longitudinal waves of deformation propagating in porous media.

Making use of the above notations for Eqs. (23.3a, b) we have

$$u_{tt} = V_P^2 u_{xx} - V_P^2 \theta \phi_x + (b_1/\rho_0)(u_x^2)_x , \tag{23.4a}$$

$$\phi_{tt} - (b_2/I) V_P^2 (u_x - \theta\phi) = (b_3/I)\phi^2 - (b_4/I)\phi . \tag{23.4b}$$

We are now in a position to solve Eq. (23.4b) for the spatial derivative of displacement. Thus, we obtain

$$u_x = \frac{I}{b_2 V_P^2}\phi_{tt} + \left(\theta + \frac{b_4}{b_2 V_P^2}\right)\phi - \frac{b_3}{b_2 V_P^2}\phi^2 . \tag{23.5}$$

Let us introduce the following nondimensional quantities:

$$\Phi = \frac{\phi}{\phi_0}, \quad X = \frac{x}{\lambda}, \quad T = \frac{V_P^2 t}{\lambda}, \tag{23.6}$$

where ϕ_0 is the initial rotation angle, λ is the wavelength.

Now, we first calculate the derivative of u_x in Eq. (23.5) with respect to x and next with respect to time. We insert the obtained expression into Eq. (23.4a). As a result, we obtain a differential equation for the rotation angle in the form

$$\left(\theta+\frac{b_4}{b_2V_P^2}\right)\Phi_{TT}=\frac{b_1}{b_2}\Phi_{XX}-\frac{I}{b_2\lambda^2}\left(\Phi_{TTTT}-\Phi_{TTXX}\right)$$

$$+\frac{b_3\Phi_0}{b_2V_P^2}\left[(\Phi^2)_{TT}-(\Phi^2)_{XX}\right]+b_1\left[\frac{\Phi_0}{V_P^2}\left(\theta+\frac{b_4}{b_2V_P^2}\right)^2\Phi^2+\aleph\right]_{XX}, \qquad (23.7)$$

where $\aleph$ contains some higher-order nonlinear terms.

The above equation contains dispersive and nonlinear terms. Both are due to the presence of defects in the medium. In general, the interplay of dispersion and nonlinearity yields soliton solutions of nonlinear equations.

Now we seek a solution of Eq. (23.7) in the form of stationary wave of rotation Φ

$$\Phi=\Psi\left(\psi=x-v_{PR}\,t\right), \qquad (23.8)$$

where v_{PR} is the velocity of the stationary wave and ψ is a new variable.

Making use of the new variable ψ, we come to the conclusion that the sought solution of Eq. (23.7) is also a solution to the following equation

$$\Psi_{\psi\psi}+Y\Psi^2+\Gamma\Psi=0, \qquad (23.9)$$

where Γ and Y are determined in the form:

$$\Gamma=\frac{b_2\lambda^2}{v_{PR}^2(v_{PR}^2-1)}\left\{v_{PR}^2\left(\theta+\frac{b_4}{b_2V_P^2}\right)-\frac{b_1}{b_2V_P^2}\right\}, \qquad (23.10a)$$

$$Y=\frac{b_2\lambda^2}{v_{PR}^2(v_{PR}^2-1)}\left\{v_{PR}^2\frac{b_3\Phi_0}{b_2V_P^2}+\frac{\Phi_0}{V_P^2}\left[\frac{b_1}{\rho_0}\left(\theta+\frac{b_4}{b_2V_P^2}\right)-\frac{b_3}{b_2}\right]\right\}. \qquad (23.10b)$$

Finally, the sought solution in the form of the rotation soliton is

$$\phi(\psi)=\Omega\cosh^{-2}\left(\frac{x-v_{PR}\,t}{\zeta}\right), \qquad (23.11)$$

where $\Omega=-3\Gamma/2Y$, and $\zeta=2/\sqrt{-\Gamma}$.

A similar problem was considered by Nikolaevskiy (1996). However, he started from a different set of equations and considered a porous medium. As a result, he obtained the Schrödinger solitons.

23.4 Conclusions

Although seismic waves have been studied for many years, their soliton nature has only recently come to wide notice. Deformation solitons propa-

gate along earthquake faults and induce earthquakes. Rotation solitons are generated in earthquake sources and propagate throughout the Earth. The conclusion to be reached from these quite disparate examples is that the research on seismic solitons is essential for investigating the propagation of seismic waves and helps understand mechanisms triggering earthquakes.

This chapter briefly presented the main results concerning seismic rotation solitons. An interesting question would be to consider the problem of stability and duration of the seismic solitons.

References

Eringen AC (1999) Microcontinuum field theories, I: Foundations and solids. Springer, New York

Erofeyev VI, Pegushin A (2003) Dispersion and nonlinearity influence on plane longitudinal wave propagation in porous materials. Proc Tenth International Congress on Sound and Vibration, 7-10 July 2003, Stockholm, Sweden

Erofeyev VI, Pegushin A (2004) Waves of deformation propagation in nonlinear viscously elastic porous material. Proc XXI ICTAM, 15-21 August 2004, Warsaw, Poland

Majewski E (1993) Thermodynamic approach to evolution. In: Dynamics of the Earth's Evolution, Teisseyre R, Czechowski L and Leliwa-Kopystynski J (eds), Vol 6 of series: Physics and Evolution of the Earth's Interior, R. Teisseyre (ser. ed.), Elsevier, Amsterdam, New York.

Majewski E, Teisseyre R (1997) Earthquake thermodynamics. Tectonophysics **277**: 219-233

Majewski E, Teisseyre R (1998) Anticrack-associated faulting in deep subduction zones. Phys Chem Earth **23**: 1115-1122

Nikolaevskiy VN (1996) Geodynamics and fluidodynamics. Kluwer, Dordrecht

Nowacki JP (1977) Theory of disclinations in elastic Cosserat media. Arch Mech **29**: 531-545

Nowacki W (1970) Theory of micropolar elasticity. Udine Courses & Lectures No 25, Springer-Verlag, Wien

Teisseyre R (2001) Deformation dynamics: continuum with self-deformation nuclei. In: Teisseyre R, Majewski E (eds), Earthquake thermodynamics and phase transformations in the earth's interior. Academic Press, San Diego

Teisseyre R (2004) Spin and twist motions in a homogeneous elastic continuum and cross-band geometry of fracturing. Acta Geophys Pol **52**: 173-183

Teisseyre R, Majewski E (eds) (2001) Earthquake thermodynamics and phase transformations in the earth's interior. Academic Press, San Diego

Teisseyre R, Majewski E (2002) Physics of earthquakes. In: Lee WHK, Kanamori H, Jennings PC, Kisslinger C (eds) International handbook of earthquake & engineering seismology, Part A, Academic Press, San Diego, pp 229-235

24 Micromorphic Continuum with Defects and Taylor–Bishop–Hill Theory for Polycrystals: Anisotropic Propagation of Seismic Waves and the Golebiewska Gauge

Jun Muto, Yusuke Kawada, Hiroyuki Nagahama

Department of Geoenvironmental Sciences, Graduate School of Science
Tohoku University, Aoba-ku, Sendai 980-8578, Japan
e-mail: mutoh@mail.tains.tohoku.ac.jp

24.1 Introduction

Internal structures and discontinuities in the earth's crust and mantle seem to have an essential influence on deformation in rocks. So, it is reasonable to believe that the notion of continuum with microstructure is an applicable tool in describing earthquake phenomena. The generalized micromorphic continuum is especially suitable for treating the microstructure (e.g. Suhubi and Eringen 1964, Eringen and Claus 1970). From this point of view, Teisseyre and Nagahama (1999) applied the micromorphic continuum to discuss the generation and propagation of the rotation seismic waves.

Basic relations of the micromorphic continuum will now be applied to another phenomenon in solid Earth, i.e. lattice preferred orientation (LPO) of polycrystals. The LPO has been observed within the polycrystals for a long time (e.g. Schmidt 1925, Sander 1930). The nature of the LPO due to the intracrystalline slip (dislocation slip and twinning) depends on geometric constrains on the deformation. The LPO of the polycrystals is applied to infer deformed conditions of the rocks, because the LPO pattern depends on several physical conditions during the deformation, such as temperature and strain rate (e.g. Lister et al. 1978). In this analysis, the Taylor–Bishop–Hill (TBH) model has been often used to simulate development of the LPO patterns (e.g. Lister et al. 1978), which was first introduced by Taylor (1938) and treated more mathematically by Bishop and Hill (1951). Based on an assumption that strain is homogeneous through the polycrystals, the TBH model has reproduced the observed LPO in

quartzite (Lister et al. 1978), calcite (Takeshita et al. 1987) and olivine (Ribe and Yu 1991). Yamasaki and Nagahama (2002) theoretically derived the TBH model with the help of differential forms and a gauge theory. However, geometrical relations between the theory of micromorphic continuum and the TBH model have not been obtained yet.

The plastic deformation or flows in the lower crust and upper mantle induces the seismic (elastic) anisotropy, which affects how fast seismic waves propagate in different directions. In the lower crust, the seismic anisotropies indicate the presence of faults or plastic shear zones (mylonite zones) (Ji and Salisbury 1993). On the other hand, the seismic anisotropies in the upper mantle reflect mantle flow related to global tectonics (see the review by Park and Levin 2002). Thus, the research on the seismic anisotropy of the rocks is essential for investigating the propagation of the seismic waves.

Here we briefly introduce the relationship between the theory of micromorphic continuum with defects and the Taylor–Bishop–Hill theory, and review the LPO development and seismic anisotropy of the deformed rocks based on the relations between the TBH model and the micromorphic continuum. Moreover, analyzing differential forms of defects, we discuss relations between the TBH model and the Golebiewska gauge according to Yamasaki and Nagahama (2002).

24.2 Micromorphic Continuum with Defects

In the micromorphic continuum it is assumed that a body possesses a certain microstructure. After Suhubi and Eringen (1964), we define the following strain measures (see also Teisseyre 1973, 1974, 1995, Teisseyre and Nagahama 1999, Nagahama and Teisseyre 1998, 2000, 2001a, b): strain tensor e_{nl}, microstrain tensor ε_{nl} , and microstrain moment tensor γ_{klm}. From compatibility conditions for the strains and microstrains, we obtain:

$$
\begin{aligned}
e_{nl} &= \frac{1}{2}\left(\frac{\partial u_n}{\partial x_l} + \frac{\partial u_l}{\partial x_n}\right), \\
\varepsilon_{nl} &= \frac{\partial u_l}{\partial x_n} + \varphi_{nl}, \\
\gamma_{klm} &= -\frac{\partial \varphi_{kl}}{\partial x_m},
\end{aligned}
\tag{24.1}
$$

where u_n is a displacement and φ_{kl} is a microdisplacement. Here we will confine ourselves to a linear theory and the Cartesian coordinate system.

For rotation, we have

$$\omega_{ij} = \frac{1}{2}\left(\frac{\partial u_i}{\partial x_j} - \frac{\partial u_j}{\partial x_i}\right), \tag{24.2}$$

while the bend twist κ_{mi} (gradient of rotation) is defined as follows:

$$\begin{aligned} \kappa_{mi} &= \frac{\partial \omega_i}{\partial x_m} = \frac{1}{2} \in_{ikl} \frac{\partial u_l}{\partial x_k \partial x_m}, \\ \omega_i &= \frac{1}{2} \in_{ijk} \omega_{jk}. \end{aligned} \tag{24.3}$$

Moreover, from Eq. (24.1), the total plastic strain is obtained by a sum of two strains (macrostrain and microstrain) and rotation

$$\varepsilon_{ij} = e_{ij} + \omega_{ij} + \varphi_{ij}. \tag{24.4}$$

Now we assume that the microdisplacement φ_{ij} and the microstrain moment tensor γ_{ijk} are independent sources of incompatibilities (Nagahama and Teisseyre 2001a: case II). In such a case, we obtain

$$\alpha_{sn} = -\frac{1}{2} \in_{smk} \left(\frac{\partial \varphi_{kn}}{\partial x_m}\right). \tag{24.5}$$

In this case, disclinations also appear and we shall relate the disclinations to moments of the microstrains:

$$\begin{aligned} \kappa_{kq} &= \in_{qst} \gamma_{stk}, \\ \theta_{pq} &= - \in_{pmk} \frac{\partial \kappa_{kq}}{\partial x_m} = - \in_{pmk} \in_{qst} \frac{\partial \gamma_{stk}}{\partial x_m}. \end{aligned} \tag{24.6}$$

From Eqs. (24.5) and (24.6), dislocation density α_{sn} and disclination density θ_{pq} are related to the microdisplacement φ_{ij}, and the deformation of the micromorphic continuum leads to an appearance of defects (i.e. dislocations and disclinations).

24.3 Taylor–Bishop–Hill Model

The derived formula on the theory of micromorphic continuum with defects is applied to the lattice preferred orientation (LPO) of the polycrystals described by the Taylor–Bishop–Hill (TBH) model. In this section, we briefly introduce the TBH model (Gil Sevillano et al. 1980, Van Houtte and Wagner 1985, Fleck et al. 1994).

External rotation must be created in the case of polycrystal deformation, because the deformation of each grain in the polycrystals is constrained by the surrounding grains (Fig. 24.1). The simplest model for the constrained deformation in the polycrystals is the Taylor homogeneous deformation hypothesis. Thus, the development of LPO is a natural outcome in the TBH model. In the TBH model, we assume that a material deforms through the crystal lattice by the intracrystalline slip and that the lattice undergoes the rotation. The basic relation in the TBH model used extensively in plasticity of the polycrystals is given by

$$\mathrm{d}\tilde{u}_i = \mathrm{d}\tilde{u}_i^{\mathrm{S}} + \mathrm{d}\tilde{u}_i^{\mathrm{R}} , \tag{24.7}$$

where

$$\mathrm{d}\tilde{u}_i^{\mathrm{S}} \equiv \tau_{ij}\,\mathrm{d}\tilde{x}_j , \qquad \mathrm{d}\tilde{u}_i^{\mathrm{R}} \equiv \varphi_{ij}\mathrm{d}\tilde{x}_j . \tag{24.8}$$

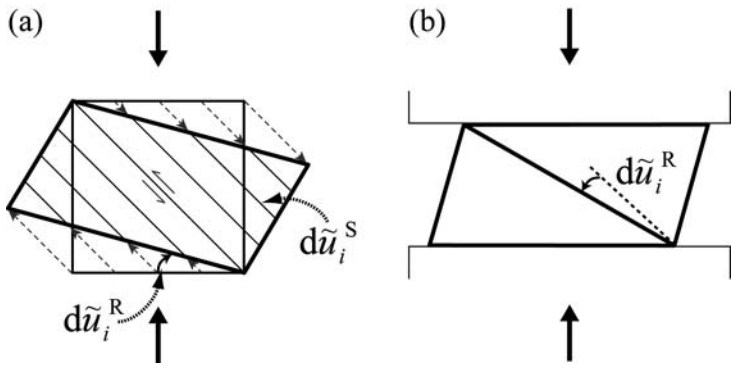

Fig. 24.1 Schematic models for the additional crystalline lattice rotation $\mathrm{d}\tilde{u}_i^{\mathrm{R}}$ with the intracrystalline slip $\mathrm{d}\tilde{u}_i^{\mathrm{S}}$: (a) The case when a crystal is not constrained by the external displacement. The base of the square rotates clockwise following the torque of the intracrystalline slip; (b) The case when the bases of the crystal are fixed by the piston. In this boundary condition, the crystal rotates counterclockwise against the torque of the intracrystalline slip. In the polycrystals, the piston is replaced with other crystals (modified from Wenk et al. 1986)

Here, $\mathrm{d}\tilde{u}_i^{\mathrm{S}}$ is the relative displacement due to the intracrystalline slip and $\mathrm{d}\tilde{u}_i^{\mathrm{R}}$ is due to an additional lattice rotation for bringing the crystal lattice to rotate. In Eq. (24.8), $\mathrm{d}\tilde{u}_i^{\mathrm{S}}$ is linearly related to $\mathrm{d}\tilde{x}_j$ via a slip tensor τ_{ij} and $\mathrm{d}\tilde{u}_i^{\mathrm{R}}$ is related to $\mathrm{d}\tilde{x}_j$ via a rotation tensor φ_{ij}. A particular slip system (α) is specified by a slip vector s_i and a vector of the slip plane normal n_j. The slip tensor τ_{ij} is associated with an amount of the slip $\tau^{(\alpha)}$ on each of the active slip systems, hence

$$\tau_{ij} = \sum_{\alpha} \tau^{(\alpha)} s_i^{(\alpha)} n_j^{(\alpha)}, \tag{24.9}$$

where the summation is taken over all active slip systems.

The physical meaning of these equations is that the imposed strain in each crystal $\mathrm{d}\tilde{u}_i$ (i.e. macroscopic strain in the Taylor model) can be accommodated by the strain created by multiple slips in the crystals $\mathrm{d}\tilde{u}_i^{\mathrm{S}}$ and the additional lattice rotation $\mathrm{d}\tilde{u}_i^{\mathrm{R}}$ generating the LPO. In other words, the strain compatibility leads to the appearance of the lattice rotation. From Eqs. (24.4) and (24.7), we have the correspondences of the variables, i.e.

$$\mathrm{d}\tilde{u}_i \Leftrightarrow \varepsilon_{ij}, \qquad \mathrm{d}\tilde{u}_i^{\mathrm{S}} \Leftrightarrow e_{ij} + \omega_{ij}, \qquad \mathrm{d}\tilde{u}_i^{\mathrm{R}} \Leftrightarrow \varphi_{ij}. \tag{24.10}$$

One-to-one correspondence (24.10) shows that the deformation of the micromorphic continuum is related to the TBH model. Moreover, the microdisplacements φ_{ij} is equivalent to the additional lattice rotation $\mathrm{d}\tilde{u}_i^{\mathrm{R}}$, and the deformation of the micromorphic continuum creates anisotropic textures in the polycrystals.

24.4 Quartz *c*-axis Preferred Orientation in Quartz Schist

Since quartz is the most abundant mineral in the upper crust, its rheological properties govern the rheological structures of the upper crust. In this section, we briefly review the results of quartz *c*-axis preferred orientation in quartz schist from the Sambagawa metamorphic belt, Japan, according to Tagami and Takeshita (1998).

In each sample the *c*-axis orientations of 350 recrystallized quartz grains were measured with a universal stage which permits tilting of a thin section at any angle for measuring the optical structure of a crystal in three -dimensions, using *XZ* thin sections (*X* is parallel to the fabric lineation direction, and *Z* is chosen perpendicular to the foliation plane). Aspect ratio (ratio of long axis to short one) of quartz grains were also measured for estimation of strain magnitude. From the acquired mean aspect ratios, natural

octahedral strain ε was determined according to Nadai (1963). Moreover, fabric intensity I (Lisle 1985) was also measured.

Figure 24.2 displays the c-axis fabric diagrams of four specimens. The measured c-axis fabrics can be classified as type I crossed girdles (Lister et al. 1978). This fabric consists of symmetrically arranged 15-30º small circle girdles around the Z axis and a connecting girdle across the Y axis. This fabric pattern in the observed samples can be reproduced by the Taylor model quartzite B of Lister and Hobbs (1980) (see also Price 1985). The active slip systems in the model quartzite B are basal <a>, rhomb <a> and rhomb <a+c> (Lister and Hobbs 1980). These slip systems are in fact

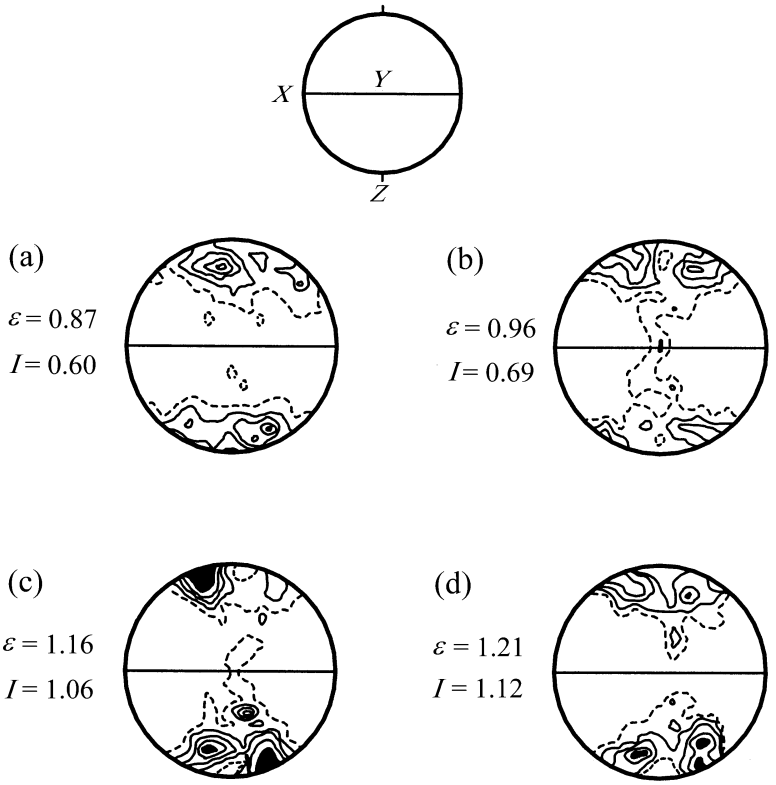

Fig. 24.2 Quartz c-axis fabric diagrams, strain magnitude ε, and fabric intensities I of four specimens on quartz schist in the Sambagawa metamorphic belt, Japan. Contour intervals: 1, 2, 3, 4, 5%. Broken lines represent 1%, and black regions above 5%. Top circle represents the main structural direction in the diagrams; X: parallel to the fabric lineation direction, Y: perpendicular to the fabric lineation direction, Z: perpendicular to the foliation plane (modified from Tagami and Takeshita 1998)

proven to have been active in the natural quartzite deformed under a greenschist facies condition, based on the crystallographic orientations of the rotation axis of misorientation in the recrystallized grains (or subgrains) (e.g. Lloyd and Freeman 1991, 1994, Fliervoet and White 1995). In Fig. 24.2, the strain magnitude ε and fabric intensity I of four specimens are also shown. The fabric intensity I increases with increasing the strain magnitude ε in four specimens. In other words, the increase in the plastic deformation intensifies the degree of the concentration of the quartz c-axis orientations.

24.5 Seismic Anisotropy due to LPO in Deformed Rocks

Here, in this section, we briefly introduce the relations between the LPO of the minerals and the seismic anisotropies of the mantle rocks (i.e. lherzolite) according to Barruol and Kern (1996). Laboratory seismic velocity measurements were made in a cubic pressure apparatus using a pulse transmission technique. Cubic samples (43 mm edge) were cut parallel to main structural directions X, Y and Z. The P- and S-wave velocities were measured at high temperature (up to 600 or 700ºC) and 600 MPa confining pressure.

A lherzolite sample from the Ivrea zone (northern Italy) was selected for the laboratory seismic measurements. It is characterized by a typical coarse granular texture and displays an evidence of the plastic deformation. The sample numbers, along with the modal composition of the rocks and the P-wave anisotropy, are shown in Fig. 24.3. Olivine shows an LPO with strong maxima of [010]-axes close to a pole of the foliation whereas the [100] are parallel to the lineation (X direction). The LPO pattern of orthopyroxene is typical of the upper mantle rocks (e.g. Boudier et al. 1984): the a-axes are grouped in a maximum close to the pole of the foliation (Z direction). The c-axes form a girdle in the foliation plane with a maximum close to the lineation (X direction). The P-wave properties are controlled by olivine, which represents the major volume of the rock (about 80%). The slow P-wave direction (V_P = 7.95 km/s) is parallel to the olivine [010]-axes, while the fast P-wave direction (V_P = 8.87 km/s) is parallel to the lineation direction characterized by the concentration of the olivine [100]-axes (fast P-wave direction in the olivine single crystal). From these analyses, the LPO of main constituents (olivine) induces the seismic anisotropy in the upper mantle rocks.

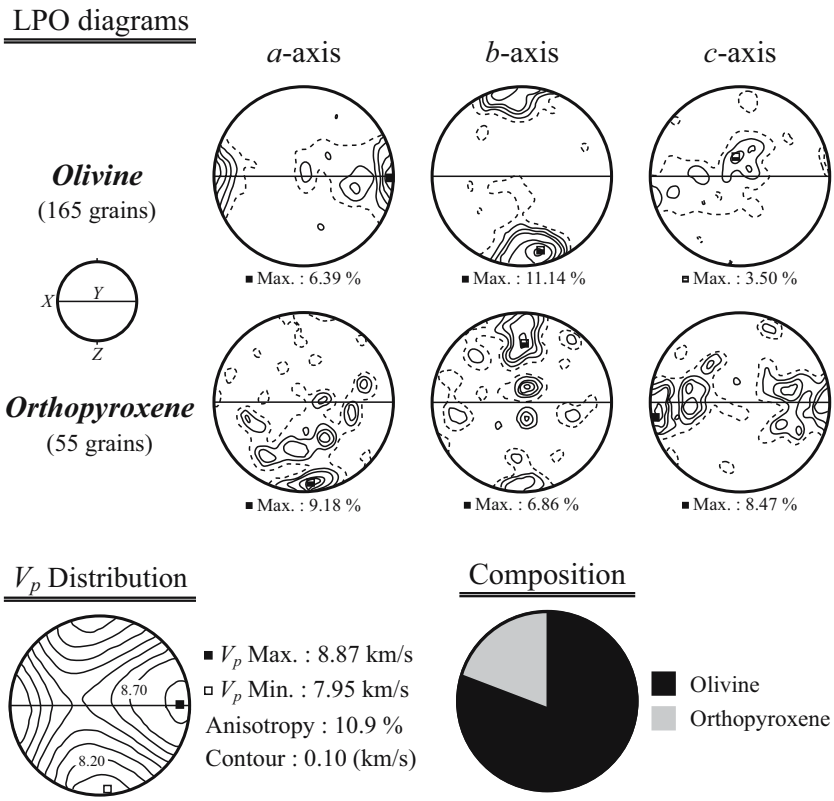

Fig. 24.3 Lattice preferred orientation (LPO) diagrams, *P*-wave velocity distribution, and modal composition of a lherzolite sample in the Ivrea area. In the LPO diagrams, contour intervals: 1, 2, 3, 4, 6, 8, 10%, and broken lines represent 1%. A left small circle represents the main structural direction in the LPO diagrams and the *P*-wave velocity distribution. The modal composition is displayed in a pie diagram (modified from Barroul and Kern 1996)

24.6 Discussion

The deformation of the micromorphic continuum leads to the appearance of the defects. In Sections 24.2 and 24.3, we reconsidered the TBH models from the view point of the theory of micromorphic continuum with defects. Then we briefly reviewed the results of the natural LPO developments and seismic anisotropies of the polycrystals (quartz schist and lherzolite). In the LPO of quartz schist, the fabric intensity I increases with the plastic strain ε increasing. Moreover the LPO of olivine which is the main

constituent of lherzolite induces the seismic anisotropy of lherzolite. In the theory of micromorphic continuum, the plastic strain ε_{ij} is composed of the sum of the strain e_{ij}, rotation ω_{ij} and microdisplacement φ_{ij} corresponding to the additional lattice rotation $\mathrm{d}\tilde{u}_i^{\mathrm{R}}$. Thus, the increase in the deformation, i.e. the increase in the plastic strain ε_{ij}, leads to the increase in the additional lattice rotation $\mathrm{d}\tilde{u}_i^{\mathrm{R}}$ in Eq. (24.7). As a result, the fabric intensity I increases with increasing the plastic strain ε. Regarding the seismic anisotropy in lherzolite, since the fast P-wave direction corresponds to the direction of the olivine [100]-axes (fast P-wave direction in the olivine crystal), the LPO of the main constituent by the plastic deformation induces the seismic anisotropy of lherzolite. Thus, the results of the LPO developments and seismic anisotropies of the deformed rocks (i.e. quartzite and lherzolite) are concordant with our theoretical considerations. As above mentioned in Sects. 24.2 and 24.3, the microdisplacements φ_{ij} in the micromorphic continuum correspond to the additional lattice rotation $\mathrm{d}\tilde{u}_i^{\mathrm{R}}$ in the polycrystals, and the deformation of the micromorphic continuum induces the anisotropic textures and seismic anisotropy in the polycrystals.

In the mathematical description of defect fields, the gauge theory has played main roles (e.g., Golebiewska-Lasota and Edelen 1979, Kadić and Edelen 1983, Nagahama 2001, Yamasaki and Nagahama 2002). In the gauge theory, gauge potential field introduces a topological phase in direct analogy with the potential field in electromagnetism. Based on the analogy, Golebiewska-Lasota and Edelen (1979) demonstrated the gauge transformation of defect (i.e. dislocations and disclinations) dynamics. Yamasaki and Nagahama (2002) derived the TBH model from the Golebiewska gauge transformation. In the differential form, a physical quantity ψ^i can be transformed under the Golebiewska gauge transformation, as follows:

$$\psi^i = \psi_e^i - \mathrm{H}\left(\Gamma_j^i \wedge \psi^j\right), \tag{24.11}$$

where ψ_e^i is called an exact part of ψ^i, H is a linear homotopy operator, Γ_j^i is a connection 1-form and a symbol $\wedge$ denotes an exterior product. From the differential geometrical description of a deformed medium including the defect field (Edelen and Lagoudas 1988), the physical quantities in the strain space-time can be expressed as follows: $\psi^i = B^i$ and $\Gamma_j^i \wedge \psi^j = K^i$, where B^i and K^i represent the distortion-velocity 1-form and bend-twist-spin 2-form, respectively. From the definitions $\mathrm{H}B^i = u^i$, $\mathrm{H}K^i = r^i$, the relation (24.11) can be rewritten:

$$B^i = \mathrm{d}u^i - r^i. \tag{24.12}$$

Equation (24.12) means that the total distortions B^i are given by a difference of two terms: the gradient of displacement $\mathrm{d}u^i$ and an internal rotation r^i. From one to one correspondences between Eqs. (24.7) and (24.12), the Golebiewska gauge transformation corresponds to another expression of the TBH model in the strain space-time (Yamasaki and Nagahama 2002).

24.7 Conclusion

Here we briefly introduced the relationships between the theory of micromorphic continuum with defects and the Taylor–Bishop–Hill theory. The deformation of the micromorphic structure (continuum) induces the appearance of the defects (dislocations and disclinations). In the Taylor –Bishop–Hill theory for the polycrystals, the total strain of the polycrystals is decomposed into the multiple slips in the crystals and into the additional lattice rotation. From the correspondence between the theory of micromorphic continuum and the TBH model, the microdisplacement in the theory of micromorphic continuum with defects corresponds to the additional lattice rotation which creates the anisotropic texture (i.e. LPO). Then, from the view point of the correspondences between the micromorphic continuum and the TBH model, we reviewed the development of the natural LPO and seismic anisotropies of the deformed rocks (i.e. quartz schist and lherzolite). On the basis of the differential form of the defects, we pointed out that the additional lattice rotation in the TBH model is another expression of the Golebiewska gauge in the strain space-time.

We would like to thank Elsevier for a permission to reproduce the aforementioned materials for Figs. 24.2 and 24.3. We are also grateful to an anonymous reviewer for insightful comments which improve our manuscript. The first author (JM) is financially supported by JSPS for Young Scientists. This work was conducted as a part of the 21st Century Center -of-Excellence program, “Advanced Science Technology Center for the Dynamic Earth”, of Tohoku University.

References

Barruol G, Kern H (1996) Seismic anisotropy and shear-wave splitting in lower-crustal and upper-mantle rocks from the Ivrea Zone – experimental and calculated data. Phys Earth Planet Inter **95**: 175-194

Bishop JFW, Hill R (1951) A theory of the plastic dislocation of a polycrystalline aggregate under combined stresses. Philos Mag **42**: 414-427

Boudier F, Jackson M, Nicolas A (1984) Structural study of the Balmuccia massif (western Alps): a transition from mantle to lower crust. Geol Mijnbouw **16**: 179-188

Edelen DGB, Lagoudas D (1988) Gauge theory and defects in solids. Elsevier, Amsterdam

Eringen AC, Claus WD Jr (1970) A micromorphic approach to dislocation theory and its relation to several existing theories. In: Simmons JA, DeWit R, Bullough R (eds) Fundamental aspects of dislocation theory. Nat Bur of Stand Publ, Washington DC **317**, 2: 1023-1040

Fleck NA, Muller GM, Ashby MF, Hutchinson JW (1994) Strain gradient plasticity: theory and experiment. Acta Metall Mater **42**: 475-487

Fliervoet TF, White SH (1995) Quartz deformation in a very fine grained quartzofeldspathic mylonite: a lack of evidence for dominant grain boundary sliding deformation. J Struct Geol **17**: 1095-1109

Gil Sevillano J, Van Houte P, Aernoudt E (1980) Large strain work hardening and textures. Prog Mater Sci **25**: 69-412

Golebiewska-Lasota AA, Edelen DGB (1979) On the gauge transformations admitted by the equations of defect dynamics. Int J Engng Sci **17**: 335-339

Ji S, Salisbury MH (1993) Shear-wave velocities, anisotropy and splitting in high-grade mylonites. Tectonophysics **221**: 453-473

Kadić A, Edelen DGB (1983) A gauge theory of dislocations and disclinations. Springer, Berlin

Lisle RJ (1985) The use of the orientation tensor for the description and statistical testing of fabrics. J Struct Geol **7**: 115-117

Lister GS, Hobbs BE (1980) The simulation of fabric development during plastic deformation and its application to quartzite: the influence of deformation history. J Struct Geol **2**: 355-370

Lister GS, Paterson MS, Hobbs BE (1978) The simulation of fabric development in plastic deformation and its application to quartzite: the model. Tectonophysics **45**: 107-158

Lloyd GE, Freeman B (1991) SEM electron channeling analysis of dynamic recrystallization in a quartz grain. J Struct Geol **13**: 945-953

Lloyd GE, Freeman B (1994) Dynamic recrystallization of quartz under greenschist conditions. J Struct Geol **16**: 867-881

Nadai A (1963) Theory of flow and fracture of solids. McGraw-Hill, New York

Nagahama H (2001) Gauge theory of dislocational electromagnetic field in earthquake preparation zone. Acta Geophys Pol **49**: 437-448

Nagahama H, Teisseyre R (1998) Micromorphic continuum, rotational wave and fractal properties of earthquakes and faults. Acta Geophys Pol **46**: 277-294

Nagahama H, Teisseyre R (2000) Micromorphic continuum and fractal fracturing in the lithosphere. Pure Appl Geophys **157**: 559-574.

Nagahama H, Teisseyre R (2001a) Seismic rotation waves: dislocations and disclinations in a micromorphic continuum. Acta Geophys Pol **49**: 1, 119-129; Erratum. Acta Geophys Pol **49**: 2, 275

Nagahama H, Teisseyre R (2001b) Micromorphic continuum and fractal properties of faults and earthquakes. In: Teisseyre R, Majewski E (eds) Earthquake

thermodynamics and phase transformations in the Earth's interior. Academic Press, San Diego, pp 425-440

Park J, Levin V (2002) Seismic anisotropy: tracing plate dynamics in the mantle. Science **296**: 485-489

Price GP (1985) Preferred orientations in quartzites. In: Wenk HR (ed) Preferred orientation in deformed metals and rocks: an introduction to modern texture analysis. Academic Press, London, pp 385-406

Ribe NM, Yu Y (1991) A theory for plastic deformation and textural evolution of olivine polycrystals. J Geophys Res **96**, B5: 8325-8335

Sander B (1930) Gefügekunde der Gesteine. Springer, Wien

Schmidt W (1925) Gefügestatistik. Tschermaks Miner Petrogr Mitt **38**: 342-423

Suhubi ES, Eringen AC (1964) Nonlinear theory of micro-elastic solids, II. Int J Eng Sci **2**: 389-404

Tagami M, Takeshita T (1998) *c*-Axis fabrics and microstructures in quartz schist from Sambagawa metamorphic belt, central Shikoku, Japan. J Struct Geol **20**, 11: 1549-1568

Takeshita T, Tomé C, Wenk HR, Kocks UF (1987) Single-crystal yield surface for trigonal lattices: application to texture transitions in calcite polycrystals. J Geophys Res **92**, B12: 12,917-12,930

Taylor GI (1938) Plastic strain in metals. J Inst Metal **62**: 307-324

Teisseyre R (1973) Earthquake processes in a micromorphic continuum. Pure Appl Geophys **102**: 15-28

Teisseyre R (1974) Symmetric micromorphic continuum wave propagation, point source solution and some applications to earthquake processes. In: Thoft -Christenen P (ed) Continuum mechanics aspects of geodynamics and rock fracture mechanics. D Riedel Pub, Dordrecht, pp 201-244

Teisseyre R (1995) Micromorphic model of a seismic source zone, 2. Symmetric micromorphic theory; applications to seismology. In: Teisseyre R (ed) Theory of earthquake premonitory and fracture processes. PWN, Warszawa, pp 616-627

Teisseyre R, Nagahama H (1999) Micro-inertia continuum: rotations and semi-waves. Acta Geophys Pol **47**: 3, 259-272

Van Houtte P, Wagner F (1985) Development of textures by slip and twinning. In Wenk HR (ed) Preferred orientation in deformed metals and rocks: an introduction to modern texture analysis. Academic Press, London, pp 233-258

Wenk HR, Takeshita T, Van Houtte P, Wagner F (1986) Plastic anisotropy and texture development in calcite polycrystals. J Geophys Res **91**, B3: 3861-3869

Yamasaki K, Nagahama H (2002) A deformed medium including a defect field and differential forms. J Phys **A**: Math Gen **35**: 3767-3778

25 Seismic Ray Theory for Structural Medium based on Kawaguchi and Finsler Geometry

Takahiro Yajima, Hiroyuki Nagahama

Department of Geoenvironmental Sciences, Graduate School of Science
Tohoku University, Aoba-ku, Sendai 980-8578, Japan
e-mails: yajima@dges.tohoku.ac.jp; nagahama@dges.tohoku.ac.jp

25.1 Introduction

In seismological studies, ray theory for high frequency wave has been discussed and extended by many researchers (e.g. Achenbach et al. 1982, Červený 2002). The seismic ray can be obtained either by solving the elasto-dynamic equations, (i.e. Euler–Lagrange equation or Hamilton equation) or by using a generalization of Fermat's variational principle (Bóna and Slawiński 2003). These geometrical ray theories are similar to the previous seismic ray theory (Teisseyre 1955, Babich 1961, 1994) and the other ray theories in acoustic ray (Ugincius 1972, Meyer and Schroeter 1981) and light (Babich 1987, Joets and Ribotta 1994).

Since a micromorphic continuum (Eringen and Suhubi 1964) can express a continuum with microstructure such as earthquake structure (Teisseyre 1973, Nagahama and Teisseyre 2000) and an anisotropic texture and seismic anisotropy in polycrystals (Mainprice and Nicolas 1989, Siegesmund et al. 1989, Muto et al. 2005), a new theory of the micromorphic continuum is needed for the propagation theory of seismic wave. The seismic wave propagating through the anisotropic medium can be regarded as a velocity vector field on each material point.

The geometry of the medium consists of the crustal material point and the direction of the velocity attached on each point, and seismic rays are geodesics in Finsler space (Bernstein and Gerver 1978, Hanyga 1984). Moreover, Antonelli et al. (2003) have introduced the seismic Finsler metric for anisotropic and inhomogeneous medium. From standpoints of higher-order geometry, the intrinsic behaviour of the ray velocity attached toeach point can be represented by the base connection in Kawaguchi space (Kawaguchi A 1931, 1966, Kawaguchi M 1962).

Here, we discuss a new seismic ray theory from the view point of higher-order geometry. Firstly, we introduce the Finsler geometry for seismic ray, and point out that the intrinsic behaviour of seismic ray velocity can be given by two covariant derivatives in higher-order space. Then, we proposed a relation between a metric of Kawaguchi space and a seismic Finsler metric. From the view point of the differential geometry, we discuss how to estimate the anisotropy of crustal materials (structural medium) from seismic ray path. This section is an extensional version of our previous study (Yajima and Nagahama 2004).

25.2 Finsler Geometry and Seismic Ray

The seismic ray path is regarded as an arclength along a curve $x^i = x^i(t)$, where $i = 1, 2, 3$ and t is a traveltime. This geometrical interpretation is expressed by the theory of higher-order space called Kawaguchi space (Kawaguchi A 1931; 1966; Kawaguchi M 1962). In Kawaguchi space of order α, the arclength is defined by

$$s = \int F(x^i, x^{(1)i}, \cdots, x^{(\alpha)i})\,\mathrm{d}t\,, \tag{25.1}$$

where $x^{(\alpha)i} = \mathrm{d}^\alpha x^i/\mathrm{d}t^\alpha$, and F denotes a fundamental function or Lagrangian. In order to investigate the seismic ray, we will regard the Lagrangian F as a function of not only the position but also its velocity vector. In this case, the Lagrangian $F(x^i, x^{(1)i}, \ldots, x^{(\alpha)i})$ reduces $F(x^i, x^{(1)i}) = F(x^i, v^i)$, where $\mathbf{x} = (x^i)$ is the position and the quantities $\mathbf{v} = (v^i) = (\mathrm{d}x^i/\mathrm{d}t)$ which are tangent to the ray represent the component of group velocity for seismic ray (Červený 2002). In this case, since the ray is invariant under change of parameter t, the Lagrangian F is homogeneous of degree one in the variable v^i. Geometrically, the space defined by the function $F(x^i, x^{(1)i})$ is called Finsler space, i.e. higher-order space of order 1. Therefore, the seismic ray theory is geometrized in higher-order space. Here, the Latin indices refer to the general curvilinear coordinates and we use the Einstein summation convention.

Now, in Finsler space, when we chose the variables $(\mathbf{x}, \mathbf{v})$, then the $\mathbf{v}$-dependence of seismic ray is geometrically represented by the connection coefficient C^i_{jk} given by the following covariant derivative for an arbitrary vector field $\boldsymbol{\xi} = (\xi^i)$ and $i = 1, 2, 3$:

$$\mathrm{D}\xi^i = \mathrm{d}\xi^i + \Gamma^i_{jk}\xi^j\mathrm{d}x^k + C^i_{jk}\xi^j\mathrm{d}v^k\,, \tag{25.2}$$

where Γ^i_{jk} and C^i_{jk} denote the Finsler connection coefficients and characterize $\mathbf{x}$-field and $\mathbf{v}$-field, respectively (Cartan 1934, Rund 1959). Then, we

consider the intrinsic behaviour of group velocity **v** whose parallelism distinguishes from the covariant derivative Eq. (25.2). Therefore, we introduce a new parallelism of *v*. This new parallelism can be expressed by a base connection of the group velocity **v** in Kawaguchi space. The base connection δv^i is defined by

$$\delta v^i = \mathrm{d}v^i + \Delta^i_{jk} v^j \mathrm{d}x^k + E^i_{jk} v^j \mathrm{d}v^k = P^i_{\ k} \mathrm{d}x^k + G^i_{\ k} \mathrm{d}v^k, \tag{25.3}$$

where the new Finsler connection coefficients Δ^i_{jk} and E^i_{jk} are different from the coefficients of Eq. (25.2), respectively, i.e. $\mathrm{D}v \neq \delta v$. We also put $P^i_k = \Delta^i_{jk} v^j$ and $G^i_k = \delta^i_k + E^i_{jk} v^j$. The coefficients Δ^i_{jk} and E^i_{jk} are functions of x^i and v^i. Here, from the general standpoints, we don't assume the homogeneity conditions $C^i_{jk} v^j = 0$ and $E^i_{jk} v^j = 0$ as Cartan's theory of Finsler geometry (Cartan 1934). Since $\mathrm{D}v \neq \delta v$, the covariant derivative δ**v** is regarded as the intrinsic parallelism of group velocity **v** and we can consider the influence of structural medium on the group velocity. When the condition δ**v** = 0 holds, neighbouring vectors {**v**} are displaced parallel each other. This state corresponds to the oriented seismic ray velocity. If **v** is orientable as a function of **x** from the condition δ**v** = 0, then we get non-linear connection $N^l_k = P^j_k (G^{-1})^l_j$ obtained by $\partial v^l / \partial x^k = -N^l_k$ and Eq. (25.2) is reduced to

$$\mathrm{D}\xi^i = \mathrm{d}\xi^i + \Pi^i_{jk} \xi^j \mathrm{d}x^k, \tag{25.4}$$

where $\Pi^i_{jk} = \Gamma^i_{jk} - N^l_k C^i_{jl}$. It is found that the **x**-field Γ^i_{jk} and **v**-field C^i_{jk} are unified into one field Π^i_{jk} which expresses anisotropy in the crustal materials. In this case, the coefficient Π^i_{jk} is related to the non-linear connection N^l_k expressed by the intrinsic property of group velocity **v** from the base connection Eq. (25.3).

In this section, we considered the seismic ray in higher-order space. The behaviour of **x**-field and **v**-field is given by the covariant derivative (Eq. 25.2). Moreover, the intrinsic behaviour of **v**-field can be expressed by the base connection δ**v** (Eq. 25.3) in higher-order space. When the condition δ**v** = 0 holds, a geometrical structure is expressed by Eq. (25.4).

25.3 Seismic Finsler Metric and Kawaguchi Space

The covariant derivative derives the geodesic equation. In Eq. (25.4), we put the vector ξ^i on the contravariant component of ray velocity v^i. Then,

the covariant derivative $Dv^i/dt = 0$ is the geodesic equation. In this case, the condition $\delta v^i = 0$ holds good. Then, the torsion tensor $T^i_{jk} = 2\Pi^i_{[kj]}$ appears, and this space becomes generalized Berwald space which is a kind of Finsler space (Wagner 1943).

Here, we define Lagrangian for seismic ray as follows:

$$F(x^i, v^i) = \frac{\sqrt{v^j v^j}}{V(x^i, v^i)}, \tag{25.5}$$

where the ray velocity function $V(\mathbf{x}, \mathbf{v})$ is divided into the spatial function $h(x^i)$ and direction function $\varphi(v^i)$, i.e. $V \equiv h(x^i)\,\varphi(v^i)$. Especially, the torsion tensor is given by semi-symmetric tensor $T^i_{jk} = \delta^i_j \sigma_k - \delta^i_k \sigma_j$, where $\sigma_i \equiv \partial\sigma/\partial x^i$ is an arbitrary contravariant vector, $\sigma = \sigma(x^i)$ is a scalar function of position and δ^i_j is Kronecker's delta. When we impose the Cartan's condition, the space becomes Wagner space which is a kind of generalized Berwald space (Wagner 1943). In Wagner space, the Lagrangian can be written by (Hashiguchi 1977)

$$F = \mathrm{e}^{\sigma(x^j)} \overline{F}(v^i), \tag{25.6}$$

where e^{σ} and $\overline{F}$ are spatial and velocity dependence part of F, respectively.

In the two-dimensional case (x^1: horizontal axis; x^3: vertical axis), we write $(x^i) = (x^1, x^2, x^3) = (x, 0, z)$ and the contravariant component of group velocity $(v^i) = (v^1, v^2, v^3) = (\dot{x}, 0, \dot{z})$. Moreover, we assume that the spatial change depends on only the depth z, i.e. $h(x^3) = h(z) = c_1 + c_2\, z$, where c_1 and c_2 are positive constants. From Eq. (25.5) and Eq. (25.6), the Lagrangian is expressed by

$$F = \mathrm{e}^{-\ln h(z)} (\dot{x}^m + \dot{z}^m)^{\frac{1}{m}}, \tag{25.7}$$

where $\sigma(x^3) = -\ln h(z) = -\ln(c_1 + c_2\, z)$ and $\overline{F} = (\dot{x}^m + \dot{z}^m)^{1/m}$, m is not an index and is an even integer, $m \geq 2$. This space is called seismic Finsler space (Antonelli et al. 2003). The Lagrangian equation (25.7) is a special 1-form metric, i.e. m-th metric (Matsumoto and Shimada 1978). In Wagner space, the geodesic equation with m-th metric is given by (Antonelli and Shimada 1991)

$$\frac{\mathrm{d}^2 x^i}{\mathrm{d}t^2} + 2\delta^i{}_j \sigma_k \frac{\mathrm{d}x^j}{\mathrm{d}t}\frac{\mathrm{d}x^k}{\mathrm{d}t} - \overline{F}^2 \sigma_j \overline{g}^{ij} = 0, \tag{25.8}$$

where $\overline{g}^{ij}$ is the inverse of $\overline{g}_{ij} = \partial^2 \overline{F}^2 / 2\partial v^i \partial v^j$. This equation is the geodesic equation for seismic ray related to Eq. (25.4). Hence, the oriented direction states $\delta v^i = 0$ for ray velocity is a necessary condition for Wagner space with seismic Finsler metric.

More generally, the *m*-th metric can be derived from Kawaguchi space. We show a relation between the Antonelli's seismic Finsler metric (Eq. 25.7) and a special metric of Kawaguchi space. Hokari (1936, 1940) proposed a special form of fundamental function *F*

$$F = \left(\sum_{\beta=0}^{K} {}_K C_\beta b_\beta a_{i_1} \cdots a_{i_{K-\beta}} x^{(a)i_1} \cdots x^{(a)i_{K-\beta}} \right)^{1/p}, \tag{25.9}$$

where ${}_K C_\beta = K!/\{(K-\beta)!\beta!\}$, and K, p and β are not indices and are constants. Moreover, b_β and a_i are functions of x, $x^{(1)}$ $\cdots$, $x^{(\alpha-1)}$, respectively. Here, we can derive the Antonelli's seismic Finsler metric from the following conditions:

$$\begin{aligned} &\alpha = 1, \quad a_i a_j = \delta_{ij} \mathrm{e}^{-\ln h(z)}, \\ &b_\beta = 1 \quad (\beta = 0); \quad b_\beta = 0 \quad (\beta \neq 0). \end{aligned} \tag{25.10}$$

Moreover, since the dimension of the quantities in Eq. (25.7) must be concordant with that in Eq. (25.9), we should put $K = p = m$ after Eq. (25.10) applied Eq. (25.9). Under this constraint, the fundamental function Eq. (25.9) can be easily reduced to that in Eq. (25.7). From the view point of seismology, the *m*-value in Eq. (25.7) expresses the anisotropy of seismic wavefront, which is discussed in the next section.

25.4 Discussion

In Section 25.3, we derived the Antonelli's seismic Finsler metric from a special form of the fundamental function in Kawaguchi space. The Berwald's Gauss curvature scalar *R* (Berwald 1947) for Antonelli's seismic Finsler metric is given by

$$R = \frac{m(c_2)^2 \dot{z}^{2-2m} [(m-2)\dot{x}^m - m\dot{z}^m]}{4(m-1)^2 (\dot{x}^m + \dot{z}^m)^{(2-m)/m}}, \tag{25.11}$$

(Antonelli et al. 2003). Here, the *m*-value in Eq. (25.11) corresponds to the *m*-value in Eq. (25.7). For $m > 0$ and $c_2 > 0$, the seismic ray angle θ can be determined where the curvature vanishes:

$$R = 0 \Leftrightarrow \frac{\dot{x}}{\dot{z}} \equiv \tan\theta = \left(1 - \frac{2}{m}\right)^{-\frac{1}{m}}. \tag{25.12}$$

Therefore, from Eq. (25.12), the ray angle θ depends on the radical sign m, and the m-value corresponds to the p-value in the special Kawaguchi space (Eq. 25.9). The case $m = 2$ is Euclidean, and $m > 2$ is Finslerian. The fundamental function (Eq. 25.7) can be related to the Minkowski metric. The two-dimensional Minkowski metric is expressed by

$$D_m = \left[|\dot{x}|^m + |\dot{z}|^m \right]^{\frac{1}{m}}. \tag{25.13}$$

The set points for $D_m = 1$ are called the unit ball of the metric (Anderberg 1973). For $m = 2$, the metric is Euclidean and the unit ball is the circle. When the even integer m takes $2 < m < \infty$, the unit ball is a convex curve. For $m \to \infty$, the unit ball approaches the square and from Eq. (25.12) the ray angle is $\pi/4$, i.e. a vertex of the square. Thus, in Eq. (25.7), at fixed point **x**, if we put $m = 2$, the group velocity surface $F = 1$ (Červený 2002), $F = \exp[-\ln h(z)](\dot{x}^2 + \dot{z}^2)^{1/2} = 1$ describes a circle in the $(\dot{x}, \dot{z})$ – group velocity space, and the wavefront propagates isotropic. On the other hand, $m > 2$ as $m \to \infty$, the circle approaches a square which defines the group velocity surface and the velocity space is anisotropic. Thus, the m-value in Eq. (25.7) means the anisotropy of seismic wavefront. Moreover, from a seismic ray path based on m-value, we can estimate the seismic anisotropy in structural medium (a continuum with microstructure) such as the earthquake structure (Teisseyre 1973, Nagahama and Teisseyre 2000) and the seismic anisotropy of polycrystalline rocks (Mainprice and Nicolas 1989, Siegesmund et al. 1989, Muto et al. 2005).

References

Achenbach JD, Gautesen AK, McMaken H (1982) Ray methods for waves in elastic solids: with applications to scattering by cracks. Pitman Advanced Publishing Program, Boston, London and Melbourne

Anderberg MR (1973) Cluster analysis for applications. Academic Press, New York and London

Antonelli PL, Shimada H (1991) On 1-form Finsler connections with constant coefficients. Tensor, N.S. **50**: 263-275

Antonelli PL, Bóna A, Slawiński MA (2003) Seismic rays as Finsler geodesics. Nonlinear Analysis: Real World Applications **4**: 711-722

Babich VM (1961) Propagation of Rayleigh wave along the surface of a homogeneous elastic body of arbitrary shape. Doklady Akad Nauk SSSR **137**: 1263-1266 (in Russian)

Babich VM (1987) Finsler geometry application to geometrical-optics of non-homogeneous anisotropic media. Vestnik Leningrad Univ Mat Mekh Astronom **3**: 19-23 (in Russian)

Babich VM (1994) Ray method of calculating the intensity of wavefronts in the case of a heterogeneous, anisotropic, elastic medium. Geophys J Int **118**: 379-383

Bernstein IN, Gerver ML (1978) On a problem of integral geometry for a family of geodesics and on an inverse kinematic problem of seismics. Doklady Akad Nauk SSSR **243**: 302-305 (in Russian), Doklady Earth Science Sections **243**: 10-12

Berwald L (1947) Ueber Finslersche und Cartansche Geometrie IV: Projektivkrümmung allgemeiner affiner Räume und Finslersche Räume skalarer Krümmung. Ann Math **48**: 755-781

Bóna A, Slawiński MA (2003) Fermat's principle for seismic rays in elastic media. J Appl Geophys **54**: 445-451

Cartan É (1934) Les espace de Finsler exposé de géométrie. Hermann, Paris

Červený V (2002) Fermat's variational principle for anisotropic inhomogeneous media. J Appl Geophys **46**: 567-588

Eringen AC, Suhubi ES (1964) Nonlinear theory of simple micro-elastic solids-I. Int J Eng Sci **2**: 189-203

Hanyga A (1984) Seismic wave propagation in the Earth. PWN – Elsevier, Warszawa – Amsterdam

Hashiguchi M (1977) On conformal transformations of Wagner spaces. Rep Fac Sci Kagoshima Univ (Math Phys Chem) **10**: 19-25

Hokari S (1936) Die Geometrie des Integrals $\int\left(a_i a_j x''^i x''^j + 2ba_i x''^i + c\right)^{\frac{1}{p}} \mathrm{d}t$. Proc Imp Acad Japan **12**: 209-212

Hokari S (1940) Die Theorie des Kawaguchischen Raumes mit der Massbestimmung von einer bestimmten Gestalt. J Fac Sci Hokkaido Imp Univ **7**: 63-78

Joets A, Ribotta R (1994) A geometrical model for the propagation of rays in an anisotropic inhomogeneous medium. Opt Commun **107**: 200-204

Kawaguchi A (1931) Theory of connections in the generalized Finsler manifold. Proc Imp Acad Japan **7**: 211-214

Kawaguchi A (1966) Connections and their invariants in higher-order spaces. In: Hoffmann B (ed) Perspectives in geometry and relativity: essays in honor of Václav Hlavatý. Indiana University Press, Bloomington, pp 192-200

Kawaguchi M (1962) An introduction to the theory of higher order spaces I: the theory of Kawaguchi space. In: Kondo K (ed) RAAG memoirs of the unified study of basic problems in engineering and physical sciences by means of geometry, vol 3. Gakujyutsu-Bunken Fukkyukai, Tokyo, pp 718-734

Mainprice D, Nicolas A (1989) Development of shape and lattice preferred orientations: application to the seismic anisotropy of the lower crust. J Struct Geol **11**: 175-189

Matsumoto M, Shimada H (1978) On Finsler spaces with 1-form metric I. Tensor, NS **32**: 161-169

Meyer R, Schroeter G (1981) The application of differential geometry to ray acoustics in inhomogeneous and moving media. Acustica **47**: 105-113

Muto J, Kawada Y, Nagahama H (2005) Micromorphic continuum with defects and Taylor-Bishop-Hill theory for polycrystals: anisotropic propagation of seismic waves and Golebiewska gauge. In: Teisseyre R, Takeo M, Majewski E (eds) Earthquake source asymmetry, structural media and rotation effects. Springer-Verlag, Berlin

Nagahama H, Teisseyre R (2000) Micromorphic continuum and fractal fracturing in the lithosphere. Pure Appl Geophys **157**: 559-574

Rund H (1959) The differential geometry of Finsler spaces. Springer-Verlag, Berlin

Siegesmund S, Takeshita T, Kern H (1989) Anisotropy of V_p and V_s in an amphibolite of the deeper crust and its relationship to the mineralogical, microstructural and textural characteristics of the rock. Tectonophysics **157**: 25-38

Teisseyre R (1955) Optico-geometrical approximation for seismic waves in non-homogeneous media. Acta Geophys Pol **3**: 161-166

Teisseyre R (1973) Earthquake processes in a micromorphic continuum. Pure Appl Geophys **102**: 15-28

Ugincius P (1972) Ray acoustics and Fermat's principle in a moving inhomogeneous medium. J Acoust Soc Am **51**: 1759-1763

Wagner V (1943) On generalized Berwald spaces. Compt Rend Acad Sci URSS **39**: 3-5

Yajima T, Nagahama H (2004) Seismic ray path in anisotropic medium based on higher-order geometry. Proceeding of Workshop on "Probing Earth Media Having Small-Scale Heterogeneities", November 22-23, 2004, Sendai, Japan, pp 62-65

26 From Non-Local to Asymmetric Deformation Field

Hiroyuki Nagahama[1], Roman Teisseyre[2]

[1]Department of Geoenvironmental Sciences, Graduate School of Science
Tohoku University, Aoba-ku, Sendai 980-8578, Japan
e-mail: nagahama@dges.tohoku.ac.jp

[2]Institute of Geophysics, Polish Academy of Sciences
ul. Księcia Janusza 64, 01-452 Warszawa, Poland
e-mail: rt@igf.edu.pl

26.1 Introduction

Internal structures and discontinuities in the lithosphere have an essential influence on fracturing. Hence, it is reasonable to believe that the notion of continuum with microstructures can be a suitable tool in describing earthquake phenomena (Teisseyre 1973). Generalized micromorphic continuum is especially suitable for introducing microstructure (Suhubi and Eringen 1964). When the deformations imposed on a microstructural element favour its elongation rather than rotation during fracturing, the symmetric micromorphic continuum is suitable to our considerations on the role of microstructures in a seismic source zone (Teisseyre 1973, Nagahama and Teisseyre 2000, 2001). Takeo and Ito (1997) have discussed rotational effect by using continuous dislocation theories, which can be connected with the theory of micromorphic continuum (Teisseyre 1973, 1974). Moreover, when friction motion along precuts occurs during earthquakes, it is better to use the asymmetric micromorphic continuum (similar to the micropolar mechanics: Teisseyre 1973, Shimbo 1978, Iesan 1981, Pasternak et al. 2003, 2004). For earthquakes, however, these theories have not been considered or unified using the concept of non-locality, asymmetry and inner -rotation of deformation.

In this chapter, we will reconsider the continuum with microstructures taking into account the concepts of non-locality, asymmetry and inner -rotation of deformation from the viewpoint of the differential geometry of high-order spaces. Then we will discuss relations between the earthquake

phenomena and the continuum with microstructures, and between the characteristics of fractal patterns (faults or earthquakes) and the characteristic length of structure caused by macrodislocations and microdisclinations.

26.2 High-Order Spaces and Non-Locality of Deformation

The high-order space (or the Kawaguchi space: Kawaguchi 1931, 1937, 1962) of order M (= 1, 2, 3, ...) is a metrical space $K_n^{(M)}$ in which the arc lengths along a curve $x^\kappa = x^\kappa(t)$ (t is an arbitrary parameter) is given by the integral

$$S = \int F\left(\mathbf{x}, \mathbf{x}^{(1)}, \mathbf{x}^{(2)}, \mathbf{x}^{(3)}, \ ..., \mathbf{x}^{(M)}\right) \mathrm{d}t\,, \tag{26.1}$$

where F means the fundamental function satisfying some homogeneity conditions and $x^{(\alpha)i} (\equiv \mathrm{d}^\alpha x^i / \mathrm{d}t^\alpha\,;\ \alpha = 1, 2, ..., M \le n-1)$ is an independent internal variable. Of course, this space is regarded as a generalized Riemannian or Finsler space non-localized by $\mathbf{x}^{(\alpha)}$ (here $\mathbf{x}^{(1)}$ is a vector, but $\mathbf{x}^{(\alpha)}$ ($\alpha \ge 2$) are the tensors). It turns out that the Riemannian space is a higher-order space of order 0, the Finsler space is a higher-order space of order 1, and the Cartan space is a higher-order space of order $\alpha = n-1$. Moreover, when we regard the non-Riemannian space and $\mathbf{x}^{(\alpha)}$ as a base space and a fiber, respectively, this high-order space is a fiber bundle space (Kawaguchi 1931, 1937, 1962).

We shall consider a geometrical grasp of the inherent law of an independent internal variable. At first, we shall write such laws of $x^{(\alpha)\kappa}$ in the form

$$\delta x^{(\alpha)\kappa} = M_\lambda^{(\alpha)\kappa} \left(\mathrm{d}x^\lambda + \sum_{\beta=1}^{\alpha} N_{(\beta)\mu}^\lambda \, \mathrm{d}x^{(\beta)\mu} \right), \tag{26.2}$$

which are essentially regarded as the base connections of high order spaces (Kawaguchi 1962). In this equation, $M_\lambda^{(\alpha)\kappa}$ and $N_{(\beta)\mu}^\lambda$ represent the interactions between each order of the internal variables. Concerning the concept of "non-locality", this is carried by the internal variable such as $x^{(\alpha)}$, so that a "non-local" field advanced by Yukawa (1950) can be obtained by attaching an internal variable to each point of a local (or Riemannian) field. This way of thinking descends from the theory of high order spaces (Kawaguchi 1931, 1962).

Finsler space can be regarded as a generalization of Cosserat continua (Cosserat and Cosserat 1909). When an independent internal variable $\mathbf{x}^{(1)}$ is a vector attached to each point of the continuum, the space can be regarded as ordinary Cosserat continua. When an independent internal variable $\mathbf{x}^{(1)}$ is a deformable director attached to each point of the continuum, we can get the theory of continuum mechanics of oriented media (Ericksen and Trusdell 1958). Moreover, when an independent internal variable $\mathbf{x}^{(1)}$ is a tensor attached to each point of the continuum, we can derive the multipolar theory (Green and Rivlin 1964). More generally, when an independent internal variable $\mathbf{x}^{(1)}$ is a *m*-dimensional manifold attached to each point of the continuum, we can derive Capriz's continuum with microstructures (Capriz 1989).

26.3 An Interaction Field Between Microscopic and Macroscopic Deformation Fields

In this section, we shall derive an interaction field between microscopic and macroscopic fields based on the base connections of high order spaces.

At first, we shall consider an interaction field between microscopic deformation field $\xi^i (\equiv x^{(1)i})$ and macroscopic deformation field x^λ (in our notation the Latin index letter refers to the microscopic deformation field and the Greek one to the macroscopic deformation field). When microscopic deformation fields ξ^j satisfy the inherent laws, we can put $\delta\xi^j = 0$. In this case, the base connection becomes

$$\mathrm{d}x^\lambda = A_i^\lambda \, \mathrm{d}\xi^i \,, \tag{26.3}$$

where A_i^λ is the interaction coefficient between microscopic and macroscopic deformation fields and is equivalent to $N_{(1)i}^\lambda$. The interaction coefficient A_i^λ is non-symmetrical in general.

Next, based on the differential geometry methods (Kondo 1953), we shall consider geometrical backgrounds of the inner-rotation. If small disturbances alone are considered, the deformation state of macroscopic deformation field can be grasped by the metric $g_{\lambda\kappa}$ and the coefficient of connection after deformation in the form:

$$g_{\lambda\kappa} = A_\lambda^j A_\kappa^i \delta_{ji} = \delta_{\lambda\kappa} + 2\varepsilon_{(\lambda\kappa)} \,, \qquad \varepsilon_{\lambda\kappa} \equiv \beta_\lambda^i \, \delta_{i\kappa} \,, \tag{26.4}$$

$$\Gamma^{\kappa}_{\mu\lambda} = A^{\kappa}_{i}\partial_{\mu}A^{i}_{\lambda} = \partial_{\mu}\varepsilon^{\kappa}_{\lambda}, \qquad \varepsilon^{\kappa}_{\lambda} \equiv \beta^{i}_{\lambda}\delta^{\kappa}_{i}, \tag{26.5}$$

where $\varepsilon_{(\lambda\kappa)}$ is an ordinary strain, β^{i}_{λ} represents deformation.

The antisymmetric strain does not represent the metric imperfection, but the rotational characteristic of microelements. Moreover, using the symmetric and antisymmetric strains, the coefficient of connection after deformation can be expressed in the form:

$$\Gamma_{\mu\lambda\kappa} = \partial_{\mu}\varepsilon_{\lambda\kappa} = \partial_{\mu}\varepsilon_{(\lambda\kappa)} + \partial_{\mu}\varepsilon_{[\lambda\kappa]}. \tag{26.6}$$

Thus, antisymmetric strains affect the metric imperfection, but the coefficient of connection after deformation remains unchanged. Let us introduce the inner-rotation $\phi_{\kappa\lambda}$; the relation between the strain and the inner -rotation is generally given by

$$\varepsilon_{\lambda\kappa} = \partial_{\lambda}u_{\kappa} + \phi_{\kappa\lambda}. \tag{26.7}$$

Therefore, the object of anholonomity in the macroscopic deformation field after deformation can be expressed by

$$\Omega_{\mu\lambda\kappa} = -\Gamma_{[\mu\lambda]\kappa} = -\partial_{[\mu}\phi_{\lambda]\kappa}. \tag{26.8}$$

This shows the geometrical object for the inner-rotation.

In the so-called Cosserat continuum (Cosserat and Cosserat 1909), the deformation and rotation tensors are given by

$$\begin{aligned} \varepsilon_{(\lambda\kappa)} &= \partial_{(\lambda}u_{\kappa)} + \phi_{(\lambda\kappa)} = \partial_{(\lambda}u_{\kappa)}, \\ \varepsilon_{[\lambda\kappa]} &= \partial_{[\lambda}u_{\kappa]} + \phi_{[\lambda\kappa]} = \partial_{[\lambda}u_{\kappa]} + \omega_{\lambda\kappa}, \end{aligned} \tag{26.9}$$

where u_{κ} is the displacement of a material element and $\omega_{\lambda\kappa}$ is the rotation independent of the rotation $\partial_{[\lambda}u_{\kappa]}$ originating from the displacement. In the micromorphic continuum theory (Suhubi and Eringen 1964), the deformations are represented not only by the displacement vector u_{κ}, but also by a new tensor that describes deformations and rotations of microelements (e.g., grains, blocks or some internal surface defects). It is a microdisplacement tensor $\varphi_{\lambda\kappa}$. The deformation can be now expressed by the following strain measures (e.g. Eringen 1968):

strain tensor $$e_{\lambda\kappa} = \partial_{\lambda}u_{\kappa}, \tag{26.10}$$

microstrain tensor $$\varepsilon_{\lambda\kappa} = \partial_{\lambda}u_{\kappa} + \varphi_{\lambda\kappa}, \tag{26.11}$$

microstrain moment tensor $\gamma_{\kappa\lambda\mu} = -\partial_\mu \varphi_{\lambda\kappa}$. (26.12)

The microdisplacement tensor $\varphi_{\lambda\kappa}$ represents the relative deformation between microscopic and macroscopic fields. Regarding the microdisplacement tensor $\varphi_{\lambda\kappa}$ as the inner-rotation $\phi_{\lambda\kappa}$, Eq. (26.11) is equivalent to Eq. (26.9). In this case, the order of the microstrain moment is the order of the coefficient of connection, and microdisplacement tensor $\varphi_{\lambda\kappa}$ plays an important role as the inner-rotation or the object of anholonomity in the macroscopic deformation field after deformation.

26.4 Asymmetry and Anholonomity of Deformation

Based on the base connections of high order spaces and the non-locality of deformation, an interaction field between microscopic and macroscopic deformation fields can be grasped by the (x^λ, A_i^λ)-fields as non-local fields. Moreover, based on the differential geometry methods (Kondo 1953), the inner-rotations as asymmetric fields can be derived from the (x^λ, A_i^λ)-fields , and the geometrical backgrounds of the inner-rotation are considered. Therefore, the interaction coefficient A_i^λ can be used to investigate the correlation between the macroscopic deformation field and the microscopic deformation field with microstructures. The metric and the coefficient of connection in strain space are dual to the stress and couple stress in stress space, respectively (Amari and Kagekawa 1964, Yamasakai and Nagahama 2002). This means that the asymmetrical fields originate from the non-local fields: an interaction field between microscopic and macroscopic deformation fields is a non-local field with internal variables as the inner-rotations $\phi_{\lambda\kappa}$ or $x^{(\alpha)}$. This internal variable $x^{(\alpha)}$-dependence is combined, in general, not only with the concept of "non-locality" but also the concept of "anisotropy" (Takano 1968).

In the micromorphic continuum theory (Suhubi and Eringen 1964), owing to the axiom of affine motion, and by analogy with the deformation gradients, the microdisplacement as the inner-rotation is linked to the relative deformation defined by the position of a material point of the microvolume relative to the center of mass of the macrovolume of the body. In this case, non-linear or irreversible behaviours with the inner-rotation have not been clear and not been linked to anholonomity in an interaction field between microscopic and macroscopic deformation fields. According to

the theory of the physical interaction field (Ikeda 1972, 1975, Muto and Nagahama 2004), the inner-rotation plays an important role in the object of anholonomity in the macroscopic deformation field after deformation. The object of anholonomity can describe the non-linear or irreversible behaviour of an interaction field between microscopic and macroscopic fields, because the interaction coefficient A_i^{λ} is non-symmetric in general.

26.5 Discussion

To complete our study of earthquake structures, we demand that deformations imposed on a microstructural element allow its elongation and rotation. This justifies our choice of micromorphic continuum in which length deformations of the Cosserat directors are also allowed. A new microdisplacement tensor $\varphi_{\lambda\kappa}$ describes deformations and rotations of microelements (e.g., grains, blocks or some internal surface defects: see Twiss and Unruh 1998, Twiss et al. 1991, 1993). In particular, while considering a focal region and its deformations, the micropolar theory (rotation only: $\varphi_{\nu\sigma} = -\varphi_{\sigma\nu}$) is rather inadequate for seismological problems (Teisseyre 1973, Nagahama and Teisseyre 2000, 2001). But considering the friction motion along precuts, the asymmetric micromorphic continuum is suitable (micropolar mechanics: Shimbo 1978, Iesan 1981, Teisseyre 1995a, b, Pasternak et al. 2003, 2004). All these continuum definitions satisfy our non-local continuum theory discussed in this paper.

For the past several years, the rotation seismic wave has become again a subject considered from theoretical and observational points of view (Takeo and Ito 1997, Moriya and Teisseyre 1999, Teisseyre 2002). Defects and internal structure contribute to processes of generation and propagation of rotation waves. In the case of non-ideal elasticity, the seismic rotational waves appear due to defect content (the non-symmetric disclinations) in a medium or due to internal structure of a medium (micromorphic or micropolar media) of the source zone.

In the classic approach to ideal elasticity, these waves would become rapidly attenuated. However, when introducing the elastic bonds for rotation of particles, the antisymmetric stresses (or stress moments) will appear (an additional constitutive law joining such stresses with rotations will be introduced), and such attenuation of rotation waves will appear only as an effect of the inadequate theory (Teisseyre 2004, 2005).

Another possibility is provided by coupling between the seismic body waves and defects or micromorphic structures of medium just beneath ob-

servation sites. Teisseyre and Nagahama (1999) discussed such a coupling in micro-inertia continua defined as special cases of micromorphic/micropolar continuum. In these researches, the concept of the inner-rotation, non-locality and asymmetry plays an important role.

Kagan (1992, 1994) compared the properties (e.g., scale-invariance, symmetry and hierarchy) of seismicity with those of the turbulence of a fluid flow, and pointed out that: *Most earthquake deformation is the effect of dislocations (translational defects), whereas disclinations (rotational defects) play a subordinate role. In turbulent motion of fluid, vortices (disclinations) are primary vehicles of deformation*. He believes that two modes of condensed matter deformation will yield significant new insight into the mechanics of both phenomena, and determined statistical features (spatial pattern $T(3)$ and rotation $SO(3)$) of earthquakes by analyzing earthquake catalogs. These properties (e.g., symmetry and hierarchy) of seismicity are consistent with the concept of asymmetry and non-locality of deformation mentioned above.

The Lagrangian of these defects is invariant with respect to three -dimensional rotations $SO(3)$ and spatial translations $T(3)$ (Kadi'c and Edelen 1983), and the deformation of micromorphic structure (continuum) induces the appearance of dislocations and disclinations, $SO(3) \triangleright T(3)$. These structural defects are related to anholonomity caused by the inner-rotation (microdisplacement or microstrains moment) in the form:

$$\Lambda_{\kappa\lambda} = -\in_{\lambda\mu\nu} \partial_{\mu} \varphi_{\kappa\nu} , \tag{26.13}$$

where $\Lambda_{\kappa\lambda}$ denotes the microdislocation density (Nagahama and Teisseyre 2001), $\in_{\lambda\mu\nu}$ is Eddington's epsilon (the skew-symmetric tensor; 0, 1, –1).

Therefore, the internal nuclei (dislocations, disclinations, vacancies, thermal nuclei or electric nuclei) are the objects/sources that create internal stresses (self stresses) (Teisseyre 2002).

On the other hand, we shall note the differences in the scales of these defects (Nagahama and Teisseyre 2001). The shear band model and macrodislocations can be combined into a consistent model in which the gauge dislocations of a superlattice are replaced by macrodislocations. A micromorphic structure leads to formation of macrodislocations related to the characteristic length of structure L; we only need to replace the superlattice constant Λ by L. The macrodislocations could reach the value of the Burgers vector b up to the characteristic length of the structure (Nagahama and Teisseyre 2001):

$$b \leq \Lambda \Rightarrow L . \tag{26.14}$$

This characteristic length of structure L is consistent with the concept of non-locality of deformation mentioned above. On a computational grid of cells as a discrete numerical system, the spatio-temporal complex slip, which induces scale-invariance, disappears in the well-defined continuum limit as the cell size diminishes (Rice 1993). If we can regard this cell size as the characteristic length of structure caused by internal variables (macrodislocations and microdisclinations), this characteristic length of structure may become the characteristic length of fractal patterns (faults or earthquakes).

References

Amari S, Kagekawa K (1964) Dual dislocations and non-Riemannian stress space. RAAG Research Notes Third Ser No. 82: 1-24

Capriz G (1989) Continua with microstructure. In: Trusdell C (ed) Springer Tracts in Natural Philosophy Vol 35. Springer-Verlag, Berlin

Cosserat E, Cosserat F (1909) Téorie des corps déformables. Librairie Scientifique A, Hermann, Paris

Ericksen JL, Trusdell C (1958) Exact theory of stress and strain in rods and shells. Arch Rational Mech Anal **1**: 295-323

Eringen AC (1968) Theory of micropolar elasticity. In: Liebowitz H. (ed) Fracture, Vol. 2. Acadmic Press, New York, pp 621-729

Green AE, Rivlin RS (1964) Multipolar continuum mechanics. Arch Rational Mech Anal **17**: 113-147

Iesan D (1981) Some applications of micropolar mechanics to earthquake problems. Int J Engng Sci **19**: 855-864

Ikeda S (1972) A geometrical construction of the physical interaction field and its application to the rheological deformation field. Tensor NS **24**: 60-68

Ikeda S (1975) Prolegomena to applied geometry. Mahā Shobō, Saitama

Kadi'c A, Edelen DG (1983) Gauge theory of dislocations and disclinations. Springer-Verlag, Berlin

Kagan YY (1992) Seismicity: Turbulence of solids. Nonlinear Sci Today **2**: 2-13

Kagan YY (1994) Observational evidence for earthquakes as a nonlinear dynamic process. Physica **D 77**: 160-192

Kawaguchi A (1931) Theory of connections in a Kawaguchi space of higher order. Proc Imper Acad Japan **13**: 237-240

Kawaguchi A (1937) Beziehung zwischen einer metrischen linearen Uebertragung und einer nicht-metrischen in einem allgemeinen metrischen Raum. Proc Kon Akad Wet **40**: 596-601

Kawaguchi M (1962) An introduction to the theory of higher order spaces I: The theory of Kawaguchi space. In: Kondo K (ed) RAAG memoirs of the unified study of basic problems in engineering and physical sciences by means of geometry Vol. III, 3-Div Misc Gakujyutsu-Bunken Fukkyukai, Tokyo, pp 718-734

Kondo K (1953) On the geometrical and physical foundations of the theory of yielding. Proc 2nd Japan Nat Congr Appl Mech, held 1952, pp 41-47

Moriya T, Teisseyre R (1999) Discussion on the recording of seismic rotation waves. Acta Geophys Pol **47**: 351-362

Muto J, Nagahama H (2004) Dielectric anisotropy and deformation of crustal rocks: physical interaction theory and dielectric mylonites. Phys Earth Planet Inter **141**: 27-35

Nagahama H, Teisseyre R (2000) Micromorphic continuum and fractal fracturing in the lithosphere. Pure appl geophys **157**: 559-574

Nagahama H, Teisseyre R (2001) Micromorphic continuum and fractal properties of faults and earthquakes. In: Teisseyre R, Majewski E (eds) Earthquake thermodynamic and phase transformations in the earth's interior. Academic Press, New York, pp 559-574

Pasternak E, Mühlhaus H-B, Dykin AV (2003) Apparent strain localization and shear wave dispersion in elastic fault gouge with microrotations. In: Sloot PMA et al (eds) Computational science - ICCS 2003, LNCS 2659. Springer -Verlag, Berlin, pp 873-882

Pasternak E, Mühlhaus H-B, Dykin AV (2004) On possibility of elastic strain localisation in a fault. Pure appl geophys **161**: 2309-2326

Rice JR (1993) Spatio-temporal complexity of slip on a fault. J Geophys Res **98** B6: 9885-9907

Shimbo M (1978) A geometrical formation of granular media. Theor Appl Mech **26**: 473-480

Suhubi E S, Eringen A C (1964) Nonlinear theory of micro-elastic solids II. Int J Engng Sci **2**: 389-404

Takano Y (1968) Theory of fields in Finsler spaces. I. Prog Theor Phys **40**: 1159-1180

Takeo M, Ito HM (1997) What can be learned from rotational motions excited by earthquakes? Geophys J Int **129**: 319-329

Teisseyre R (1973) Earthquake processes in a micromorphic continuum. Pageoph **102**: 15-28

Teisseyre R (1974) Symmetric micromorphic continuum: wave propagation, point source solution and some applications to earthquake processes. In: Thoft -Christensen (ed) Continuum mechanics aspects of geodynamics and rock fracture mechanics. D. Riedel Publ, Holland, pp 201-244

Teisseyre R (1995a) Micromorphic model of a seismic source zone, 1. Introduction. In: Teisseyre R (ed) Theory of earthquake premonitory and fracture processes. Polish Scientific Publ, Warszawa, pp 613-615

Teisseyre R (1995b) Micromorphic model of a seismic source zone, 2. Symmetric micromorphic theory; application to seismology. Theory of earthquake premonitory and fracture processes. Polish Scientific Publ, Warszawa, pp 616-627

Teisseyre R (2002) Continuum with defect and self-rotation fields. Acta Geophys Pol **50**: 51-68

Teisseyre R (2004) Spin and Twist motions in a homogeneous elastic continuu and cross-band geometry of fracturing. Acta Geophys Pol **52**: 173-183

Teisseyre R (2005) Asymmetric continuum mechanics: Deviations from elasticity and symmetry. Acta Geophys Pol **53**: 115-126

Teisseyre R, Nagahama H (1999) Micro-inertia continuum: Rotations and semi-waves. Acta Geophys Pol **47**: 259-272

Twiss RJ, Unruh JR (1998) Analysis of fault slip inversions: Do they constrain stress or strain rate? J Geophys Res **103**, B6: 12205-12222

Twiss RJ, Protzman GM, Hurst SD (1991) Theory of slickenline patterns based on the velocity gradient tensor and microrotation, Tectonophys **186**: 215-239

Twiss RJ, Souter BJ, Unruh JR (1993) The effect of block rotations on the global seismic moment tensor and the patterns of seismic P and T axes. J Geophys Res **98**, B1: 645-674

Yamasaki K, Nagahama H (2002) A deformed medium including a defect field and differential forms. J Phys A: Math Gen **35**: 3767-3778

Yukawa H (1950) Quantum theory of non-local fields. Part I. Free fields. Phys Rev 77: 219-226; Quantum theory of non-local fields. Part II. Irreducible fields and their interaction. Phys Rev **80**: 1047-1052

27 Earthquake Hazard in the Valley of Mexico: Entropy, Structure, Complexity

Cinna Lomnitz, Heriberta Castaños

National University of Mexico, UNAM, 04510 Mexico, DF, Mexico
e-mail: cinna@prodigy.net.mx

27.1 Introduction

Disasters are complex events that occur in complex 3-D environments. The structure of central Mexico involves an offshore subduction zone, a volcanic belt, an efficient *Lg* waveguide, several tectonic terranes that accreted in different geological periods, and a variety of complicated local structures (Kennett and Furumura 2002, Ottemöller et al. 2002). Disasters such as the 1985 earthquake strike Mexico City as a result of a combination of unusual factors. First, the city was located several hundred kilometers inland from the epicenter of a damaging subduction earthquake off the Pacific coast. Second, the waves that caused the damage were coherent, monochromatic, high-amplitude surface waves of very long duration. These characteristic wave trains were recorded only on soft lake sediments in the downtown urban area.

Finally, severe structural damage occurred mainly in modern, multistory office and apartment buildings. Traditional masonry construction performed quite well, and so did low-income housing.

The high degree of surprise still commonly associated with disasters is due to unexpected combinations of causes and circumstances. Some modern views of disasters reflect the embarrassing puzzlement of specialists in their preference for paradoxical explanations – such as that "nature, technology and society interact to generate vulnerability and resilience to hazard" (Burton et al. 1993). The very concept of vulnerability is being questioned. The 1985 Mexico earthquake selectively destroyed the most highly developed part of the country and within it, those structures designed by engineers in accordance with a building code widely regarded as the most advanced in the world – while 300-year old Colonial churches and monuments survived.

27.2 Seismology: a Science in Trouble?

After the 1906 San Francisco earthquake the Seismological Society of America was founded. At the same time a new discipline – earthquake engineering – was born. It was initially very successful in controlling earthquake hazard, and in reducing human and economic sufferings from earthquake disasters. The vigorous response of society after the 1906 earthquake disaster was yielding concrete benefits. At the mid-century point there was optimism that the threat from earthquakes would soon be a thing of the past.

However, about 1955 or 1960 it was discovered that the losses from earthquakes had started climbing again. Presently they exceed all earlier world records. The cause of this upset is uncertain. It has been attributed to the population "explosion" or to urbanization, but it could also be related to some unfamiliar features in disaster causation, such as complexity, technology, and environmental change. Or, it might be due to our reluctance to face these changes in a more effective way. The 2005 Katrina hurricane has brought these considerations to the attention of a broader public.

Take the development of seismological instrumentation. In the last 20 years or more there has been no relevant technological innovation in the recording and interpretation of seismic signals. Yet other disciplines, such as astronomy, not only expanded significantly the width of the spectrum of observations beyond the visual range but also raised the level of description of the signals, for example, in the case of Very Large Telescope Interferometry (VLTI).

After the 1985 Mexico earthquake an increasing amount of earthquake damage was observed on soft ground, yet no specific new instrumentation for recording rotational ground motions on soft ground has become available. The last important advance in seismic instrumentation was arguably Hugo Benioff's strain seismograph, developed in 1935.

Another aspect of the same problem is what we actually do with the observations. Hypocentral location has been the bread-and-butter activity of seismology at least since Zoeppritz (1907). However, as the plane-earth approximation can no longer be sustained, the problem of earthquake location becomes ill-posed (Lomnitz 2005). Various stopgap procedures have been used in an attempt to restore the posedness of the problem, but large location errors remain common. The uncertainty in earthquake location contaminates estimates of earth structure and earthquake hazard.

Seismologists reacted by retreating behind the laws of geometrical optics. The influential textbook by Aki and Richards (1980) redefined seismology as the science of seismograms, and thus the ultimate purpose of

seismologists became a strenuous effort to fit or "synthesize" seismograms by a superposition of linear effects of reflection, refraction, and scattering. The physics of earthquakes shrunk to the status of a minor and esoteric specialty.

27.3 Disasters in General, and Mexico City in Particular

Disasters are extreme phenomena that occur at the nature-society interface. Nature and society are interacting complex systems. Wolf Dombrowsky (1984) has suggested that a disaster may be seen as a negation of progress. The idea is that progress is falsified when the system can hit back. Relevant properties of the system are ignored at our peril.

Thus complex systems are creative: they have emergent properties. The term emergence refers to patterns or properties that cannot in general be predicted from the initial conditions, or from the rules of the system or systems. This implies that there are several levels of description of the system. Emergent phenomena are unexpected and unpredictable, not in general but in terms of some lower-level description.

For example, a lower-level description of the 1985 Mexico earthquake might involve a source *S*, a path *P,* and a site or receiver *R* (Fig. 27.1). The seismogram, or seismic record, is assumed to be a convolution of source

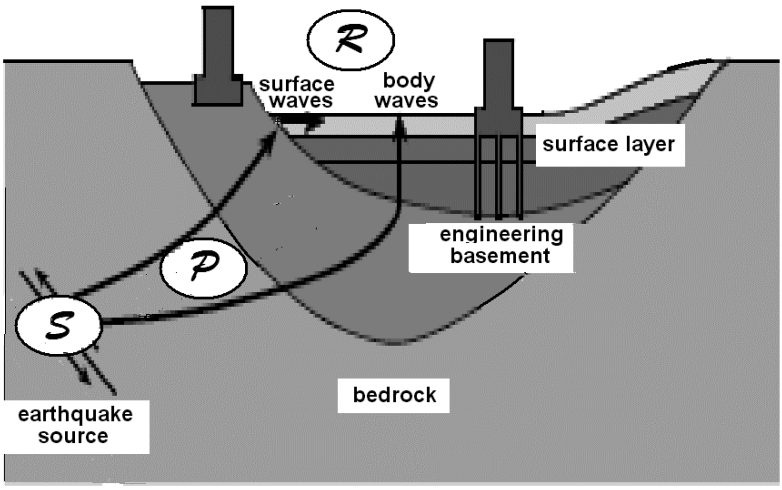

Fig. 27.1 A lower-level description of the 1985 Mexico earthquake as a convolution of source effects *S*, path effects *P*, and receiver effects *R*. The geology is highly idealized. Modified after Yoshida and Iai (1998)

effects *S*, path effects *P*, and receiver effects *R*:

$$F(\omega) = S(\omega) \cdot P(\omega) \cdot R(\omega)\,, \tag{27.1}$$

where ω is frequency. The structure of the earth between the source and the receiver is assumed to be fully contained in the path function *P*.

Actually the deep structure under Mexico City is controversial and a concave basement is unlikely, as there is no evidence of a former river valley. On the other hand, complex 3-D structures, especially when found in the neighbourhood of a site, are widely recognized to have complicated effects on the focusing and defocusing of seismic energy. But it is merely a matter of harnessing more computing power: *the local influence of sedimentary basins is large but needs fine scale representation* (Kennett and Furumura 2002). This approach ignores the evidence on the enormous increase of seismic energy that is observed on soft ground in Mexico City, and which cannot be accounted for at this level of description.

Consider pairs of seismograms written on identical instruments at nearby stations for the same seismic event (Fig. 27.2). The epicentral distance of the Mexican coastal earthquake in the figure was not quite 400 km

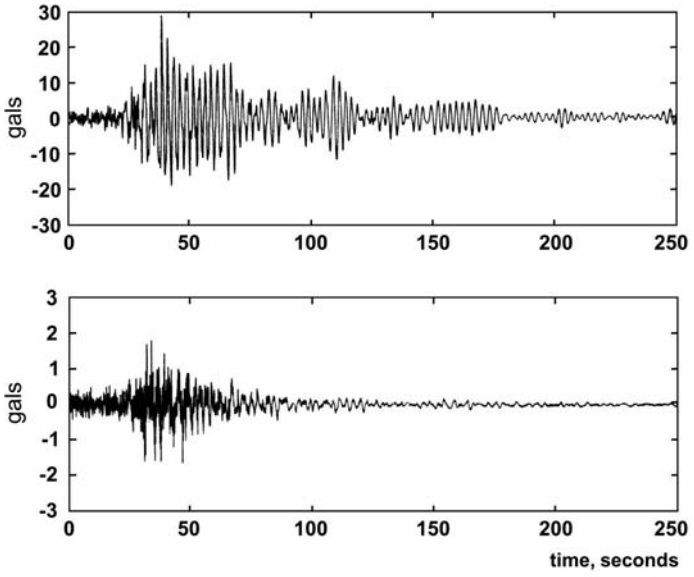

Fig. 27.2 Radial component recordings of the off-Michoacan, Mexico, earthquake of 11 January 1997, M7.1, at two stations in the Mexico City basin. *Top*: station on soft ground at Texcoco seismic array. *Bottom:* Texcoco station on hard ground. Epicentral distance was about 380 km. Distance between stations was less than 10 km. Both records were produced on identical FBA23 accerelographs. Note that the acceleration scales differ by a factor of 10

and the distance between stations was less than 10 km. Both stations were located in the Valley of Mexico, but the lower record was written on hard ground while the upper one was on soft ground nearby. The thickness of the soft layer was less than the wavelength of regional surface or body waves: thus one might expect that all three functions *S, P,* and *R* should have been similar or identical. Yet the two seismograms are very different. The amplitude ratio is very significant for two neighbouring stations in the same sedimentary basin. Note that the amplitude scale differs by a factor of 10. Perhaps more important is the fact that the prominent monochromatic phase which dominates the signal on soft ground appears to be absent on hard ground.

Singh and Ordaz (1993) attempted to minimize the importance of such differences by suggesting that the seismograms on hard ground can also have long durations. It is merely a matter of turning up the gain. The implication was that the large signal observed in the sedimentary basin might have been generated by incoming surface waves. However, Chavez-Garcia and Bard (1994) proved that 1-D amplification of ground motion cannot explain the long duration of strong shaking; and Barker et al. (1997) showed from 2-D and 3-D array analysis that the waves in the soft-ground area of downtown Mexico City originate mostly from the near edges of the soft layer, not from incoming surface waves. Independently of their back-azimuth, waves from the far edges are systematically damped out. Thus, the high-amplitude surface waves which caused severe damage in Mexico City represent a strictly local phenomenon.

In conclusion, a nagging question remains: where did all the energy in the former lake area come from?

27.4 A Higher Level of Description

Whenever a lower explanatory level is exhausted, we may feel entitled to search for a higher level of description of the system. This is true for hardware (telescopes or molecular machinery) as well as for software. It is true of disaster science.

Societies build bridges to nature in order to dominate or exploit it, or parapets to protect themselves against the onslaughts of nature. This frontier between nature and society is known as technology. It is where disasters attack.

The Mexico City building code was believed to be among the most modern in the world. The technology of reinforced concrete-frame structures was thought to be well understood. Yet after the 1985 disaster the

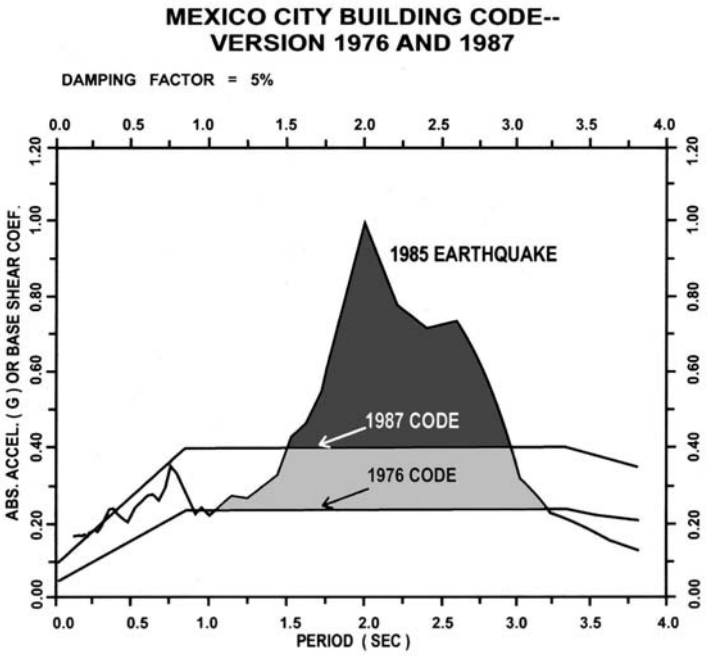

Fig. 27.3 Response spectrum for the 1985 earthquake recorded at station SCT1 on soft ground. The design spectra for the 1976 and 1987 versions of the Mexico City Building Code are given for reference. Both versions predict a broad, flat-topped response spectrum which falls short of the recorded 1985 spectrum

engineers (including the authors of the building code) recognized that the ordinances had been inadequate. The 1987 amendments to the Mexico City Building Code raised the peak spectral design accelerations by up to 66% (Fig. 27.3). But the code still predicted ground motions based on geometrical optics.

Geometrical optics is based on a high-frequency approximation. Surface features the size of a wavelength, such as the mud layer under Mexico City, will cause problems, as will features like edges. The next higher level of description which we may invoke is the waveguide. A waveguide is a conductor of wave energy. It differs from an optical ray bundle in that it has discrete propagation modes.

In Fig. 27.4 we show a diagram representing the 1985 Mexico earthquake in terms of two waveguides: (a) a regional or crustal waveguide which includes the source and the upper 2 kilometers of the continental crust, and (b) a local waveguide consisting in a flat layer of soft mud. Layer (b) is embedded in the crustal waveguide (a). When the crustal waveguide is excited by a seismic transient the two waveguides may

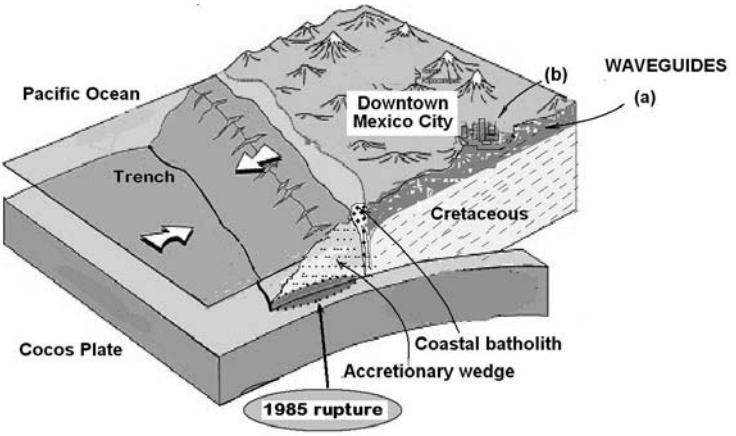

Fig. 27.4 Subduction model of the 1985 earthquake. An E-W idealized geological section is shown. In a large earthquake, efficient transmission of seismic energy inland over the regional *Lg* waveguide (a) enables 0.4 Hz modes to be trapped in an embedded soft local waveguide (b) which underlies downtown Mexico City. Severe damage is caused by prolonged excitation of monochromatic, coherent, short surface waves of very long duration

couple and seismic energy at a specific frequency f_c may flow from waveguide (a) into waveguide (b). Under certain conditions which have to do with the number of propagating and evanescent modes at the boundaries, the mode of frequency f_c may be trapped in the shallow waveguide. If the rate of inflowing energy exceeds the attenuation in the mud, seismic energy of frequency f_c will accumulate in the waveguide for the duration of the earthquake. In other words, the duration of the earthquake will be defined by the time span during which the influx of energy exceeds the rate of energy expended in damping and in causing damage to structures.

Before we proceed, let us attempt to consolidate our argument. Firstly, it might be argued that the waveguide model contributes no new features since "the trapping of waves within sedimentary basins is well known and leads to complex, elongated wavetrains" (Kennett and Furumura 2002). This is quite true, but a bundle or packet of rays should reach a sedimentary basin with a fairly uniform power cross-section. Optical trapping cannot explain large power variations between neighbouring points within a basin such as those observed in Fig. 27.2.

Secondly, coupling between modes seems to require or to imply some nonlinear behaviour, as linear modes in 1-D layered systems are orthogonal. Uniform wavetrain solutions of the nonlinear Schrödinger equation would most likely be unstable, as Infeld and Rowlands (2000) have found

for 1-D deep-water gravity waves. However, seismic signals are transients. As Infeld and Rowlands also pointed out, in time the higher unstable modes tend to decay and transfer their energy to the fundamental mode. Indeed the seismogram becomes quasi-cyclic, as can also be observed in water waves ("Fermi-Ulam-Pasta recurrence").

Finally, given a fixed amount of earthquake energy at the source, why should a system prefer one form of energy transfer over another? It seems that coupled modes in waveguides might represent a very lossy mechanism as compared to straightforward seismic propagation with optical amplification due to impedance contrasts.

The latter objection is of particular interest and will be discussed here.

27.5 Nonlinearity and Non-Equilibrium Thermodynamics

A complex system provides many options or routes of evolution. How does the system choose among these options? An answer may be found in the emerging field of non-equilibrium thermodynamics (Kleidon and Lorenz 2005).

Consider the work output of a complex system such as the earth. It is governed by heat flow and by the Carnot efficiency for that heat flow. For this system to be found in a steady state, the frictional dissipation must balance the work production. But circulation of heat and of matter is a combination of many flow modes.

Let the *i*th mode be characterized by a heat transport F_i and a loss by dissipation L_i. Some modes may be very efficient (low *L/F*) while others may be very inefficient (high *L/F*). If the work output and the dissipation are to be balanced, we must have $L \leq F \cdot \Delta T/T$ at steady state (Lorenz 2005).

But this condition can be achieved in many different ways. In other words, the steady state can be reached by many microscopic combinations of modes, especially when the steady state has a high work output and a high dissipation. Suppose that all possible combinations are populated with equal probability: then the most likely states are those with higher dissipation. This is called the Principle of Maximum Entropy Production (Dewar 2003)[*)].

[*)] In a popular form this may be expressed as Murphy's Law: If anything can go wrong, it will. Another version is as follows: *If there is a possibility of several things going wrong, the one that will cause the most damage will be the one to go wrong — and if there is a worse time for something to go wrong, it will happen then.*

The validity of the principle is quite general but there has been some confusion with the "principle of minimum entropy production" formulated by Prigogine (1962). Actually there is no contradiction. Prigogine's work applies to linear systems with fixed boundary conditions near equilibrium. Such systems have one unique steady state, which indeed represents a state of minimum entropy production with respect to neighbouring non-steady state conditions. But disasters involve nonlinear processes far from equilibrium that can have an infinity of degrees of freedom, and thus of steady states — among which the state of maximum entropy production is selected. Note that the argument by Kleidon and Lorenz applies also to transient processes such as earthquakes.

But why should one wish to invoke nonlinearity when a linear approach will do? The answer to this objection is fundamental if we wish to understand the causes of disasters. Let us consider the specific case of the 1985 Mexico earthquake, which we may later attempt to extend to disasters in general.

Unlike rocks, soil is a nonlinear material. The stress-strain curvature at the origin is negligible for rocks, and a maximum for soils. The stress-strain propagation behaviour in soils may be represented by an empirical 1-D equation of state (Lomnitz 1994):

$$\frac{\mathrm{d}\sigma}{\mathrm{d}\varepsilon} = c\left(\frac{\sigma}{\varepsilon}\right)^{d}, \tag{27.2}$$

where σ is a shear strain component, ε is the corresponding stress component, and d is a fractal dimension. Note that this equation contains elastic waves ($d = 0$) as well as gravity waves in fluids ($\mathrm{d}\sigma/\mathrm{d}\varepsilon = 0$). It also contains the Hardin and Drnevich (1972) empirical equation for soils ($d = 2$).

Soils as well as other soft condensed matter behave as solids at low strains, and as liquids at high strains. As ε tends to infinity, the shear modulus $\mu = \mathrm{d}\sigma/\mathrm{d}\varepsilon$ decays to zero. This is known as shear-modulus degradation.

Mexico City mud has a substantial rate of shear-modulus degradation. Under realistic conditions the rigidity μ will be halved after every three or four strain cycles. Also, the initial value of μ is extremely low, as the shear velocity is around $V_s = \sqrt{\mu/\rho} \approx 50\,\mathrm{m/s}$. Thus, during a large earthquake, the shear strength will be further reduced, and only the molecular forces known as cohesion will prevent the material from flowing like saturated sand. The proper terminology for this behaviour is cyclic mobility, as opposed to liquefaction in sands. Cyclic strain value estimated in the 1985 earthquake on the linear assumption (i.e., assuming μ not to decay during

the earthquake) were around 0.3% but the actual values were certainly much larger, as was also found in Japanese earthquakes (Yoshida and Iai 1998).

In addition, because of the large impedance contrast between the mud layer and the underlying volcanic tuff, there was a very substantial passive amplification. This behaviour was well known and had been specified in the Mexico City Building Code. Nonlinear behaviour was not foreseen, however. The important effects of nonlinearity are not primarily in the amplitude but in other dynamic effects. Gravity must be considered in very soft materials.

Weakly nonlinear wave propagation in soils is governed by the Schrödinger equation, a universal nonlinear equation of wave propagation (Infeld and Rowlands 2000, Chap. 5). In the case of the Mexican earthquake we may write the wave potential Φ as

$$\Phi(x,t) = a(x,t)\exp[\mathrm{i}(kx - \omega t)], \tag{27.3}$$

where k and ω represent the wavenumber and frequency of the marginally stable mode (here the fundamental shear resonance of the mud layer), and the nonlinear effects are in the amplitude factor a.

Nonlinearity may be introduced in a number of ways. For example, Ewing et al. (1957) invoked coupling between acoustic waves and Rayleigh waves in a soft soil layer when the Rayleigh phase velocity is lower than the speed of sound in air. This coupled mode is monochromatic and is known in petroleum prospecting as ground roll. But nonlinearity in the stress-strain relations is probably the most obvious cause of coupling between two waveguides.

Coupling enables a receiver – in this case, the mud layer – to trap incoming modes that match the resonant modes in the layer, as when an antenna is tuned to a specific frequency. The Mexican Volcanic Belt, with a thickness of around 2 km, has a major impedance contrast with the underlying Cretaceous limestones found at sea level. The crustal waveguide propagates multiply reflected and refracted body waves known as *Lg* from epicenters in the subduction zone toward Mexico City. Propagation is particularly efficient in the frequency range of 0.3 to 1 Hz (Campillo et al. 1989). The Mexico City mud layer is embedded in this waveguide.

The mud layer is around h = 30 m thick and its shear-wave velocity is around V_S = 50 m/s. Thus the incoming *Lg* waves can excite the mud layer at its quarter-wavelength resonance $f = 50/(4\cdot 30) \approx 0.4$ Hz. When the influx of energy from the *Lg* waveguide cannot make up for losses from attenuation in the mud the strong-motion output is short-lived. However, for earthquakes of magnitude 6.5 and above, the energy trapped in the mud

layer will exceed the damping loss. The higher the magnitude, the more energy is trapped in the surface layer. The result is a strong, coherent, monochromatic wave train of very long duration.

Because of shear-modulus degradation in the mud, the shear-wave velocity decays at near-constant input frequency and the wavelength shortens during the earthquake. As it approaches the characteristic wavelength for gravity waves in shallow water, gravity competes with elasticity as a restoring force and visual observations of slowly traveling pseudo-gravity waves are reported. Long structures such as freeways or aqueducts sway or buckle and elongated buildings capsize. As the amplitude fades, the wavy ground motion freezes and permanent deformations of up to 20 m wavelength are left in the downtown area. Similar observations have been made in other large earthquakes on soft ground (see, e.g., Matuzawa 1925).

The interaction between natural and social phenomena in disasters is still poorly understood. The more we claim to understand disasters, and that we are on the verge of being able to predict them in terms of probability, the worse is disaster's revenge. Most authors agree that the response of society to extreme events "should be re-examined", and that our methods "cry out for refinement" (Burton et al. 1993). Similar criticisms were voiced after the 2005 Katrina disaster. However, examples of collaborative disaster research between social and natural scientists are still rare.

To summarize, we propose a new model of disaster causation for the 1985 Mexico earthquake. Our model invokes a nonlinear interaction between higher-level structures, rather than a passive response of lower-level structures to linear wave propagation. Interaction between geology and social structures remains a major unsolved problem.

In order to buttress our argument, we have suggested a variety of new effects based on insights in mechanics of guided-wave propagation and non-equilibrium thermodynamics. Some of these effects had been noted many years ago but were not fully explored by seismologists. As a notable example, Lord Rayleigh recognized that surface waves propagated as guided waves, and he noted in his *Theory of Sound* that:

Anything that confines the sound will tend to diminish the falling off of intensity. Thus over the flat surface of still water, a sound carries further than over broken ground; the corner between a smooth pavement and a vertical wall is still better; but the most effective of all is a tube-like enclosure, which prevents spreading altogether. . . Sound might be thus conveyed with little loss to very great distances.

We submit that when two waveguides couple during an earthquake, seismic energy at 0.4 Hz can flow from one waveguide to the other. The receiver layer acts as a filter or antenna that soaks up and traps shear

modes at resonant frequencies. Structures built upon the receiver will be excited to the extent that their own eigenfrequencies match the frequencies in the ground. Reinforced concrete structures are particularly vulnerable to resonance as their intrinsic damping is quite low, usually below 5% of critical. To bring such buildings to the point of structural collapse, as in the 1985 Mexico earthquake, extreme seismic inputs are essential.

From the observations of the behaviour of structures made after the disaster it appears that the very long duration of strong ground shaking played a major unexpected role in causing the damage. Another unforeseen factor was the presence of coherent monochromatic wave trains. Finally, the presence of prograde surface waves similar to water waves may have introduced some unforeseen factors such as the excessive swaying of tall buildings, and the whiplash effect in the upper stories.

Let us now address the main objection to this argument, namely that our model is contrived and that it needlessly invokes nonlinearity, wave-wave coupling and other emergent features of complex systems.

27.6 A Theory of Disasters as Unexpected Events

Consider the following reasoning:

Proposition 1:	All disasters are unexpected.
Proposition 2:	Unexpected events occur.
Conclusion:	Always expect the unexpected.

Let us overlook some formal objections for the moment and consider the above reasoning as an example of empirical logic. Else Barth (1985) has pointed out that real arguments and real debates deserve to be studied as such, and that the suitability of a social science approach to argument does not in the least derogate from the importance of logical pursuits. We argue that disasters may occur because they are unexpected, and that they are preventable to the extent that a multiplicity of possible combinations of causative factors can be anticipated or foreseen.

As we are dealing with complex systems having a virtually inexhaustible number of modes, the chances of anticipating all possible disasters are slim. But one approach to prevention may always be effective, namely strengthening society against all types of adversity. If there is social cohesion, if there are no obvious social inequalities, if there is security, and if there is a vigorous economy with access to opportunity for all, such a society will take all needed precautions and develop the necessary resilience against disasters of every kind.

Of course, the above conclusion ("always expect the unexpected") may be regarded as sophistry, or as an example of Russell's Paradox, since one can hardly expect the unexpected without eliminating all unexpected events. This contradicts Proposition 2. However, an imaginative solution of this apparent contradiction might be the only practical way of preventing disasters.

Against all evidence, it has sometimes been maintained that disasters such as the 1985 Mexico earthquake, the 2004 Indian Ocean tsunami or the 2005 Katrina hurricane were predicted. The large number of casualties and the degree of damage to society seem to point in a different direction. A valid disaster prediction can be socially usefully on condition that there is a way of telling it apart from the large amount of similar predictions that are regularly issued and which fail to materialize. As far as the 1985 Mexico earthquake is concerned, it is true that the Mexican subduction zone had been recognized as a source of large earthquakes but the specific epicentral area of Michoacan had also been tentatively designated as inactive (Singh et al. 1980). The hazardous soft-ground area in downtown Mexico City had been mapped and duly labeled. The prescribed design accelerations in the Mexico City Building Code were much stricter in the hazardous area. They took into account the well-known fact that some builders would attempt to cut corners. Yet the earthquake demolished many buildings that had been designed under earthquake regulations while sparing neighbouring structures that hadn't.

Prior to the 1985 Mexico earthquake it had been widely believed that high damping in soft soil should reduce the seismic amplitude as compared to sites on rock (Finn 1991). Peak accelerations on soft ground were revised sharply upward after the Mexico and Loma Prieta earthquakes. Yet the number of full-fledged seismic stations on soft ground remains negligible worldwide as compared to stations on rock.

Disasters are not caused by recklessness, nor can they be attributed to a single physical event such as a hurricane or an earthquake. A study of specific disasters and major "accidents" suggests that there is a chain of seemingly unconnected and unlikely physical and social circumstances which we have called a Perrow chain (Perrow 1999). The following Perrow chain appears to fit this description.

1. The earthquake occurred at almost 400 km in an area where geophysicists had not expected the next large seismic event to occur.
2. It hit hardest in the capital and in the heart of the most advanced modern area of the country, but it caused only moderate damage in the epicentral area and in underdeveloped regions.

3. It caused severe structural damage in a relatively small urban area on soft ground, which had been correctly identified and recognized as hazardous in the Building Code.
4. It destroyed exclusively modern reinforced concrete high-rise buildings designed and built by professionals according to seismic regulations believed to be among the most advanced in the world. No traditional old masonry structures collapsed.
5. The strong ground motion in the soft-ground area of Mexico City was monochromatic, coherent and of extremely long duration.
6. So-called "visible surface waves" in the same area were described as similar to water waves. Residual wavy deformation was observed on pavement.
7. Important critical facilities such as hospitals, schools, telephone and communications hubs and emergency centers collapsed. The number of casualties was extremely high.

Most of these circumstances were unexpected. Our hypothesis may provide an adequate causative link to this Perrow chain, thus helping to account for the element of surprise. No two earthquakes ever affect society in the same way. Charles Richter used to say that earthquakes tend to recur in the same place but are never the same events. This might be due to the fact that both earth and society are evolving complex systems. Social change outpaces and overtakes geological change. Mexico City today is a different city than it was in 1985, and Mexican society is a different society.

We submit that the objection against a nonlinear approach to disaster causation amounts to a misuse of Occam's Razor. The fact that many scientists have agreed on a linear approach for explaining the 1985 Mexico earthquake disaster should not be used as an argument to rule out a different approach, particularly when the linear approach failed to account for a crucial element in disaster causation, namely its extremely long duration. Even if the linear approach were able to explain all features of the disaster but this particular one, it would fail because no wholesale collapse of buildings would have occurred if the duration of the earthquake had been normal. Kant warned against reductionism and argued that the variety of being should not rashly be reduced.

Disasters are not ordinary events. They cannot be prevented unless we are prepared to recognize the relevance of many modes of causation. In a sense, the Mexico earthquake has a history that goes back to the foundation of Mexico City in 1325. In searching for likely Perrow chains it is sensible to keep in mind the principle of maximum entropy production.

27.7 Disasters and Society

Burton et al. (1993) have compared disaster trends in different countries and concluded that *the long-term thrust of development in nations is toward reducing the social cost of hazard to society – but in periods of rapid transition, society becomes peculiarly vulnerable to hazard*. Translation: disaster strikes mainly in developing countries.

The basic idea, due to White (1945), is that the risk R (or probable loss) is proportional to the hazard H times the vulnerability V:

$$R = H \cdot V \,, \tag{27.4}$$

where H represents the contribution of nature and V that of society. This linear concept of disasters represented a substantial advance at the time and it is still widely accepted. But it implies, against all evidence, that natural and social factors are independent. This sounds logical until we take a closer look. The years 2004 and 2005 were the worst disaster years in history. The Indian Ocean tsunami caused an estimated 270,000 deaths, yet in terms of the incidence of damaging events 2004 was rated an "average year" (Münchener Rück 2005). The worst 2004 disasters did not occur in developing countries but in industrial nations such as the United States (hurricanes Charley, Frances, Ivan and Jeanne, $68 billion) and Japan (Niigata earthquake, $30 billion, typhoons Songda, Tokage and Chaba, $18.5 billion). The Indian Ocean earthquake and tsunami disaster caused an estimated damage of $10 billion, and damage in the 1985 Mexico earthquake was rated at $4 billion.

Thus the statement that disaster hazard is inversely related to economic development needs to be qualified. In the case of the 1985 Mexico earthquake the main damage occurred in the most highly developed part of the country. Some industrial installations were damaged in the epicentral area and two people were killed in a highway accident due to loss of steering.

The 7- to 20-story reinforced concrete buildings which collapsed in Mexico City were designed by engineers trained in the U.S. after a code which followed U.S. standards (Suh 1985). Tens of thousands of homes self-built by the poor, using scavenged materials, and hundreds of age-old churches and palaces were also built on soft ground and survived the earthquake.

Casualties also followed an unexpected pattern. The poor were largely spared. Most of the victims belonged to the urban middle class. They had made the mistake of investing their modest savings in modern "earthquake-proof" apartments. Fortunately the earthquake occurred at 7:19 a.m. when most of the working population was on their way to work, before

office hours and before schools had opened. But several modern hospital buildings collapsed. Days after the earthquake, 16 newborn babies were rescued alive from the Juarez Hospital maternity ward. Many young women were killed in buildings that harboured illegal sweatshops of the garment industry. One survivor, a young girl, was rescued alive by friends but died ten years later of AIDS. She had received a blood transfusion. Thus disaster assistance can contribute to spreading epidemics.

Relatives found that they were not allowed to bury their dead as they had no proof of identity. As a result of clandestine burials, the number of victims is not even approximately known. There was no official investigation of the disaster.

Not everybody was surprised by the disaster. The chief geophysicist of a major European reinsurance corporation came to Mexico City five years ahead of the earthquake and took some notes on a walk downtown. When the earthquake struck his advance estimate of damage turned out to have been within 5% of the true amount. Experience of disasters can certainly lead to preventive action.

Social scientists are often misunderstood because they are immersed in their object of study, which happens to be society. Social science is self-referential (Habermas 1981). This awkward situation is not necessarily a drawback. After all, our ideas on the natural world seem to be changing at least as rapidly as those on society. No two disasters are alike, and it seems to be impossible to anticipate all the combinations of adverse situations that might occur. However, actively hardening the resilience of society against all kinds of mishaps is presently the only rational response to disasters.

References

Aki K., Richards PG (1980) Quantitative seismology: theory and methods. WH Freeman and Company, San Francisco, CA

Barker JS, Singh SK, Quaas R. (1997) Array analysis of wave propagation in the Lake Zone of Mexico City (abstract). Seismol Res Lett **68**: p 302

Barth EM (1985) A New Field: Empirical Logic. Bioprograms, Iogemes and Logics as Institutions. Synthese **63**: 375-388

Bunde A, Kropp J, Schellnhuber HJ (eds) (2002) The science of disasters: climate disruptions, heart attacks, and market crashes. Springer, Berlin pp 453

Burton I, Kates RW, White GF (1993) The environment as hazard. Guilford Press, New York

Campillo M, Gariel JC, Aki K, Sanchez-Sesma FJ (1989) Destructive strong ground motion in Mexico City: source, path and site effects during the great 1985 Michoacan earthquake. Bull Seism Soc Am **79**: 1718-1735

Casagrande A (1936) Characteristics of cohesionless soils affecting the stability of slopes and earth fills. J Boston Soc Civ Eng

Chavez-Garcia FJ, Bard P-Y (1994) Site effects in Mexico City eight years after the September 1985 Michoacan earthquakes. Soil Dyn Earthquake Eng **13**: 229-247

Chavez-Garcia F, Salazar L (2002) Strong motion in Central Mexico: A model based on data analysis and simple modeling. Bull Seism Soc Am **92**: 1116-1126

Daley DJ, Vere-Jones D (2003) An introduction to the theory of point processes.. Springer, Heidelberg

Davies P (1989) Glossary in the new physics. Cambridge University Press, Cambridge

Dewar RC (2003) Information theory explanation of the fluctuation theorem, maximum entropy production, and self-organized criticality in non-equilibrium stationary states. J Physics **A 36:** 631-641

Dombrowsky W, Clausen L (eds) (1984) Einführung in die Soziologie der Katastrophen Osang-Verlag Bonn

Ewing MW, Jardetzky WE, Press F (1957) Elastic waves in layered media. McGraw-Hill Book Company, New York, pp380

Green NB (1987) Earthquake-resistant building design and construction. Elsevier, Amsterdam

Habermas J (1981) Theorie des kommunikativen Handelns, vol 1, Suhrkamp, Frankfurt am Main

Hardin BO, Drnevich VP (1972) Shear modulus and damping in soils: design equations and curves. J Soil Mech Found Div, Proc Am Soc Civ Eng, SM7 98: 667-692

Infeld E, Rowlands G (2000) Nonlinear waves, solitons and chaos. 2nd ed. Cambridge University Press, Cambridge

Kennett BLN, Furumura T (2002) Propagation of seismic waves away from earthquakes. In: Matsu'ura M, Nakajima N, Mora P (eds) Proc. 2nd ACES Workshop, APEC Cooperation for Earthquake Simulation, Brisbane

Kleidon A, Lorenz RD (2005) Entropy production by earth system processes. In: Kleidon A, Lorenz RD (eds) Non-equilibrium thermodynamics and the production of entropy. Springer, Heidelberg

Lomnitz C (1994) Fundamentals of earthquake prediction. John Wiley, New York, pp 326

Lomnitz C (2005) Three theorems of earthquake location. Bull Seism Soc Am **95** (in print)

Lord Rayleigh (1877) The theory of sound in two volumes. Dover Publications, New York, vol 1, pp 480; vol 2, pp 504

Lorenz EN (1975) Climate predictability, the physical basis of climate and climate modelling. WMO Report 16, p. 132 Geneva

Lorenz RD (2005) Entropy production in the planetary context. In: Kleidon A, Lorenz RD (eds) Non-equilibrium thermodynamics and the production of entropy. Springer, Heidelberg, p 147-160

Matuzawa T (1925) On the possibility of gravitational waves in soils and allied problems. J Inst Astron Geophys **3**: 161-174

Münchener Rück (2005) Münchener Rückversicherungs-Gesellschaft. Jahresrückblick Naturkatastrophen 2004

Ottemöller L, Shapiro N, Singh SK, Pacheco J (2002) Lateral variation of Lg wave propagation in southern Mexico. J Geophys Res **107**: B1, doi: 10.1029/2001JB0002-6

Perrow C (1999) Normal accidents. Princeton University Press, Princeton

Prigogine I (1962) Introduction to non-equilibrium thermodynamics. Wiley Interscience, New York

Rosenblueth E, Ordaz M, Sánchez-Sesma FJ, Singh SK (1989) Design spectra for Mexico's Federal District. Earthq Spectra **5**: 258-272

Singh SK, Ordaz M (1993) On the origin of long coda observed in the lake-bed strong-motion records of Mexico City. Bull Seism Soc Am **83**: 1298-1306

Singh SK, Yamamoto J, Havskov J, Guzman M, Novelo D, Castro R (1980) Seismic gap of Michoacan, México. Geoph Res Let **7**: 69-72

Snow CP (1959) The two cultures and the scienctific revolution. Cambridge University Press, Cambridge

Suh NP (1985) Statement before the Senate Subcommittee for Science, Research and Technology, Congressional Record. Proceedings and Debates, 99th Congress, Washington DC, October 3, 1985

White GF (1945) Human adjustment to floods: A geographical approach to the flood problem in the United States. Research Paper 29, University of Chicago, Chicago

Yoshida N, Iai S (1998) Nonlinear site response and its evaluation and prediction. Proc. 2nd Symp. Surface Geol. Ground Motion, Yokosuka, Japan, 71-90

Zoeppritz K (1907) Über Erdbebenwellen II. Laufzeitkurven. Nachrichten der Königlichen Gesellschaft der Wissenschaften zu Göttingen, Mathematisch-physikalische Klasse 529-549

PART V

SEISMIC ROTATIONAL MOTIONS: RECORDING TECHNIQUES AND DATA ANALYSIS

28 Note on the Historical Rotation Seismographs

Graziano Ferrari

SGA Storia Geofisica Ambiente
Via del Battiferro 10b 40129 Bologna, Italy
e-mail: ferrari@sga-storiageo.it

28.1 Introduction

Various authors, even in the pre-scientific age, hypothesised the existence of rotational waves, or at least the existence of "vortical motions". As the evidence of such motions, scientists have always distinguished the rotation of pinnacles and other ornamental elements of churches and monumental buildings. That kind of rotation is cited in various direct observation reports on the effects of Italian earthquakes.

Numerous sources that document the effects of historical earthquakes describe this type of events within some complex descriptive frameworks, affected by the cultural and scientific context inside which the sources were produced. Even when the strangeness of these effects was observed and stressed, the sources do not always put forward any hypotheses as to the causes. Although specific research has not been performed on these aspects, a thorough systematic research into historical seismology for the creation of the Catalogue of Strong Earthquakes in Italy (Boschi et al. 2000) provides a large case history of occurrences of such effects. It was necessary to wait until the mid-19 century in Italy to have reports of rotational movements written with a "scientific" intention. Pedini (1742), on the occasion of the Livorno earthquake (Northern Italy) on 27 January 1742 recalls that it was as though the earth had "a vortical motion". But it was only after the Lisbon earthquakes (1 November 1755) and those of Calabria (5 February – 28 March 1783) that the scientists' attention started to be focused on the effects induced by the so-called "vortical" waves. Perhaps the most famous report as to the effects is the one relating to the rotation of two obelisks (Fig. 28.1) of the Charterhouse of Serra San Bruno in Calabria. This effect is documented in the account of Michele Sarconi (1784) about the mission of scientists guided around the places struck by

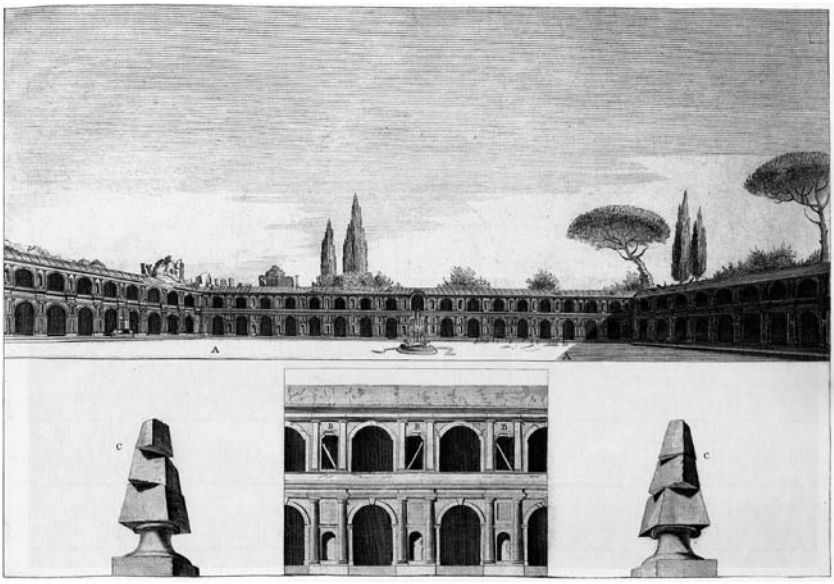

Fig. 28.1 The 1783 Calabrian earthquake. Rotation of two ornamental obelisks of the Charterhouse of Serra San Bruno in Calabria, in an etching contained in the "Atlante" by Schiantarelli and Stile (1784). This famous image was reproduced and commented on by many scholars of the earth sciences in the early 20th century, but only a few of them traced it back to the "rotational" waves caused by the earthquakes

the earthquakes in February–March 1783 and by one of the etchings on the effects on the villages and the natu-ral environment, contained in the "Atlante" (Schiantarelli and Stile 1784, etching XXI) enclosed in the report by Sarconi. In many other points of his report, Sarconi (1784) makes explicit reference to the vortex movement of the earth caused by the earthquake.

The image in Fig. 28.1 was referred to by several authors and cited as an example of vortical movements induced by earthquakes; among the first and most illustrious were Charles Lyell (1797–1875) Charles Darwin (1809–1882), Robert Mallet (1810–1881), and Alexander Von Humboldt (1769–1859).

Charles Lyell, who published a reproduction of the two rotated obelisks within a broad treatise on the Calabria earthquakes wrote in his work "Principles of Geology" (Lyell 1830): *It appears that the wave-like motions, and those which are called vorticose or whirling in a vortex, often produced effects of the most capricious kind.*

Even Charles Darwin goes back upon the issue of the vortex motions in the description of the effects of the 20 February 1835, earthquake in Concepcion (Chile): *Some square ornaments on the coping of these same walls, were moved by the earthquake into a diagonal position. A similar circumstance was observed after an earthquake at Valparaiso, Calabria, and other places, including some of the ancient Greek temples. This twisting displacement, at first appears to indicate a vorticose movement beneath each point thus affected; but this is highly improbable*. (Darwin 1845)

Robert Mallet, who was inspired by Lyell in many of his studies, contested Lyell's interpretation of the movements of the obelisks, being in agreement with the perplexities expressed by Darwin (Ferrari and McConnell 2005). Subsequently, Mallet honed an original method for the determination of the epicenter and the hypocenter of an earthquake starting from the study of the direction of the collapses, the shifting or the rotation of objects, buildings or parts of them (Mallet 1862, Ferrari and McConnell 2005) (Fig. 28.2).

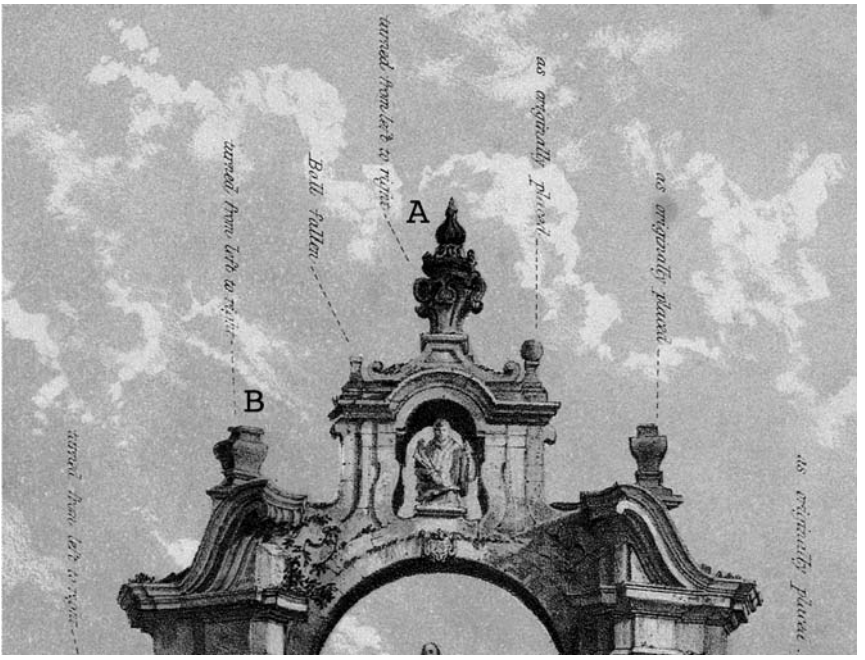

Fig. 28.2 Particular of an etching depicting the archway of San Bernardo in Padula (Salerno, Southern Italy) in which R. Mallet indicated the behaviour of the ornamental parts. In particular, note the pinnacles A and B that Mallet reports "turned from left to right"

It is in the wake of the interest and the emotions aroused by the Calabria earthquakes of 1783 that some scholars dealt with the design and the testing of seismic instruments, not the very first ones, but among the first.

At that time, however, it was still too early, to find instruments predisposed for the recording of "vortex" motions induced by earthquakes. The very first instruments of which we have reports that they have actually being made and used, are those of Jean de Hautefeuille in 1703, Nicola Cirillo in 1731 and Andrea Bina in 1751 (see Ferrari 1992). These instruments were very simple and exploited the principle of simple pendulum and the transfer of liquids from receptacles. It was necessary to wait until the mid-19 century, and in particular the mid-1870s, for the complex and pioneering phase of seismometry in which numerous scientists around the world became engaged in designing and testing of seismoscopes and seismographs, paying particular attention to the directions and components of the seismic motion. In 1875 one of these scholars, Filippo Cecchi, the director of the Ximeniano Observatory of Florence, designed the first instrument with an apparatus specially prepared to record the "vortical mo-

Fig. 28.3 The Cecchi electrical seismograph with sliding smoked paper (Cecchi 1875), after restoration

tions" as well (of the rotational waves): Cecchi's electrical seismograph with sliding smoked paper (Fig. 28.3). The instrument, described later on, still exists in two specimens: one is in Rome at the Ufficio Centrale di Ecologia Agraria and the other, is the prototype preserved at the Ximeniano Observatory in Florence. The first one was restored in 2002 by SGA and exposed at the ESC General Assembly in Genoa.

28.2 Electrical Seismograph with Sliding Smoked Paper

The electrical seismograph with sliding smoked paper was developed by P. Filippo Cecchi, the director of the Osservatorio Ximeniano of Florence, in 1875. Models of this instrument have operated at the following Observatories: Ximeniano of Florence and Seminario of Fiesole (Florence, Northern Italy), Geodinamico of the Collegio "Carlo Alberto" of Moncalieri (Turin, Northern Italy), and Meteorologico "Vincenzo Nigri" of Foggia (Southern Italy).

The equipment (Fig. 28.3) allowed for a great deal of information to be collected regarding the earthquake components movements (horizontal, vertical and "whirling"), the number of shocks, the intensity, the timing of the first two shocks, each one's duration and the interval between them.

At our present state of knowledge, only two specimens of this instrument have survived: the one of the Osservatorio Ximeniano of Florence and that of the Collegio "Carlo Alberto" at Moncalieri, kept today in the Museum of Ufficio Centrale di Ecologia Agraria (UCEA) in Rome. The former is the prototype designed by Filippo Cecchi, which has been in use at the Observatory from 1875, identical to the description Cecchi made of it in three articles (Cecchi 1875, 1876, 1877), and which was subsequently followed up with reference to Fig. 28.3. The second instrument, which operated at the Moncalieri Observatory from 1875 until the early 20 century is, however, significantly different in terms of its recording start-up system.

The part of the apparatus dedicated to the detection and the recording of the horizontal movement components is formed by two pendulums oscillating on planes N-S and E-W. Each pendulum is formed by a rectangular iron triangle, with the minor cathetus as the axis of oscillation and the opposite vertex occupied by a lenticular mass to which a circular arch (made of chromed brass) is attached, whose radius is equal to the pendulum length. At the end of the arch a silk string is attached wrapped around a pulley to which it transmits the movement of the pendulum. An arm is attached to the pulley, and in turn connected to a pen-nib that records the

movements of the pendulum on the smoked paper amplifying them threefold. The coupling pendulum-pulley recording mechanism lengthens the period of the oscillating system by about 1 second. The movements of the two pendulums are recorded on smoked glass plates or sheets of smoked paper, placed on the faces of a hollow metal square-based parallelepiped, capable of sliding vertically by means of 4 small wheels, along an internal groove. The 40 cm long parallelepiped is connected by means of an iron rectangle to a string that from the fixed pulley wraps itself round a drum, ending up with a weight.

The vertical movements are detected by the apparatus that consists of a small brass and leaden cylinder, axially driven by a barrel, only free to move vertically thanks to the presence of 4 pulleys placed in two pairs below and above the cylinder. The upper extremity of the barrel is attached to a silk thread, that is twice wrapped around a fixed pulley and is tied to a spiral spring encased by a tube and fixed to the top. The axis of pulley carries a spring with pen-nib function that lies on a smoked sheet, placed on a third face of the parallelepiped, tracing the curve of the vertical movement.

The so-called "whirling" or torsion movements are recorded on the fourth face of the parallelepiped (Fig. 28.4). These movements had been hypothesized by some authors, including F. Cecchi, to explain the rotation effects of parts of columns, pinnacles in the facades of the churches, etc. The movement recorded is that of a balance-wheel having two large leaden

Fig. 28.4 Particular of the Cecchi electrical seismograph with sliding smoked paper (Cecchi 1875) showing the recording system (on the left) and the apparatus for the surveying of the so-called "rotational" movements

lenticular masses at the extremities. This balance-wheel can move horizontally, and from one of the two lenses there extends a string that wraps a horizontal pulley placed behind the parallelepiped and terminates with a spiral spring fixed to the wall. A pen-nib protrudes from the horizontal pulley, tracing the "whirling movement" on a fourth smoked sheet.

The recording parallelepiped, stationary under conditions of stillness, starts moving in the event of an earthquake falling 20 cm in 20 seconds. The axis of drum bears a cogged wheel that moves a perpetual screw. The axis of this screw is prolonged upwards and with a protruding arm fitted with a long slit makes the conical pendulum turn, serving as a movement regulator. This pendulum hangs by means of a cardan joint *I* and carries two weights, so that its movement is not disturbed even by the strongest seismic events.

This instrument recorded the main tremor of the earthquake on 23 February 1887. The recording, published in Denza (1887), concerns the EW component (Fig. 28.5), while according to Denza himself, the recordings of the remaining 3 components (NS, Z and "whirling movements") did not present significant traces.

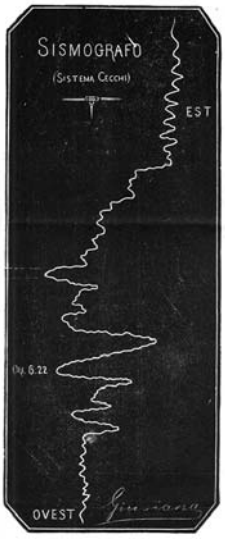

Fig. 28.5 Seismogram of the Ligurian earthquake of 23 February 1887, recorded at the Moncalieri Observatory with the UCEA's restored Cecchi electrical seismograph with sliding smoked paper. The recording, published in Denza (1887) regards the EW component, while Denza himself states that the recordings of the remaining 3 components (NS, Z and "whirling movements") did not present significant traces

28.3 Electrical Seismograph with Sliding Smoked Paper – Second Model

This instrument, of which there is only one surviving specimen at the Museum of the UCEA (Fig. 28.6), is reminiscent of the electrical seismograph with sliding smoked paper, described above.

Following the perfecting of the design, first of all the device appears more compact, more sophisticated in its recording mechanism of several shocks and endowed with greater amplification. The recording occurs on a sheet of smoked paper wrapped around a rotating drum. Unlike most of the instruments designed by Cecchi, this one does not have its published description with it. The instrument, subjected to conservative and integrative restoration, had some parts missing; that made its complete reconstruction and proper functioning all the more difficult.

The instrument is installed on a wooden column painted with a fake marble design, having a square base (30 cm sides), 250 cm in height.

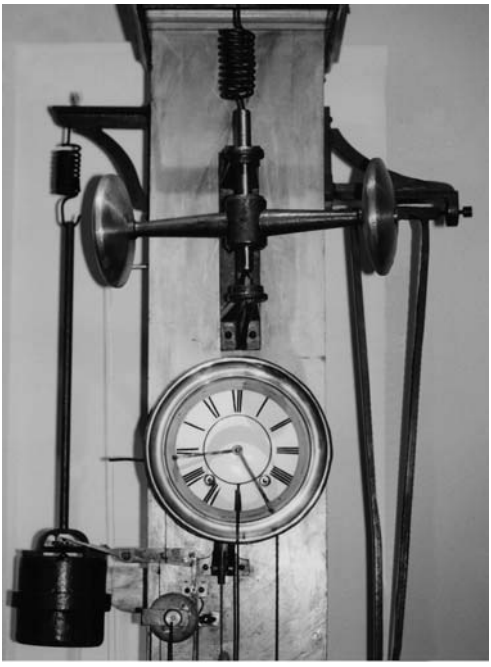

Fig. 28.6 The Cecchi electrical seismograph with sliding smoked paper – second model (1880s), particular of the detection system of the so-called "rotational" movements

Akin to the instrument from which it is derived, this seismograph is capable of recording the three components of the seismic movement and the so-called "whirling movements" (Fig. 28.6).

The part of the instrument dedicated to the detection of the horizontal movements is formed by two pendulums that are wholly identical to those of the previously described instrument, oscillating on two orthogonal planes, generally arranged N-S and E-W, one fixed to the right-hand face of the column and one to the rear side, and thus not visible. The pendulums transmit their movement to two pulleys equipped with a writing pen-nib onto a sheet of smoked paper wrapped around the recording drum, a vertical cylinder.

The vertical movements are detected by a mechanism made up of a vertical spiral spring, about 80 cm long, held tight in the lower part by a mass.

The part of the apparatus dedicated to the "whirling movements" is made up of a balance-wheel, equipped with two lenticular masses at the extremities, which have been restored in that they had gone missing. The movement of that balance-wheel is limited to the horizontal plane; by one of the two masses it horizontally expands a string that goes through a pulley and from this is directed towards a lower pulley upon which it accomplishes a rotation ending up connected to a weight which guarantees its traction. A fourth pen-nib protrudes from the latter, which akin to the others, transforms the movement of the balance-wheel into a recording on the smoked paper.

These instruments have worked for several years without ever observing in either type of instrument the functioning of the apparatus for the "rotational waves". The research hitherto performed on the seismic instruments designed and developed in Italy over the last 200 years seem to show the uniqueness of Cecchi's attempts to make instruments suited to recording or even just evidencing rotational waves.

References

Boschi E, Guidoboni E, Mariotti D, Ferrari G, Mariotti D, Valensise G, Gasperini P (2000) Catalogue of strong Italian earthquakes from 461 B.C. to 1997. Annali di Geofisica **43**: 4, 609-868

Cecchi F (1875) Sismografo elettrico a carte affumicate scorrevoli. In: Bullettino meteorologico dell' Osservatorio del R. Collegio Carlo Alberto in Moncalieri, vol X, n 9, 30 September 1875, Turin

Cecchi F (1876) Sismografo elettrico a carte affumicate scorrevoli. In: Atti della Pontificia Accademia de' Nuovi Lincei, A.XXIX (1875-76), Rome, pp 421-428

Cecchi F (1877) Sismografo elettrico a carte affumicate scorrevoli. In: L'Elettricista, I, N.1 January. Florence
Darwin C (1845) The Voyage of the Beagle, London
Denza F (1887) Alcune notizie sul terremoto del 23 febbraio 1887, Turin
Ferrari G (1992) Two Hundred Years of seismic instruments in Italy (1731-1940), Bologna
Ferrari G, McConnell A (2005) Robert Mallet and the "Great Neapolitan Earthquake" of 16th December 1857. Notes and Records Roy Soc London, January 2005, 45-64
Lyell C (1830) Principles of Geology, vol I. London
Mallet R (1862) The Great Neapolitan Earthquake of 1857. The First Principles of Observational Seismology, London; anastatic reprint. In: Guidobonie E, Ferrari G (eds) Mallet's macroseismic survey on the Neapolitan earthquake of 16th December 1857. Bologna
Pedini PR (1742) Lettera scritta al Molto Rev. Padre D.Claudio Fremond Camaldolense Pubblico Professore nell'Università di Pisa, in cui si dà ragguaglio dei Terremoti seguiti in Livorno dal dì 16 al dì 27 Gennajo 1742 con alcune osservazioni fatte, e raccolte dal Rev. Sig. Pasqual Ranieri Pedini Maestro dei Chierici dell'Insigne Collegiata di detta Città, Pisa
Sarconi M (1784) Istoria de' fenomeni del tremoto avvenuto nelle Calabrie, e nel Valdemone nell'anno 1783 posta in luce dalla Reale Accademia delle Scienze, e delle Belle Lettere di Napoli
Schiantarelli P, Stile I (1784) Atlante. Attached to the above work by Sarconi M.

29 Ring Laser Gyroscopes as Rotation Sensors for Seismic Wave Studies

K. Ulrich Schreiber[1], Geoffrey E. Stedman[2], Heiner Igel[3], Asher Flaws[3]

[1]Forschungseinrichtung Satellitengeodäsie der TU- München,
Arcisstr. 21, 80333 München, Germany
e-mail: schreiber@wettzell.ifag.de

[2]Department of Physics and Astronomy,
University of Canterbury, Private Bag 4800, New Zealand
e-mail: geoffrey.stedman@canterbury.ac.nz

[3]Department für Geo- und Umweltwissenschaften, Sektion Geophysik,
Ludwig-Maximilians-Universität München,
Theresienstr. 41, 80333 München, Germany
e-mail: heiner.igel@geophysik.uni-muenchen.de

29.1 Introduction

Although their importance was understood (Aki and Richards 2002), rotations have long been neglected in seismic studies because no suitable sensors existed. The technology for seismometers exploiting the inertia of a test mass, on the other hand, is well established and such sensors are nowadays sensitive, reliable and reasonably cheap. In general, there is a variety of different concepts for rotation sensors available, such as a pendulum, micromechanic tuning fork gyros, fiber optic gyros and ring lasers. The latter, when scaled up, have the advantage of an extremely high sensitivity.

Over the last 40 years, ring laser gyroscopes have become one of the most important instruments in the field of inertial navigation and precise rotation measurements. They have a high resolution, good stability and a wide dynamic range. Furthermore, no spinning mechanical parts are required, so these sensors can be manufactured in a very robust way. These properties made them very suitable for aircraft navigation. For more than 10 years, very large perimeter ring laser gyroscopes have been specifically developed for applications in geodesy and geophysics (Schreiber et al.

2001). By increasing the effective ring laser area by up to a factor of 24,000 over the size of an aircraft gyro, the sensitivity of these ring lasers to rotation has improved by at least 5 orders of magnitude, while the drift rate of the instruments has been reduced substantially. With several of these highly stable large ring lasers, very small periodic signals coming from polar motion, solid Earth tides and ocean loading have been successfully measured (Schreiber et al. 2003, 2004a). However, rotational signal signatures caused by remote earthquakes are stronger than these small perturbations of Earth rotation (McLeod et al. 1998, Pancha et al. 2000). The range of angular velocities to be covered is very wide: 10^{-14} rad/s $\leq \Omega_s \leq$ 1 rad/s, with the required frequency bandwidth for the seismic waves in the range of 3 mHz $\leq f_s \leq$ 10 Hz (Schreiber et al. 2004b). Currently, the large ring lasers are the only available rotation sensors which fulfil these demands. Three such devices mounted in orthogonal orientations may eventually provide the quantitative detection of rotations from shear, Love and Rayleigh waves. These properties inspired the development of a highly sensitive ring laser gyro dedicated to seismological applications. It is important to note that ring laser gyroscopes are sensitive only to rotations around their area normal vector. From that point of view, they provide additional information.

The goal of the GEOsensor project was the construction and evaluation of a field-deployable demonstrator unit, which will eventually provide access to all 6 degrees of freedom of motion. The recording of the (complete) earthquake-induced rotational motion is expected to be particularly useful for: (1) further constraining earthquake source processes when observed close to the active faults (Takeo and Ito 1997); (2) estimating permanent displacement from seismic recordings (Trifunac and Todorovska 2001); (3) estimating local (horizontal) phase velocities from collocated observations of translations and rotations (Igel et al. 2005). Because of the relatively short duration of an earthquake, such ring lasers do not need a long term stability over weeks or months, which is difficult and expensive to obtain. An instrumental stability of approximately one hour during a seismic event is sufficient. Therefore it is possible to use a steel structure attached to a solid concrete platform as the main components of the Sagnac interferometer. As indicated above, ring lasers for seismic studies require a high data rate of at least 20 Hz, because of the wide bandwidth of seismic frequencies near an earthquake source. While large ring lasers for geodetic applications are usually optimized for measuring variations in the rotation rate of the Earth in a frequency band below 1 mHz, autoregressive algorithms can be used to determine the Sagnac frequency with a resolution below the Nyquist limit. While this method can still be employed for the strongly bandwidth limited teleseismic signals (McLeod et al. 2001), an

entirely different detection scheme is needed for the data evaluation of regional or local seismic events.

29.2 Properties of Ring Lasers

Ring lasers are active Sagnac interferometers, where two monomode laser beams circulate around a triangular or square closed cavity in opposite directions (Aronowitz 1971, Stedman 1997). If the whole apparatus is placed on a platform rotating with respect to inertial space, the effective cavity length differs between the co-rotating and the anti-rotating laser beams and one obtains a frequency splitting of the two counter propagating optical waves, the magnitude of which is directly proportional to the rate of rotation. The Sagnac frequency δf is

$$\delta f = \frac{4A}{\lambda P}\,\mathbf{n}\cdot\Omega\,, \tag{29.1}$$

where A is the area, P is the perimeter enclosed by the beam path and λ is the optical wavelength of the laser oscillation. Ω is the angular velocity at which the instrument is turning and $\mathbf{n}$ is the normal vector to the laser beam plane. In order to understand the functions of such a Sagnac interferometer with respect to applications in seismology, one can distinguish three independent mechanisms contributing to the measured beat frequency δf. These are: scale factor $4A/\lambda P$, orientation $\mathbf{n}\cdot\Omega$, and rotation velocity $\Omega(t)$.

29.2.1 Scale factor

A number of helium/neon ring lasers with square resonators have been successfully constructed over the last 15 years. Basic design features common to all of them are laser cavities with an extremely high Q around 10^{12} ($Q = \omega\,\tau$, with ω the optical frequency and τ the cavity decay time) and a rf-plasma excitation scheme. All these ring lasers are operated near laser threshold, using mode competition as a natural selection criterion to ensure single longitudinal mode operation for each sense of rotation (Stedman 1997). The lock-in threshold is well below 1 Hz; therefore, all of these rings are always unlocked at the rate bias generated from the rotating Earth. From Eq. (29.1) one can see that the geometrical stability of the ring laser cavity is very important, because small variations in the scale factor impact on the Sagnac frequency. For relatively small ring lasers, which can

be manufactured from a monolithic Zerodur body such as C-II (A = 1 m^2) and G (A = 16 m^2), it is possible to fulfil this condition. However, for very large ring lasers, namely UG1 (A = 367 m^2) and UG2 (A = 832 m^2) it is impossible to keep the scale factor constant. These instruments are made from stainless steel tubes mounted on small concrete piers inside the Cashmere Cavern in Christchurch, New Zealand. Apart from distortions of the cave caused by changes in temperature and atmospheric pressure, such a ring laser is also exposed to a variable strain field induced by the gravitational forces of the moon.

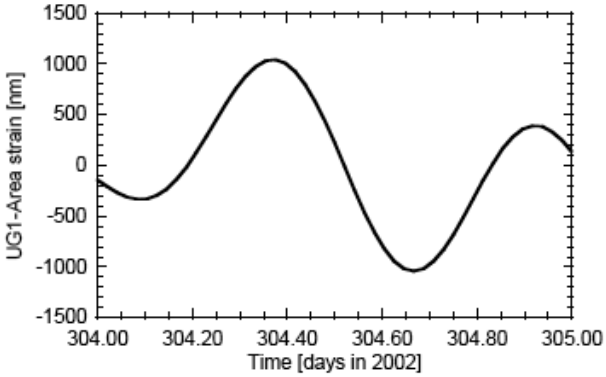

Fig. 29.1 Area strain for the UG1 ring laser location computed from global model for the day 304 in 2002. The maximum peak to peak variation of the perimeter is around 2.5 μm

Figure 29.1 shows an example for the modelled area strain acting on the UG1 ring laser. The perimeter changes by as much as 2.5 μm as a result of the deformation of the Earth crust caused by lunar attraction. However this is not the only effect. Atmospheric pressure changes also cause deformations to the Cashmere cavern. A way to analyse these variations of the ring laser perimeter is to operate the ring laser in two neighbouring longitudinal modes and the measurement of the resultant beat frequency, which corresponds to the free spectral range (FSR) of the cavity. The FSR is defined as FSR = C/P and when measured can be used to determine the perimeter (P) of the ring laser accurately. For the UG1 ring laser the FSR is 3.8969041 MHz. In order to allow a detailed study of the variation of the cavity length this rf-signal was downconverted to an audio signal of around 282 Hz with a help of a GPS-stabilized signal generator. Figure 29.2 shows the result.

Good agreement has been obtained between model and measurement. Since the atmospheric pressure constantly dropped over the time of the measurement, it was included into the analysis as a linear drift. As a result

of this investigation one can conclude that it is impossible to keep the perimeter and therefore the scale factor constant for very large rings.

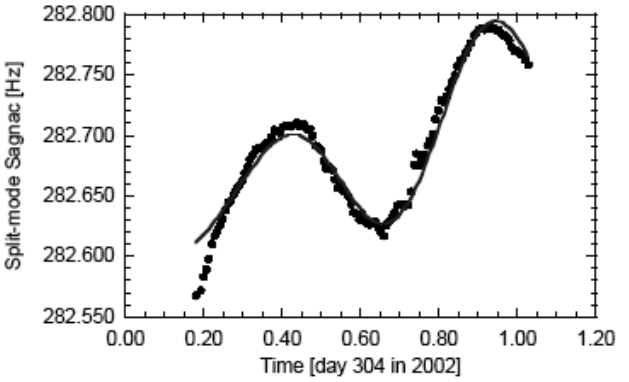

Fig. 29.2 Area strain for the UG1 ring laser location computed from a global model extended with a linear drift from atmospheric pressure changes (solid curve) superimposed on FSR measurements of the ring laser cavity (dotted curve)

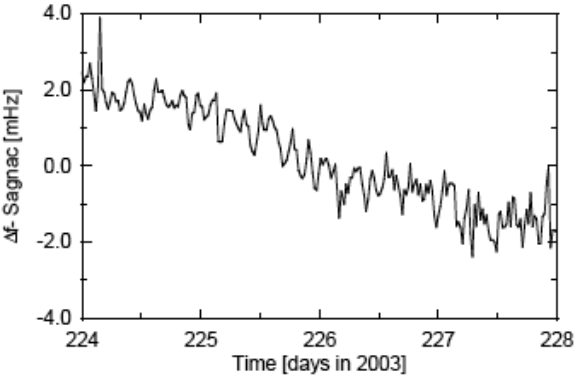

Fig. 29.3 Example of a timeseries of the Sagnac frequency variations from UG1. here is a general sensor drift apparent, but strain related scale factor changes are not present

Figure 29.3 shows an arbitrary example of a longer timeseries of Earth rotation measurements from the UG1 ring laser. One can see that there are no apparent contributions of the scale factor variations in this dataset. Since Fig. 29.3 has a measurement resolution of approx. 1 ppm (part per million) of the measurement quantity, this is surprising. According to the ring laser equation, Eq. 29.1, the scaling factor is depending on the perimeter and area. The wavelength of the laser is given by

$$\lambda = \frac{P}{I}, \tag{29.2}$$

where P is the perimeter and I the index of the longitudinal mode. For a square cavity and under the assumption that any change in area also reflects in the corresponding change of the perimeter (that is, in the absence of distortions of the ring laser), one finds that the scaling factor is independent of the wavelength and the ring laser dimensions as long as the same longitudinal index of the laser mode is maintained. The Sagnac formula then can be written as

$$\delta f = \frac{4IA}{P^2}\mathrm{n}\cdot\Omega, \tag{29.3}$$

For an exact square cavity, where one side is a, the scale factor reduces to $I/4$. Since area and perimeter changes correspond to each other in general, this means that the scale factor variations of this type do not appear in the Sagnac frequency as long as the longitudinal mode index does not change. This is usually the case. As the area changes, the perimeter and the instantaneous optical frequency inside the laser cavity will respond to compensate for the changes. This means, the large ring lasers are suitable instruments for seismic studies.

29.2.2 Ring laser orientation

Because of the inner product in Eq. 29.1, the value of the measurement quantity also depends on the projection of the rotation vector on the ring laser normal vector. Geophysical signals such as the solid Earth tides, ocean loading and diurnal polar motion become measurable via the variation of this projection (Schreiber et al. 2003, 2004a). Therefore, it is also important to look at this effect for the interpretation of seismic wave detections. Figure 29.4 gives an example of a $M = 6.8$ earthquake that occurred in Algeria on May 21 in 2003. It was recorded at the G ring laser facility of the geodetic observatory Wettzell in Southern Germany.

The upper part of the diagram shows the Sagnac frequency converted to a rotation rate as measured during the earthquake. The lower part of the diagram was obtained by taking the simultaneously recorded tiltmeter readings (referenced to local g) and converting them to a projection-induced variation of the rotation rate. In comparison, one can see that this tilt signal contributes less than 5% to the total signal. For an earthquake with a large epicentral distance, this effect is smaller, but for much closer earthquakes it may well become a dominant signal source. This again

shows how important it will be to measure all 6 degrees of freedom of motion close to an earthquake source.

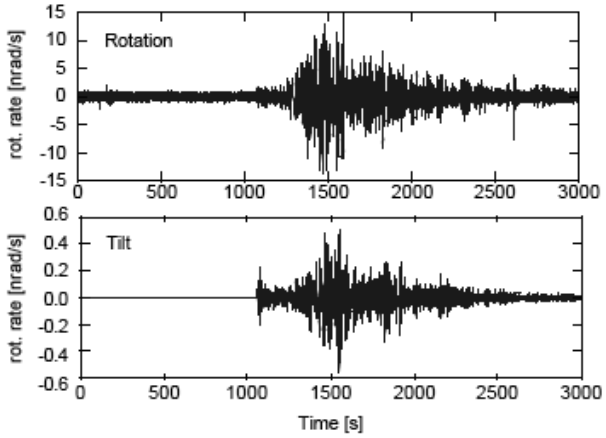

Fig. 29.4 Ring laser seismogram of an earthquake in Algeria ($M = 6.8$) of 21 May 2003, recorded by the G ring laser in Wettzell. The tilt induced contribution to the measurement quantity is as large as 5%

29.2.3 Instrumental dynamic range

Unlike seismometers, the concept of a Sagnac interferometer is not based on mass inertia. As a consequence, ring lasers have no moving mechanical parts. This has the advantage that there is no restitution process required for the extraction of the true ground motion from the transfer function of the measurement device. In order to distinguish true measured ground rotations from possible unknown sensor artefacts, two independent ring lasers were co-located and operated at the same place. The first ring laser is C-II, a monolithic solid body structure with an effective area of 1 m^2, the second ring is the heterogeneous UG1, built on many small independent concrete pedestals around the inner perimeter of the Cashmere cave. UG1 has an effective area of 467 m^2. C-II is placed inside UG1 and the area normal vectors of both ring laser planes are collinear.

According to the ring laser equation, the relationship between the obtained Sagnac frequency and the input rotation rate is linear over a wide dynamic range. The $M = 7.7$ earthquake near the Fiji Islands on 19 August 2002, was recorded on both ring lasers simultaneously. Figure 29.5 shows the first 15 seconds of this earthquake. The measured raw Sagnac frequency as a function of time was converted to rotation rate in nanoradians per second using Eq. (29.1). Apart from this conversion the data has not

been modified. The dataset from the C-II ring laser is much more noisy than the data from UG1, because there is almost a factor of 20 difference in the respective scale factors. Nevertheless one can see that both ring lasers measure exactly the same signal in phase as well as in amplitude. It has to be stressed again that apart from the unit conversion, the comparison in Fig. 29.5 uses raw data only.

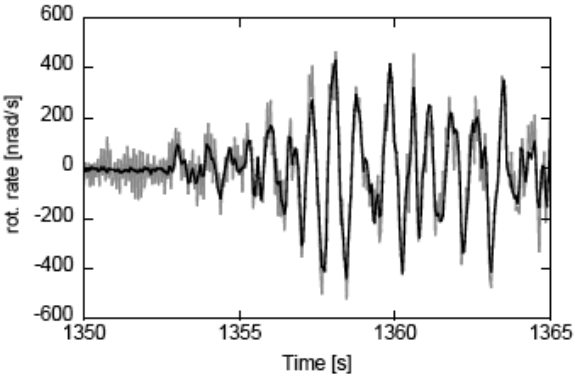

Fig. 29.5 Comparison of two ring laser seismograms from the same $M = 7.7$ earthquake near Fiji on 19 August 2002. Both ring lasers were located in the same place with identical orientation. Apart from the higher noise level of the smaller instrument the recordings are identical

29.2.4 Detection properties

Ring lasers provide optical interferograms where the external rate of rotation is proportional to the rate of change of the fringe pattern. This signal becomes available as an audio-frequency at the output of a photomultiplier tube. In seismology it is important to detect the rate of change of this frequency at 50 ms intervals (20 Hz) very accurately. Since frequency counting techniques do not provide a sufficient resolution at such short averaging intervals, a frequency demodulation concept has been developed. A voltage controlled oscillator is phase locked to the Sagnac frequency of the ring laser, exploiting the fact that Earth rotation provides a constant rate bias in the absence of any seismically induced rotation signals. In the event of an earthquake, one obtains the rate of change of the Sagnac frequency at the feedback line of the voltage controlled oscillator. This voltage can be digitized and averaged at the required 20 Hz rate or higher. Currently, the upper limit for the detectable rate of change from a large ring laser is not set by the rotation sensor itself but by the frequency extraction process.

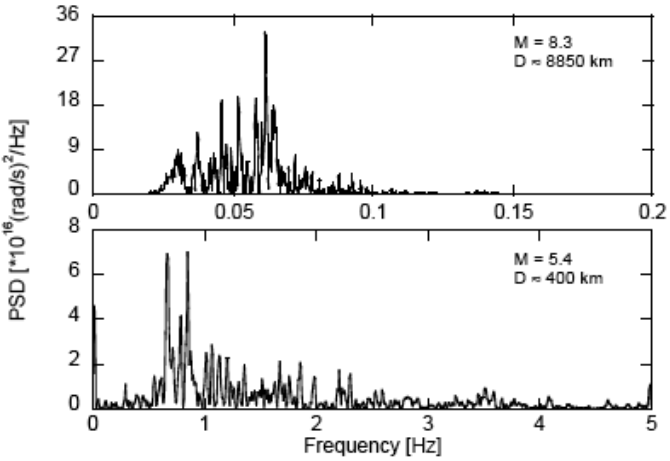

Fig. 29.6 Comparison of recorded rotation spectra from an teleseismic event (Hokkaido: 9 September 2003) and a regional earthquake (France: 22 February 2003). The much higher bandwidth of the rotational wave spectra requires alternative data acquisition techniques such as the demodulator

To outline the importance of the frequency demodulation technique two earthquakes with distinctly different properties are compared. Figure 29.6 shows an example for a teleseismic event and an example from a much closer regional earthquake. While for the remote earthquake the spectral power density essentially drops off to zero above frequencies of 0.1 Hz, one can still see some signal signature up to about 4 Hz for the regional event. Frequencies with a rate of change above 2 Hz, however, are already outside the regime of reliable representation in phase and amplitude by conventional frequency counting and second order autoregression frequency analysis (McLeod et al. 2001).

29.3 Detection of Seismic Signals

For example, the 4×4 m^2 ring laser G installed in the Geodetic Observatory Wettzell has a sensor resolution of $\delta\varphi = 9\times10^{-11}\,\mathrm{rad/s^{1/2}}$. This outstanding sensitivity is appropriate for the detection of both teleseismic waves and near source seismic signals. Typical seismic signals require a high sensor stability for up to one hour of continuous data acquisition. This requirement is much reduced as compared to the long-term stability necessity of the instrument G for the geodetic applications for which it has been built.

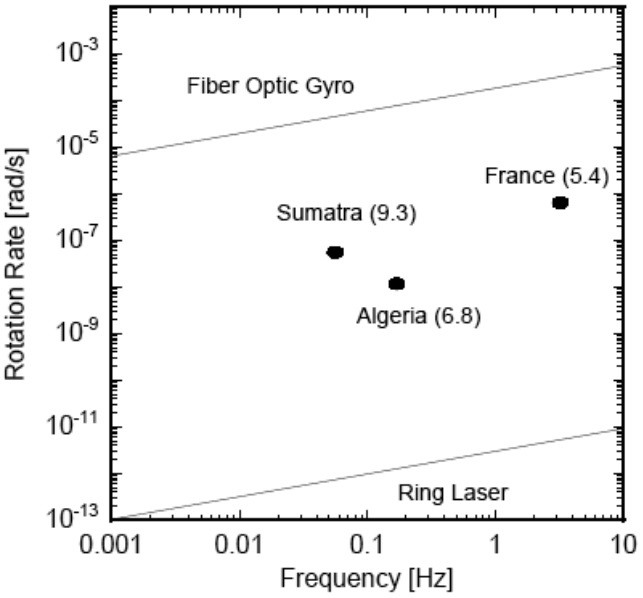

Fig. 29.7 Sensor resolution of different rotation sensor concepts in relation to the observed signal strength of some earthquakes at different epicentral distances

Figure 29.7 illustrates some basic characteristics for the detection of rotations from seismic signals. The diagram shows most of the measurement range of interest for seismic studies. The relevant frequency window is plotted horizontally, while the magnitude of the respective rotation rates is displayed on the vertical. In order to keep this diagram simple the strong motion region is not shown. In the lower part of the plot one can see a line which indicates the resolution limit for current ring lasers. Depending on the actual scale factor, the sensitivity differs from one ring laser to another. However, within the *y*-scale of this chart this line gives a good representation for the existing large ring lasers in general. The current high quality fiber optic gyros (FOG) exhibit a sensor resolution $\delta\varphi = 0.1°/\mathrm{h}^{1/2}$ or slightly less. The upper line was derived from test measurements of a sample FOG type instrument: μFORS-1 manufactured by LITEF in Germany. Both lines are sloping over the frequency range of interest. This reflects the improvement resulting from longer integration as the frequency of interest reduces. To give an idea of the real sensor requirement, three very different examples of earthquakes are indicated on the graph. The details of these earthquakes are given in Table 29.1. Since the Earth crust acts as a lowpass filter one can see that the earthquakes at the right side of the Fig. 29.7 plot are the closest.

Table 29.1 Details of some earthquakes recorded in Germany

Source	Magnitude	Distance [km]
Sumatra	9.3	> 10000
Algeria	6.8	1550
France	5.4	400

All events listed here produced datasets with good signal to noise ratio on the G ring laser. Figure 29.8 shows a raw dataset as an example.

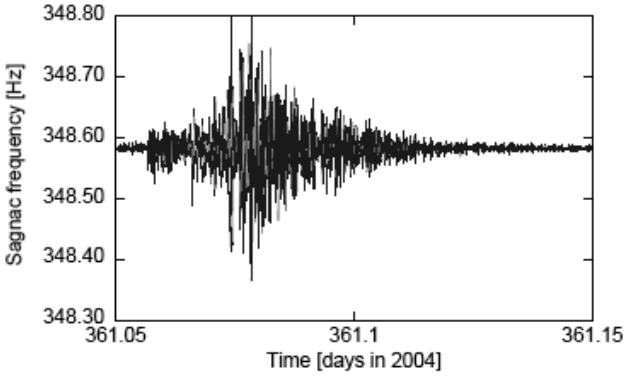

Fig. 29.8 The raw rotation measurement of the $M = 9.3$ Sumatra earthquake from 26 December 2004. The dataset was recorded with a good signal to noise ratio

None of these events would have been within the sensor resolution of FOG. As clearly seen in Fig. 29.7, the application of FOGs for seismic studies is currently possible only for strong motion applications.

29.4 GEOsensor

Based on the discussion of the previous sections one can formulate a concept for a sensitive seismic rotation sensor. In order to obtain a stable interferogram of the two laser beams, the cavity length has to be kept constant to within a fraction of a wavelength. Therefore, usually ring laser bodies are made from Zerodur, a glass ceramic which exhibits a very small relative thermal expansion of $\alpha = 5 \times 10^{-8}$ per K. Since a ring laser for seismic applications requires an enclosed area of more than 1 m^2, a monolithic ring construction would be both too expensive and not transportable.

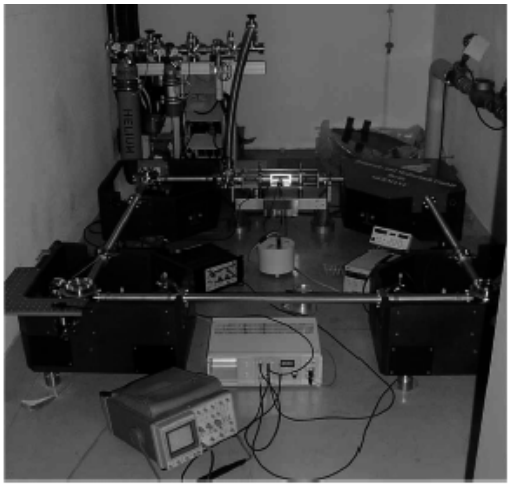

Fig. 29.9 Photo of the GEOsensor ring laser during sensor integration

Figure 9 shows the actual ring laser hardware. The laser cavity has the shape of a square. The four adjustable mirrors are each located in a solid corner box for maximum mechanical stability. The adjustable mirrors are located inside steel containers which in turn are connected together with stainless steel tubes, forming an evacuated enclosure for the laser beams. In the middle of the far side the steel tubes are reduced to a small glass capillary of 4 mm in diameter and a length of 10 cm, which is required for gain medium excitation. When operated, the ring laser cavity is first evacuated and then filled with a mixture of helium and neon reaching a total gas pressure of approximately 6 hPa. In the background of Fig. 29.9 the vacuum pump and filling station can be seen. Other subsystems like the seismometer, the rf-transmitter and the beampower stabilizer are placed inside the ring laser boundary. The following two important considerations are unique for the GEOsensor design:

- Since the ring laser is constructed from several components, it requires a stable concrete platform base at the location of deployment. Such a pad is simple to specify and can be prepared totally independently of the actual GEOsensor deployment.
- The actual area of the ring laser component is not predetermined by the design. The instrument can be built according to the available space at the host observatory. Different GEOsensor realizations may therefore have different size and consequently different instrumental resolution. The length of the current instrument is 1.6 m on a side, which provides an area of 2.56 m^2.

In order to operate the GEOsensor, the cavity must be evacuated, baked and filled with a He/Ne gas mixture. This procedure requires a turbo molecular pump system and a manifold with a supply of ^{4}He, ^{20}Ne and ^{22}Ne. The pump system is not required during the operation of the GEOsensor, but is necessary for the preparation of the instrument and once or twice a year in order to change the laser gas. Laser excitation itself is achieved via a high frequency generator, matched to a symmetrical high impedance antenna at the gain tube. A feedback loop maintains the level of intensity inside the ring laser and ensures monomode operation. When the ring laser is operated it detects the beat note caused by Earth rotation as a rate bias. The magnitude of this beat frequency depends on $\sin\Phi$, with Φ the latitude of the ring laser location. Table 29.2 shows the value of the Earth's rate bias for a few locations of interest, for the GEOsensor with 1.6 m arms.

Table 29.2 Earth rotation bias for some GEOsensor locations

Location	Frequency [Hz]
Wettzell, Germany (49.145 N)	138
Pinon Flat, CA (33.6 N)	102
Tokyo, Japan (35.4 N)	106
Cashmere, NZ (43.57 S)	127

To date, the GEOsensor has been operated at the first two locations. Since the Earth rotation acts like a rate bias on our ring laser measurements, any rotations caused by earthquakes will show up as a frequency modulation around the measured Earth rate.

Acknowledgement. The combined ring laser results were possible because of a collaboration of Forschungseinrichtung Satellitengeodäsie, Technische Universität München, Germany, University of Canterbury, Christchurch, New Zealand and Bundesamt für Kartographie und Geodäsie, Frankfurt, Germany. The GEOsensor was funded under the programme GEOTECHNOLOGIEN of BMBF and DFG, Grant 03F0325 A-D. The authors would also like to acknowledge the IQN Program by the German Academic Exchange Service and the Leibniz Computing Centre Munich for providing access to their supercomputers. University of Canterbury research grants, contracts of the Marsden Fund of the Royal Society of New Zealand and also grants from the Deutsche Forschungsgemeinschaft (DFG) are gratefully acknowledged.

References

Aronowitz F (1971) The laser gyro. In: Ross M (ed) Laser applications, vol 1. Academic Press, New York, pp 133-200

Aki K, Richards PG (2002) Quantitative Seismology, 2nd ed. University Science Books, Sausalito, CA

Igel H, Schreiber KU, Flaws A, Schuberth B, Velikoseltsev A, Cochard A (2005) Rotational motions induced by the M8.1 Tokachi-oki earthquake, September 25, 2003. Geophys Res Lett **32:** L08309, doi:10.1029/2004GL022336

McLeod DP, Stedman GE, Webb TH, Schreiber KU (1998) Comparison of standard and ring laser rotational seismograms. Bull Seism Soc Amer **88**: 1495-1503

McLeod DP, King BT, Stedman GE, Schreiber KU, Webb TH (2001) Autoregressive analysis for the detection of earthquakes with a ring laser gyroscope. Fluctuations and Noise Letters **1**: 1, R41-R50

Pancha A, Webb TH, Stedman GE, McLeod DP, Schreiber U (2000) Ring laser detection of rotations from teleseismic waves. Geophys Res Lett **27**: 3553-3556

Schreiber U, Schneider M, Rowe CH, Stedman, GE, Schlüter W (2001) Aspects of ring lasers as local earth rotation sensors. Surveys in Geophysics **22**: 5-6, 603-611

Schreiber KU, Stedman GE Klügel T (2003) Earth tide and tilt detection by a ring laser gyroscope. J Geophys Res **108**: B2, 10.1029/2001JB000569

Schreiber KU, Velikoseltsev A, Rothacher M, Klügel T, Stedman GE, Wiltshire DL (2004a) Direct measurement of diurnal polar motion by ring laser gyroscopes. J Geophys Res **109**: B6, 10.1029/2003JB002803, B06405

Schreiber U, Velikoseltsev A, Stedman GE, Hurst RB, Klügel T (2004b) Large ring laser gyros as high resolution sensors for applications in geoscience. Proc. 11th Intern Conf on Integrated Navigation Systems, St. Petersburg, 326-331

Stedman GE (1997) Ring laser tests of fundamental physics and geophysics. Rep Progr Phys **60**: 615-688

Takeo M, Ito HM (1997) What can be learned from rotational motions excited by earthquakes? Geophys J Int **129**:319–329

Trifunac MD, Todorovska MI (2001) A note on the usable dynamic range of accelerographs recording translation. Soil Dyn Earth Eng **21**: 275-286

30 Rotational Motions in Seismology: Theory, Observation, Simulation

Alain Cochard[1], H. Igel[1], B. Schuberth[1], W. Suryanto[1], A. Velikoseltsev[2], U. Schreiber[2], J. Wassermann[1], F. Scherbaum[3], D. Vollmer[3]

[1]Department of Earth and Environmental Sciences
Ludwig-Maximilians-Universität
Theresienstr. 41, 80333 München, Germany
e-mail: alain@geophysik.uni-muenchen.de

[2]Forschungseinrichtung Satellitengeodäsie
Technical University of Munich, Fundamentalstation Wettzell
Sackenriederstr. 25, D-93444 Kötzting, Germany

[3]Institut für Geowissenschaften, Universität Potsdam
Karl-Liebknecht-Str. 24/25, 14476 Golm, Germany

30.1 Introduction

The rotational part of earthquake-induced ground motion has basically been ignored in the past decades, compared to the substantial research in observing, processing and inverting translational ground motions, even though there are theoretical considerations that suggest that the observation of such motions may indeed be useful and provide additional information. In the past years, interest in this potentially new observable for seismology has risen, primarily because – with modern acquisition technology such as fiber-optical or ring laser gyros – rotational motions have actually been observed, the resolution is steadily increasing, and the observations are becoming consistent with collocated recordings of translational ground motions. Even though the real benefit to Earth sciences is still under investigation, recent results suggest that collocated measurements of rotations and translations may allow the estimation of wavefield properties (such as phase velocities, direction of propagation) that otherwise can only be determined through array measurements or additional strain observations. In this paper we focus on studies of the vertical rotational component (twist, spin, or rotation around a vertical axis) and review recent results on the

fundamental concepts that are necessary to understand the current broadband observations of a wide distance and magnitude range, and show that the classical theory of linear elasticity is sufficient to explain these observations. In addition to direct measurements of rotational motions using ring laser technology, we describe the method to derive rotational motions from seismic arrays and present some initial results. Sophisticated 3D modelling of the rotational ground motions of teleseismic events illustrate the accuracy with which observed horizontal phase velocities match with theoretical predictions, even though the precise waveforms are quite different due to inaccuracies in crustal models or kinematic rupture properties. This may have implications for sparse networks or situations where extremely few or even single-station observations are taken (e.g., in remote areas or planetary seismology).

To fully characterize the motion of a deformable body at a given point in the context of infinitesimal deformation, one needs three components of translation, six components of strain, and three components of rotation, a vectorial quantity. Rotational motions induced by seismic waves have been essentially ignored for a long time, first because rotational effects were thought to be small (Bouchon and Aki 1982), and second because sensitive measuring devices were not available. Indeed, Aki and Richards (1980, p. 489) point out that *the state-of-the-art sensitivity of the general rotation sensor is not yet enough for a useful geophysical application*.

However, there have been many reports of rotational effects associated with earthquakes (like twisting of tombstones, or statues). It is certainly possible that some of these effects are due to the asymmetry of the construction. Indeed, as is well known, when the center of mass is not located at the geometric center, a mere translation may induce a local rotation of that structure. However, some field evidences suggest that it is at least not always the case (Galitzin 1914, p. 172). The rotational angles calculated by Bouchon and Aki (1982) for realistic cases of earthquake scenarios (about 10^{-4} radians) seem indeed too small to be responsible for damages, except, maybe for the case of long structures. However, as, roughly speaking, rotations are proportional to displacement divided by the phase velocity (see Section 30.2.3), when the wave velocity becomes smaller, rotations become comparatively larger. This happens in soft or unconsolidated sedimentary and/or fluid-infiltrated porous media, where wave speeds might be as low as about 50 m/s, hence smaller than usual by about a factor of 50. Thus, it is not implausible that, near seismic sources – where rotations and strains become relatively large even in normal media – rotations and strains become really large and be responsible for the above mentioned damages (there is also growing seismological evidence that rotational amplitudes have been underestimated (Castellani and Zembaty 1996)). Obvi-

ously, in such a situation, the assumption of infinitesimal deformation would then fail and the theory of finite deformations would be necessary.

As an attempt to measure rotational motions with high sensitivity, in the past years ring laser gyroscopes were developed, primarily to observe variations in Earth's absolute rotation rate with high precision (Stedman et al. 1995, Stedman 1997). One of these instruments – located near Christchurch, New Zealand – recorded seismically induced signals of ground rotation rate for several large earthquakes (McLeod et al. 1998, Pancha et al. 2000). These observations gave evidence that the optical sensors indeed provide sufficient accuracy to record seismic rotations. However, they were not fully consistent in phase and amplitude with translational motions recorded with collocated seismometers, the limited consistency being obtained only in a narrow frequency band. Earlier attempts to observe ground rotations with other devices (e.g., solid state rotational velocity sensors, fiber-optical gyros) were limited to large signals close to artificial or earthquake sources (Nigbor 1994, Takeo 1998) and did not lead so far to an instrument of general interest. This explains why Aki and Richards (2002, p. 608) note that *as of this writing seismology still awaits a suitable instrument for making such measurements*. However, the subsequent development of ring laser technology indicates that a significant part of the gap has recently been filled, as demonstrated by Schreiber et al. (2003b) and Igel et al. (2005b) and exemplified later in this paper. Rotations can also be determined with array measurements, but with important limitations; see Section 30.3.1 and Suryanto et al. (2005).

The recording of even small, non potentially damaging, rotational motions is expected to be very useful. First, translation recordings are polluted by rotations. There is a purely geometrical effect (the reference axis of the seismometer is rotated), introducing a cosine factor, hence negligible for very small deformations, but which could become significant in case of very strong ground motion. More importantly, there is also an inertial contribution. It is well known that surface tilt (horizontal rotation – see Section 30.2.2) induces a translational signal (Aki and Richards 2002, p. 604). A similar effect exists for vertical rotation (Trifunac and Todorovska 2001). Measuring the three components of rotation allows in principle to correct for these effects. Second, as the measure of rotation provides additional information, it helps constraining physical models. For example, the measure of vertical rotation and horizontal acceleration allows the estimation of the local Love wave phase velocity and of its propagation direction (see Section 30.2.3 and Igel et al. 2005a). It is also expected (Takeo and Ito 1997) that the measure of rotations will allow to better constrain earthquake rupture histories.

The above discussion has been deliberately restricted to classical elasticity, for which the stress and strain tensors are symmetric. In some extreme cases (e.g., large stress gradient) near crack tips or in granular materials, the material can no longer be treated as a continuum. A continuous formalism may still be used for an effective medium in which additional – intrinsic – rotations (i.e., not related to displacement) may exist. In such Cosserat/micropolar media, the stress and strain tensors are no longer symmetric. See, e.g., Dyszlewicz 2004, Nowacki 1986, Maugin 1998, Lakes 1995, Teisseyre and Majewski 2001, Teisseyre et al. 2003, and other papers in this monograph. In the following of this chapter we remain in the framework of classical elasticity.

30.2 Fundamental Theory

In the framework of classical elasticity, and further assuming infinitesimal deformations, displacement of a point $\mathbf{x}$ is related to that of a neighbouring point $\mathbf{x}+\delta\mathbf{x}$ by (e.g., Aki and Richards 2002, p. 13)

$$\begin{aligned}\mathbf{u}(\mathbf{x}+\delta\mathbf{x}) &= \mathbf{u}(\mathbf{x}) + \mathbf{G}\,\delta\mathbf{x} \\ &= \mathbf{u}(\mathbf{x}) + \boldsymbol{\varepsilon}\,\delta\mathbf{x} + \boldsymbol{\Omega}\,\delta\mathbf{x} \\ &= \mathbf{u}(\mathbf{x}) + \boldsymbol{\varepsilon}\,\delta\mathbf{x} + \boldsymbol{\omega}\times\delta\mathbf{x}\,,\end{aligned} \tag{30.1}$$

where $\mathbf{G}$, $\boldsymbol{\varepsilon}$, $\boldsymbol{\Omega}$ are the gradient, strain, and rotation second order tensors, respectively, and

$$\boldsymbol{\omega} = \frac{1}{2}\nabla\times\mathbf{u}(\mathbf{x}) \tag{30.2}$$

is a (pseudo-) vector which does not enter Hooke's law and represents the angle of rigid rotation generated by the disturbance. This illustrates that one needs three components of translation, six components of strain and three components of rotation to fully characterize the change in the medium around point $\mathbf{x}$.

30.2.1 Rotations and strain due to a double couple point source

Aki and Richards (2002, Fig. 4.4 and Eqs. 4.32 and 4.33) give the expression for the displacement $\mathbf{u}(\mathbf{x})$ generated by a point source shear dislocation (double couple) in an infinite, homogeneous, isotropic medium. The dislocation is in the *xy* plane with slip along *x* (Fig. 30.1).

Following the same notations, we can then determine the rotation as

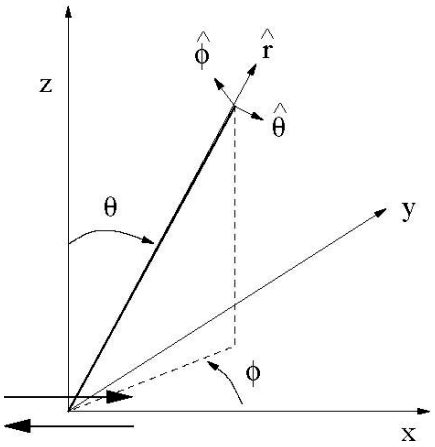

Fig. 30.1 Geometry and notations for the double couple expressions

$$\begin{aligned}\boldsymbol{\omega}(\mathbf{x},t) &= \frac{1}{2}\nabla\times\mathbf{u}(\mathbf{x},t)\\ &= \frac{-\mathbf{A}^R}{8\pi\rho}\left[\frac{3}{\beta^2 r^3}M_0\left(t-\frac{r}{\beta}\right)+\frac{3}{\beta^3 r^2}\dot{M}_0\left(t-\frac{r}{\beta}\right)+\frac{1}{\beta^4 r}\ddot{M}_0\left(t-\frac{r}{\beta}\right)\right],\end{aligned} \tag{30.3}$$

where

$$\mathbf{A}^R = \cos\theta\sin\phi\,\hat{\boldsymbol{\theta}} + \cos\phi\cos 2\theta\,\hat{\boldsymbol{\phi}} \tag{30.4}$$

is the radiation pattern of the three components of rotation (the radial component being zero). Likewise, the divergence (or trace of the strain tensor, representing volumetric change) is given by

$$\nabla\cdot\mathbf{u}(\mathbf{x}) = \frac{-A^D}{4\pi\rho}\left[\frac{3}{\alpha^2 r^3}M_0\left(t-\frac{r}{\alpha}\right)+\frac{3}{\alpha^3 r^2}\dot{M}_0\left(t-\frac{r}{\alpha}\right)+\frac{1}{\alpha^4 r}\ddot{M}_0\left(t-\frac{r}{\alpha}\right)\right], \tag{30.5}$$

where

$$A^D = \cos\phi\,\sin 2\theta \tag{30.6}$$

is the radiation pattern of the divergence.

Figure 30.2 shows displacement, velocity, divergence and rotation, and divergence and rotation rates, as a function of time at a given point (see caption for details).

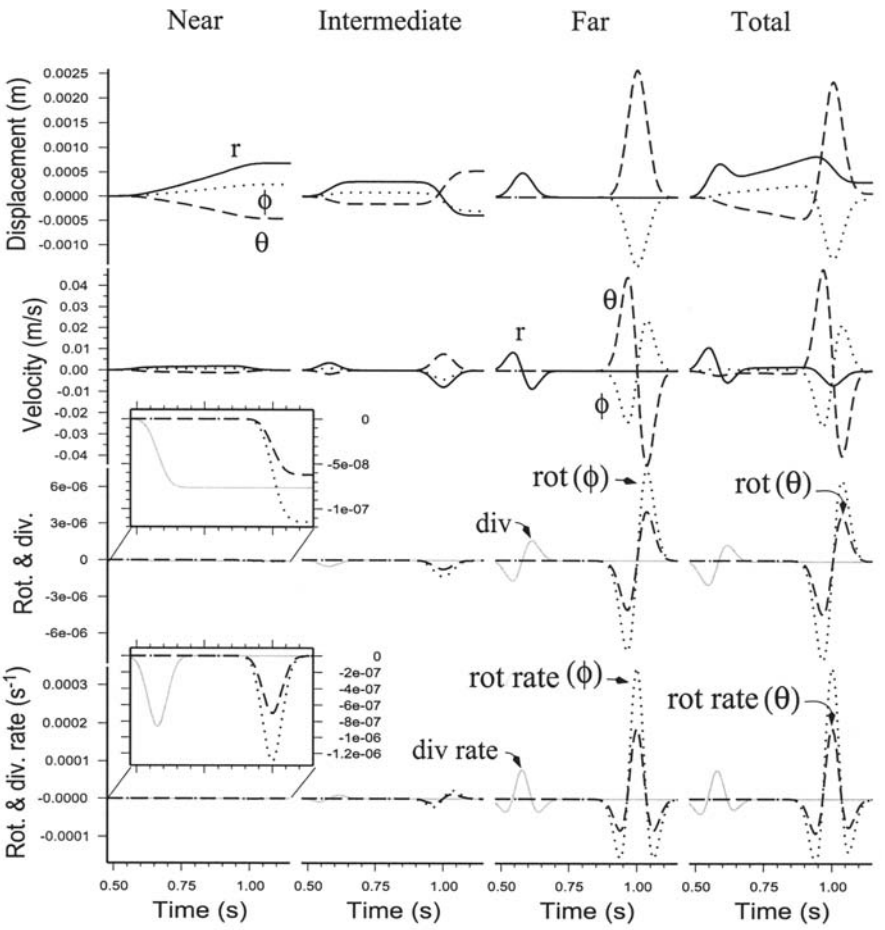

Fig. 30.2 From top to bottom: Displacement, velocity, divergence and rotation, divergence and rotation rates, as a function of time at a given point due to a double couple in an infinite, homogeneous, isotropic medium. The dislocation is in the *xy* plane with slip along *x*, as in Aki and Richards (2002, Fig. 4.4) and in Fig. 30.1. The observation point is defined as $(r, \theta, \phi) = (3 \text{ km}, \pi/8, \pi/8)$ in spherical coordinates. The moment is 10^{15} N·m ($M \approx 4$) and the source time function rate is a Gaussian of the form $\exp(-(t/T)^2)$ with $T = 0.05$ s. The density of the medium is $\rho = 2800$ kg/m^3, the *S* and *P* wave velocities are $\beta = 3$ km/s and $\alpha = \sqrt{3}\beta$. Concerning displacement and velocity, the usual terminology is used for the near, intermediate, and far fields, but not concerning divergence and rotation (and their rates) (see text). The radial components (along $\hat{\mathbf{r}}$) are plotted black, the $\hat{\boldsymbol{\theta}}$ components, dashed, and the $\hat{\boldsymbol{\phi}}$ components, dotted; the divergence and divergence rate evolutions are plotted gray

Since the gradient tensor is merely split into symmetric and antisymmetric tensors, we intuitively derive from Eq. (30.1) and see from the figure, that rotations and strains are of the same order of magnitude.

Not surprisingly, rotations are zero at the *P* wave front, and only start at the *S* wave arrival (and have no radial component), even in the displacement near field region (this is also true for, e.g., single forces or single couples). This could however appear strange at first sight, as, e.g., the rotation associated with the far field *P* term is not zero. This is obvious when looking at its radiation pattern (Fig. 4.5a of Aki and Richards 2002) and is in fact given by $-\mathbf{A}^R \dot{M}_0(t-r/\alpha)/(4\pi\rho\alpha^3 r^2)$. It turns out that this contribution cancels out with part of the curl of the intermediate field at the *P* front, the other part canceling in turn with the near field contribution. (Nevertheless, rotations may not be obtained by taking the curl of only the transverse displacement terms in Eq. 4.32 of Aki and Richards 2002.) Analogous comments may be made for strains, which are active around the *P* front only. Therefore, the usual classification for displacement in near, intermediate, and far field terms cannot be applied to rotations and strains. As rotations and strains comprise terms proportional to $1/r$, $1/r^2$, $1/r^3$, it is convenient to refer to them as far, intermediate, and near field terms, respectively, which has been done in Fig. 30.2. However, this could be misleading, since, if the far and intermediate displacement fields also decrease as $1/r$ and $1/r^2$, respectively, the near field displacement term, proportional to $(1/r^4)\int_{r/\alpha}^{r/\beta} \tau M_0(t-\tau)\,\mathrm{d}\tau$ essentially decreases as $1/r^2$, not $1/r^3$.

We conclude the section by noting that the rotation radiation pattern $\mathbf{A}^R$ can be calculated from the transverse (or *S*) far field radiation pattern $\mathbf{A}^{FS} = \cos 2\theta \cos\phi\,\hat{\boldsymbol{\theta}} - \cos\theta \sin\phi\,\hat{\boldsymbol{\phi}}$ (Eq. 4.33 of Aki and Richards 2002, p. 78) as $\nabla \times \mathbf{A}^{FS} = \mathbf{A}^R/r$; thus, $\mathbf{A}^{FS}$ and $\mathbf{A}^R$ are orthogonal. Similarly, A^D is related to the radial (or *P*) far field radiation pattern $\mathbf{A}^{FP} = A^D\mathbf{r}$.

30.2.2 Effect of free surface — rotation and tilt

Assuming the surface corresponds to the *xy* plane, the zero traction boundary condition at the free surface implies that $\sigma_{i3} = 0$ ($i = x, y, z$). Direct application of Hooke's law $\sigma_{ij} = \lambda\varepsilon_{kk}\delta_{ij} + 2\mu\varepsilon_{ij}$ in a homogeneous, isotropic medium leads to

$$\frac{\partial u_x}{\partial z} = -\frac{\partial u_z}{\partial x}\ , \qquad \frac{\partial u_y}{\partial z} = -\frac{\partial u_z}{\partial y}\ , \qquad \frac{\partial u_x}{\partial z} = \frac{\lambda}{\lambda + 2\mu}\left(\frac{\partial u_x}{\partial x} + \frac{\partial u_y}{\partial y}\right). \tag{30.7}$$

It then directly follows (Eq. 30.2) that

$$\omega_x = \frac{\partial u_z}{\partial y} \quad , \quad \omega_y = -\frac{\partial u_z}{\partial x} \quad , \tag{30.8}$$

hence that at the Earth's surface, horizontal rotation corresponds to tilt.

As a consequence, *P* waves generate horizontal rotation at the surface whereas they are irrotational in the bulk. There is an additional contribution to horizontal rotation due to *P*-to-*SV* converted waves at the surface (also due to the free surface boundary condition). It is still an open question what technology is best for the various components of rotation. For the vertical component, the results presented here and in other studies suggest that the optical devices are the way to go. Those optical devices could be advantageous compared to classical tiltmeters for the horizontal components as well (regardless of metrological characteristics – accuracy, sensitivity, etc. – which remain to be assessed): indeed, classical tiltmeters measure a change of angle with respect to the local vertical, determined by gravity; thus, they cannot discriminate between true rotation and a pure change in the local gravity (e.g., due to mass redistribution).

30.2.3 Comparison of rotation and translations

Obviously, if we know, or assume we know, the full expression for displacement **u**, we can determine rotation **ω** from the measurement of **u** (Eq. 30.2) by differentiating. If we do not fully know **u**, the measurement of **ω** brings in additional information.

First, consider the case of a transversely polarized plane wave with displacement $\mathbf{u}(x, y, z, t) = (0, u_y(t - x/c), 0)$ propagating in the x direction, with c being the horizontal phase velocity. Rotation is thus given as $\boldsymbol{\omega}(x,y,z,t) = (1/2)\nabla \times \mathbf{u}(x,y,z,t) = (0,0,-\dot{u}_y(t - x/c)/(2c))$. Thus we have

$$\omega_z(x,y,z,t) = -\frac{\dot{u}_y(x,y,z,t)}{2c} \quad . \tag{30.9}$$

Surface waves are composed of both Love waves, with horizontal transverse polarization, and Rayleigh waves, with displacement in a vertical plane assuming elastic isotropy. So Rayleigh waves do not generate a vertical component of rotation. Thus, for a given earthquake for which the distance to the station is large enough compared with the source dimension and the wavelength of interest so that the plane wave assumption is valid, from the measurement of rotation and displacement of a surface wave train one can in principle infer both the phase velocity and the direction of the

incoming wave train. In practice, we have so far dealt only with earthquakes of known location, and have assumed that the surface trains were traveling along the great circle, thus providing the direction (Igel et al. 2005b, and Section 30.4 below). There are now observations of ground rotations of several dozens of earthquakes with a wide magnitude and epicentral distance range. The accuracy of the phase velocity estimates is currently under investigation by comparison with complete wave simulations (see below), and array-derived phase velocities (Suryanto et al. 2005) as well as theoretical predictions of Love-wave dispersion for local Earth models.

30.3 Rotational Measurements

Rotational ground motions can be observed by (1) finite-differencing of seismic array data or (2) directly (ring laser, fiber-optical or mechanical gyros). In this section we briefly review both approaches and give relevant references.

30.3.1 Array derived rotations

One way of estimating the components of the deformation gradient **G**, hence of computing strains and rotations, is through array measurements (e.g., Spudich et al. 1995, Bodin et al. 1997, Huang 2003). Using the first of Eqs. (30.1) with a non infinitesimal quantity **R** as the position vector between two points in place of $\delta\mathbf{x}$, we get $\mathbf{d} = \mathbf{u}(\mathbf{x}+\mathbf{R}) - \mathbf{u}(\mathbf{x}) = \mathbf{G}^{FD}\mathbf{R}$ where $\mathbf{G}^{FD}$ is a first order approximation of **G**, i.e., exact if **u** varies linearly between **x** and **x** + **R**. Using three non aligned points, one gets two such vectorial equations (six equations in Cartesian coordinates) with a common point, relating, say, $\mathbf{d}_1$ and $\mathbf{d}_2$ to $\mathbf{R}_1$ and $\mathbf{R}_2$, and one can then solve for the six approximations of the partial derivatives in the plane defined by the three points. Specifically, if we measure the ground displacement at three stations on the surface, whose relative positions are known, we can determine (without using the free surface boundary condition) estimations of $\partial u_x/\partial x$, $\partial u_x/\partial y$, $\partial u_y/\partial x$, $\partial u_y/\partial y$, $\partial u_z/\partial x$, $\partial u_z/\partial y$. This is what is commonly used in finite element methods to calculate the spatial derivatives in triangular cells (e.g., Cook 1974); for example, one gets $\partial u_x/\partial y = (d_{2x}R_{1x} - d_{1x}R_{2x})/(2S)$, where S is the surface of the triangle.

In particular, we can determine an estimation of the vertical component of rotation

$$\omega_z = \frac{1}{2}\left(\frac{\partial u_x}{\partial y} - \frac{\partial u_y}{\partial x} \right) . \tag{30.10}$$

When more than three stations are used, the equations $\mathbf{d}_i = \mathbf{G}^{FD}\mathbf{R}_i$ (where $i+1$ is the number of stations) can be solved by using a least square procedure (e.g., Spudich et al. 1995). This is how we proceed in Sect. 30.4.2.

Note that the rotation-induced translational signals, as explained in the introduction, affect the array-derived rotation calculations as described just above. It should be possible to devise an iterative procedure to correct for this effect, but this has not been attempted in this paper.

Using the free surface boundary condition, one can also estimate the horizontal components of rotation, and, if further assuming the quantity $\lambda/(\lambda+2\mu)$ known, $\partial u_z/\partial z$ (cf. Sect. 30.2.2). Note that ω_z cannot be determined by means of tiltmeters or strainmeters. Array-derived rotations are subjected to an important limitation. The instruments should be as close as possible for the finite difference approximations to be as close as possible to the true gradients. However, for a given instrumental noise level, the uncertainty in the gradients will be larger if the instruments are closer; see Suryanto et al. (2005) for a more in-depth discussion of noise contribution. Finally, the assumption of linearity of the displacement will be greatly affected by site effects at the stations.

30.3.2 Ring laser rotational measurements

In 1913, G. Sagnac showed that two counter-propagating light beams, steered around a closed area A inside an interferometer, generated a phase shift when the instrument was rotating at an angular frequency $\dot{\boldsymbol{\omega}}$ with respect to an inertial frame. In our active square laser cavities, lasing at a single mode per sense of rotation is achieved when an integral number of wavelengths circumscribe the ring perimeter. Since the path length is slightly different for the co-rotating and counter-rotating laser beams, we obtain a beat frequency $\Delta\nu$ instead of the phase shift. This has the advantage that, technically, a frequency can be measured much more precisely than a phase shift. With P the perimeter of our instrument, the Sagnac equation for an active ring laser cavity reads

$$\Delta\nu = \frac{4A\,\mathbf{n}\cdot\dot{\boldsymbol{\omega}}}{\lambda P} , \tag{30.11}$$

where λ is the rest wavelength of the laser and $\mathbf{n}$ is the unit vector perpendicular to the ring laser area. Inherently, this equation has three contri-

butions which reflect upon the beat frequency $\Delta\nu$. Variations of the scale factor $(4A/\lambda P)$ have to be avoided by making the instrument mechanically as rigid and stable as possible. Changes in orientation enter the beat frequency via the inner product. Finally, variations in $\dot{\boldsymbol{\omega}}$ are representing the most dominant contribution to changes in $\Delta\nu$ and are the focus of our seismic studies here. Technically, our rings are realized as high Q Helium/Neon lasers, operated close to laser threshold in order to satisfy the single mode condition (Stedman 1997). The body is made from Zerodur, a glass ceramic with extremely low thermal expansion, to ensure the required scaling factor stability. Mirrors with a total loss of around 15 ppm each are used to minimize errors arising from coupling between the two counter-rotating beams through backscattered light. The larger the ring laser can be made, the higher is the sensitivity to rotation (Schreiber et al. 2003c).

All ring lasers are rigidly attached to bedrock and very small changes of orientation caused by Earth tides, ocean loading (Schreiber et al. 2003a) and, in particular, diurnal polar motion (Schreiber et al. 2004) were successfully detected. Ring lasers have two major advantages for applications in seismic studies. They are measuring absolute rotation with respect to the local universe and they do not depend on accelerated masses. In particular this last property ensures an extremely wide dynamic range of operation, reaching from a few μHz for geophysical signals up to more than 10 Hz as obtained from regional earthquakes.

30.4 Observations and Simulations of Rotational Motions

In this section we shall present direct (ring laser) and array-derived rotations and compare them with observations of transverse acceleration and theoretical rotation rate calculated for a 3D Earth model.

30.4.1 Ring laser observation of rotational motions, comparison with simulations

In the last years the capabilities of simulating the propagation of seismic waves resulting from earthquakes on a global scale have improved significantly. This is not only due to the still increasing computer resources, but also due to improved and highly sophisticated numerical methods. The "spectral element method" (Komatitsch 1997, Komatitsch and Tromp 2002a, b), for example, allows very accurate modelling of elastic waves in

three-dimensional model structures of the Earth's interior, additionally incorporating various effects, such as topography/bathymetry, anelasticity, anisotropy, ocean loading and rotation as well as gravitation of the Earth. The method proved to give very good results in terms of fit to observed data when using current 3D tomographic Earth models (Komatitsch et al. 2003, Igel et al. 2005b, Schuberth et al. 2005). For this study, we used a modified version of the spectral element program SPECFEM3D, in which we implemented the calculation and output of rotational ground motions for comparison with the ring laser data from Wettzell, Germany. The actual computation of the rotations in the code is straightforward, the spatial derivatives of the displacement $\partial u_x / \partial x$ etc. being already available as they are needed for the calculation of the translational motions. Thus we can easily obtain the rotational motion as the curl of the displacement field (Eq. 30.2).

For this study, simulations were carried out using a finite source model of the M7.3 Irian Jaya earthquake in Indonesia on 7 February 2004 (Ji et al. 2002, Ji 2004). Most of the available options described above were incorporated in the model, thus including 3D models for the crust and the mantle (crust2.0 and S20RTS, respectively), attenuation, transverse isotropy, topography/bathymetry, ocean loading as well as gravity and rotation of the Earth. The resolution of the model allowed for numerical seismograms accurate down to periods of 20 s.

As shown in Section 30.2.3, the rate of rotation and the transverse component of acceleration at the same location should be in phase for an incoming plane wave. Furthermore, when assuming a horizontally propagating wave, one can estimate the phase velocity. The results of the simulation demonstrate this in a very clear way, as the seismograms are inherently noise free. Figure 30.3 shows the comparison of observed rotation rate (gray) and transverse acceleration (black) for the M7.3 Irian Jaya earthquake of 7 February 2004. The real data (top left) were filtered between 1000- and 20-second periods, that lower limit being controlled by the accuracy of the synthetic data. The amplitudes of acceleration were scaled by an arbitrary phase velocity of 3000 m/s. Shown in the lower left part of the figure is the correlation coefficient of a 30-second sliding window. Despite the relatively low signal-to-noise ratio in the ring laser data, the normalized correlation coefficient reaches values close to one (perfect match) for most of the surface wave train between 3200 s and 4200 s. The right part of the figure shows the same for the modeled data which is inherently noise free. The correlation is higher for the simulated data, but showing a similar behaviour for the body and surface wave parts of the seismogram. The synthetic data do not fit exactly the observed data, but show some

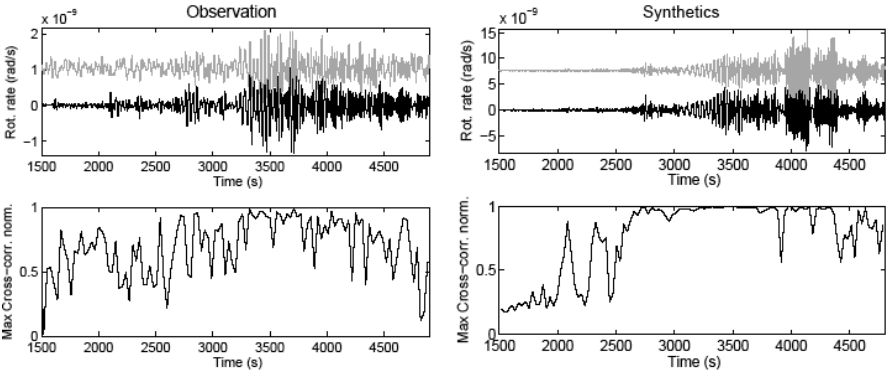

Fig. 30.3 Comparison of correlation coefficients, obtained with a 30-s sliding window, of acceleration and rotation rate for the M = 7.3 Irian Jaya (Indonesia) earthquake of 7 February 2004. *Left*: observed; *right*: synthetics. *Top*: scaled (see text) transverse acceleration (black) and rotation rate (gray – shifted for legibility)

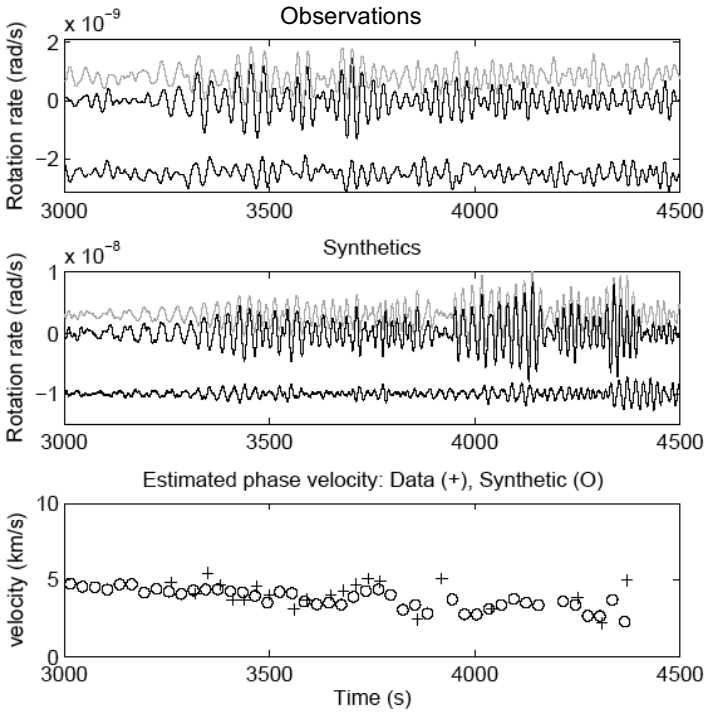

Fig. 30.4 Estimation of phase velocities (lower plot shows velocities from observed data as crosses and velocities from simulation as circles) by correlation of observed rotation rate (gray) and transverse acceleration (black) in upper plots (the bottom trace is the residual). The chosen time window only displays part of the whole seismogram where mainly surface waves appear. See text for more details

strong similarities in the surface waves, where the signal-to-noise ratio (especially for the ring laser) gets better. The difference between synthetic and real data may either be due to an inaccurate model of the rupture process and/or to incorrect crustal or mantle models.

In Fig. 30.4, horizontal phase velocities are estimated by sliding a 30 s time window along the time series of rotation rate and transverse acceleration and dividing peak amplitudes in time windows where the waveform fit is good (normalized maximum correlation coefficient greater than 0.95). The figure shows observed rotation rate and scaled transverse acceleration (top), theoretical rotation rate and scaled transverse acceleration (mid) and the phase velocity estimates (bottom) in a time window containing Love waves. Despite the difference in waveform and amplitude between synthetics and observations, the time-dependent phase velocities match surprisingly well the observations, supporting the conclusions from the analysis of another large event (Igel et al. 2005b). The Love wave phase velocity curve as a function of frequency is expected to reflect the material properties of some volume around the receiver location and may well be used for structural inversion if other information is not available. However, the uncertainties of this phase-velocity estimations still need to be investigated.

30.4.2 Array based determination of rotational motion

As explained in Section 30.3.1, all three components of rotation can in theory be derived from data acquired by an array of three-component seismometers at the Earth's surface. Indeed, in several array studies, rotation rate of seismic wavefields after large earthquakes was estimated (e.g., Huang 2003). However, there is only one study where array-derived rotation rate was compared with direct measurements (Suryanto et al. 2005) and the results indicate that – as expected – array derived rotation is sensitive to noise. As indicated above and shown in Igel et al. (2005b), with appropriate scaling the broadband transverse acceleration can be almost identical to rotation rate provided that the assumption of plane wave propagation holds. Here we compare array-derived rotation rate with transverse acceleration scaled with the appropriate phase velocity, to match the rotation rate amplitudes. This complements the studies of consistency between rotations and translations in phase and amplitude.

In December 2003 an array of seismometers was installed in Wettzell, about 150 km NE of Munich, Germany (Fig. 30.5) around the location of the ring laser. The radius of the array was about 1.5 km. A broadband seismometer of the German Regional Seismic Network (GRSN) is colloca-

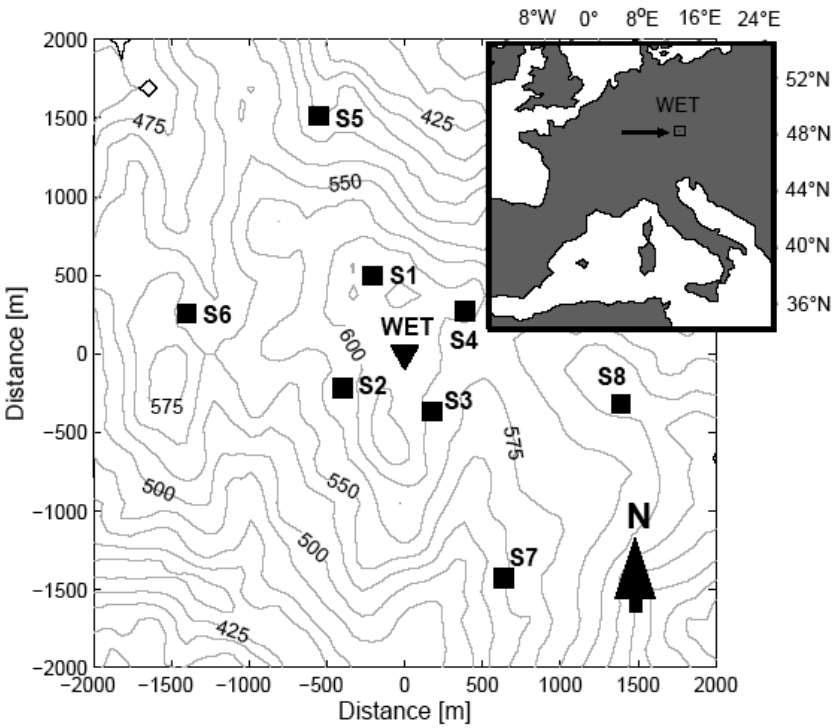

Fig. 30.5 Topographic map of the Wettzell area, SE Germany. The Fundamental Wettzell Station (WET) is denoted by a triangle. The ring laser and the broadband GRSN seismometer are both located in WET (about 250 m away from each other)

ted with the ring laser. The experiment ran up to early March 2004. The observational system consisted of 3 components of a Le3D-5s velocity sensor having a flat response in velocity between 0.2 and 40 Hz, with a 400 V/m/s generator constant. The seismometers were either buried in soft ground at a bottom depth of about 50 cm or put on outcropping igneous rock boulders. The GRSN station is using a STS-2 instrument, with a flat response of the ground velocity from 8.33 mHz (120 s) to 50 Hz.

Several teleseismic events with magnitude larger than 5.5 were observed during the experiment. Here we analyze one event: the M = 6.6 Bam (Iran) earthquake of 26 December 2003, with an estimated moment of $M_0 = 6.6\times10^{18}$ N·m and an epicentral distance of 4425 km. Rotations were determined as described in Sect. 30.3.1. In this study, we use four stations for both events to derive the rotation rates (Fig. 30.6).

In Section 30.2.3 we have shown that, assuming a plane wave propagation, the transverse horizontal acceleration and the vertical component of

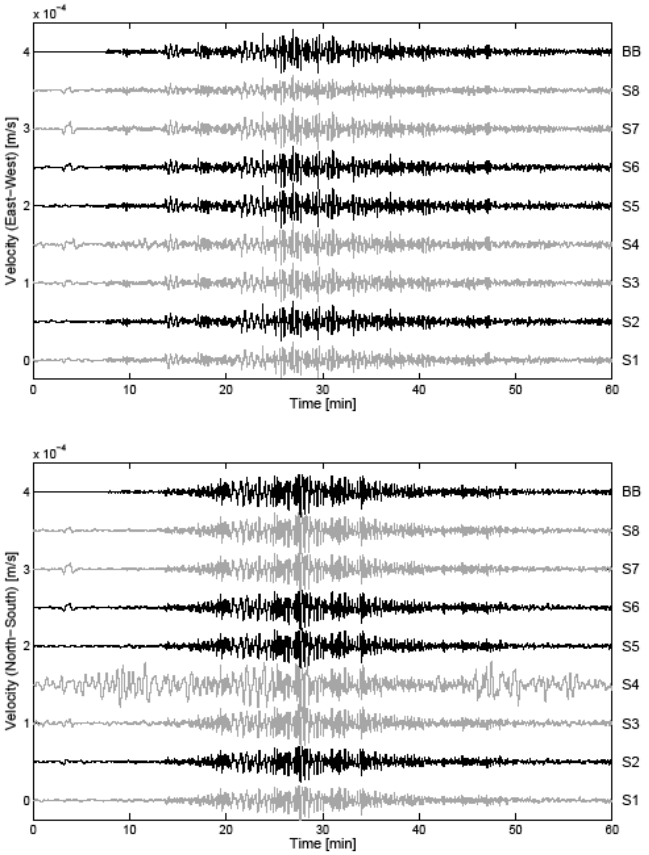

Fig. 30.6 Horizontal components of the velocity recorded by the array seismometers for the 26 December 2003, Bam (Iran) earthquake. The data from stations 2, 5, 6 and broadband are used to derive the rotations. *Top*: E-W components, *bottom*: N-S components

rotational rate should be in phase and their ratio equal to twice the horizontal phase velocity. Since the data from the ring laser was not available for this event, we use the transverse acceleration data to compare with the calculated array-derived rotational rate. This is justified given the substantial fit between rotation rate and transverse acceleration reported by Igel et al. (2005b) and Igel et al. (2005a) particularly for time windows containing the surface wave trains. For this purpose, a band pass filter (0.03–0.08 Hz) is used to isolate the main phase of the surface waves contained in the seismograms. The transverse acceleration is scaled (i.e., converted to rotation rate) by dividing by twice a constant phase velocity (5000 m/s). Figure 30.7 shows the computed time histories of the scaled transverse accelera-

tion (black lines) superimposed with the vertical component of ground rotation rate (gray lines) across the array for the Bam earthquake. There is considerable phase match (maximum correlation coefficient above 0.9) between array-derived rotation rate and scaled transverse acceleration. This suggests and further supports the conclusion that the array seismograms, the broadband sensor and the ring laser (Suryanto et al. 2005) consistently provide the same information on the rotational part of the wave field.

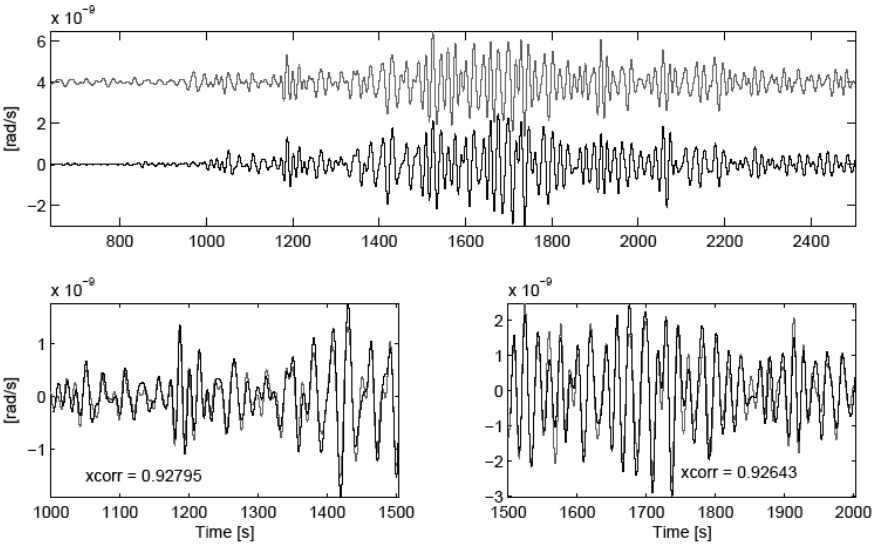

Fig. 30.7 Comparison of collocated (scaled) transverse acceleration (black) observed by the GRSN broadband seismometer with array derived rotation rate (gray) for the Bam earthquake

30.5 Discussion and Conclusions

Are measurements of rotational ground motions useful for seismology and related fields in the earth sciences? While the tremendous success of research on the translational part of ground motions in the past decades would suggest that this is not the case, the question posed can only now be addressed in the context of real observations. The ring laser technology that was extended towards high resolution measurements of absolute rotations in the past years (Schreiber et al. 2003a, 2004) with the major aim of measuring changes of the Earth's rotation rate, was successfully transferred to the field of seismology, which required adaptation in terms of ac-

quisition parameters and timing accuracy. The resolution of ring laser type measurements is now such that observations can be directly compared with those from broadband standard seismometers. In broadband global seismology we do not expect major information gain from rotation sensors as seismic network densities are ever increasing and many of the wavefield properties can be extracted by array processing. However – given the fact that we are dealing with a new observable – long period teleseismic broadband data provide an excellent opportunity to test the consistency of this new observable, thus the correct measurement of the ring laser instrument and its potential applicability in other domains of seismology (e.g., strong ground motion, source inversion, etc.).

As motivated in the theoretical section, assuming plane wave propagation, we can directly compare rotation rate with transverse acceleration as they should be in phase and related by a factor proportional to phase velocity. The first earthquake-induced observations with the German ring laser system (Igel et al. 2005b) demonstrate that indeed – particularly for time windows containing the transversely polarized Love surface waves – the fit between those independent observations is almost perfect, providing the test for phase consistency. The amplitude relation between acceleration and rotation rate can be used to estimate horizontal phase velocities as well as propagation directions. As shown in Fig. 30.4 these phase velocities match well those predicted by the most sophisticated forward modelling possible today. The accuracy and uncertainties of phase velocity estimates are still being investigated but it is important to note that – with collocated measurements of translation and rotation – it is thus possible to extract information from the wavefield that otherwise could only be obtained through seismic arrays. This may be useful in case of a very sparse network or when only single stations are possible, a situation likely in planetary seismology, but current technology would not yet allow a light sensor with the required sensitivity given the payload restrictions of space missions.

Sampling the seismic wavefield at the Earth's surface with an appropriate array allows the estimation of the rotational part by finite differencing the three components of ground motion for the given array geometry. While the first – surprisingly successful – direct comparison of ring-laser-based direct observation and array-derived rotational motions is given by Suryanto et al. (2005), it is clear that the logistic effort to determine rotations from array is considerably larger than direct measurements. This holds particularly for temporary arrays when the installation may be heterogeneous in terms of station quality. However, the fact that we are sampling the same rotation wavefield properties with the ring laser, broadband sensor and the array is further supported by the results shown in Fig. 30.7.

The rotation rate converted from the broadband transverse acceleration is close to the array-derived rotation rate as expected from theory.

We consider these studies as a contribution towards the demonstration of the accuracy and consistency of a new observable quantity in broadband seismology: the vertical component of rotation. While the acquisition technology will continue to improve, there are still many open questions that need to be answered before it is clear what the new observable is good for. These questions involve: (1) the sensitivity of rotations *vs*. translations with respect to the Earth structure; (2) the importance of ground rotations in shaking hazard issues particularly in the presence of very unconsolidated low-seismic-velocity near surface structures; (3) the effects of strongly scattering structures and anisotropy; (4) the sensitivity of rotations with respect to finite fault scenarios; (5) the development of low-resolution portable sensors with the appropriate sensitivity for near source (e.g., aftershock) studies. Many of these issues can now be addressed using modern wave propagation simulation technology as was used in this study to model teleseismic observations.

Acknowledgments. This work was supported by the German Ministry of Research and Education (BMBF-Geotechnologien). We also acknowledge the support by the German Academic Exchange Service (IQN-Georisk), and by the KONWIHR project. We are grateful to J. Tromp and D. Komatitsch for providing their SEM code and to Ji Chen for the finite source parameters. We acknowledge the contributions of the Bundesamt für Kartographie und Geodäsie (BKG) towards the installation and operation of the G ring laser at the geodetic observatory Wettzell. Thanks to the Munich Leibniz Computing Center for providing access to their supercomputing facilities.

References

Aki K, Richards PG (1980) Quantitative seismology: theory and methods. W.H. Freeman and Company, San Francisco, CA

Aki K, Richards PG (2002) Quantitative seismology. University Science Books, 2nd ed, Sausalito, CA

Bodin P, Gomberg J, Sing SK, Santoyo M (1997) Dynamic deformations of shallow sediments in the valley of Mexico. Part I. Three-dimensional strains and rotations recorded on a seismic array. Bull Seism Soc Am **87**: 528-539

Bouchon M, Aki K (1982) Strain, tilt, and rotation associated with strong ground motion in the vicinity of earthquake faults. Bull Seism Soc Am **72**: 1717-1738

Castellani A, Zembaty Z (1996) Comparison between earthquake spectra obtained by different experimental sources. Engng Struct **18**: 597-603

Cook RD (1974) Concepts and applications of finite element analysis. John Wiley & Sons, New York

Dyszlewicz J (2004) Micropolar theory of elasticity. Springer, Berlin–New York

Galitzin F (1914) Vorlesungen über Seismometrie. BG Teubner, Leipzig–Berlin (in German)

Huang B-S (2003) Ground rotational motions of the 1999 Chi-Chi, Taiwan earthquake as inferred from dense array observations. Geophys Res Lett **30**: 1307-1310, doi:10.1029/2002GL015157

Igel H, Flaws A, Cochard A, Wassermann J, Schreiber U, Velikoseltsev A (2005a) Rotational and translational motions induced by local, regional and global seismic events. I. Observations and processing (in preparation)

Igel H, Schreiber U, Flaws A, Schuberth B, Velikoseltsev A, Cochard A (2005b) Rotational motions induced by the M8.1 Tokachi-oki earthquake, September 25, 2003. Geophys Res Lett **32**: L08309, doi:10.1029/2004GL022336

Ji C (2004) URL http://www.gps.caltech.edu/˜jichen

Ji C, Wald DJ, Helmberger DV (2002) Source description of the 1999 Hector mine, California earthquake. Part I. Bull Seism Soc Am **92**: 4, 1192-1207

Komatitsch D (1997) Méthodes spectrales et éléments spectraux pour l'équation de l'élastodynamique 2D et 3D en milieu hétérogène (Spectral and spectral -element methods for the 2D and 3D elastodynamics equations in heterogeneous media). PhD thesis, Institut de Physique du Globe, Paris, France

Komatitsch D, Tromp J (2002a) Spectral-element simulations of global seismic wave propagation – I. Validation. Geophys J Int **149**: 390-412

Komatitsch D, Tromp J (2002b) Spectral-element simulations of global seismic wave propagation – II. 3-D models, oceans, rotation, and self-gravitation. Geophys J Int **150**: 303-318

Komatitsch D, Tsuboi S, Ji C, Tromp J (2003) A 14.6 billion degrees of freedom, 5 teraflops, 2.5 terabyte earthquake simulation on the Earth Simulator. Proc. ACM/IEEE Supercomputing SC'2003 conference. Published on CD-ROM and at www.sc-conference.org/sc2003

Lakes RS (1995) Experimental methods for study of Cosserat elastic solids and other generalized continua. In: Mühlhaus HB (ed) Continuum models for materials with microstructure, Chap 1, pp 1-22. John Wiley & Sons, London

Maugin GA (1998) On the structure of the theory of polar elasticity. Phil Trans R Soc **356**: 1367-1395

McLeod DP, Stedman GE, Webb TH, Schreiber U (1998) Comparison of standard and ring laser rotational seismograms. Bull Seism Soc Am **88**: 1495-1503

Nigbor RL (1994) Six-degree-of-freedom ground-motion measurement. Bull Seism Soc Am **84**: 1665–1669

Nowacki W (1986) Theory of asymmetric elasticity. Pergamon Press–Oxford and PWN–Warszawa

Pancha A, Webb TH, Stedman GE, McLeod DP, Schreiber KU (2000) Ring laser detection of rotations from teleseismic waves. Geophys Res Lett **27**: 3553-3556

Schreiber KU, Klügel T, Stedman GE (2003a) Earth tide and tilt detection by a ring laser gyroscope. J Geophys Res **108**: 21-32, 10.1029/2001JB000569

Schreiber KU, Velikoseltsev A, Igel H, Cochard A, Flaws A, Drewitz W, Muller F (2003b) The GEOsensor: A new instrument for seismology. In: GEO-TECHNOLOGIEN Science Report No. 3: Observation of the System Earth from Space, Status Seminar, Programme and Abstracts. Munich, 12-13 June, Bavarian State Mapping Agency (BLVA)

Schreiber KU, Velikoseltsev A, Stedman GE, Hurst RB, Klugel T (2003c) New applications of very large ring lasers. In: Sorg H (ed) Symposium Gyro Technology, pp 8.0-8.7

Schreiber KU, Velikoseltsev A, Rothacher M, Klügel T, Stedman GE, Wiltshire DL (2004) Direct measurement of diurnal polar motion by ring laser gyroscopes. J Geophys Res **109**: B06405

Schuberth B, Ewald M, Igel H, Treml M, Wang H, Brietzke G (2005). Computational seismology: narrowing the gap between theory and observations. In: Bode A, Durst F (eds) High performance computing in science and engineering – Garching 2004. Springer, Heidelberg, pp 251-262

Spudich P, Steck LK, Hellweg M, Fletcher JB, Baker LM (1995) Transient stresses at Park-field, California, produced by the m 7.4 Landers earthquake of June 28, 1992: Observations from the UPSAR dense seismograph array. J Geophys Res **100**: 675-690

Stedman GE (1997) Ring laser tests of fundamental physics and geophysics. Reports Progr Phys **60**: 615-688

Stedman GE, Li Z, Bilger HR (1995) Sideband analysis and seismic detection in a large ring laser. Appl Opt **34**: 7390-7396

Suryanto W, Igel H, Wassermann J, Cochard A, Schubert B, Vollmer D, Scherbaum F (2005) Comparison of seismic array-derived rotational motions with direct ring laser measurements. Bull Seismol Soc Am (submitted)

Takeo M (1998) Ground rotational motions recorded in near-source region of earthquakes. Geophys Res Lett **25**: 789-792

Takeo M, Ito HM (1997) What can be learned from rotational motions excited by earthquakes. Geophys J Int **129**: 319-329

Teisseyre R, Majewski E (2001) Earthquake thermodynamics and phase transformation in the earth's interior. Academic Press, San Diego

Teisseyre R, Suchcicki J, Teisseyre KP, Wiszniowski J, Palangio P (2003) Seismic rotation waves: basic elements of theory and recording. Annali di Geofisica **46**: 671-685

Trifunac MD, Todorovska MI (2001) A note on the useable dynamic range of accelerographs recording translation. Soil Dyn and Earth Eng **21**: 275-286

31 Absolute Rotation Measurement Based on the Sagnac Effect

Leszek R. Jaroszewicz, Zbigniew Krajewski, Lech Solarz

Institute of Applied Physics, Military University of Technology
ul. Kaliskiego 2, 00-908 Warszawa, Poland
e-mail: jarosz@wat.edu.pl

31.1 Introduction

This chapter deals with technical aspects of absolute rotation measurement based on the Sagnac effect. Starting from a brief description of this effect, its explanation based on different physical approaches is presented. Overviews of optical gyroscopes as a technical implementation of the Sagnac effect for angular position measurement are shown. Differences between gyro and rotation measurements are pointed out. On this basis, fundamental investigations connected with attainable accuracy of the designed fibre-optic rotational seismometers (FORS) are presented. Sensitivity, resolution, noise and drift phenomena are discussed. Finally, technical implementation of different constructions of FORS are proposed.

31.2 Sagnac Effect

The absolute rotation measurement is based on the Sagnac effect (Sagnac 1913). The Sagnac effect is a consequence of the fact that an optical path length difference is experienced by light beams propagating in opposite directions in a rotating frame. It is the measurement of this optical path difference (proportional to the absolute rotation) that forms the basis of all the optical gyros.

31.2.1 Sagnac effect in a vacuum

For simplicity, the usual explanation of the Sagnac effect starts by considering a circular ring interferometer in vacuum (Post 1967). The light entering the system is divided into two counter-propagating waves which return

in phase after having travelled along the same path in opposite directions (Fig. 31.1a). When the interferometer rotates (about an axis perpendicular to the interferometer plane) with angular velocity Ω, an observer at rest in the inertial reference frame sees the light entering the interferometer at point P (Fig. 31.1b). Then the light travels with the same vacuum velocity c_0, in opposite directions, but, during the transit time through the loop, the beamsplitter has moved to P', and our observer sees that the co-rotating wave has had to propagate over a longer path than the counter-rotating one. The optical path length difference, ΔL, experienced by light propagating in opposite directions along the interferometer (Sagnac 1913, Post 1967) is given by

$$\Delta L = \frac{4\mathbf{A}}{c_0}\boldsymbol{\Omega}\,, \tag{31.1}$$

where $\mathbf{A}$ is the vector of the geometrical area $|A| = \pi R^2$ enclosed by the wave path, c_0 is the velocity of light in vacuum, $\boldsymbol{\Omega}$ is the rotation vector.

The rigorous derivation of this formula (Post 1967) is based on the propagation of light in a rotating frame, i.e., an accelerating frame of reference, where the general theory of relativity must be used to perform the exact calculation. However, a simple way of explaining this formula (Post 1967) is to consider the ring interferometer shown in Fig. 31.1 as a rotating disc. At a given point on the perimeter, designed by P in Fig. 31.1a, identical photons are sent in the counter-directions (*ccw* and *cw*) along the perimeter. If $\Omega = 0$, the photons traveling at the speed of light, c_0, will arrive at the starting point P after covering an identical distance $2\pi R$ in the same time $t = 2\pi R/c_0$. In the presence of angular rotation Ω (Fig. 31.1b), the *ccw* photons will arrive at the starting point on the disc, now located at point P',

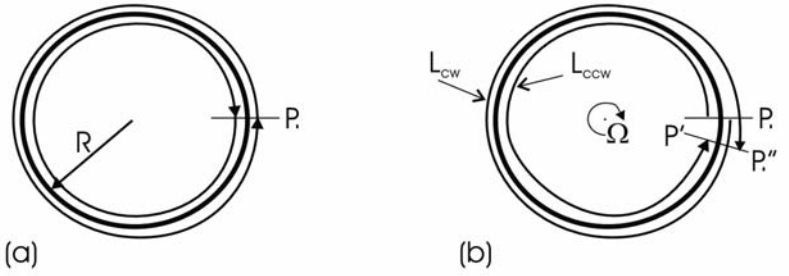

Fig. 31.1 Sagnac effect in a circular ring interferometer: (a) at rest in an inertial frame of reference; (b) rotating with respect to an inertial frame of reference. Notation: R – radius of loop, L_{cw} – distance in clockwise direction, L_{ccw} – distance in counter-clockwise direction, Ω – angular velocity of interferometer rotation

after covering distance L_{ccw}, which is shorter than the perimeter $2\pi R$, given by

$$L_{ccw} = 2\pi R - R\Omega t_{ccw} = c_{ccw} t_{ccw} , \tag{31.2}$$

where $R\Omega$ is the tangential velocity of the ring and t_{ccw} is the time taken to cover the distance L_{ccw}. It should be noted that L_{ccw} is also given by the product of the velocity of light c_{ccw} in the *ccw* direction and t_{ccw}. For propagation in a vacuum, $c_{ccw} = c_0$.

Similarly, the photons propagating in the *cw* direction will arrive at the starting point now located at P'' and will experience a longer effective perimeter L_{cw} given by

$$L_{cw} = 2\pi R + R\Omega t_{cw} = c_{cw} t_{cw} , \tag{31.3}$$

where t_{cw} is the time taken to cover the distance L_{cw} , and again $c_{cw} = c_0$ for propagation in a vacuum.

The last two equations can be solved for t_{ccw} and t_{cw} , and we can obtain the difference, Δt, between clockwise and counter-clockwise propagation

$$\Delta t = t_{cw} - t_{ccw} \approx \frac{4\pi^2 R^2}{c_0^2} = \frac{4\pi R^2 \Omega}{c_o^2} = \frac{4A}{c_0^2}\Omega . \tag{31.4}$$

Hence, the path length ΔL travelled by light in a time Δt is

$$\Delta L = c_0 \Delta t = \frac{4A}{c_0}\Omega , \tag{31.5}$$

which is identical with Eq. (31.1) for rotation speed perpendicular to the disc area.

31.2.2 Sagnac effect in a medium

If light propagates in a medium, it can be demonstrated that the Sagnac results are unchanged (Post 1967, Arditty and Lefevre 1981a, b). Because the waves travel n times slower (n is the index of refraction for the medium), the splitter point has moved n times further when the waves recombine. The path difference is then longer than in the vacuum. But the medium is also moving, and there is a Fizeau drag that increases the velocity for the longer path and decreases it for the shorter path. The magnitude of this drag is such that it may completely eliminate the effect of the medium. An electrodynamic approach using propagation equation in a rotating frame of reference (Arditty and Lefevre 1981b, Lefevre and Arditty 1982) confirms this result.

In order to give an orientation about the magnitude of ΔL, we present in Table 31.1 the data for different characteristic rotation speeds under the assumption that an area $A = 100$ cm^2.

Table 31.1 The magnitude of ΔL for different rotation speeds Ω

Rotation speed Ω	Magnitude of ΔL	Comment
1.00 rad/s	1.3×10^{-8} cm	
1.00 rad/h	3.7×10^{-12} cm	
0.26 rad/h	9.7×10^{-13} cm	Earth rotation rate
0.01 deg/h	1.0×10^{-15} cm	Navigation grade performance
1.0×10^{-8} rad/s	2.0×10^{-16} cm	Expected magnitude of seismic rotational waves

We see that this distance is very small indeed, especially when compared with the wavelength of light, which is about 5×10^{-5} cm, or the diameter of hydrogen atom, which is about 10^{-8} cm.

31.3 Optical Gyroscopes as Systems Utilizing the Sagnac Effect

The practical application of the Sagnac effect is the construction of an optical gyroscope designed to detect the angular position changes in three-dimensional space. This is accomplished by detecting rotation rate via the Sagnac effect measurement, and calculating angular position in integration process over a given time range. Because distance ΔL generated by the Sagnac effect is extremely small, special interferometric methods are applied for its measurement. In general, all these methods can be divided into passive and active ones, as shown in Fig. 31.2.

31.3.1 Passive resonator method

The passive resonator method (Meyer et al. 1983) of measuring ΔL in fiber-optic implementation is shown in Fig. 31.2c. In this case, light having a frequency f enters the resonator at one-directional coupler, along the *cw* (or +) direction and also along the *ccw* (or –) direction. The light excites the fiber resonator at the same coupler, as shown in the figure. In the absence of rotation, the resonance frequencies of the cavity for (+) and (–) propagation are identical and given by f_q

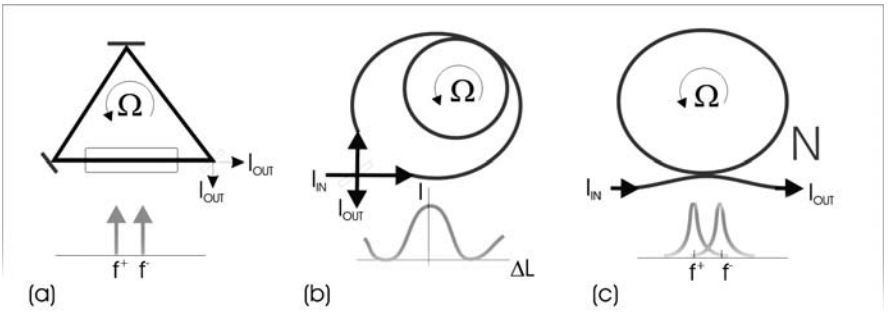

Fig. 31.2 Interferometric systems for Sagnac effect detection: (a) active method in ring-laser approach, (b) passive method in two-beam interferometer approach, (c) passive method in passive resonator approach. Parameters I_{IN}, I_{UOT} are the intensities of input and output beams, respectively

$$f_q = q\frac{c_0}{nP}\ , \tag{31.6}$$

where nP is the optical perimeter of the resonator, n is the refractive index of the fiber and q is an integer representing the longitudinal mode number for the fiber resonator.

In the presence of rotation normal to the plane of the fiber resonator, the optical perimeter nP will be different for (+) and (–) propagation directions as predicted by the Sagnac effect (Eq. 31.5). In other words, $\Delta P = nP^+ - nP^- = \Delta L$ and it generates a frequency difference, Δf, between the (+) and (–) resonances of the cavity, given by

$$\Delta f = f^+ - f^- = q\frac{c_0}{nP^+} - q\frac{c_0}{nP^-} = -\frac{4A}{\lambda_q nP}\Omega\ , \tag{31.7}$$

where $\lambda_q = c_0/f_q$. The width of each resonance shown in the bottom part of Fig. 31.2c is determined by the loss in the resonator. Moreover, for the N-turn fiber resonator the frequency difference Δf is identical with that for the single-turn resonator.

To measure rotation using the resonator method, it is necessary to measure Δf using some external means.

31.3.2 Ring-laser method

The ring-laser set up for the measurement of ΔL, shown in Fig. 31.2a, is similar to the passive resonator set up, except that an optical amplifier is

included within the resonator (Rosenthal 1962, Macek and Davis 1963, Killpatrick 1966). Such an amplifier enables laser oscillation at f_q along the (+) and also (–) directions within the resonator (bottom part of Fig. 31.2a).

In the presence of rotation Ω, we get the frequency difference Δf, given by

$$\Delta f = f^+ - f^- = q\frac{c_0}{P^+} - q\frac{c_0}{P^-} = -\frac{4A}{\lambda_q P}\Omega \ . \tag{31.8}$$

The advantage of the ring-laser method is that no external means are needed to measure Δf, since f^+ and f^- are automatically generated within the ring laser and may be coupled out through one of the mirrors. To obtain Δf, one simply beats the f^+ and f^- outputs outside the ring laser.

The ring-laser approach using a He-Ne amplifier (Aronowitz 1971) was the first successful optical gyroscope and is now being used in a number of civilian and military inertial navigation systems. To avoid mode competition when the cavity resonances at centre of the gain curve, two isotopes of Ne are used (Aronowitz 1971). Since the isotope shift of 500 MHz is smaller than the 1.5 GHz bandwidth of the Ne amplifying transition, stable oscillations can simultaneously take place along both directions of propagation.

31.3.3 Two-beam interferometer method

The fiber-optic version (Vali and Shorthill 1976) of two-beam interferometer method applies the fiber loop interferometer configuration with a 3 dB fiber coupler as input-output gate for optical beam (Fig. 31.2b). In such a system, a phase shift is produced between *cw* and *ccw* propagating light of magnitude $\Delta\phi$, given by

$$\Delta\phi = \frac{2\pi}{\lambda_0}\Delta L = \frac{8\pi A}{\lambda_0 c_0}\Omega \ , \tag{31.9}$$

where λ_0 is the wavelength on the light in vacuum.

The bottom part of Fig. 31.2b shows the cosinusoidal variation of the output intensity from this interferometer, I_{OUT}, as a function of Ω. Therefore, to measure Ω, we need to measure the change in I_{OUT}. In the case of a fiber interferometer, however, it is possible to loop the fiber many times (Vali and Shorthill 1976), say N times, before returning to the fiber coupler. In this case, Δt, as well as ΔL, become N times longer and the corresponding $\Delta\phi$ becomes

$$\Delta\phi = \frac{2\pi}{\lambda_0}\Delta L\, N = \frac{8\pi AN}{\lambda_0 c_0}\Omega \ . \tag{31.10}$$

For a fiber of length L wound in a coil of diameter D, we have

$$A = \frac{\pi D^2}{4} \quad \text{and} \quad N = \frac{L}{\pi D} \ . \tag{31.11}$$

Substituting the above into Eq. (31.10), we get

$$\Delta\phi = \frac{8\pi AN}{\lambda_0 c_0}\Omega = \frac{2\pi LD}{\lambda_0 c_0}\Omega \ . \tag{31.12}$$

In other words, the sensitivity of the Sagnac interferometer in this approach is enhanced by a factor of N. The limit on the magnitude of N will of course depend on the loss in the fiber.

31.4 Fundamental Measurement Limits

Since the magnitude of Δf or $\Delta\phi$ can be very small, depending on the precision required, it is worthwhile to examine what determines the fundamental limit in such a measurement. For the fiber-optic interferometer with perfect components, the measurement limit is imposed by the shot noise in the light as measured by the detector (Davis and Ezekiel 1978, Lin and Giallorenzi 1979). In other words, $\delta\Omega$ which represents the uncertainty in the measurement of Ω is generated by uncertainty in the measurement of the Sagnac phase shift and can be expressed by the formula presented in Table 31.2 (Davis and Ezekiel 1979). In the case of passive multiturn fiber resonator with perfect components, the fundamental limit is determined by the uncertainty in the measurement of Δf due to the shot noise on the light at the detectors (Lin and Giallorenzi 1979). For this method the formula for $\delta\Omega$, in a simplified form, is presented in Table 31.2, too. The last for-

Table 31.2 Fundamental measurement limits for different methods. (Symbols explained in the text)

Fiber-optic interferometer gyro	Passive resonator gyro	Ring-laser gyro
$\delta\Omega \approx \frac{c_0}{LD}\frac{\lambda_0/2}{\sqrt{n_{ph}\eta_D\tau}}$	$\delta\Omega \approx \frac{\sqrt{2}\lambda_0 nP}{4A}\frac{\Gamma_c}{\sqrt{n_{ph}\eta_D\tau}}$	$\delta\Omega \approx \frac{\sqrt{2}\lambda_0 P}{4A}\frac{\Gamma_c}{\sqrt{n_{ph}\tau}}$
(31.13)	(31.14)	(31.15)

mula in Table 31.2 describes fundamental limit on $\delta\Omega$ for the ring-laser gyro which is imposed by the uncorrelated jitter in the counterpropagating laser frequencies (Dorschner et al. 1980) which limits the measurement of Δf. Under ideal conditions, it is the spontaneous emission generated in the laser amplifier.

Simplified expressions for $\delta\Omega$ are shown in Table 31.2, using the following notation: n_{ph} is the number of photons/s arriving at the detector, η_D is the photodetector quantum efficiency, τ is the averaging time, Γ_c is the cavity linewidth, and the other parameters are as defined in Eqs. (31.7) and (31.12).

As can be seen, the fundamental limit on Ω in the ring laser gyro is very close to that for the passive resonator gyro, assuming the same A, P, λ, Γ_c, n_{ph} and τ. The technical abilities for increasing the system sensitivity (i.e., decreasing $\delta\Omega$) are connected with enlarging the system area A. In this way, practical solution can be obtained only in the case of fiber-optic interferometer, because this can be accomplished by extending fiber length L without dramatical growth in size of all the system.

31.5 Fiber-Optic Rotational Seismometer (FORS)

For the above reason, the idea of seismic rotation waves recording based on the Sagnac effect in an optical system seems to be an attractive proposition. The main advantage of such a system is the measurement of the absolute rotation rate around any axis perpendicular to the optical path plane, nonsensitive to the uniform linear motion or distortion (Post 1967). The comparison of standard seismograms and a ring laser as a sensor for rotational events has shown some advantages of the latter (McLeod et al. 1998), mainly in its extremely high sensitivity (Cochard et al. 2003). However, such a ring laser is as expensive as a motionless device.

Therefore, the relatively cheap version of fiber-optic rotational seismometer (FORS), made in fiber-optic technique seems to be a better solution. The sensors described below are based on configuration well known from the classic fiber-optic gyroscope (FOG) system (Ezekiel and Arditty 1982). The success of FOG is due to the Sagnac interferometer, a common-path, reciprocal configuration that is inherently highly stable. Its accuracy is generally limited by a small number of extraneous effects arising from undesirable properties of the loop fiber, namely Rayleigh backscattering (Cutler et al. 1980) and the Kerr (Lefevre 1993, Burns 1994), Faraday (Lefevre 1993) and Shupe (1981) effects. These deleterious effects induce short-term noise and/or long-term drift in the gyro output, which limit

the ability to accurately measure small rotation rates over long periods of time. These issues have been successfully resolved with clever engineering solutions. However, the basic FORS optimization for detection of the rotation only, without conversion for angular changes, distinguishes this system from gyro applications (Jaroszewicz and Krajewski 2002). On the other hand, the compact system construction makes the device movable that is advantageous in comparison with the ring laser system. Thus, the contents of this chapter is mainly focused on the fiber-optic rotational seismometer designed to be used for two antiparallel pendulum seismometers (TAPS) (Moriya and Teisseyre 1999) as well as for detection of seismic rotational effects (SRE). A new method of TAPS calibration and some conclusions obtained basing on the first tests of the SRE registration simultaneously by the TAPS and the FORS are also presented.

31.5.1 Application of FORS for standard rotational seismometer investigation

An application of the fiber-optic Sagnac interferometer as the fiber-optic rotational seismometer may be an attractive proposition for the TAPS calibration; however, the system must be optimized for seismic area of operation. For the above reason, a special construction of optical part of the system as well as signal processing is required. According to optical part of the system, the main parameter is the maximum sensitivity (in the range of 10^{-7}–10^{-10} rad/s), so the sensor loop should contain a long section of the optical fiber wound in the shape of a loop with maximum radius and extremely high-power optical sources. Compatibility with the standard seismic recording unit (KST), appropriate band of detection and sampling scheme are the main parameters for the constructed signal processing unit.

For the above reason, the existing construction of FOG has been adopted for introductory investigation of its usefulness for SRE detection according to the scheme shown in Fig. 31.3.

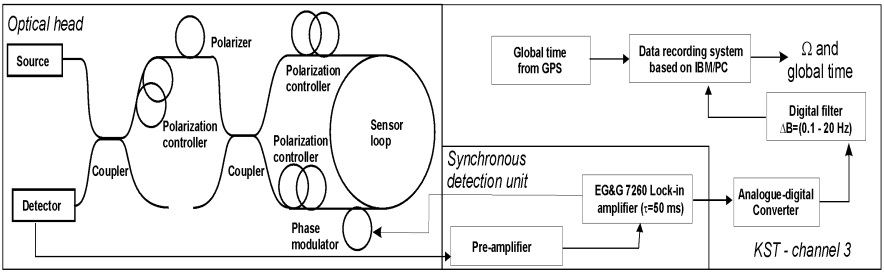

Fig. 31.3 General scheme of the FORS-I system

This system, named FORS-I, uses 1.0 mW light source operating at wavelength $\lambda = 1300$ nm and a sensor loop with radius $R = 0.1$ m containing $L = 400$ m PANDA fiber. The detection unit, based on lock-in amplifier 7260 (EG and G), carries out the synchronic detection throughout the phase modulator operating at 147.7 kHz. Because the calculated total optical loss was about 30 dB, the theoretical system sensitivity connected with the noise level is 6.8×10^{-7} rad/s$^{1/2}$ (Jaroszewicz and Krajewski 2002). The practical system calibration has been made basing on the constant Earth rotation component detection for Warsaw latitude ($\varphi = 52^{o}20''$), as described in detail by Jaroszewicz and Krajewski (2002). Because the Sagnac effect detects only the absolute rotation speed in plane of interferometric loop (Post 1967), the FORS-I placed in the north or the south direction should give rotation signal $\Omega_E = \pm 11.86$ deg/h, and in the west-east direction (see Fig. 31.4a) should be 0 deg/h. The calibration procedure gives the signal equal to 400 mV and 20 mV for the FORS-I placed in the N-S and the W-E directions, respectively, as shown in Fig. 31.4b. These data have been used for calculation of FORS-I sensitivity; it is equal to 2.3×10^{-6} rad/s which is twice worse than expected for this system in the applied detection band. The main source of this error is the occurrence of fluctuations of polarization parameters of the light source used (Jaroszewicz et al. 2003). Finally, the standard seismic recording unit KST has been used for the data processing. The analogue-digital converter samples the signal with frequency 1 kHz and after re-sampling stores it with frequency $f_s = 100$ Hz.

The drift phenomenon is a well-known problem for the fiber-optic loop interferometer applied as an optical gyroscope, because all the FOG systems give angular position as a result of time integration of the detected ro-

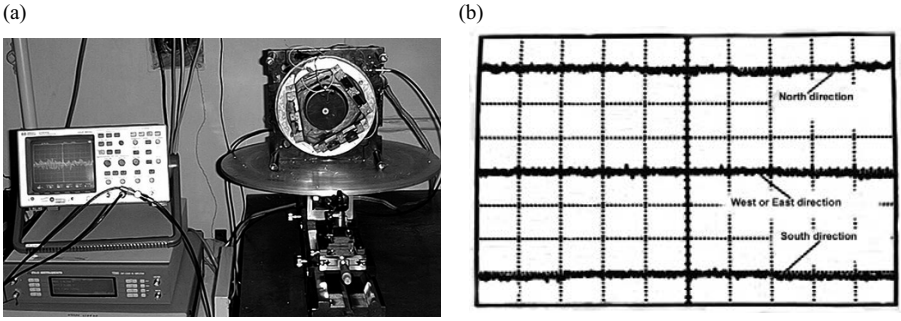

Fig. 31.4 (a) The FORS-I positioned in W-E direction, and (b) oscillogram of electronic signals from the FORS-I system during calibration (Jaroszewicz and Krajewski 2002)

tation speed. Therefore, the final system accuracy is very sensitive to the integration process. The system's sensitivity grows with narrowing integration time, but the drift minimisation needs an opposite operation – the time widening (Ezekiel and Arditty 1982). Hence, the drift connected with the constant component of the output signal has an influence on final FOG accuracy and must be taken into consideration. The application of the fiber-optic loop interferometer such as the FORS, where the final parameter is rotation speed directly obtained from the Sagnac phase shift (Post 1967), does not require the integration process. This gives a possibility to eliminate the drift influence on the system accuracy by a suitable choice of band of output signal. The digital filter included to the KST provides such a selection because its lower frequency of 0.1 Hz generally eliminates environmental fluctuation of the fiber-optic loop interferometer (Jaroszewicz 2001), whereas the upper frequency of 20 Hz is just equal to the frequency put by lock-in system (for time constant $\tau = 50$ ms used by lock-in). It is worth mentioning that the above frequency band is connected with the expected frequency characteristic of rotational seismic effects (Teisseyre et al. 2003).

Comparison of TAPS and FORS-I systems in the laboratory

The FORS-I system has been used for the TAPS testing. Figure 31.5a shows the TAPS and the FORS-I placed on the rotation table in such a way that the rotational event is dominated by displacement. The rotation with a speed equal to the Earth rotation for Warsaw latitude (i.e., about 12.86 deg/h) gives 400 mV signal generated in KST: in-phase signals from the TAPS channels. These data have been used for the evaluation of rotation components with additional TAPS left channel equalisation by the following method (Teisseyre 2002)

$$u_L' \geq u_L \sqrt{\sum u_R u_R \Big/ \sum u_L u_L} \,, \tag{31.16}$$

where u_R and u_L are two SEM recorded by right and left seismometer of TAPS.

The results presented in Fig. 31.5b show good conformity of TAPS and FORS-I for the above events; however, the TAPS system seems to generate worse response to rotation. As one can see, the rotational signal obtained from the TAPS is fuzzed, whereas the signal from the FORS-I is very smooth. This results show the advantage of direct method of rotation measurement by the FORS in comparison to the differential method realised by the TAPS. Hence, the sources of disturbances in the TAPS opera-

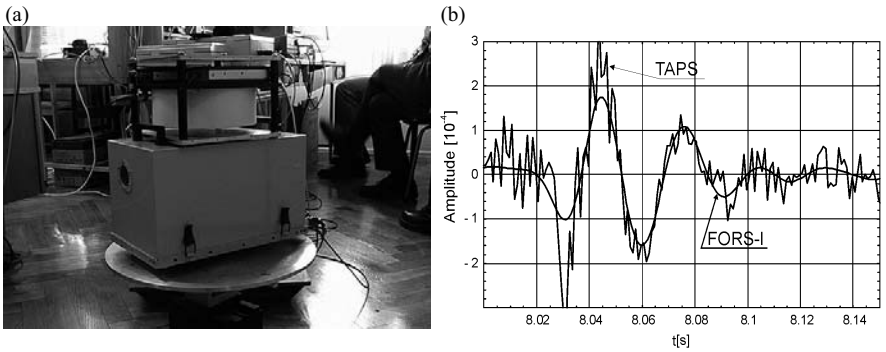

Fig. 31.5 (a) The rotation table with the TAPS (bottom box) and the FORS-I system (top box), and (b) output signals from the FORS-I and the TAPS after proper numerical processing (Jaroszewicz and Krajewski 2002)

tion should be analysed and some methods of their minimization should be proposed.

Estimation of the main error sources of TAPS operation

Most probably, the non-identical characteristics of two seismographs used in the TAPS construction are the main source of the fluctuation. The applied channel's equalisation method described by Eq. (31.16) seems to be too weak. It should be noticed that correlation like (31.16) is not adequate to the presented data, because it minimizes the mean square of the sum u_L and u_R, which contains the anticorrelated rotational components; thus, relation (31.16) minimizes at the same time both the errors and the rotations,

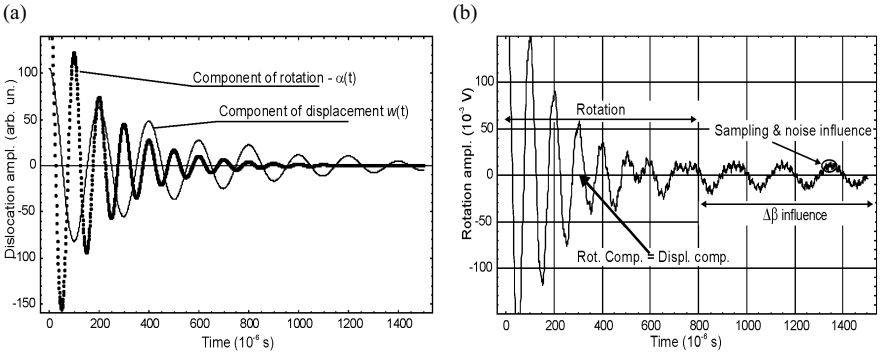

Fig. 31.6 (a) Simulated rotational and displacement components of a seismic event, and (b) rotation signal detected by TAPS system (Jaroszewicz et al. 2003)

destroying the latter. Moreover, our simulation analysis (Jaroszewicz et al. 2003) has shown that this procedure can be ineffective, especially if the TAPS system components have different attenuation characteristics. In such a situation, the existing finite components sensitivities connected with signal sampling procedure used during the data recording generate error signal, as shown in Fig. 31.6. In this simulation, the difference between left and right seismographs attenuation, $\Delta\beta$, has been assumed to be equal to 0.05. Moreover, two seismographs as elements with different noise levels have been considered.

As one can see, the main error signal exists in the region where the rotational components have small amplitude in comparison to the displacement. Because, in fact, it is the expected region of the rotational seismic effects, the method of TAPS calibration is a crucial problem for credibility of its operation.

Method of improving the TAPS performance

The reasons signalized in the preceding section have led to a search for other methods of improving the TAPS performance. The recent propositions apply, for example, the filtering procedure in the FFT domain (Teisseyre et al. 2003) or the time-domain (Nowożyński and Teisseyre 2003). However, these methods use the so-called test positioning of the TAPS (the seismographs of the system are turned so as to make them situated in the parallel-parallel position), that generally changes the conditions of the TAPS operation. For this reason, another procedure of the recorded data processing has been proposed (Solarz et al. 2004). Generally speaking, this procedure is based on smoothing by the spline functions (Kojdecki 2002, Eubank 2000). The recorded digital data $\mathbf{Y} = \{Y_i,\ i = 0,\ \ldots,\ N\}$ with sampling at Δt is smoothed by the spline function

$$S(t) = a_j\tau^3 + b_j\tau^2 + c_j\tau + d_j\,, \quad j\Delta t \le t \le (j+1)\Delta t\,, \qquad (31.17)$$
$$\tau = t - j\Delta t, \qquad j = 0, \ldots, N-1\,.$$

In this way, the functional

$$F[S] = p\int_0^{N\Delta t}\left[S''(t)\right]^2 \mathrm{d}t + \sum_{i=0}^{N} p_i\left[S(i\Delta t) - Y_i\right]^2\,, \qquad (31.18)$$
$$p \ge 0, \qquad p_i > 0$$

reaches its minimum. It should be emphasized that there exists a relation between parameter p of the above functional and mean square error ε (Kojdecki 2002) defined as

$$\varepsilon = \sqrt{\frac{1}{N+1}\sum_{i=0}^{N} p_i \left[Y_i - S(i\Delta t)\right]^2} \Bigg/ \sqrt{\frac{1}{N+1}\sum_{i=0}^{N} p_i Y_i^2} \quad . \tag{31.19}$$

This relation calculated for $p_i = 1$ ($i = 0, \ldots, N$) (Kojdecki 2002) by implementation of the falsi method (Flannery 1998) is shown in Fig. 31.7a. As one can see, the smoothing procedure generates an error by one order of magnitude greater for TAPS than for FORS-I.

The effectiveness of this method for improving the recording of rotation events by TAPS (in comparison with the method presented in Fig. 31.5b) is shown in Fig. 31.7b. For the spline function, the parameter p equal to 5×10^{-6} has been chosen as optimum for smoothing. It is high enough for rotational component smoothing without decreasing the really existing displacement component (see Fig. 31.7c) (Solarz et al. 2004). It should be noticed that rotational effects have been by one order of magnitude higher than the displacement ones. Such a situation is possible during laboratory

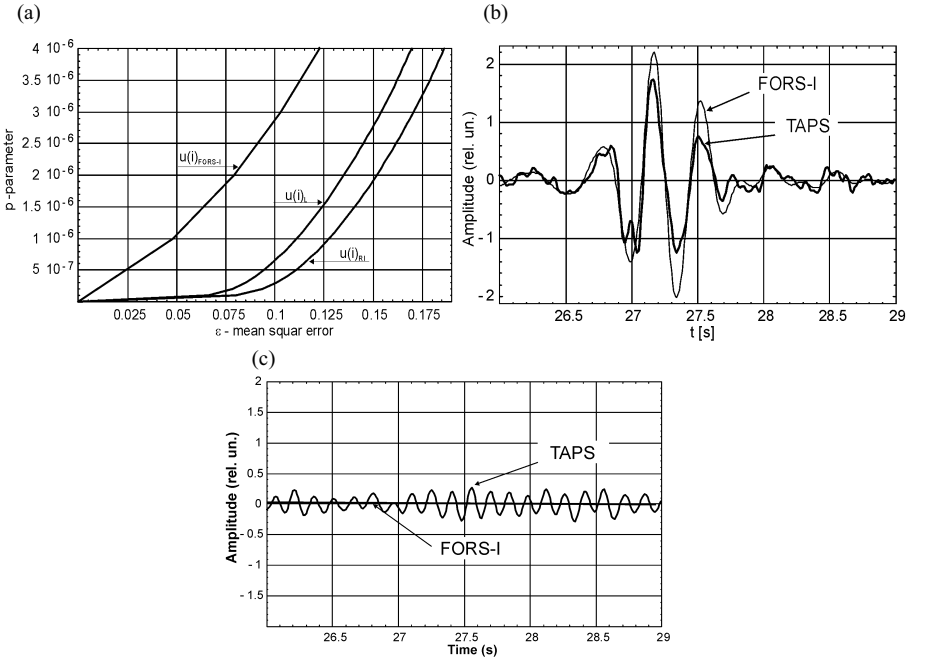

Fig. 31.7 (a) Dependence between the mean square error ε and parameter p for TAPS and FORS-I systems, (b) the rotational component recorded during the test presented in Fig. 31.5b after smoothing, and (c) additional displacement effect recorded by TAPS

tests only; in practice, the relation between these events is reversed (Bouchon and Aki 1982).

31.5.2 Usefulness of FORS for seismic rotational effects investigation

The results presented above have shown the usefulness of FORS-I in application to the standard rotational seismometer TAPS. Unfortunately, the data recorded in the period of 2002–2003 by the FORS-I at the Książ Seismic Observatory (Poland) during small earthquakes showed that this sensor has too small sensitivity to record SRE. For this reason, a new construction of a high-sensitivity fiber-optic rotational seismometer, named FORS-II, has been proposed (Jaroszewicz et al. 2005).

We will now briefly discuss the FORS-II system construction as well as its application for detection and investigation of SRE. It should be noticed that the presented analysis is based on the data obtained simultaneously by the FORS-II and the TAPS during the seismic events recorded between 18 August 2004 and 4 January 2005. On this ground, new aspects of the SRE are discussed.

Design of the fibre-optic rotational seismometer FORS-II

Figure 31.8 shows the FORS-II system representing again a classical fiber-optic gyroscope configuration (Jaroszewicz et al. 2005). Application of a

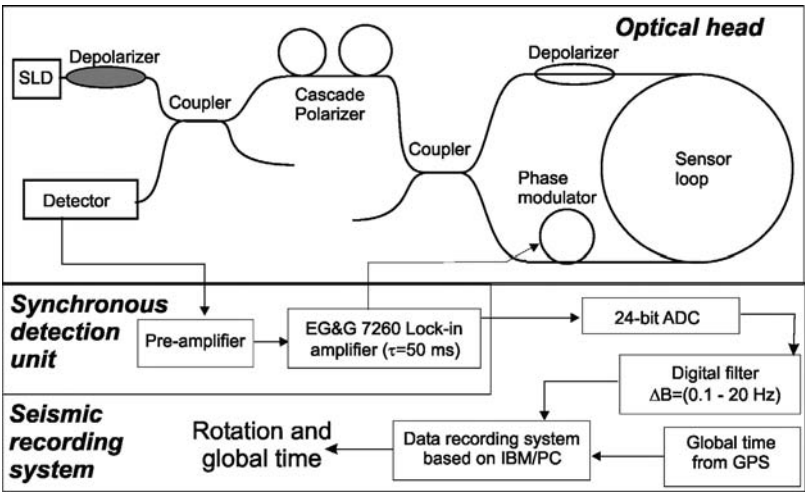

Fig. 31.8 General scheme of the FORS-II system

standard single-mode fiber 11,130 m long in 0.63 m diameter sensor loop, high optical power source (superluminescent diode, SLD, of 10.2 mW power and 35.1 nm spectral-band operating at 1285 nm) and the total optical loss equal to 21 dB gives a theoretical sensitivity of the system equal to 4.4×10^{-9} rad/s$^{1/2}$. Moreover, a cascade polarizer consisting of two fiber-optic polarizers (Phoenix Photonics of extinction ratio equal to 49 dB and 40.9 dB) and special loop wind for Shupe effect reduction (Xuhan et al. 2002) has been used for minimization of the drift phenomenon. Moreover, because the sensor loop is extremely long, the system operates on depolarized light, which allows to reduce the polarization influence on the output signal (Urlich 1994). For this reason, the system of two fiber depolarizers has been applied. One of them (Phoenix Photonics) with extinction ratio equal to 0.05 dB is placed behind the source. The second one is the sensor loop whose operation is equivalent to the depolarization for the applied wide-band source (Krajewski et al. 2005). The detection unit, based on lock-in amplifier 7260 (EG and G) realizes synchronic detection with optimization for frequency equal to 9.0 kHz (Jaroszewicz et al. 2005). The

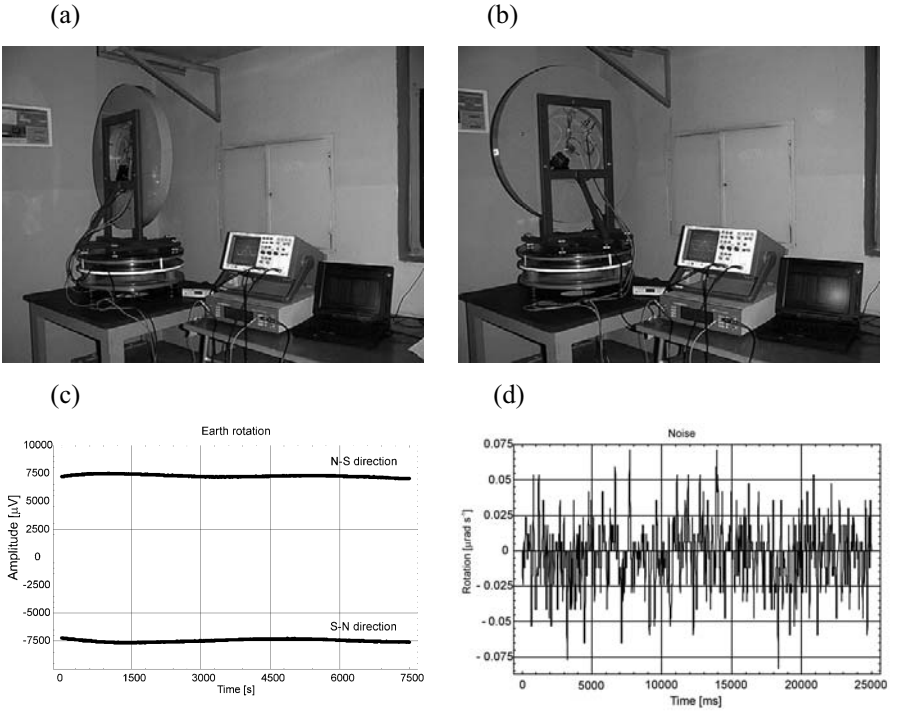

Fig. 31.9 (a) General view of FORS-II system during the calibration process: N-S direction, (b) the output signal for the Earth rotation rate measurement, (c) the system directed W-E, and (d) the measured noise level of the system

output signal is stored in IBM/PC by the seismic recording system, which contains 24-bit Sigma-Delta type ADC (with 2 μV resolution and input signal range ± 10 V). The recording system samples a signal with frequency of 1 kHz and after the re-sampling it stores the signal with the frequency f_s = 100 Hz. The digital filter included in the system provides a suitable band selection (from 0.1 to 20 Hz) for the frequency characteristic of the SRE (Teisseyre 2002). Additional system contains a clock synchronized by a DCF77 radio signal or by a GPS receiver for the precise global time recording (with 1 ms resolution).

The laboratory FORS-II investigation has confirmed the achievement of the required system sensitivity (Jaroszewicz et al. 2004). The system of calibration basing on the Earth rotation (Fig. 31.9a) indicates that the sensor used for measuring the Earth rotational component in Warsaw (i.e., 4.45×10^{-5} rad/s for latitude 52°20′) provides an output signal equal to 7500 μV, as shown in Fig. 31.9c. Because the noise level for the FORS-II directed E-W (Fig. 31.9c), i.e. the direction for which Earth component is zero, is 7.2 μV, the estimated FORS-II sensitivity is 4.27×10^{-8} rad/s (for 2σ) in the used 20 Hz detection band, as shown in Fig. 31.9d. The obtained sensitivity is two times worse than the theoretical one. This is caused mainly by inefficient depolarisation of light in the system.

Results of the SRE recording in Ojców

The FORS-II and a set of two TAPS have been installed in Ojców Seismic Observatory (see Fig. 31.10a) in order to record the SRE. The initial impact test showed that all the electronic channels of the seismic recording system give the same time delay, as shown in Fig. 31.10b (Jaroszewicz et

(a) (b)

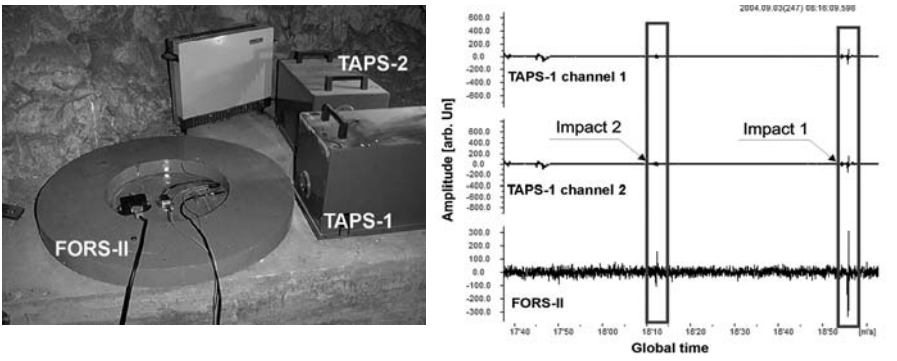

Fig. 31.10 (a) The FORS-II and a set of two TAPS in Ojców, (b) and seismogram of the impact test on 3 September 2004 at 08^h16^m

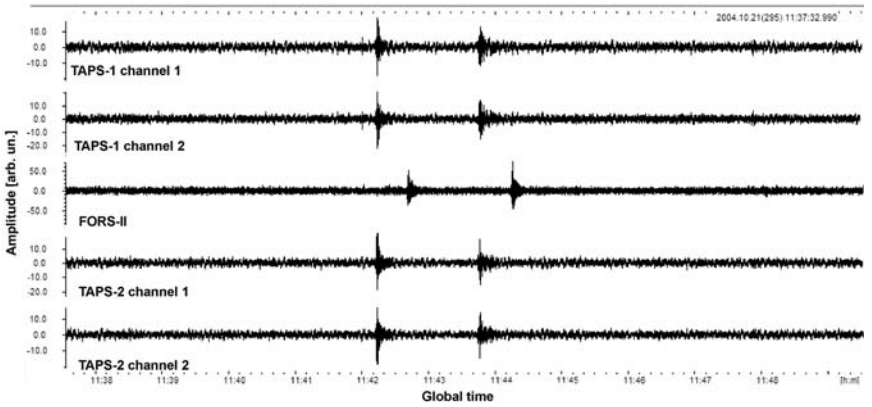

Fig. 31.11 Seismograms of the seismic events recorded on 21 October 2004 at 11^h37^m

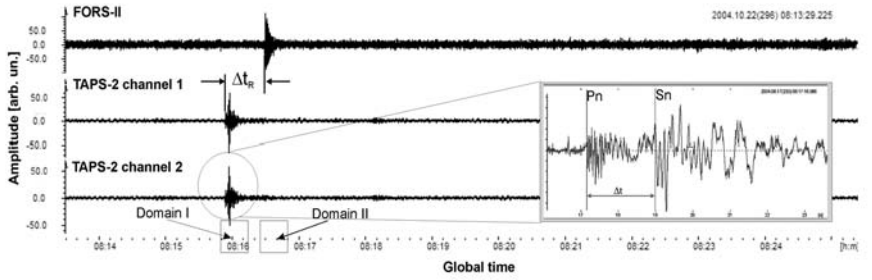

Fig. 31.12 Seismograms of the seismic events recorded on 22 October 2004 at 08^h13^m by FORS-II and the TAPS-2 with two domains selected for future considerations. Additional windows show the method of time delay identification between *S* waves (*Sn* line) and *P* waves (*Pn* line)

al. 2005). It should be noticed that only the FORS-II shows the rotational component in a direct way. The rotational components from the TAPS systems are calculated basing on the recorded linear motion by two channels, applying a suitable mathematical procedure, which is widely described in the previous paper (Solarz et al. 2004).

The data shown in Figs. 31.11 and 31.12 are examples of seismic events recorded in Ojców on 21 October 2004 at 11^h44^m and on 22 October 2004 at 8^h18^m, respectively. The source of these events is a quarry situated near Ojców. Because a set of two TAPS has been installed in Ojców (one perpendicular to the other), Fig. 31.11 presents five seismograms (two for TAPS-1, and two for TAPS-2, separated by FORS-II).

As one can see, all the recorded data resulting from the real seismic events show that the FORS-II has registered the SRE time delay (Δt_R) with respect to the characteristic linear motion of this earthquake registered by the TAPS channels, as shown in Fig. 31.12. The final results of the numerical processing (spline function approximation with $\varepsilon = 0.3$; Solarz et al. 2004) applied for the data presented in Fig. 31.12, oriented towards calculation of the rotational component by the TAPS, is shown in Fig. 31.13. In general, Fig. 31.13 concerns the data for two time domains of the seismic events shown in Fig. 31.12. Figures 31.13a, b, c have been obtained

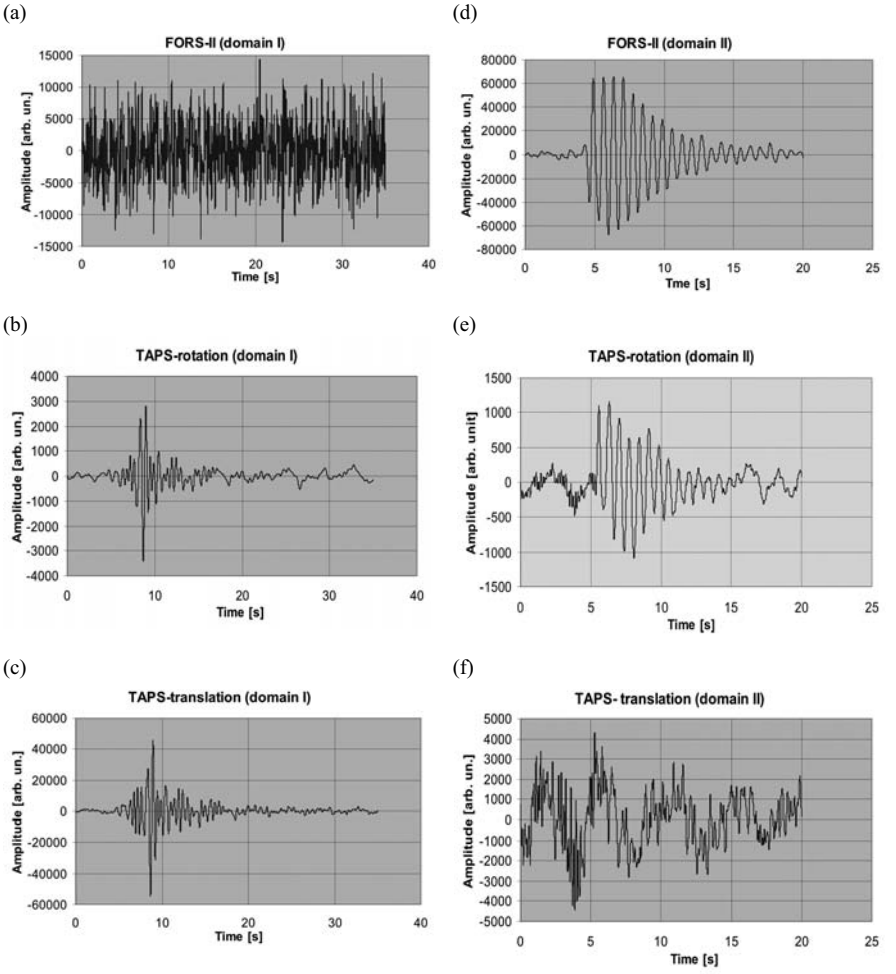

Fig. 31.13 Recognition of SRE by the TAPS-2 and FORS-II from the data presented in Fig. 31.12. Panels (a, b, c) for domain I; (d, e, f) for domain II

from the data from FORS-II and TAPS in domain I, i.e., at the moment when the TAPS registered the linear motion (40 s following $8^h15^m50^s$). Figures 31.13d, e, f present the calculations in the domain II, i.e., at the moment when the FORS-II recognized the rotation motion (25 s following $8^h16^m30^s$). Moreover, the calculated spectra of all the signals presented in Fig. 31.13 are shown in Fig. 31.14 with the same table structure as in Fig. 31.13.

An analysis of the above data shows that the rotational components recorded by the TAPS system in domain I (at $8^h15^m50^s$) are connected only with the system sensitivity to the linear motion (classic seismic waves). In these moments there exist strong translational components (Fig. 31.13c). Because the FORS-II has not recorded any rotation and the spectra of the rotational and translational components recorded by the TAPS have the

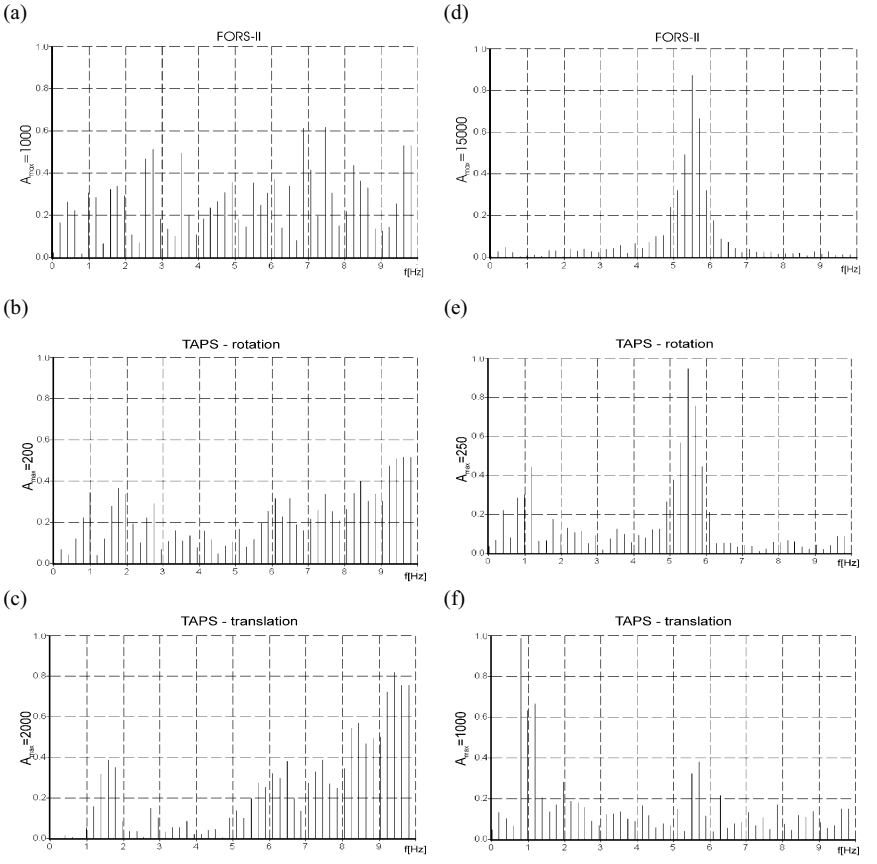

Fig. 31.14 Spectra of components of the seismic events presented in Fig. 31.13. Panels (a, b, c) for domain I; (d, e, f) for domain II

same frequency and amplitude characteristics (see Fig. 31.14b and c), the rotation calculated from the TAPS represents only the error related to different characteristics of the two channels (Jaroszewicz et al. 2003).

On the other hand, the numerical calculation performed using the data obtained in domain II (at $8^h16^m30^s$) reveals the existence of a rotational component in the FORS-II as well as in the TAPS records. In this region there does not exist a translational component (see Fig. 31.13f). Moreover, the characteristics recorded by the TAPS and the FORS-II are the same (also in the spectrum range – see Fig. 31.14e and f). On this ground we conclude that SRW exists only at this moment and its amplitude is contained in the range of 4×10^{-7} rad/s, as shown in Fig. 31.15.

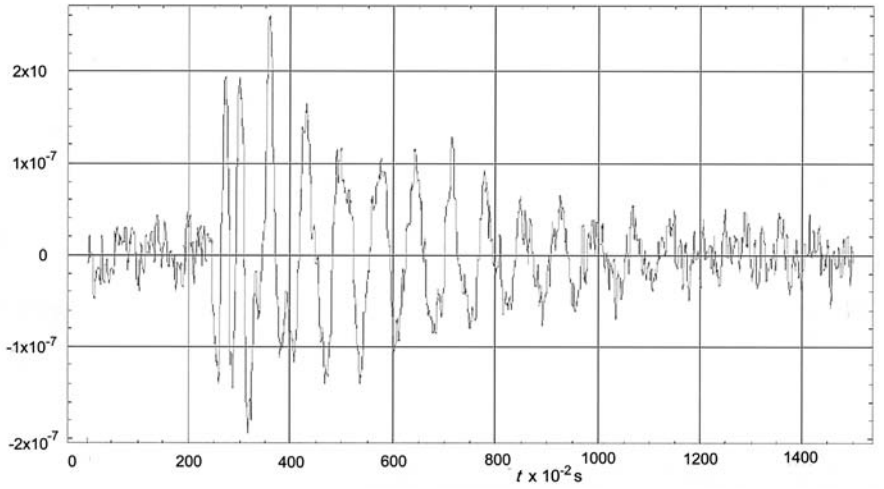

Fig. 31.15 Amplitude of the SRW calculated basing on the FORS-II recordings

31.6 Investigation of the SRE Propagation Velocity

The main conclusion to be drawn from the above results is that the SRE are seismic events which propagate with velocities different from the classical longitudinal or transversal seismic waves.

Because the seismic *S* waves have higher velocity than the *P* waves and both of them have different attenuation and frequency characteristics, the delay time between them (Δt – see windows in Fig. 31.12) may be used for calculating the distance from the seismic events epicentre as $L = 7.86\ \Delta t$. Additionally, for each recorded seismic event, the time delay Δt_R between the *P* waves and the SRE may also be calculated according to the scheme

shown in Fig. 31.12 (Jaroszewicz et al. 2005). The results of the above estimation for the SRE in the seismic events recorded in the Ojców seismic observatory are summarized in a graphical form in Fig. 31.16 as a dependence between the distance from the event epicentre and the time delay.

The data presented in Fig. 31.16 show the appearance of a linear dependence between the time delay Δt_R and the distance L from the seismic wave sources. Such results suggest the existence of a different velocity of SRE in comparison to the classical seismic waves (S or P types), which can be calculated from the following formula:

$$V_R = \frac{V^P L}{V^P \Delta t_R + L}, \tag{31.20}$$

where V^P is the velocity for the P waves, which (basing on Jeffreys-Bullen travel-time curves; Bullen 1963) is equal to 5500-5800 m/s for the seismic events from the Silesia mining region and 5900-6000 m/s for the Lubin mining region. For distant seismic events, V^P is equal to 8000-10,000 m/s. The results of the estimation of SRW parameters in the seismic events recorded in Ojców are summarized in Table 31.3. As one can see, for the near events (the Silesia or Lubin regions) the SRE velocity is contained within the range of 400 m/s , determined with the error δV_R estimated at 5-8%, while for the distant seismic events V_R it is of about 580 m/s with the measurement error of 1%. Unfortunately, we have not collected more representative data about the last events, so these estimates should be confirmed in future research.

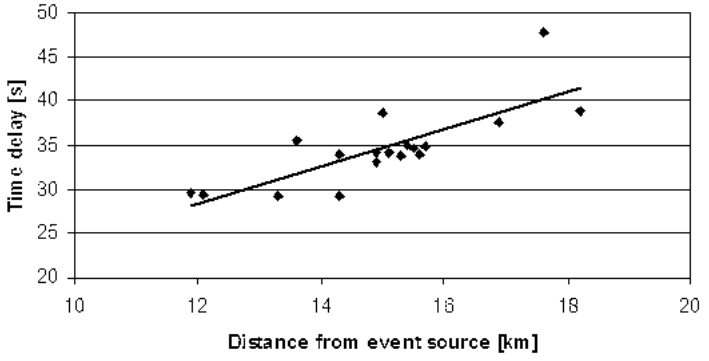

Fig. 31.16 Time delays *versus* the distance from the seismic event epicentre of the SRE for the data recorded in Ojców

Table 31.3 Parameters of the SRE calculated basing on the events recorded in the Ojców Seismic Observatory (Poland)

Initial time Year(Day)Time	V^P [m/s]	$\Delta t = \|Sn\text{-}Pn\|$ [s]	$L = 7.86\ \Delta t$ [s]	Δt_R [s]	V_R [m/s]	δV_R [%]
04 (230) 08:17:17.2[a]	5500	1.82	14.3	33.92	391.57	6.9
04 (232) 11:51:18.9[a]	5500	1.91	15	38.6	362.96	6.6
04 (232) 12:00:52.4[a]	5500	2.32	18.2	38.83	431.9	5.4
04 (238) 11:28:30.9[a]	5500	1.89	14.9	33.1	416.1	6.6
04 (239) 11:28:02.7[a]	5500	1.99	15.6	34	423.49	6.3
04 (239) 12:17:16.6[a]	5500	2.15	16.9	37.68	414.7	5.9
04 (243) 11:29:36.5[a]	5500	1.97	15.5	34.58	414.46	6.4
04 (247) 08:09:12.8[a]	5500	2.24	17.6	47.77	345.3	5.6
04 (247) 08:16:59.1[a]	5500	2.00	15.7	34.9	415.84	6.3
04 (260) 11:28:57.3[a]	5500	1.90	14.9	34.1	404.79	6.6
04 (264) 08:19:02.8[a]	5500	1.96	15.4	35	407.41	6.4
04 (260) 08:17:55.9[a]	5500	1.95	15.3	33.7	419.39	6.5
04 (273) 08:14:31.2[a]	5500	1.92	15.1	34.2	408.71	6.5
04 (274) 11:15:33.2[a]	5500	1.82	14.3	29.2	449.69	6.9
04 (295) 11:42:11.7[a]	5500	1.69	13.3	29.2	420.64	7.4
04 (295) 11:43:44.9[a]	5500	1.51	11.9	29.6	374.64	8.3
04 (296) 08:15.54.1[a]	5500	1.74	13.6	35.5	358.15	7.3
04 (296) 11:38.52.1[a]	5500	1.55	12.1	29.4	382.91	8.1
04 (364) 12:26.56.8[a]	5500	2.40	18	36	458.33	5.5
04 (366) 04:03.09.2[b]	5900	13.60	109	168	584.53	1
04 (366) 10:03.25.1[a]	5500	6.40	50	206	232.46	2
05 (003) 12:06.23.0[a]	5500	3.40	26	120	208.46	3.8
05 (003) 12:42.10.5[a]	5500	4.50	34	105	305.81	3
05 (004) 09:24.26.4[c]	10000	1017.80	8000	402	6658.6	0.7

[a] Seismic events from the Silesia mining region
[b] Seismic events from the Lubin mining region
[c] Seismic events from the Andaman region

The physical confirmation of different velocities of the SRE treated as seismic rotational waves in comparison to the classical ones may be performed basing on the theoretical work by Teisseyre et al. (2003), where the velocity of the SRE is estimated as $4\ \mu^*/\rho$. The recorded difference between V_R and V^P suggests that μ^* (rotation rigidity) is smaller than the μ rigidity. Such an approach opens a new area for investigation of the SRE as well as their role during the earthquakes.

31.7 Conclusions

The idea and the first experimental results of the fiber-optic loop interferometer application for detecting the SRE presented in this chapter are very

promising for several reasons. Firstly, the presented FORS system is designed to detect absolute rotation, which is probably impossible to realise in another way. It seems that the data obtained are clear for identification. Moreover, FORS is a system operating in real time, so it gives immediate information about such events, that is an additional advantage. Secondly, it can be used for investigation of other kinds of rotational seismometers, for example, the TAPS. The presented results have become an impulse for developing a new method of analysis of data recorded by the TAPS. This method, based on smoothing by the spline function, gives more clear results of rotational events measured by the TAPS system.

The FORS-II system is characterized by a sensitivity of 4.27×10^{-8} rad/s in 20 Hz detection band and it seems to be a very promising device for the rotational seismic events investigation, because it ensures detection of the absolute rotation, which is probably impossible to realize in other way. The data obtained by this sensor are clear for identification. In comparison to the laser ring rotational seismometer, the presented fiber-optic system is cheaper and easily moveable.

The results obtained in the Ojców seismic observatory are very promising. The data recorded simultaneously by the TAPS and the FORS-II during the earthquakes show that SREs propagate with different velocities than the longitudinal or shear seismic waves. It was shown that SRE are delayed in time in comparison to the classical seismic waves of earthquakes. Moreover, it has been evaluated that SRE connected with near seismic events have an amplitude of about 4×10^{-7} rad/s and velocity about 400 m/s. In the authors' opinion, the experimentally confirmed conclusions are the first reports touching this aspect of SRE nature. Unfortunately, the collected data are not representative for different types of earthquake sources and they are mainly limited to the near seismic events. In consequence, extension of this estimate for other seismic events should be confirmed in future research. We expect that by analogy to the Jeffreys-Bullen travel-time curves for classic seismic waves, the seismic rotational waves should present a similar dependence – different velocities depending on their distance and location in relation to the source of an event.

References

Arditty HJ, Lefevre HC (1981a) Sagnac effect in fiber gyroscopes. Optics Lett **6**: 401-403

Arditty HJ, Lefevre HC (1981b) Theoretical basis of Sagnac effect in fiber gyroscope. Springer Ser. in Optical Sciences **32**: 44-51

Aronowitz F (1971) The laser gyro. In: Ross M (ed) Laser Applications, vol. 1. Academic Press, New York, pp 133-200

Bouchon M, Aki K (1982) Strain, tilt, and rotation associated with strong ground motion in the vicinity of earthquake faults. Bull Seism Soc Am **72**: 1717-1738

Burns W (1994) Optical fiber rotational sensing. Academic Press, Boston

Cochard A, Schreiber U, Igel H, Flaws A, Bethmann F (2003) Observations and simulations of rotational motions recorded by a ring laser. EGS-AGU-EUG Joint Assembly 2003 (Nicea, France 7-11 April 2003) EAE03-A-13160

Cutler CC, Newton SA, Shaw HJ (1980) Limitation of rotation sensing by scattering. Opt Lett **5**: 488-450

Davis JL, Ezekiel S (1978) Techniques for shot-noise-limited inertial rotation measurement using a multiturn fiber Sagnac interferometer. Proc SPIE **157**: 131-136

Dorschner TA, Haus HA, Holz M, Smith IW, Statz H (1980) Laser gyro at quantum limit. IEEE J Quant Electronics **QE-16**: 1376-1379

Eubank RL (2000) Spline regression. In: Schimek MG (ed) Smoothing and regression: approaches, computation, and application. John Wiley & Sons Inc, New York, pp xix + 607

Ezekiel S, Arditty HJ (1982) Fibre optic rotational sensors and related technologies. Springer, New York

Jaroszewicz LR (2001) Polarisation behavior of different fiber-optic interferometer configurations under temperature changes. Opt Applicata **31**: 399-423

Jaroszewicz LR, Krajewski Z (2002) Possibility of fibre-optic rotational seismometer design. Proc SPIE **4900**: 416-423

Jaroszewicz LR, Krajewski Z, Solarz L, Marć P, Kostrzyński T (2003) A new area of the fiber-optic Sagnac interferometr application. International Microwaves and Optoelectronics Conference IMOC-2003, Iguazu Falls, Brazil, pp 661-666

Jaroszewicz LR, Krajewski Z, Solarz L (2004) The fibre-optic Sagnac interferometer application for recognition of the rotational seismic events. Proc SPIE **5459**: 272-280

Jaroszewicz LR, Krajewski Z, Solarz L, Teisseyre R (2005) Application of the FORS-II for investigation of the seismic rotation waves. Proc SPIE **5776**: 385-393

Killpatrick JE (1966) The laser gyro. IEEE Spectrum **67**: 44-55

Kojdecki MA (2002) Private communication, Warsaw

Krajewski Z, Jaroszewicz LR, Solarz L (2005) Optimization of fiber-optic Sagnac interferometer for detection of rotational seismic events. Proc SPIE **5952**: paper-32 (in press)

Lefevre HC (1993) Fiber optic gyroscope. Artech House, Boston

Lefevre HC, Arditty HJ (1982) Electromagnetisme des milieux dielectriques lineaires en rotation et application a la propagation d'ondes guides. Appl Optics **21**: 1400-1409

Lin SC, Giallorenzi TG (1979) Sensitivity analysis of the Sagnac effect optical -fiber ring interferometer. Appl Optics **18**: 915-931

Macek WM, Davis Jr DTM (1963) Rotation rate sensing with travelling wave ring laser. Appl Phys Lett **2**: 67-71

McLeod DP, Stedman GE, Webb TH, Schreiber U (1998) Comparison of standard and ring laser rotational seismograms. Bull Seism Soc Am **88**: 1495-1503

Meyer RE, Ezekiel S, Stowe DW, Tekippe VJ (1983) Passive-fiberoptic ring resonator for rotation sensing. Opt Lett **8**: 644-646

Moriya T, Teisseyre R (1999) Discussion on the recording of seismic rotation waves. Acta Geophys Pol **47**: 351-362

Nowożyński K, Teisseyre KP (2003) Time-domain filtering of seismic rotation waves. Acta Geophys Pol **51**: 51-61

Post EJ (1967) Sagnac effect. Rev Modern Physics **39**: 475-494

Press WH, Flannery BP, Teukolsky SA, Vetterling WT (1989) Numerical recipes in Pascal: The art of scientific computing. Cambridge University Press, Cambridge, pp 759 + xxii, http://www.nrcom.

Rosenthal AH (1962) Regenerative circulatory multiple-beam interferometry for the study of light propagation effect. J Opt Soc Am **52**: 1143-1148

Sagnac G (1913) L'ether lumineux demontre par l'effet du vent relatif d'Etherdanus un interferometre en rotation uniforme. Compte-rendus a l'Academie des Sciences **95**: 708-710

Shupe DM (1981) Fiber resonator gyroscope: sensitivity and thermal nonreciprocity. Appl Optics **20**: 286-289

Solarz L, Krajewski Z, Jaroszewicz LR (2004) Analysis of seismic rotations detected by two antiparallel seismometers: Spline function approximation of rotation and displacement velocities. Acta Geophys Pol **52**: 198-217

Teisseyre R, Suchcicki J, Teisseyre KP (2003) Recording the seismic rotation waves: reliability analysis. Acta Geophys Pol **51**: 37-50

Urlich R (1994) Polarization and birefringence effects. In: Burns WK (ed) Optical fiber rotation sensing. Academic Press Inc, New York, pp 31-79

Vali V, Shorthill RW (1976) Fiber ring interferometer. Appl Optics **15**: 1099-1100

Xuhan D, Xiaolin Z, Bingchu C, Guoguang Y, Kejiang Z, Chen L (2002) Quantitative analysis of the Shupe reduction in a fiber-optic Sagnac interferometer. Opt Eng **41**: 1155-1156

32 Design of Rotation Seismometer and Non-Linear Behaviour of Rotation Components of Earthquakes

Takeo Moriya[1], Roman Teisseyre[2]

[1]Graduates School of Science, Hokkaido University
e-mail: moriya@ep.sci.hokudai.ac.jp

[2]Institute of Geophysics, Polish Academy of Sciences
ul. Księcia Janusza 64, 01-452 Warszawa, Poland; e-mail: rt@igf.edu.pl

32.1 Introduction

Rotation component of seismic waves is one of the strain components (extension, rotation and twist-bend) caused by the seismic waves passing through the observation site. Our interests have been inspired by the fact that tombstones and small rigid bodies had been rotated after strong earthquakes. It is suggested that destruction of the buildings might be caused not only by a strong motion, but also by a strong dynamic strain. Takeo and Ito (1997) and Teisseyre (1973) have discussed the importance of rotation motions caused by the earthquakes. The conventional translation seismometers, however, cannot observe the rotation component of seismic waves. Therefore, rotation seismometer is required to investigate the nature of rotation components. There are many sensors to measure rotation movement, such as gyro-sensor (Henkel 1993), laser-gyro for car navigation and airplane control (e.g., GYROSTAR produced by Murta Ltd.). They are sensitive to pure rotation motion, but their sensitivity is too low to observe seismic waves. However, the very strong vibrations have been observed (Nigbor 1994). Hence, the gyro-sensor is useful as a calibrating tool. In this situation, we decided to design the rotation seismometer (Moriya and Marumo 1998, Moriya and Teisseyre 1999). Overcoming some difficulties, we were able to design and manufacture the rotation seismometer and observe local earthquakes at three observation sites where surface geological conditions were different.

32.2 Design of the Rotation Seismometer

We intended to measure not only the rotation component but also the twist-bend component (Moriya and Teisseyre 1999). We used two pairs of seismic translation sensors to obtain spatial differentiation of the seismic waves. The rotation component R around the normal axis is defined as

$$R = A - B \tag{32.1}$$

while the twist-bend component T is

$$T = A + B\,, \tag{32.2}$$

where $A = \frac{1}{2}\frac{\partial u_x}{\partial y}$, $B = \frac{1}{2}\frac{\partial u_y}{\partial x}$, and u_x and u_y are the horizontal spatial derivatives along east-west and north-south directions of the ground. To measure A and B, two seismic sensors have to be set at a small distance (22 cm). Then to obtain R and T, outputs A and B of the two pairs of sensors must be added and subtracted. The problem is, however, that the amplitude and phase characteristics of seismic sensors are not the same or at least similar enough for detecting the spatial differentiation. For this reason, many seismologists have abandoned the idea of measuring rotation component. We developed a technique to select the seismic sensors with the same amplitude and phase characteristics; moreover, by using electronic equalizer circuit we managed to obtain seismic sensors which have almost the same amplitude and phase characteristics.

32.2.1 Equalization of the sensors

Selection of the sensor

While constructing the rotation seismometer, a great difficulty is the lack of sensors whose characteristics, sensitivity, phase characteristics, coil resistance, and the like, would be perfectly the same. Out of many L22d seismometers (Mark Products Ltd.), we must select appropriate pairs, by comparing their sensitivities, and phase differences from observation of the microtremor spectrum. We tested about 60 of L22d seismometers and found that 1/4 of them have phase characteristics differing by less than 1 degree.

Equalization by electronic circuits

To reduce the small differences of the selected L22d instruments, the overdamping and integration method (Moriya et al. 1998a) was applied. The

strong over-damping is achieved by connecting to the negative input an impedance amplifier (Sakurai and Shimoda 1984), and applying negative and positive feedbacks to the operational amplifier. The integration is made by band-pass filter ($T_0 = 5.0$ s, $Q = 0.7$). The electric parts, resistors and condensers, are selected to be perfectly the same. The circuit diagram of the electronics is shown in Fig. 32.1. Figure 32.2 shows difference of spectra of microtremors observed by a single EW horizontal component sensor and subtraction component obtained by two EW translation sensors. The translation resonance frequency of 2.44 Hz of the laboratory building is canceled by subtraction, and the rotation resonance frequency of 2.60 Hz is preserved. Four L22d seismometers are set rigidly on the aluminum plate 11 cm apart from the center of the plate (Fig. 32.3). Therefore, the twist-bend component is observed through the rigidity of the aluminum plate. The rotation seismometers were calibrated by the spectrum comparison method with the gyro-sensor. Five-minute averaged spectra of two sensors were obtained by manual rotation of the sensors on the rotation table. Through this experiment, we confirmed that the rotation seismometer has a sensitivity for rotation velocity of 300 mV/deg·s^{-1} at 4 Hz, which is 8.91 dB higher than that of the gyro-sensor (Fig. 32.4). The equality of two rotation sensors was confirmed by comparing the spectra of microtremor (Fig. 32.5).

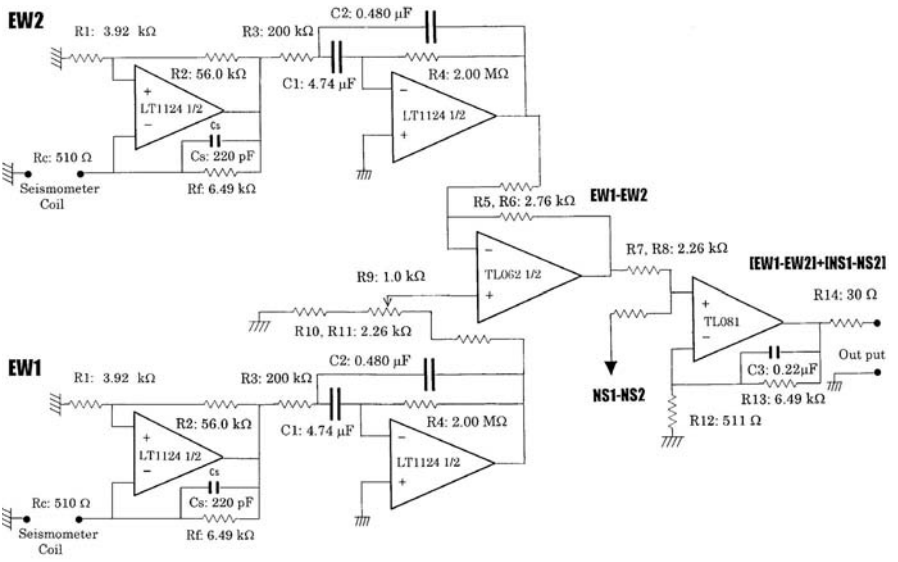

Fig. 32.1 Circuit diagram of negative input impedance and band-pass filter

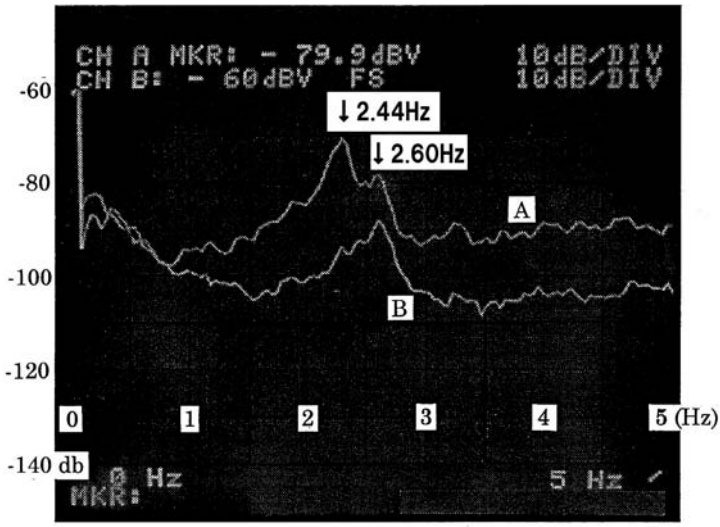

Fig. 32.2 Spectra of microtremor observed by single EW translation (A) and subtraction (B, amplified 22 dB) components by two EW sensors set apart 22 cm

Fig. 32.3 Photograph of three-axis rotation seismometers

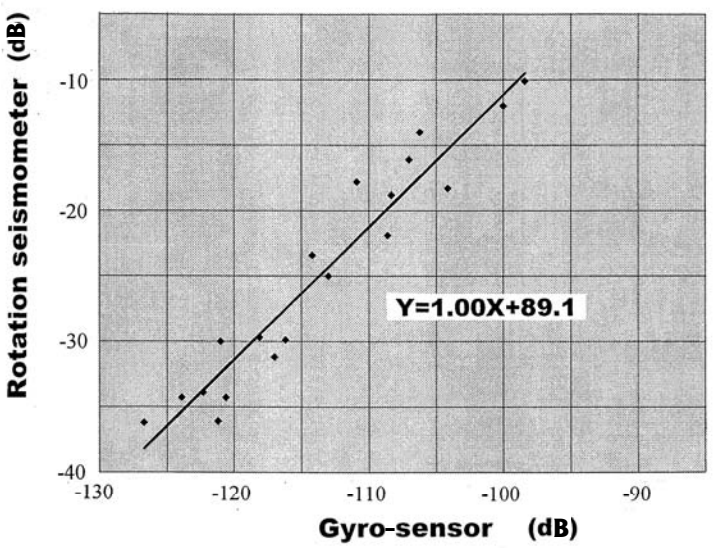

Fig. 32.4 Calibration of the rotation seismometer by comparison with gyro-sensor

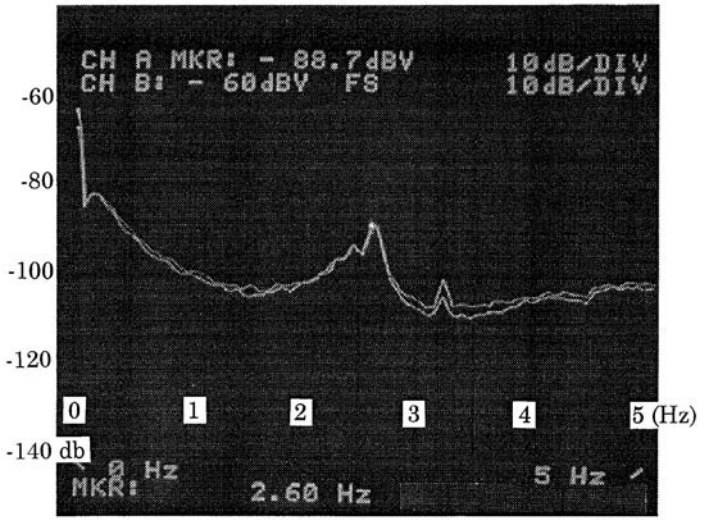

Fig. 32.5 A comparison of the spectra of microtremor observed by two rotation seismometers, showing two instruments have almost the same characteristics. A peak of 2.60 Hz is a rotational resonance frequency of the building

32.3 Absolute Rotation Component Amplitudes for Earthquakes Observed at Sites of Different Surface Geological Conditions

32.3.1 Temporary observation

To examine the absolute rotation amplitudes of earthquakes, we executed temporary earthquake observations at three stations. Observation sites were selected in places where the crustal structure has been investigated.

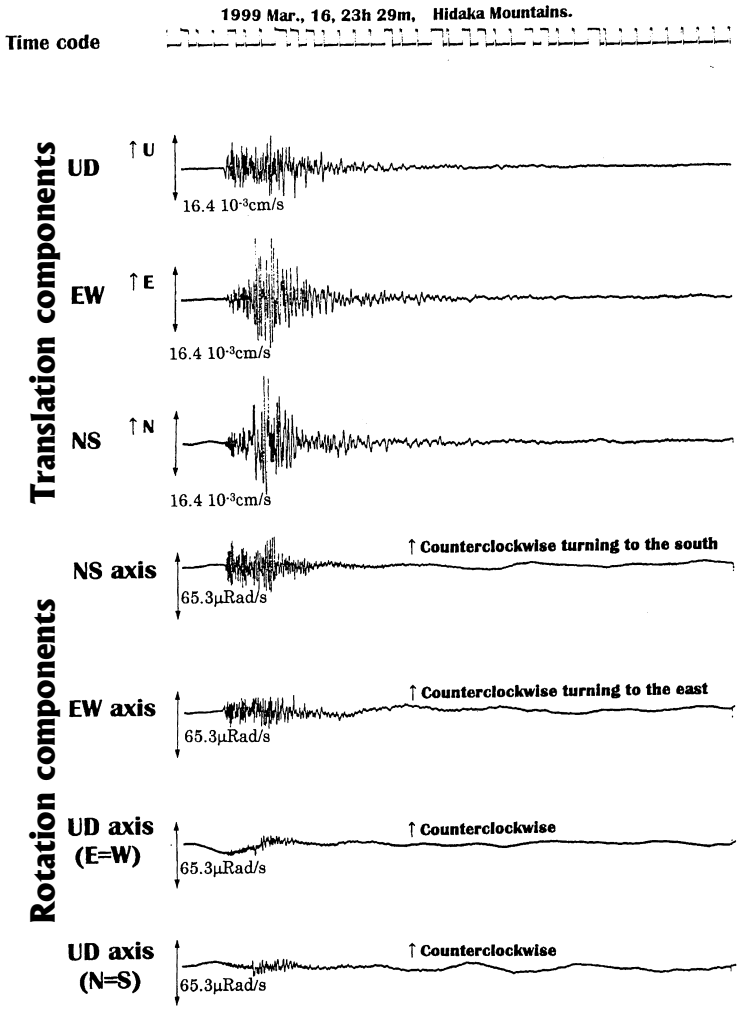

Fig. 32.6a Seismograms of earthquake which occurred in southern Hokkaido, observed by three translation and rotation seismometers

These were: Mitsuishi (MUJ), Obihiro (OBI), and Showa-Shinzan (SWZ) in Hokkaido. Station MUJ was situated on the foot of the Hidaka Mountains where the crusts of Northern Honshu and Kurile have collided, and the complicated structure was ascertained (e.g., Moriya et al. 1998b, Iwasaki et al. 2004). Station OBI was situated in the Tokachi plane where thick sedimentary layers have been developed. Station SWZ is situated very close to the Showa-Shinzan and Usu volcanoes and is covered by lava, where we observed volcanic earthquakes accompanied by the eruption of Usu volcano in March 2000. We used three components of translation and rotation seismometers. At MUJ, we tentatively recorded subtraction components (A and B of Eq. 32.1) of normal axis. Figures 32.6a, b and c show seven-component seismograms of two local and one distant

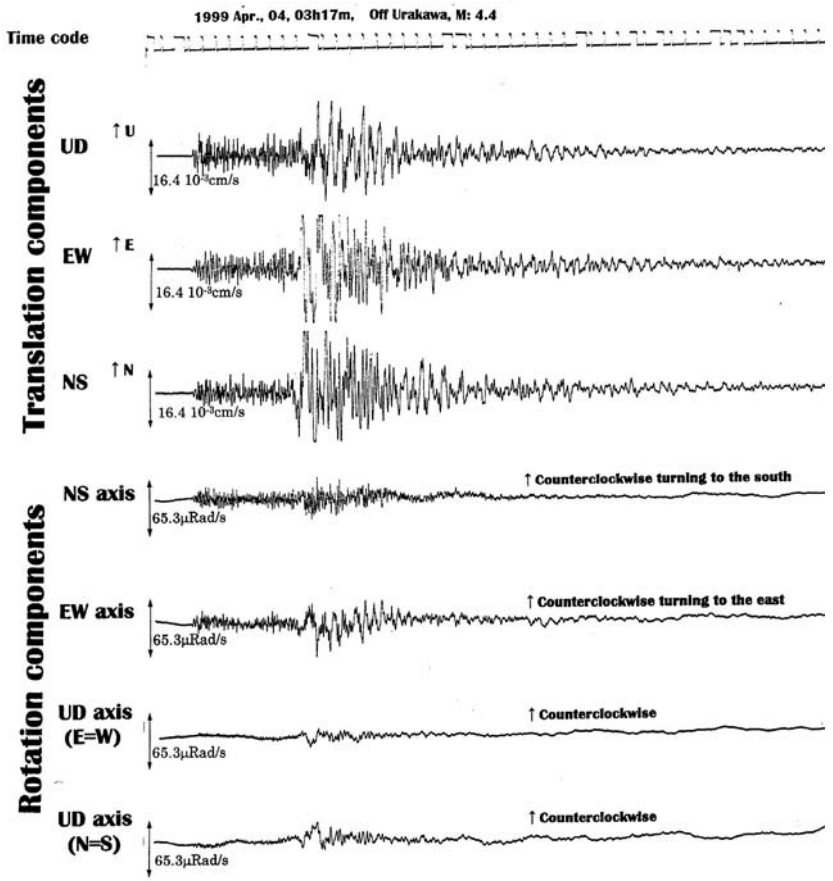

Fig. 32.6b Same as Fig. 32.6a, but for earthquake which occurred south off Hokkaido

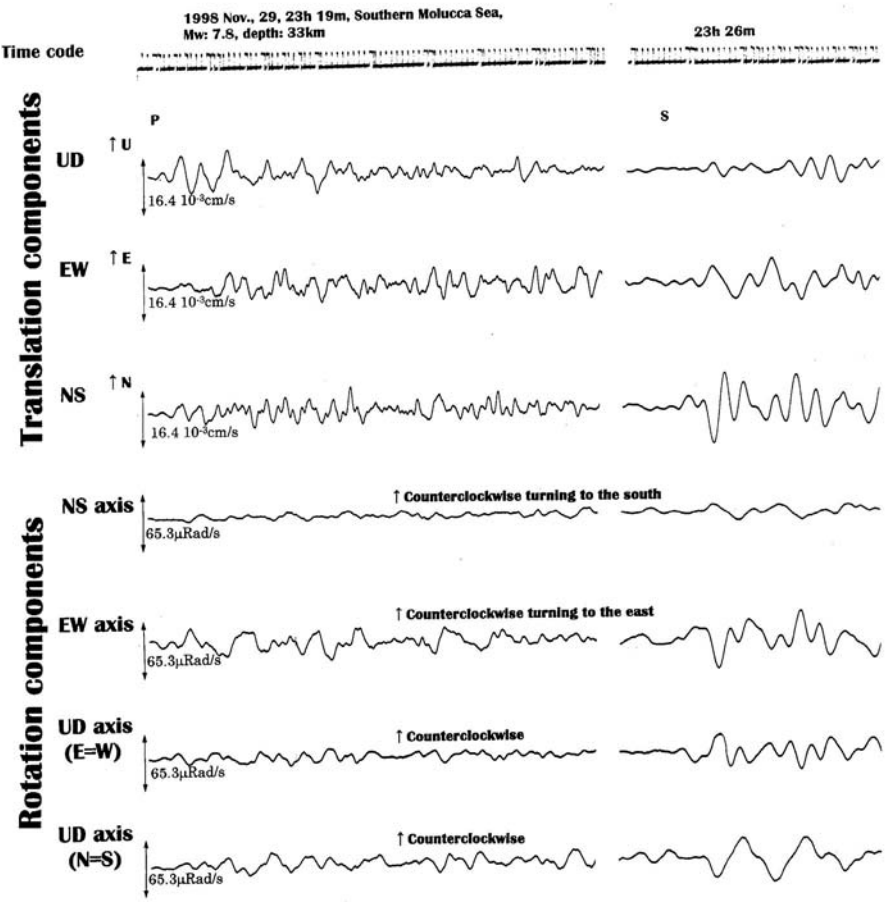

Fig. 32.6c Same as Fig. 32.6a, but for earthquake which occurred in Molucca sea

earthquake observed at MUJ. Subtraction traces (lower two traces in Figs. 32.6a, b and c) of seismograms, which correspond to A and B of (31.1) and (31.2), show slight differences between the two traces, suggesting the existence of twist-bend mode (Moriya and Teisseyre 1999); however, those differences are very small, almost at the level of critical values of the sensor's resolution.

32.3.2 Relation between amplitudes of translation and rotation components

From the seismograms obtained by temporary observations we inferred rough estimates of amplitudes of rotation velocity movements, which

amounted to several tens of micro radians per second for felt earthquakes (Japanese Standard Intensity of 1–2). To obtain a relation between amplitudes of translation and rotation observed at three stations, we read the maximum amplitude of seismograms. Figures 32.7a, b and c show relations between maximum amplitudes of translation and rotation of the same phases observed at the three stations – MUJ, OBI and SWZ. The absolute amplitudes of rotation component vary between 3 and 300 μrad/s; these values are very small, as expected. Apparently, rotation amplitude A_r and translation amplitude A_t are linked by the empirical relation

$$\log A_r = m \log A_t \tag{32.3}$$

We obtained the following values: $m = 1.4$ at MUJ, $m = 1.2$ at OBI, and $m = 0.84$ at SWZ. The relation suggests that on the site of complicated surface geology, m takes a large value. If the empirical relation holds in the range of very large intensities, 5-6 (Japanese Standard Seismic Intensity), the rotation amplitude could reach 0.3-3 rad/s. It is not clear whether the rotation amplitude of 0.3-3 rad/s is enough to make tombstones rotate, but a very strong rotation movement can occur when a very strong seismic wave shakes the ground. This means that the ground is distorted by a seis-

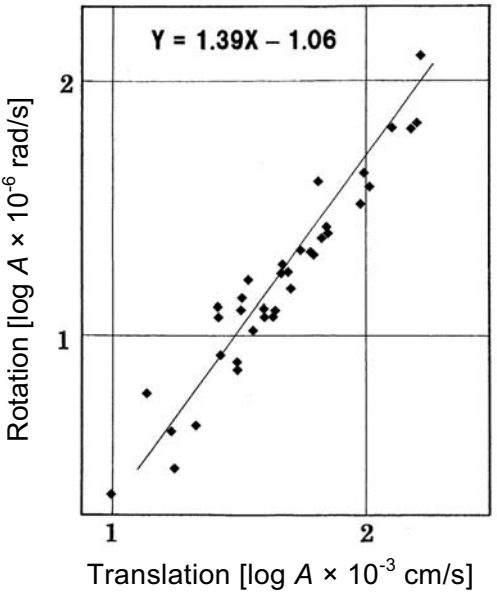

Fig. 32.7a Plots of amplitudes of rotation against translation of earthquakes observed at MUJ observatory

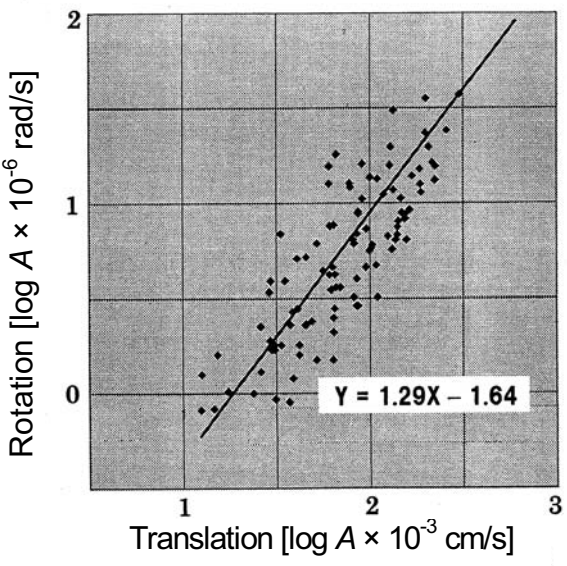

Fig. 32.7b Same as Fig. 32.7a, but for earthquakes observed at OBI observatory

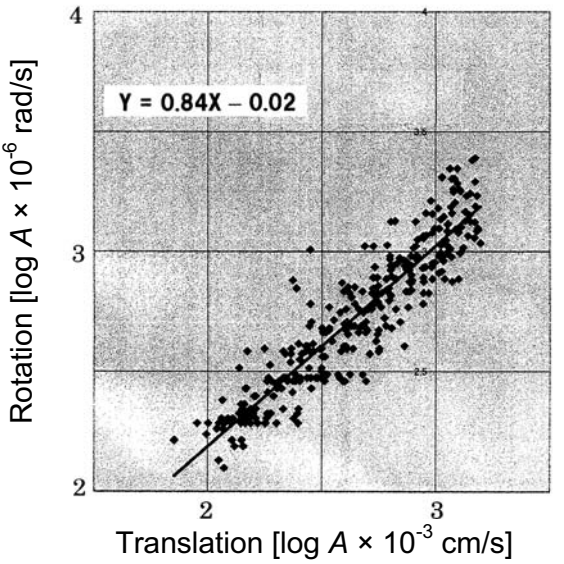

Fig. 32.7c Same as Fig. 32.7a, but for earthquakes observed at SWZ observatory

mic wave passing through. On a more complicated surface geology, the seismic wave generates stronger rotation strain. We have found that some tombstones and small constructions were rotated after a strong earthquake. Our observation suggests that rotation of the constructions by large earthquakes is not accidental. If empirical relation (32.3) is valid, *m* represents one of the parameters of inhomogeneity of the surface and shallow underground structure. Abrupt amplitude changes of translation components of propagating seismic waves have been thought to be caused by complicated and inhomogeneous structure. We think that the rotation amplitude corresponds to dynamic strain caused by seismic waves and is inversely proportional to wavelength; hence, parameter *m* is a new geophysical parameter to characterize the transmission of seismic waves in inhomogeneous media.

32.4 Results and Future Scope

We have demonstrated that our rotation seismic sensors are reliable and have high sensitivity for observing local and distant earthquakes. To confirm the validity of relation (32.3) for strong earthquakes, a strong motion rotation/twist-bend seismometer is required because the rotation seismometer designed here is saturated at about 3000 μrad/s. The strong motion rotation/twist-bend seismometer will become a tool for examining the relation between strain of the ground associated with strong earthquakes and the disaster, because a seismic disaster is caused not only by strong vibration, but also large dynamic strain of the ground.

References

Henkel SL (1973) Gyro-on-a-chip acts as Colioli's sensor. SENSORS: May, 6

Iwasaki T, Adachi K, Moriya T, Miyamachi H, Matsushima T, Miyashita K, Takeda T, Taira T, Yamada T, Ohtake K (2004) Upper and middle crustal deformation of arc-arc collision across Hokkaido, Japan, inferred from seismic refraction/wide-angle reflection experiments. Tectonophysics **388**: 59-73

Moriya T, Marumo T (1998) Design for rotation seismometers and their calibration. Geophys Bull Hokkaido Univ **61**: 99-106

Moriya T, Teisseyre R (1999) Discussion on the recording of seismic rotation waves. Acta Geophys Pol **47**: 4, 351-362

Moriya T, Okada H, Suqun L, Kon Y, Nakano O (1998a) Evaluation for the overdamping and integration method by a negative shunt resistance to prolong the

natural period of pendulum of the seismometer. Geophys Bull Hokkaido Univ **61**: 107-114

Moriya T, Okada H, Matsushima T, Asano S, Yoshii T, Ikami A (1998b) Collision structure in the upper crust beneath the southwestern foot of the Hidaka Mountains, Hokkaido, Japan, as derived from explosion seismic observations. Tectonophysics **290**: 181-196

Nigbor RL (1994) Six-degree-of-freedom ground-motion measurement. Bull Seism Soc Am **84**: 1665-1669

Sakurai K, Shimoda K (1984) Applied electronics. Shokabo, 1-358

Takeo M, Ito HM (1997) What can be learned from rotational motion exited by earthquakes? Geophys J Int **129**: 319-329

Teisseyre R (1973) Earthquake processes in a micromorphic continuum. Pure Appl Geophys **102**: 1, 15-28

33 Rotation and Twist Motion Recording – Couple Pendulum and Rigid Seismometers System

Jan Wiszniowski

Institute of Geophysics, Polish Academy of Sciences
ul. Księcia Janusza 64, 01-452 Warszawa, Poland
e-mail: jwisz@igf.edu.pl

33.1 Introduction

The measurement of rotation has been discussed by Aki and Richards (1980), who raised doubts as to the possibility of measuring rotation either by seismometers with mass in the center or by an array of seismometers (Saito 1968). In the latter case, the attention was drawn to the shallow heterogeneities in the Earth's structure.

There are several papers dealing with the rotation measurement, mainly relating to the near-source regions (Bouchon and Aki 1982, Nigbor 1994, Minoru 1988). Source-related rotations quickly decrease with distance. The measurements reported here concern rotation in the far-field, connected with seismic waves. The measurement of that rotation was dealt with by Smith and Kasahara (1969) or Saito (1968), mainly with the aim of separating the *SH* waves.

The aim of measurements with the use of sensors described here was not only to detect the *S*-wave rotation, but also to measure the proper rotations generated by seismic waves and rotations that propagate as waves (Moriya and Teisseyre 1999). Therefore, we used the pendulum sensors which are able to measure transient deformation related to seismic waves, yet sensitive enough to measure very small values.

The pendulum sensors are being used as tiltmeters. They are very well described by Dunkan (1986). They have been applied to the measurement of very slow rotations or very long seismic waves. In contrast to those measurements, we were interested in rotations of higher frequencies, covering the frequencies of seismic waves. Hence, the main problem was how to distinguish the signal due to rotation from that due to straight-line vibrations.

33.2 Behaviour of a Pendulum Seismometer During Measurement of Rotations – Static Approach

Figure 33.1 shows a schematic of a simple pendulum electromagnetic seismometer discussed in this chapter. The pendulum moves relative to the seismometer's enclosure in the plane of the diagram. Additionally, we show the centre of inertia of a simple pendulum, which will be useful for our further analysis. In seismometry, the operation of seismometer is usually discussed with the help of a simple (mathematical) pendulum model, in which the mass is reduced to one point (Bullen and Bolt 1985, Aki and Richards 1980). Such an approach is sufficient when we study a simple, linear movement and the rotation is measured by many seismometers. In the next section we will describe a seismometer employing a compound pendulum model.

Movements in all the figures are seen from an inertial coordinate system, relative to which the earth rotates.

Figure 33.2 shows the mechanism of movement of a seismometer with a simple pendulum. The following elements are considered: the pivot of the

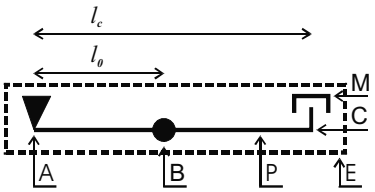

Fig. 33.1 Schematic of simple pendulum electromagnetic seismometer; l_0 is the reduced length of pendulum, l_c is the length of pendulum from its pivot to the coil. The seismometer consists of: pendulum P, pivot (axis of rotation) A, magnet M, coil C, mass center B and enclosure E

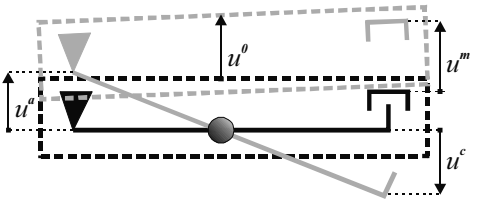

Fig. 33.2 Motion of units of a simple pendulum seismometer; u^a is the displacement of the pivot of seismometer, u^0 is the displacement of the enclosure of seismometer at the point of reduced length of pendulum, u^m is the displacement of the magnet, and u^c is the displacement of the coil. Grey colour refers to the seismometer after displacement

pendulum with displacement u^a, and magnet with displacement u^m, both rigidly fixed to the enclosure, and the pendulum with a coil which is movable relative to the enclosure.

$$u^m = u^a + l_c \varphi , \tag{33.1}$$

where φ is the rotation of the Earth's surface and thereby the seismometer. We have denoted rotation by symbol φ to make it distinct from the rotation γ as used by Teisseyre *et al*. (2003a), since we treat seismometer's parts as rigid bodies. The displacement and rotations are treated as very small.

The centre of inertia of a simple pendulum does not move. The reduced length of the pendulum counted from the pendulum's pivot is denoted by l_0. The pendulum's coil is movable. This movement is related to the movement of the pivot through the relation

$$\frac{u^c}{l_c - l_0} = \frac{u^a}{l_0} , \tag{33.2}$$

where u^c is the displacement of coil.

The seismometer records the coil displacements U relative to the magnet:

$$U = u^m + u^c . \tag{33.3}$$

Substituting Eqs. (33.2) and (33.1) to (33.3) we obtain the formula for the signal recorded by the seismometer, composed of the rotational component and displacement,

$$U = \frac{l_c}{l_0}\left(u^a + l_0 \varphi\right). \tag{33.4}$$

A similar formula was presented by Moriya and Teisseyre (1999). The seismometer records displacement of the pivot of the pendulum and rotation.

It is also possible to present a formula for recording the displacement component alone, without rotation. Provided that changes of the stress tensor along the seismometer pendulum are negligible, we may assume that

$$u^0 = u^a + l_0 \varphi , \tag{33.5}$$

where u^0 is the displacement in the point of inertia centre, and we get

$$u^0 = \frac{u^a \left(l_c - l_0\right) + u^m l_0}{l_c} . \tag{33.6}$$

Using Eqs. (33.1), (33.4) and (33.6), we obtain

$$U = \frac{l_c}{l_0} u^0 \,. \tag{33.7}$$

The pendulum seismometer is then equivalent to a seismometer with straight-line movement of inertial mass placed in the centre of inertia of a simple pendulum.

In the next section we will describe the measurement by a pair of seismometers where the position of seismometers will mean the position of inertial mass of seismometer pendulum. The main problem is how to obtain rotation signal by eliminating the linear motion. Both seismometers will record velocity.

33.3 Measurement of Rotations by a Pair of Seismometers – Influence of Seismic Waves on Signal

We expect from the rotation recording instruments to be able to measure both the linear motions and proper rotation. At the same time we are aware of the fact that the seismometers in pairs are excited by linear vibrations of both the rotation-free *P* waves and the rotation-bearing *S* waves, and perhaps also the proper rotation waves.

The principle of the rotation measurement is the following: two sensors record ground motions of velocities v_{g1} and v_{g2}, which differ from each other, and then the linear signal is eliminated by using the calculated difference in the signals recorded by these seismometers. These signals contain both linear and rotational vibrations. At first we assume that the instrument' responses are ideally the same. The effect of differences in responses will be analysed in the next section.

We assume that the two seismometers are located at opposite sides in a continuous elastic medium penetrated by plane seismic *P* and *S* waves (Fig. 33.3). The angle between the *P*-wave direction and the line of seismometers is α (Fig. 33.3a).

The second seismometer is shifted by vector $\delta\mathbf{x} = (\delta x, \delta y, \delta z)$ relative to the first one (for instance, in Fig. 33.3 we have $\delta z = 0$). We assume that this vector is relatively small. The velocity increment $\delta\mathbf{v}$ between the two seismometers is

$$\delta\mathbf{v} = \left(\delta\mathbf{x} \cdot \nabla\right)\mathbf{v} \,. \tag{33.8}$$

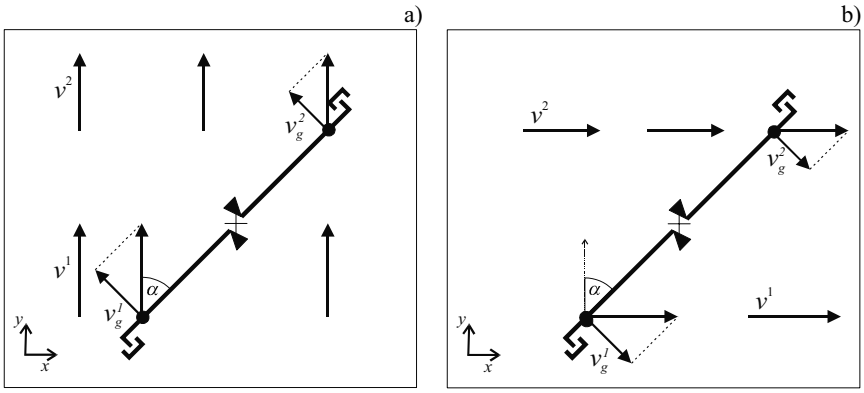

Fig. 33.3 Excitation of the pair of seismometers by *P* waves (a) and *S* waves (b). Notation: v^1 – ground motion velocity for the first seismometer, v_g^1 – the component of vibrations acting on the first seismometer, v^2 – ground motion velocity for the second seismometer, v_g^2 – component of vibrations acting on the second seismometer, α – the angle between the seismometer pair and the direction of the arriving wave. The wave travels in the *y* direction, and the particle vibrations are in the *y* direction for the *P* wave and *x* for the *S* wave

The pendulums of the two seismometers move in the direction described by versor $\mathbf{n}_g$, so the velocity recorded by the seismometers is

$$v_g = \mathbf{v} \cdot \mathbf{n}_g \,. \tag{33.9}$$

In the pair of seismometers positioned for the rotation measurement, the direction of seismometer's motion is perpendicular to the seismometers line, hence

$$\delta\mathbf{x} \cdot \mathbf{n}_g = 0 \,. \tag{33.10}$$

For two ideal seismometers, the velocity difference is

$$\delta v_g = \left(\delta\mathbf{x} \cdot \nabla\right)\mathbf{v} \cdot \mathbf{n}_g \,. \tag{33.11}$$

For the *P* wave from Fig. 33.3a, the measured signal will be

$$\delta v_g = \frac{1}{2} L \sin 2\left(\alpha \frac{\partial v_y}{\partial y}\right), \tag{33.12}$$

where $L = |\delta\mathbf{x}|$ is the distance between the mass centers of the mathematical pendulums. For a sine wave, we have

$$\left|\delta v_g\right| = \frac{\pi L |v|}{\lambda} \sin 2\alpha \,, \tag{3.13}$$

where λ is the wavelength. This means that the difference in signals from the two seismometers will be nonzero also for non-rotational waves. It will depend on the angle at which the wave arrives. This difference will be zero for waves coming from the direction of seismometers line and perpendicular to it. The value measured by the pair of seismometers corresponds to the compressional deformations when the rotation is zero.

For the *S* wave (Fig. 33.3b) the measured value of the signal will be

$$\delta v_g = L\cos^2(\alpha)\frac{\partial v_x}{\partial y}\,. \tag{33.14}$$

In this case the term $\partial v_x/\partial y$ corresponds to rotation. For the *S* wave the value of the rotation measurement depends on the direction and is correct only for the wave coming from the direction of seismometers line. For the wave coming perpendicularly to it, nothing should be recorded.

If we use two pairs of seismometers, the second pair being rotated by 90° relative to the first one, then the sum of differences defined as rotation *R* by the formula (Teisseyre et al. 2003b)

$$R = \frac{\delta v_g^1 + \delta v_g^2}{2} \tag{33.15}$$

is

$$R = \frac{1}{4}L\sin(2\alpha)\frac{\partial v_y}{\partial y} + \frac{1}{4}L\sin\big(2\,(\alpha+90)\big)\frac{\partial v_y}{\partial y} = 0\,, \tag{33.16}$$

for the *P* wave from Fig. 33.3a, and

$$R = \frac{1}{2}L\cos^2(\alpha)\frac{\partial v_x}{\partial y} + \frac{1}{2}L\cos^2\big(\alpha+90\big)\frac{\partial v_x}{\partial y} = \frac{1}{2}L\frac{\partial v_x}{\partial y}\,,$$

for the *S* wave from Fig. 33.3b.

Generally speaking, on the basis of relations (33.10), (33.11) and (33.15), for the four seismometers positioned in the above manner, we obtain $R = \frac{1}{2}L\mathbf{n}_s \cdot \operatorname{rot}\mathbf{v}$, where $\mathbf{n}_s$ is the normal to the plane at which the seismometers are located. For the example of Fig. 33.3 this gives the following value:

$$R = \frac{1}{2}L\left(\frac{\partial v_x}{\partial y} - \frac{\partial v_y}{\partial x}\right). \tag{33.17}$$

It follows from the above that the sum of signals from the ideal four seismometers is zero for the *P* waves and corresponds to the *S*-wave rotation regardless of the direction the waves arrive.

Twist is defined as a difference in the signals from the seismometer pairs (Teisseyre et al. 2003b)

$$T = \frac{\delta v_g^1 - \delta v_g^2}{2} . \tag{33.18}$$

For the *P* wave the twist will be

$$T = \frac{1}{4} L \sin(2\alpha) \frac{\partial v_y}{\partial y} - \frac{1}{4} L \sin\left(2(\alpha + 90)\right) \frac{\partial v_y}{\partial y} = \frac{1}{2} L \sin(2\alpha) \frac{\partial v_y}{\partial y} , \tag{33.19}$$

while for the *S* wave it will be

$$T = \frac{1}{2} L \cos^2(\alpha) \frac{\partial v_x}{\partial y} - \frac{1}{2} L \sin^2(\alpha) \frac{\partial v_x}{\partial y} = \frac{1}{2} L \cos(2\alpha) \frac{\partial v_x}{\partial y} .$$

In general, for the waves in Fig. 33.3 we have

$$T = \frac{1}{2} L \sin(2\alpha) \left(\frac{\partial v_y}{\partial y} - \frac{\partial v_x}{\partial x} \right) + \frac{1}{2} L \cos(2\alpha) \left(\frac{\partial v_x}{\partial y} + \frac{\partial v_y}{\partial x} \right) . \tag{33.20}$$

For both, the *P* and *S* waves, the value of *T* depends on the direction α of the wave arrival.

Let us now consider a more general case. The seismometers are placed at edges of a regular polygon of side length *L*. Figure 33.4 shows such a distribution for a square. According to the Stokes formula, if we assume that for each side

$$L v_g = \int_L \mathbf{v} \mathrm{d}\mathbf{l} , \tag{33.21}$$

and that the polygon surface is relatively small and rotation can be treated as constant, we obtain

$$\mathrm{rot}\, \mathbf{v} = \frac{L}{A} \sum_{i=1}^{N} v_g^i , \tag{33.22}$$

where v_g^i is the velocity measured by the *i*-th seismometer, *N* is the number of sides, and *A* is the surface area. For the four seismometers from Fig. 33.4 the rotation is

$$\mathrm{rot}\, \mathbf{v} = \frac{1}{L} \sum_{i=1}^{4} v_g^i . \tag{33.23}$$

Hence, the sum of signals from the four evenly distributed seismometers corresponds to rotation of ground motions, in accordance with (33.17).

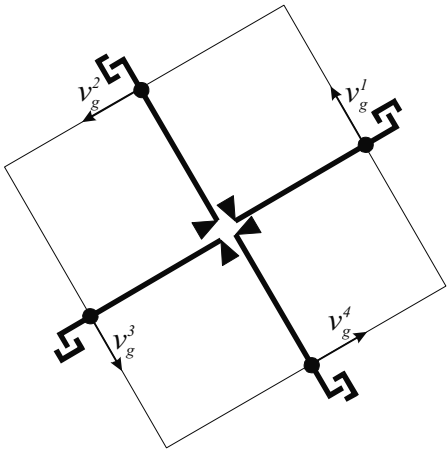

Fig. 33.4 System of four seismometers; rotation is calculated on the periphery of the square

For the measurement of rotation it is enough to have three seismometers in a triangle; however, in order to ensure the fulfillment of assumption (33.21) and because of differences in the seismometr's responses, it is better to use a greater number of seismometers distributed on a regular polygon. When the distribution is arbitrary, we must use scaling coefficients. Saito (1968) uses coefficients that minimize the difference between $\partial/\partial x$ and coefficients.

Instead of a great number of seismometers, we can use a Sagnac interferometer (Jaroszewicz et al. 2001, and McLeod et al. 1998), where a pulse of light is sent in opposite directions around a circular loop and the difference in time (Δt) of the pulse arrivals is measured. It amounts to

$$\Delta t = \oint \frac{\mathrm{d}\mathbf{r}}{c+v} - \oint \frac{\mathrm{d}\mathbf{r}}{c-v} = \oint \frac{\boldsymbol{\nu}\mathrm{d}\mathbf{r}}{c^2-v^2} \approx \frac{A}{c^2}\mathrm{rot}\,\boldsymbol{\nu}\,, \tag{33.24}$$

where c is the speed of light.

The above analysis gives grounds for concluding that it is improper to determine rotation on the basis of seismometer pair, since we do not have any information on the motion parallel to the seismometer pair. Still, the measurement of rotation by a pair of seismometers can be made when the seismometers are placed on a rigid body.

For measurements described by Teisseyre et al. (2003a), a double-pendulum seismometer in one trunk (Fig. 33.5) was applied. The problem how

the continuous medium affects a rigid body is complicated and disputable. The solid body is treated as part of the continuous medium for which the deformation tensor is zero (Aki and Richards 1980). It is a problem of discussion how the body affects the continuous medium. If the solid body is part of a continuous medium, then the instrument base rotates by the angle

$$\omega = \frac{1}{2}\left(\frac{\partial v_x}{\partial y} - \frac{\partial v_y}{\partial x}\right)$$

(Smith and Kasahara 1969); the other option is to assume that the interaction takes place through elastic support points. At the same time, the cavity in which the sensor is placed has an influence on the creation of various vibrations, including rotational ones (Dunkan 1986, Harrison 1976). We assume that the excitation of the solid body of the sensor takes place through the support points. The problem of connection with the basement applies to the Sagnac interferometer too.

The construction shown in Fig. 33.5 is fixed to the ground in three points. It is a solid body stimulated through the support points. In such a situation, in order to ensure the recording of rotation of seismic waves regardless of their arrival angle, these points must be evenly distributed relative to the mass center. The sensors used for the measurement of rotation and twist waves have the support points in the shape of a plane triangle, which makes the signal dependent on the wave direction. In such a case, in order to measure rotation we need two such sensors, yet the measurement of twist (33.18) by those two sensors is then possible**.** In the next sections, the seismometer pair and the rigid seismometer will be treated as rigid bodies.

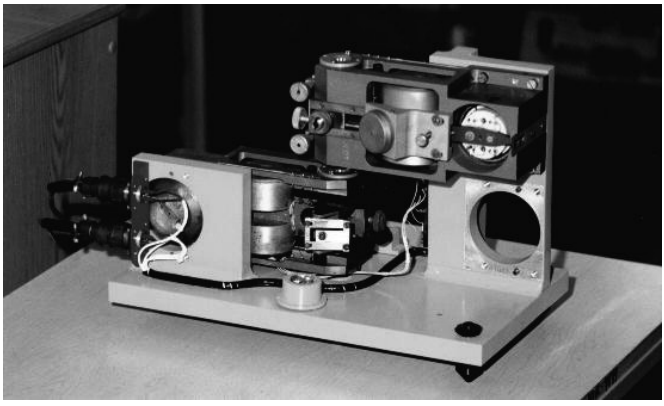

Fig. 33.5 Double pendulum horizontal electromagnetic seismometer

33.4 Influence of Small Differences in Channel Responses on Rotation Measurement – Dynamic Approach

The two-seismometer system can measure rotation, provided that the response functions of the two pendulums are the same. Unfortunately, the responses of seismometers and recording channels are not the same.

In the recording path, we can specify the following elements: sensor (seismometer) S, analogue amplifiers-filter F, sampling device P, analog -digital converter A and digital filters D. In fact, we can vary only the recorded digital signals c_1 and c_2 , so that

$$c_i = v^g{}_i \circ S_i \; F_i \circ P_i \circ C \circ D = v^g{}_i \circ H_i \,. \tag{33.25}$$

Elements S, F, P, C, D are dynamic, so sign $\circ$ means convolution in time domain as well as multiplication in the frequency or S (Laplace transform) domain.

Digital filters are identical by assumption. The analog-digital converter is one for all channels in the applied recording device. These two elements can be ignored. Responses of the remaining parts have an influence on the difference of channels. Additionally, noise of seismometers and recording device adds to error of difference. As a result, the difference of signals (33.25) is

$$\begin{aligned} \delta c = A \circ D \circ (S_1 \circ F_1 \circ P_1 - S_2 \circ F_2 \circ P_2) \circ v^g \\ + A \circ D \circ S \circ F \circ P \circ L\,\dot{\varphi} + e = c^{err} + c^R + e \,, \end{aligned} \tag{33.26}$$

where e is the noise of recording device, c^R is the signal from rotation recorded by the device, and c^{err} is the linear motion that was not eliminated because of differences of seismometers. A large value of c^{err} precludes a correct determination of rotation, so the most important problem is to translate the signals so as to make this value very small, or to separate frequencies of large c^{err} from frequencies of $\dot{\varphi}$.

33.4.1 Differences in seismometer responses

We adopt a standard seismometer model, in which the dependence of voltage E_s on ground motion frequency is given by the formula

$$E_s = S(s)\,v = \frac{s^2 G_s}{s^2 + 2s\omega_0\alpha_0 + \omega_0^2}\,v \,, \tag{33.27}$$

where G_s is the electromotive constant of the main coil, ω_0 is the circular frequency of free vibrations, and α_0 is the damping coefficient.

When the recording is made by two seismometers, coefficients in Eq. (33.27) will have different values. In the sensors, we used pendulums of seismometers SM-3. The coefficients of the two seismometers were the following: $G_s \approx 135$ Vs/m, $\omega_0 \approx 2\pi/1.5$ Hz, $\alpha_0 \approx 0.7$.

In the classical operation of seismometers, while the linear vibrations are measured, it is enough for the coefficients of seismometers to differ by no more than 5%. Such an error is too high for rotation measurements.

To eliminate the linear component from the recorded signal, it is not enough to correct the gain G_s. The response of the signal created by difference of the values recorded by sensors whose free periods and damping differ by 5% is shown in Fig. 33.6. The gain was assumed to be 1. We see that the difference for channels for which the damping and free period differ by only 5%, may produce a signal that is only 20 times smaller than the linear signal coming into the sensors. This means that signal $C_{err} \approx 0.05 C_r$ may be much higher than $L\, C_{rr}$ and will jam the rotational signal.

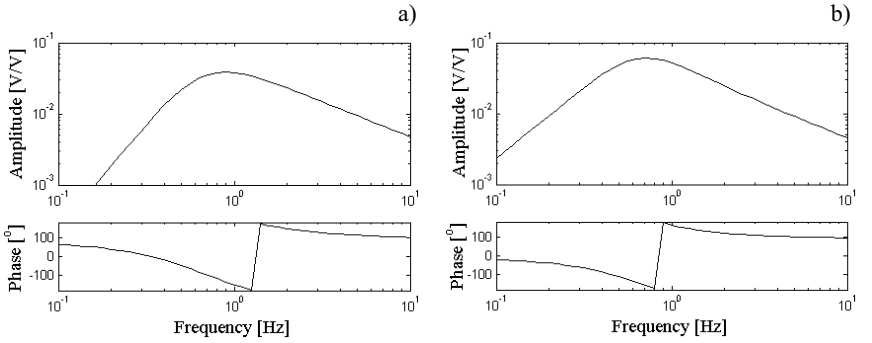

Fig. 33.6 Differences in responses of seismometers S_1 and S_2: (a) the damping of the second seismometer differs from that of the first by 5%; (b) the free period of the second seismometer differs from that of the first by 5%

One of the methods to eliminate this problem was to apply a very large damping of seismometer with the use of negative resistance. This causes the extension of the poles of the response (33.27) beyond the recording band and diminishes the effect of ω_0 and α_0 on the error of the difference (33.26). The differences of the response are not only lower, but also displaced beyond the frequency recording band (Fig. 33.7). This method gives good results for measurements of strong signals close to epicenter, since it amplifies the noise of recording.

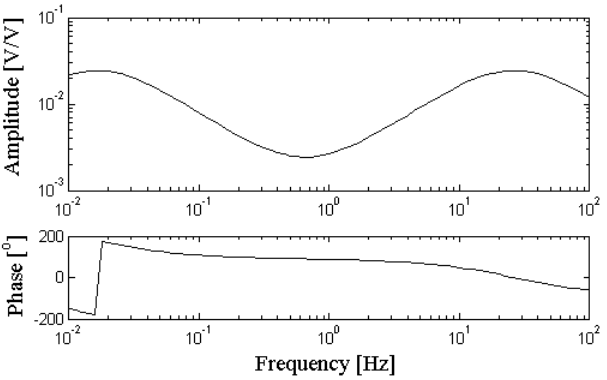

Fig. 33.7 Difference in responses of seismometers overdamped by $\alpha = 20$, whose free period differs by 5%

Another approach is to use long-period seismometers, in which the poles of the response are for low frequencies, below the band of measured rotation vibrations.

33.4.2 Sampling delays between channels

The delay between channels resulting from signal multiplexing and a single sampling device causes the time-lag between the signal samples. For adjacent channels of the recording system, it amounts to 1/12800/3 s (26 μs) (Wiszniowski 2002). For a frequency of, say, 10 Hz, the phase lag between any channels will be $\Delta c \times 0.094°$ ($\Delta c \times 0.0016$ rad), where Δc is the difference in channel number (of course, $\Delta c = 1$ for channels 1 and 2). For the instrument WiRek-HDD, the delay between the adjacent channels is 31.25 μs. The maximum phase lag for channels 1 and 8, for frequency of 10 Hz, will be 0.014 rad. We should keep in mind that for a sine signal

$$A\cos\big(\omega(t+\tau)\big) - A\cos\omega t = -2A\sin\left(\frac{\omega\tau}{2}\right)\sin\left(\omega t + \frac{\omega\tau}{2}\right), \qquad (33.28)$$

which means that the difference in sine signals, one with a phase shift τ, gives a signal of the same period (with about 90° phase shift) and the amplitude

$$A_\tau = \omega\,\tau A\,. \qquad (33.29)$$

This means that for 10 Hz the maximum error associated with the shift of sampling will be $C_{err} \approx 0.0016C$ for the instrument MK-6 (two chan-

nels) and $C_{err} \approx 0.0059C$ for the instrument WiRek (four channels). Figure 33.8a shows the seismic signal sampled at a rate of 100 sps and its difference from the signal shifted by 31.5 μs.

The relative delay resulting from sampling is known and it may be removed by resampling.

The same method can be used to adjust the channels recorded by different sampling systems, as in the case of recording from two seismometers at Ojców and Książ. In this case, it is necessary to know the exact time of sampling.

Resampling is performed by the spline method (de Boor 1978) with the use of Matlab. It is not possible to reconstruct the situation before the delay because of filtration and sampling of the signal. However, as seen in Fig. 33.8b, the error due to the time shift between the channels can be effectively reduced.

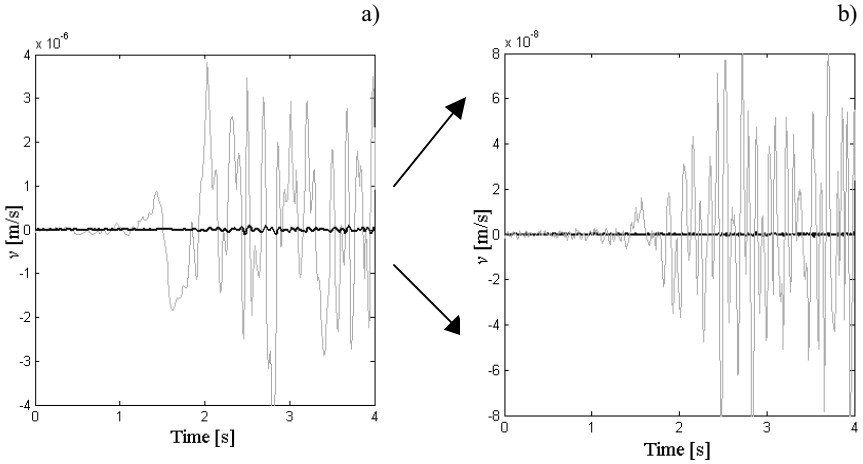

Fig. 33.8 Effect of time shift of sampling on the signal differences and the result of error correction through the resampling spline: a) – original signal sampled at 100 Hz (grey) and a difference for the same signal but sampled with 31 μs delay (black); b) – enlarged difference of signals from panel a) (grey), and difference of signals after the delay has been corrected with the spline method (black)

In this manner we can eliminate constant and known time shifts resulting from the multiplexer effect and the use of different converters for various channels. I think, however, that it is not safe to estimate the time-lag between the channels to eliminate, for instance, the differences in responses, since we can confuse the time-lag in the recording channel responses with the delay in the wave onsets when the wave is recorded by one sensor. We have

$$f(\omega t + x/\lambda), \tag{33.30}$$

where x is the distance and v is the wave velocity, while for the other sensor at this time we have

$$f\left[\omega(t+\tau)+\varphi+(x+L)/\lambda\right] = f\left[(\omega t + x/\lambda)+(\omega\tau+\varphi+L/\lambda)\right], \tag{33.31}$$

where L is the distance between the sensors, φ is the rotation, and τ is the time-lag between the channels.

The effect of sampling delay is the same as that of rotation. However, the *S*-wave signal should be recorded as twist vibrations and an attempt at estimating the delay treated as differences in channel recordings may lead to elimination of these vibrations. An exception is the method of seismometer paralleling (Teisseyre et al. 2003b).

A separate problem of the same kind is a comparison of signals recorded by the A/C converters with independent sampling. The sampling moments may differ by no more than half the sampling period; in our case by 5 ms. Knowing the exact time of signal sampling, synchronized by DCF or GPS, one should make resampling before summing the signals.

33.4.3 Methods of measurement of seismometer response differences and their reduction

One approach is to estimate seismometer responses and make their correction before the signal is subtracted. In the course of measurements we examined several ways of determining the relative response of seismometers:

- Through sine-signal calibration of the two seismometers;
- Through transposition of the seismometer to a parallel position and estimation of differences in responses under the assumption that in the parallel position they record the same signal. In this method, there are various ways of estimating the response difference.

Calibration by a sine signal should give fairly good results, since the calibrating signal is related to the ground vibration accelerations according to the formula:

$$a_c = \frac{I_c G_c l_0}{K_s}, \tag{33.32}$$

where G_c is the electromotive force of the calibration coil and I_c is the calibration current. It follows from this formula that if the current signal is

given in series on calibration coils of all the seismometers, their excitation will differ by a constant value only. This will enable us to determine the dynamic parameters of the seismometers in an exact manner.

An attempt at using this method for two seismometer pairs at Książ failed. This was a consequence of very specific conditions prevailing there. Because of high humidity, reaching 100%, and the presence of calcium salts, the calibration coils were not insulated from measurement coils, and the calibration signal acted not only through acceleration but had a direct electrical influence as well.

The other method consists in the following:

- parallel positioning of seismometers, so that they will record the same signal,
- determining their relative responses,
- positioning of seismometers in the opposite arrangement,
- calculating the signal difference, taking into account the earlier measurements.

In Fig. 33.5 we see the construction adjusted to such measurements. The method was described by Teisseyre et al. (2003b)

Basing on the measurement we can search for a filter to eliminate the linear term from the signal, as it was done by Nowożyński and Teisseyre KP (2003), or eliminate ΔR in the frequency domain, as done by Teisseyre et al. (2003a, b). Those solutions can be characterized by non parametric approach.

Another approach is to modify the seismometer to attain elimination of linear motions already during recording.

33.5 The Pendulum Seismometer for Measurement of Rotations Alone

A simple (mathematical) pendulum model of seismometer, which assumes that the moment of inertia relative to the pendulum's barycentre, I_s , is zero, is not sufficient for our further analysis. The motion of the barycentre of a compound (physical) pendulum is schematically shown in Fig. 33.9. The physical pendulum has a mass m_s and a moment of inertia I_s relative to the barycentre, situated at a distance l_s from the pendulum pivot. The displacement of coil in relation to the magnet is

$$U = l_c \left(\frac{u^a l_s m_s}{K_s} + \varphi \right), \tag{33.33}$$

where $K_s = m_s l_s^2 + I_s$ is, according to Steiner's theorem, the moment of inertia of the pendulum relative to the pendulum pivot. Adopting the reduced pendulum length

$$l_0 = \frac{l_s K_s}{K_s - I_s} = \frac{K_s}{m_s l_s} , \tag{33.34}$$

formula (33.33) simplifies to (33.4).

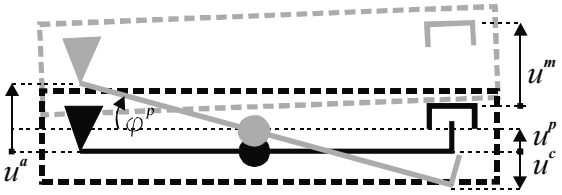

Fig. 33.9 Diagram of motion of the units of compound pendulum seismometer. Notation: u^a is the displacement of the seismometer's pivot, u^p is the displacement of the barycentre of seismometers pendulum, φ^p is the rotation angle of the pendulum, u^m is the displacement of the magnet and u^c is the displacement of the coil. Grey color marks seismometer after displacement

Having a possibility of adjusting l_s, we can control, in a proportional manner, the ratio of rotations to the linear motion in the signal recorded by the seismometer. We can simplify Eq. (33.33) to Eq. (33.7), which does not contain the rotation component, but the displacement will then be measured at the point which is at a distance equal to the reduced pendulum length l_0 in formula (33.34). This point may even be located beyond the seismometer. Of course, large metrics do not make sense for elastic media.

When we place the barycentre on the seismometer pivot, then $l_s \to 0$ and $K_s \to I_s$, and

$$U = l_c \varphi , \tag{33.35}$$

which means that such a seismometer will record nothing else but rotations.

The signal recorded by the seismometer can be written as a sum of dislocations and rotation functions

$$U = U(u^a) + U(\varphi) . \tag{33.36}$$

We will now define the quantity that would represent the compliance of a pendulum seismometer to rotation measurement; it will be the ratio of the rotation motion function to the linear motion function in the signal recorded by the seismometer:

$$C_R = \frac{\partial U/\partial \varphi}{\partial U/\partial u^a} \,. \tag{33.37}$$

Let us name this quantity the rotation compliance C_R. For a simple pendulum seismometer $C_R = l_0$. For example, for seismometer SM-3, the rotation compliance is $C_R = 0.083$ m. Figure 33.10 demonstrates the dependence of the reduced length of the pendulum on the distance from the barycentre to the pendulum pivot, according to formula (33.34) (we assume I_s = constant). It may be seen that the increase of C_R may be achieved in two ways: we can either move the barycentre farther away from the pivot (thus enlarging the size of pendulum and seismometer) or bring the pivot closer to the barycentre. The latter option is more convenient because it is possible to reach a large value of C_R without creating a gigantic seismometer. For an ideal solution, when the barycentre is at the pendulum axis, $C_R = \infty$.

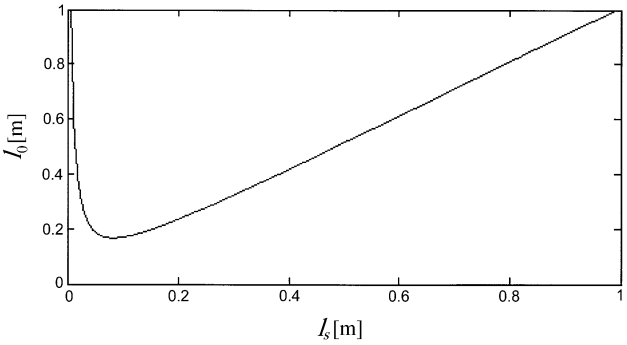

Fig. 33.10 The reduced length of pendulum l_0 as a function of distance of barycentre from the pivot of physical pendulum l_s

The construction we propose, fulfilling the demand of rotational motion measurement (large C_R), is a seismometer with the pendulums rigidly joined with each other (Fig. 33.11). Therefore, we named it the rigid seismometer (RS).

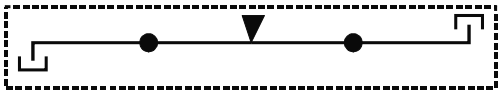

Fig. 33.11 Schematic of rigid seismometer made up of two pendulums joined together

In our design, the barycentre is at the rotation axis. The moment of inertia is

$$K_s \approx I_s = 2 l_{s0}^2 m_s \,, \tag{33.38}$$

where l_{s0} means here the reduced length of each pendulum, and m_s is the mass of each pendulum. On the basis of Eqs. (33.33), (33.37) and (33.38), the rotation compliance is

$$C_R = \frac{2 l_{s0}^2}{l_s} \,, \tag{33.39}$$

where l_{s0} is the deviation of positioning of the pivot (metric of the barycentre of both pendulums to the pivot).

If we want C_r to be a thousand times larger than that for seismometer SM-3 ($l_0 = 8.3$ cm), then l_s must be less than 0.083 mm. Adjustments of l_s were realized by adding small weights whose bearings were controllable on screws. The balance is tested by investigating the stability of location of the pendulum for different directions of the seismometer.

The basic problem relating to the seismometer of this type is its ability to record the signal. At stations of the Institute of Geophysics in Poland, the *S* waves of the recorded signals achieve, roughly speaking, a value of ~3 μm/s for 3.5 magnitude earthquakes. We have the relationship (Teisseyre et al. 2003a):

$$\dot{\gamma} \approx \frac{\mathrm{d}\dot{u}}{\mathrm{d}x} \approx -\frac{C}{V}\frac{\mathrm{d}\dot{u}}{\mathrm{d}t} \,, \tag{33.40}$$

where V is the *S*-wave velocity (emergence) and C is the coefficient taking into account the site effect ($C = 1$ for pure rotation of torsional waves). The signal recorded by a seismometer corresponds to the velocity of rotational motions multiplied by the pendulum length up to the coil position l_c. According to Eq. (33.40), the angular velocity is equal to

$$\omega l_c \approx -\frac{C l_c}{V}\frac{\mathrm{d}v}{\mathrm{d}t} = -\frac{C l_c a}{V} \,, \tag{33.41}$$

where v is the velocity and a is the acceleration of ground vibrations. We can expect the seismograph to be able to measure signals of the order of ~1 nm/s, for the *S*-wave frequency of 1-2 Hz, $l_c = 14$ cm, provided that there is a lack of rotation other than the pure *S*-wave rotation ($C = 1$). The measured values may be 2-3 thousand times smaller than the measured dislocations. The problems relating to measurement of a very small signal against noise of seismometer with amplifier have been discussed by Rod-

gers (1994), and it has been demonstrated how difficult it is to measure a signal below nm/s.

The values of mass m_s and spring parameters were selected so as to obtain the free vibration period of RS equal to that of SM-3 (i.e., about 1.5 s). Results of measurements by this seismometer were presented by Wiszniowski et al. (2003).

33.6 Conclusions

To measure rotation, it is better to use a system with two seismometers in one enclosure, evenly (at three or more points) fixed to the basement. To measure rotation and twist, however, it is better to use a system of four independent seismometers (separately fixed to the basement), or a system fixed to the basement in a manner enhancing a specified direction.

The measurement by a pair of sensors is based on the difference of signals. The main problem for the seismometer pair is how to eliminate differences in the seismometer's responses and their recording paths. Another approach is to eliminate signals already in the sensor. This function is performed by a rigid seismometer whose two arms are mechanically balanced.

It should be kept in mind that the seismometers operate an inhomogeneous medium, at the Earth's surface or in caves. Already this gives rise to twist waves. Also the housing of sensors, while excited by linear vibrations, generates the twist vibrations.

References

Aki K, Richards PG (1980) Quantitative seismology: theory and methods. WH Freeman and Co, San Francisco, CA

Bouchon M, Aki K (1982) Strain, tilt, and rotation associated with strong ground motion in the vicinity of earthquake faults. Bull Seism Soc Am **72**: 1717-1738

Bullen KE, Bolt BA (1985) An introduction to the theory of seismology, part 9 – Seismometry. Cambridge University Press, Cambridge

de Boor C (1978) A Practical Guide to Splines. Springer Verlag, New York

Dunkan CA (1986) Strainmeters and tiltmeters. Rev Geophys **24**: 679-624

Harrison JC (1976) Cavity and topographic effects in tilt and strain measurement, J Geophys Res **81**: 2, 319-328

Jaroszewicz LR, Krajewski Z, Świłło R (2001) Application of fiber-optic Sagnac interferometer for detection of rotational seismic events. Molecular and Quantum Acoustic **22**: 133-144

McLeod DP, Stedman GE, Webb TH, Schreiber U (1998) Comparison of standard and ring laser rotational seismograms. Bull Seism Soc Am **88**: 1495-1503

Minoru T (1998) Ground rotational motions recorded in near-source region of earthquakes. Geophys Res Lett **25**: 789-792

Moriya T, Teisseyre R (1999) Discussion on the recording of seismic rotation waves. Acta Geophys Pol **48:** 351-362

Nigbor RL (1994) Six-degree-of-freedom ground-motion measurement. Bull Seism Soc Am **84:** 1665-1669

Nowożyński K, Teisseyre KP (2003) Time-domain filtering of seismic rotation waves. Acta Geophys Pol **51**: 51-62

Rodgers PW (1994) Self-noise spectra for 34 common electromagnetic seismometer / preamplifier pairs. Bull Seism Soc Am **84**: 222-228

Saito M (1968) Synthesis of rotational and dilatational seismograms. J Phys Earth **16**: 53-62

Smith SW, Kasahara K (1969) Wave and mode separation with strain seismographs. Bull Earthq Res Inst **47**: 831-848

Teisseyre R, Suchcicki J, Teisseyre KP (2003a) Recording of seismic rotation waves: reliability analysis. Acta Geophys Pol **51:** 37-50

Teisseyre R, Suchcicki J, Teisseyre KP, Wiszniowski J, Palangio P (2003b) Seismic rotational waves: basic elements of theory and recording. Ann Geophys **46**: 671-685

Wiszniowski J (2002) Broadband seismic system: effect of transfer band on detection and recording of seismic waves. Publs Inst Geophys Pol Acad Sc **B-27**: 339, pp 180

Wiszniowski J, Skrzyński A, Suchcicki J (2003) Recording rotations with a pendulum seismometer: A sensor with reduced sensitivity to linear motions. Acta Geophys Pol **51**: 433-446

34 Equation of Pendulum Motion Including Rotations and its Implications to the Strong-Ground Motion

Vladimir M. Graizer

California Geological Survey
801 K Street, MS 12-32, Sacramento, CA, USA
e-mail: graizer@pacbell.net

34.1 Introduction

In contrast to classical seismological measurements where ground displacements do not usually exceed 1 mm and accelerations are less than 1 mg, amplitudes of strong ground motion can exceed 1 m of displacement and acceleration of more than 1g. Most instruments recording strong ground motion are pendulum accelerographs operating on the same principles as classical seismographs. Strong-motion data are used in seismological studies and in earthquake engineering. For many years, from its birth in the 1930s, strong-motion seismology was mostly oriented toward earthquake engineering with very little impact on seismology. On the other hand, strong-motion also means that records are obtained in the near-field of an earthquake or explosion, and therefore seismologists started using near-field strong-motion records as a tool to study the earthquake source process. Compared to teleseismic records, near-field data present an opportunity to take a close look at a seismic source with much less distortion by the wave propagation path. Source studies also lead investigators to look at the possibilities of extracting more information from the records than what is possible with classical strong-motion data processing (Trifunac 1971, Trifunac and Lee 1973, Shakal et al. 2003). New methods of data processing were developed, allowing determination of ground motion including residual displacement from accelerograms (Bogdanov and Graizer 1976, Graizer 1979, Iwan et al. 1985, Boore 2001).

Strong-motion seismometry employed the same pendulum type instruments as used in classical seismology. The main differences between strong-motion and weak-motion seismometers are that (1) strong-motion

instruments are less sensitive to the ground motion, and (2) their output is proportional to the acceleration as opposed to velocity or displacement in classical seismology. During the 1930s the assumptions used in classical weak-motion seismology were simply transposed onto the area of strong-motion. The most questionable perception brought from classical seismology into strong-motion is the assumption of simple linear input motion of the ground, with rotational (tilt) component being negligible. These assumptions lead to two consequences: After 70 years of recording strong motion: (1) we still have very primitive knowledge about this important component of strong ground motion, with only theoretical or indirect assessments about the rotational components (Trifunac 1982, Bouchon and Aki 1982, Lee and Trifunac 1985, 1987, Niazi 1986, Oliveira and Bolt 1989); (2) we approximate the output of the instruments as translational acceleration. As a result, by integrating this signal we have to assume that this results in translational velocity and displacement.

In real near-field of an earthquake, the rotational components may not be negligible as compared to accelerations of the linear motion. As a result, the records that are assumed to represent translational accelerations are actually a sum of acceleration and tilt. (It is well-known that the same type of pendulums can also be used as tiltmeters in the low frequency range, for example, for frequencies lower than 0.01 Hz).

Evidently, in the near-field of an earthquake it is necessary to measure all six components of motion: three linear and three rotational. There are different ways of implementing this (Golitsyn 1912, Kharin and Simonov 1969, Farrell 1969, Bradner and Reichle 1973, Graizer 1987, 1989, 1991, Nigbor 1994). The general solution is to combine the three linear motion sensors with the corresponding three rotational ones at the same point of measurement. Another way is to assure that the seismic sensors are moving strictly linearly in space, for example, by using a gyroscopic platform (similar to the inertial navigation).

The need to consider rotational motions becomes especially important now because of the new trends in technology and data processing. The high-resolution digital accelerographs developed recently provide new possibilities for data processing. Processing and analysis of those data must be performed with full understanding of the basics and the possible errors in data recording. Different groups of researchers apply various techniques of acceleration data processing, including permanent displacement calculations, but this can be done only if certain conditions apply.

34.2 Theory of the Pendulum

Looking at the basic equation of pendulum motion one can discover the following interesting fact: It is written differently in different classical seismological sources (Golitsyn 1912, Rodgers 1968, Aki and Richards 1980).

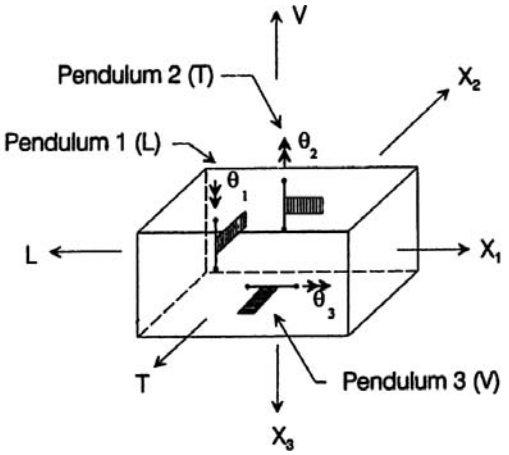

Fig. 34.1 Schematic representation of three transducers in an accelerograph. The coordinate axes X_1, X_2 and X_3 serve to describe the motion of the L, T and V transducers, respectively. Angles θ_1, θ_2 and θ_3 describe the deflection of the transducer pendulums (modified from Trifunac and Todorovska 2001)

Figure 34.1 shows a schematic representation of an accelerograph. The differential equation of a horizontal pendulum oscillating in a horizontal plane can be written as (coordinate system is preliminarily oriented to the static state of the pendulum):

$$\text{L:}\quad y_1'' + 2\omega_1 D_1 y_1' + \omega_1^2 y_1 = -x_1'' + g\psi_2 - \psi_3'' l_1 + x_2'' \theta_1 , \tag{34.1a}$$

$$\text{T:}\quad y_2'' + 2\omega_2 D_2 y_2' + \omega_2^2 y_2 = -x_2'' + g\psi_1 - \psi_3'' l_2 + x_1'' \theta_2 , \tag{34.1b}$$

where: y_1 is the recorded response of the instrument, θ_1 is the angle of pendulum rotation, l_1 is the length of pendulum arm, $y_1 = \theta_1 l_1$, ω_1 and D_1 are, respectively, the natural frequency and fraction of critical damping of the *i*th transducer, g is the acceleration due to gravity oriented vertically, x_1'' is the ground acceleration in 1th direction, ψ_1 is the angle of rotation of the ground surface about x_i axis.

Equations (34.1a) and (34.1b) for the two horizontal directions L (longitudinal) and T (transverse) describe the pendulum response to low ampli-

tude motions when $\sin\psi_1 \approx \psi_1$. Directions 1 and 2 are horizontal (L and T), and direction 3 is vertical (V).

Sensitivity of the vertical pendulum to tilts is different. For small tilts it is proportional to

$$1-\cos\psi \quad \text{and} \quad \cos\psi \approx 1-\psi^2/2 .$$

The equation of the vertical pendulum can be written as follows:

$$\text{V:} \quad y_3'' + 2\omega_3 D_3 y_3' + \omega_3^2 y_3 = -x_3'' + g\psi_1^2/2 - \psi_1'' l_3 + x_2'' \theta_3 .$$

Thus, the vertical pendulum is sensitive to the vertical acceleration, angular acceleration, and cross axis motion, but is less sensitive to tilts (for small tilts). Neglecting $g\psi_1^2/2$ gives

$$\text{V:} \quad y_3'' + 2\omega_3 D_3 y_3' + \omega_3^2 y_3 = -x_3'' - \psi_1'' l_3 + x_2'' \theta_3 . \tag{34.1c}$$

Thus, the horizontal pendulums (34.1a) or (34.1b) are sensitive to the acceleration of linear motion, tilt, angular acceleration, and cross-axis excitations. Regrettably, the completeness of representing Eq. (34.1) in the seismological literature varies. For example, Golitsyn (1912) does not take into account the cross-axis sensitivity, while Aki and Richards (1980) ignore the angular acceleration term. The difference in tilt sensitivity of vertical and horizontal pendulums is well known to the instrument designers, but is usually ignored in data analysis.

For correct interpretation of strong-motion recordings, it is important to study the sensitivity of a pendulum to the second, third and fourth terms on the right-hand side of Eqs. (34.1a), (34.1b) and (34.1c). In teleseismic studies using typical seismometers, the effect of these terms is usually considered to be small enough to be neglected (Golistyn 1912, Rodgers 1968, Aki and Richards 1980). The question is then: Is this also true for the strong-motion in the near-field studies? If the answer is "No", then: Which terms on the right-hand side of the equations will influence the output of the strong-motion instrument?

Possible impacts of different terms in the right-hand side of Eqs (34.1) were studied by Graizer (1989), Trifunac and Todorovska (2001), Wong and Trifunac (1977) and Todorovska (1998). Based on numerical simulations performed for a number of typical strong-motion instruments, Graizer (1989) concluded that tilts could influence significantly the output of the horizontal pendulums. The effect of angular acceleration is significant for instruments with a long pendulum arm l_i, as in the case of classical seismometers (VBP: l_i = 65 cm, S5S: l_i = 42.5 cm, SKM-3: l_i = 16.5 cm, SM-3: l_i = 8.5cm), but is small for typical accelerometers

with a short pendulum arm (SSRZ: l_i = 2.4 cm) (Fig. 34.2a). The effect of cross-axis sensitivity may reach few percents for accelerations higher than 2g, and for accelerometers with a natural frequency of 25 Hz (Fig. 34.2c). Cross-axis sensitivity is almost negligible for modern accelerometers that have natural frequency of about 100 Hz and short pendulum arm. The terms caused by tilting are always present for the horizontal pendulum, and cannot be neglected (Fig. 34.2b).

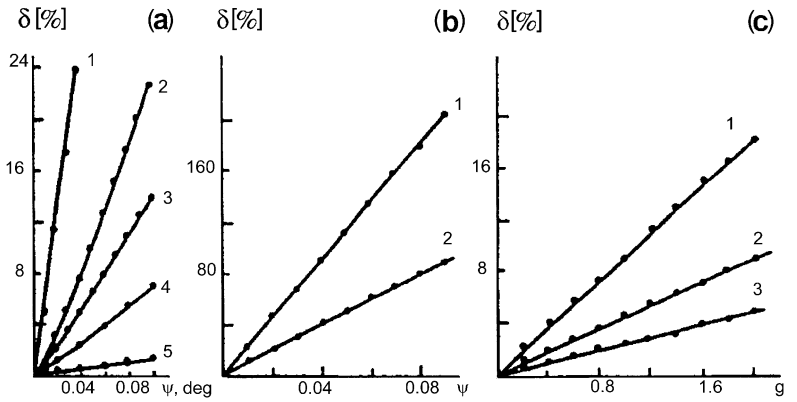

Fig. 34.2 Effect of angular acceleration (a): tilt (b) and cross axis sensitivity (c) on response of pendulum for different types of seismographs and accelerographs. Panel (a): 1 – seismograph VBP, 2 – S5S, 3 – SKM-3, 4 – SM-3 and 5 – accelerograph SSRZ; Panel (b): 1 – seismograph SM-3, and 2 – accelerograph SSRZ; Panel (c): 1 – accelerographs with natural frequencies of 10 Hz, 2 – of 15 Hz and 3 – of 20 Hz

For small oscillations, the vertical seismometer is almost not sensitive to tilts, and neglecting the cross-axis sensitivity terms simplifies the differential equations of the horizontal and vertical pendulums to:

$$\text{L:} \quad y_1'' + 2\omega_1 D_1 y_1' + \omega_1^2 y_1 = -x_1'' + g\psi_2 \ , \tag{34.2a}$$

$$\text{T:} \quad y_2'' + 2\omega_2 D_2 y_2' + \omega_2^2 y_2 = -x_2'' + g\psi_1 \ , \tag{34.2b}$$

$$\text{V:} \quad y_3'' + 2\omega_3 D_3 y_3' + \omega_3^2 y_3 = -x_3'' \ . \tag{34.2c}$$

Thus, in a typical strong-motion tri-axial instrument the two horizontal sensors are responding to the combination of inputs corresponding to horizontal accelerations and tilts, while the vertical sensor is mainly respond-

ing to the vertical acceleration. This may have important consequences, and raises the following questions when dealing with strong-motion records from earthquakes:

– To what extent is tilt responsible for the differences between horizontal and vertical components in long periods during a real earthquake?
– Is there a principal difference in spectral content of horizontal and vertical motions, or does this difference mainly result from errors in recording horizontal accelerations which are contaminated with tilt?

The horizontal sensor (see Eqs. (34.2a) and (34.2b)) is sensitive to the second derivative of displacement and to tilt. This means that double integration of Eqs. (34.2a) or (34.2b) will produce the sum of displacement and double integrated tilt. Assuming that tilt is proportional to velocity (Trifunac and Todorovska, 2001), double integration will give results proportional to the integral of displacement, and the result can look like long-period noise.

Based on Eqs. (34.2a)–(34.2c) we suggest performing a simple test of tri-axial accelerograms: Compare long-period components of the two horizontal and one vertical records. The true vertical and horizontal motions generated by an earthquake are expected to have similar low frequency content. If their recorded levels are of the same order, this can give us more confidence in attributing long periods to ground displacement. If the recorded level of long-period motion is significantly higher in the horizontal components, this could possibly be due to tilts.

34.3 Residual Displacements and what can be Done in Absence of Recorded Rotations (Tilts)

Consider the differential equation of pendulum motion in the absence of rotations. In this case Eqs. (34.2a) and (34.2b) can be simplified and will be similar to (34.2c) for both, vertical and horizontal, components:

$$\mathrm{y}'' + 2\omega D\mathrm{y}' + \omega^2 \mathrm{y} = -Vx'', \tag{34.3}$$

where V represents a magnification factor. The ground displacement $x(t)$ can be found by integrating recorded output of the instrument $y(t)$.

The first algorithm for computation of residual ground displacements from recorded strong motion accelerograms appears to have been given by Bogdanov and Graizer (1976), and later modified by Graizer (1979). A key part of the proposed method involves baseline correction that can be accomplished by minimizing the functional W which is based on realistic

assumptions about minimum velocity at the beginning and at the end of an earthquake ground motion:

$$W = \int_0^{T_1} [x'(t)]^2 \, \mathrm{d}t + \int_{T_2}^{T} [x'(t)]^2 \, \mathrm{d}t \,, \tag{34.4}$$

where T is the length of the recorded signal and T_1 and T_2 are times such that $0 < T_1 < T_2 < T$. This approach is based on the assumption that time intervals $[0, T_1]$ and $[T_2, T]$ can be found during which the ground motion is small (<10-15%) compared to the strongest amplitudes on the record (Graizer, 1979). Recent strong-motion accelerographs have enough preevent memory and also continue recording after acceleration is below a certain level. A baseline was first approximated by polynomials of up to the third degree, and later up to the higher degrees. In real applications of this method, polynomials of the 2nd to 5th degrees were used for baseline correction.

The challenging part was to convince the seismological community that it is possible to recover residual displacement from records of real accelerographs. The first series of tests were performed with the Soviet analog-type accelerograph SSRZ (very similar to the SMA-1). The instruments were placed on a shake-table (or a specially designed cart), and their permanent displacements were recorded independently by a ruler or a special gauge. The results of the tests were published in a series of papers (Bogdanov and Graizer 1976, Graizer 1979) and reports. Two tests of this type are shown in Fig. 34.3. In those two experiments the actual motion of the shake-table (1) was independently recorded together with the response of an accelerograph (2). Accelerogram was first digitized and processed to get displacement using Graizer's method (3). In those tests performed with analog-type accelerographs the error of residual displacement calculation was less than 25%. This is the most convincing classical way of testing the methods of data processing. The shake-table tests proved that residual displacement could be recovered from the record. Later, similar tests were performed in 1991 at the Institut de Physique du Globe (Strasbourg, France) and in 1993 with the Kinemetrics FBA, Terra Tech SSA-302, Sundstrand SSD3 and Teledyne SA-220 sensors in cooperation with W. Lee of the U.S. Geological Survey in Menlo Park (1993).

During the first series of experiments performed at the end of the 1970s, we "discovered" (Bogdanov and Graizer 1976, Graizer 1979) that if the instrument is even slightly tilted during its movement, it makes recovery of permanent displacement almost impossible. First, series of tests were simply performed by sliding the accelerograph along the surface of the table. In this case, to overcome the static friction at the beginning of the motion,

tilting of the instrument may occur. To avoid this problem a cart or shake-table was used in later tests (Graizer 1979, 1989, 1991). Comparisons were also made of results obtained from different instruments installed at the same place, for example, from accelerograph and seismograph (Graizer 1979).

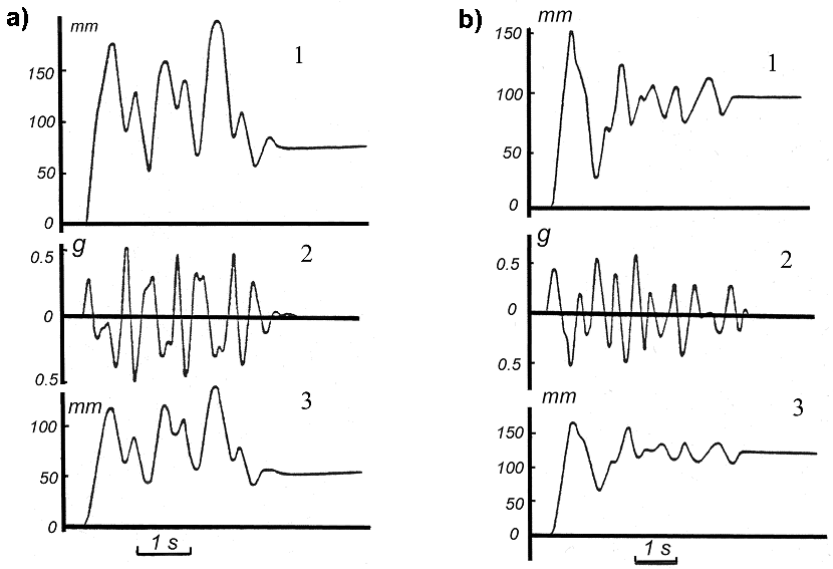

Fig. 34.3 Comparison of the shake-table displacements with calculated displacements for the two tests (a) and (b): true independently recorded displacement of the shake-table (1), recorded acceleration (2), results of displacement calculations using Graizer's method (3)

Another group of analyses was performed by numerical testing of the algorithm. In this case the ideal (calculated) response of the instrument was distorted by systematic and random errors. This group of tests is valuable because it allows to study the effects of each factor separately. It also allowed formulation of the requirements for the quality (dynamic range) of the records necessary to obtain permanent displacements. These tests also showed that random errors in acceleration can result in long-period disturbance after double integration (Graizer 1979). In this set of tests it was assumed that random errors have normal distribution with zero mean (Trifunac et al. 1971). Double integrated random noise may results in additional errors in permanent displacement calculations. Similar to this result, Boore (2003) concluded that analog-to-digital conversion of the signal can introduce significant drifts in displacements derived from digitally recorded accelerations.

The results of all these tests lead to conclusion that the processing of real accelerograms to get true ground displacement (including permanent displacement) requires the following conditions to be satisfied:

1. The input ground motion must be purely translational without any tilting or any other natural distortions.
2. The record must contain clear beginning and ending parts with relatively small amplitudes to allow the baseline correction.
3. The signal-to-noise level of the record must be high enough, at least 40 dB.

Compliance with the second and third conditions is usually possible (and can be verified), especially for digital records. But the first condition cannot be verified unless independent measurements of rotations are performed.

34.4 Numerical Tests of the Effects of Tilt on Computations of Displacement

Tests were performed to study the influence of tilt on the ability of numerical algorithms to compute displacements, including permanent displacement (Gaizer 2005). Figure 34.4 shows the first test in which the acceleration record was "contaminated" by tilt. The record was produced by correcting the accelerogram of the Northridge earthquake, recorded at Los Angeles – University Hospital Grounds (LAU). The test record was processed using the standard CSMIP procedure of filtering (same as the procedure of Trifunac 1971). This test acceleration record does not have any long periods, and when integrated twice it does not produce permanent displacement (Fig. 34.4c, dashed line).

The ideal test acceleration record (Fig. 34.4a) was contaminated by tilt record shown in Fig. 34.4b. The maximum amplitude of tilt was 0.6^{o}, and had a simple shape of one period of a sinusoid (with a period of ~0.7 s). The maximum amplitude of acceleration resulting from tilt alone is about 2% of the peak translational acceleration. The displacement calculated by double integration of the acceleration record "contaminated" by tilt (ideal record + tilt record) produces displacements (Fig. 34.4c, full line) that look like a perfect case of displacement with permanent displacement.

The results of another test are shown in Fig. 34.5. The record that contains permanent displacements (Fig. 34.5a) was "contaminated" by tilt. This record was created by using the corrected displacement curve from the Hector station during the Hector Mine earthquake (N-S component,

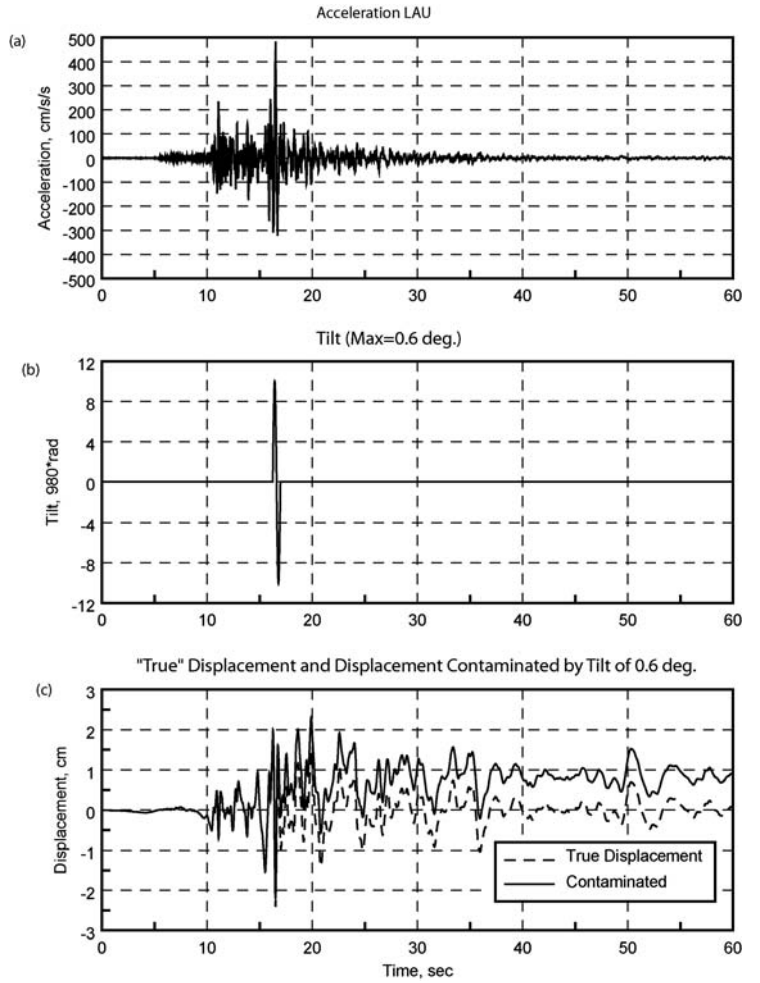

Fig. 34.4 Comparison of the "true" displacement and displacement calculated using accelerogram contaminated by "realistic" tilt: (a) test acceleration, (b) tilt with maximum amplitude of 0.3^{o}, (c) true displacement calculated from the test acceleration (dashed line) and displacement calculated from the record contaminated by tilt (full line)

HEC-N). It was assumed that this specific solution is an ideal ground motion with the corresponding ideal acceleration shown in Fig. 34.5a. The tilt record was generated based on the assumption that the tilt spectrum is proportional to the ground velocity spectrum (Trifunac and Todorovska 2001). The ground velocity curve was normalized to the maximum amplitude corresponding to the tilt of 0.1^{o}. In this case, the maximum amplitude

of tilt motion ($g\psi$) was less than 1% of peak translational acceleration. Figure 34.5c shows the following three curves: true or ideal displacement (dashed line), displacement obtained by double integration of true acceleration contaminated by tilt (dotted line), displacement calculated using Graizer's algorithm for baseline correction (full line).

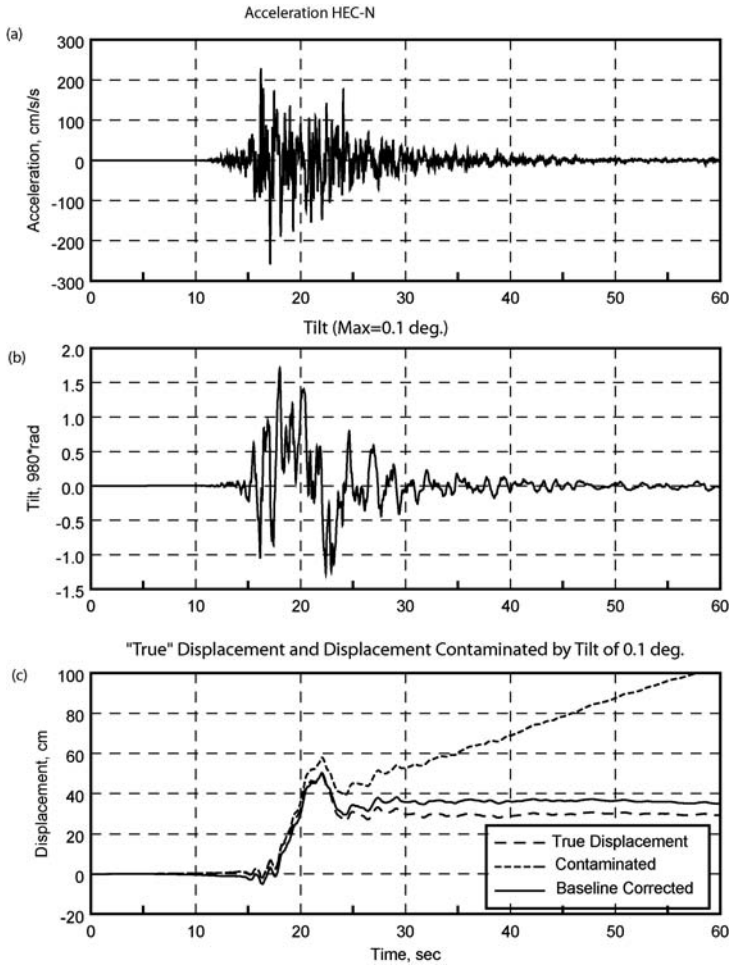

Fig. 34.5 Comparison of the "true" displacement and displacement calculated using accelerogram contaminated by "realistic" tilt: (a) test acceleration, (b) tilt with maximum amplitude of 0.1°, (c) true displacement calculated from the test acceleration (dashed line) and displacement calculated from the record contaminated by tilt (dotted line), and displacement obtained using Graizer's algorithm for baseline correction (Graizer 1979)

Application of the baseline correction algorithm (Graizer 1979) makes the displacement solution look very real, but it produces an error of about 21% in permanent displacement calculation.

These test examples are applicable to accelerograms from horizontal sensors. The results shown in Figs. 34.4 and 34.5 clearly demonstrate that tilt of the instrument during an earthquake motion can contaminate results of ground motion calculations with what resembles permanent displacement. Their influence will result in non-reliable permanent displacement. Results of these experiments (Figs. 34.4 and 34.5) show that short and long tilting of the instrument during an earthquake motion can result in what appears as permanent displacement of the ground. If tilting occurs during the strong motion it may look like a realistic permanent ground displacement.

Tilt can also result in differences in the long-period component of the horizontal and vertical motions, since the vertical pendulum is much less sensitive to tilts than the horizontal ones. Thus, only records of vertical sensors (for tilts less than $\sim 10^{o}$) can be used for permanent displacement calculations.

The above results show that only a six-component accelerometer (measuring three translations and three rotations) or a three-component accelerometer in combination with gyroscopes (similar to those used in inertial navigation) allow reliable measurements of permanent displacements from recorded accelerograms. Coming back to the analysis of existing three component accelerograms, it is possible to conclude that conservative procedure developed by Trifunac and Lee (Trifunac 1971, Trifunac and Lee 1973) and other similar ones are the only way for routine processing of existing strong-motion data.

34.5 Conclusions

Analysis of the response of pendular accelerometers to complex input motion that includes translational and rotational components was performed. It is shown that even for small oscillations the pendulum is sensitive to the translational acceleration, angular acceleration, cross axis motion and tilt.

Strong-motion instruments which are used in seismological and earthquake engineering measurements are sensitive not only to the translational motion, but also to tilt. This sensitivity can be neglected in some far-field measurements, but must be included in the near-field studies. Numerical experiments demonstrate that ignoring the tilt effects in strong-motion studies can introduce long-period errors, especially for calculation of re-

sidual displacements. In contrast to horizontal sensors, vertical sensors are less sensitive to tilt. This makes them potentially more usable for the long-period and residual displacement calculations.

If: (1) the input ground motion is purely translational, (2) the recorded acceleration has a relatively high signal-to-noise ratio and (3) it also contains beginning and ending part to allow for baseline correction, it is possible to calculate displacement including permanent one. A number of recently recorded near-field digital strong-motion records comply with the second and third conditions, but the first condition cannot be verified unless independent measurements of rotations are performed.

Conservative methods of strong-motion data processing that involve filtering in a limited frequency band have a clear advantage for routine data processing, because digital filters can eliminate the long-period components partially introduced by tilting.

Thus it is desirable to start measuring the rotational components of the strong-ground motion in combination with measurements of translational motion in the vicinity of active faults.

Acknowledgements. I would like to thank Mihailo Trifunac for his suggestions and support of this publication. Special thanks go to my former colleagues Valery Bogdanov, Konstantin Pletnev and Oleg Kuznetsov from the Institute of the Physics of the Earth in the former Soviet Union for their support and help. I would also like to thank anonymous reviewer of the manuscript for his comments that lead to improvements.

References

Aki K, Richards PG (1980) Quantitative seismology, vols. I and II. Freeman, San Francisco

Bogdanov VI, Graizer VM (1976) Determination of residual displacement of the ground from a seismogram. Reports USSR Acad Sci **229**: 1, 59-62 (in Russian)

Boore DM (2001) Effect of baseline corrections on displacements and response spectra for several recordings of the 1999 Chi-Chi, Taiwan, earthquake. Bull Seism Soc Am **91**: 1199-1211

Boore DM (2003) Analog-to-digital conversion as a source of drifts in displacements derived from digital recordings of ground acceleration. Bull Seism Soc Am **93**: 2017-2024

Bouchon M, Aki K (1982) Strain, tilt, and rotation associated with strong ground motion in the vicinity of earthquake faults. Bull Seism Soc Am **72**: 1717-1738

Bradner H, Reichle M (1973) Some methods for determining acceleration and tilt by use of pendulums and accelerometers. Bull Seism Soc Am **63**: 1-7

Farrell WE (1969) A gyroscopic seismometer: measurements during the Borrego earthquake. Bull Seism Soc Am **59**: 1239-1245

Golitsyn BB (1912) Lectures on seismometry. Russ Acad Sci, St. Petersburg

Graizer VM (1979) Determination of the true displacement of the ground from strong-motion recordings. Izv USSR Acad Sci, Physics Solid Earth **15**: 12, 875-885

Graizer VM (1987) Determination of the path of ground motion during seismic phenomena. Izv USSR Acad Sci, Physics Solid Earth **22**: 10, 791-794

Graizer VM (1989) Bearing on the problem of inertial seismometry. Izv USSR Acad Sci, Physics Solid Earth **25**: 1, 26-29.

Graizer VM (1991) Inertial seismometry methods. Izv USSR Acad Sci, Physics Solid Earth **27**: 1, 51-61

Graizer VM (2005) Effect of tilt on strong motion data processing. Soil Dyn Earthq Eng **25**: 197-204

Iwan WD, Moser MA, Peng C-Y (1985) Some observations on strong-motion earthquake measurement using a digital accelerograph. Bull Seism Soc Am **75**: 1225-46.

Kharin DA, Simonov LI (1969) VBPP seismometer for separate registration of translational motion and rotations. Seismic Instruments **5**: 51–66 (in Russian)

Lee VW, Trifunac MD (1985) Torsional accelerograms. Soil Dyn Earthq Eng **4**: 132-142

Lee VW, Trifunac MD (1987) Rocking strong earthquake accelerations. Soil Dyn Earthq Eng **6**: 75-89

Niazi M (1986) Inferred displacements, velocities and rotations of a long rigid foundation located at El Centro differential array site during the 1979 Imperial Valley, California earthquake. Earthquake Eng Struc **14**: 531-542

Nigbor RL (1994) Six-degree-of-freedom ground-motion measurements. Bull Seism Soc Am **84**: 1665-1669

Oliveira CS, Bolt BA (1989) Rotational components of surface strong ground motion. Earthquake Eng. Struc **18**: 517-526

Rodgers PW (1968) The response of the horizontal pendulum seismometer to Rayleigh and Love waves, tilt and free oscillations of the earth. Bull Seism Soc Am **58**: 1384-1406

Shakal AF, Huang MJ, Graizer VM (2003) Strong-motion data processing. In: Lee WHK et al. (eds) International book of earthquake & engineering seismology, part B. Academic Press, Amsterdam, pp 967-981

Todorovska MI (1998) Cross-axis sensitivity of accelerographs with pendulum like transducers – mathematical model and the inverse problem. Earthquake Eng Struc **27**: 1031-1051

Trifunac MD (1971) Zero baseline correction of strong-motion accelerograms. Bull Seism Soc Am **61**: 1201-1211

Trifunac MD (1982) A note on rotational components of earthquake motions for incident body waves. Soil Dyn Earthq Eng **1**: 11-19

Trifunac MD, Lee VW (1973) Routine computer processing of strong-motion accelerograms. Earthq Engin Res Lab, Report EERL 73-03

Trifunac MD, Todorovska MI (2001) A note on the usable dynamic range of accelerographs recording translation. Soil Dyn Earthq Eng **21**: 275-286

Trifunac MD, Udwadia FE, Brady AG (1971) High frequency errors and instrument corrections of strong-motion accelerograms. Earthq Enging Res Lab, Report EERL 71-05, p 49

Wong HL, Trifunac MD (1977) Effect of cross-axis sensitivity and misalignment on response of mechanical-optical accelerographs. Bull Seism Soc Am **67**: 929-956

35 Strong Motion Rotation Sensor

Jiří Buben, Vladimír Rudajev

Institute of Rock Structure and Mechanics, Acad. Sc. Czech Rep.
V Holešovičkách 41, 182 09 Praha 8, Czech Republic
e-mail: rudajev@irsm.cas.cz

35.1 Introduction

Rotation components of seismic vibrations can be radiated from the source, or can be generated when seismic waves propagate through anisotropic (micromorphic) rock massif; they can also appear as a response of structures to translation excitation.

Rotation components of strong vibrations could cause a non-negligible contribution to the whole earthquake hazard to building structures in near-source zones. The excitation of rotation vibration depends on the structure of subsoil, the dynamic response of building structures and built-in components. This is especially true for high structures of prevailing linear shape, such as pipelines and rail rapid transit lines, for objects with great seismic risk (e.g. nuclear power facilities), great seismic vulnerability (e.g. astronomical instruments) and for buildings of great historical value.

In order to experimentally study the rotation components, we constructed a new sensor of strong motion rotational vibrations, which is briefly described here. The pickup we constructed is based on the principle of flywheel, which must be balanced very accurately to attain a very high rotation-to-translation sensitivity ratio. The rotation oscillatory system is realized as a strong motion electromagnetic converter. The instrument is constructed from cooling air blower, which is a standard component of PC.

35.2 Experimental Setup

The prototype is made by slightly reconstructed cooling air blower SUNON 12V 2.8W, KDE 1029 PTS1 (external dimensions: 120 x 120 x 35 mm). The bearing of rotation shaft is composed of very precise ball

bearings (external diameter of 8 mm, internal diameter of 2 mm and height of 2 mm). The restoring momentum of the airscrew is produced by magnetic attraction force between the magnetic ring and the electromagnetic armature of the air blower. The permanent magnetic ring is fixed to the rotation shaft and the armature is fixed to the frame.

Mechanic reconstruction of the blower consists only in switching-over the electromagnet coil tags, connected in series to output clips. Their electric resistance is R_S = 82 Ohm and inductivity L_S = 0.15 H. This instrument is described in greater detail by Buben and Rudajev (2004).

The voltage sensitivity was determined by measuring the angular deflection dα as a function of the applied voltage dV on the coil. The measurement yielded the sensitivity dV/dα = 0.180 V/deg.

The natural vibration frequency f_S = 4.76 Hz of this system was determined from the variation of free vibrations exited by Dirac's impulse (Fig. 35.1).

The damping constant D = 0.12 was determined from the relation

$$D = 0.733 \frac{\log v}{\sqrt{1 + (0.733 \log v)^2}} \approx 0.733 \log v \,,$$

where $v = A_i / A_{i+1}$ is the ratio of successive amplitudes at an interval of one period T.

The two parameters of the pickup, i.e., damping D and natural frequency f_S , can be adjusted in the ranges $0.07 < D < 0.6$ and $1 \text{ Hz} < f_S < 5$ Hz. Damping can be enlarged by submerging the pickup into a vessel with mineral oil, while the frequency can be reduced by an additional fly wheel. Frequency of 1 Hz can be adjusted by using duralumin flywheel with dia-

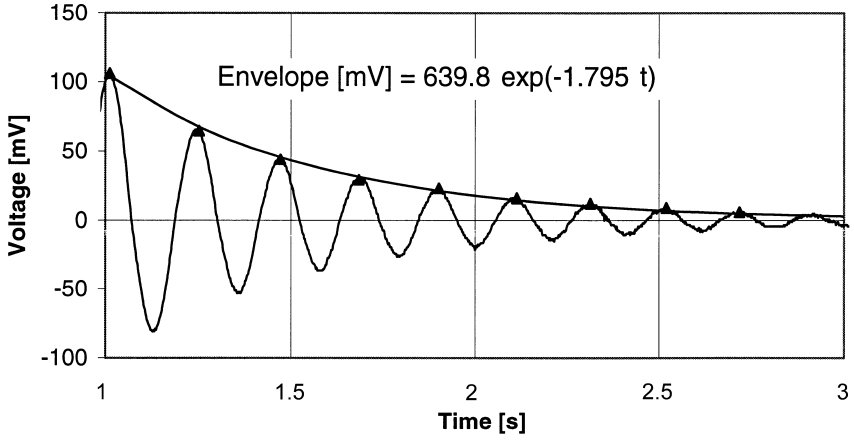

Fig. 35.1 Response of rotation sensors to Dirac's impulse

meter of 120 mm and a height of 5 mm. The course of free vibration is illustrated in Fig. 35.1.

The envelope of the amplitude curve (Fig. 35.1) can be described by the exponential function:

$$mV(t) = a\exp(-bt) = 639.8\exp(-1.795t),$$

and the damped harmonic oscillation by the relation:

$$v = (A_i / A_{i+1}) = \exp(-bT).$$

Substitution of the measured values b and period T gives

$$v = \exp(-1.795 \cdot 0.210) = 0.686$$

From this equation it follows that $D = 0.733 \log v = 0.12 = 0.733 \cdot 0.164$. The method of determining D from the envelope curve uses statistical approaches and yields reliable results.

35.3 Experimental Records

The pickup with $f_S = 4.7$ Hz and $D = 0.12$ was tested both in laboratory and in the field.

Laboratory testing

The rotation sensor was sited on a seismic pillar in the cellar of the Institute's building in Prague. Its induction coil was connected to the analogue input of the BR3 recorder (Brož et al. 2003) adjusted to the gain of 40 dB.

Figure 35.2 illustrates the records of artificially generated signal and its Fourier spectrum. The vibrations were excited by low hops (20 cm) of a person on the concrete floor at a distance of about 2 m from the pillar. The recording was made by a pickup with vertically oriented rotation axis (this means, the system was sensitive to horizontal movement). The maximum voltage amplitude on the coil of pickup is $\mathrm{d}V = 0.25$ mV

Taking into account the pickup sensitivity $\mathrm{d}V/\mathrm{d}\alpha = 0.180$ V/deg, the maximum angular amplitude is $\alpha = 0.0014$ deg = 5″. The maximum voltage amplitude on the coil of pickup is $\mathrm{d}V = 0.5$ mV.

The maximum spectral amplitude is observed for frequencies of about 5.0–5.5 Hz. For this frequency band, the dynamic magnification C of the pickup is $C = ½\ D = 4.17$. With regard to this dynamic magnification, the amplitude of vibration was 5″/ 4.17 ≈ 1.2″.

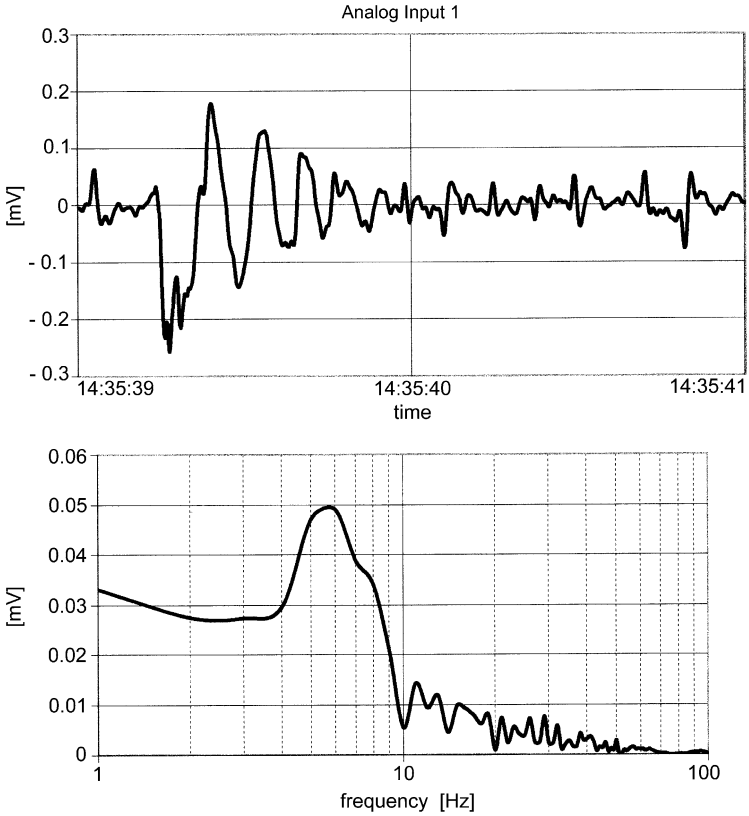

Fig. 35.2 Records of man-made signal at a distance of 2 m

Records of production blasting in the Špička quarry

Millisecond blasting of 1588 kg charge (102 kg per one step, time intervals of 17 and 8 ms) was fired on 10 December 2004 at 12:30:31 UTC in Špička stone quarry (latitude $\varphi = 50°$N, longitude $\lambda = 14.323°$E, $Z = 296$ m above sea level) situated in the vicinity of Radotín village near Praha. The straight line of 16 boreholes (21 m deep) was oriented in approximately SW-NE direction, and the free face surface of the quarry was in the SE direction. The focal distance from the focus to the measuring point was 327 m and the azimuth of the line from focus to the station was 215°.

The rotation sensor with vertical rotation axis was sited on the concrete floor of a cellars shanty. Its induction coil was connected to the analogue input of the BR3 recorder (Brož et al. 2003) adjusted to the gain of 40 dB.

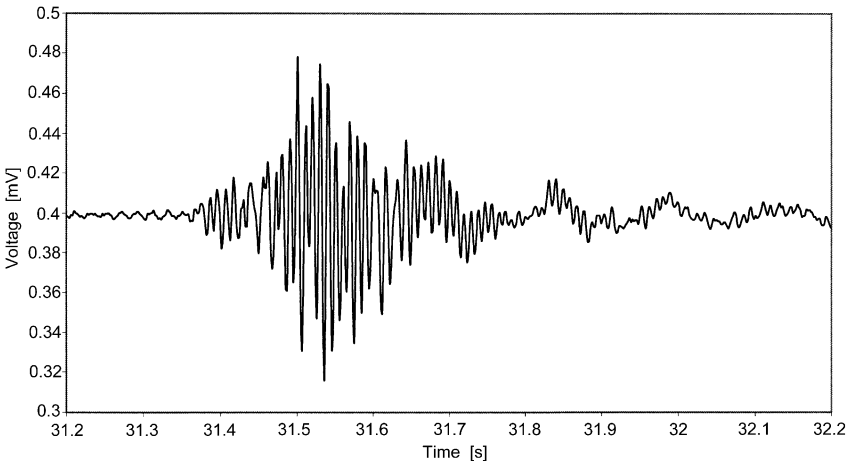

Fig. 35.3 Wave trace of horizontal rotation component excited by blasting

The signal amplifier with flat (±3 dB) frequency band in the range 0-45 Hz was installed in the recorder. The analog-to-digital convector ADS8341 had a discrimination of 16 bit (1:65536) and input range of ±5V.

All functions are controlled by microprocessor PIC16F877 with frequency of 20 MHz. Data are stored in the binary code on the memory card MMC (16-128 MB). Data reading is carried out by PC through interface SPI. Pre-event time is realized by RAM memory, which is continuously rewritten (FIFO). The record of rotation component is shown in Fig. 35.3.

The maximum amplitudes of the amplifier input voltage reach $dV \approx 0.08$ mV. The prevailing frequency of maximum amplitudes is about 11 Hz. The maximum angular amplitude is

$$\alpha = dV/0.18\ V/\text{deg} = 0.00044\ \text{deg} = 1.6''.$$

The described experiments proved the existence of rotational ground motion with measurable amplitudes, generated both by impacts and blasting.

35.4 Conclusions

A special pickup for recording rotational components of strong motion was constructed. This instrument was tested in laboratory and in the field. In both cases, the existence of rotational components was proved. The production of this pickup is technically easy and therefore a great number of such instruments can be available for investigation of rotational waves

generated by various sources. The use of such pickups the in networks or seismic profiles makes it possible to study attenuation of rotational amplitudes with distance.

The robustness and simple application of sensors with automated digital records is suitable for installing on building or engineering structures and monitoring their rotational response in the case of dangerous earthquakes.

Acknowledgement. Authors would like to thank Mr. Libor Žanda for realization of field measurements.

This work was supported partially by the project of the Academy of Sciences of the Czech Republic No. S3046201: "Experimental determination of seismic vibration attenuation in the Bohemian massif" and Institutional Research Plan No. A VOZ30460519.

References

Brož M, Štrunc J, Žanda L, MálekJ, Čermák L (2003) Using of BR-3 recorder for seismic profiles measurement. Proc. of the 12th regional conference with international participation: "New results of seismological, geophysical and geotechnical survey", Ostrava 2003, pp 39-42 (in Czech)

Buben J, Rudajev V (2004) Recorder of rotational ground vibration. Acta Geodyn Geomater **1**: 133, 143-147

36 High-Resolution Wide-Range Tiltmeter: Observations of Earth Free Oscillations Excited by the 26 December 2004 Sumatra -Andaman Earthquake

Marek Kaczorowski

Space Research Centre, Polish Academy of Sciences
ul. Bartycka 18A, 00-716 Warszawa, Poland
e-mail: marekk@cbk.waw.pl

36.1 Introduction

Observations of plumb line variations phenomenon have been carried out in the Low Silesian Geophysical Observatory in Książ by means of quartz horizontal pendulums for thirty years. The observations were adjusted with the help of least square method. The thirty-year-long permanent observations made it possible to determine interaction between tidal waves and the Earth core, improve the model of ocean indirect effects (Kaczorowski 1991), investigate the tidal waves seasonal modulation (Chojnicki 1991a, 1991b, 1999b, and Kaczorowski 1989), as well as investigate seasonal variations of the ocean indirect effects (Kaczorowski 1989). However, because of limitations of quartz horizontal pendulums, mainly their low sensitivity and instrumental drift, our investigations had to be concentrated on tidal phenomena only.

In 1997, taking into account possibilities of installing a long water-tube tiltmeter as well as expected improvements of measurements, we began to construct new instruments. The water-tube tiltmeter consists of two perpendicular tubes, 65 and 83 m long, partially filled with water. The idea of measurements applies the principle of hydrostatic equilibrium. Inside the hydrodynamic system of the instrument, the Luni-Solar forces as well as some great-scale geodynamic phenomena produce variations of water level. The water level changes are measured at the ends of the tubes with the interference technique (Kaczorowski 1999a, b). The water-tube tiltmeter has very advantageous properties, such as high sensitivity of measurement, lack of instrumental drift, and absolute units of measurement (length of wave of He-Ne laser light). These properties result from applying the

interference method of measurement of water variations in the hydrodynamic system of the instrument. The accuracy of measurements is close to single nanometers. For the hundred-meter long tube, changes of water level of the order of 10^{-9} m correspond to plumb line variations of the order of 10^{-3} mas (millisecond of arc). This precision allows us to determine plumb line variations with an accuracy better than 10^{-2} mas, being the most sensitive method of measurements of plumb line variations (Bower 1973). Simultaneously, this method possesses the property of absolute measurements technique. We obtained verification of measurement system of the instrument after the very strong earthquake (8.6 magnitude) which took place on 25 September 2003 near Japanese coast as well as after the Sumatra-Andaman catastrophic earthquake (9.1 magnitude) of 26 December 2004 (Sect. 36.8). Both earthquakes generated free oscillations in the Earth body (Pekeris and Jarosch 1958, and Alterman et al. 1959), causing plumb line variations of a few mas. Effects of plumb line variations associated with Earth free oscillations were registered by long water-tube. In the water system of the instrument, the low-pass filters were installed to diminish the rate of water level waving and to reduce the number of cycle-slip effects during the main phase of free oscillations.

36.2 Natural Conditions in the Low Silesian Geophysical Observatory

In the case of long water-tube tiltmeter, the measurements of plumb line variations are related to the Earth crust. The measurements of this kind require high mechanical stability of the orogen, fixed firmly with deeper geological structure. The geological and morphological conditions of the Low Silesian Geophysical Observatory are as follows:

- The bedrock is mechanically stable. Tunnels of the observatory were made in hard-fixed Devonian conglomerates joined with deeper layers of the Earth's crust.
- The thickness of the rocky cover of the underground amounts to 52 m.
- Entrance to the underground is situated 338 m above sea level and about 40 m above the bottom of the valley.
- The observatory is situated in the central part of the Sudeten Mountains, about 5 kilometers west of the Sudetic marginal fold.
- Geographical coordinates are $50^{o}51''$N and $16^{o}18''$E.
- The temperature variations are less than 0.5^{o}C during the year, and the average temperature is 7.8^{o}C.

- Variations of relative humidity in the undergrounds range from 85% to 94%.

36.3 Principle of Operation of the Long Water-Tube Tiltmeter

The principle of operation of the long water-tube tiltmeter takes advantage of fluids property (Moulton 1919), concerning the response of fluid free surface under the influence of mass forces. The construction of the hydrodynamic system of tiltmeter (Section 36.4) assures that fluid, particularly water, preserves free surface along the full length of the system. We will present the behavior of the fluid with free surface under the influence of the field of potential forces resulting from the second-order tidal potential W_2. In the equilibrium state of fluid, the velocity $v = 0$ and the Euler equation of motion will take the form:

$$-\operatorname{grad} W_2 = \frac{1}{\rho}\operatorname{grad} p\,, \tag{36.1}$$

where p is the pressure, and ρ is the fluid density. Let us discuss the equation of state of a fluid, $\rho = \rho(p, t)$, where t is temperature. For isothermal or adiabatic processes, $t = \text{const}$ or $t = t(p)$, we will get the equation of state in the form $\rho = \rho(p)$. For $\rho = \rho(p)$ there exists differentiable function $V(p)$ in the form of definite integral over the pressure variations $\int_{p_0}^{p} \frac{\mathrm{d}p}{\rho}$. The gradient of function $V(p)$ is

$$\operatorname{grad} V(p) = \frac{1}{\rho}\operatorname{grad} p\,. \tag{36.2}$$

Substituting Eq. (36.2) into (36.1) we will get $\operatorname{grad}(V(p)) + \operatorname{grad}(W_2) = 0$. Hence,

$$V(p) + W_2 = \text{const}\,. \tag{36.3}$$

From Eq. (36.3) it follows that if the fluid surface is the equipotential surface $W_2 = \text{const}$, then the function $V(p)$ is constant. In such a case, from Eq. (36.2) it follows that p and $\rho(p)$ are constant. Thus, the fluid is in hydrostatic equilibrium state. Inversely, if the fluid is in hydrostatic equilibrium state, i.e., $p = \text{const}$ and $\rho = \rho(p) = \text{const}$, then by virtue of Eq. (36.2), function $V(p)$ is constant, so the tidal potential W_2 is also constant. Thus, in the hydrostatic equilibrium state, the free surface of the fluid is an equipotential surface.

This law is the principle of operation of the long water-tube tiltmeter. When we measure the variations of the fluid free surface in the state close to hydrostatic equilibrium (quasi-equilibrium-approximation of adiabatic process), we simultaneously determine the variations of equipotential surface. The influence of tidal forces resulting from potential W_2 on the Earth globe causes, among other phenomena, the following two effects:

- Appearance of a horizontal component of gravity, which causes variation of the absolute direction of the plumb line;
- Deformation of the shape of the Earth and generation of absolute tilt of the Earth surface.

We will apply solutions of the linear theory of elasticity for radially symmetric Earth model (Love 1911).

Changes of the absolute direction of the plumb line caused by tidal potential W_2 (Love 1927), described with help of Love's numbers h and k, are as follows:

$$\alpha_{NS} = \frac{1+k}{g}\,\frac{1}{a}\,\frac{\partial W_2}{\partial \theta} \tag{36.4}$$

for the meridian component, and

$$\alpha_{EW} = \frac{1+k}{a\,g\sin\theta}\,\frac{\partial W_2}{\partial \lambda} \tag{36.5}$$

for the parallel component. At the same time, the absolute tilts of the Earth surface are:

$$\beta_{NS} = \frac{1}{g}\,\frac{h}{a}\,\frac{\partial W_2}{\partial \theta} \tag{36.6}$$

for the meridian component, and

$$\beta_{EW} = \frac{h}{a\,g\sin\theta}\,\frac{\partial W_2}{\partial \lambda} \tag{36.7}$$

for the parallel component. Considering both phenomena, the plumb line variations ψ measured in relation to the Earth's crust are:

$$\alpha_{NS} - \beta_{NS} = (1+k-h)\,\frac{1}{g}\,\frac{1}{a}\,\frac{\partial W_2}{\partial \theta} \tag{36.8}$$

for the meridian component, and

$$\alpha_{EW} - \beta_{EW} = (1+k-h)\,\frac{1}{g\sin\theta}\,\frac{1}{a}\,\frac{\partial W_2}{\partial \lambda} \tag{36.9}$$

for the parallel component (see Fig. 36.1).

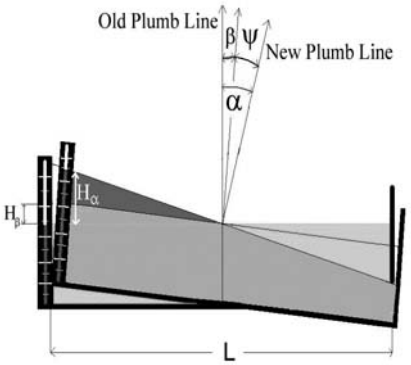

Fig. 36.1 Determination of angle ψ of plumb line variations on the basis of measurement of water level variations

The combination of Love's numbers (1+*k*–*h*) in Eqs. (36.8) and (36.9) is the tidal amplitude factor γ of plumb line variations. Factors $(1/a)\,\partial W_2/\partial\theta$ and $(1/a\sin\theta)\,\partial W_2/\partial\lambda$ are horizontal components of the additional gravity, resulting from the second order tidal potential W_2.

In the case of the long water-tube the variations of water free surface are measured relative to the base lens (Fig. 36.2). The lens is rigidly connected to the surrounding orogen as well as to the Earth's crust. The observed variations of water level H result from the two effects: changes H_α of water level caused by changes of absolute direction of the plumb line, and changes H_β of water level caused by tilts of the Earth surface (Fig. 36.1)

$$H = H_\alpha - H_\beta\,. \tag{36.10}$$

Dividing Eq. (36.10) by half length of the tube, $L/2$, we get the approximation for small angles:

$$\psi = \alpha - \beta \approx \frac{2}{L}\left(H_\alpha - H_\beta\right), \tag{36.11}$$

where ψ is the plumb line variation measured in relation to the Earth's crust. Therefore, on the basis of formula (36.11), measurements of the water level changes H allow us to determine angle $\psi = \alpha - \beta$ of plumb line variations. The quality of approximation of the water-surface to the equipotential surface depends on the rate of changes of the field of potential forces, the hydrodynamic parameters of the system, the viscosity of the applied fluid, as well as the level of local-origin disturbances. We made a large effort to adjust the hydrodynamic system of the long water-tube tiltmeter to measurements of the phenomena whose periods are longer than one minute (Sects. 36.4 and 36.8).

36.4 The Hydrodynamic System of the Long Water-Tube Tiltmeter

The main elements of the tiltmeter are two independent hydrodynamic systems consisting of two perpendicular tubes, 65.24 and 83.51 m long, situated at azimuths –31.4° and –121.4° The hydrodynamic system of the tiltmeter contains many vents compensating differences of the air pressure inside the tubes and the surroundings. While constructing the tiltmeter, our aim was to preserve free surface of the fluid in the whole length of the hydrodynamic system. The reasons of selecting water instead of other fluids are the following:

- The viscosity of water is sufficiently low to make it possible to register phenomena whose periods are longer than hundred seconds.
- The high relative humidity in the underground (Sect. 36.2) preserves the constant mass of water in the hydrodynamic system. At such the mass of other fluids such as alcohols would grow. Otherwise, the viscosity of oils at a temperature of 8°C is too high.
- The values of diffraction factors on the air-water and water-glass boundaries are close to each other (Sect. 36.5), which ensures high level of contrast of images.
- Ecological aspects, as well as availability of water in the underground.

The tubes were divided into fifteen or more four-meter long sections, separated by division walls. Water can flow between sections through the holes and narrow tubes in the division walls. These elements act as low-pass filters in the hydrodynamic system. The low-pass filters reduce the rate of phase variations of interference images. That is why the number of cycle-slip effects has been significantly diminished (Sect. 36.6.4). The most critical place of the interferometer is the measurement chamber. The chamber is half filled with water. The reflecting lens is located at its bottom (Fig. 36.2).

36.5 The Optic Module of Interference Gauge of the Water Level Variations Measurements

In the long water-tube, measurements of water-level variations are carried out using the interference method. The interference system of measurement consists of the four modules:

1. Base plate module.
2. TV camera module.

3. Laser module with the light-separating plate and a system of the laser beam shaping.
4. Reflecting-lens module.

The base plate module consists of a granite plate and three adjusting screws. The reflecting lens module is fixed to the base plate (Fig. 36.2). The camera module is situated upon the surface of the base plate. It registers the interference images created directly on CCD element of the camera. This solution minimizes the number of optical elements as well as enables us to avoid additional reflections, interferences, and deformations of images. We are able to move the camera module in the plane of the base plate to choose the fragments of the interference images that are most suitable for further analyses.

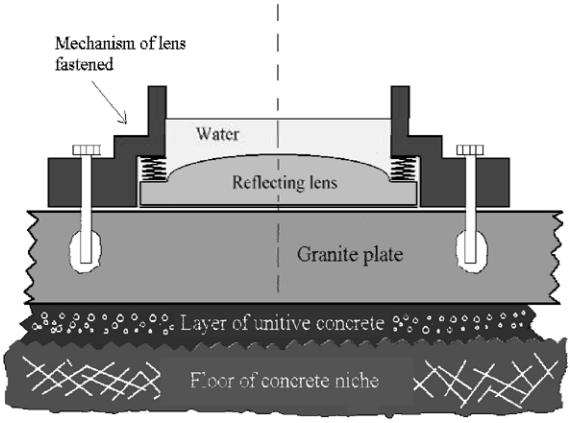

Fig. 36.2 The reflecting lens module

The laser module contains the following elements:

- The He-Ne laser (632.8 nm) of single mode of work and high stability of light wavelength.
- The optic system of the laser beam shaping.
- The light-separating plate.
- The heating system to prevent against moisture on the light-separating plate.

The reflecting lens module contains:

- The body of the lens module.
- The fixing system of the reflecting lens.
- The reflecting lens.
- The system of connections of the measurement chamber to the main tube.

The reflecting lens module connects the interferometer with the main water-tube. We chose radius of reflecting lens curvature so as to obtain three Newtonian rings on CCD element of camera (Fig. 36.3).

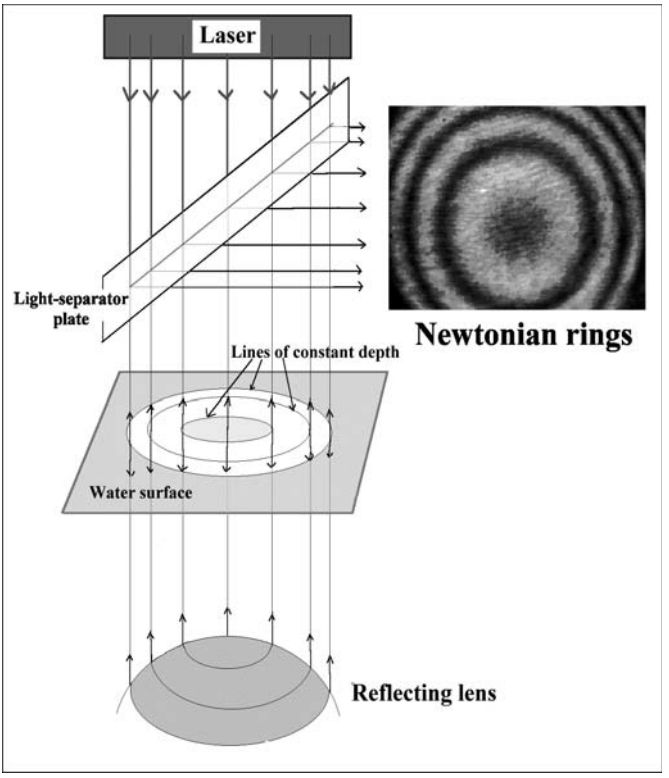

Fig. 36.3 The optic system of Newtonian interferometer

The measurement chamber is situated under the laser module inside the lens module. On the bottom of the chamber, about 8 mm under the water surface, there is a fixed flat-convex reflecting lens. Interference occurs between the light beam reflected from the convex surface of the lens and the light beam reflected from the water surface (Fig. 36.3). On account of the analysis it is important to obtain interference images with a central interference ring. To obtain central rings we must fulfill the two conditions: perpendicularity of the light beam to the water surface, as well as the co-linearity of the light beam with radius of the reflecting lens curvature. We can find the central position of interference rings applying the following motions:

- Inclinations of the base plate. These motions help us to fulfill the perpendicularity of the laser beam to the water surface.
- The flat displacement of the laser module relative to the reflecting lens module to attain co-linearity of the light beam with the radius of reflecting lens curvature.

The Newtonian rings correspond to isolines of depth of the water above the reflecting lens. The water level variations are observed as "floating" of the interference rings (Fig. 36.4).

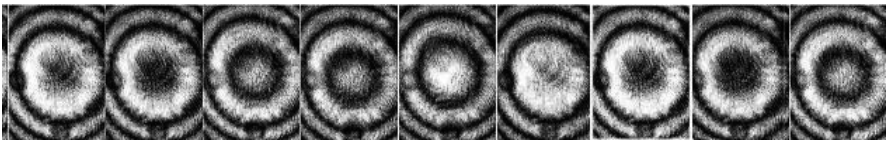

Fig. 36.4 Ten-second interval sequence of the images representing a decreasing water level

The process of measurement of water level variations is based on the registration of time series of interference images. We determine from them the series of phases of interference images applied to calculate the water level changes. Our discussion is concentrated on the function of brightness distribution $\omega(r)$ of the interference images as well as on the relation between variations of the interference image phases and changes of the water layer thickness. The optic model of the interferometer was related to the situation in which flat monochromatic wave propagates along axis Z of Cartesian system XYZ (Fig. 36.5). The flat wave reflects from the water surface (plane $z = 0$), and then from the surface of the convex lens of curvature radius R. After propagation through the water layer, the wave reflected from the lens interferes with the wave directly reflected from the water surface.

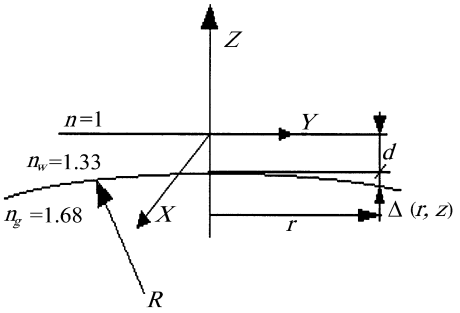

Fig. 36.5 Scheme of interference system in Cartesian coordinates XYZ

The position of axis Z of the coordinate system was selected on the prolongation of the curvature radius of the reflecting lens. Therefore, axis Z is the axis of symmetry of the optic system.

We adopted the following values of the diffraction factors: $n_1 = 1$ of air, $n_w = 1.33$ of water, and $n_g = 1.68$ of the RG7 glass. From the formula:

$$\rho = \left(\frac{n_2 - n_1}{n_2 + n_1} \right)^2 , \tag{36.12}$$

we calculated the reflection factors on the air-water and water-glass boundaries, getting the following values: $\rho_w \approx 0.02$ and $\rho_g \approx 0.0135$, respectively. We assume that the optical system (Fig. 36.5) is lit up by a monochromatic flat wave described by the formula:

$$U(x, y, z, t) = A_0 \exp(-\mathrm{i}\varphi) . \tag{36.13}$$

The phase element is given by the equation $\varphi = \omega t - kz - kn\Delta_a(x, y, z)$, where ω is the angular velocity of a light wave, $k = 2\pi/\lambda$ is the wave number, and λ is the wavelength in vacuum. The phase element $-kn\Delta_a(x, y, z)$ contains the wave number, the factor of air diffraction $n_1 = 1$, and a function describing aberration of the wave's front as well as a small discrepancy of the beam. Part of the light beam is reflected at the boundary of air-water environments. Function

$$U_1(x, y, z, t) = \rho_w A_0 \exp(\mathrm{i}\varphi) , \tag{36.14}$$

describes the wave directly reflected from the water surface. The rest of the wave, passing through water, is described by the function:

$$U'(x, y, z, t) = (1 - \rho_w) A_0 \exp(-\mathrm{i}\varphi) . \tag{36.15}$$

After propagation through the water layer, this wave is reflected from the water-glass boundary, and passes again through the water layer and air-water boundary; this is described by the formula:

$$U_2(x, y, z, t) = \rho_g (1 - \rho_w)^2 A_0 \exp\left[\mathrm{i}(\delta + \varphi)\right] . \tag{36.16}$$

The amplitude of the wave $U'(x, y, z, t)$ (Eq. 36.15) was multiplied by the factor $\rho_g(1-\rho_w)$. This results from the reflection of the wave on the water-glass boundary (factor ρ_g) and propagation of the wave through air-water boundary (factor $1-\rho_w$). In the phase module of Eq. (36.16) there appeared component δ resulting from the change of the wave phase caused by reflection of the wave from the lens spherical surface, as well as from double-passing of the wave through the layer of water.

$$\delta(r) = 2kn_w\left(d + \frac{r^2}{2R}\right), \tag{36.17}$$

where n_w is the water diffraction factor, r is the distance from the axis of symmetry Z of Cartesian system, d is the distance between the top of the reflecting lens and the water surface. The phase element δ describes the difference of phases between the reflected waves $U_1(x, y, z, t)$ and $U_2(x, y, z, t)$. According to the coherent waves summation law, the function of brightness distribution $\omega(r)$ is expressed by the equation:

$$\omega(r) = U_1U_1^* + U_2U_2^* + U_1U_2^* + U_2U_1^*, \tag{36.18}$$

where $*$ denotes the complex conjugate. The function of brightness distribution $\omega(r)$ is radial symmetric on account of axial symmetry of the problem. From the property of complex numbers we get

$$\omega(r) = U_1U_1^* + U_2U_2^* + 2\,\mathrm{Re}\{U_1U_2^*\}\cos(\delta), \tag{36.19}$$

where Re is the real part of the expression $\{U_1U_2^*\}$. Hence, the function of brightness distribution for the thickness d of water layer is given by the equation:

$$\omega(r) = A + B\cos\delta(r), \tag{36.20}$$

where the phase element is

$$\delta(r) = n_w k\left(2d + \frac{r^2}{R}\right). \tag{36.21}$$

Constants A and B, describing the level of background brightness and the amplitude of brightness of interference rings are given by the equations:

$$A = U_1U_1^* + U_2U_2^* \sim \rho_w^2 + \rho_g^2(1-\rho_w)^4$$

and

$$B = 2R_e\{U_1U_2^*\} \sim 2\rho_w\rho_g(1-\rho_w)^2.$$

We can express the thickness of water layer above the lens in the form:

$$d = n_wN\lambda + \Delta d, \tag{36.22}$$

where $N\lambda$ is the multiplicity of light wavelength and Δd is the residuum. After substitution of Eq. (36.22) into (36.21), the equation of phase will take the form:

$$\delta(r) = 2\pi N + 2\pi \frac{n_w}{\lambda R} r^2 + 4\pi \frac{n_w}{\lambda} \Delta d \,. \tag{36.23}$$

The function of brightness distribution will be

$$\omega(r) = A + B\cos\left[Cr^2 + \Delta F(\Delta d) \right], \tag{36.24}$$

where $C = \dfrac{2\pi n_w}{\lambda R}$. The variable element of phase $\Delta F(\Delta d) = 4\pi \dfrac{n_w}{\lambda} \Delta d$ is a linear function of the water level variations Δd. Therefore, the determination of the phase change $\Delta F(\Delta d)$ enables us to calculate the water level variations Δd from the formula:

$$\Delta d = \frac{1}{4\pi} \frac{\lambda}{n_w} \Delta F(\Delta d) \,. \tag{36.25}$$

Substituting the numerical values into the right-hand side of Eq. (36.25) and converting angle 4π into the angular measure we obtain:

$$\frac{1}{720} \frac{\lambda}{n_w} = 0.6608 \text{ nm/deg} \,.$$

Hence, the formula describing the relation between variation of phase $\Delta F(\Delta d)$ of the following interference images and the variation of water level Δd is

$$\Delta d = 0.6608\,[\text{nm/deg}]\, \Delta F(\Delta d) \,. \tag{36.26}$$

Equation (36.26) was applied in an algorithm to calculate time series of the water level changes on the basis of time series of interference image phase variations.

36.6 Determination of the Function of Plumb Line Variations

The initial result of the measurements of the water-tube tiltmeter is the time series of interference images. The time series of images contains information about water level variations in the hydrodynamic system of the instrument. Determination of the time series of water level variations enables us to calculate the final product, i.e., plumb line variation. One of the main problems with processing the long water-tube observations is the necessity of processing 12 million files of interference images in yearly

series. The number of images results from the necessity of supporting registration on four channels with a frequency of one photo per ten seconds. Taking into account the quality of registration, the frequency ought to be as high as possible. For the high frequency of registration, cycle-slip effects (Sect. 36.6.4) will never appear. The chosen frequency of registration results from technical limitations of computer such as the number of stored files as well as image-processing abilities. The observations are performed under the control of the MS Windows 2000 system applying the Pentium 4 with 2.7GB clock. The main algorithms applied in data processing programs are presented further on.

36.6.1 Determination of brightness profiles of interference images

The time-consuming element of the observation analysis is the determination of the series $\{\bar{\omega}_n(r,t)\}$ of brightness profiles distribution of interference images, where r is the distance from the center of symmetry of interference image, and t is the parameter denoting the time of image generation. During the registration, the collection of images was divided into few-week long blocks. For each block, the following three parameters were manually chosen:

- Locations of the centers of the brightness section independently for each series.
- Angle of tilt of brightness section in relation to interference image.
- Color of brightness section.

Picking up the location of profile, we choose the low-noise area of the image; it should be as long as possible, while the distance of the profile from the center of symmetry of interference images should be small (Fig. 36.6). To obtain high dynamics of the brightness function $\bar{\omega}_n(r,t)$, we choose the color of section without exceeding the scale of brightness (range < 0-255 >). Due to the invariability of location of the symmetry axis of the Newtonian rings in epoch of a few weeks as well as to the invariable location of the interference noise on the images, it is enough to select the location of the section of brightness only at the beginning of the analyzed several-week long data block.

A possible displacement of the location of the brightness section in relation to the image axis of symmetry causes a shift of the whole few-week series by a constant. However, it does not affect the result of the final analysis.

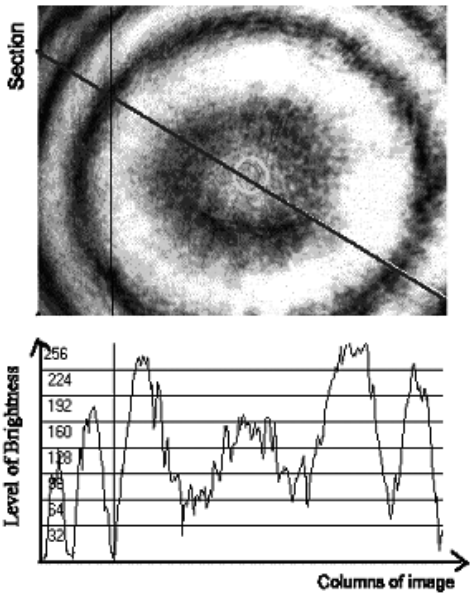

Fig. 36.6 Profile of brightness $\overline{\omega}_n$ (r, t) of interference image

36.6.2 Division of daily series of brightness profiles into similarity classes

Time series of brightness profiles $\{\overline{\omega}_n(r,t)\}$ of interference images are the initial data for calculating – with the help of the least square method – the time series of theoretical brightness profiles $\{\omega_n(r,t)\}$ as well as for determining time series $\{F_n(t)\}$ of the phases of interference images (Sect. 36.6.3). Because the process of determining the phase F of a single interference image is time-consuming, we perform time series of brightness profiles $\{\overline{\omega}_n(r,t)\}$ before the analysis. The applied algorithm is based on the repeatability of the interference images as well as repeatability of their brightness profiles $\overline{\omega}(r)$.

The profiles of brightness of interference images are not differentiated when their phases differ by the full angle. Basing on this property, we introduce equivalent relation "to be similar to" into the series of brightness profiles $\{\overline{\omega}_n(r,t)\}$.

The equivalent relation divides series of brightness profiles into disjoined classes. Each class contains the images whose brightness profiles

are similar. Next, applying adjustment process, we determine for each class one phase F of brightness profiles of pattern image (Sect. 36.6.3).

The number of classes generated by the algorithm in a series of profiles depends on the value of similarity coefficient. When the number of classes is too small, the smoothness of the function of plumb line variations (quantification of values) is violated; when it is too large, the process of further elaboration is significantly prolonged. The experience has shown that the optimum number of brightness profile classes is between 400 and 600 (Fig. 36.7).

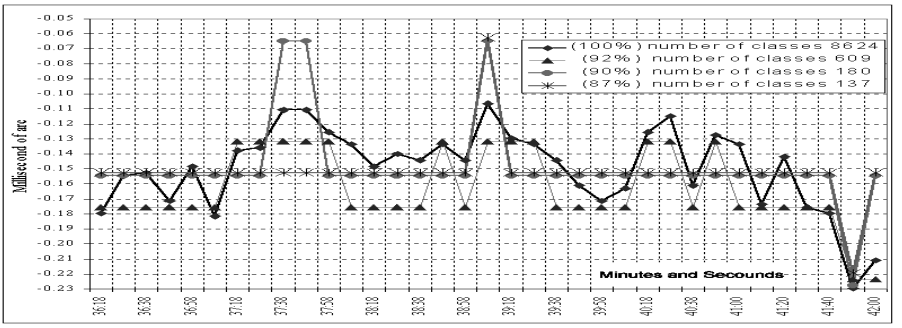

Fig. 36.7 Influence of the number of classes on quantification of data

The algorithm automatically chooses the value of similarity coefficient to obtain the appropriate number of classes. Application of the division of daily series of brightness profiles into similarity classes reduces the number of necessary adjustments of the brightness function $\omega(r)$ from 34,000 to about 2,000 per day.

36.6.3 Determination of phase F of the interference image on the basis of brightness profiles $\bar{\omega}(r)$

Adjustment of the theoretical function $\omega(r)$ (Eq. 36.24) of brightness profiles requires that the observed brightness function $\bar{\omega}(r)$ be normalized before analysis. The normalization improves the contrast of interference rings, eliminates inhomogeneity of the image brightness as well as decreases the effects of interference noise created in laser optic, the light-separating plate, and water surface pollutions. The algorithm determines the mean value of brightness and then introduces correction to normalize the level of brightness. To determine phase F of interference images, we compared empirical function $\bar{\omega}(r)$ of brightness profile with the theoretical function of brightness profile $\omega(r)$. We assume that conformability

between the empirical and theoretical images will be reached when the square function of the difference of empirical $\bar{\omega}(r)$ and theoretical $\omega(r)$ functions of brightness reaches minimum. The mathematical formula for the condition of the images conformability was expressed by putting the first derivatives of the sum of squares of differences equal to zero. We applied the theoretical function of brightness (Eq. 36.24).

$$\omega(r) = A + B\cos(Cr^2 + F)\,. \tag{36.27}$$

Variable r is the distance from the image axis of symmetry. The amplitude coefficients, A and B, represent the level of background brightness and the amplitude of brightness of interference rings. Constant C is given by the formula: $C = 2\pi n_w/\lambda R$ (Sect. 36. 5). The phase variable F is associated with water level variations above the reflecting lens (Sect. 36.5). The difference of empirical $\bar{\omega}(r)$ and theoretical $\omega(r)$ functions is given by the formula

$$\Delta\omega(r) = \bar{\omega}(r) - A - B\cos(Cr^2 + F)\,. \tag{36.28}$$

Applying the identity

$$B\cos(Cr^2 + F) = B\cos(Cr^2)\cos(F) - B\sin(Cr^2)\sin(F)$$

and substituting the formulae:

$$V_1 = B\cos(F)\,, \qquad V_2 = B\sin(F)\,,$$

$$X_1 = \cos(Cr^2)\,, \qquad X_2 = \sin(Cr^2)\,,$$

we obtained Eq. (36.28) in a new form:

$$\Delta\omega(r) = \bar{\omega}(r) - A - X_1V_1 + X_2V_2\,. \tag{36.29}$$

After squaring and differentiating Eq. (36.29) with respect to A, V_1, V_2 we obtained three differential equations. To fulfill the requirement of extremum, the differential equations were equated to zero.

$$\begin{aligned}
\frac{\partial\Delta\omega(r)}{\partial A} &= 2\left[\bar{\omega}(r) - A - X_1V_1 + X_2V\right](-1) = 0\,,\\
\frac{\partial\Delta\omega(r)}{\partial V_1} &= 2\left[\bar{\omega}(r) - A - X_1V_1 + X_2V\right](-X_1) = 0\,,\\
\frac{\partial\Delta\omega(r)}{\partial V_2} &= 2\left[\bar{\omega}(r) - A - X_1V_1 + X_2V\right](-X_2) = 0\,.
\end{aligned} \tag{36.30}$$

For each point of the brightness profile $\bar{\omega}(r)$ we defined a system of equations identical to (36.30). Next, we summed up the corresponding components of equation system. The solutions of system (36.30) allowed us to determine variables A, V_1, V_2. To calculate phase F of theoretical interference image best fitting to the real image, we used the formula:

$$\operatorname{arctg}(V_2 / V_1) = F\,. \tag{36.31}$$

The algorithm of calculation of the real image phase F gives the phase in angular measure. The resolution of calculation is equal to one degree and variable F is an integer from the interval 0 to 359.

36.6.4 The calculation of time series of progressive phases $\{S_n(t)\}$ of interference images

After calculation of time series $\{F_n(t)\}$ of interference image phases, the next step is to calculate the time series of progressive phases $\{S_n(t)\}$. This is realized in several iterations. The first is based on the principle of choosing "the shorter step". We chose the following formulae for calculating the next element of the series of progressive phases $\{S_{n+1}(t)\}$:

for $\left|F_{n+1} - F_n\right| \le 180^{\circ}$

$$S_{n+1}(t) = S_n(t) + F_{n+1} - F_n\,; \tag{36.32}$$

for $\left|F_{n+1} - F_n\right| > 180^{\circ}$

$$\begin{aligned} S_{n+1}(t) &= S_n(t) + F_n + (360^{\circ} - F_{n+1}) \quad \text{when} \quad F_{n+1} > 180^{\circ}, \\ S_{n+1}(t) &= S_n(t) + F_{n+1} + (360^{\circ} - F_n) \quad \text{when} \quad F_n > 180^{\circ}\,. \end{aligned} \tag{36.33}$$

The greater the reliability of correctness of "the shorter step" choice, the smaller the value of $\left|F_{n+1} - F_n\right|$. In the case of tidal phenomena, the rate of the image phase variations never exceeds 100 deg/min. For 10-second period of sampling images (Sect. 36.6) and for tidal periods, we obtain: $\left|F_{n+1} - F_n\right| < 10^{\circ}$. For slow variations of image phases $\left|F_{n+1} - F_n\right| \ll 180^{\circ}$ there is a real chance that the chosen method of progressive phases determination is correct. Incidentally, due to local as well as some geodynamic effects we observe differences of phases $\left|F_{n+1} - F_n\right|$ close to 180° or larger (Sect. 36.8). For differences $\left|F_{n+1} - F_n\right| > 100^{\circ}$ the application of "the shorter step" principle becomes controversial. Therefore, in the case of

high-dynamics phenomena, producing large and rapid variability of phases, the process of sticking successive phases is a source of errors (Sect. 36.8). The errors of sticking process resulting from discontinuity of phases $\{F_n(t)\}$ are called cycle-slip effects.

The second iteration of the determination of series of progressive phases $\{S_n(t)\}$ is the elimination of some discontinuities (jumps) arisen because of errors of sticking process (first iteration). In the case of typical discontinuities, the algorithm automatically detects and eliminates such errors. Other errors can be partially eliminated by comparing signals obtained from opposite ends of the tube or by comparing the signal with tidal ephemerides function.

36.6.5 Determination of series of plumb line variations $\{T_n(t)\}$ on the basis of series of progressive phases $\{S_n(t)\}$ measured on one side of the tube

To determine time series of plumb line variations $\{T_n(t)\}$, the series $\{S_n(t)\}$ of progressive phases were multiplied by the coefficient of proportionality K (in mas/deg). The coefficient K was calculated from Eq. (36.26). Both sides of Eq. (36.26) were divided by half lengths of the water-tubes, $L / 2$ (Eq. 36.11). Next, the radians were converted into millisecond of arc (mas).

For the tube in azimuth –121.4°, whose length is 65.24 m, the coefficient is

$$K_{A1} = 2.089 \times 10^{-3} \text{ mas/deg}. \tag{36.34}$$

For the tube in azimuth –31.4°, whose length is 83.51 m, the coefficient is

$$K_{B1} = 1.632 \times 10^{-3} \text{ mas/deg}. \tag{36.35}$$

For tube $A1$ located in azimuth –121.4°, the time series of plumb line variations $\{T_n(t)\}$ is calculated from the formula

$$\{T_n(t)\}_{A1} = 2.089 \times 10^{-3} \text{ [mas/deg]} \ \{S_n(t)\}_{A1}. \tag{36.36}$$

For tube $B1$ located in azimuth –31.4°, the time series of plumb line variations $\{T_n(t)\}$, are calculated from the formula

$$\{T_n(t)\}_{B1} = 1.632 \times 10^{-3} \text{[mas/deg]} \ \{S_n(t)\}_{B1}. \tag{36.37}$$

Sensitivity of the tiltmeter in azimuth –121.4° (the shorter tube) is 78% of that of the tiltmeter in azimuth –31.4° (the longer tube). Equations (36.36) and (36.37) determined limits of the long water-tube measure-

ments. If the accuracy of determination of time series $\{S_n(t)\}$ is close to several degrees, then we are able to determine plumb line variations with an accuracy better than 10^{-2}mas in single measurement. For comparison, the accuracy of measurements of the quartz horizontal pendulums approaches 0.8 mas in yearly series of observations.

36.6.6 The difference method of plumb line variations measurements

In the previous section we described the method of determination of plumb line variations on the basis of single series of observations of water level variations obtained from one end of the tube. Simultaneous measurements of water changes on both sides of the tube enable us to apply the difference method of measurements. The measurements on both ends of the tube open additional possibilities of signals verification. The signals of plumb line variations consist of local signals as well as large-scale signals of geodynamic origin. The geodynamic phenomena such as direct and indirect tides, meteorological-origin loading effects, and Earth free oscillations, generate large scale signals of plumb line variations.

On account of the relation between the length of the tube (tens of meters) and tilt waves associated with large-scale phenomena (thousands of kilometers), the effects of water level variations generated at the ends of the tube are opposite (increasing and decreasing). The water-tube stays all the time on one slope of the tilt wave; never on both slopes. Therefore, the water level changes generated by large-scale phenomena are exactly correlated in opposite phases. Otherwise, local signals originated in the surroundings of the instrument or inside the hydrodynamic system of the instrument produce signals of conformable phases or signals appearing at one end of the tube only. All local signals (noise) were interpreted as a source of errors. On the basis of the series of progressive phases $\{S_n(t)\}_{A11}$ and $\{S_n(t)\}_{A12}$ obtained on the opposite ends of the tube, we determine the time series of plumb line variations $\{T_n(t)\}_{A12}$, from the formula

$$\{T_n(t)\}_{A12} = 2.089\times10^{-3}[\text{mas/deg}]\ \frac{\{S_n(t)\}_{A11} - \{S_n(t)\}_{A12}}{2}\ . \qquad (36.38)$$

Likewise, for the second tube, on the basis of progressive phases series $\{S_n(t)\}_{B11}$ and $\{S_n(t)\}_{B12}$, we calculate time series of plumb line variations $\{T_n(t)\}_{B12}$, from the formula

$$\{T_n(t)\}_{B12} = 1.632\times10^{-3}[\text{mas/deg}]\ \frac{\{S_n(t)\}_{B11} - \{S_n(t)\}_{B12}}{2}\ . \qquad (36.39)$$

Simple subtraction of signals from opposite ends of the tube (Eqs. 36.38 and 36.39) causes double amplification of all large scale geodynamic signals and partial reduction of local signals (noise). On the other hand, the summation of series of progressive phases $\{S_n(t)\}_{A11}$ and $\{S_n(t)\}_{A12}$, as well as the summation of series of progressive phases $\{S_n(t)\}_{B11}$ and $\{S_n(t)\}_{B12}$, caused elimination of large-scale geodynamic signals and summation errors. These errors originated mainly from the surroundings of the instrument and errors of data processing, such as cycle-slip effects. The time series of errors $\{\varepsilon_n(t)\}_{A12}$ and $\{\varepsilon_n(t)\}_{B12}$, are given by the formulae:

$$\{\varepsilon_n(t)\}_{A12} = 2.089\times10^{-3}[\text{mas/deg}]\ \frac{\{S_n(t)\}_{A11} + \{S_n(t)\}_{A12}}{2}\ , \qquad (36.40)$$

$$\{\varepsilon_n(t)\}_{B12} = 1.632\times10^{-3}[\text{mas/deg}]\ \frac{\{S_n(t)\}_{B11} + \{S_n(t)\}_{B12}}{2}\ . \qquad (36.41)$$

Basing on the comparative method we try to separate series of errors $\{\varepsilon_n(t)\}_{A12}$ and $\{\varepsilon_n(t)\}_{B12}$ into two channels, associated with the two ends of the tube. Applying the comparative method we are looking for effects which were registered only in one channel and effects whose plots have conformable shapes and conformable phases. If the process of separating series of errors into two channels is correct, we obtain an opportunity to additionally improve the large-scale geodynamic signals.

36.7 Determination of tidal wave coefficients on the basis of the long water-tube measurements

To determine the tidal wave coefficients we made a standard analysis of the 2003 yearly series of plumb line variations. The values of amplitude and phase coefficients were applied in the following section to calculate tidal ephemeredes and to separate plumb line variations of tidal and non-tidal origin, while the Earth free oscillations were of 26 December 2004. The tidal analysis of the 2003 yearly series was made with the help of the algorithm of Chojnicki (1977), basing on the least-squares method. The accuracy of tidal wave parameters was obtained from the Fourier analysis of residuum (Chojnicki 1978). For tidal adjustment we applied expansion of tidal potential given by Cartwright and Tayler (1971). The data adjustment was made independently for each of the tubes in their azimuths, -121.4° and -31.4°, calculated from north to west. The interval of observations applied in the adjustment process amounts to 13 months in the years 2003/2004. The tidal waves spectrum was divided into 18 groups, repre-

senting main tidal waves. From the tidal analysis we determined the values of amplitude coefficients and phase retardations for 18 tidal waves. We also obtained the mean square errors of all the observations. For both tubes, the results of adjustment showed relatively large values of mean square errors of tilt signals, close to 0.5 mas (Kaczorowski 2004, 2005). We explain the relatively large values of mean square errors (in comparison to sensitivity of measurement system – Sect. 36.6.5) by local effects associated with the phenomenon of air pressure compensation between the outside and the underground. This thesis is well confirmed by a coincidence of windy days and days of increased level of noise in registrations of plumb line variations. Other sources of errors are associated with cycle-slip effects in the progressive phases determination.

36.8 Observations of anomalous plumb line variations associated with Earth free oscillations on 26 December 2004

Phenomenon of the Earth free oscillations is generated by extremely strong seismic events. Dozen or so hours after the earthquake of MS equal to 9.1, which took place near the coast of Sumatra-Andaman Islands on 26 December 2004 (Seismological Bulletin 2004), we observed non-tidal plumb line variations. The Earth free oscillations are associated with several effects such as body waves, surface waves, compressions and dilatations of the Earth medium (Pekeris and Jarosch 1958, Alterman et al. 1959). Simultaneously, there are generated gravity and inertial accelerations as well as plumb line variations. Plumb line variations related to the Earth crust consist of tilt effects produced by surface waves and horizontal components of gravity and inertial accelerations.

Over two hours after the first seismic signals onset, that is, at $01^h\,11^m$ UT, we observed strong inertial signals. Horizontal components of inertial signals produced tilts and rotation of water surface in the measurement chamber of instrument (Sect. 36.5). Sequence of the following images showed displacements of the centers of Newtonian rings as well as their deformations from circular into elliptical shape (Fig. 36.8). Duration of inertial impulses amounted to just single seconds, and did not affect the water level in hydrodynamic system of tiltmeter. During the later phase of free oscillations, we did not observe inertial effects. The Sumatra -Andaman earthquake provided an opportunity to verify the hydrodynamic system of tiltmeter (Sect. 36.4). The results of observations show that the low-pass filters considerably reduce the contribution of short-period effects and effectively protect the hydrodynamic system against resonance.

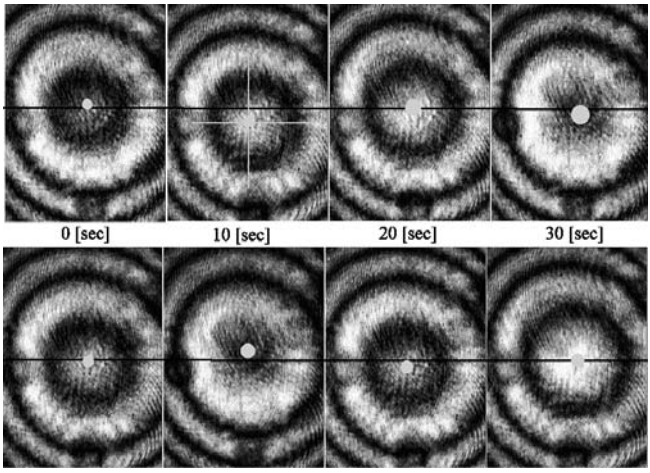

Fig. 36.8 Sequence of the Newtonian rings during the first hour of Earth free oscillations on 26 December 2004, as obtained from the water-tube situated in azimuth -121.4^{o}

This circumstance enables us to register a later phase of free oscillations (Figs. 36.9, 36.10, and 36.11). During the first two hours of the event we observed rapid variations of water level caused by the passing of surface waves (periods from hundred seconds up to tens of minutes) as well as effects of additional gravity and inertial accelerations. Accidentally, variations of water level became too rapid to be firmly registered. The ten-second period of interference image sampling was too long and we obtained a significant number of cycle-slip errors. Two hours later, the cycle-slip errors became incidental.

In Figs. 36.10 and 36.11, plots of plumb line variations registered by both tubes on 26 December 2004 are shown. Black plots represent the observed plumb line variations – difference of signals from ends of the tubes (Sect. 36.6.6). Dark grey plots describe noise – the sum of signals. Light grey lines present the modeled tide calculated on the basis of ephemerid obtained from the previous observations (Sect. 36.7). Results of subtraction of tidal signals from observations are shown in Figs. 36.12 and 36.13. The upper plots represent non-tidal-origin plumb line variations associated with free oscillations. The maximum amplitude observed reached 5 mas and decreases to 0.5 mas after two and a half hours. The lower plots describe the noise level (Sect. 36.6.6). These plots contain errors of data treatment caused by cycle-slip effects mainly. During the first two hours, amplitudes of errors caused by cycle-slip effects were close to the amplitudes of plumb line variations.

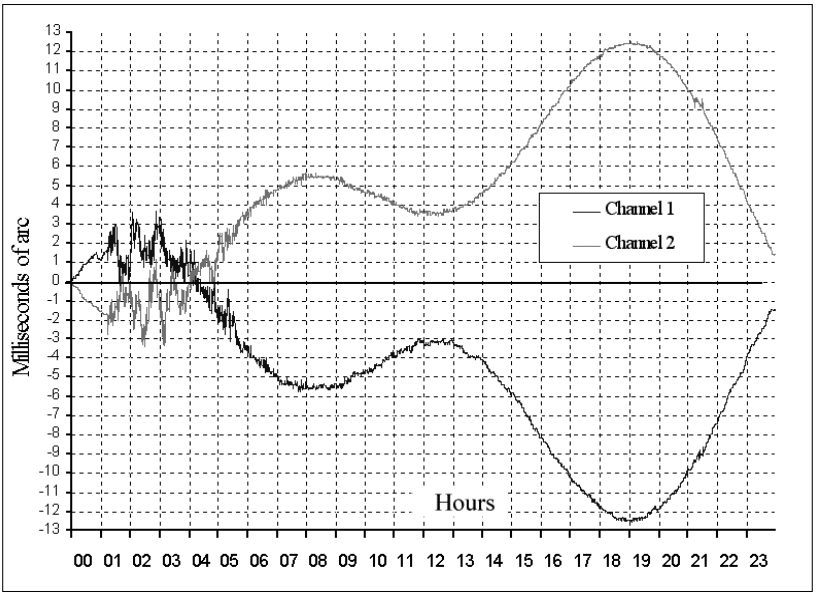

Fig. 36.9 Water level variations reduced to milliseconds of arc (mas) of plumb line variations obtained from two ends of the tube (channels 1 and 2) placed in azimuth –121.4°

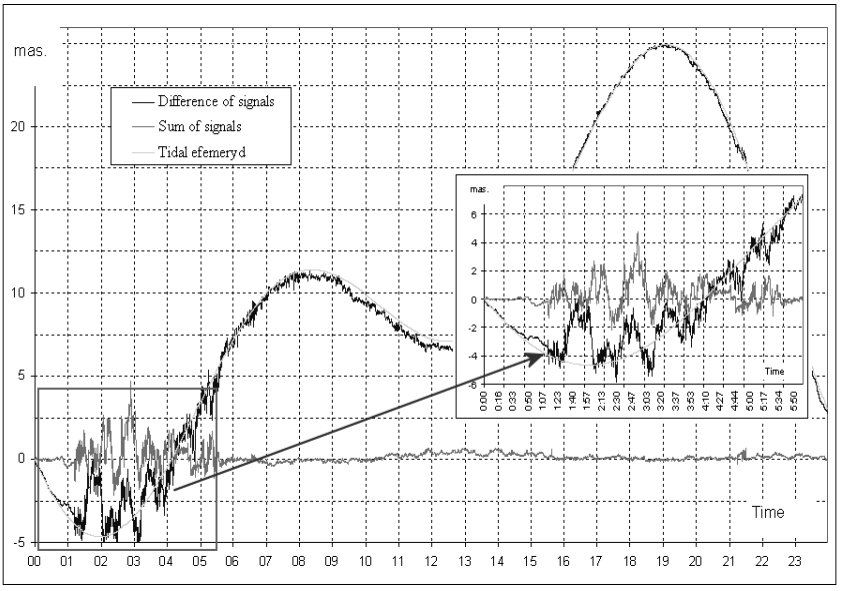

Fig. 36.10 The plumb line variations in azimuth –121.4° on 26 December 2004. Visible anomaly of plumb line variations associated with Earth free oscillations

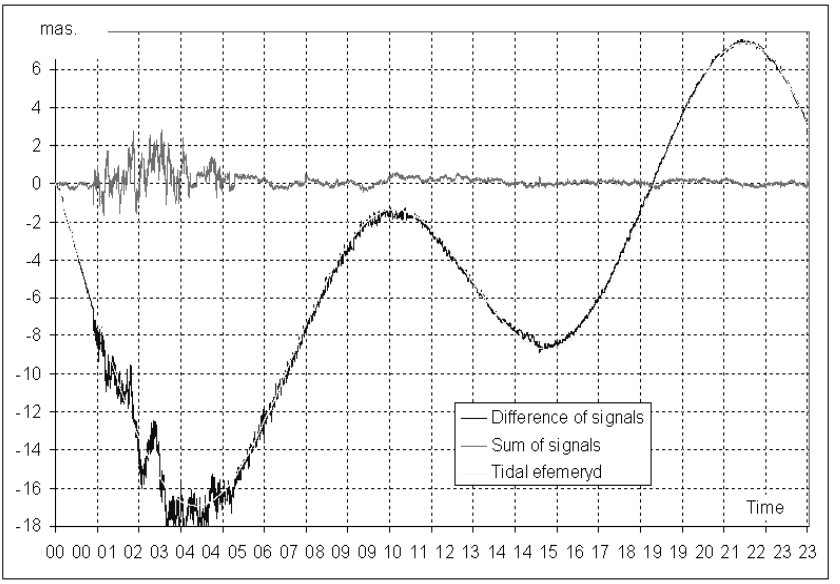

Fig. 36.11 The plumb line variations in azimuth –31.4° on 26 December 2004. Visible anomaly of plumb line variations associated with Earth free oscillations

In a later phase of the event, the level of noise decreased to tenth of mas. On the basis of data obtained from both water-tubes we assembled a plot of plumb line variations in space (Fig. 36.14). On this figure, the tubes are situated exactly on the axis of coordinates. The plumb line variations were shown in azimuths of measurements: azimuths of the tubes –31.4° and –121.4°. The magnified fragment of plot shows large complications of tilts signals affecting the instrument. The presented fragment was chosen from the end of third hour of the event and spread over fifteen minutes. During this interval, the amplitude of non-tidal plumb line variations was close to one mas. Then, the amplitudes of non-tidal tilt waves reduced to several tenth of mas. From Fig. 36.14 we can notice that non-tidal signals slightly affected tidal trends and that tilt waves associated with free oscillations cause only around-tidal variations of plumb line.

36.9 Conclusions

Several years of measurements carried out with the long water-tube tiltmeter confirm attractive features of this instrument (Kaczorowski 2004**)**. The long water-tube construction provides us with measuring system whose internal accuracy of measurement is close to several thousandths mas

(Sect. 36.6.5). Application of difference method for data processing eliminated the effect of instrumental drift (Sect. 36.6.6). The comparison of results of observations from previous years confirmed the high stability of the measurement system sensitivity.

We obtained a perfect correlation between tidal signals observed on 26 December 2004 and modelled tides calculated on the basis of observations from previous years (Figs. 36.10 and 36.11). Discrepancies between plots are associated with non-tidal plumb line variations of the Earth free oscillations. Several years of experience provided information about positive features of new instrument as well as information about some drawbacks of measuring system.

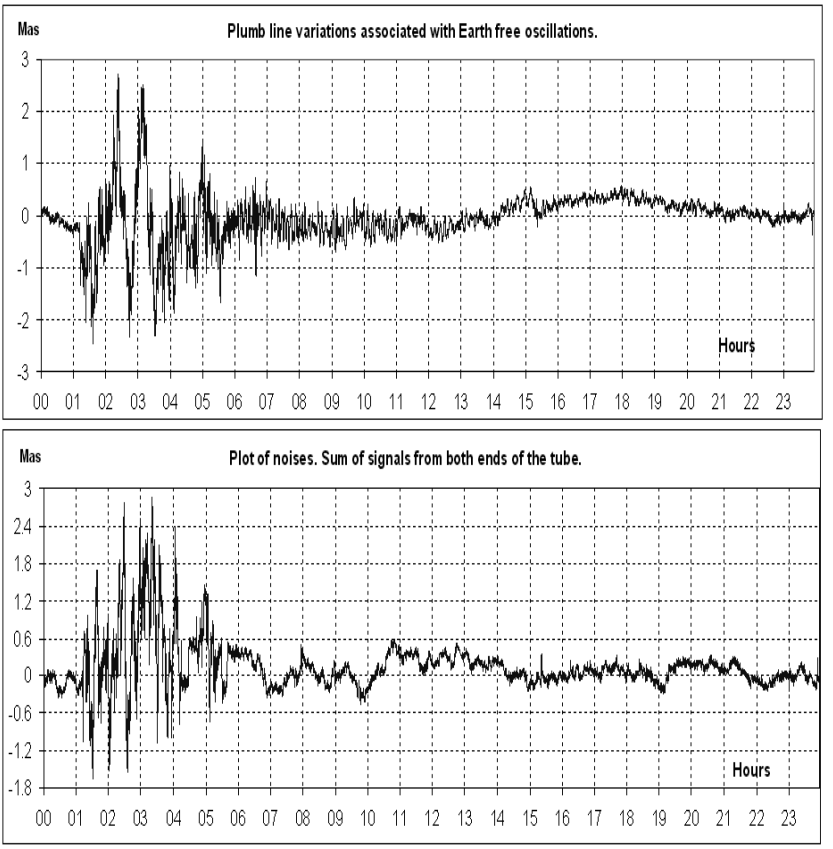

Fig. 36.12 Plots of differences and sum of signals from both ends of the tube in azimuth -121.4^{o} after subtraction of the tidal signal. Differences of signals (upper plot) represent effect of plumb line variations caused by Earth free oscillations. Sum of signals (lower plot) represents the noise level (Sect. 36.6.6)

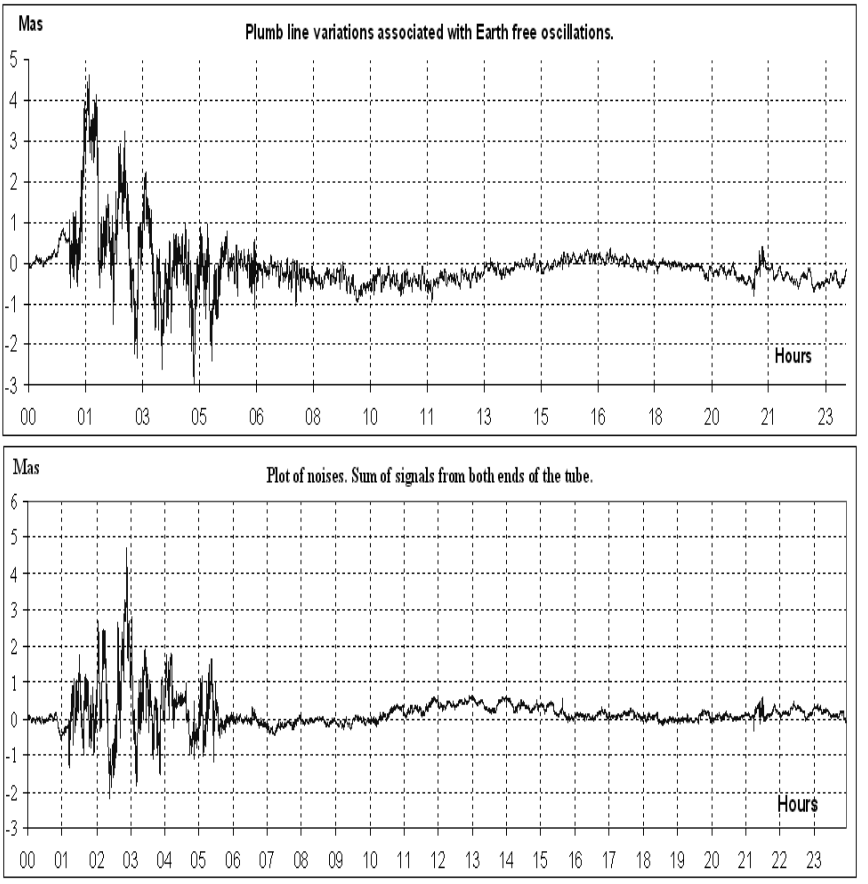

Fig. 36.13 Plots of differences and sum of signals from both ends of the tube in azimuth -31.4^{o} after subtraction of the tidal signal. Differences of signals (upper plot) represent effect of plumb line variations caused by Earth free oscillations. Sum of signals (lower plot) represents the noise level (Sect. 36.6.6)

There are two main problems of measurement: the cycle-slip effects (Sect. 36.6.4) and the pressure gradient appearing along the water-tubes of instrument. The pressure gradient disturbs water free surface through the inverse barometric effect. Gradient of the order of 10^{-6} hPa/m can be erroneously interpreted as plumb line variations. Both problems can be solved. Cycle-slip effects will be eliminated by changing the method of image registration from regular (every ten seconds) into irregular control by phase variations between the succeeding interference images. Application of a new system of registration will reduce the number of cycle-slip effects as well as the number of stored images. The second problem related to

pressure gradient in underground tunnels can be solved by limitating the air exchange between underground and the outside. The phenomenon of air pressure compensation in the underground plays the main role in generating the water free surface disturbances producing signals of the order of 0.5 mas (values of the mean square errors – see Sect. 36.7). For this purpose, we are going to build two partition walls separating tunnels with the instrument from the rest of the underground. Our experiences with the long water-tube tiltmeter confirm particular properties of the new instrument, such as high sensitivity, lack of instrumental drift, constant and well determined sensitivity of measuring system, constant and well known azimuth of measurements as well as effectiveness of damping the system for short-period seismic effects. Simultaneously, differential method of data treatment helps us to reduce the level of errors of instrumental origin (Section 36.6.6). The features of the long water-tube confirmed the usefulness of our instrument for investigation of wide range of long-period geodynamic phenomena such as Earth free oscillations, tidal effects, as nonperiodic loading effects of atmospheric origin as well as tectonic plates motions.

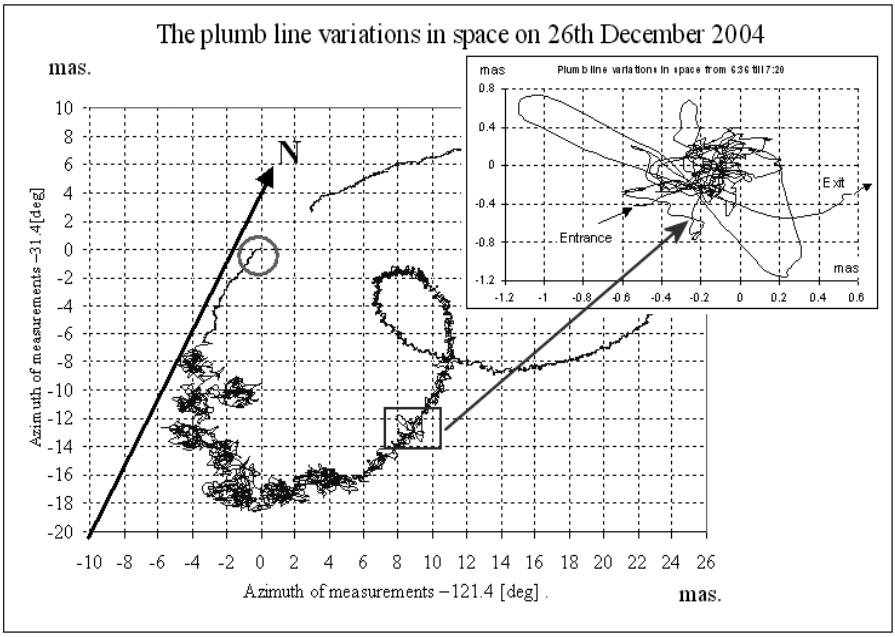

Fig. 36.14 Plumb line variations in space, assembled on the basis of measurements from the two water-tubes

References

Alterman Z, Jarosch H, Pekeris CL (1959) Oscillations of the earth. Proc Roy Soc London **A 252**: 80

Bower DR (1973) A Sensitive water-level tiltmeter. Measurem, Interpretat, Changes of strain in the Earth. Phil Trans Roy Soc **A 274**: 1239, 223-226

Cartwright DE, Tayler RJ (1971) New computations of the tidal-generating potential. Geophys J Roy astron Soc **23**: 45-73

Chojnicki T (1977) Sur l'analyse des observations de marees terrestres. Ann Geophys **33**: 157-160

Chojnicki T (1978) Estimation of accuracy of tidal data adjustment results based on a residual spectrum. Publs Inst Geophys Pol Acad Sc **F-4**: 129, 3-9

Chojnicki T (1991a) Détermination des variations des amplitudes des ondes de marées. Bull Inform Marees Terr, no 109, Obs Royal de Belgique, Bruxelles, 7877-7884

Chojnicki T (1991b) Modulation of some tidal waves of horizontal constituents. Proceed of the XI Intern Symp on Earth Tides, Helsinki '89, E Schw Verlagsb Stuttgart, Germany, 249-255

Kaczorowski M (1989) Seasonal variations of the ocean indirect effects, Proc 11th Intern Symp on Earth Tides, Helsinki, 321-334

Kaczorowski M (1991) The ocean indirect effect model for European tidal stations. Publs Inst Geophys Pol Acad Sc **F-17**: 237, 103-124

Kaczorowski M (1999a) The long water-tube clinometer in Książ Geophysical Station. Promotion of the works. Artificial Satellites **33**: 2, 77-93

Kaczorowski M (1999b) The results of preliminary tilt measurements by use of the long water-tube clinometer in Książ Geophysical Station. Artificial Satellites **33**: 2, 77-93

Kaczorowski M (2004) Water tube tiltmeter in Low Silesian Geophysical Observatory results of preliminary observations. Artificial Satellites **39**: 2, 147-154

Kaczorowski M (2005) Discussion on the results of analyses of yearly observations (2003) of plumb line variations from horizontal pendulums and long water-tube tiltmeters. Acta Geodyn Geomater **2**: 3 (139), 1-7

Love AEH (1911) Some problems of geodynamics. Cambridge University Press, Cambridge, pp. XXVIII+180

Love AEH (1927) A treatise on the mathematical theory of elasticity. Cambridge University Press, Cambridge, pp XVIII+643

Moulton FR (1919) Theory of tides in pipes on a rigid earth. Astroph Journ **50**: 346-355

Ozawa I (1967) On the tidal observation by means of a recording water-tube tiltmeter. Journ Geod Soc Japan **12**: 151-156

Pekeris C, Jarosch H (1958) The free oscillations of the earth. In: Benioff H, Ewing M, Howell BF, Press F (eds) Contributions in Geophysics, Pergamon Press, London, pp 171-192

Seismological Bulletin 2004, Publs Inst Geophys Pol Acad Sc (in print)

37 Fiber Optic Sensors for Seismic Monitoring

William B. Spillman Jr.[1], Dryver R. Huston[2], Junru Wu[1]

[1]Physics Department, University of Vermont, Burlington, VT, USA
e-mails: wspillma@vt.edu; jun-ru.wu@uvm.edu

[2]Mechanical Engineering, University of Vermont, Burlington, VT, USA
e-mail: drhuston@verizon.net

37.1 Introduction

Damage in civil structures due to earthquakes is a serious problem. New approaches in active damping of earthquake induced structural vibrations can mitigate this problem if sufficient warning time is given for an impending earthquake. A number of approaches have been implemented in seismic sensing technology to provide this warning. Seismic sensing is also critical in detecting and characterizing underground nuclear tests. Most approaches employ either a single point sensor or an array of such sensors. In this paper, we explore the possibility of using very long gauge length fiber optic sensing technology to create very high sensitivity seismic sensors that have the ability to focus on particular fault regions or nuclear test sites through the use of particular spatial antenna configurations.

37.2 Seismic Monitoring

Detection of seismic waves has been found to be one of most effective ways for the earthquake prediction. Compared with other physical phenomena associated with earthquakes such as heat flow, static displacement, strain and electromagnetic radiation, seismic waves have the following advantages (Aki and Richards 1980): 1. The high resolution and accuracy are attainable as seismic waves have the shortest wavelength of any wave that can be observed after passing through structures inside the earth; 2. Seismic waves undergo the least distortion in waveform and the attenuation in amplitude.

Generally speaking, the three types of earthquake waves (*P*, *S* and Rayleigh waves) are generated during an earthquake; *P* waves travel

fastest and are followed by *S* waves and Rayleigh waves. Thus, *P* waves are also called the primary waves. Analysis and interpretation of seismograms can help to determine the epicenter and strength of an earthquake. Since the wavelengths of all three waves are usually long, the very long gauge length fiber optical detectors have obvious advantage compared with other detectors. A schematic showing characteristic detected amplitudes from an earthquake are shown in Fig. 37.1. Also shown is a characteristic signature from an underground nuclear test such as have been carried out recently by India and Pakistan. As can be seen, a clear distinction can be made between the natural and artificial events.

The conventional method of sensing seismic motions is to use an array of accelerometers that measure the accelerations at a particular point. Seismic accelerations are fairly difficult to measure because of the wide dynamic amplitude ranges that occur between earthquakes and tremors and the sub-Hertz frequencies that have to be measured and the rarity and short duration of strong earthquakes. Nonetheless, these problems have been largely overcome through the use of carefully selected accelerometer proof masses, springs, triggering mechanisms and storage media. Measuring seismic behaviour over an extended region requires using an array of synchronized accelerometers. This is a fairly expensive proposition, but has been accomplished successfully for a few strong earthquakes, such as the El Centro earthquake. An alternative point sensor array technique is to use an array of voice-coil velocimeters known as geophones. Geophone arrays are commonly used in seismic exploration for oil with detonated charges.

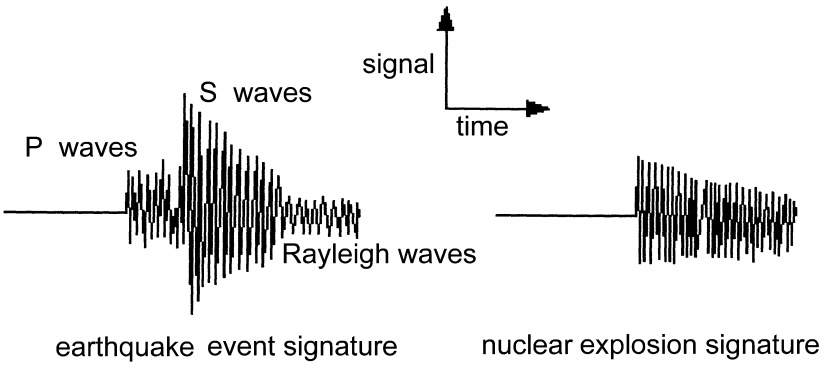

Fig. 37.1 Different types of seismic waves

37.3 Sensor/Ground Coupling

The interaction of a seismic event and a civil structure, such as a building, bridge or dam, is quite complicated due to the traveling of elastic waves through non-homogeneous soil and rock media into a flexible solid structure with its own dynamic stiffness, damping and inertia. Depending on the level of complexity required, several different types of engineering models of soil-structure interaction are used. The simplest model is one where it is assumed that the dynamics of the structure do not appreciably affect the soil motions at the base of the structure. In this case, the ground motions are simply used as an input into the structure, thereby causing an inertial loading in the form of base excitation. The ground motions that occur in an earthquake can vary quite widely from location to location. The variation is attributed to the ability of the localized soil elasticity to amplify the ground motions. Site amplification is particularly bad when there is a soft soil layer over a solid rock base, such as in Mexico City. An additional complication arises if the structure is of sufficient size so that the localized site motions are appreciably different at different parts of the structure. An example would be a long suspension bridge. In this case, the different base motions must be accounted for in the analysis, by methods such as pseudo-static functions. If the stiffness and inertia of the structure appreciably affect ground motion, then a set of coupled field equations between the elasto-dynamics of the soil and structure has to be solved. With the exception of a few simple geometries, the analysis requires numerical simulation.

37.4 Fiber Optic Sensing

The field of fiber optic sensing was born in the late 1970's as an adjunct to fiber optic telecommunications (Miller and Chynoweth 1979). Optical fibers are very small cylinders of glass of arbitrary lengths that are essentially lossless transmission media for optical signals of the appropriate wavelength. In general, optical fibers have an inner glass core region in which light travels more slowly than in a surrounding glass cladding region. The glass fiber is protected from the environment by a non-glass buffer coating. A fiber optic sensor consists of an optical source, optical fiber to carry the light from the optical source to the sensing region, a transducer to couple the parameter of interest to changes in the optical signal, a fiber to take the modulated optical signal to a signal processing location where the optical signal is then converted to a digital electrical signal

and a computer which processes the digital signals to extract the information of interest. If the light is extracted from the fiber by the transducer, modulated and then re-injected into the fiber, the sensor is called an extrinsic fiber optic sensor. If, on the other hand, the light never leaves the fiber, the sensor is called an intrinsic fiber optic sensor. Fiber optic sensors possess a number of advantages including:

– arbitrary separation between sensing location and signal processing location (lossless transmission),
– immunity to electromagnetic interference,
– high sensitivity and large dynamic range,
– small size and light weight,
– scalability,
– non-metallic and electrically passive (secure signal transmission),
– geometric flexibility,
– ability to be multiplexed,
– ability to sense a wide spectrum of different parameters.

37.4.1 Types of fiber optic sensors

The light traveling through an optical fiber has a number of characteristics that can be modulated by a transducer to encode information about the parameter of interest. These include the intensity of the light, its polarization state, its wavelength (frequency), its coherence and its speed. It is important to note, however, that in the final analysis what is always detected is the intensity of the light as a function of time. The light may be interfered with a reference signal, passed through a polarizer or reflected off a grating to disperse its different wavelength components into different directions, but in the end, one converts an optical intensity signal into a digital electrical signal that is analyzed appropriately to extract information about some parameter or parameters of interest.

Since the inception of the field of fiber optic sensing, a very large number of different transducer mechanisms have been proposed and investigated, too many to list here. However, some of the more significant types of fiber optic sensors that have been demonstrated include:

- Mach–Zhender interferometric sensors: these were the first practical fiber optic sensors that were developed. These sensors are now the basis of extremely sensitive hydrophone arrays deployed by the U.S. Navy and others. This type of sensor is based upon a measurement of a difference in travel times between a sensing fiber optic pathway and a reference pathway. The speed in the sensing arm is modulated by stress-

induced changes in the refractive index and length of the optical fiber. When the signal from the sensing arm is compared with a signal that has passed through the reference arm (interfered), the integrated stress along the sensing fiber can be inferred. Since the basic effect is very small, very long lengths of fiber must be used, although they are generally wrapped around small mandrels, making these sensors essentially sensors which only measure changes at a point.

- Sagnac interferometers: these sensors are used to measure rotation rate in a highly accurate manner. This type of sensor is based upon the fact that if a loop of fiber is rotated, one end of the fiber moves away from the optical signal transmission direction and the other end moves towards the optical signal transmission direction. This results in a difference in transit time for signals going clockwise and anti-clockwise. When this difference in transit time is determined (by interfering the two signals), the rotation rate can be inferred. This type of sensor is currently installed and used on a number of different types of aircraft.
- Photoelastic sensors: these sensors are based upon the fact that many materials, when stressed, have different speeds of light depending upon whether the direction of electric field of the light is parallel to or perpendicular to the stress direction. Glass, polycarbonate and many other materials exhibit this effect. Sensors of this type have been used as fluid level monitors in large oil containment vessels in China.
- Grating based sensors: these types of sensors rely on the properties of gratings to modulate optical signals. The relative motion of two gratings can be used to modulate the intensity of an optical signal. The rotation of a diffraction grating can be used to modulate the wavelength distribution of an optical signal to encode rotary position, while a spatially chirped grating can be used to encode linear displacement. One of the more successful grating based sensors is called the fiber Bragg grating sensor. In this sensor, periodic index of refraction (speed) variations are created in an optical fiber in a very small region. When the period of the grating is one half the wavelength of light in the fiber, constructive interference occurs and a large backscattered signal results. If the grating period is changed due to some parameter of interest, the wavelength of backscattered light changes accordingly, assuming that a broadband (large number of wavelengths) was incident on the grating to begin with. These types of sensors have been used to monitor many different composite and civil structures.
- Fabry–Perot sensors: this type of sensor was first developed in the late 1980's. It is based upon the fact that an optical cavity with partially re-

flecting boundaries will transmit or reflect light in a way that is extremely well characterized and depends only on the reflectivity of the boundaries and the distance across the cavity. If the distance across the cavity is modulated, then this can be detected as either an intensity modulation (for a monochromatic signal) or a wavelength modulation (if a broadband signal is used). This kind of sensor has been utilized in a number of applications and is part of the product lines of a number of commercial enterprises.

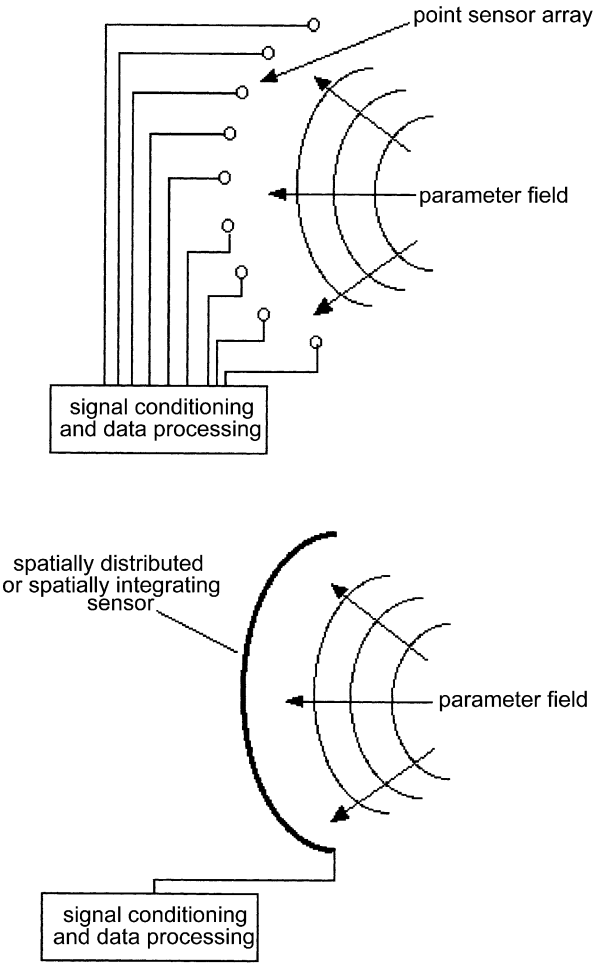

Fig. 37.2 Point *versus* distributed sensor systems

37.4.2 Point *versus* long gauge length sensing

There are numerous ways in which sensing systems can be configured. These are: single point sensor, multiple single point sensors, point sensors configured into a spatially ordered array, quasi-distributed sensors, spatially integrating distributed sensors and fully distributed sensors. To appreciate the advantages and disadvantages of some of these system types, we consider the use of a number of point sensors configured into a spatially ordered array *versus* a spatially integrating distributed sensor for the purposes of monitoring a spatially confined source of seismic signals. This situation is shown in Fig. 37.2. As can be seen, both systems are configured so that signals from the seismic source arrive in phase to the sensors. For the case of the point sensor array, however, each individual sensor has its own dedicated transmission path to the signal conditioning and data processing location. The summing of all the sensor signals is done electronically to provide the final output. In the case of the spatially distributed integrating sensor, however, only one transmission path is required and the summing of signals is done directly along that transmission path. This results in a significant reduction in the cost and complexity of the integrated system *versus* the point sensor array as can be seen. In order for this situation to be effective, however, domain knowledge must exist as to the location and distribution of the potential source of seismic waves of interest.

37.4.3 Simple displacement sensing

Some of the earliest seismic monitors involved a proof mass attached to a spring, with a pen attached to the mass that wrote on a long strip of paper that continuously scrolled by. A modern version of this type of monitor could be made using optics as shown in Fig. 37.3. This type of sensor has been demonstrated for the purposes of very high sensitivity underwater acoustic detection (Spillman 1981). The technique, as shown in Fig. 37.3, involves the use of a pair of equivalent optical absorption gratings that are offset by one quarter of a grating period. One grating is free to move (attached to the spring and proof mass) while the other grating is fixed. When the moving grating moves towards alignment with the fixed grating, the optical signal transmitted through the grating pair increases. When the moving grating moves in the opposite direction, the optical signal transmitted through the grating pair decreases. Motions of the proof mass will then modulate the intensity of any optical signal transmitted through the grating pair. The dynamic range of such a system will be equal to displacements of one quarter of a grating period at the maximum end and approximately

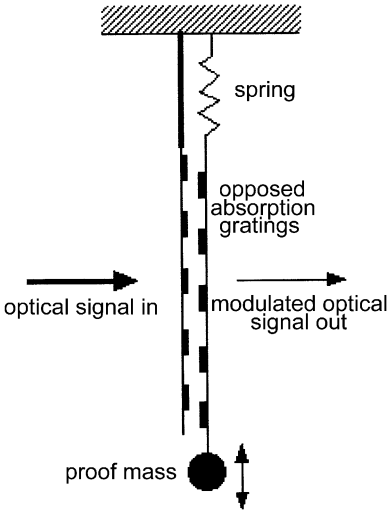

Fig. 37.3 Conceptual optical point seismic transducer

a million times smaller than that for minimum displacement detection (assuming a relatively low power shot noise limited source and no other sources of vibration noise). In the acoustic sensor work previously noted, the grating period was of the order of 5 μm, which gives an indication of how sensitive optical techniques can be when applied in a simple fashion to the problem of the detection of displacements due to seismic disturbances.

37.4.4 Statistical mode (STM) sensing

One of the better ways to carry out spatially distributed integrating sensing is to use fiber optic technology. Numerous different types of sensors have been developed which can be configured with very long gauge lengths. We have investigated what is called a statistical mode sensor (STM) for this purpose. In this type of sensor, coherent light is injected into a multimode fiber. Since there are many propagation modes with different propagation constants, the light exiting the fiber exhibits a complex interference pattern. Perturbation of the fiber changes the distribution of optical power within the output cone but not its integrated value. Since the change in pattern is due to relative phase changes, perturbations along the fiber sum and the device output depends upon the integrated perturbation, *P*. The STM device essentially takes a picture of the output power distribution and

stores it. It then takes a second picture and sums the absolute values of the differences between all of the small corresponding elements of the two pictures. The first picture is then replaced by the second, a new picture is taken and the process is repeated. It has been shown (Spillman et al. 1989) that the STM output is directly proportional to the absolute value of first time derivative of the integrated perturbation, i.e.

$$\text{signal} = C\left|\frac{\mathrm{d}P}{\mathrm{d}t}\right|. \tag{37.1}$$

A schematic diagram of this kind of sensing is shown in Fig. 37.4

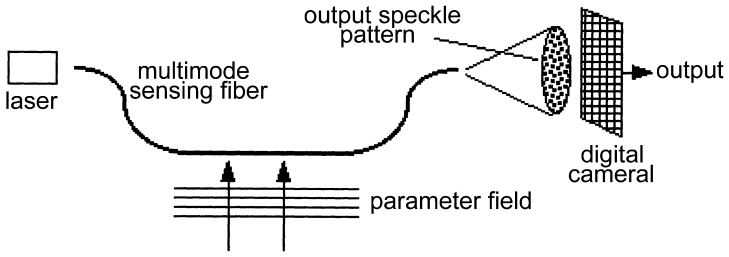

Fig. 37.4 Schematic diagram of STM spatially integrating fiber optic sensor

37.4.5 High order mode excitation (HOME) sensing

Another method of using fiber optics to perform spatially distributed integrating sensing involves the use of modal conversion. In HOME sensing (Herczfeld et al. 1990), light is injected into a multimode fiber so that only the higher order (high angle) modes are excited. In the absence of perturbation, light exiting the fiber forms an annulus when projected on a screen. Perturbation of the fiber converts some of the higher order modes into low order modes, i.e. optical power appears in the what was the un-illuminated center of the annulus. If a large area detector is placed so that it only intercepts the inside of the original annulus, it will produce a signal that is directly proportional to the perturbation integrated along the fiber, i.e.

$$\text{signal} = C\,P(t)\,. \tag{37.2}$$

A schematic diagram of this kind of sensing is shown in Fig. 37.5

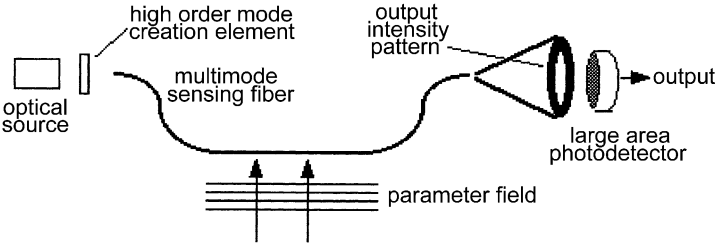

Fig. 37.5 Schematic diagram of HOME spatially integrating fiber optic sensor

37.4.6 Combined large dynamic range STM/HOME sensing

Both the STM and HOME sensors have advantages and disadvantages. The STM sensor, which is basically a multi-path optical interferometer, has extremely high sensitivity up until the point when the effect of the integrated perturbation causes phase shifts greater than 2π between the interfering modes. This point represents the upper limit of the dynamic range of this type of sensor. The HOME sensor, on the other hand, requires rather large physical displacements of the fiber before the mode conversion mechanism becomes significant. It is possible, however, to combine both techniques into a single sensor as shown in Fig. 37.6. In this case high order coherent modes are created in the fiber, resulting in an output annulus having a speckle pattern. If this is projected onto a digital camera and processed in the same fashion as a standard STM sensor, a high sensitivity output will result. When the perturbations become so large as to saturate the STM technique, modal conversion comes into play, with the summed intensity of the previously unilluminated pixels at the center of the annulus providing the equivalent of a HOME sensor output. This type of hybrid

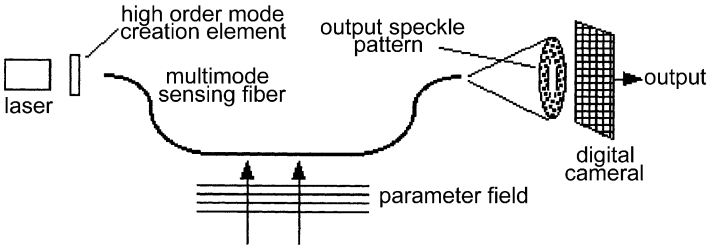

Fig. 37.6 Combined STM/HOME spatially integrating fiber optic sensor

sensor possesses the advantages of both types of spatially distributed integrating sensor while providing a greatly extended dynamic range (Meissner and Spillman 2004).

37.5 Matched Filtering/Antenna Gain

Very long gauge length sensors can be configured so that they serve as matched filters for spatially distributed parameter fields of interest. This has previously been demonstrated for particular mode signal enhancement in simply supported vibrating beams (Spillman and Huston 1995) and for vehicle identification (Spillman and Huston 1996). If one wishes to detect and discriminate for a given parameter field as shown in Fig. 37.7, then both the spatial configuration and sensitivity weighting of the long gauge length sensor must be optimized.

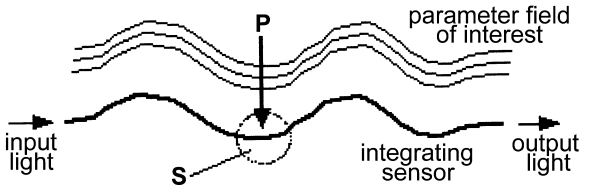

Fig. 37.7 Matched filtering

In order to see this, it will be assumed that the parameter field of interest is given by the parametric function $P[\mathbf{x}_P(s)]$, where s ranges from 0 to L, and is zero elsewhere. It is also assumed that there is a long gauge length sensor described by the parametric function of sensitivity $S[\mathbf{x}_S(s')]$, where s' ranges from 0 to L, but the functional dependency, $\mathbf{x}_S(s')$, is undetermined. The sensor output will be given by the integration of the value of the parameter field of interest times the sensitivity along the sensor length at those positions where the two functions spatially overlap, i.e.

$$\text{signal} = \int_0^L \mathrm{d}s \int_0^L \mathrm{d}s'\, P\left[\mathbf{x}_P(s)\right] S\left[\mathbf{x}_s(s')\right] \mathrm{d}\left[\mathbf{x}_p(s) - \mathbf{x}_s(s')\right]. \tag{37.3}$$

The sensor output is clearly maximized when $\mathbf{x}_S(s') = \mathbf{x}_P(s)$ or $\mathbf{x}_S(L - s') = \mathbf{x}_P(s)$, i.e. the sensor gives the maximum output when it is spatially configured to match the spatial distribution of the parameter field it is trying to detect.

Once the sensor is spatially configured to match the parameter field of interest, one must consider how to optimize the sensitivity distribution to select for $P[\mathbf{x}_P(s)]$ as opposed to other parameter fields that might be present. If the sensor is spatially matched to the desired parameter field, then

$$\text{signal} = \int_0^L \mathrm{d}s \; P[s]\, S[s]. \tag{37.4}$$

If P and S are unrelated (uncorrelated), then they can each be replaced by their expectation values and the signal will be ($L<P><S>$). If S is some constant value, S_0, then the signal would be [$LS_0<P>$]. Finally, if S is completely correlated with P (i.e. $S = P$), then the signal would be [$L<P^2>$]. To compare these, consider that both P and S are normalized and uniformly distributed on the interval [0,1]. Their expectation values would then be $<S> = <P> = 0.5$. Also assume that $S_0 = 0.5$ (i.e., its expectation value is the same as for the uncorrelated case). Then for both the uncorrelated S and the constant S cases, the signal would be [0.25 L]. For the complete correlated case, the signal would be given by

$$\text{signal} = L < P^2 > = L \int_0^L \mathrm{d}\mathbf{x}\, \mathbf{x}^2 = 0.333\, L\,. \tag{37.5}$$

It is then clear that by making the sensitivity distribution of the long gauge length sensor equal to the parameter distribution sought, the signal output is enhanced by 33% over what would be produced by an uncorrelated parameter distribution in the same spatial configuration. For optimum matched filtering with long gauge length integrating sensors:

– Sensor spatial distribution must be matched to desired parameter spatial distribution;
– Sensor sensitivity distribution must be matched to desired parameter distribution.

In order to better understand the matched filtering concept, we modeled a seismic signal from a distant source in two ways, as a circular wave (near field) and as a plane wave (far field). A square tone burst was used as the signal function. In the circular wave case, the wave was modeled so as to have its energy density fall off as a function of r^{-2} from some point source. The plane wave was assumed to have a uniform energy density. The effect of each type of wave on two different types of spatially distributed integrating sensor configurations was calculated, a circular antenna segment and a linear antenna segment, both of the same length. The effects of both

rotation and displacement of the antenna segments relative to the incident waves were considered. In Fig. 37.8, a circular wave is shown impinging upon a circular antenna segment. During rotation, the segment is rotated around a point on the midpoint of the segment cord on the *x*-axis. In Fig. 37.9, a plane wave is shown impinging on a straight line antenna segment. During rotation, the segment is rotated around a point on the midpoint of the segment on the *x*-axis. For zero rotation, both segments were assumed to intersect the *x*-axis at the same point. The interactions of a plane wave with a circular antenna segment and a circular wave with a straight line antenna segment were also calculated.

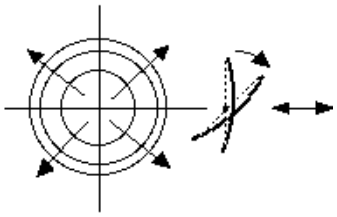

Fig. 37.8 Circular antenna segment in a circular wave field

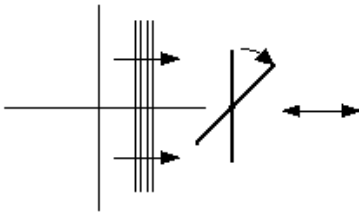

Fig. 37.9 Straight line antenna segment in a circular wave field

Figure 37.10 shows the effects of rotation of a circular antenna segment centered on a circular wave signal source. Only for 0 degree rotation is the true signal recovered. For other angles, phase cancellation occurs and the signal duration expands as the antenna segment intercepts the wave for longer and longer periods of time. In Fig. 37.11, the same circular wave is intercepted by a straight line antenna. The square tone burst envelope is lost for this configuration and frequency information is only present for low angles of rotation. Similarly, when a plane wave is incident upon a straight line antenna segment (Fig. 37.12), the true signal is recovered for 0 degree rotation, but for other angles. Frequency information is lost along with an accurate measure of the tone burst envelope. When the plane wave is incident on the circular antenna segment (Fig. 37.13), frequency infor-

mation is only present for low angles of rotation and information about the actual tone burst envelope is not lost.

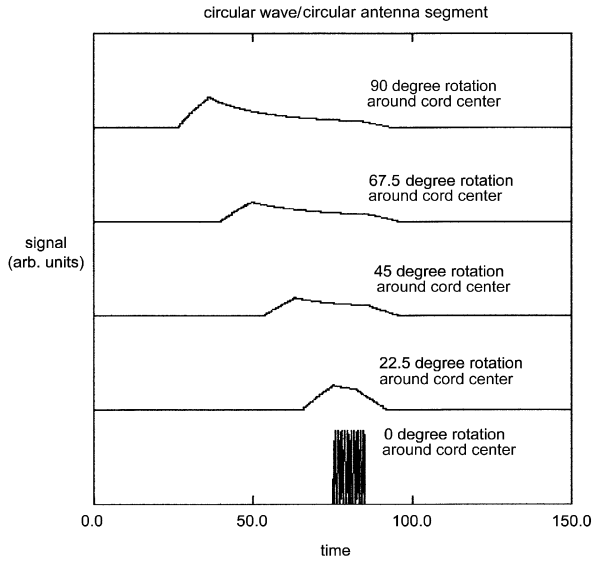

Fig. 37.10 Circular antenna segment response to a circular wave as a function of rotation

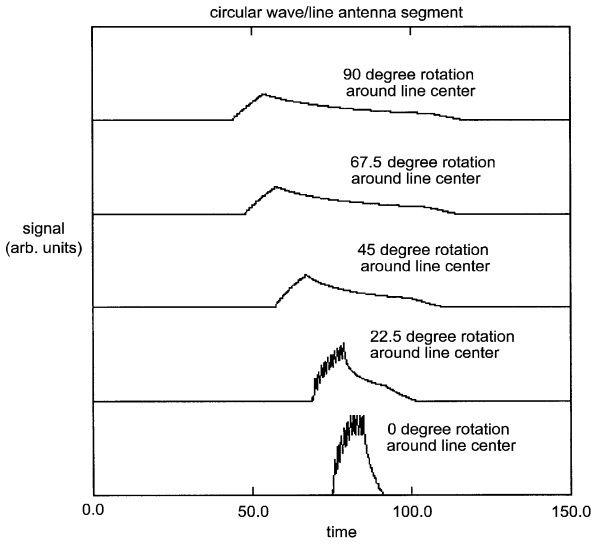

Fig. 37.11 Straight line antenna segment response to a circular wave as a function of rotation

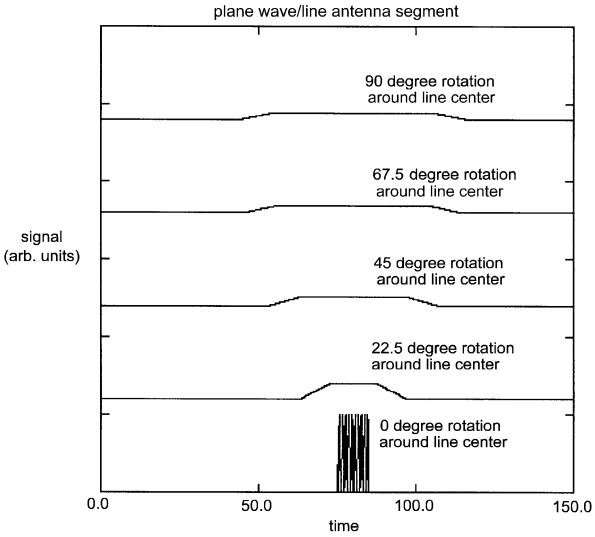

Fig. 37.12 Straight line antenna segment response to a planar wave as a function of rotation

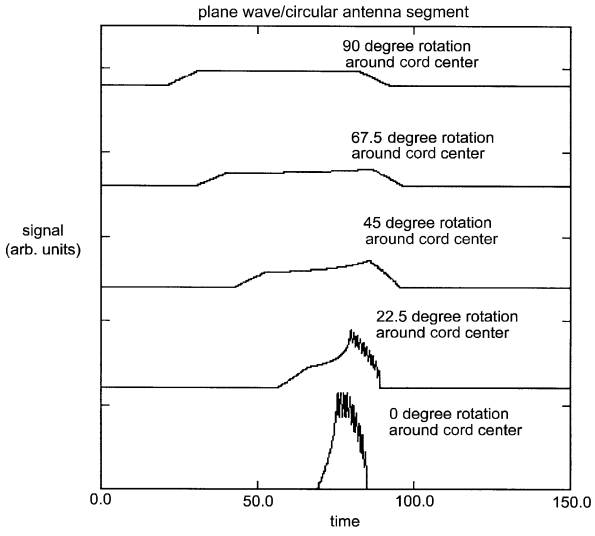

Fig. 37.13 Circular antenna segment response to a planar wave as a function of rotation

When the antenna segments are fixed at 0 degrees rotation and then relatively displaced along the *x*-axis, a different kind of behaviour is observed. In Fig. 37.14 with a circular wave incident upon a circular antenna segment, signal detection delay as a function of displacement is clearly seen. The true signal is only recovered when the antenna segment lies on a circle whose center is the center of the circular wave disturbance. Otherwise, the signal is largest when nearest the source (r^{-2} behaviour) and significant dc signal components are present. In Fig. 37.15, where the circular wave intercepts the straight line antenna segment, signal detection delay is also observed, basic signal shape remains the same with its amplitude falling off as r^{-2}. In Fig. 37.16, only signal detection delay is observed since the plane wave has uniform energy density. The true signal is recovered in every case. For a plane wave impinging upon a circular antenna segment, the signal is distorted due to the mismatch between wave shape and antenna shape, signal detection delay is observed and signal shape and amplitude remain constant.

As can be seen, only when the antenna shape precisely matches the shape of the parameter field will the actual wave function be recovered (matched filtering)

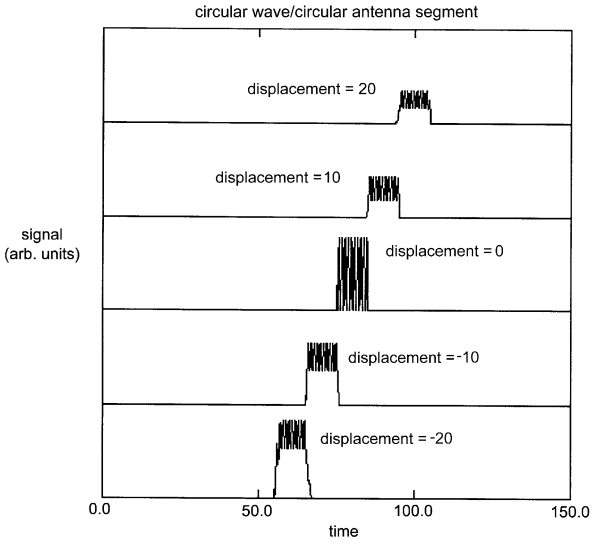

Fig. 37.14 Circular antenna segment response to a circular wave as a function of displacement

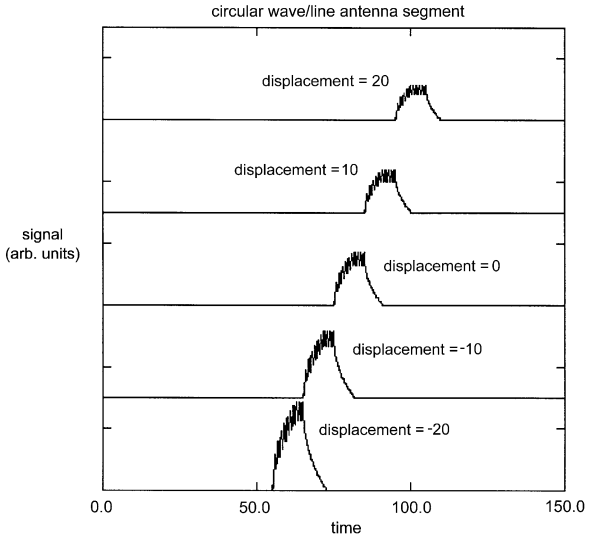

Fig. 37.15 Straight line antenna segment response to a circular wave as a function of displacement

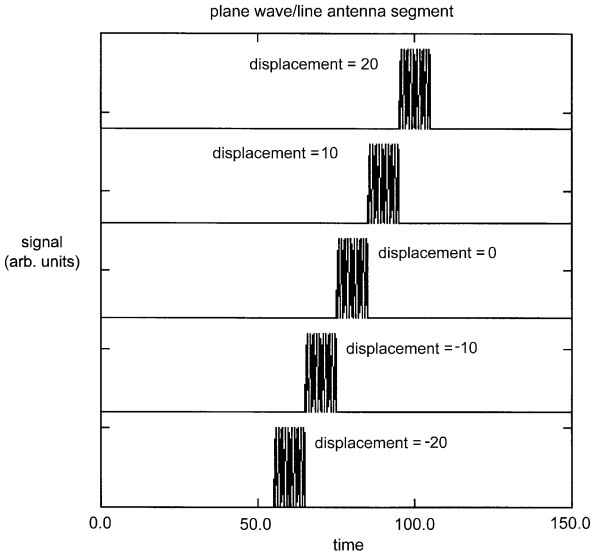

Fig. 37.16 Straight line antenna segment response to a planar wave as a function of displacement

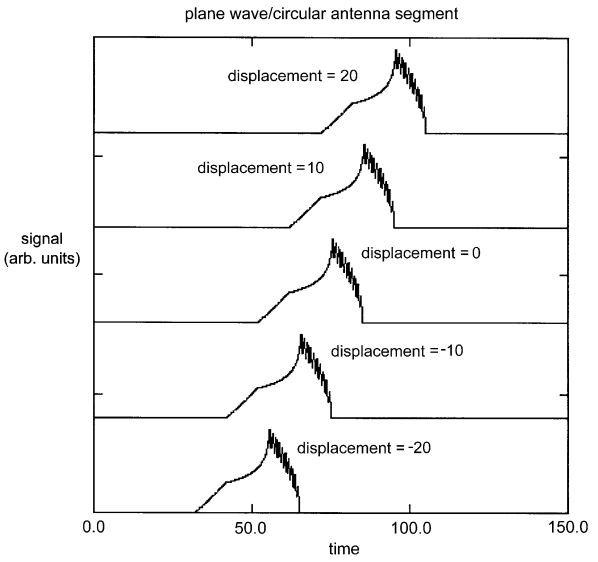

Fig. 37.17 Circular antenna segment response to a planar wave as a function of displacement

37.6 Physical Simulation Results Using STM

An experiment was set-up to physically simulate Rayleigh seismic wave antenna interactions in a subscale fashion. A square wooden tank, 109 x 109 x 5 cm was fabricated and lined with plastic. The tank was then leveled and filled with water to a depth of 1 cm. The integrated sensing length was taped to piece of plastic on the surface of the water in either a linear or circular arc antenna configuration. Waves generated on the surface of the water in the tank perturbed the sensing length in the same way that a Rayleigh earthquake wave would perturb a much larger sensing element.

Seismic wavefronts seen at a sensing location depend upon the proximity of the sensor to the event. All Rayleigh waves will consist of circular waves propagating outward from the epicenter. To lowest order, near the epicenter, Rayleigh waves will exhibit significant curvature when measurement lengths of the order of a kilometer are considered. As the distance from the epicenter increases, the amount of curvature over a kilometer length begins to approximate a plane wave. The subscale simulatation was then designed to produce and to detect both circular and linear (plane) transverse waves.

In order to detect the linear and circular waves produced in the simulation, linear and circular arc antennas were created by taping sensor lengths to the plastic on the surface of the water in the appropriate configurations. The linear length and circular arc length were made the same for the purposes of direct comparison.

The antenna was a single strand of 200/240 μm multimode fiber optic cable. The fiber was excited by a multimode laser diode operating at 780 nm and the output speckle pattern was detected and processed using a CCD array (STM sensing configuration). The sensor output was digitized and analyzed using a Macintosh computer. Linear waves were produced with a long aluminum meter stick while circular waves were produced with a 10 cm high x 13 cm diameter plexiglass cylinder having a solid bottom with the exception of a 2 cm centered hole.

Linear waves were generated by uniform motion of the meter stick through the water to produce a linear wave propagating normal to the axis of the linear antenna and parallel to the walls of the tank. Circular waves were produced by supporting the plexiglass cylinder at the surface of the water centered over the center of the circle incorporating the circular arc antenna. The cylinder was rapidly forced to the bottom of the tank, which resulted in the creation of the circular wave. Since there was variation in this manual generation of waves, eight sets of measurements were taken for each of the four experimental configurations to permit statistical comparisons.

Typical experimental results for the simulated seismic detection with antenna gain are shown in Figs. 37.18–37.21.

Figure 37.18 shows a typical output for a circular wave interacting with a circular antenna segment while Fig. 37.19 shows the result of a circular wave interacting with a straight line antenna segment. In Fig. 37.20, the signal resulting from a plane wave incident on a straight line antenna segment is shown. One can see the original signal detection, the detection of the wave reflected from the near tank wall and on the far right side of the plot the second wave reflection (from the far wall). Finally, Fig. 37.21 shows the signal resulting from the interaction of a plane wave with the circular antenna segment. Since the distances of the walls from the antenna were known, this allowed calculation of the wave speed of 33 cm/s. Calculations were done on the 8 runs for each experiment type to determine the mean value of the maximum of the sensor output in each case and the standard deviation. In terms of mean value of maximum $\pm 1\sigma$, the calculations yielded: 3316.6±268.4 for linear wave/linear antenna, 2117.9±277.5 for linear wave/circular antenna, 883.7±214.3 for circular wave/linear antenna, and 2055.9±188.5 for circular wave, circular antenna. The ratio of average maxima for linear wave/linear antenna to linear wave/circular an-

tenna was 1.57 and the ratio of maxima for circular wave/circular antenna to circular wave/linear antenna was 2.47.

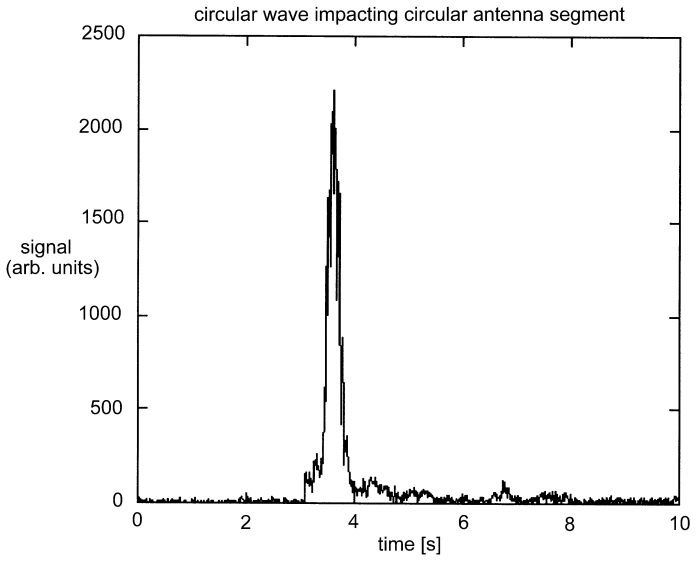

Fig. 37.18 Typical response from circular wave/circular antenna segment interaction

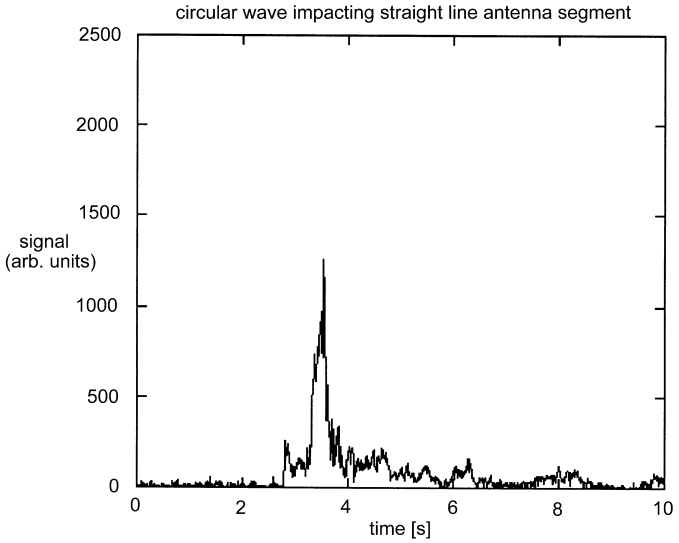

Fig. 37.19 Typical response from circular wave/straight line antenna segment interaction

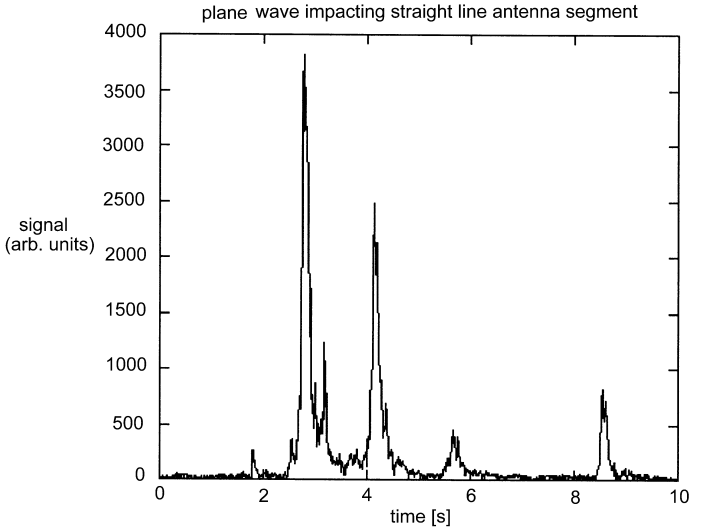

Fig. 37.20 Typical response from planar wave/straight line antenna segment interaction

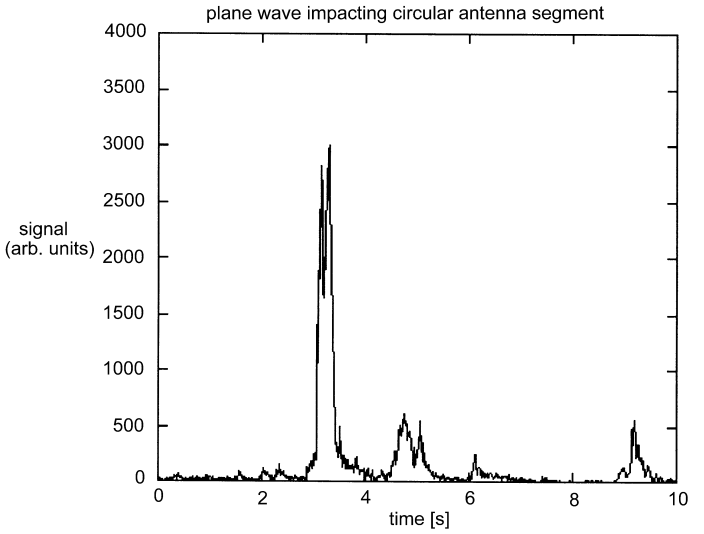

Fig. 37.21 Typical response from planar wave/circular antenna segment interaction

37.7 Discussion and Summary

Both the model results and the subscale experimental simulation results demonstrate the potential for the creation of very long gauge length seismic sensors based using antenna gain. The tone burst model predicted that when an antenna segment intercepted a wave to which it was matched, a signal increase of more than a factor of 2 could be expected over detection of equivalent power waves to which it was not matched. The average enhancement factor from the experiments for the linear antenna segment was 1.57, while for the circular antenna segment it was 2.47. The variance between the model and experimental subscale simulation results could be due to several factors. The assumption in the model based on summing the z direction displacements due to the presence of the wave of all of the antenna segments from their equilibrium points might not be correct. Weighting of different portions of the antenna might be non-uniform, i.e. bending at the antenna ends might contribute more to the output than common displacements (between adjacent segments) toward the middle of the antenna. Another contributing factor could be edge effects in linear wave propagation, creating curvature in the wave, thereby reducing the physical difference between it and a pure circular wave. Nonetheless, antenna gain has clearly been shown.

There are numerous ways in which very long gauge length sensing can be carried out, both electrical (TDR) and optical (OTDR, interferometry, polarimetric sensing). Optical techniques are attractive because the gauge lengths that can be used can be arbitrarily long for all practical purposes due to the very low loss nature of optical fiber transmission. The same is not true of electrical techniques in which gauge lengths greater than a few hundred meters are probably not achievable. We shall therefore limit our consideration to fiber optic techniques for fieldable fiber optic seismic sensing systems.

Early in the development of fiber optic sensors, it was assumed that the amount of fiber that could be used as sensing element only depended upon the loss characteristics of the fibers used. Predictions were made that fiber optic magnetic field sensors would soon surpass the performance of SQUID devices. In fact the fiber optic device performance never came within more than a few orders of magnitude of the SQUID devices. The reason for this was shown to be statistical fluctuations in the index of refraction of the fiber optic sensing element which increased as the length of the sensing element increased, eventually becoming the dominant noise source (Glenn 1989). When that occurred, increased signal due to increased length was exactly compensated for by increased noise level in the

same proportion, resulting in a static signal to noise ratio. This effect was minimized in Mach–Zehnder hydrophones due to the fact that the very long gauge length of fiber was confined to a relatively small uniform temperature volume around a mandrel. For seismic sensing, in which the long gauge length will be spatially distributed, the noise due to thermal fluctuations, even within the Earth, will be much more of a problem. In order to optimize sensor design, thermal fluctuation caused changes in the optical path length will have to be considered.

Although there are numerous different possible spatially distributed integrating fiber optic seismic sensing techniques, the combined STM/HOME technique offers particular advantages. It exhibits high interferometric sensitivity that could allow the detection of relatively low energy precursor signals while at the same time being able to detect and characterize the large amplitude signals present in the waves from the seismic event itself. In addition, the sensitivity of a combined STM/HOME sensor can be enhanced in two ways. First, the gauge length can be increased up to the point at which thermal noise fluctuations come into play. Secondly, the sensitivity can be increased by optimizing the ground/sensor coupling, i.e. burying the buffer clad sensing fiber in soil whose particle size is selected to optimize that coupling (the particles would have diameters that matched one of the microbending loss periods in the fiber). These types of sensitivity enhancements are shown schematically in Fig. 37.22. In addition to these types of advantages, the combined STM/HOME sensor has the potential to be wireless (Spillman et al. 2004) and very cost effective.

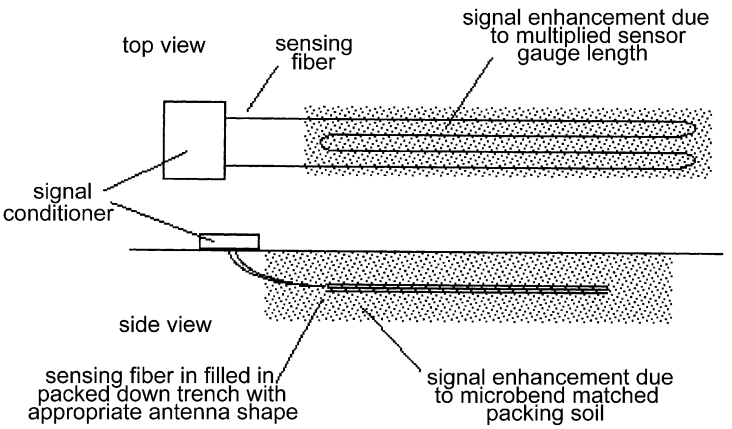

Fig. 37.22 Implementation options for spatially distributed integrating fiber optic seismic sensing

The scaling up of systems from the laboratory to the field will require attention to both issues of scale and practical issues of field deployment. The issues of scale depend largely on those related to sensing the large motions over large distances. A typical measurement may be to detect a 1 Hz seismic signal in a medium with a wave speed of 3.5 km/s (typical for *S* waves), with a 1 g acceleration. The sensor must then be sensitive to a relative motion on the order of a 0.2 to 0.5 m over a 3.5 km distance. Field installation requires the deployment of a ruggedized, possibly specialized non-communication style, fiber optic cable over an extended range. Using existing communication, utility or transportation structures as a backbone may reduce the cost of the system.

Depending on the particular requirements, it may be very useful to design antenna arrays that are particularly sensitive to certain types of waves. The distinction of *S* and *P* waves is an important consideration in detecting underground nuclear blasts. The large scale coherence of *S* waves has implications in structural safety in earthquakes. The measurement of Rayleigh waves can be useful in identifying mechanical properties of surface materials. The *P*, *S* and surface waves are all manifested differently on the surface of the Earth. *P* waves appear as a compressive and extensional motion where relative surface points move closer together and then farther away. *S* waves appear as a shearing motion where relative points on the surface move sideways and vertically relative to one another. If the antenna array can be configured to be sensitive to either compressive or shear motions, then it can be selectively sensitive to either *S* or *P* waves.

References

Aki K, Richards PG (1980) Quantitative seismology: theory and methods. WH Freeman and Company, New York

Glenn WH (1989) Noise in interferometric optical systems - An optical Nyquist theorem. IEEE J Quantum Elect **25**: 1218-1224

Herczfeld PR, Elsherif MA, Kawase LR, Ko FK, Bobb L (1990) An embedded fiber optic sensor utilizing the modal power distribution technique. J Opt Lett **15**: 21, 1242-1244

Meissner KE, Spillman Jr WB (2004) Dual-mode optical fiber vibration sensor. Proc Intern Symp on Photonics in Measurement, Frankfurt

Miller SE and Chynoweth AG (1979) Optical fiber telecommunications. Academic Press, New York

Spillman Jr WB (1981) Multimode fiber optic hydrophone based on a Schlieren technique. Applied Optics **20**: 3, 465-467

Spillman Jr WB, Huston DR (1995) Scaling and antenna gain in integrating fiber optic sensors, J Lightwave Technol **13**: 7, 1222-1230

Spillman, Jr WB, Huston DR (1996) Pattern detection through the use of long gauge length spatially weighted fiber optic sensors. Proc. Society of Photooptical Instrumentation Engineers 2838, 178-187

Spillman Jr WB, Kline BR, Maurice LB, Fuhr PL (1989) Statistical mode sensor for fiber optic vibration sensing applications. Applied Optics **28**: 15, 3166-3176

Spillman Jr WB, Mayer M, Bennett J, Gong J, Meissner KE, Davis B, Claus RO, Muelenaer Jr AA, Xu X (2004) A 'smart' bed for non-intrusive monitoring of patient physiological factors". J Meas Sci Technol **15**: 8, 1614-1620

PART VI

ROTATIONS
AND ENGINEERING SEISMOLOGY

38 Deriving Seismic Surface Rotations for Engineering Purposes

Zbigniew Zembaty

Faculty of Civil Engineering, Technical University of Opole
ul. Mikołajczyka 5, 45 233 Opole, Poland; e-mail: zet@po.opole.pl

38.1 Introduction and Formulation of the Problem

In conventional earthquake engineering, seismic loads on structures are formulated only in terms of the three translational components of ground motion. Of these three, the two horizontal actions are usually decisive in structural design because civil engineering structures are much stiffer in the vertical direction than in the horizontal ones. In addition, with only a few exceptions (e.g. the 1995 Northridge earthquake) the vertical component is generally less intensive than any of the two horizontal ones.

Nevertheless, each site on the surface of the ground can be subjected to six motions: three translations along x, y and z axes as well as three rotations about these axes. The rotation about vertical axis z will be called here torsion while the rotations about two horizontal axes will be called rockings. In the mid seventies of the past century, Penzien and Watabe (1975) have introduced a system of the so-called principal axes on the surface of the ground (Fig. 38.1) in which horizontal axis x is directed towards epicenter, the second horizontal axis, perpendicular to x, is denoted by y, and z represents vertical axis. Penzien and Watabe have shown that the three components of ground motions, $u(t)$, v(t) and $w(t)$, along the respective x, y and z axes may be regarded as uncorrelated. Furthermore, when analyzing spatial seismic effects at two points, A and B, on the ground surface, the respective coherence matrix transforms as a tensor with changes of the coordinate system (e.g. Zembaty 1997). This convenient system of coordinates shown in Fig. 38.1 will be applied throughout this paper. Only two rotational components, i.e., rocking about the y axis, ψ, and torsion about the z axis, φ, are usually analyzed, as there is a rationale for their existence when considering the respective wave decomposition at the ground surface.

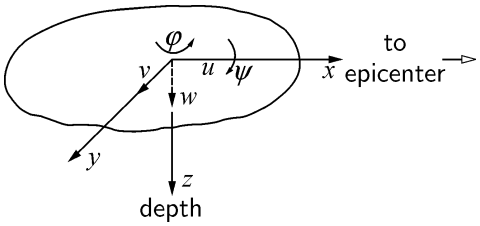

Fig. 38.1 Principal axes and two rotations on the ground surface (after Zembaty et al. 1993)

The most natural way to obtain these rotations would be to differentiate the spatial field of strong motion with respect to spatial coordinates. For these purposes, basic formulae of the continuum mechanics can be applied. For example, torsion (about the z axis) is given by the following formula:

$$\varphi = \frac{1}{2}\left(\frac{\partial v}{\partial x} - \frac{\partial u}{\partial y}\right). \tag{38.1}$$

Since the tangential strains can be assumed zero at the free surface, the surface rocking motion (about the y-axis) can be obtained as simple differentiation of vertical field of motion $w(x, y, t)$ (see e.g. Oliveira and Bolt 1989):

$$\psi = \frac{\partial w(x, y, t)}{\partial x}. \tag{38.2}$$

Consider a stiff, massive structure founded on compliant soil, under horizontal excitations (Fig. 38.2). The interaction of structural vibrations with the soil motion (soil-structure interaction) leads to structural rotations even from horizontal excitations only and can particularly be important for structures with small, massive foundations, for which the lowest (fundamental) natural frequency is just the rocking one. The rotation, although important in seismic response analyses, should however be distinguished from the actual rotational excitations analyzed here. This type of rotation during earthquakes was observed very early (e.g. Imamura 1937), but its analysis does not require considering wave propagation. It takes place during kinematic excitations of any structure with substantial moment of inertia resting on compliant soil. This effect is also observed during shaking table tests and is treated as an unwanted, spurious motion to be eliminated by the control software of the shaking table (see e.g. Juhasova et al. 2000, 2002). For in-depth analyses of these effects, one may read the vast literature on soil structure interaction (e.g. a book by Wolf 1985). This situation

shows also an evident difficulty in observing rotations or carrying out their eventual measurements.

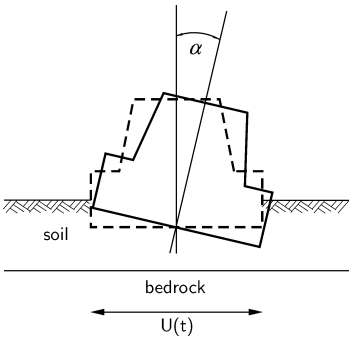

Fig. 38.2 Rocking of a massive structure on compliant soil as excited only by horizontal ground motion $U(t)$

The engineering importance of rotational components of seismic strong ground motion was noted during late sixties and early seventies of the 20th century (Newmark and Hall 1969, Newmark and Rosenblueth 1971). In their book Newmark and Rosenblueth (1971) also quote eyewitness accounts even for gravitational waves observed as slowly moving, visible waves on the surface of the ground. Such waves might easily generate rocking motion. Later an interesting contribution in this field was a simulation study of rotational effects in layered media and near-field excitations by Bouchon and Aki (1982). At a distance of a few kilometers from the fault, they estimated torsional displacements at about 3×10^{-4} rad, torsional velocity at about 1.5×10^{-4} rad/s and rocking displacements at about $7\text{-}8\times10^{-4}$ rad.

Finally, two different approaches emerged in the literature:

- Theoretical reasoning based on wave passage effects (Trifunac 1982, Lee and Trifunac 1985, 1987, Rutenberg and Heidebrecht 1985, Castellani and Boffi 1989, Zembaty et al. 1993, Castellani and Zembaty 1996).
- Experimental analyses utilizing the measurements from synchronized dense arrays of accelerometers like SMART 1 in Taiwan, leading first to stochastic models of spatial ground motion (e.g. Tamura and Aizawa 1992, Loh 1985) and then to estimations of rotational ground motion (Oliveira and Bolt 1989, Castellani and Zembaty 1994, 1996).

This paper presents an approach to modelling the rotational effects in terms of stationary stochastic processes and random fields. More general

non-stationary approach is given by Zembaty et al. (1993). The importance of applying these effects to some types of structures will also be briefly shown (Zembaty and Boffi 1994). Due to space limitations only the rocking component will be analyzed. For detailed analyses of the torsional component as excited by the incident *SH* wave propagation the reader may refer to the paper by Lee and Trifunac (1985), whereas an experimental account for the torsional surface effects may be found in Oliveira and Bolt (1989).

38.2 Spectral Decomposition of Translational Components of Seismic Ground Motion

Before proceeding with further analyses of surface rotations, the spectral decomposition of random processes representing translational accelerations of ground motion is introduced. Consider the stationary (steady) ground vibrations in the form of accelerations along the principal axes of seismic ground motion $\ddot{u}(t)$, $\ddot{v}(t)$ and $\ddot{w}(t)$ (Fig. 38.1). The classic spectral representations of the above three components of seismic motion, treated as stationary stochastic processes take the following form:

$$\ddot{u}(t)=\int_{-\infty}^{\infty}\mathrm{e}^{\mathrm{i}\omega t}\mathrm{d}\hat{\ddot{u}}(\omega)\,,\quad \ddot{v}(t)=\int_{-\infty}^{\infty}\mathrm{e}^{\mathrm{i}\omega t}\mathrm{d}\hat{\ddot{v}}(\omega)\,,\quad \ddot{w}(t)=\int_{-\infty}^{\infty}\mathrm{e}^{\mathrm{i}\omega t}\mathrm{d}\hat{\ddot{w}}(\omega) \tag{38.3}$$

in which dashed symbols are random processes in the frequency domain with orthogonal increments. This means that e.g. for $\ddot{u}(t)$ we have:

$$\left\langle \mathrm{d}\hat{\ddot{u}}(\omega_1)\,\mathrm{d}\hat{\ddot{u}}(\omega_2)\right\rangle=\begin{cases}\left\langle\left|\mathrm{d}\hat{\ddot{u}}(\omega)\right|^2\right\rangle=S_{\ddot{u}}(\omega)\mathrm{d}\omega & \text{for}\quad \omega_1=\omega_2=\omega\\ 0 & \text{for}\quad \omega_1\neq\omega_2\end{cases}\,, \tag{38.4}$$

where the symbol < > denotes mathematical expectation, an asterisk denotes complex conjugate, $S_{\ddot{u}}(\omega)$ represents power spectral density of the acceleration process $\ddot{u}(t)$ and ω is the angular frequency (in rad/s).

For two different processes, e.g. $\ddot{u}(t)$ and $\ddot{w}(t)$, formula (38.4) takes the form:

$$\left\langle \mathrm{d}\hat{\ddot{u}}(\omega_1)\mathrm{d}\hat{\ddot{w}}^{*}(\omega_2)\right\rangle=\begin{cases}\left\langle\left|\mathrm{d}\hat{\ddot{u}}(\omega)\mathrm{d}\hat{\ddot{w}}^{*}(\omega)\right|\right\rangle=S_{\ddot{u}\ddot{w}}(\omega)\mathrm{d}\omega & \text{for } \omega_1=\omega_2=\omega\\ 0 & \text{for } \omega_1\neq\omega_2\end{cases} \tag{38.5}$$

in which $S_{\ddot{u}\ddot{w}}(\omega)$ is the co-spectral density. If the Penzien and Watabe (1975) assumption of the lack of correlation of motions among the principal axes holds, then the co-spectra $S_{\ddot{u}\ddot{v}}(\omega)$, $S_{\ddot{u}\ddot{w}}(\omega)$, $S_{\ddot{w}\ddot{v}}(\omega)$ vanish.

38.3 Rocking from Body Waves Decomposition

Consider now body waves in the vertical plane containing the focus (Fig. 38.3). The in plane motions are given by two harmonic components

$$e^{i\omega\tau} d\hat{\ddot{u}}(\omega), \qquad e^{i\omega\tau} d\hat{\ddot{w}}(\omega) \tag{38.6}$$

in the frequency band interval (ω, ω+dω). The motion corresponding to this band interval can be written as the sum of *P* and *SV* wave contributions:

$$\begin{aligned} d\ddot{u} &= d\ddot{u}_P + d\ddot{u}_S, \\ d\ddot{w} &= d\ddot{w}_P + d\ddot{w}_S. \end{aligned} \tag{38.7}$$

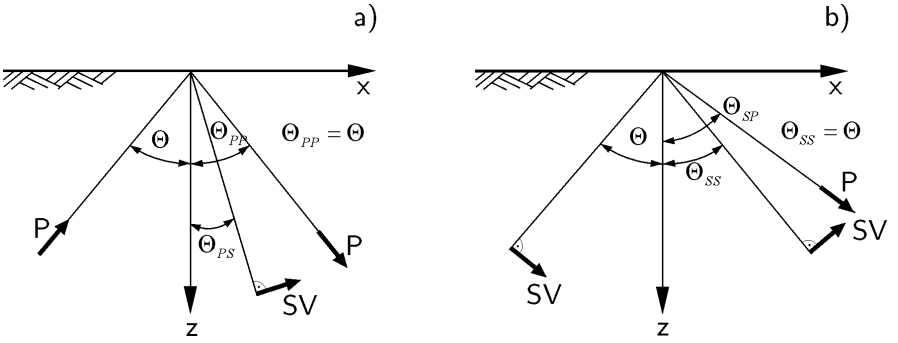

Fig. 38.3 Body waves incident on the ground surface (after Zembaty et al. 1993)

Substituting the spectral representations (38.3) for $\ddot{u}$ and $\ddot{w}$ one obtains

$$\begin{aligned} e^{i\omega\tau} d\hat{\ddot{u}}(\omega) &= U_P\, e^{i\omega\tau} d\hat{\ddot{\Phi}}_P(\omega) + U_S\, e^{i\omega\tau} d\hat{\ddot{\Phi}}_S(\omega), \\ e^{i\omega\tau} d\hat{\ddot{w}}(\omega) &= W_P\, e^{i\omega\tau} d\hat{\ddot{\Phi}}_P(\omega) + W_S\, e^{i\omega\tau} d\hat{\ddot{\Phi}}_S(\omega), \end{aligned} \tag{38.8}$$

where $\hat{\ddot{\Phi}}_P(\omega)$, $\hat{\ddot{\Phi}}_S(\omega)$ are the random functions with orthogonal increments (Eqs. 38.4 and 38.5), and U_P, U_S, W_P, W_S are the coefficients given by the following formulae (Fig. 38.3):

$$
\begin{aligned}
U_P &= (1+P_P)\sin\Theta + P_S\cos\Theta_{PS},\\
W_p &= (P_P-1)\cos\Theta + P_s\sin\Theta_{PS},\\
U_S &= (1+S_S)\cos\Theta + S_P\sin\Theta_{SP},\\
W_S &= (1-S_S)\sin\Theta - S_P\cos\Theta_{SP}.
\end{aligned}
\tag{38.9}
$$

P_P, P_S, S_P, S_S are the coefficients of body wave reflections at the free surface. They can be found in monographs on wave propagation (e.g. Achenbach 1973 or Aki and Richards 1980)

$$
P_P = \frac{-\left(\frac{1}{c_S^2}-2p^2\right)^2 + 4p^2\frac{\cos\Theta}{c_P}\frac{\cos\Theta_{PS}}{c_S}}{\left(\frac{1}{c_S^2}-2p^2\right)^2 + 4p^2\frac{\cos\Theta}{c_P}\frac{\cos\Theta_{PS}}{c_S}} \tag{38.10a}
$$

$$
P_S = \frac{4\frac{c_S}{c_S}p\frac{\cos\Theta}{c_P}\left(\frac{1}{c_S^2}-2p^2\right)}{\left(\frac{1}{c_S^2}-2p^2\right)^2 + 4p^2\frac{\cos\Theta}{c_P}\frac{\cos\Theta_{PS}}{c_S}} \tag{38.10b}
$$

$$
S_P = \frac{4\frac{c_P}{c_P}p\frac{\cos\Theta}{c_S}\left(\frac{1}{c_S^2}-2p^2\right)}{\left(\frac{1}{c_S^2}-2p^2\right)^2 + 4p^2\frac{\cos\Theta_{SP}}{c_P}\frac{\cos\Theta}{c_S}} \tag{38.10c}
$$

$$
S_S = \frac{\left(\frac{1}{c_S^2}-2p^2\right)^2 - 4p^2\frac{\cos\Theta_{SP}}{c_P}\frac{\cos\Theta}{c_S}}{\left(\frac{1}{c_S^2}-2p^2\right)^2 + 4p^2\frac{\cos\Theta_{SP}}{c_P}\frac{\cos\Theta}{c_S}}. \tag{38.10d}
$$

The angle of incidence Θ has been assumed here for simplicity to be the same for *P* and *SV* waves, and it holds only for homogeneous half space. Eventual generalization for layered media is straightforward (see e.g. papers by Haskell from fifties and sixties of the past century). The angles Θ_{PS} and Θ_{SP} are the angles of the reflected *S* and *P* waves, respectively:

$$\sin\Theta / \sin\Theta_{PS} = c_P / c_S = S\,, \tag{38.11}$$

$$\sin\Theta / \sin\Theta_{SP} = c_S / c_P\,, \tag{38.12}$$

and $p = \sin\Theta/c_P$ stands for the horizontal slowness of incident P waves for Eqs. (38.10a,b), while for Eqs. (38.10c,d) $p = \sin\Theta/c_S$ represents the horizontal slowness of incident SV waves, whereas c_P and c_S are the propagation velocities of P and S waves, respectively. The coefficients U_P, U_S represent the horizontal component of motion driven by P and SV waves, respectively, and W_P, W_S correspond to vertical motion.

Solving the system of equations (38.8) for the P and SV waves contributions one obtains the inverse of Eqs. (38.8):

$$\begin{aligned} \mathrm{e}^{\mathrm{i}\omega t}\,\mathrm{d}\hat{\ddot{\Phi}}_P(\omega) &= \frac{W_S}{D}\mathrm{e}^{\mathrm{i}\omega t}\,\mathrm{d}\hat{\ddot{u}}(\omega) - \frac{U_S}{D}\mathrm{e}^{\mathrm{i}\omega t}\,\mathrm{d}\hat{\ddot{w}}(\omega)\,, \\ \mathrm{e}^{\mathrm{i}\omega t}\,\mathrm{d}\hat{\ddot{\Phi}}_S(\omega) &= \frac{U_P}{D}\mathrm{e}^{\mathrm{i}\omega t}\,\mathrm{d}\hat{\ddot{w}}(\omega) - \frac{W_P}{D}\mathrm{e}^{\mathrm{i}\omega t}\,\mathrm{d}\hat{\ddot{u}}(\omega)\,, \end{aligned} \tag{38.13}$$

where $D = U_P W_S - W_P U_S$. Hence, the incremental vertical motion can be presented as the sum of two wave terms propagating in the x direction with different velocities

$$\begin{aligned} \mathrm{d}\ddot{w}(t,\omega,x) = {} & W_P \exp\left[\mathrm{i}\omega\left(t - \frac{x\sin\Theta}{c_P}\right)\right]\mathrm{d}\hat{\ddot{\Phi}}_P(\omega) \\ & + W_S \exp\left[\mathrm{i}\omega\left(t - \frac{x\sin\Theta}{c_S}\right)\right]\mathrm{d}\hat{\ddot{\Phi}}_S(\omega)\,. \end{aligned} \tag{38.14}$$

The incremental rocking acceleration becomes:

$$\mathrm{d}\ddot{\psi}(t,\omega,x) = \frac{\partial}{\partial x}\mathrm{d}\ddot{w}(t,\omega,x)\Big|_{x=0}\,, \tag{38.15}$$

$$\begin{aligned} \mathrm{d}\ddot{\psi}(t,\omega,x) = {} & W_P\left(-\mathrm{i}\omega\frac{\sin\Theta}{c_P}\right)\exp\left[\mathrm{i}\omega\left(t - \frac{x\sin\Theta}{c_P}\right)\right]\mathrm{d}\hat{\ddot{\Phi}}_P(\omega) \\ & + W_S\left(-\mathrm{i}\omega\frac{\sin\Theta}{c_S}\right)\exp\left[\mathrm{i}\omega\left(t - \frac{x\sin\Theta}{c_S}\right)\right]\mathrm{d}\hat{\ddot{\Phi}}_S(\omega)\,. \end{aligned} \tag{38.16}$$

Substituting $x = 0$ and taking into account Eq. (38.13) one obtains

$$
\begin{aligned}
\mathrm{d}\ddot{\psi}(t,\omega) = & W_P\left(-\mathrm{i}\omega\frac{\sin\Theta}{c_P}\right)\mathrm{e}^{\mathrm{i}\omega t}\frac{W_S}{D}\mathrm{d}\hat{\ddot{u}}(\omega) \\
& -W_P\left(-\mathrm{i}\omega\frac{\sin\Theta}{c_P}\right)\mathrm{e}^{\mathrm{i}\omega t}\frac{U_S}{D}\mathrm{d}\hat{\ddot{w}}(\omega) \\
& +W_S\left(-\mathrm{i}\omega\frac{\sin\Theta}{c_S}\right)\mathrm{e}^{\mathrm{i}\omega t}\frac{U_P}{D}\mathrm{d}\hat{\ddot{w}}(\omega) \\
& -W_S\left(-\mathrm{i}\omega\frac{\sin\Theta}{c_S}\right)\mathrm{e}^{\mathrm{i}\omega t}\frac{W_P}{D}\mathrm{d}\hat{\ddot{u}}(\omega)\,.
\end{aligned}
\tag{38.17}
$$

Introducing new coefficients

$$
\begin{aligned}
W_x &= \frac{W_P W_S}{D}\frac{\sin\Theta}{c_P} - \frac{W_P W_S}{D}\frac{\sin\Theta}{c_S}\,, \\
W_z &= \frac{U_P W_S}{D}\frac{\sin\Theta}{c_S} - \frac{W_P U_S}{D}\frac{\sin\Theta}{c_P}\,,
\end{aligned}
\tag{38.18}
$$

results in

$$
\mathrm{d}\ddot{\psi}(t,\omega) = W_x(-\mathrm{i}\omega)\,\mathrm{e}^{\mathrm{i}\omega t}\mathrm{d}\hat{\ddot{u}}(\omega) + W_z(-\mathrm{i}\omega)\,\mathrm{e}^{\mathrm{i}\omega t}\mathrm{d}\hat{\ddot{w}}(\omega)\,. \tag{38.19}
$$

Finally, after integrating in the whole frequency domain one obtains the spectral decomposition of the rocking component

$$
\ddot{\psi}(t) = \int_{-\infty}^{\infty} W_x(-\mathrm{i}\omega)\,\mathrm{e}^{\mathrm{i}\omega t}\mathrm{d}\hat{\ddot{u}}(\omega) + \int_{-\infty}^{\infty} W_z(-\mathrm{i}\omega)\,\mathrm{e}^{\mathrm{i}\omega t}\mathrm{d}\hat{\ddot{w}}(\omega)\,, \tag{38.20}
$$

which can easily be applied to obtain any stochastic characteristic of ψ, e.g. correlation function, power spectral density etc. For example, the mean square rocking acceleration is given by

$$
\begin{aligned}
\sigma^2_{\ddot{\psi}} = & \int_{-\infty}^{\infty}\left|W_x\right|^2\omega^2 S_{\ddot{u}}(\omega)\mathrm{d}\omega + 2\int_{-\infty}^{\infty} W_x W_z^*\omega^2 S_{\ddot{u}\ddot{w}}(\omega)\,\mathrm{d}\omega \\
& + \int_{-\infty}^{\infty}\left|W_z\right|^2\omega^2 S_{\ddot{w}}(\omega)\,\mathrm{d}\omega\,.
\end{aligned}
\tag{38.21}
$$

The integrand in the above equation is the power spectral density of the rocking component:

$$
S_{\ddot{\psi}}(\omega) = \left|W_x\right|^2\omega^2 S_{\ddot{u}}(\omega) + 2W_x W_z^* S_{\ddot{u}\ddot{w}}(\omega) + \left|W_z\right|^2\omega^2 S_{\ddot{w}}(\omega)\,. \tag{38.22}
$$

It can be seen from the derived formulae that the rotational spectrum is a function of the first time derivatives of the vertical and horizontal accelerations (the ω^2 multiplier), i.e., the function of the third derivative of respective displacements as $S_{\ddot{\dot{u}}}(\omega) = \omega^6 S_u(\omega)$. It should also be noted that if one follows the Penzien and Watabe (1975) assumption, the second term of Eq. (38.22) vanishes, as there is no correlation between vertical and horizontal components. In this case, Eq. (38.22) can further be simplified when assuming the same spectral density for both horizontal and vertical ground motions differing only by intensity factor η, i.e.,

$$S_{\ddot{w}}(\omega) = \eta^2 S_{\ddot{u}}(\omega). \tag{38.23}$$

This leads to

$$S_{\ddot{\psi}}(\omega) = \left(|W_x|^2 + \eta |W_z|^2\right)\omega^2 S_{\ddot{u}}(\omega). \tag{38.24}$$

The value of η can be estimated from the statistical analysis of earthquake records. For example, following Trifunac and Brady (1975) it can be taken as approximately 0.5. On the other hand, in the near field the vertical component can be as intensive as the horizontal one (e.g. the 1995 Northridge earthquake). In any case the contribution to the total rocking of vertical vs. horizontal components is controlled by the values of the coefficients W_x and W_z.

In Fig. 38.4a and b the moduli of these two coefficients are presented as functions of the incidence angle Θ of body waves (both *P* and *SV*). The plots include three sets of data given in detail in Table 38.1

Table 38.1 Data to numerical calculations (according to Zembaty et al. 1993)

	c_p = 6800 m/s	c_p = 5200 m/s	c_p = 4500 m/s
c_S [m/s]	3000	3000	3000
$S = c_P/c_S$	2.27	1.73	1.50
Poisson modulus, ν	0.38	0.25	0.10
Θ_{cr} [deg]	26.14	35.26	41.81

For $\Theta < \Theta_{cr}$ coefficient W_x is real and negative while W_z is also real but positive, although in any case the signs are lost when formulating the spectral density. It can be seen from Fig. 38.4a, b that W_x and W_z increase for an overcritical angle with considerable variation with respect to the values of Poisson's ratio ν for W_x and with little variation for W_z. In Fig. 38.4c the coefficient of formula (38.24), i.e., $|W_x|^2 + \eta |W_z|^2$ is shown for three values of ν vs. incidence angle Θ. To investigate the contribution of possible cross-correlation of horizontal and vertical components one may as-

sume (although it is unlikely) an extreme case of full (100%) correlation. In this case, formula (38.22) takes the following form:

$$S_{\ddot{\psi}}(\omega) = (|W_x|^2 + 2\eta W_x W_z^* + \eta^2 |W_z|^2)\, \omega^2 S_{\ddot{w}}(\omega)\,. \tag{38.25}$$

The multiplier of the last equation, i.e., $|W_x|^2 + 2\eta W_x W_z^* + \eta^2 |W_z|^2$ is plotted in Fig. 38.4d. It can be seen that Poisson's ratio influences the rocking response substantially.

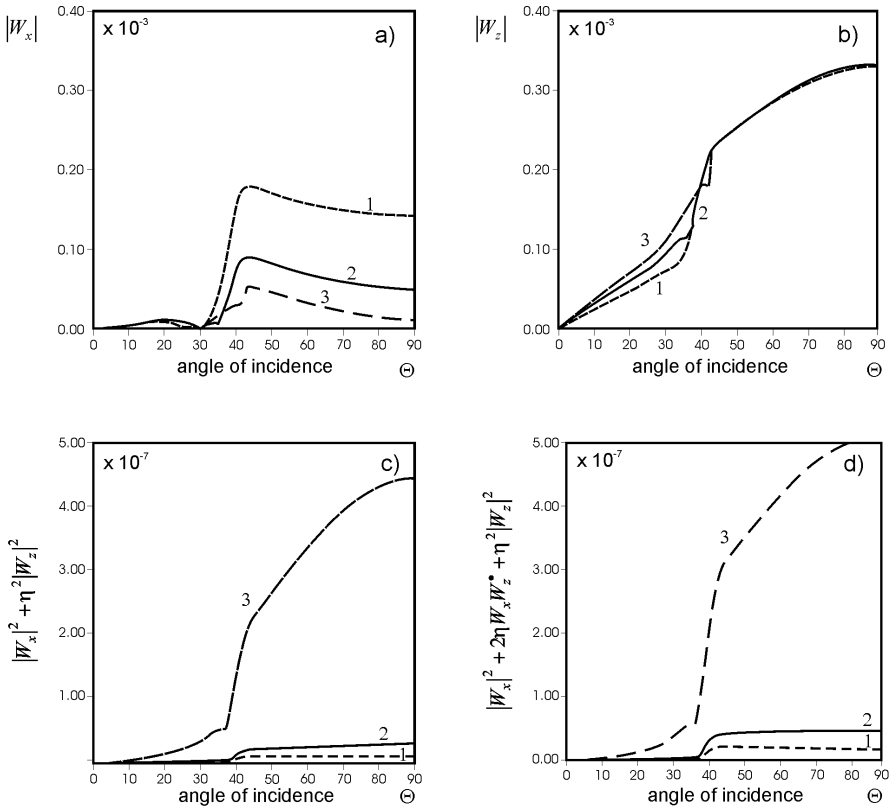

Fig. 38.4 Modulus of W_x (a) and W_z (b) and the coefficients of rocking spectral densities with zero translational correlation (c) and with full correlation (d). All data shown for three values of Poisson coefficient v: curve (1) for 0.38, curve (2) for 0.25 and curve (3) for 0.10 (according to Zembaty et al. 1993)

Particularly, the difference for $v = 0.38$ and $v = 0.25$ is substantial. It can also be seen that cross-correlation between vertical and horizontal components may increase the rocking ground motion by about 30%. All plots in

Fig. 38.4 show dramatic increase in the rocking component for greater incidence angles. On the other hand, it should be noted that when the layered media are analyzed the refracted *P* and *SV* waves at the surface would appear at smaller angles. However, the wave energy carried by surface waves would continue to be associated with large incidence angles.

38.4 Rocking from Surface Waves

A quantitative estimation of the contribution of surface waves to the total ground motion is not an easy task. Identification of the wave types for the strong events at a particular site becomes possible via dispersion analysis, when large scale measurements of ground motion are carried out as in the spatial measurements of the SMART-1 network in Lotung, Taiwan. A rough and simple idea has been proposed by Sugito et al. (1984). Analyzing some Japanese strong motion records they proposed to separate surface waves from the total ground motion by using the criterion of first arrival time t_S and band limit ω_S. Following their approach, the motion due to surface waves should be subtracted from the total motion and treated separately (Fig. 38.5).

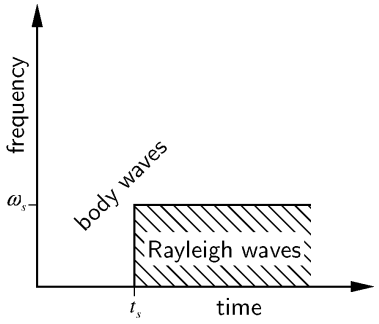

Fig. 38.5 Body and surface waves separation (from Zembaty et al. 1993)

When considering the rocking component we restrict our example to Rayleigh waves. In analogy to the earlier treatment, the acceleration due to surface waves in the frequency range (ω, $\omega+d\omega$) can be taken as a result of a wave propagating in the horizontal direction with the velocity of Rayleigh waves c_R as follows:

$$\mathrm{d}\ddot{w}_R = \exp\left[\mathrm{i}\omega\left(t - \frac{x}{c_R}\right)\right]\mathrm{d}\hat{\ddot{w}}(\omega)\,. \tag{38.26}$$

From the above equation the incremental surface rocking can be written as

$$\mathrm{d}\ddot{\psi}_R = \frac{\partial}{\partial x}\mathrm{d}\ddot{w}_R(t,\omega,x)\Big|_{x=0} = \left(-\frac{\mathrm{i}\omega}{c_R}\right)\mathrm{e}^{\mathrm{i}\omega t}\mathrm{d}\hat{\ddot{w}}(\omega)\,. \tag{38.27}$$

Since the first arrival time of Rayleigh waves is t_S, in the stationary analysis one should consider the validity of this approach only in the respective time windows. Taking into account the above criterion of wave separation leads to

$$\mathrm{d}\ddot{\psi}_R = \left(-\frac{\mathrm{i}\omega}{c_R}\right)\mathrm{e}^{\mathrm{i}\omega t}\mathrm{d}\hat{\ddot{w}}(\omega) \quad \text{for} \quad -\omega_S < \omega < \omega_S \quad \text{and} \quad t > t_S\,, \tag{38.28}$$

$$\ddot{\psi}_R = \int_{-\omega_S}^{\omega_S} W_R(-\mathrm{i}\omega)\,\mathrm{e}^{\mathrm{i}\omega t}\mathrm{d}\hat{\ddot{w}}(\omega) \quad \text{for} \quad t > t_S\,, \tag{38.29}$$

where $W_R = 1/c_R$. From this equation and Eqs. (38.4) and (38.5) one may write the equation for spectral density of the rocking acceleration contributed by the surface waves

$$S_{\ddot{\psi}}(t,\omega) = W_R^2\omega^2 S_{\ddot{w}}(t,\omega) \quad \text{for} \quad -\omega_S < \omega < \omega_S \quad \text{and} \quad t > t_S\,. \tag{38.30}$$

This formula shows only roughly the dependence between vertical and rotational spectral density on Rayleigh waves propagation. The analysis of joint effects of body and surface waves should be done in both time and frequency domain. Such a general approach, including the non-stationary, evolutionary description of stochastic processes is presented in detail by Zembaty et al. (1993).

38.5 Rocking from Spatial Field of Ground Motion

To derive the rocking component on a surface point it suffices to consider a random field with respect to time and only one spatial coordinate x (directed towards the epicenter – as in Fig. 38.1). Assuming for simplicity the stationarity with respect to time and spatial coordinates, the vertical acceleration of this point can be presented in the form of spectral representation (38.3) with an additional spatial variable x:

$$\ddot{w}(t,x) = \int_{-\infty}^{\infty}\mathrm{e}^{\mathrm{i}\omega t}\mathrm{d}\hat{\ddot{w}}(\omega,x)\,, \tag{38.31}$$

where $\hat{\ddot{w}}(\omega, x)$ is a random function with orthogonal increments defined both in time and spatial domain as follows:

$$\left\langle \hat{\ddot{w}}(\omega_1, x_A)\, \hat{\ddot{w}}^*(\omega_2, x_B) \right\rangle = \begin{cases} S_{\ddot{W}_A \ddot{W}_B}(\omega, x_A - x_B) & \text{for} \quad \begin{cases} \omega_1 = \omega_2 = \omega \\ x_A \neq x_B \end{cases} \\ S_{\ddot{W}}(\omega) & \text{for} \quad \begin{cases} \omega_1 = \omega_2 = \omega \\ x_A = x_B \end{cases} \\ 0 & \text{for} \quad \omega_1 \neq \omega_2 \end{cases} \tag{38.32}$$

where $S_{\ddot{W}_A \ddot{W}_B}(\omega, x)$ is a complex co-spectrum, $S_{\ddot{W}}(\omega)$ is the respective point spectrum (for $x_A = x_B$) which does not depend on the position along the x axis. Following Eqs. (38.31) and (38.32) one may derive a formula for the correlation function of the vertical random field:

$$\begin{aligned} K_{\ddot{w}}(t, t', x_A, x_B) &= \left\langle \ddot{w}(t, x_A)\, \ddot{w}^*(t', x_B) \right\rangle \\ &= \left\langle \int_{-\infty}^{\infty} \mathrm{e}^{\mathrm{i}\omega_1 t}\, \mathrm{d}\hat{\ddot{w}}(\omega, x_A) \int_{-\infty}^{\infty} \mathrm{e}^{-\omega_2 t'}\, \mathrm{d}\hat{\ddot{w}}^*(\omega, x_B) \right\rangle \\ &= \int_{-\infty}^{\infty} \mathrm{e}^{\mathrm{i}\omega(t-t')} S_{\ddot{W}_A \ddot{W}_B}(\omega, x_A - x_B)\, \mathrm{d}\omega \,. \end{aligned} \tag{38.33}$$

Introducing new variables $\tau = t - t'$ and $x_{AB} = x_A - x_B$ one obtains

$$K_{\ddot{w}}(\tau, x_{AB}) = \int_{-\infty}^{\infty} S_{\ddot{W}_A \ddot{W}_B}(\omega, x_{AB}) \mathrm{e}^{\mathrm{i}\omega\tau}\, \mathrm{d}\omega \,. \tag{38.34}$$

For $\tau = 0$ one has the following space correlation function

$$K_{\ddot{w}}(x_{AB}) = \int_{-\infty}^{\infty} S_{\ddot{W}_A \ddot{W}_B}(\omega, x_{AB})\, \mathrm{d}\omega \,, \tag{38.35}$$

while for both $\tau = 0$ and $x_{AB} = 0$ the mean square value is given by

$$\sigma_{\ddot{w}}^2 = \int_{-\infty}^{\infty} S_{\ddot{W}}(\omega)\, \mathrm{d}\omega \,. \tag{38.36}$$

From the time-space stationarity it follows that the point spectra are the same at points A and B, i.e., $S_{\ddot{W}_A}(\omega) = S_{\ddot{W}_B}(\omega) = S_{\ddot{W}}(\omega, x_{AB} = 0)$. Introducing then the coherence function

$$\gamma_{\ddot{w}}(\omega, x_{AB}) = \frac{S_{\ddot{W}_A \ddot{W}_B}(\omega, x_{AB})}{\sqrt{S_{\ddot{W}_A}(\omega) S_{\ddot{W}_B}(\omega)}} = \frac{S_{\ddot{W}}(\omega, x_{AB})}{S_{\ddot{W}}(\omega)} \tag{38.37}$$

one obtains

$$K_{\ddot{w}}(x_{AB}) = \int_{-\infty}^{\infty} \gamma_{\ddot{w}}(\omega, x_{AB}) \; S_{\ddot{W}}(\omega) \, \mathrm{d}\omega \,, \tag{38.38}$$

where $S_{\ddot{W}}(\omega, x_{AB})$ denotes complex co-spectrum, while $S_{\ddot{W}}(\omega)$ stands for real valued point spectrum. Separating modulus and phase of the coherence function gives

$$\gamma_{\ddot{w}}(\omega, x_{AB}) = \left|\gamma_{\ddot{w}}(\omega, x_{AB})\right| \mathrm{e}^{\mathrm{i}\phi(\omega, x_{AB})} \,. \tag{38.39}$$

Now, using the notation introduced above one may consider the rocking acceleration component as the respective spatial derivative $\ddot{\psi} = \partial / \partial x \, \ddot{w}(x, y)$ (Eq. 38.2). Substituting Eq. (38.39) into (38.33) and then $\tau = t - t'$ as well as $x_{AB} = x_A - x_B$, after some algebra one obtains for $\tau = 0$:

$$K_{\ddot{\psi}}(x_{AB}) \; = \; -\frac{\partial^2}{\partial x_{AB}^2} K_{\ddot{w}}(\tau = 0, x_{AB}) \; = \; -\int_{-\infty}^{\infty} \frac{\partial^2}{\partial x_{AB}^2} S_{\ddot{W}}(\omega, x_{AB}) \, \mathrm{d}\omega \,. \tag{38.40}$$

For $x_{AB} = 0$ the integrand in this formula can be interpreted as a spectral density function of the rocking acceleration:

$$S_{\ddot{\psi}}(\omega) = -\frac{\partial^2}{\partial x_{AB}^2} S_{\ddot{W}}(\omega, x_{AB} = 0) = -S_{\ddot{w}}(\omega) \frac{\partial^2}{\partial x_{AB}^2} \gamma_{\ddot{w}}(\omega, x_{AB} = 0) \,. \tag{38.41}$$

It is interesting to note that $S_{\ddot{W}}(\omega, x_{AB})$, although generally complex, is real for $x_{AB} = 0$ as we require for $S_{\ddot{W}}(\omega)$. It can be seen from Eq. (38.41) that for rocking spectrum one needs a spatial spectrum of the vertical surface motion. Such spectra are available from SMART-1 array measurements (e.g. Abrahamson et al. 1987). Unfortunately, most of the researchers indicate substantial reduction of accuracy of experiments at short distances. Thus, direct differentiation at $x_{AB} = 0$ should be avoided. Instead, the finite difference method seems more reasonable in this case. Applying, e.g. the second central finite difference one obtains:

$$S_{\ddot{\psi}}(\omega) \approx -\frac{\Delta^2}{\Delta x^2} S_{\ddot{W}}(\omega, x = 0)$$

$$= -\frac{1}{(\Delta x)^2}\left[S_{\ddot{W}}(\omega,-\Delta x) - 2S_{\ddot{W}}(\omega,0) + S_{\ddot{W}}(\omega,\Delta x)\right]. \tag{38.42}$$

Taking into account that $S_{\ddot{W}}(\omega,x)$ is a Hermitian complex function in both frequency and space domains one can write that $S_{\ddot{W}}(\omega,\Delta x) = S^*_{\ddot{W}}(\omega,-\Delta x)$ and consequently

$$S_{\ddot{\psi}}(\omega) \approx -\frac{1}{(\Delta x)^2}\left[2\,\mathrm{Re}\,S_{\ddot{W}}(\omega,\Delta x) - 2S_{\ddot{W}}(\omega,0)\right]. \tag{38.43}$$

Substituting $S_{\ddot{W}}(\omega,x) = \gamma_{\ddot{W}}(\omega,x)S_{\ddot{W}}(\omega)$, one finally obtains the following approximation for the spectral density of rocking component:

$$S_{\ddot{\psi}}(\omega) \approx \frac{2S_{\ddot{W}}(\omega)}{(\Delta x)^2}\left[1 - \mathrm{Re}\,\gamma_{\ddot{w}}(\omega,\Delta x)\right]. \tag{38.44}$$

The information required to calculate rocking spectral density from the spatial random field of seismic motion is the actual acceleration spectral density function of vertical accelerations as well as respective spatial coherency function.

The simplifications made in deriving Eq. (38.44) are as follows:

a) the stationarity with respect to time,
b) the stationarity with respect to space distance,
c) the arbitrariness of the assumption of finite difference parameter Δx.

The first simplification seems very crude but in fact one may say that the proportion between vertical and rocking motion may be the same whether the stationarity assumption is relaxed or not. The second and third simplifications are more serious. Particularly the third assumption seems arbitrary, but the distance parameter should be treated as a space scale parameter assumed equal to the shortest structural foundation dimension which would yield greater rotation effect.

38.6 Code Proposals and Approximate Formulae

In the modern civil engineering seismic codes, the calculation of seismic forces is usually based on the response spectrum which is a plot of maximum quantity of interest vs. natural period of a single degree of freedom (SDOF) system. In a draft version of Eurocode 8 part II (bridges) two formulae were proposed for rotational response spectra:

for the rocking response spectrum

$$R_{\psi} = r_{\psi} R(T), \qquad r_{\psi} = \frac{1.7\pi}{c_S T}, \tag{38.45}$$

for the torsional response spectrum

$$R_{\varphi} = r_{\varphi} R(T), \qquad r_{\varphi} = \frac{2.0\pi}{c_S T}, \tag{38.46}$$

where c_S is the shear wave velocity, T is the natural period of an oscillator, $R(T)$ is the pseudo-acceleration response spectrum defined for translations. As can be seen, the main parameter influencing the rotational excitations is the shear wave velocity. Unfortunately, as is usually the case for engineering codes, no explanation is given regarding the scientific justification of these formulae.

On the other hand, one may propose another approximate formula for rocking component based on the derived formula (38.44). Assuming that the ratio of rotational to vertical motion remains approximately the same for the root mean square response as for respective response spectra (Castellani and Zembaty 1996) one obtains the following approximate formula in the form of a rotational coefficient:

$$r_{\psi} = \frac{1.4}{\Delta x}\sqrt{1 - \mathrm{Re}\,\gamma_{\ddot{W}}(\omega, \Delta x)}, \tag{38.47}$$

which depends directly on the foundation separation distance Δx (as in Eq. 38.44). Formula (38.47) may be used as a multiplier for vertical response spectra, but its validity should still be verified, possibly with recorded rotations.

38.7 Application Example: A Slender Tower Under Horizontal-Rocking Excitations

Consider now the seismic response of a slender tower, a tall industrial chimney or TV-tower. Following standard structural dynamic methods (e.g. Clough and Penzien 1993) the discrete equation of motion of this structure under seismic horizontal $\ddot{u}(t)$ and rocking $\ddot{\psi}(t)$ excitations (Fig. 38.6) takes the following form:

$$\mathbf{B}\ddot{\mathbf{x}} + \mathbf{C}\dot{\mathbf{x}} + \mathbf{K}\mathbf{x} = -\mathbf{B}\mathbf{l}\ddot{\mathbf{u}}(t) - \mathbf{B}\mathbf{h}\ddot{\psi}(t) = \mathbf{p}_{eff}(t), \tag{38.48}$$

where upper and lower case bold letters denote matrices and vectors respectively, **x** is the vector of relative response of the structure, **1** is a unit vector, **h** is the vector containing heights above ground of discretized masses, **B**, **C**, **K** are the matrices of inertia, damping and stiffness, respectively.

$$\mathbf{x} = \mathbf{x}(t) = \begin{bmatrix} x_1(t) \\ x_2(t) \\ \cdots \\ \cdots \end{bmatrix}, \qquad \mathbf{l} = \begin{bmatrix} 1 \\ 1 \\ \cdots \\ \cdots \end{bmatrix}, \qquad \mathbf{h} = \begin{bmatrix} h_1 \\ h_2 \\ \cdots \\ \cdots \end{bmatrix}. \tag{38.49}$$

The solution of Eq. (38.48) was obtained by generalized response spectrum method. Details are given in the paper by Zembaty and Boffi (1994). To assess the contribution of the rocking component in the overall structural response, a 160 m reinforced concrete industrial chimney has been chosen. The data of the chimney were taken from the book by Ciesielski et al. (1968). The chimney has the external radius of 4 m at the top and 5.92 m at the bottom. The foundation has a radius of 10 m. Some realistic data on soil compliance are in turn taken from Eurocode 8 (soil profile C): c_S is 200 m/s, density of soil is 1800 kg/m^3, Poisson's ratio ν is 0.25.

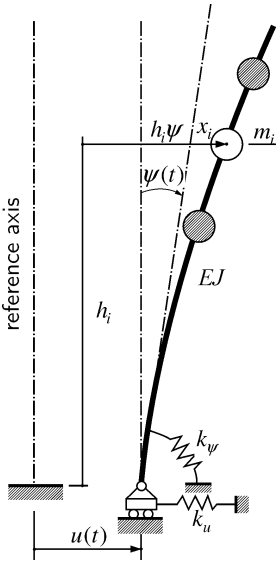

Fig. 38.6 A discrete dynamic model of a slender tower on compliant soil (Zembaty and Boffi 1994)

Discrete dynamic model of the structure is presented in Fig. 38.6 in which m_i denotes discrete mass at height h_i, k_ψ and k_h denote rocking and horizontal soil stiffness, EJ stands for bending stiffness of the chimney and $u(t)$ and $\psi(t)$ represent horizontal and rocking excitation components, respectively. Five percent structural damping ratio has been applied. The most critical response parameter describing the seismic response of a slender tower it is the bending moment appearing in the respective horizontal cross-sections of the structure. In Fig. 38.7, this bending moment is plotted vs. the height above the ground. In the computations, Eurocode 8 design response spectrum has been applied together with formula (38.45) (solid line) as well as approximation (38.47) (dashed line). It can be seen from Fig. 38.7 that the contribution of rocking excitations is quite substantial, reaching almost 50% of the total response. The bending moment as calculated by applying Eurocode 8 is slightly higher than the approximation (38.47).

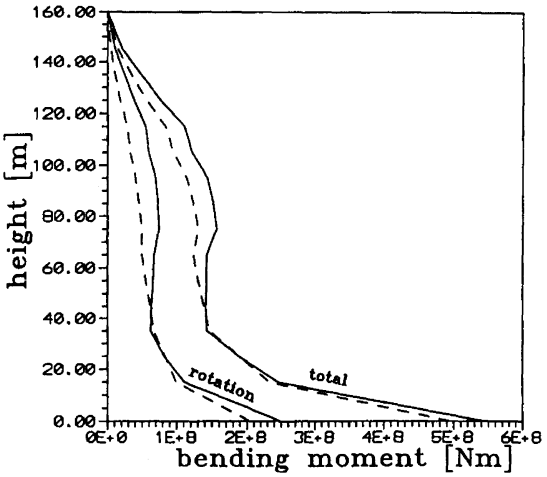

Fig. 38.7 Bending moment vs. height for a 160 m slender tower. Total value and contribution of rocking component: Eq. (38.45) – solid line, Eq. (38.47) – dashed line (Zembaty and Boffi 1994)

38.8 Summary and Conclusions

Two engineering approaches for the analyses of the rotational component of surface seismic ground motion have been presented. Rocking component of ground motion about the horizontal axis was studied in detail. The first method is based on the decomposition of the ground motion into

respective wave components and then differentiation with respect to horizontal, spatial coordinate. The resulting rocking component appeared to be a direct function the wave parameters and time derivative of translational accelerations (third derivative of displacement translations). The second method utilizes the vertical random field of ground motion from spatial arrays of the SMART-1 type. The resulting rocking component is then a function of spatial coherency of the measured vertical accelerations at a selected spatial distance.

Subsequent approximate analysis of the seismic response of a slender tower shows that rotational excitations may, in some cases, be as important as the horizontal ones applied in conventional seismic engineering.

Acknowledgements. This paper has been written in the EU sponsored Center of Structural Integrity (CESTI) at the Technical University of Opole. The support of the Commission of the European Communities under FP5, contract No. G1MA-CT-2002-04058 is gratefully acknowledged. The author wishes to thank to professor Avigdor Rutenberg from the Technion–Israel Institute of Technology, for valuable comments on the paper.

Figures 38.1, 38.3, 38.4, 38.5, 38.6 and Table 38.1 are reprinted from Zembaty et al. (1993) with permission from Elsevier.

References

Abrahamson NA, Bolt BA, Darragh RB, Penzien J, Tsai YB (1987) The Smart 1 accelerograph array (1980-1987): A review. Earthquake Spectra **3**: 263-287

Achenbach JD (1973) Wave propagation in elastic solids. North-Holland, Amsterdam

Aki K, Richards PG (1980) Quantitative seismology. W.H. Freeman, San Francisco

Bouchon M, Aki K (1982) Strain, tilt, and rotation associated with strong ground motion in the vicinity of earthquake faults. Bull Seism Soc Am **72**: 1717-1738

Castellani A, Boffi G (1989) Rotational components of seismic motion. Earth Eng Struc **18**: 785-797

Castellani A, Zembaty Z (1994), Stochastic modeling of seismic surface rotations. J Nat Hazards **10**: 181-191

Castellani A, Zembaty Z (1996) Comparison between earthquake rotation spectra obtained through different experimental sources. Eng Struc **18**: 597-603

Ciesielski R (1968) Concrete structures, vol XIII (in Polish), Arkady, Warszawa

Clough RW, Penzien J (1993) Dynamics of structures, 2nd edn. McGraw-Hill, New York

Imamura A (1937) Theoretical and applied seismology. Maruzen Co., Tokyo

Juhasowa E, Zembaty Z, Kowalski M (2000) Experimental investigations of dynamic effects on brick masonry buildings and their strengthening. Arch Civil Eng **46**: 83-106

Juhasova E, Hurak M, Zembaty Z (2002) Assessment of seismic resistance of masonry structures including boundary conditions. Soil Dyn Earthq Eng **22**: 1193-1197

Lee VW, Trifunac MD (1985) Torsional accelerograms. Soil Dyn Earthq Eng **4**: 132-139.

Lee VW, Trifunac MD (1987) Rocking strong earthquake accelerations. Soil Dyn Earthq Eng **6**: 75-89.

Loh CH (1985) Analysis of the spatial variation of seismic ground movements from SMART-1 array data. Earthquake Eng Struc **13**: 561-577

Newmark NM, Hall WJ (1969) Seismic design criteria for nuclear reactor facilities. Proc. Fourth World Conf Earthq Engrg. Santiago, Chile **2**: 37-50

Newmark NM, Rosenblueth E (1971) Fundamentals of earthquake engineering. Prentice-Hall, Englewood Cliffs

Oliveira CS, Bolt BA (1989) Rotational components of surface strong ground motion. Earthquake Eng Struc **18**: 517-526

Penzien J, Watabe M (1975) Characteristics of 3-dimensional earthquake ground motion. Earthquake Eng Struc **3**: 365-373

Rutenberg A, Heidebrecht AC (1985) Response spectra for torsion, rocking and rigid foundations. Earthquake Eng Struc **13**: 543-557

Sugito M, Goto H, Aikawa F (1984), Simplified separation technique of body and surface waves in strong motion accelerograms. Structural Engineering/Earthquake Engineering, Proc Japan Soc Civil Eng **1**: 71-76

Tamura K, Aizawa K (1992) Differential ground motion estimation using a time--space stochastic process model. Structural Engineering/Earthquake Engineering, Proc Japan Soc Civil Eng **8**: 217-223

Trifunac MD (1982) A note on rotational components of earthquake motions for incident body waves. Soil Dyn Earthq Eng **1**: 11-19

Trifunac MD, Brady AG (1975) On the correlation of seismic intensity scales with the peaks of recorded strong ground motion. Bull Seism Soc Am **65**: 139-162

Wolf J (1985) Dynamic soil-structure interaction. Prentice-Hall, Englewood Cliffs

Zembaty Z (1997) Vibrations of bridge structure under kinematic wave excitations. J Struct Eng-ASCE **123**: 479-488

Zembaty Z, Boffi G (1994) Effect of rotational seismic ground motion on dynamic response of slender towers. Eur Earthq Eng J **8**: 3-11

Zembaty Z, Castellani A, Boffi G (1993) Spectral analysis of the rotational component of earthquake motion. Probabilistic Engineering Mechanics **8**: 5-14

39 Effects of Torsional and Rocking Excitations on the Response of Structures

Mihailo D. Trifunac

Department of Civil Engineering, University of Southern California
Los Angeles, CA 90089-2531; e-mail: trifunac@usc.edu

39.1 Introduction

In traditional earthquake engineering, structures are designed to resist only simplified representation of strong earthquake ground motion, in terms of the horizontal translational components of acceleration. Occasionally, in the design of important structures with long spans, the vertical component of excitation is also considered. Rotational excitation by the torsional and rocking components of strong ground motion is almost never considered. The significance of the rotational components of strong motion for the overall response of structures can be evaluated using analytical solutions of the soil-structure interaction problems, by means of numerical modeling, or with probabilistic representations of response. At present, there are only a few isolated recordings of the rotational components of strong ground motion, and it is therefore possible only to work with their simulations.

This chapter presents the methods for construction of artificial torsional and rocking strong motion accelerations, using the theory of linear wave propagation in a layered half space. These synthetic rotational motions, along with the corresponding translational components of motion, can be used to evaluate the response of typical structures. The significance of the rotational components of excitation can be evaluated by comparing the responses computed with and without participation of rotational components in the general forcing functions.

The generation of seismic waves can be viewed from two different levels. The first is the classical macroscopic view, which starts with kinematic representation of faulting (Haskell 1969) and then follows the radiated elastic waves using the first-order linear theory of elasticity. If nonlinear phenomena occur along the wave path, and if those are investigated, the

analysis is usually restricted to the response of soft soil deposits near ground surface. The second level involves the microphysics of fracture in rocks and includes the irreversible deformations from dislocations, disclinations and micro cracks (Teisseyre and Majewski 2002). In the following review of the effects of rotational strong ground motion on the response of man-made structures, only the first, or macroscopic representation will be considered.

Rotational ground motions, accompanying seismic waves and their effects on simple objects (obelisks, grave stones) and buildings are mentioned in many older texts, which by describing the consequences of strong shaking aim to decipher its physical nature (Hobbs 1907, Davison 1927, Gutenberg 1927, Richter 1958, Imamura 1937). Deployment of strong motion accelerographs in many seismic areas of the world during the past seventy years has produced data on translational components of motion during many strong earthquakes. This data describes strong motion in three orthogonal directions (two horizontal and one vertical), but because the spacing of the recording sites is much larger than the wavelengths of the recorded motions, little is known today about the accompanying differential and rotational motions.

The effects of differential motions on man-made structures include strains (Lee 1990), curvatures (Trifunac 1990), torsion (Newmark 1969, Luco 1976, Scanlan 1976, Lee and Trifunac 1985) and rocking excitation (Lee and Trifunac 1987) of foundations, which, for flexible, extended, multiple and separate foundations (e.g. bridges) can lead to large pseudostatic shears and moments (Trifunac and Todorovska 1997a). Many structural failures and much of the damage caused by earthquakes have been linked to differential and rotational ground motions. Hart et al. (1975) showed that large torsional responses of tall buildings in Los Angeles, during the San Fernando, California, earthquake in 1971, could be ascribed to torsional excitation, while longitudinal differential motions may have caused the collapse of bridges during San Fernando 1971, Miyagi-ken-Oki 1978 (Bycroft 1980) and Northridge 1994 (Trifunac et al. 1996) earthquakes. Earthquake damage to pipelines that is not associated with faulting or landslides but is due to large differential motions and strains in the soil reflects the consequences of traveling seismic waves and of the associated large rotations and twisting of soil blocks caused by lateral spreads and early stages of liquefaction (Ariman and Muleski 1981, Trifunac and Todorovska 1997b, 1998, 1999, Trifunac 1997, 2003).

Studies of the rotational components of strong motion and of their effects on man-made structures are relatively young. Much can be anticipated and studied theoretically, but our understanding of these motions will gain sound and realistic basis only when a large number of recorded

rotational accelerograms becomes available. This may take several decades and will require deployment of a large number of new strong motion instruments, which will record all six components of motion (three translations and three rotations; Trifunac and Todorovska 2001a, b).

39.2 Rotational Strong Ground Motion

Rotational components of strong ground motion accompany the displacements induced by seismic waves. In linear elastic media, rotations are expressed by space derivatives of the displacements. Other contributions to rotational motion result from the internal structure of the medium, nonsymmetric processes of fracture, and friction (Teisseyre et al. 2003). However, once generated, these additional rotational motions are believed to attenuate quickly, and so, to be studied experimentally, they have to be recorded in the near field (Teisseyre 2002, Teisseyre and Boratyński 2002).

During the past thirty years, the inversion of recorded strong ground motion (Trifunac 1974, Trifunac and Udwadia 1974) has been developed to such a degree that it now can describe spatial and temporal variations of slip on the fault surface. Many inverse studies of the source mechanism have shown that the distribution of slip can be very irregular (Jordanovski and Todorovska 2002). Along the edges of fault planes and near abrupt changes of fault slip, tensile fractures can contribute to radiation of rotational waves (Takeo and Ito 1997). A comparison of computed and recorded rotational velocity during an earthquake swarm, in March 1997, off the shore of Izu peninsula in Japan, Takeo (1998) showed that the recorded rotations were several times larger than the simulated rotations computed from linear displacements excited by dislocations on the fault (Bouchon and Aki 1982). He showed that agreement between recorded and simulated rotations can be improved if "direct excitation of rotational motions due to spatial variations of slip velocity and due to rotational strains" is added to the rotations excited by dislocations alone.

Translational and rotational components of strong motion radiated from an earthquake source are modified along the propagation path through interference, focusing, scattering, and diffraction. For example, reflection of plane *P* and *SV* waves from half space can lead to large displacement amplitudes for incident angles between 30° and 43°, but the associated rotations (rocking for *P* and *SV* waves, and torsion for *SH* waves) change monotonically and do not lead to large amplifications (Trifunac 1982, Lin et al. 2001). Scattering and diffraction of plane waves from topographic

features can lead to focusing and to amplification for both displacements and rotations (Sanchez-Sesma et al. 2002).

Beyond the results of linear theory, in the near field the non-linear response of soil and ultimately soil failure and liquefaction can lead to large transient and permanent rotations. Four types of ground failure can follow liquefaction: lateral spreading, ground oscillations, flow failure, and loss of bearing strength. **Lateral spreads** involve displacements of surface blocks of sediment facilitated by liquefaction in a subsurface layer. This type of failure may occur on slopes up to 3° and is particularly destructive to pipelines, bridge piers, and other long and shallow structures situated in flood plain areas adjacent to rivers. **Ground oscillations** occur when the slopes are too small to result in lateral spreads following liquefaction at depth. The overlying surface blocks break one from another and then oscillate on liquefied substrate. **Flow failures** are a more catastrophic form of material transport and usually occur on slopes greater than 3°. The flow consists of liquefied soil and blocks of intact material riding on and with liquefied substrate, on land or under the sea (e.g., at Seward and Valdez during the 1964 Alaska earthquake; Trifunac and Todorovska 2003). **Loss of bearing strength** can occur when the soil liquefies under a structure. The buildings can settle, tip, or float upward, if the structure is buoyant. The accompanying motions can lead to large transient and permanent rotations, which so far have been neither evaluated through simulation nor recorded by strong motion instruments.

39.3 Recording Rotational Strong Motion

Direct instrumental data on rotational components of earthquake ground motion (Farrell 1969, Shibata et al. 1976, Teisseyre et al. 2003, Takeo 1998) and of the motions in the vicinity of large explosions (Nigbor 1994) are rare. This can be attributed to two things. First, in traditional seismology recorded motions are small because of the large epicentral distances, and thus the recording of the associated rotations has received little attention. Second, relative to the design of transducers for measurement of translational motions, it is more difficult to design transducers to measure rotations (Graizer 1989). Following the development of strong motion accelerographs since the 1930s, which was influenced by experience with the design of seismological transducers, it is now becoming clear that for complete characterization of strong motion — and in particular for computation of permanent displacements following earthquakes — in the near-

field, all three translational and three rotational motions must be recorded (Trifunac and Todorovska 2001b).

Stedman et al. (1995) observed, using a ring laser gyro, torsional ground motion excited by a magnitude 6.3 earthquake in New Zealand, at an epicentral distance of 200 km. Other ring laser interferometers (gyroscopes with zero inertial moment) for recording angular motion are described in Takeo and Ito (1997), Jaroszewicz et al. (2001) and Cochard et al. (2003).

Takeo (1998) described and analyzed three translational and three rotational components of ground velocity recorded during two earthquakes offshore of Ito on Izu peninsula, Japan, in 1997. He measured rotational motions with Systron Donner triaxial gyro sensors, with a full-scale output capacity of 8.7×10^{-1} rad/s and with flat frequency response from 0 to 75 Hz.

A rotational seismograph consisting of two penduli with opposite orientations and with identical mechanical properties (Graizer 1989, Moriya and Marumo 1998) in Ojców Observatory, Poland, recorded a small Silesian earthquake event, magnitude 1.5, at an epicentral distance of about 60 km, on 11 July 2001 (Teisseyre et al. 2003). So far, nobody has succeeded in recording strong rotational motion in the near field of large earthquakes.

Average "rotational motions" can be approximated from the differences in the recordings of at least two translational records, from an array of stations on the ground (Huang 2003, Castellani and Boffi 1986, 1989, Oliveira and Bolt 1989, Nathan and MacKenzie 1975, Droste and Teisseyre 1976) and in structures (Moslem and Trifunac 1986, Trifunac and Todorovska 2001c, Trifunac and Ivanovic 2003). Such estimates can at best approximate the average rotations over the distance separating the two translational records, and in principle they will approximate the rotations at a point only for the wave-lengths that are much longer than this separation distance. This is a limitation for the studies of rotational strong motion in the ground and in the flexible foundations of structures (Trifunac et al. 1999, Trifunac and Todorovska 2001c), but the method is a suitable and desirable form of describing relative rotations in engineering analyses of the responses of buildings in terms of inter-story drifts (Trifunac and Ivanovic 2003).

39.4 Generation of Synthetic Rotational Motions

In the following it is assumed that the x_1-axis coincides with the radial coordinate, in the plane containing the earthquake source and the recording station. The x_3-axis is perpendicular to this plane and coincides with the transverse direction relative to the earthquake source. The vertical coordi-

nate, x_2, is perpendicular to the surface of the half space. Then, in elastic isotropic, layered half space, *P*, *SV*, and Rayleigh waves will produce only horizontal x_1, vertical x_2, and rocking φ_{x_3} (about the x_3 axis) motions, while *SH* and Love waves will produce only transverse x_3 and torsional φ_{x_2} (about the x_2 axis) motions.

An early engineering suggestion, that torsional ground motion occurs during strong earthquake ground motion, may have been made by Rosenblueth (1957). The first proposal on how this torsional excitation could be estimated was made by Newmark (1969), who assumed that apparent velocities of strong motion can be approximated by one equivalent velocity, *c*, for all frequencies of transverse motion. Newmark's idea was adopted and further explored in the studies of Nathan and MacKenzie (1975), Morgan et al. (1983), Awad and Humar (1984), and Rutenberg and Heidebrecht (1985). Through spectral analyses of the responses of tall buildings during the 1971 San Fernando earthquake in California, Hart et al. (1975) showed that torsional motions can indeed contribute significantly to the overall response. Their study was limited by the fact that there was only one strong motion accelerograph on the roof of each building, which prevented them from quantitatively separating out the torsional contributions to total response. With the introduction in the mid-1970s of central recording systems that employ distributed one-channel recorders throughout the buildings, this limitation was partly eliminated, so that the recordings made since the late 1970s (e.g., Kojic et al. 1984, Trifunac and Ivanovic 2003) could be used to separate the contributions to the response of translation and the torsion of structures.

Analyses showing that the rocking response of structures is caused not only by the compliance of soil during soil-structure interaction but also by the rocking of foundations caused by the passage of *P*, *SV*, and Rayleigh waves started to appear in the earthquake engineering literature in the mid-1980s (Castellani and Bofi 1986, 1989, Lee and Trifunac 1987). Many analytical studies showed the significance of those rocking excitations for continuous (e.g., Todorovska and Trifunac 1990a, b, 1991, 1992a, b) and for the base isolated structures (Todorovska and Trifunac, 1993), but during the past 20 years the studies of rocking excitation have been outnumbered by the studies of torsional excitation and response. Proper separation of the effects of rocking excitation and the rocking associated with soil-structure interaction are essential for interpretation of the observed inter-story drifts in full-scale structures. However, with the current instrumentation in tall buildings, which typically consists only of translational transducers, this separation cannot be carried out even approximately (Trifunac et al. 2001a, b, c, Trifunac and Ivanovic 2003). For buildings with large

floor plans, warping and deformation of the foundation (Trifunac et al. 1999, Hayir et al. 2001, Todorovska et al. 2001), differential translational, and rocking seismic waves further complicate both analysis and recording of the response of full-scale structures. Further work needs to be done in this area before the role of rocking excitation can be understood and then included in engineering design.

In the absence of recorded rotational components of strong motion, it is important for engineering studies of response to have at least preliminary and physically realistic simulations of such motions. At present, the method of Lee and Trifunac (1985, 1987) meets most of these requirements, and it is outlined below.

The method of Lee and Trifunac for generation of artificial torsional and rocking accelerograms is an exact analytical method if it is accepted that (1) the motion occurs in linear elastic, layered half space and (2) that synthetic ground motion can be constructed by superposition of body *P* and *SV* and surface Rayleigh waves for rocking (Lee and Trifunac 1987), and by body *SH* and surface Love waves for torsion (Lee and Trifunac 1985). This method has been extended to predict the associated strains (Lee 1990) and curvatures near the surface over time (Trifunac 1990), during passage of seismic waves.

Synthesis of translational motions is based on the procedure proposed by Trifunac (1971) and later refined by Wong and Trifunac (1979). This procedure generates random, transient time series data, with arrival times determined by the empirical travel times of *P* and *S* waves in the area and by computed arrivals of surface waves determined from phase and group velocities in the given layered structure. After random time series have been created, their amplitudes are scaled to produce correct (desired) Fourier (or response) spectrum amplitudes, based on empirical scaling laws for such spectra in terms of earthquake magnitude, distance, and local soil and geologic site conditions (e.g., Lee 2002a). At the end, the frequency-dependent duration of each random time series is modified to agree with empirical estimates of the duration of strong motion in terms of selected empirical scaling equations for duration of strong motion (e.g., Lee 2002b). Because in this process of generating translational accelerograms all characteristics of incident body and surface waves are known, those can be used for the computation of rotations, strains, and curvograms (Lee 2002c).

39.5 Response of Structures

Computation of the dynamic response of structures to earthquake shaking requires selection of the forcing functions and of the mathematical models of structures. How close the result will be to the actual response can be determined only by full scale experiments, preferably through a comparison with recorded response during earthquake shaking. In traditional earthquake engineering only one or two translational horizontal components of strong motion acceleration are used as forcing functions. Vertical accelerations are usually neglected, because the methods of solution are formulated assuming small deflections. Combined effects of vertical, rocking, and torsional accelerations cannot be neglected in the computation of response of bridge structures (e.g., Werner et al. 1979). Thus, most earthquake engineering calculations of response do not consider the effects of gravity and vertical accelerations, and by adopting these simplifying assumptions ignore the consequences of dynamic instability (Lee 1979). Because both are significant during the collapsing stage of response, it is seen that for typical selection of forcing functions, meaningful prediction of response is possible only for relatively small response amplitudes. Excitation by rotational components of strong motion (torsion and rocking) is also usually ignored. Some analytical studies do include torsional excitation (Luco 1976, Todorovska et al. 1988), but explicit consideration of rocking excitation is very rare.

An elementary representation of simple structural systems is often based on a model with a rigid foundation slab supporting a one-dimensional set of lumped masses interconnected by massless springs, and with dashpots to simulate local dissipation of vibrational energy. Such models have been used to analyze elementary consequences of soil-structure interaction and are common in many studies and applications of the Response Spectrum Method (Biot 1942, Trifunac 2002, Gupta and Trifunac 1987a, 1990a). These models have also been studied and used in some detail to evaluate the significance of the effects of torsional excitation (Gupta and Trifunac 1987b, 1989, 1990c) and of rocking excitation (Gupta and Trifunac 1988a, 1990b, 1991). By using the order statistics of the peaks in earthquake response (Gupta and Trifunac 1988b) the contribution of torsional and rocking excitation has been characterized in terms of tens of the largest peaks of response, not just the largest peak, which forms the basis for the Response Spectrum Method. These studies have shown how significant torsional and rocking excitations can be and for what combinations of structural and soil properties. It has been shown, for example, that rocking excitation becomes important for tall structures supported by soft soil de-

posits, while torsional excitations can dominate in the response of long and stiff structures supported by soft soils.

Observations of the response of buildings during earthquake shaking lead to similar findings. For a seven-story, symmetric, reinforced concrete structure, for example, which was damaged in 1971 by the San Fernando Earthquake and again in 1994 by the Northridge earthquake, torsional response contributed up to 40 percent of motion at the roof (Trifunac and Ivanovic 2003). Coupled with the non-linear response of soils and large excentricities in soil-structure interaction, torsional and rocking excitations of ground motion contributed to significant damage to this building (Trifunac et al. 2001b, c). In another well-studied building (Hollywood Storage building) in Los Angeles, asymmetry of the foundation and strong torsional excitation by surface waves propagating essentially along the longitudinal axis of the building resulted in large torsional response (Trifunac et al. 2001a).

Recording, analysis, and interpretation of the contributions of torsional and rocking excitations to the total inter-story drifts in structures are also essential for future development of earthquake-resistant design codes. Without proper consideration of these contributions, the observed drifts may be erroneously assumed to result completely from relative displacement of structures, and this can lead to false confidence that the current design methods are “conservative” (Trifunac and Ivanovic 2003).

References

Ariman T, Muleski GE (1981) A review of the response of buried pipelines under seismic excitation. Earthquake Eng Struct Dyn **9:** 133-151

Awad AM, Humar JL (1984) Dynamic response of buildings to ground rotational motion. Canadian J of Civil Eng **2**: 48-56.

Biot MA (1942) Analytical and Experimental Methods in Engineering Seismology. ASCE Transactions **108**: 365-408.

Bouchon M, Aki K (1982) Strain and rotation associated with strong ground motion in the vicinity of earthquake faults. Bull Seism Soc Am **72**: 1717-1738

Bycroft GN (1980) Soil-foundation interaction and differential ground motions. Earthquake Eng Struct Dyn **8:** 397-404

Castellani A, Boffi G, (1986) Rotational components of the surface ground motion during an earthquake. Earthquake Eng Struct Dyn **14**: 751-767

Castellani A, Boffi G (1989) On the rotational components of seismic motion. Earthquake Eng Struct Dyn **18**: 785-797

Cochard A, Flaws A, Schreiber U, Igel H (2003) Observations and simulations of rotational motions. Geophys Res Abstr **5**, 13160

Davison C (1927) The Founders of Seismology. Cambridge University Press, Cambridge 240

Droste Z, Teisseyre R (1976) Rotational and displacement components of ground motion as deduced from data of the azimuth system of seismographs. Publs Inst Geophys Pol Acad Sci **97**: 157-167

Farrell WE (1969) A gyroscopic seismometer: Measurements during the Borrego earthquake. Bull Seism Soc Am **59:** 1239-1245

Graizer VM (1989) Ob izmerenii naklona zemnoi poverkhnosti vblizi epitsentra vzriva. Dokladi Akademii Nauk SSSR, Geofizika **305:** 2, 314-318

Gupta ID, Trifunac MD (1987a) Statistical analysis of response spectra method in earthquake engineering. Dept Civil Eng, Univ Southern California, Los Angeles CA, Report 87-03

Gupta ID, Trifunac MD (1987b) A note on contribution of torsional excitation to earthquake response of simple symmetric buildings. Earthq Eng Eng Vib **7**: 3, 27-46

Gupta ID, Trifunac MD (1988a) A note on computing the contribution of rocking excitation to earthquake response of simple buildings. Bull Indian Soc Earthq Tech **25**: 2, 73-89

Gupta ID, Trifunac MD (1988b) Order statistics of peaks in earthquake response. J Eng Mech (ASCE) **114**: 10, 1605-1627

Gupta VK, Trifunac MD (1989) Investigation of building response to translational and rotational earthquake excitations. Dept Civil Eng Univ Southern California, Los Angeles CA, Report 89-02

Gupta ID, Trifunac MD (1990a) Probabilistic spectrum superposition for response analysis including the effects of soil-structure interaction. J Probabilistic Eng Mech **5**: 9-18

Gupta VK, Trifunac MD (1990b) Response of multistoried buildings to ground translation and rocking during earthquakes. J Probabilistic Eng Mech **5**: 138-145

Gupta VK, Trifunac MD (1990c) Response of multistoried buildings to ground translation and torsion during earthquakes. European Earthq Eng **IV,** 1, 34-42

Gupta VK, Trifunac MD (1991) Effects of ground rocking on dynamic response of multistoried buildings during earthquakes. Struct Eng/Earthq Eng (JSCE) **8:** 2, 43-50

Gutenberg B (1927) Grundlagen der Erdbebenkunde. Univ Frankfurt a/M 189

Hart GC, DiJulio M, Lew M (1975) Torsional response of high-rise buildings. J Struct Div-ASCE. **101:** 397-414

Haskell NA (1969) Elastic displacements in the near field of a propagating fault. Bull Seism Soc Am **59**: 865-908

Hayir A, Todorovska MI, Trifunac MD (2001) Antiplane response of a dyke with flexible soil-structure interface to incident SH-waves. Soil Dyn Earthq Eng **21:** 7, 603-613

Hobbs WH (1907) Earthquakes. An Introduction to Seismic Geology. Appleton and Co., New York pp 336

Huang BS (2003) Ground rotational motions of the 1999 Chi-Chi, Taiwan earthquake as inferred from dense array observations. Geophys Res Letters **30:** 6, Art. No. 1307, 40-1, 40-4.

Imamura A (1937) Theoretical and applied seismology. Maruzen Co., Tokyo 358

Jaroszewicz LR, Krajewski Z, Swillo R (2001) Application of fiber-optic Sagnac interferometer for detection of rotational seismic events. Mol Quantum Acoust **22:** 133-144

Jordanovski LR, Todorovska MI (2002) Inverse studies of the earthquake source mechanism from near-field strong motion records. Indian Soc Earthq Technol J **39:** 1-2, 73-91

Kojic S, MD Trifunac, Anderson JC (1984) A post earthquake response analysis of the imperial county services building. Dept Civil Eng Univ Southern California, Los Angeles CA, Report CE 84-02

Lee VW (1979) Investigation of three-dimensional soil-structure interaction. Dept Civil Eng Univ Southern California, Los Angeles CA, Report 79-11

Lee VW (1990) Surface strains associated with strong earthquake shaking. Proc Japan Soc Civil Eng **422n:** 1-14, 187-194

Lee VW (2002a) Empirical scaling of strong earthquake ground motion-part I: Attenuation and scaling of response spectrum. Indian Soc Earthq Technol J **39:** 4, 219-254

Lee VW (2002b) Empirical scaling of strong earthquake ground motion - part II: Duration of strong motion. Indian Soc Earthq Technol J **39:** 4, 255-272

Lee VW (2002c) Empirical scaling of strong earthquake ground motion - part III: Synthetic strong motion. Indian Soc Earthqe Technol J **39:** 4, 273-310

Lee VW, Trifunac MD (1985) Torsional accelerograms. Int J Soil Dynam & Earthq Eng **4**: 3, 132-139

Lee VW, Trifunac MD (1987) Rocking strong earthquake accelerations. Int J Soil Dynam & Earthq Eng **6:** 2, 75-89

Lin CH, Lee VW, Trifunac MD (2001) Effects of boundary drainage on the reflection of elastic waves in a poroelastic half space saturated with non-viscous fluid. Dept Civil Eng Univ Southern California, Los Angeles CA, Report No. CE 01-04

Luco JE (1976) Torsional response of structures to obliquely incident seismic SH waves. Earthquake Eng Struc **4**, 207-219

Morgan JR, Hall WJ, Newmark NM (1983) Seismic response arising from traveling waves. J Struct Div-ASCE **109:** 4, 1010-1027

Moriya T, Marumo R (1998) Design for rotation seismometers and their calibration. Geophys Bull Hokkaido Univ **61**: 99-106

Moslem K, Trifunac MD (1986) Effects of soil-structure interaction on the response of buildings during strong earthquake ground motion. Dept Civil Eng Univ Southern California, Los Angeles CA, Report No. CE 86-04

Nathan ND, MacKenzie JR (1975) Rotational components of earthquake motion. Can J Civil Eng **2:** 430-436

Newmark NM (1969) Torsion in symmetrical buildings. Proc Fourth World Conference on Earthquake Eng **II**, A3/19 - A3/32

Nigbor RL (1994) Six-degree-of-freedom ground-motion measurement. Bull Seism Soc Am **84**: 1665-1669
Oliveira CS, Bolt BA (1989) Rotational components of surface strong ground motion. Earthquake Eng Struct **18**: 517-526
Richter CF (1958) Elementary seismology. Freeman and Co., San Francisco CA
Rosenblueth E (1957) Comments on torsion. Procs Convention Struct Eng Assoc Southern California 36-38
Rutenberg A, Heidebrecht AC (1985) Rotational ground motion and seismic codes. Can J Civil Eng **12**: 3, 583-592
Sanchez-Sesma FJ, Palencia VJ, Luzon F (2002) Estimation of local site effects during earthquakes: An overview. Indian Soc Earthq Technol J **39**: 3, 167-194
Scanlan RH (1976) Seismic wave effects on soil-structure interaction. Earthquake Eng Struct **4**: 379-388
Shibata H, Shigeta T, Sone A (1976) A note on some results of observation of torsional ground motions and their response analysis. Bull Earthquake Resistant Struct Research Center **10**: 43-47
Stedman GE, Li Z, Bilger HR (1995) Sideband analysis and seismic detection in a large ring laser. App Optics **34**: 5375-5385
Takeo M (1998) Ground rotational motions recorded in near-source region. Geophys Res Lett **25**: 6, 789-792
Takeo M, Ito HM (1997) What can be learned from rotational motions excited by earthquakes? Geophys J Int **129:** 319-329
Teisseyre R (2002) Continuum with defect and self rotation fields. Acta Geophys Pol **50**: 51-68
Teisseyre R, Boratyński W (2002) Continuum with self-rotational nuclei: Evolution of defect fields and equations of motion. Acta Geophys Pol **50**: 223-230
Teisseyre R, Majewski E (2002) Physics of earthquakes. In: Lee WHM et al. (eds) International Handbook of Earthquake and Engineering Seismology, part A. Academic Press, Amsterdam, pp 229-235
Teisseyre R, Suchcicki J, Teisseyre K, Wiszniowski J, Palangio P (2003) Seismic rotation waves: Basic elements of theory and recording. Ann Geophys **46**: 4, 671-685
Todorovska MI, Trifunac MD (1990a) Analytical model for in plane incident building foundation soil interaction: Incident P, SV, and Rayleigh waves, Dept Civil Eng Univ Southern California, Los Angeles CA, Report 90-01
Todorovska MI, Trifunac MD (1990b) A note on the propagation of earthquake waves in buildings with soft first floor. J Eng Mech-ASCE **116**: 4, 892-900
Todorovska MI, Trifunac MD (1992a) The system damping, the system frequency and the system response peak amplitudes during in-plane building-soil interaction. Earthquake Eng Struct **21**: 2, 127-144
Todorovska MI, Trifunac MD (1992b) Effect of the base input base rocking on the relative response of long buildings on embedded foundations. Europ Earthq Eng **VI**: 1, 36-46
Todorovska MI, Trifunac MD (1993) The effects of wave passage on the response of base-isolated buildings on rigid embedded foundations. Dept Civil Eng Univ Southern California, Los Angeles CA, Report CE 93-10

Todorovska MI, Trifunac MD, Lee VW (1988) Investigation of earthquake response of long buildings. Dept Civil Eng Univ Southern California, Los Angeles CA, Report No. CE 88-02

Todorovska MI, Hayir A, Trifunac MD (2001) Antiplane response of a dike on flexible embedded foundation to incident SH-waves. Soil Dyn Earthq Eng **21**: 7, 593-601

Trifunac MD (1971) A method for synthesizing realistic strong ground motion. Bull Seism Soc Am **61**: 1755-1770

Trifunac MD (1974) A three-dimensional dislocation model for the San Fernando, California earthquake of February 9, 1971. Bull Seism Soc Am **64**: 149-172

Trifunac MD (1982) A note on rotational components of earthquake motions for incident body waves. Soil Dyn Earthq Eng **1**: 1, 11-19

Trifunac MD (1990) Curvograms of strong ground motion. J Eng Mech-ASCE **116**: 6, 1426-1432

Trifunac MD (1997) Differential earthquake motion of building foundations. J Struct Eng-ASCE **4**, 414-422

Trifunac MD (2002) 70th anniversary of Biot spectrum. Indian Soc Earthq Technol J **40**: 1, 19-50

Trifunac MD (2003) Non-linear soil response as a natural passive isolation mechanism, Paper II – the 1933 Long Beach, California earthquake. Soil Dyn Earthq Eng **23**: 7, 549-562

Trifunac MD, Ivanovic SS (2003) Analysis of drifts in a seven-story reinforced concrete structure. Dept Civil Eng Univ Southern California, Los Angeles CA, Report No. CE 03-01

Trifunac MD, Todorovska MI (1997a) Response spectra and differential motion of columns. Earthquake Eng Struct **26**: 2, 251-268

Trifunac MD, Todorovska MI (1997b) Northridge, California, earthquake of 17 January 1994: Density of pipe breaks and surface strains. Soil Dyn Earthq Eng **16:** 3, 193-207

Trifunac MD, Todorovska MI (1998) Non-linear soil response as a natural passive isolation mechanism – the 1994 Northridge, California Earthquake. Soil Dyn Earthq Eng **17**: 1, 41-51

Trifunac MD, Todorovska MI (1999) Reduction of structural damage by nonlinear soil response. J Struct Eng-ASCE **125**: 89-97

Trifunac MD, Todorovska MI (2001a) Evolution of accelerographs, data processing, strong motion arrays and amplitude and spatial resolution in recording strong earthquake motion. Soil Dyn Earthq Eng **21:** 6, 537-555

Trifunac MD, Todorovska MI (2001b) A note on useable dynamic range in accelerographs recording translation. Soil Dyn Earthq Eng **21**: 4, 275-286

Trifunac MD, Todorovska MI (2001c) Recording and interpreting earthquake response of full scale structures. In: Erdik M et al. (eds.) Proc NATO Advanced Research Workshop on Strong Motion Instrumentation for Civil Eng Structures, Istanbul, Turkey, June 2-5 1999, Kluwer Acad Publ, Dordrecht, pp 131-155

Trifunac MD, Todorovska MI (2003) Tsunami source parameters of submarine earthquakes and slides. In: Locat J and Mienert J (ed.) Proc First Intern Symp

on Submarine mass movements and their consequences, EGS-AGU-EUG Joint Meeting, Nice, France, April 7-11, Kluwer Academic Publ, Dordrecht, pp 121-128

Trifunac MD, Udwadia FE (1974) Parkfield, California earthquake of June 27, 1966: A three-dimensional moving dislocation. Bull Seism Soc Am **64:** 511-533

Trifunac MD, Todorovska MI, Ivanovic SS (1996) Peak velocities, and peak surface strains during Northridge, California earthquake of 17 January 1994. Soil Dyn Earthq Eng **15:** 5, 301-310

Trifunac MD, Ivanovic SS, Todorovska MI, Novikova EI, Gladkov A(1999) Experimental evidence for flexibility of a building foundation supported by concrete friction piles. Soil Dyn Earthq Eng **18:** 3, 169-187

Trifunac MD, Hao TY, Todorovska MI (2001a) Response of a 14 story reinforced concrete structure to excitation by nine earthquakes: 61 years of observation in the Hollywood storage building, Dept Civil Eng Univ Southern California, Los Angeles CA, Report CE 01-02

Trifunac MD, Ivanovic SS, Todorovska MI (2001b) Apparent periods of a building, Part I: Fourier analysis. J Struct Eng-ASCE **127**: 5, 517-526

Trifunac MD, Ivanovic SS, Todorovska MI (2001c) Apparent periods of a building, part II: Time-frequency analysis. J Struct Eng-ASCE **127**: 5, 527-537

Werner SD, Lee LC, Wong HL, Trifunac MD (1979) Structural response to traveling seismic waves, J of Struct Div-ASCE **105**, ST12, 2547-2564

Wong HL, Trifunac MD (1979) Generation of artificial strong motion accelerograms. Int J Earthq Eng Struct Dynamics **7**: 509-527